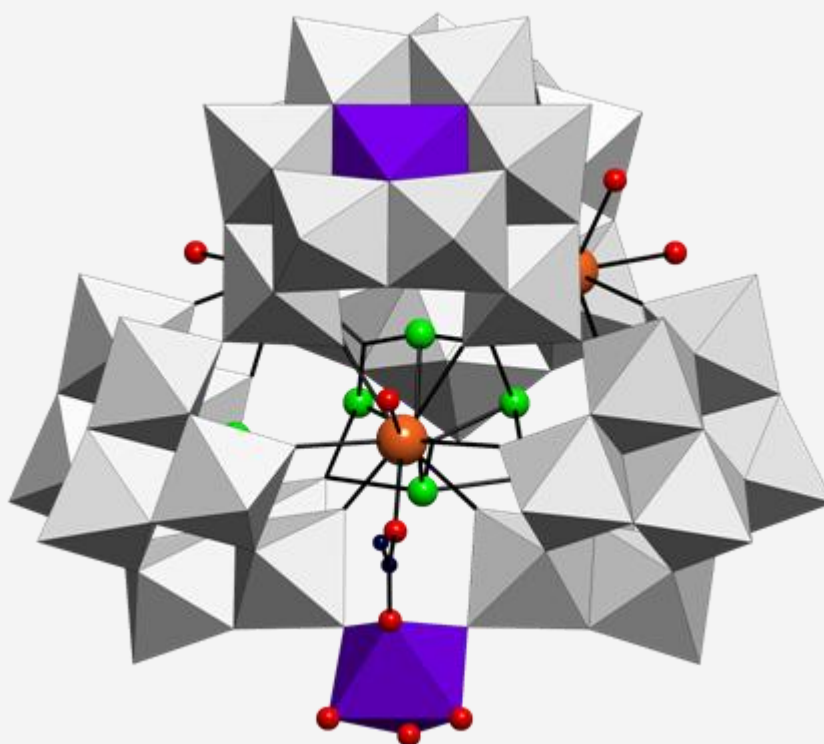


Systematic Studies on 3d- and 4f-Metal Containing Polyoxometalates Suitable for Organic Derivatization



BEÑAT ARTETXE ARRETXE

Ph.D. thesis

June 2014



ZTF-FCT

Zientzia eta Teknologia Fakultatea
Facultad de Ciencia y Tecnología

Kimika Ezorganikoa Salla
Departamento de Química Inorgánica

eman la zabal zazu



Universidad
del País Vasco

Euskal Herriko
Unibertsitatea

Systematic Studies on 3d- and 4f-Metal Containing Polyoxometalates Suitable for Organic Derivatization

Memoria presentada por

Beñat Artetxe Arretxe

para optar al grado de

Doctor por la Universidad del País Vasco / Euskal Herriko Unibertsitatea

Leioa, Junio 2014

ACKNOWLEDGEMENTS

I would like to use these lines to express my deepest gratitude to all of you.

En primer lugar quisiera transmitir mi más profundo agradecimiento a mis directores, los Dres. Juan M. Gutiérrez-Zorrilla López y Santiago Reinoso Crespo, Catedrático e Investigador Contratado del Departamento de Química Inorgánica de la Facultad de Ciencia y Tecnología de la Universidad del País Vasco UPV/EHU, respectivamente. Al primero por todo la confianza depositada en mi, su continua aportación de ideas, por invitarme a su grupo cuando todavía era un joven estudiante de apenas 20 años, y sobre todo, haber conseguido transmitirme toda esa pasión que siente por el conocimiento en general, y la ciencia en particular. Al segundo por todo su apoyo, conocimiento, paciencia, rigurosidad y capacidad para guiarme. Gracias a ambos por haber hecho de todo esto una realidad.

A la Dra. Leire San Felices y Pablo Vitoria, por toda la ayuda proporcionada durante estos años. Su experiencia, trabajo diario y apoyo han sido indispensables para, no solo la realización de este trabajo, sino también mi formación como investigador.

I wish to express my gratitude to Prof. Tianbo Liu for providing me the opportunity to work in his research group at the University of Akron, Akron, OH, USA for three months. I would like to thank Dr. Liu and Fadi Haso for all their support, friendliness and for introducing me in the field of light scattering.

Al Dr. José Angel García, Catedrático del Departamento de Física Aplicada II de la UPV/EHU por abrirme las puertas de su laboratorio de fotoluminiscencia, así como por su trato e implicación.

Quiero agradecer el trabajo de todas aquellas personas que han realizado las medidas aquí presentadas, y especialmente, a los técnicos de los servicios Generales de Investigación de la UPV/EHU (SGIker). Dra. Leire San Felices y Pablo Vitoria por las medidas de difracción de rayos X en monocristal. Dres. Aitor Larrañaga y Fco. Javier Sangüesa por las medidas de rayos-X en muestra policristalina. Dres. Sonia García de Madinabeitia y Luis Bartolomé por medidas de ICP-MS y análisis elemental CHN, respectivamente. Dr. Iñaki Orue por las medidas de susceptibilidad magnética. Dra. Isabel Collado por las medidas de $^1\text{H-NMR}$. Por otra parte, querría también agradecer al Dr. Luis Lezama, Catedrático del Departamento de Química Inorgánica de la UPV/EHU, por todo lo relacionado con el magnetismo y las medidas de EPR, así como su apoyo y disposición a la discusión científica. Al Dr. Cristian Vicent (Universitat Jaume I, Castellón) por las medidas de ESI-MS, así como por su disponibilidad para aclarar todas las dudas que me surgieron alrededor de una técnica que me era extraña. A los Dres. Maite Insausti y Santiago Reinoso por las medidas de termogravimetría. A la Dra. Izaskun Gil de Muro por las micrografías de TEM Finally, I would also like to thank Prof. Ulrich Kortz and Ali Haider (Jacobs University, Bremen, Germany) for the $^{183}\text{W-NMR}$ spectrum.

Al Dr. Diego M. Guérin de la Unidad de Biofísica CSIC-UPV/EHU y Dr. José Luis Vilas del Departamento de Química Física de la UPV/EHU por permitirme realizar medidas preliminares de DLS en sus laboratorios.

Al Dr. Pascual Román, director de departamento y en general, a todo el Departamento de Química Inorgánica de la Facultad de Ciencia y Tecnología de la UPV/EHU.

Eusko Jaurlaritzako Hezkuntza, Hizkuntza Politika eta Kultura Sailari (garai hartan Hezkuntza, Unibertitate eta Ikerketa Saila) doktoretza-aurreko bekagatik.

A D. Teo del Servicio de Reprografía por toda su ayuda y a D. Justo San Felices por los derechos de imagen de la contraportada.

Bereziki aipatu nahiko nituzke urte luze guzti hauetan zehar lankide izan ditudan Aroa, Amaia eta Jagoba. Beraien laguntzagatik, laborategian pasatako une on eta txarreatatik, egindako bidaiengatik...; eskerrik asko bihotz-bihotzez! Ezin ahaz ditzaket, era berean, taldekide diren edo izan diren, Eder, Ainhoa, Sergio eta Saioa.

Sin esfuerzo no hay recompensa y sin estos compañeros de departamento no hubiese habido tesis. *Mundua konpontzen* eta gure etorkizuna zuzentzen pasatako momentu on guztiengatik, hartutako kafeengatik eta zuen aholku guztiengatik: Aipatu ditudan Aroa, Amaia eta Jagoba, baina baita Ricardo, Javi C., Sonia, Xabi, Vero, Paula, Javi S., Mónica, Iturrondo, Dorle, Idoia, Paulita, Dani, Jintxa, Aritza eta Maider. Eskerrik asko!

Kimikaren munduan (eta bertatik kanpo) elkarrekin emandako lehen pasuengatik nire lagun Eder eta Imanoli agur bero bat.

I would like to thank Fadi, Ali, Roy, YY, Baofang, Jing, Panchao, Pushkar and Alankar, for those three *awesome* months in Akron and for making me feel at home.

Ezin ahaztu hainbeste urtetan zehar nire ondoan egon diren *Pastoreak*. Aritz, Cami, Dei, Garp, Iban, Igor, Iker, Haitz, Iñigo, Josu, Kere, Larre, Pitter, Ruben, Talorro, eta Xabier. Aupa zuek!

Azkenik gogoan beti ditudan, eta izango ditudan, familiari, baina bereziki, ama, aita, aitite eta amamari, beraiek gabe sekula ezin izango nintzatekeelako naizena izan. Eskerrik asko Maite danagatik, *por ocuparte de que el día a día siguiera su curso para que yo pudiera dedicar a este trabajo todo ese tiempo que debería haber empleado en vosotros*. Zuengatik eta zuentzako delako egiten dudana guztia.

ESKERRIK ASKO nire inguruan zaudeten guztioi

Beñat Artetxe Arretxe

Aititeri

Dedicated to the memory of my grandfather

Jaime Arretxe Soriano (1930–2013)

RESUMEN

Los polioxometalatos (POMs) son clústeres aniónicos formados por metal y oxígeno que constituyen una clase de compuestos única, tanto por su complejidad estructural, como por su versatilidad topológica, electrónica y reactiva, lo que hace que hayan encontrado importantes aplicaciones en campos tan diversos como la catálisis, magnetismo, medicina o ciencia de materiales. Los POMs exhiben una gran diversidad estructural (Figura I) que abarca desde especies pequeñas y sencillas como los aniones dimetalato hasta grandes y complejos clústeres del tamaño de una proteína. Desde un punto de vista estructural, pueden describirse como compuestos de condensación de unidades MO_x poliédricas mediante compartición de vértices y/o aristas. Los números de coordinación de los centros generalmente oscilan entre 4 y 7, siendo la octaédrica la geometría de coordinación más frecuente. Los elementos metálicos que pueden actuar como centros M se limitan a aquellos que poseen una combinación favorable de radio iónico y carga, así como orbitales d vacantes y accesibles para la formación de enlaces π M-O. Por tanto, quedan restringidos a metales de transición en estados de oxidación elevados, fundamentalmente V(V), Mo(VI), y W(VI).

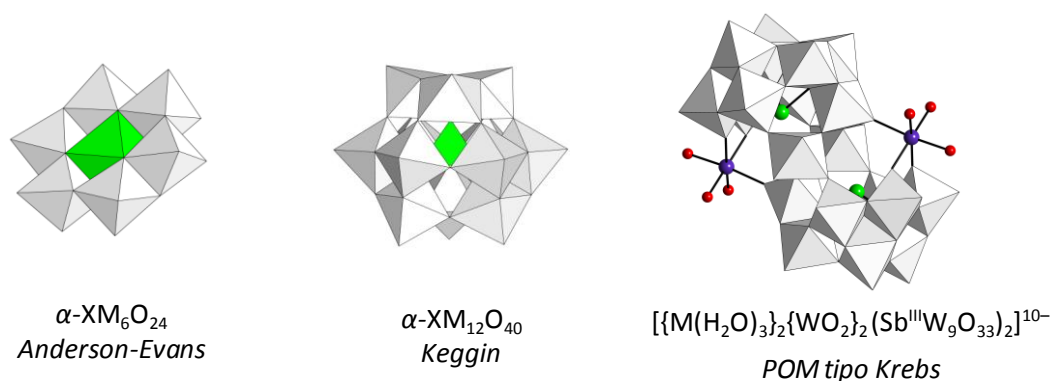


Figura I. Estructuras de algunos de los tipos de POMs más representativos.

La funcionalización de POMs con grupos orgánicos constituye uno de los campos más activos y prometedores dentro de la química de polioxometalatos debido a que los híbridos resultantes han sido identificados como factores clave para la incorporación de este tipo de clústeres en diversos materiales (polímeros, nanotubos de carbono), e incluso para su interacción con superficies o nanopartículas metálicas. Esta estrategia puede dar lugar a la formación de nuevos materiales multifuncionales. Con el fin de obtener POMs híbridos, se han seguido diversas rutas sintéticas entre las que destacan las siguientes: i) empleo de grupos organosililo, -germilo, -fosforilo o -estannilo con polioxowolframatos lacunarios; ii) sustitución de los oxígenos superficiales por ligandos N- u O-dadores; iii) coordinación de complejos metalorgánicos a los oxígenos superficiales del clúster; iv) coordinación de ligandos orgánicos a POMs que contienen centros metálicos 3d o 4f accesibles.

Basándose en esta última aproximación, el objetivo de este trabajo es comprobar la viabilidad de la funcionalización orgánica de clústeres conocidos con centros metálicos accesibles por medio de química de coordinación clásica, así como preparar nuevos POMs que contengan metales 3d o 4f que sean susceptibles a una potencial derivación orgánica. Los 39 nuevos compuestos que se describen en este estudio muestran características interesantes que van desde sus propiedades luminiscentes a la capacidad de auto-ensamblarse en disolución para dar estructuras de tipo *blackberry*. El trabajo se ha dividido en dos partes bien diferenciadas: en el Capítulo 2 se aborda el estudio sistemático de la

funcionalización orgánica de POMs tipo-Krebs disustituidos con metales de transición frente a ligandos N,O-quelantes y diversos ligandos puente. Por otro lado, los capítulos 3 y 4 tratan sobre la síntesis de nuevos polianiones con metales del bloque f (Capítulo 3), entre los que se incluyen estructuras gigantes que contienen más de 100 átomos de wolframio por fórmula unidad, o clústeres heterometálicos que contienen metales 3d y 4f como parte del propio esqueleto inorgánico (Capítulo 4).

En el **Capítulo 2**, se presenta el estudio de la funcionalización orgánica de POMs tipo-Krebs disustituidos con metales de transición, $[\{M(H_2O)_3\}_2\{WO_2\}_2(Sb^{III}W_9O_{33})_2]^{10-}$ (donde $M^{II} = Mn, Co, Ni, Zn$) frente a ligandos aniónicos N,O-quelantes o ligandos puente. Debido a que este tipo de clústeres cuenta con dos centros M en posiciones externas cuyas esferas de coordinación presentan tres moléculas de agua terminales, se ha evaluado su reactividad frente a diferentes tipos de ligandos orgánicos con objeto de determinar i) si los clústeres son susceptibles de ser funcionalizados mediante química de coordinación clásica, y ii) qué tipo de ligando es el más adecuado. Para ello, se han escogido ligandos aromáticos planos con capacidad quelante (minimización de impedimentos estéricos), y más concretamente, derivados carboxilato de heterociclos N-dadores de 5 y 6 miembros: diazolcarboxilatos como 1H-imidazol-4-carboxilato (imc) o 1H-pirazol-3-carboxilato (pzc); piridincarboxilatos como el picolinato (pic); y diazincarboxilatos como piridazin-3-carboxilato (pydc), pirimidin-4-carboxilato (pymc) o pirazin-2-carboxilato (pyzc). Además, también han sido estudiados diferentes ligandos puente como la 4,4'-bipiridina (4,4'-bpy), piracin-2,3-dicarboxilato (2,3-pyzdc) y piracin-2,5-dicarboxilato (2,5-pyzdc).

La reacción entre polioxometalatos (preformados o sintetizados *in situ*) y ligandos orgánicos se ha llevado a cabo en medio tamponado de NaOAc bajo condiciones normales de laboratorio. Se ha determinado el éxito o fracaso de la funcionalización orgánica del POM mediante espectroscopia infrarroja (FT-IR) a todo producto sólido (cristalino o no) obtenido de las reacciones anteriores. Esta técnica resulta ideal para este cometido puesto que i) las bandas características de los clústeres inorgánicos y los ligandos orgánicos aparecen en regiones bien diferenciadas del espectro, y ii) la huella dactilar del POM experimenta variaciones significativas tras su funcionalización.

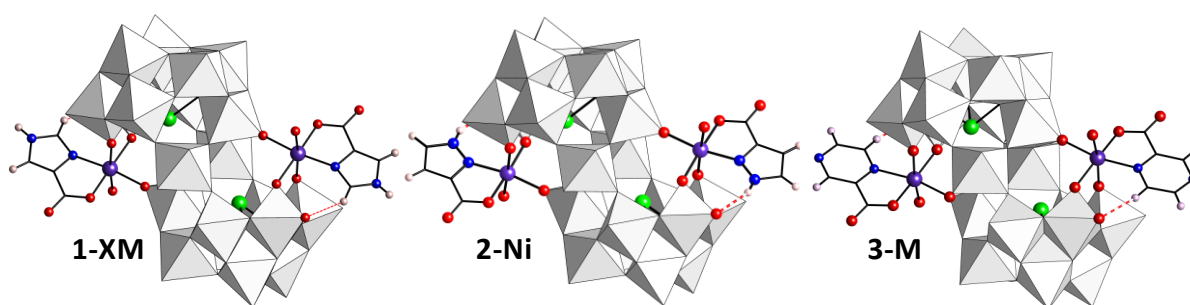


Figura II. Estructura molecular de los polioxometalatos híbridos **1-XM**, **2-Ni** y **3-M** (enlaces de hidrógeno intramoleculares representados como líneas rojas discontinuas).

Los resultados obtenidos del empleo de los ligandos N,O-quelantes muestran que la funcionalización de este tipo de POMs es extremadamente dependiente de la naturaleza exacta del ligando. El anión pic es inerte frente a los POM tipo Krebs, mientras que los ligandos diazincarboxilato pydc y pymc cuando reaccionan con el clúster, lo hacen para promover su descomposición parcial y generar el complejo monomérico $[ML_2(H_2O)_2]$ neutro correspondiente. Por su parte, el ligando diazincarboxilato restante (pyzc) no da lugar a complejos, sino que se muestra

selectivo hacia la funcionalización de los polioxometalatos de Co y Zn. Los ligandos diazolcarboxilato muestran reactividades completamente diferentes con sólo variar la posición relativa de los dos átomos de nitrógeno del ciclo. Así, el ligando pzc se muestra selectivo hacia la funcionalización del clúster de Ni, mientras que su reactividad hacia el resto de polioxometalatos o bien es nula (Mn, Zn), o bien implica descomposición y consiguiente formación de complejo neutro. Por el contrario, el ligando diazolcarboxilato imc se ha revelado como el “ligando universal” puesto que es capaz de coordinarse a cualquiera de los polioxometalatos tipo Krebs estudiados independientemente del metal de transición presente o del método sintético empleado. Más aún, se han llevado a cabo reacciones sustituyendo Sb^{III} por Te^{IV} para evaluar la influencia de un cambio en la carga del heteroátomo sobre la reactividad final y se ha constatado que la formación de las correspondientes especies híbridas también tiene lugar.

Por consiguiente, de los citados estudios sistemáticos, se han obtenido un total de 9 fases cristalinas puras de POM-híbridos caracterizadas mediante análisis elemental (CHN y metales), termogravimetría y difracción de rayos X sobre monocristal (XRD). Los compuestos de fórmula general $[\{\text{ML}(\text{H}_2\text{O})_2(\text{WO}_2)_2(\text{B}-\beta\text{-XW}_9\text{O}_{33})_2\}]^n$ pueden clasificarse como: **1-SbM**, donde L = imc, X = Sb, n = 12 y M = Mn, Co, Ni, Zn; **1-TeM**, donde L = imc, X = Te, n = 10 y M = Mn, Co; **2-Ni**, donde L = pzc, X = Sb, n = 12 y M = Ni; **3-M**, donde L = pyzc, X = Sb, n = 12 y M = Co, Zn. De acuerdo con estudios de XRD, los ligandos empleados (pyzc, pzc, imc) se incorporan a las posiciones M externas sustituyendo las mismas dos moléculas de agua de coordinación, de tal modo que los anillos aromáticos adoptan una orientación prácticamente idéntica respecto al esqueleto wolframio-oxígeno que facilita la formación de un puente de hidrógeno intramolecular de tipo C–H...O o N–H...O en función del ligando orgánico empleado (Figura II). Además, la estabilidad en disolución acuosa de este tipo de POM-híbrido se ha confirmado por medio de medidas de resonancia magnética nuclear de protón (^1H -RMN) sobre los derivados diamagnéticos.

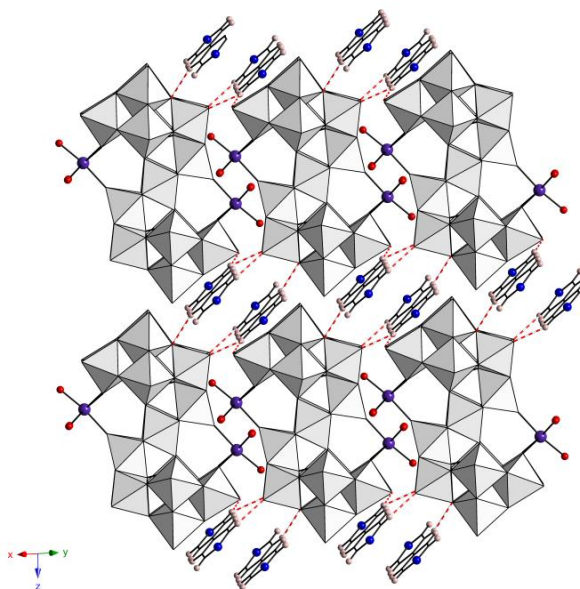


Figura III. Vista de la estructura cristalina de los compuestos **4-M** a través de la dirección [110].

En el caso de los ligandos puente empleados en nuestros estudios de reactividad, también se han encontrado comportamientos diferentes. El ligando N-bis(monodentado) 4,4'-bpy se ha mostrado inerte frente a los polioxometalatos tipo Krebs, de tal modo que se ha obtenido una familia de compuestos de fórmula $\text{Na}_{10}[\{\text{M}(\text{H}_2\text{O})_3\}_2(\text{WO}_2)_2(\text{SbW}_9\text{O}_{33})_2] \cdot 2(4,4'\text{-bpy}) \cdot 32\text{H}_2\text{O}$ (**4-M**, M = Mn, Co,

Ni, Zn) en los que, de acuerdo con la determinación estructural a partir de medidas XRD, las moléculas 4,4'-bpy ocupan espacios intersticiales entre los clústeres tipo Krebs “desnudos” (Figura III). Respecto a los ligandos puente N,O-quelantes pirazindicarboxilato 2,3-pyzdc y 2,5-pyzdc, cabe destacar que mientras el segundo es inerte, el primero muestra una reactividad singular hacia los polioxometalatos tipo Krebs. El ligando 2,3-pyzdc se ha mostrado selectivo únicamente hacia el clúster de Ni. El ataque del ligando promueve una reorganización completa en el esqueleto wolframio-oxígeno, dando lugar al polianión híbrido $[\mu\text{-}\{2,3\text{-pyzdc}\}_2\{\text{Ni}_2(\text{H}_2\text{O})\text{Sb}_2\text{W}_{20}\text{O}_{70}\}_2]^{24-}$ (**5-Ni**). Esta especie dimérica, en la que dos ligandos puente 2,3-pyzdc unen dos subunidades polioxometalato $\{\text{Ni}_2(\text{H}_2\text{O})\text{Sb}_2\text{W}_{20}\text{O}_{70}\}$, presenta átomos de sodio lábiles incorporados en la estructura del clúster, lo que podría permitir utilizar este POM como un macroligando híbrido en reacciones de intercambio iónico de sodio por otros centros metálicos (Figura IV). La subunidad $\{\text{Ni}_2(\text{H}_2\text{O})\text{Sb}_2\text{W}_{20}\text{O}_{70}\}$ es absolutamente novedosa dentro de la química de polioxometalatos, y las uniones entre los diferentes fragmentos wolframio-oxígeno que la forman no tienen precedente. El estudio del comportamiento en disolución de **5-Ni** mediante espectrometría de masas de ionización por electrospray (ESI-MS) muestra que la entidad dimérica se descompone para dar los monómeros correspondientes en disolución acuosa. Asimismo, sus propiedades magnéticas pueden ser descritas por medio del desdoblamiento a campo nulo de los centro de Ni^{II}.

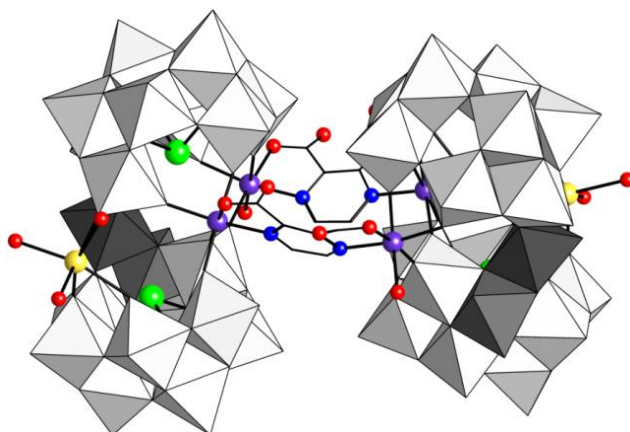


Figura IV. Estructura molecular del compuesto híbrido dimérico **5-Ni** (átomos de sodio en amarillo; grupo $\{\text{W}_2\text{O}_{10}\}$ incorporado en la subunidad trilacunaria en gris oscuro).

Como se muestra en el **Capítulo 3**, la reacción entre iones lantánido(III), níquel(II), GeO_2 y Na_2WO_4 en una disolución tamponada de acetato sódico, da lugar un amplio abanico de isómeros $[\text{Ln}_2(\text{GeW}_{10}\text{O}_{38})]^{6-}$ consistentes en fragmentos dilacunarios de tipo-Keggin estabilizados por la coordinación de metales 4f a las posiciones vacantes. Este tipo de clústeres muestra una gran habilidad de sufrir procesos de auto-ensamblaje dirigidos por cationes alcalinos. Los lantánidos más ligeros (de Ce a Sm) dan lugar a arquitecturas hexaméricas $[\text{Na}\{\text{Ln}_2(\text{H}_2\text{O})_4(\beta\text{-GeW}_{10}\text{O}_{38})\}_6]^{35-}$ (**6-Ln**, Ln = Pr, Nd) de tipo corona en presencia de Na^+ exclusivamente, mientras que la adición de K^+ da como resultado un ensamblaje similar para Sm $[\text{K}\{\text{Sm}_2(\text{H}_2\text{O})_4(\beta\text{-GeW}_{10}\text{O}_{38})\}_6]^{35-}$ (**7-Sm**) y estructuras dodecaméricas gigantes $[\text{K}\{\text{K}_7\text{Ln}_{24}\text{Ge}_{12}\text{W}_{120}\text{O}_{444}(\text{OH})_{12}(\text{H}_2\text{O})_{56}\}]^{52-}$ para Ce, Pr y Nd (**8-Ln**). Éstas últimas están formadas por núcleos hexaméricos $\text{K}\{\text{Ln}_2(\text{H}_2\text{O})_4(\beta\text{-GeW}_{10}\text{O}_{38})\}_6$ a los que se unen seis subunidades $\{\gamma\text{-GeW}_{10}\text{O}_{38}\}$ mediante las esferas de coordinación de los lantánidos. A partir de la misma reacción, se han obtenido otros dos tipos de arquitecturas para los lantánidos más pesados (de Gd a Lu) en ausencia de Ni^{2+} : entidades diméricas $[\text{Ln}_4(\text{H}_2\text{O})_6(\beta\text{-GeW}_{10}\text{O}_{38})_2]^{12-}$ (**9-Ln**, Ln = Tb to Lu)

en presencia de Na^+ y tetraméricas $[\{\text{Ln}_4(\text{H}_2\text{O})_5(\text{GeW}_{10}\text{O}_{38})_2\}]^{24-}$ (**10-Ln**, Ln = Ho to Lu) tras la adición de Cs^+ (Figura V). Cabe destacar que dos tipos de tetrámeros **10-Ln** coexisten en estado sólido, la forma $\alpha\beta$ y $\beta\beta$.

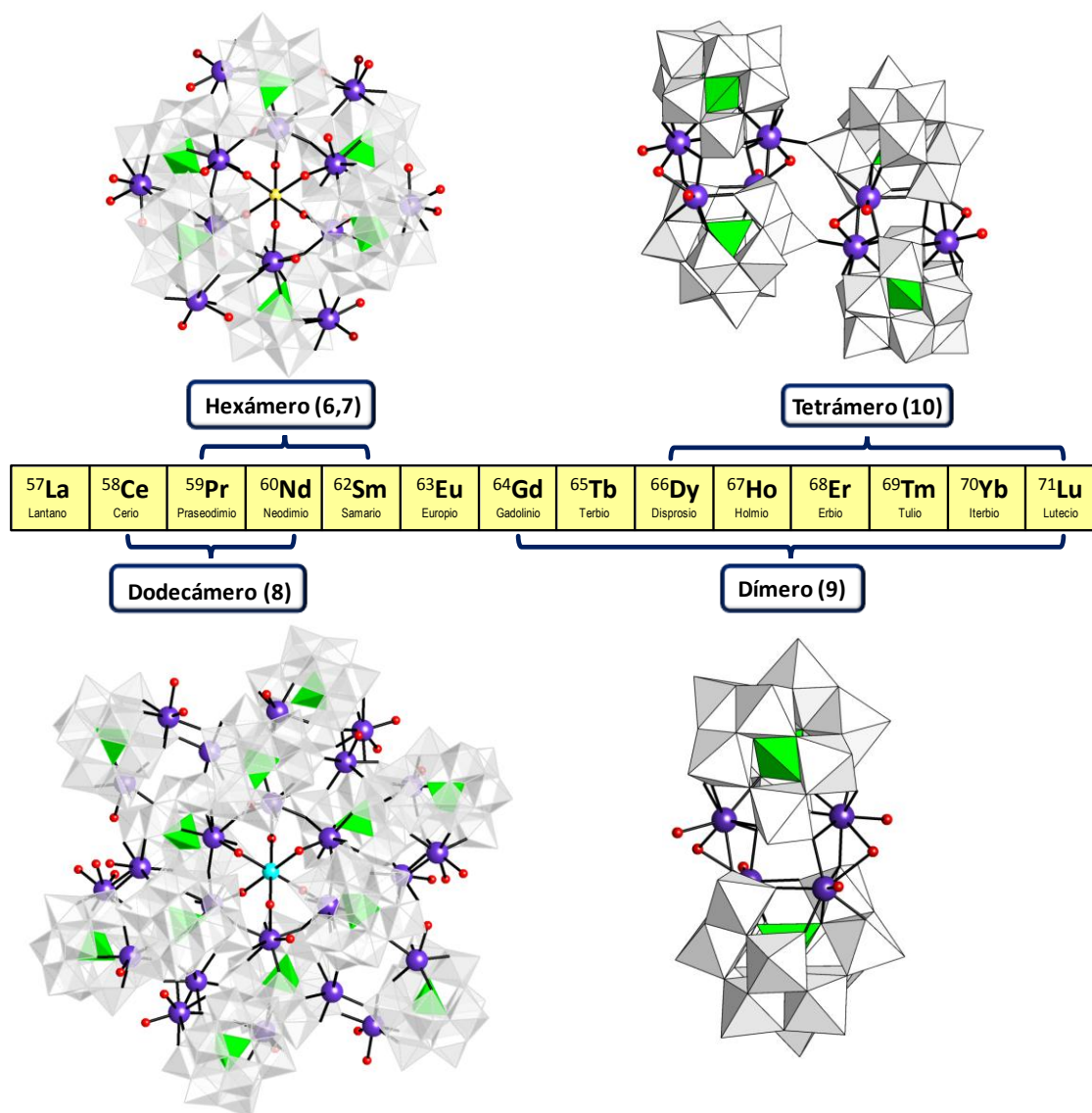


Figura V. Representación esquemática de los compuestos obtenidos en el Capítulo 3.

Todos los compuestos obtenidos en este capítulo, se han caracterizado mediante análisis elemental y térmico, FT-IR y XRD. En relación a las diversas características de cada uno de los compuestos, se han estudiado las propiedades luminiscentes de **7-Sm**, **9-Tb** y **9-Dy**, las propiedades magnéticas de la serie **9-Ln** y el comportamiento en disolución de la familia **8-Ln** (Ln = Ce, Pr, Nd) y la especie **9-Ho**. Los resultados obtenidos en medidas de conductividad y experimentos de ESI-MS indican que los aniones dodecaméricos **8-Ln** se disocian en disolución acuosa dando lugar a monómeros y hexámeros. En disoluciones diluidas, estas especies hexaméricas se auto-ensamblan en agregados vesiculares esféricos, huecos y monocapa denominados estructuras tipo *blackberry*. La formación de las *blackberry* se monitorizó mediante técnicas de dispersión de luz dinámica (DLS) y estática (SLS). La naturaleza esférica y hueca de los agregados se confirmó tanto mediante los valores obtenidos en estudios de DLS y SLS, como de imágenes de microscopía electrónica de transmisión

(TEM). El empleo de acetona como co-disolvente hace que las especies **8-Ln** se mantengan estables en disolución como se observa por ESI-MS y den lugar a su vez a estructuras de tipo *blackberry*. El tamaño de estas estructuras en mezclas de agua-acetona aumenta con el contenido de acetona, o lo que es lo mismo, con la inversa de la constante dipolar del medio. En referencia a los aniones obtenidos con los lantánidos más pequeños, la combinación de estudios de ESI-MS y ^{183}W -NMR indica que los tetrámeros **10-Ln** se fragmentan en dímeros de tipo **9-Ln** en disolución acuosa. Estos últimos sufren una disociación parcial, estableciéndose un equilibrio monómero/dímero, que es seguido por una isomerización $\beta \rightarrow \alpha$, tal como se confirma por medio de las fases $\alpha\alpha$ -**9-Ln** aisladas en estado sólido.

Por último, tal y como se muestra en el **Capítulo 4**, la combinación de POMs tipo-Krebs disustituidos con metales de transición ($M = \text{Co}, \text{Ni}$ y Zn) con tierras raras (de La^{3+} a Gd^{3+}) en un medio tamponado de acetato sódico da lugar a la formación de la familia de clústeres heterometálicos 3d-4f $[\text{Sb}_7\text{W}_{36}\text{O}_{130}(\text{OH})_3\text{Ln}_3\text{M}_2(\text{OAc})(\text{H}_2\text{O})_8]^{14-}$ (**11-LnM**, $\text{Ln} =$ de La a Gd , $M = \text{Co}$; $\text{Ln} = \text{Ce}$, $M = \text{Ni}, \text{Zn}$). Los compuestos **11-LnM** (Figura VI), que se obtienen a partir de la descomposición y posterior reorganización del precursor tipo Krebs, han sido caracterizados mediante análisis elemental, termogravimetría y espectroscopía FT-IR. Estructuralmente, esta familia de clústeres puede describirse como ensamblajes tetraméricos de tres subunidades trilacunarias $\{\text{SbW}_9\text{O}_{33}\}$ de tipo Keggin unidas mediante dos metales 4f y un dímero $\{\text{LnM}(\text{OAc})\}$, más un fragmento $\{\text{M}^{\text{II}}\text{W}_6\text{O}_{24}\}$ tipo Anderson-Evans que se conecta a las subunidades trilacunarias por medio de tres centros *cis*- $\{\text{WO}_2\}$ adicionales para “cerrar” la estructura inorgánica. A su vez, el clúster encapsula una unidad $\{\text{Sb}_4\text{O}_4\}$ en su interior, que confiere quiralidad al anión **11-LnM** mediante su disposición en dirección horaria o anti-horaria. El anión **11-CeCo** es estable en disolución acuosa, tal y como se observa en las medidas de ESI-MS, y da lugar a estructuras tipo *blackberry* en disoluciones diluidas como indican los estudios de DLS, SLS y TEM. Finalmente, se ha constatado que los resultados obtenidos por medio de la espectroscopia paramagnética electrónica están en buen acuerdo con la disposición que adoptan los polianiones en el empaquetamiento cristalino.

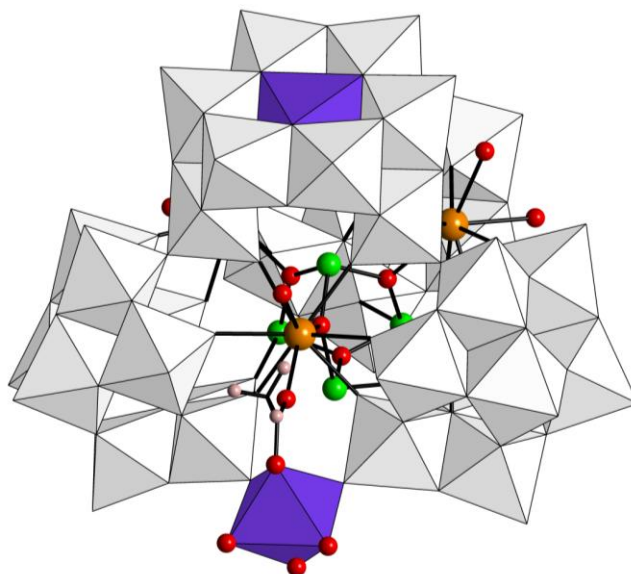


Figura VI. Representación de la estructura molecular del clúster aniónico **11-LnM**.

Table of Contents

1. GENERAL INTRODUCTION	1
1.1. Polyoxometalates	2
1.2. The Keggin Anion	5
1.3. Organic Functionalization of POMs	7
1.3.1. <i>p</i> -block organoderivatives	7
1.3.2. Substitution of surface oxygen atoms	10
1.3.3. Grafting of the transition metal complexes at POM surface	12
1.3.4. Organic functionalization of 3d- or 4f-metal substituted POMs	13
1.4. Summary and Aim of the Work	15
1.5. References	19
2. STRAIGHTFORWARD ORGANIC FUNCTIONALIZATION OF KREBS-TYPE POLYOXOMETALATES	26
2.1. Introduction	27
2.2. Experimental Section	30
2.2.1. Synthesis	30
2.2.2. X-ray crystallography	35
2.3. Results and Discussion	38
2.3.1. Reactions of Krebs-type POMs with organic N,O-chelating ligands	38
2.3.2. Reactions of Krebs-type POMs with organic bridging ligands	54
2.4. Conclusions	64
2.5. References	65
3. STRUCTURAL DIVERSITY IN LANTHANIDE-CONTAINING TUNGSTOGERMANATE ASSEMBLIES	68
3.1. Introduction	69
3.1.1. Lanthanide containing isopolyoxotungstates	69
3.1.2. Lanthanide containing heteropolyoxotungstates	70
3.1.3. Organically derivatized lanthanide containing POMs	72
3.1.4. Properties and applications	73
3.1.5. Giant POMs	74
3.1.6. Aim of the work	77
3.2. General Synthetic Aspects	79
3.3. POM assemblies containing early lanthanides	80
3.3.1. Experimental Section	80
3.3.2. Results and discussion	83
3.4. POM assemblies containing mid-to-late lanthanides	105
3.4.1. Experimental Section	105
3.4.2. Results and discussion	109
3.5. Conclusions	127
3.6. References	129

4. HETEROMETALLIC 3d-4f POLYOXOMETALATES DERIVED FROM THE 3d-METAL DISUBSTITUTED KREBS-TYPE FRAMEWORK	134
4.1. Introduction	135
4.2. Experimental Section	139
4.2.1. Synthesis	139
4.2.2. X-ray crystallography	142
4.3. Results and Discussion	143
4.3.1. Synthesis	143
4.3.2. Molecular structure of 11-LnM	146
4.3.3. Crystal packing of 11-LnM	155
4.3.4. Solution behavior of 11-CeCo	156
4.3.5. ESR spectroscopy studies on 11-CeCo and 11-GdCo	157
4.4. Conclusions	160
4.5. References	160
5. FINAL REMARKS AND FUTURE PERSPECTIVES	163
5.1. Final Remarks	164
5.2. Future Perspectives	166

APPENDICES

A1. Synthesis and characterization of transition metal complexes with N,O-chelating ligands	168
A2. Materials and methods	179
A3. Nomenclature of dilacunary units	204
A4. Lanthanide-oxygen bond lengths of compounds included in Chapter 3	207

General Introduction

- 1.1. Polyoxometalates
- 1.2. The Keggin anion
- 1.3. Organic functionalization of polyoxometalates
- 1.4. Summary and aim of the work
- 1.5. References

ABSTRACT: Polyoxometalates (POMs) are a well-known family of anionic metal-oxygen clusters with large compositional, structural and electronic versatility. These features make POMs unique compounds with a wide range of potential applications in fields like catalysis, magnetism, materials science or biomedicine. In this chapter a brief overview of the POM chemistry is given with strong focus on the Keggin-type anion which constitutes one of the most studied polyanions. Derivatization of POMs with additional organic functions represents one of the current hot topics in the field. The resulting hybrid derivatives have been identified as a key factor for the clusters to be suitably incorporated into materials like polymers or carbon nanotubes, and also to interact with diverse surfaces or metallic nanoparticles. The most usual methods for the organic functionalization of POMs are discussed, including the use of *p*-block organoderivatives, substitution of the shell-oxygen atoms, the grafting of transition-metal complexes and replacement of labile water molecules on 3d-/4f-metal substituted POMs with exposed metal centers. The chapter is completed with a short description of the aim of this work, which is based on the last synthetic approach mentioned above.

1.1. POLYOXOMETALATES

Polyoxometalates (POMs) are a well-known family of anionic metal-oxygen clusters with a large compositional, structural and electronic variety.¹ These features make POMs unique compounds with a wide range of potential applications in fields like catalysis², magnetism³, materials science⁴ or biomedicine.⁵ It is commonly thought that J. J. Berzelius was the first to synthesize a polyoxometalate back in 1826 (the ammonium salt of the $[\text{PMo}_{12}\text{O}_{40}]^{3-}$ anion).⁶ However the Elhuyar brothers had already prepared a POM almost 40 years before (1783), describing it as a bitter, spicy, yellow salt containing tungsten.⁷ It is worth mentioning in this context that the Elhuyar brothers were the discoverers of the element W, which they named *wolfram*. There was not any structural evidence of a POM cluster until 1933, when J. F. Keggin determined the crystal structure of the $\text{H}_3[\text{PMo}_{12}\text{O}_{40}]$ acid by using powder X-ray diffraction.⁸ Based on M. T. Pope's seminal work^{1,9} in the 80's, POM chemistry has expanded very quickly in the last two decades as can be exemplified by the large number of books¹⁰ and special thematic issues in some of the most prestigious journals within the inorganic chemistry,¹¹ as well as by the growing number of published works or reviews in the last 20 years. Therefore, POM chemistry can be considered as one of the most dynamic fields of the inorganic chemistry at present.

The preparation of this kind of anions goes from simple one-pot procedures to highly sophisticated flow-system approaches or integrated 3D-printed reactionwares.¹² This has resulted in a huge variety of structures comprising from small and simple M_2O_7 dimetalate anions to complex clusters showing sizes comparable to those of proteins (Figure 1.1).

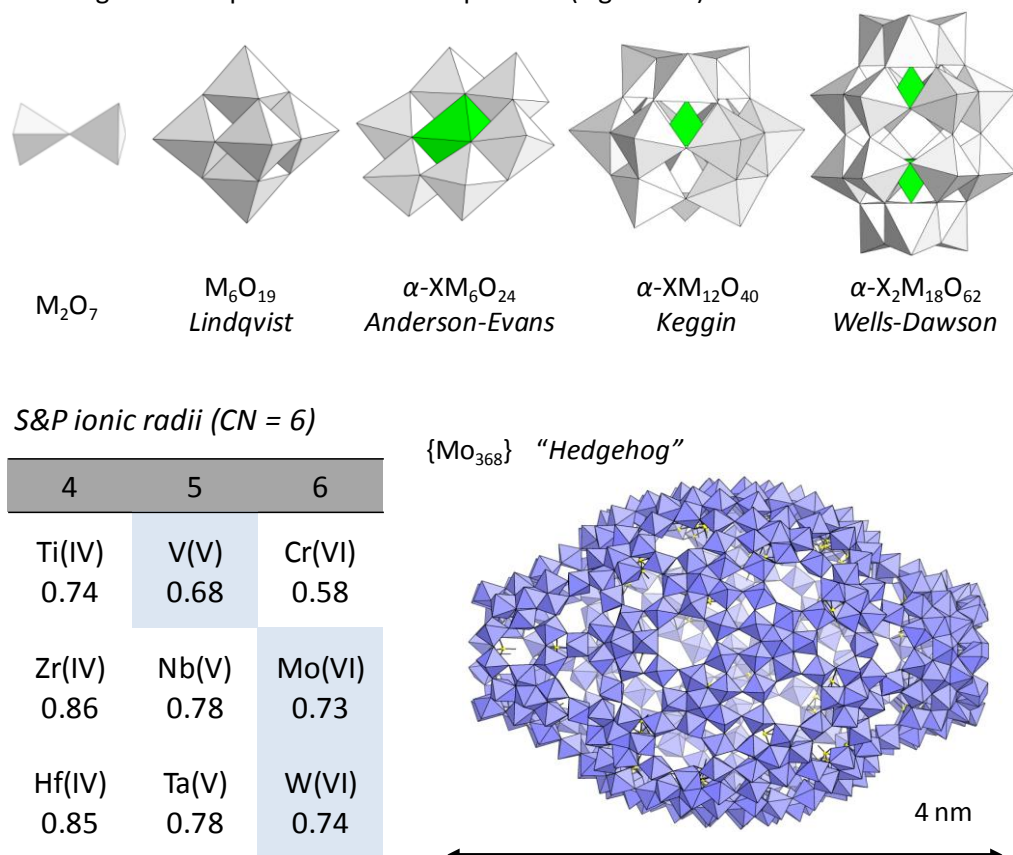
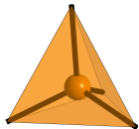
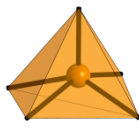
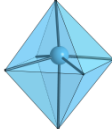
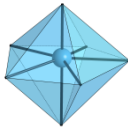


Figure 1.1. Structural diversity in POMs. Inset: Shannon & Prewitt ionic radii for transition metals of groups 4- 6 in coordination number six. The most usual metals found in POMs are highlighted in pale blue. Color code: $\{\text{MO}_x\}$, pale grey; $\{\text{XO}_n\}$, green; $\{\text{MO}_x\}$ in Mo-Blue, blue.

POMs are composed of early transition metals (M, so-called *addenda* metals) from groups 5 and 6, usually in their highest oxidation states. Traditionally, Mo, W or V, but Nb or Ta can also act as *addenda* metals.¹³ These metals show a suitable combination of charge and ionic radius as well as empty and accessible *d* orbitals available for electronic back-donation in the formation of π M–O bonds. Recently, some examples of noble metal POMs have been reported including polyoxopalladates, -platينات and -aurates.¹⁴ Among the unconventional POMs, the family of actinyl clusters has also grown very quickly during the last decade.¹⁵

Structurally, classical POMs are formed by the condensation of polyhedral MO_x units, where the coordination numbers of the metallic centers are between 4 and 7 and the octahedral is the most common geometry (Table 1.1.). The $\{\text{MO}_x\}$ units can condense sharing vertices or edges (exceptionally faces), in such a way that a maximum of two oxygen atoms per octahedron can be left unshared (Lipscomb's principle),¹⁶ which minimizes the strong *trans*-effect of the terminal M–O bonds and avoids the dissociation of the cluster. The *addenda* metals Mo^{VI} and W^{VI} can also occupy a seven-coordinate $\{\text{O}=\text{M}(\text{O}_6)\}$ polyhedron in POMs, and this has led to the development of several macrosized giant-POMs, including i.e. the ring-like $\{\text{Mo}_{154}\}$,¹⁷ hollow icosahedral “Keplerates” $\{\text{Mo}_{60}\text{W}_{72}\}$,¹⁸ or the “blue hedgehog” $\{\text{Mo}_{368}\}$.¹⁹ All polyhedral units show a certain degree of distortion due to the *d* orbitals taking part in the M–O bond. Each metal center located in a MO_x environment is displaced towards the terminal oxygen atoms as a result of the π M–O bonding, in such a way that two types of polarization can be distinguished: toward a single terminal oxygen atom (*class I*) or toward two terminal oxygen atoms located in relative *cis* configuration (*class II*). This results in polyanions with very different electronic properties. The LUMO orbitals of the *class I* clusters are non-bonding and therefore, these POMs are more easily and reversibly reduced by chemical, photochemical or electrochemical methods. Certain POM structures are reducible to mixed-valence “blue” or “brown” species with retention of the POM skeleton. On the contrary, reduction of *class II* clusters is more difficult and shows irreversible nature.²⁰

Table 1.1. Usual coordination polyhedra of metal centers in POMs.

Coordination number	4	5	6	7
	Tetrahedron	Square pyramid	Octahedron	Pentagonal bipyramid
Polyhedron				
Found in	Metavanadates	Polyvanadates	Most POMs	Keplerates, Mo-Blues

Despite the wide variety of structures, most POMs exhibit some features in common:⁹

- (i) Usually, they show high charge, size and symmetry, as well as thermal and solution stability.
- (ii) The formation equilibria of POMs are highly dependent on the concentration of the reactants, pH, ionic strength, presence of extra ligands, counterions employed, temperature or pressure (hydrothermal synthesis, microwave assisted reactions). It is highly usual that different POM species coexist in solution at a given pH value.
- (iii) Species containing alkaline counterions are usually water soluble, whereas organic counterions confer high solubility in organic solvents on the polyanions.

(iv) POMs can be used as inorganic ligands due to their ability to coordinate cations, anions or neutral molecules with the oxygen atoms located at the surface.

Depending on their composition, POMs can be classified into two main groups:

A) Isopolyoxometalates (iso-POMs), of general formula $[M_mO_y]^{q-}$, are exclusively constituted by early transition metals and oxygen. The structures of most iso-POMs are derived from the $M_{10}O_{28}$ decametallate anion *via* elimination of octahedral units. The parent POM cluster is formed by ten edge-sharing MO_6 octahedra arranged in D_{2d} symmetry.²¹ Examples of most common iso-POMs include the β - M_8O_{26} octametallate, M_7O_{24} heptametallate (parametallate-A) and the M_6O_{19} hexametallate (Lindqvist-type structure) anions.²² Furthermore, some other iso-POMs whose structures are not directly derived from the $M_{10}O_{18}$ cluster include the $H_2W_{12}O_{42}$ isopolyanion, (paratungstate-B) which is formed from the rearrangement of the $W_7O_{24}^{6-}$ heptatungstate cluster in solution.²³ Meta- and polyvanadates are also worth to be mentioned in this context.²⁴

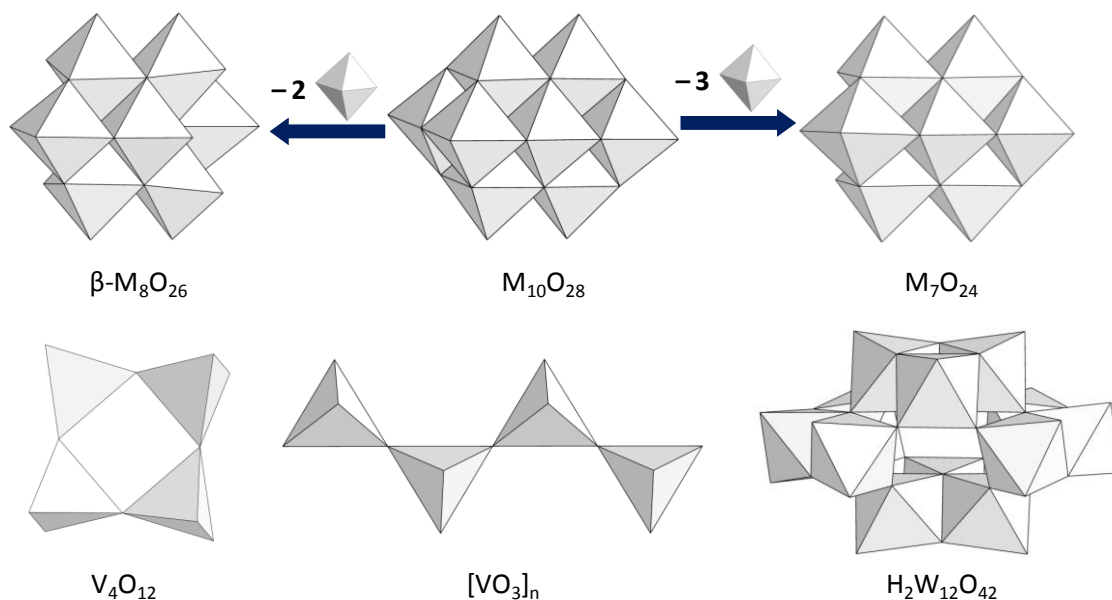


Figure 1.2. Polyhedral representation of the structures of some iso-POMs.

B) Heteropolyoxometalates (hetero-POMs), of general formula $[X_xM_mO_y]^{q-}$, contain not only metal and oxygen, but also additional elements known as heteroatoms (X). The nature of X does not show any specific restriction as many of the elements of the periodic table with the exception of noble gases are known to be able to act as heteroatoms. Examples of well-known heteropolytungstates include the $[XM_6O_{24}]^{n-}$ Anderson-Evans anion, which contains an octahedral heteroatom ($X =$ first row transition metals, Al^{III} , Ga^{III} , Rh^{III} , Pt^{IV} , Sb^V , Te^VI , I^{VII});²⁵ the Keggin anion $[XW_{12}O_{40}]^{n-}$, which contains a tetrahedral heterogroup (usually $X = B^{III}$, Si^{IV} , Ge^{IV} , P^V , As^V);⁸ and the Wells-Dawson anion $[X_2W_{18}O_{62}]^{n-}$ derived from the Keggin structure and showing two tetrahedral heteroatoms ($X =$ typically from the group 15).²⁶

In a typical stepwise formation of polyoxotungstates (the most studied POMs due to their higher stability in solution), the transformation of the tetrahedral tungstate oxoanions $[WO_4]^{2-}$ to octahedral $\{WO_6\}$ units at acidic pH is followed by the condensation of cited units involving the release of water molecules. Considering the common linkage modes between $\{MO_6\}$ octahedra,

corner sharing offers flexibility, while edge sharing confers certain degree of rigidity on the cluster formed (Figure 1.3). This oligomerization is not infinite; due to the polarization of the peripheral tungsten centers toward the outer oxygen shell, vacant and accessible d orbitals of the metal allow for the formation of terminal W=O double bonds, preventing the subsequent formation of bridges with additional octahedra.

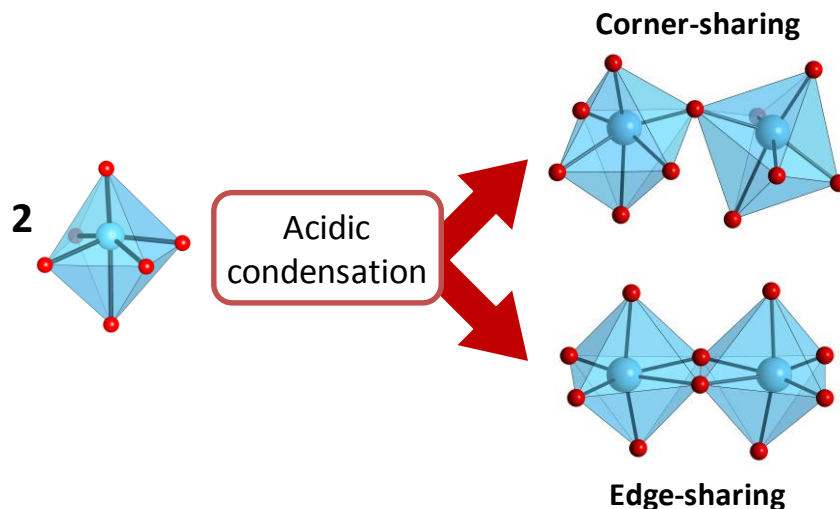


Figure 1.3. Schematic representation of the two common linkage modes between octahedral $[WO_6]$ units: corner-sharing (top right) and edge-sharing (bottom right).

1.2. THE KEGGIN ANION

Acidic condensation of WO_6 units in the presence of tetrahedral $[XO_4]^{n-}$ oxoanions usually results in $\{\alpha-XM_{12}O_{40}\}$ Keggin-type structures. The Keggin anion is constituted by four $\{M_3O_{13}\}$ trimers formed by three edge-sharing WO_6 octahedra. These trimers are linked to each other and to the central tetrahedron through corner-sharing in an ideal T_d symmetry (Figure 1.4).

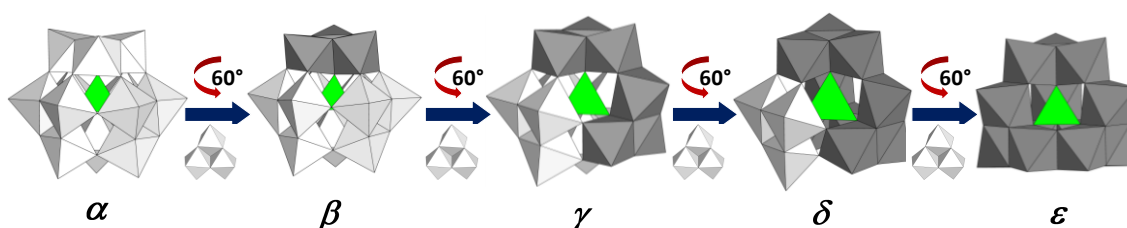


Figure 1.4. Baker-Figgis isomers of the Keggin-type $\{XM_{12}O_{40}\}$ structure. Rotated trimers in dark grey.

Keggin-type heteropolyanions have five structural isomers, known as Baker-Figgis isomers. These isomers result from the 60° rotation of one (β), two (γ), three (δ) or four (ϵ) M_3O_{13} trimers from the parent α -Keggin anion. The α and β isomers are the most stable from the five, because they do not show any edge-sharing linkages between different M_3O_{13} trimers. The α , β and γ isomers of Keggin-type tungstosilicates can be readily synthesized and have been successfully characterized both in solution and in the solid state.²⁷ On the contrary, the less stable δ -Keggin-type structure has only been observed for the $[AlO_4Al_{12}(OH)_{24}(H_2O)_{12}]^{7+}$ cationic cluster,²⁸ whereas the lanthanide stabilized phosphomolybdates $[\epsilon-PMo_{12}O_{36}(OH)_4\{Ln(H_2O)_4\}_4]^{4+}$ ($Ln = La$ to Sm)²⁹ and the aluminium $[MO_4Al_{12}(OH)_{24}(H_2O)_{12}]^{n+}$ ($M = Al, Ga, Ge$) polyoxocations,²⁸ represent the only structurally characterized examples of the ϵ -isomer isolated as independent cluster.

Some POM structures are derived from larger parent cluster by removing one or more addenda metal atoms from the shell, resulting in defect structures known as *lacunary species*. Lacunary polyanions can act as multidentate ligands toward different electrophiles (like 3d- and 4f-metals) through the oxygen atoms delimiting the vacant sites. Incorporation of electrophiles in these sites to regenerate the parent cluster results in *substituted species*.³⁰ Nine lacunary species can be obtained by removing one or more octahedra from the parent plenary $\text{XM}_{12}\text{O}_{40}$ Keggin anion. From the α -isomer mono- ($\text{XM}_{11}\text{O}_{39}$) and trivacant species (XM_9O_{34}) can be generated upon elimination of one or three octahedra respectively. The α - XM_9O_{34} anions show two different isomers named as *A- α* , or *B- α* depending on whether the WO_6 octahedra eliminated belong to $\{\text{M}_3\text{O}_{13}\}$ edge-sharing trimer or to a $\{\text{M}_3\text{O}_{15}\}$ corner-sharing triad, respectively. Similar species can be isolated for the β -isomer. However, the lower symmetry of the β - $\{\text{XM}_{12}\text{O}_{40}\}$ allows for three different monolacunary species to be formed depending on the position of the vacant site. The vacant position in the β_1 -monolacunary species is located in the triad opposite to the 60° rotated trimer, whereas for the β_2 and the β_3 forms it lies at the central belt and the rotated trimer, respectively. Up to now, only the dilacunary $\text{XM}_{10}\text{O}_{36}$ species has been isolated from the γ isomer. The chemical equilibria of Keggin-type tungstosilicates in water solution are summarized in Figure 1.5 to illustrate the complexity of the interconversion pathways between plenary and lacunary POMs. All the ten species represented can be prepared and isolated as alkaline salts from mixtures of silicate and tungstate sources as a function of the pH, by following the procedures reported by Téze & Hervé.²⁷

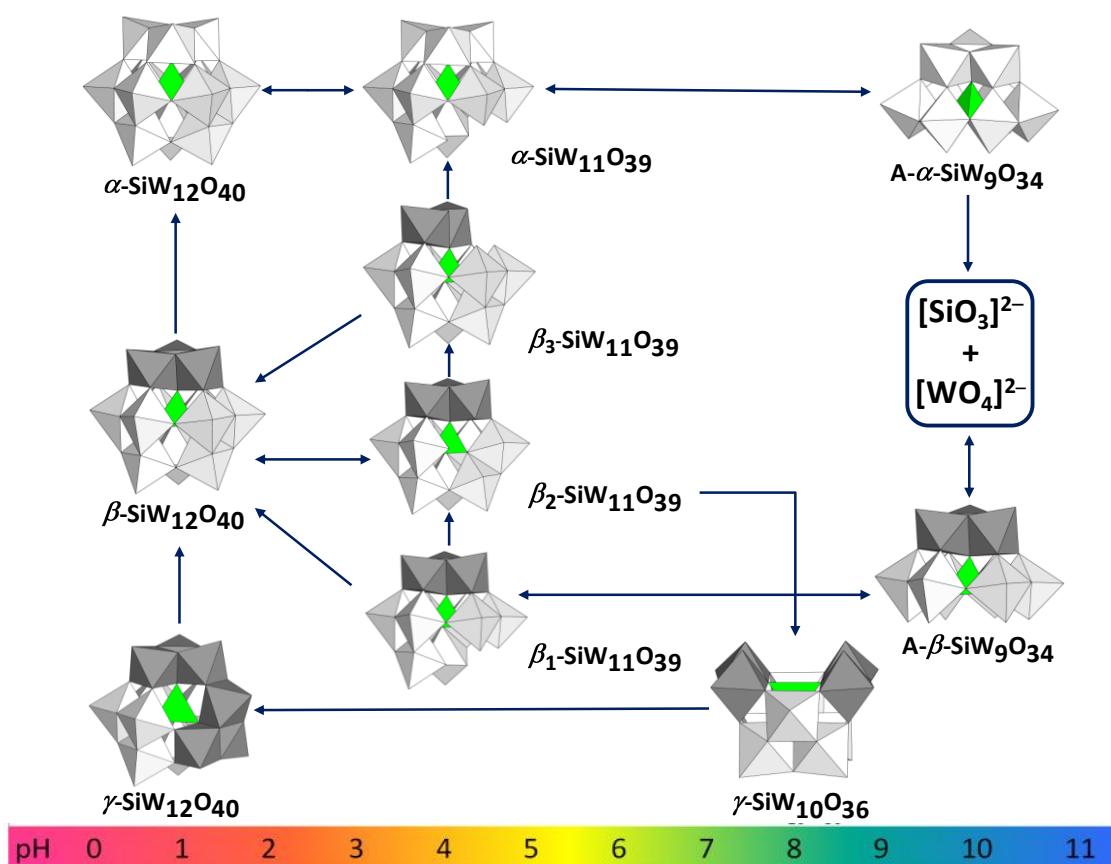


Figure 1.5. Scheme of the chemical equilibria between different plenary and lacunary Keggin-type tungstosilicates.

For some specific heteroatoms like As^{III}, Sb^{III}, Te^{IV} or Se^{IV}, the presence of a lone pair of electrons precludes the full closure of the Keggin shell, so that only *B*-XW₉O₃₃ trivacant species can be formed.³¹ In some other cases, lacunary species can undergo further condensation reactions, leading to new types of heteroPOMs. For example, the X₂M₁₈O₆₂ Wells-Dawson cluster is formed by two *A*- α -XM₉O₃₄ (X = group 15 heteroatoms) trilacunary units sharing corners through the belt WO₆ octahedra (Figure 1.1). Several isomers and lacunary species derived from the Wells-Dawson structure are also known.^{9, 27, 32}

1.3. ORGANIC FUNCTIONALIZATION OF POMs

Derivatization of POMs with additional organic functions represents one of the current hot topics in the field. The resulting hybrids have been identified as a key factor for POM clusters to be suitably incorporated into materials like polymers or carbon nanotubes, and also to interact with diverse surfaces (silica, silicon, gold, alumina, graphite) or metallic nanoparticles *via* covalent interactions.³³ This strategy might pave the way for new multifunctional devices (e.g. immobilized catalysts, photoactive systems for energy conversion, sensors), but it usually requires elaborate organic functions that can be only achieved via multistep synthetic work on the so-called preformed hybrid POM platforms.³⁴ Hybrid POMs with attached organometallic catalysts (e.g. metallo-salen, Wilkinson-type or Pd-NHC moieties) have been described as more active and/or selective than their related organometallic complex precursors.³⁵ Furthermore, the presence of POM facilitates the removal of the catalyst by precipitation with organic solvents or nanofiltration processes.³⁶ There is also a great interest in combining POMs and photosensitizers for the design of new luminescent systems, photocatalysts or materials for photovoltaic cells.³⁷

Two different classes of POM-based organic-inorganic hybrid compounds have emerged during the last decades, in which this specific field of the POM chemistry has undergone remarkable development. The first class gathers all the systems where only electrostatic interactions, hydrogen bonds, or van der Waals interactions are established between organic and inorganic components. In the second class, the organic and inorganic moieties are linked via strong covalent bonds. For example, some organic ligands can substitute oxo groups of the POM surface and get directly linked to the addenda metal center. The nucleophilic character of the oxygen atoms located on the surface of the POM clusters can also lead to covalent interactions with electrophilic moieties bearing organic antenna groups. In this way, different approaches have been applied to prepare well-defined, solution-stable hybrid POMs in a precursor scale.

1.3.1. p-block organoderivatives

One of the most extensively explored routes consists in combining lacunary polyoxotungstates with p-block organoderivatives such as organosilyl, -germyl, -phosphoryl, -stannyl or -stibyl moieties (Figure 1.6). The nucleophilic character of the oxygen atoms delimiting the lacunae is significantly increased compared to those of the plenary anion, and this greatly favors the reaction with electrophilic groups. In order to incorporate custom-designed organic moieties to the clusters, two strategies are usually followed. The first strategy consists in preparing the desired p-block organoderivative, followed by its reaction with lacunary POMs. In the second strategy, the p-block organoderivative with a reactive pendant group is first inserted in the vacant site of the cluster and the resulting POM is then used as a platform for further postfunctionalization.

For the non-metallic Si, Ge and P-derivatives, two main approaches have been used for the synthesis of hybrid POM species. In the first synthetic approach, the lacunary POM is phase transferred in a suitable organic solvent (acetonitrile, DMF) and then reacted with the corresponding p-block organotrichloro derivative. The second approach is exclusive for organosilyl groups and consists in the direct reaction of the lacunary heteroPOM and an organotrialkoxosilane in a mixture of solvents like CH₃CN/H₂O or CH₃OH/H₂O in the presence of an acid.

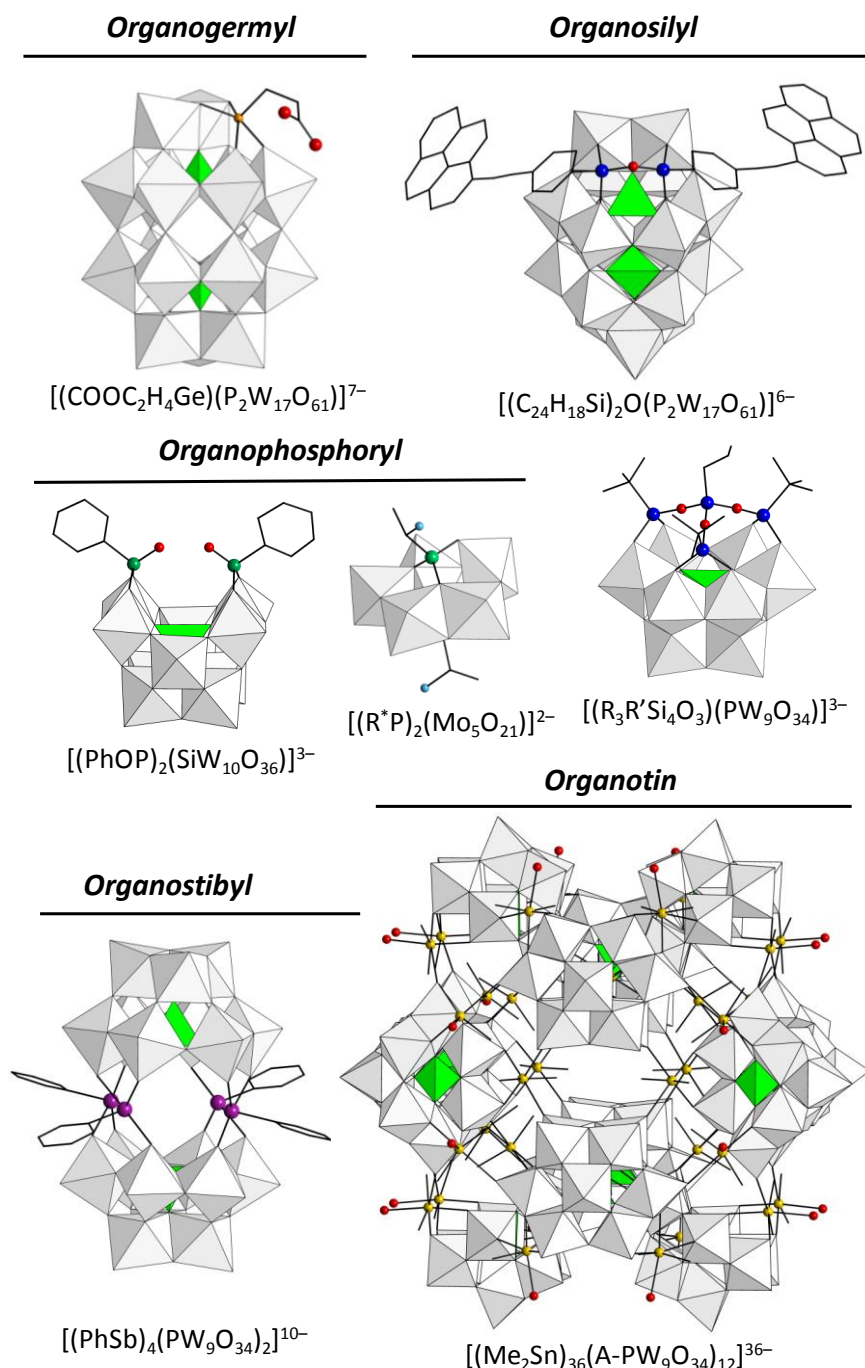


Figure 1.6. Representative examples of hybrid POMs with p-block organoderivatives (R = C₄H₁₂; R' = C₃H₇; R* = R,R-CH₃CHNH₃; Ph = phenyl; Me = Methyl). Color code for the p-block elements of the organic fragments: Ge, orange; Si, blue; P, green; Sb, purple; Sn, yellow.

Since Knoth described the series $[\text{SiW}_{11}\text{O}_{39}\{\text{O}(\text{SiR})_2\}]^{4-}$ ($\text{R} = \text{C}_2\text{H}_5, \text{C}_6\text{H}_5, \text{NC}(\text{CH}_2)_3, \text{C}_3\text{H}_5$) as the first organosilyl derivatives in 1979,³⁸ a large variety of groups have been incorporated into monolacunary Keggin- or Wells-Dawson-type structures. Some different molecular hybrid POMs containing one or two SiR moieties or even one dimeric μ -oxo-bridged $(\text{RSi})_2\text{O}$ unit per vacant site have been reported to date.³⁹ Moreover, four organosilyl groups have been inserted into di- or trilacunary Keggin units.⁴⁰ Some of these hybrid POMs have been post-functionalized to attach additional organic groups, linked to gold or latex nanoparticles, or even incorporated into polymers.⁴¹ In contrast to organosilyl groups, only a few papers describe the functionalization of POMs with organogermyl moieties.⁴²

Organophosphonate ligands have been widely used for the functionalization of Strandberg-type polyoxomolybdates, lacunary polyoxotungstates derived from the Keggin structure or diverse polyxovanadates. The resulting hybrid clusters have shown optical activity or molecular capsule shape among other features.⁴³ Closely related to organophosphonates, bisphosphonates are by themselves great therapeutic agents and well-known as drugs towards bone-loss diseases, so that their combination with POMs could open the way for the design and development of new and efficient drugs.⁴⁴ As indicated in a recent review, most of bisphosphonate-based POMs show open structures with the hetero groups located on the surface of the polyanion instead of encapsulated in the metal-oxo framework.⁴⁵ Methylene-bisphosphonate and its derivatives (e.g. etidronate, alendronate...) are the most employed species which can be found in diverse structures and have led to POM derivatives with applications as antitumoral agents, in the facile synthesis of nanoparticles, or even for film electrodeposition.⁴⁶ As an advantage of organophosphonate-POM derivatives, it is worth noting the possibility of the hybrid clusters for being studied in solution by means of ^{31}P -NMR spectroscopy.

Organotin compounds have also been extensively used in the past years to synthesize hybrid polyoxometalates. These organometallic moieties show some noticeable advantages like: (i) the high stability of the Sn-C bond in aqueous media; (ii) the similar size of Sn^{IV} and W^{VI} and consequent aptitude of the former to substitute addenda metal centers in POM skeletons; (iii) the possibility of using ^{119}Sn -NMR spectroscopy to characterize the hybrid species in solution. The syntheses of these derivatives are basically performed in water by direct reaction of organotin reagents with lacunary polyoxometalates. Knoth's group first, and Liu and coworkers later, both studied the reactivity of commercial mono-organotin groups with mono-, di- and trivacant Keggin polyoxotungstates or monovacant Wells-Dawson species.⁴⁷ Pope et al. also worked in those systems, and besides applied transmetallation reactions to obtain (RSn) -substituted Tourné- or Lindqvist-type anions.⁴⁸ Taking a step forward, Hasenknopf et al. reported series of lacunary Wells-Dawson POMs with monoorganotin moieties showing pendant reactive groups (e.g. carboxylic acids, alkynes or azides) to graft a large variety of organic functions upon postfunctionalization via amide formation or click chemistry.⁴⁹ Over the past decade, the group of Kortz has been one of the main contributors to the development of the chemistry of organotin containing POMs. Dimethyltin moieties were employed in combination with polylacunary POM frameworks leading to structures of large size or dimensionality.⁵⁰ The use of diorganotin linkers allows for the formation of outstanding species like the dodecameric $[\{\text{SnMe}_2(\text{H}_2\text{O})\}_{24}\{\text{SnMe}_2\}_{12}(\text{A-XW}_9\text{O}_{34})_{12}]^{36-}$ ($\text{X}^{\text{V}} = \text{P}, \text{As}$) ball-shaped anion.⁵¹ It is also worth highlighting the role of guanidinium counterions as structure directing agents *via* hydrogen bonding, for the selective crystallization of some minor species in solution or even the preparation of

new molybdate or hexatungstate hybrid-iso-POMs.⁵² This group is also the responsible for the two only reports on organostibyl POM derivatives to date.⁵³ The potential biological activity as antimicrobial agents has been evaluated in these hybrid species showing organometallic moieties trapped between two trilacunary units.

1.3.2. Substitution of surface oxygen atoms

Another elegant strategy to covalently attach organic groups to the POM skeleton involves replacement of shell O atoms with O- or N- donor ligands, as exemplified by trisalkoxo capped Anderson-Evans clusters, Lindqvist-type polyoxovanadates or $[H_4P_2V_3W_{15}O_{62}]^{5-}$ anions (V₃-Wells-Dawson) and also by organoimido/diazenido derivatives of Lindqvist-type molybdates (Figure 1.7). For the Anderson-Evans derivatives, hybrid structures are obtained by reaction of the preformed clusters with the appropriate trisalkoxo ligand in refluxing organic solvent. Trisalkoxo ligands with pendant reactive groups like -NH₂ can be grafted on the polyoxometalate and then get involved in imination or amidation reactions for postfunctionalization. Organic moieties can be linked to both sides of the plane defined by the metal atoms in idealized D_{3d} symmetry, in such a way that the trisalkoxo ligand caps the two opposite triangular faces of the central $\{XO_6\}$ octahedron. This type of hybrid POMs are known as δ isomers and have only been obtained for trivalent transition metal containing polyoxomolybdates ($X^{III} = Fe^{III}, Mn^{III}, Cr^{III}$). A wide range of organic functionalities have been incorporated, like alkyl chains, alkenes, amines, alcohols, nitro groups, or even more complex architectures (terpyridines, pyrenes).⁵⁴ Some of these functionalities have allowed further derivatization by coordination to catalytic centers like Pd or Ru, whereas others have endowed the cluster with photoactive properties or the ability to form vesicles in solution.⁵⁵ When the organic ligand caps one tetrahedral cavity on each side of the Anderson-Evans cluster, the resulting hybrid with ideal C_{2h} symmetry is known as χ isomer. There is only one report on this kind of functionalization authored by Hasenknopf et al. who prepared the χ isomer hybrid for divalent metal containing polyoxomolybdates ($X^{II} = Zn, Ni$).⁵⁶ Recently single-side and asymmetric functionalization for δ isomers have been achieved by Wei's and Cronin's groups respectively.⁵⁷ Trisalkoxo groups have also been used to synthesize Lindqvist-type hexavanadates difunctionalized in *trans* fashion, including porphyrin/polyoxovanadate hybrids, fluorescent compounds or catalytically active metal-coordination-polymers.⁵⁸ Although only scarce examples have been published to date, the *cis*-functionalization has also been observed.⁵⁹

The same approach has been applied for preparing V₃-Wells-Dawson hybrid anions where the $\{V_3O_{13}\}$ trimer is capped by the tris(hydroxymethyl) (Tris) ligand.⁶⁰ The use of linear bis-Tris bridging ligands has resulted in "dumbbell" hybrids composed of two V₃-Wells-Dawson-type clusters linked to each other, which can self-assemble into vesicles in acetone/water solutions.⁶¹ Analogously, functional dendrimers and polymers were prepared by using linkers of higher dimensionality.⁶² The V₃-Wells-Dawson POM has also allowed the covalent attachment of amide groups. Relatively small organic molecules showing amide and diol groups $\{RCONHC_5H_9(OH)_2\}$ can substitute the bridging O atoms of the $\{V_3O_{13}\}$ trimer with the two oxygen atoms from the hydroxo groups and the carbonyl oxygen of the amide function.⁶³ Other examples worth to be mentioned show caboxylate O atoms from amino acids replacing the POM-shell O atoms, like in Kortz's hexamolybdates containing lone-pair heteroatoms or An's octamolybdates.⁶⁴

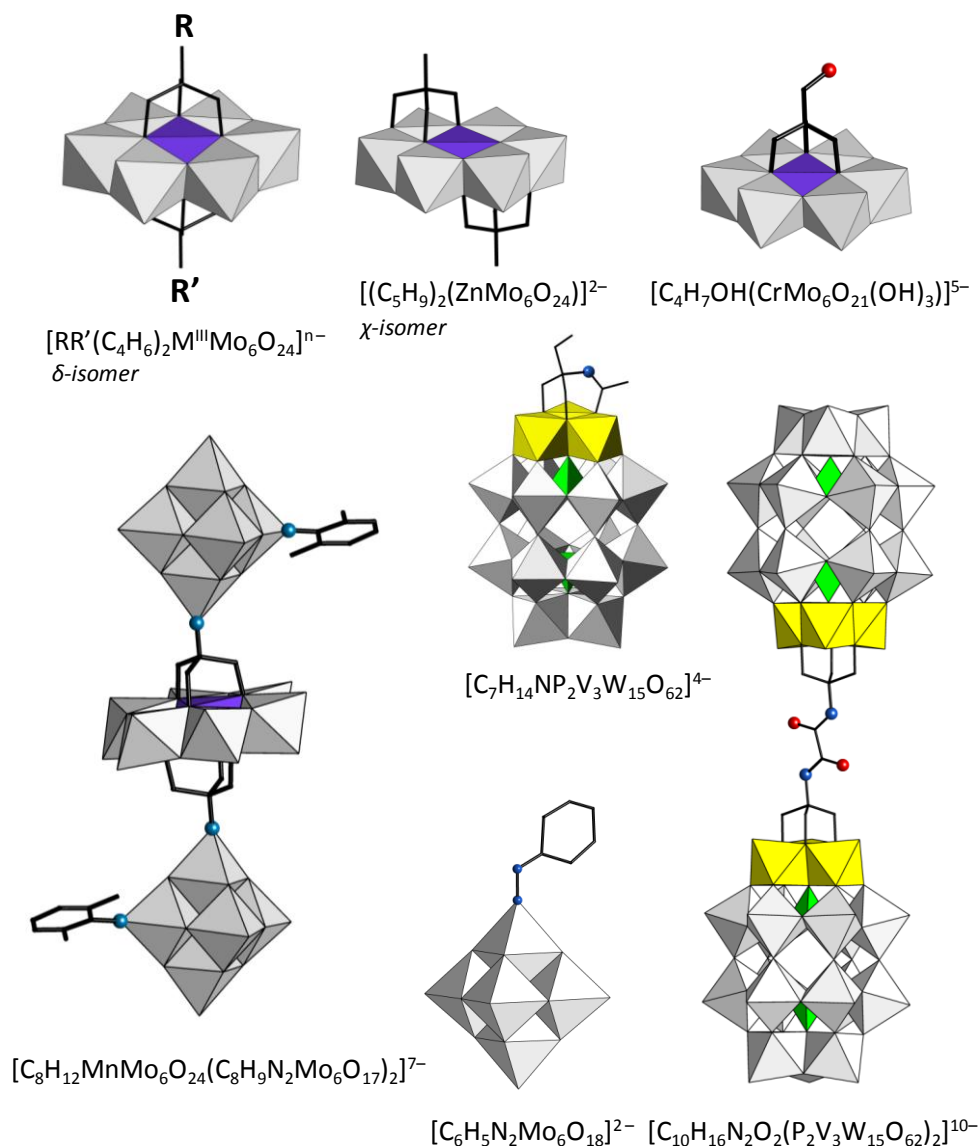


Figure 1.7. Representative examples of hybrid POMs with surface O-atoms replaced with organic fragments (R = R' symmetric functionalization; R = R' asymmetric functionalization). Color code: VO₆, yellow octahedra.

Regarding the N-donor ligands, the first example and the first X-ray structural characterization of an organoimido derivative of the Lindqvist-type molybdate were reported in the late 80's by Zubieta and Maatta, respectively.⁶⁵ These reports paved the way to a large and still growing family of hybrid POM derivatives. These hybrids were first prepared by refluxing the Lindqvist-type precursor in pyridine with variable equivalents of organic isocyanates, resulting in mono- or di-organoimido derivatives.⁶⁶ Organoimido-polyoxometalates were even introduced as pendant groups in organic polymers.⁶⁷ A more efficient synthetic process was later developed by Peng. This method is based on the use of dicyclohexylcarbodiimide (DCC) in acetonitrile and has become the standard procedure for the functionalization of hexamolybdates.⁶⁸ The DCC additive acts as dehydrating agent and activates the Mo—O bonds toward the inorganic isocyanates. A recent study has demonstrated that not only terminal oxo ligands, but also bridging O atoms can be replaced with organic imido ligands.⁶⁹ Potential applications of this family of compounds as antitumoral or herbicidal agents, and in nonlinear optical activities have also been evaluated.⁷⁰

Interestingly, the cited synthetic methodology was recently applied for the preparation of chiral rod-like molecular triads, formed by two Lindqvist-type molybdates connected to a central Anderson-Evans POM *via* Tris ligands. The trisalkoxo group of the ligand reacts with both sides on the Anderson-Evans cluster, whereas the pendant amino groups take part in the formation of imide linkages with the hexamolybdate units.⁷¹ In contrast to organoimido derivatives, related organodiazenido derivatives are less studied, but analogously prepared starting from a phosphazine precursor. In some cases, this kind of derivatization has led to compounds showing non-linear optical response.⁷²

1.3.3. Grafting of the transition metal complexes at POM surface

Several groups including ours have studied the synthesis of hybrid species via grafting of 3d-metal complexes at POM surfaces to incorporate additional catalytically or magnetically active centers to the system. *Decoration* can result in molecular hybrid-POMs or extended structures depending on the nature of the organic ligand (Figure 1.8). In the last decades a huge number of structures synthesized by hydrothermal methods have been reported. This work was initiated by Zubietta and co-workers, who first focused their studies on polyoxomolybdates and specially vanadates, and later extended them to tungstates.⁷³ The systematic studies carried out in our group include compounds prepared under mild bench conditions or by hydrothermal synthesis. The former comprises compounds derived from the assembly of plenary Keggin-type tungstosilicates or copper(II)-monosubstituted $[\text{SiW}_{11}\text{O}_{39}\text{Cu}(\text{H}_2\text{O})]^{6-}$ species and the dinuclear cationic complexes $[\{\text{Cu}(\text{phen})(\text{H}_2\text{O})_2\text{OAc}\}_2]^{2+}$ and $[\{\text{CuL}(\text{H}_2\text{O})_2\}_2\text{ox}]^{2+}$ (L = phenantroline, 2,2'-bipyridine). Molecular complexes, chain-like coordination polymers or extended two-dimensional coordination networks can be found among these compounds. Interestingly, the influence of the counterions of the acetate buffer solutions on the nature of hybrid compounds was also evaluated.⁷⁴ On the other hand, hydrothermal conditions were successfully applied in the preparation of hybrid organic-inorganic compounds based on Keggin-type tungstosilicates or -germanates and copper complexes bearing different N-donor ligands. These include the bidentate 2,2'-bipyridine, 1,10-phenanthroline and 2,9-dimethyl-1,10-phenanthroline (neocuproine); the bridging 4,4'-bipyridine and 1,2-bis(4-pyridil)ethane; and tetradentate cyclam, or diamino-dipyridin-type species.⁷⁵ Very recently, we have reported some examples of single-crystal-to-single-crystal transformations promoted by reversible dehydration processes observed for the compounds derived from diamino-dipyridine ligands.⁷⁶

It is also worth mentioning some other striking structures reported in the literature, like the “porphyrin hamburger” constituted by a $[\text{SiW}_{12}\text{O}_{40}]^{4-}$ anion decorated by two porphyrin-metal complexes in a *trans*-fashion; compounds showing accessible catalytic Ru or Ag centers; porous frameworks with unusual sorption properties; or compounds derived from the inclusion of chiral natural ligands (e.g. L-proline) onto achiral POMs with potential applications in asymmetric catalysis.⁷⁷ However, this type of hybrid compounds derived from the grafting of transition metal complexes at POM surfaces usually displays some major drawbacks in terms of predictability and applicability, which are originated from the limited control of the anchoring position or the formation of insoluble solid phases with extended structures.

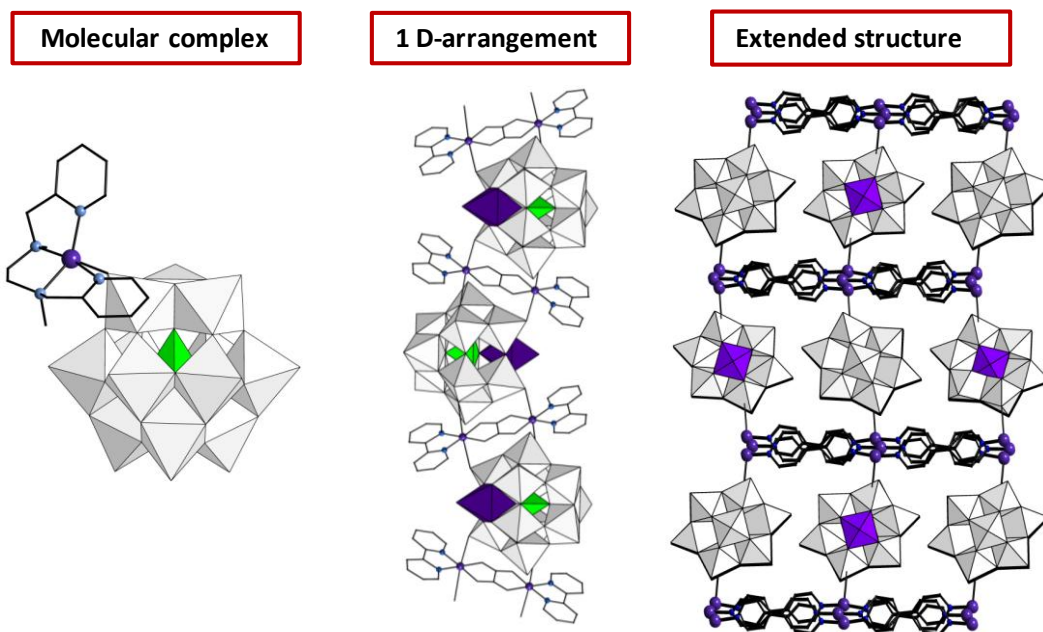


Figure 1.8. Representative examples of hybrid compounds with transition metal complexes grafted at the surface of the POM. Left: Molecular $[\text{Cu}(\text{bpmen})\text{SiW}_{12}\text{O}_{40}]^{2-}$ anion; center: mono-dimensional $\{(\text{CuSiW}_{11}\text{O}_{39})(\text{Cu}_2\text{bpy}_2\text{ox})\}$ arrangement; right: extended $\{(\text{CuSiW}_{11}\text{O}_{39})(\text{Cu}(\text{bpy})_3)\}$ framework.

1.3.4. Organic functionalization of 3d- or 4f-metal substituted POMs

The incorporation of transition metals or lanthanides in vacant polyoxoanions is one of the oldest and most studied reactions in POM chemistry. Examples of metal-substituted POMs range from simple mono-substituted monolacunary Keggin-type anions to complex structures like the tetradecanuclear copper cluster encapsulated between four trilacunary $[\text{SiW}_9\text{O}_{34}]^{10-}$ Keggin units (Figure 1.9).^{30c,d} Lanthanide containing POMs and their hybrid derivatives will be briefly reviewed in Chapter 3.

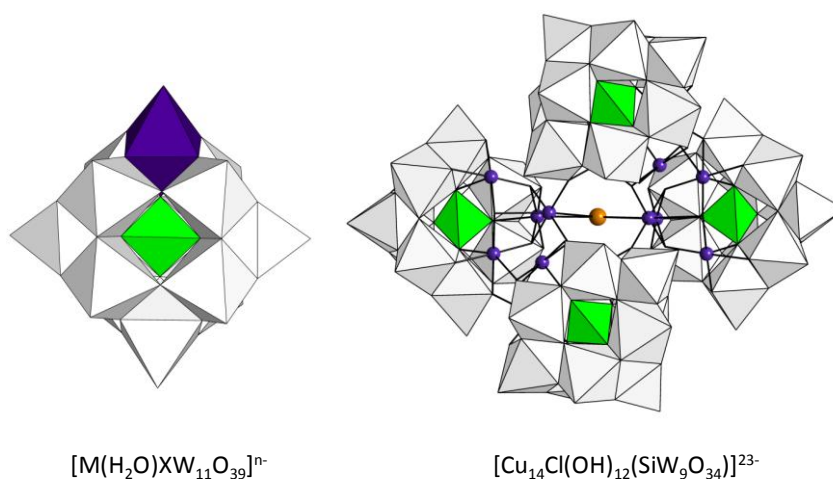


Figure 1.9. Two examples of transition metal substituted POMs.

There are three main approaches to achieve the organic functionalization of these clusters: i) performing ligand replacement of labile solvent molecules (or acetate anions) on suitable 3d- or 4f-metal substituted POMs with exposed metal centers; ii) adding transition metal complexes bearing organic ligands to lacunary POMs; iii) employing one-pot procedures by mixing the corresponding oxoanion, a heteroatomic source, a 3d-metal salt and the organic ligand together (Figure 1.10).

The first approach seems to be the less used so far, due to the difficulty of finding solution stable POM precursors with accessible metal centers. The first studies in this approach were carried out with the aim of substituting the single water molecule of 3d-metal mono-substituted Keggin-type $[M(H_2O)(XW_{11}O_{39})]^{n-}$ anions with N-donor ligands like pyridine or imidazol derivatives. More recently, the replacement of this water molecule with ligands like 4,4-bipyridine under hydrothermal conditions has been reported.⁷⁸ Ruthenium monosubstituted species have been one of the most studied species due to their potential catalytic activity and the ability to form Ru-C bonds.⁷⁹ Regarding classical sandwich-type structures, monodentate N-donor ligands like imidazole, pyridine or pending ethylenediamine ligands have been widely used to substitute the water molecules of Weakley- $[M_4(H_2O)_2(XW_9O_{34})_2]^{n-}$ and Hervé-type $[M_3(H_2O)_3(XW_9O_{33})_2]^{n-}$ POMs.⁸⁰

The first examples of polyoxometalate structures that incorporate embedded chelated metals were reported by Pope. Those include ethylenediamine chelated Co centers encapsulated between two $\{PW_9O_{34}\}$ or $\{PW_{10}O_{38}\}$ lacunary Keggin units or lacunary hexamolybdates.⁸¹ Analogously, Wang described a hexamethylenetetramine bridged decanuclear Fe^{III} cluster sandwiched by two previously unknown $\{P_2W_{13}O_{51}\}$ anions.⁸² Complete transition metal chelate encapsulation within a dilacunary Keggin POM has been observed as a result of the one-pot reaction of tungstate and phosphate and a Ni^{II} salt with the multifunctional N,N'-bis(2-hydroxyethyl)piperazine (bhep) ligand. Similar reaction at higher pH (pH = 6) allows to isolate a dimeric cluster formed by two trilacunary Keggin-type $\{PW_9O_{34}\}$ tungstophosphate subunits containing 9 Co^{II} ions bridged by three bhep ligands.⁸³

Preparation of chiral compounds is nowadays a hot topic in POM-chemistry due to their high potential in asymmetric catalysis, nonlinear optical materials, molecular recognition or biomedical applications.⁸⁴ Following this target, Hill and coworkers reported two enantiomerically pure compounds formed by tartrate or malate ligands coordinated to Zr^{IV} -substituted POMs where the Zr centers are linking two lacunary $\{P_2W_{15}O_{46}\}$ Wells-Dawson units.⁸⁵ It is also worth highlighting the systematic studies carried out by the group of Versailles in quest of a general method for the functionalization of 3d-substituted POMs with carboxylate ligands under mild conditions. The β -alanine or γ -aminobutyric aminoacids, and the 3-thiopheneacetate, p-phenylenediacetate or glutarate ligands were linked to trilacunary $\{B-\alpha-XW_9\}$ Keggin units substituted by multiple Cu or Ni centers, leading to hybrid compounds of different dimensionalities.⁸⁶ All these compounds can be considered as model systems for the linkage of POM cluster to substrates possessing carboxylate functions.

Steric effects and repulsion between anionic ligands and POMs make complexation of exposed metal centers in POM clusters challenging. Overall, negatively charged and bulky ligands will react less favorably than small neutral ligands. This can be overcome by using a large excess of ligand, as exemplified by several acetate containing clusters that are readily prepared in acetate buffered solutions.⁸⁷ However, the high affinity of metal ions toward some specific ligands can lead to the isolation of the corresponding transition metal complexes instead of the desired hybrid POM. Even though only a few crystal structures have been reported, the synthesis of organically functionalized POMs in organic solvents has succeeded in some cases.⁸⁸ Alternatively, hydrothermal techniques were efficiently used by Yang and coworkers for the formation of extended POMOF (POLyoxometalate-Metal-Organic-Framework) networks. Hybrid $\{Ni_6PW_9\}$ building blocks stabilized by ethylenediamine, 1,2-diaminopropane or Tris molecules were interconnected using benzenedi-, -tri-

and -tetracarboxylate ligands, giving rise to unprecedented molecular cages or porous materials with potential applications as catalysts or gas absorption agents.⁸⁹ Following similar approaches, ligand coordinated high-nuclear transition metal clusters (Co, Ni, Cu, Zn) have also been embedded between trilacunary $\{B-\alpha-XW_9O_{34}\}$ (X = Si, Ge, P) subunits.⁹⁰

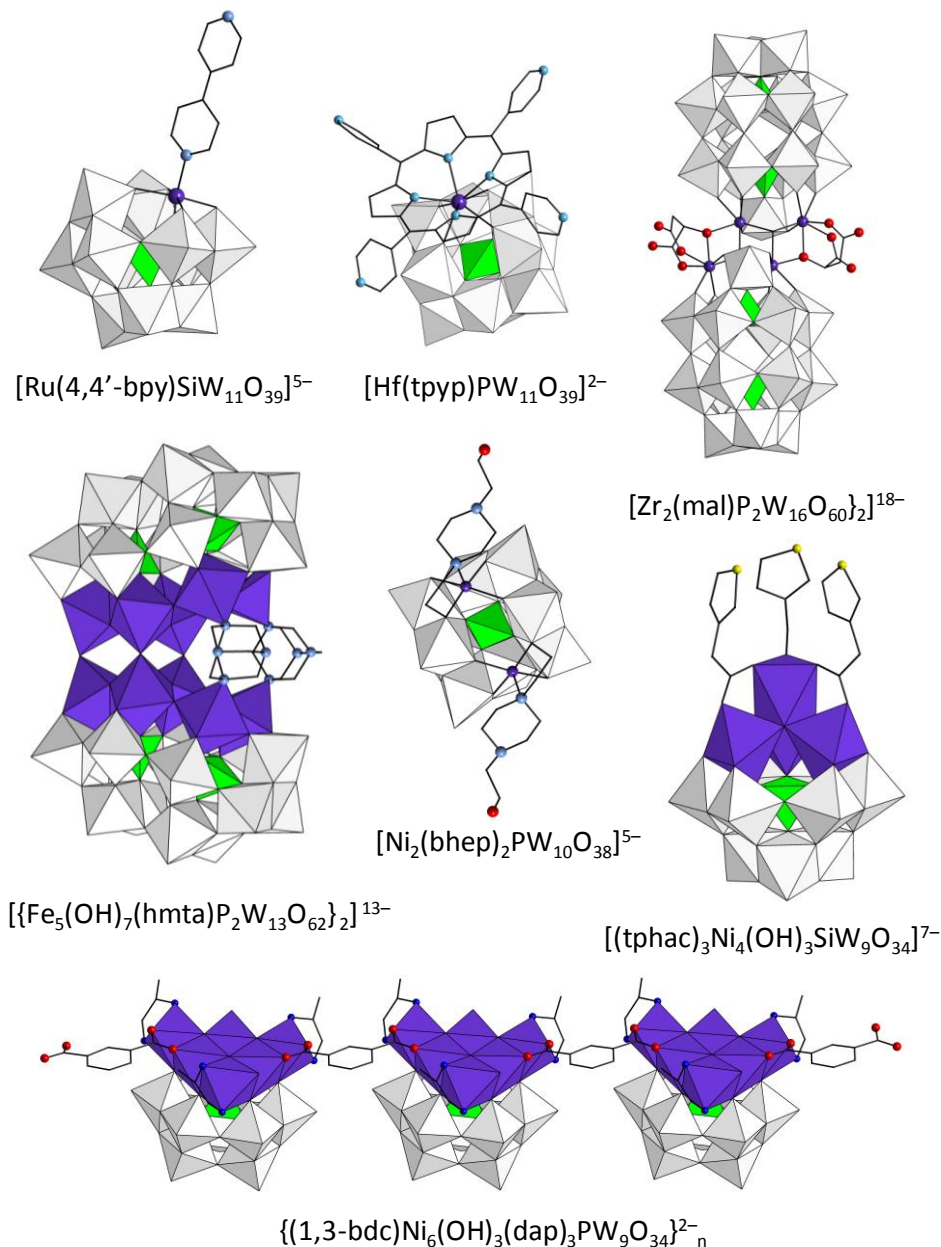


Figure 1.10. Representative examples of organic functionalization in 3d-metal containing POMs. (Ligands: 4,4'-bpy, 4,4'-bipyridine; tpyp, meso-tetra-(4-pyridil)-porphyrine; mal, malate; hmta, hexamethylene-tetraamine; bhep, N,N'-Bis(2-hydroxyethyl) piperazine; en, ethylenediamine; 1,4-bdc, 1,4-benzenedicarboxylate; tphac, 3-thiophene-acetate).

1.4. SUMMARY AND AIM OF THE WORK

This dissertation fits within one of the research lines of *Departamento de Química Inorgánica de la Facultad de Ciencia y Tecnología de la Universidad del País Vasco UPV/EHU*. This line consists in the synthesis and structural characterization of organic-inorganic hybrid compounds based on the interaction between POMs and metal-organic complexes, and its main objective is to combine both

type of components in quest of new properties or structural motifs to enrich the field of POM chemistry. As mentioned before, previous studies in this group involved the preparation of POM hybrids via grafting of transition-metal complexes on POM surfaces.⁷⁴⁻⁷⁶ The limited control of the anchoring position and the formation of insoluble compounds with extended structures were found to be major drawbacks in terms of predictability and applicability. To overcome these drawbacks, it was decided to apply an alternative approach consisting in the ligand replacement of labile solvent molecules on suitable d- or f-substituted POMs with exposed metal centers. Based on this synthetic approach, **the aim of this work is: i) to evaluate the viability of the organic functionalization of well-known clusters with accessible 3d- or 4f-metal centers via simple coordination chemistry, and ii) to prepare new clusters that could be potentially suitable for this kind of organic derivatization.** The resulting compounds could show interesting properties like catalytic activity, luminescence and single-molecule magnet behavior, or could be good candidates to undergo further self-assembly processes in solution. As part of a new research line implemented in the group, the hybrid-POMs prepared could also be incorporated into polymeric surfaces for preparing new advanced multifunctional materials.

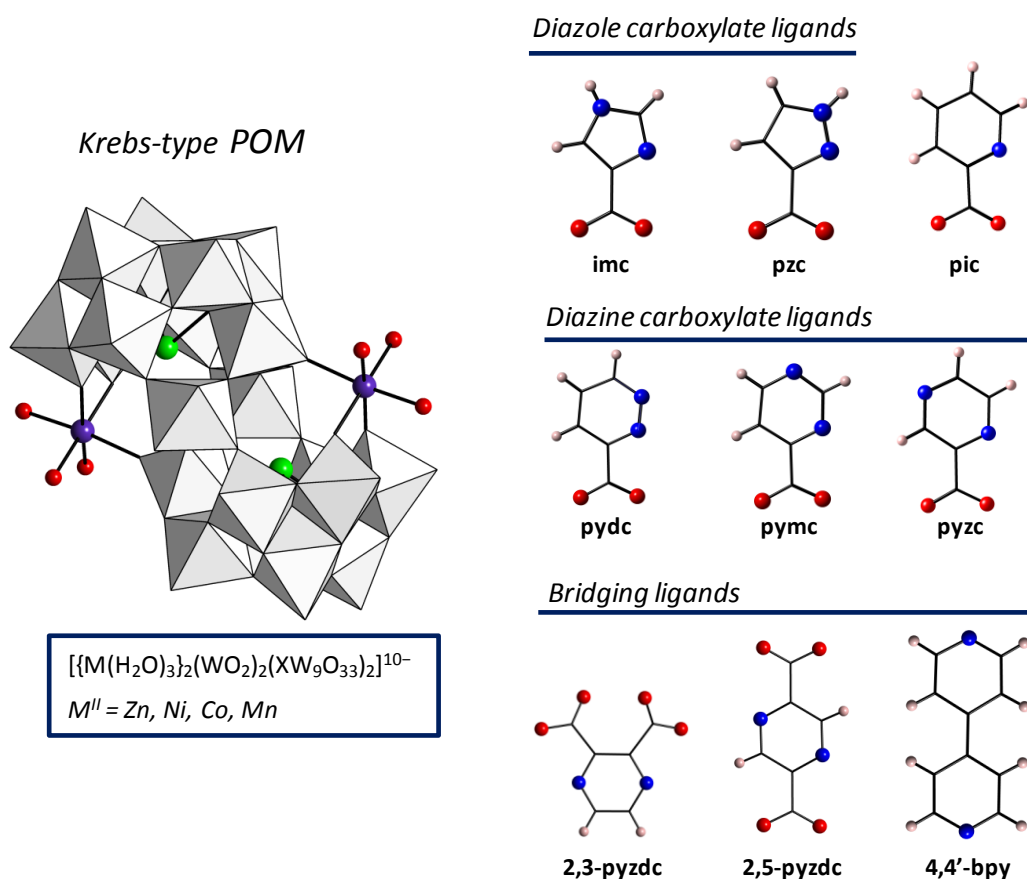


Figure 1.11. Organic ligands and POM precursors employed in the first part of this work (Chapter 2).

The work has been divided in two well-differentiated parts. In the first section (Chapter 2), a systematic study on the organic functionalization of the well-known family of transition-metal di-substituted Krebs-type tungstoantimonates(III) has been performed. The $[\{ M(H_2O)_3 \}_2 (WO_2)_2 (SbW_9O_{33})_2]^{n-}$ ($M^{II} = Zn, Ni, Co, Mn$) framework displays two accessible transition metal center with three labile water molecules each, that appears to be suitable for organic ligand substitution. Krebs-type POMs were selected as ideal candidates for performing such ligand replacement studies

CHAPTER 1

because they can be prepared in precursor scale, they are stable in solution in a wide pH range and their structure allows for systematic compositional variations. Carboxylate derivatives of N-donor heterocycles with N,O-chelating capability were tested. These include diazolecarboxylates like 1H-imidazole-4-carboxylate (imc) and 1H-pyrazole-3-carboxylate (pzc); the pyridincarboxylate picolinate (pic); and the diazinecarboxylates pyridazine-3-carboxylate (pydc), pyrimidine-4-carboxylate (pymc) and pyrazine-2-carboxylate (pyzc). Chapter 2 also includes results obtained with three selected bridging ligands, namely 4,4'-bipyridine (4,4'-bpy), pyrazine-2,5-dicarboxylate(2,5-pyzdc) and pyrazine-2,3- dicarboxylate (2,3-pyzdc) (Figure 1.11). The compounds isolated have been characterized by elemental and thermal analyses, infrared spectroscopy, and single-crystal X-ray diffraction. To elucidate whether these hybrid POMs are stable in water solution or undergo decomposition processes, $^1\text{H-NMR}$ studies and Electrospray Ionization-Mass Spectrometry (ESI-MS) experiments were carried out on different derivatives. Magnetic properties have also been studied by magnetic susceptibility measurements.

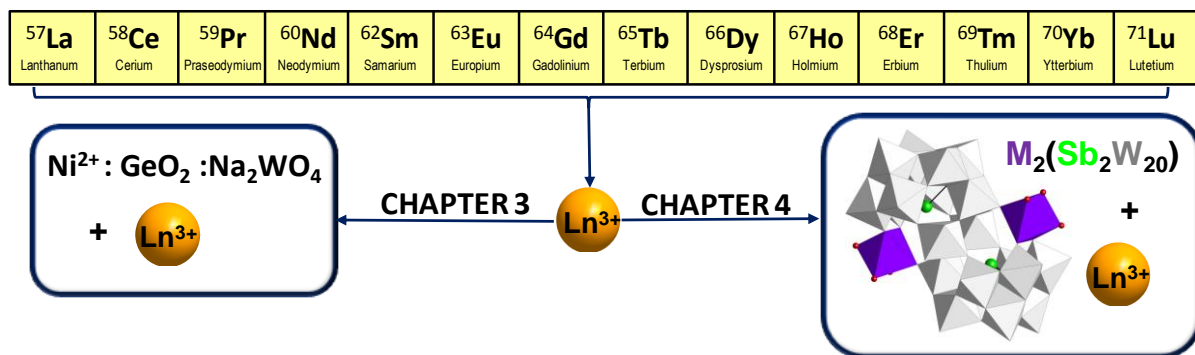


Figure 1.12. Schematic representation of the studies included in Chapter 3 and Chapter 4.

In the second part (Chapters 3 and 4), the preparation of clusters with accessible metal centers showing two or more water molecules that could be suitable for further organic functionalization is discussed. On the one hand, Chapter 3 includes the synthesis of a series of 4f-metal containing tungstogermanates and the effect of the lanthanide and counterion employed in the final structures is evaluated. On the other hand, Chapter 4 contains the results obtained for some heterometallic 3d-4f clusters synthesized from the reaction of transition-metal di-substituted Krebs-type POMs with lanthanides (Figure 3.12). As for the hybrid POMs included in Chapter 2, transition metal and/or lanthanide containing POMs described in Chapters 3 and 4 have also been characterized by elemental and thermal analyses, infrared spectroscopy, and single-crystal X-ray diffraction. Different properties of these clusters, such as photoluminescence, magnetism, or solution behavior have been analyzed by luminescence studies, magnetic susceptibility measurements, electron spin resonance spectroscopy (ESR), ESI-MS experiments, $^{183}\text{W-NMR}$ spectroscopy and Laser Light Scattering (LLS) techniques.

To sum up, a total number of 39 compounds are reported in this dissertation. Table 1.2 compiles all these compounds, together with their formulae, codes and graphical representations.

	Code	Compound	Schematic representation
CHAPTER 2	1-SbMn	$\text{Na}_{12}[\{\text{Mn}(\text{imc})(\text{H}_2\text{O})\}_2(\text{WO}_2)_2(\text{SbW}_9\text{O}_{33})_2] \cdot 44\text{H}_2\text{O}$	
	1-SbCo	$\text{Na}_{12}[\{\text{Co}(\text{imc})(\text{H}_2\text{O})\}_2(\text{WO}_2)_2(\text{SbW}_9\text{O}_{33})_2] \cdot 44\text{H}_2\text{O}$	
	1-SbNi	$\text{Na}_{12}[\{\text{Ni}(\text{imc})(\text{H}_2\text{O})\}_2(\text{WO}_2)_2(\text{SbW}_9\text{O}_{33})_2] \cdot 44\text{H}_2\text{O}$	
	1-SbZn	$\text{Na}_{12}[\{\text{Zn}(\text{imc})(\text{H}_2\text{O})\}_2(\text{WO}_2)_2(\text{SbW}_9\text{O}_{33})_2] \cdot 44\text{H}_2\text{O}$	
	1-TeMn	$\text{Na}_7\text{K}_3[\{\text{Mn}(\text{imc})(\text{H}_2\text{O})\}_2(\text{WO}_2)_2(\text{TeW}_9\text{O}_{33})_2] \cdot 39\text{H}_2\text{O}$	
	1-TeCo	$\text{Na}_7\text{K}_3[\{\text{Co}(\text{imc})(\text{H}_2\text{O})\}_2(\text{WO}_2)_2(\text{TeW}_9\text{O}_{33})_2] \cdot 39\text{H}_2\text{O}$	
	2-Ni	$\text{Na}_8\text{K}_4[\{\text{Ni}(\text{pzc})(\text{H}_2\text{O})\}_2(\text{WO}_2)_2(\text{SbW}_9\text{O}_{33})_2] \cdot 36\text{H}_2\text{O}$	
	3-Co	$\text{Na}_6\text{K}_6[\{\text{Co}(\text{pyzc})(\text{H}_2\text{O})\}_2(\text{WO}_2)_2(\text{SbW}_9\text{O}_{33})_2] \cdot 32\text{H}_2\text{O}$	
	3-Zn	$\text{Na}_6\text{K}_6[\{\text{Zn}(\text{pyzc})(\text{H}_2\text{O})\}_2(\text{WO}_2)_2(\text{SbW}_9\text{O}_{33})_2] \cdot 32\text{H}_2\text{O}$	
	4-Mn	$\text{Na}_{10}[\text{Mn}_2(\text{H}_2\text{O})_6(\text{WO}_2)_2(\text{SbW}_9\text{O}_{33})_2] \cdot 32\text{H}_2\text{O} \cdot 2(4,4'\text{-bpy})$	
5-Ni	$\text{Na}_{24}[\mu\text{-}\{(2,3)\text{pyzdc}\}_2[\text{Ni}_2(\text{H}_2\text{O})\text{Sb}_2\text{W}_{20}\text{O}_{70}]_2] \cdot 91\text{H}_2\text{O}$		
CHAPTER 3	6-Pr	$\text{Na}_{31}\text{Ni}_2[\text{Na}\text{-}\text{Pr}_{12}\text{Ge}_6\text{W}_{60}\text{O}_{228}(\text{H}_2\text{O})_{24}] \cdot 145\text{H}_2\text{O}$	
	6-Nd	$\text{Na}_{31}\text{Ni}_2[\text{Na}\text{-}\text{Nd}_{12}\text{Ge}_6\text{W}_{60}\text{O}_{228}(\text{H}_2\text{O})_{24}] \cdot 145\text{H}_2\text{O}$	
	7-Sm	$\text{Na}_{27}\text{K}_4\text{Ni}_2[\text{K}\text{-}\text{Sm}_{12}\text{Ge}_6\text{W}_{60}\text{O}_{228}(\text{H}_2\text{O})_{22}] \cdot 123\text{H}_2\text{O}$	
	8-Pr	$\text{Na}_{40}\text{K}_6\text{Ni}_3[\text{K}\text{-}\text{K}_7\text{Pr}_{24}\text{Ge}_{12}\text{W}_{120}\text{O}_{444}(\text{OH})_{12}(\text{H}_2\text{O})_{64}] \cdot 280\text{H}_2\text{O}$	
	8-Nd	$\text{Na}_{40}\text{K}_6\text{Ni}_3[\text{K}\text{-}\text{K}_7\text{Nd}_{24}\text{Ge}_{12}\text{W}_{120}\text{O}_{444}(\text{OH})_{12}(\text{H}_2\text{O})_{64}] \cdot 280\text{H}_2\text{O}$	
	9-Gd	$\text{Na}_{12}[\text{Gd}_4(\text{H}_2\text{O})_6(\beta\text{-GeW}_{10}\text{O}_{38})_2] \cdot 44\text{H}_2\text{O}$	
	9-Tb	$\text{Na}_{12}[\text{Tb}_4(\text{H}_2\text{O})_6(\beta\text{-GeW}_{10}\text{O}_{38})_2] \cdot 44\text{H}_2\text{O}$	
	9-Dy	$\text{Na}_{12}[\text{Dy}_4(\text{H}_2\text{O})_6(\beta\text{-GeW}_{10}\text{O}_{38})_2] \cdot 44\text{H}_2\text{O}$	
	9-Ho	$\text{Na}_{12}[\text{Ho}_4(\text{H}_2\text{O})_6(\beta\text{-GeW}_{10}\text{O}_{38})_2] \cdot 44\text{H}_2\text{O}$	
	9-Er	$\text{Na}_{12}[\text{Er}_4(\text{H}_2\text{O})_6(\beta\text{-GeW}_{10}\text{O}_{38})_2] \cdot 44\text{H}_2\text{O}$	
	9-Tm	$\text{Na}_{12}[\text{Tm}_4(\text{H}_2\text{O})_6(\beta\text{-GeW}_{10}\text{O}_{38})_2] \cdot 41\text{H}_2\text{O}$	
	9-Yb	$\text{Na}_{12}[\text{Yb}_4(\text{H}_2\text{O})_6(\beta\text{-GeW}_{10}\text{O}_{38})_2] \cdot 41\text{H}_2\text{O}$	
	9-Lu	$\text{Na}_{12}[\text{Lu}_4(\text{H}_2\text{O})_6(\beta\text{-GeW}_{10}\text{O}_{38})_2] \cdot 41\text{H}_2\text{O}$	
10-Ho	$\text{Cs}_7\text{Na}_{17}[\{\text{Ho}_4(\text{H}_2\text{O})_5(\text{GeW}_{10}\text{O}_{38})_2\}_2] \cdot 66\text{H}_2\text{O}$		
10-Er	$\text{Cs}_6\text{Na}_{18}[\{\text{Er}_4(\text{H}_2\text{O})_5(\text{GeW}_{10}\text{O}_{38})_2\}_2] \cdot 66\text{H}_2\text{O}$		
10-Tm	$\text{Cs}_5\text{Na}_{19}[\{\text{Tm}_4(\text{H}_2\text{O})_5(\text{GeW}_{10}\text{O}_{38})_2\}_2] \cdot 63\text{H}_2\text{O}$		
10-Yb	$\text{Cs}_6\text{Na}_{18}[\{\text{Yb}_4(\text{H}_2\text{O})_5(\text{GeW}_{10}\text{O}_{38})_2\}_2] \cdot 63\text{H}_2\text{O}$		
10-Lu	$\text{Cs}_5\text{Na}_{19}[\{\text{Lu}_4(\text{H}_2\text{O})_5(\text{GeW}_{10}\text{O}_{38})_2\}_2] \cdot 63\text{H}_2\text{O}$		
CHAPTER 4	11-LaCo	$\text{Na}_{17}[\text{Sb}_7\text{W}_{36}\text{O}_{133}\text{La}_3\text{Co}_2(\text{OAc})(\text{H}_2\text{O})_8] \cdot 63\text{H}_2\text{O}$	
	11-CeCo	$\text{Na}_{17}[\text{Sb}_7\text{W}_{36}\text{O}_{133}\text{Ce}_3\text{Co}_2(\text{OAc})(\text{H}_2\text{O})_8] \cdot 63\text{H}_2\text{O}$	
	11-PrCo	$\text{Na}_{17}[\text{Sb}_7\text{W}_{36}\text{O}_{133}\text{Pr}_3\text{Co}_2(\text{OAc})(\text{H}_2\text{O})_8] \cdot 63\text{H}_2\text{O}$	
	11-NdCo	$\text{Na}_{17}[\text{Sb}_7\text{W}_{36}\text{O}_{133}\text{Nd}_3\text{Co}_2(\text{OAc})(\text{H}_2\text{O})_8] \cdot 63\text{H}_2\text{O}$	
	11-SmCo	$\text{Na}_{17}[\text{Sb}_7\text{W}_{36}\text{O}_{133}\text{Sm}_3\text{Co}_2(\text{OAc})(\text{H}_2\text{O})_8] \cdot 63\text{H}_2\text{O}$	
	11-EuCo	$\text{Na}_{17}[\text{Sb}_7\text{W}_{36}\text{O}_{133}\text{Eu}_3\text{Co}_2(\text{OAc})(\text{H}_2\text{O})_8] \cdot 63\text{H}_2\text{O}$	
	11-GdCo	$\text{Na}_{17}[\text{Sb}_7\text{W}_{36}\text{O}_{133}\text{Gd}_3\text{Co}_2(\text{OAc})(\text{H}_2\text{O})_8] \cdot 63\text{H}_2\text{O}$	
	11-CeNi	$\text{Na}_{17}[\text{Sb}_7\text{W}_{36}\text{O}_{133}\text{Ce}_3\text{Ni}_2(\text{OAc})(\text{H}_2\text{O})_8] \cdot 63\text{H}_2\text{O}$	
	11-CeZn	$\text{Na}_{17}[\text{Sb}_7\text{W}_{36}\text{O}_{133}\text{Ce}_3\text{Zn}_2(\text{OAc})(\text{H}_2\text{O})_8] \cdot 63\text{H}_2\text{O}$	

1.4. REFERENCES

- [1] Pope, M. T. *Heteropoly and Isopoly Oxometalates*; Springer-Verlag: Berlin, 1983.
- [2] (a) Neumann, R.; Dahan, M. *Nature* **1997**, *388*, 353. (b) Kozhevnikov, I. in *Catalysis by Polyoxometalates*; Roberts, S. M., Ed.; Catalysts for Fine Chemical Synthesis (Vol. 2); John Wiley & Sons: Chichester, U.K., 2002. (c) Kamata, K.; Yonehara, K.; Sumida, Y.; Yamaguchi, K.; Hikichi, S.; Mizuno, N. *Science* **2003**, *300*, 964. (d) Yin, Q.; Tan, J. M.; Besson, C.; Geletti, Y. V.; Musaev, D. G.; Kuznetsov, A. E.; Luo, Z.; Hardcastle, K. I.; Hill, C. L. *Science* **2010**, *328*, 342. (e) Carraro, M.; Sartorel, A.; Ibrahim, M.; Nsouli, N.; Jahier, C.; Nlate, S.; Kortz, U.; Bonchio, M. in *Innovative Catalysis in Organic Synthesis: Oxidation, Hydrogenation, and C–X Bond Forming Reactions*; Andersson, P. G., Ed.; Wiley-VCH: Weinheim, Germany, 2012. (f) Misono, M. *Stud. Surf. Sci. Catal.* **2013**, *176*, 97. (g) Sun, M.; Zhang, J.; Putaj, P.; Lefebvre, F.; Pelletier, J.; Basset, J.-M. *Chem. Rev.* **2014**, *114*, 981. (h) Stracke, J. J.; Finke, R. G. *ACS Catal.* **2014**, *4*, 909.
- [3] (a) Müller, A.; Peters, F.; Pope, M. T.; Gatteschi, D. *Chem. Rev.* **1998**, *98*, 239. (b) Clemente-Juan, J. M.; Coronado, E. *Coord. Chem. Rev.* **1999**, *193-195*, 1776. (c) Kortz, U.; Müller, A.; van Slageren, J.; Schnack, J.; Dalal, N. S.; Dressel, M. *Coord. Chem. Rev.* **2009**, *253*, 2315. (d) Clemente-Juan, J. M.; Coronado, E.; Gómez-García, C. J. *Chem. Soc. Rev.* **2012**, *41*, 7464.
- [4] (a) Coronado, E.; Gómez-García, C. J. *Chem. Rev.* **1998**, *98*, 273. (b) Long, D.-L.; Burkholder, E.; Cronin, L. *Chem. Soc. Rev.* **2007**, *36*, 105. (c) Miras, H. N.; Yan, J.; Long, D.-L.; Cronin, L. *Chem. Soc. Rev.* **2012**, *41*, 7403. (d) Song, Y.-F.; Tsunashima, R. *Chem. Soc. Rev.* **2012**, *41*, 7384. (e) Ammam, M. *J. Mater. Chem. A* **2013**, *1*, 6291.
- [5] (a) Rhule, J. T.; Hill, C. L.; Judd, D. A.; Schinazi, R. F. *Chem. Rev.* **1998**, *98*, 327. (b) Hasenknopf, B. *Front. Biosci.* **2005**, *10*, 275. (c) Yamase, T. *Prog. Mol. Subcell. Biol.* **2013**, *54*, 65. (d) Stroobants, K.; Absillis, G.; Moelants, E.; Proost, P.; Parac-Vogt, T. N. *Chem. Eur. J.* **2014**, *20*, 3894.
- [6] Berzelius, J. J. *Poggend. Ann. Phys. Chem.* **1826**, *6*, 369.
- [7] (a) De Luyart, F.; De Luyart, J. J. *Extractos de las Juntas Generales celebradas por la R.S.B.A.P.* **1783**, 46. (b) Román, P. *Los hermanos Delhuyar, la Bascongada y el Wolframio* R.S.B.A.P., Bilbao, 2000. (c) Goya, P.; Martín, N.; Román, P. *Nature Chemistry*, **2011**, *3*, 336.
- [8] Keggin, J. F. *Nature* **1933**, *132*, 351.
- [9] (a) Pope, M. T. in *Comprehensive Coordination Chemistry*; Wilkinson, G., Gillard, R.D., McCleverty, J.A., Eds.; Pergamon Press: New York, NY, USA, 1987; pp. 1023-1058. (b) *Polyoxometalates: from Platonic Solids to Anti Retroviral Activity*; Pope, M. T., Müller, A., Eds.; Kluwer: Dordrecht, The Netherlands, 1994. (c) Pope, M. T. in *Encyclopedia of Inorganic Chemistry*; King, R. B., Ed.; John Wiley & Sons: Chichester, UK, 1994; pp. 3361-3371.
- [10] (a) *Polyoxometalate Chemistry: From Topology via Self-Assembly to Applications*; Pope, M. T., Müller, A., Eds.; Kluwer: Dordrecht, The Netherlands, 2001. (b) *Polyoxometalate Chemistry for Nano-Composite Design*; Yamase, T., Pope, M. T., Eds.; Kluwer: Dordrecht, The Netherlands, **2002**. (c) *Polyoxometalate Molecular Science*; Borrás-Almenar, J. J., Coronado, E., Müller, A., Pope, M. T., Eds.; Kluwer: Dordrecht, The Netherlands, 2003. (d) Pope, M. T. in *Comprehensive Coordination Chemistry II*; McCleverty, J. A., Meyer, T. J., Eds.; Elsevier: Oxford, UK, 2004; pp. 1023-1058. (e) *Complexity in Chemistry and Beyond: Interplay Theory and Experiments*; Hill, C. L., Musaev, D. G., Eds.; Springer: Dordrecht, The Netherlands, 2012. (e) *Polyoxometalate Chemistry: Some Recent Trends*; Sécheresse, F., Ed.; World Scientific: Singapore, 2013.
- [11] Special monographic issues on POMs: (a) Hill, C. L., Ed. *Chem. Rev.* **1998**, *98*, issue 1. (b) Kortz, U., Ed. *Eur. J. Inorg. Chem.* **2009**, issue 34. (c) De-Liang, L.; Cronin, L., Eds. *Dalton Trans.* **2012**, *41*, issue 33. (d) Cronin, L.; Müller, A., Eds. *Chem. Soc. Rev.* **2012**, *41*, issue 22. (e) Kortz, U.; Liu, T., Eds. *Eur. J. Inorg. Chem.* **2013**, issue 10-11.
- [12] (a) Richmond, C. J.; Miras, H. N.; Ruiz de la Oliva, A.; Zhang, H.; Sans, V.; Paramonov, L.; Makatsoris, C.; Inglis, R.; Brechin, E. K.; Long, D.-L.; Cronin, L. *Nature Chem.* **2012**, *4*, 1037. (b) Symes, M. D.; Kitson, P. J.; Yan, J.; Richmond, C. J.; Cooper, G. J. T.; Bowman, R. W.; Vilbrandt, T.; Cronin, L. *Nature Chem.* **2012**, *4*, 349.

- [13] (a) Lindqvist, I.; Aronsson, B. *Ark. Kemi* **1953**, *7*, 49. (b) Filipowitz, M.; Ho, R. K. C.; Klemperer, W. G.; Shum, W. *Inorg. Chem.* **1979**, *18*, 93. (c) Nyman, M.; Bonhomme, F.; Alam, T. M.; Rodriguez, M. A.; Cherry, B. R.; Krumhansl, J. L.; Nenoff, T. M.; Sattler, A. M. *Science* **2002**, *297*, 996. (e) Nyman, M. *Dalton Trans.* **2011**, *40*, 8049.
- [14] Izarova, N. V.; Pope, M. T.; Kortz, U. *Angew. Chem. Int. Ed.* **2012**, *51*, 9492.
- [15] (a) Nyman, M.; Burns, P. C. *Chem. Soc. Rev.* **2012**, *41*, 7354. (b) Qiu, J.; Burns, P. *Chem. Rev.* **2013**, *113*, 1097.
- [16] Lipscomb, W. N. *Inorg. Chem.* **1965**, *4*, 132.
- [17] Müller, A.; Krickemeyer, E.; Meyer, J.; Bögge, H.; Peters, F.; Plass, W.; Diemann, E.; Dillinger, S.; Nonnenbruch, F.; Randerath, M.; Menke, C. *Angew. Chem. Int. Ed. Engl.* **1995**, *34*, 2122.
- [18] Scäffer, C.; Merca, A.; Bögge, H.; Todea, A. M.; Kistler, M. L.; Liu, T.; Thouvenot, R.; Gouzerh, P.; Müller, A. *Angew. Chem. Int. Ed.* **2009**, *48*, 149.
- [19] Müller, A.; Beckmann, E.; Bögge, H.; Schmidtman, M.; Dress, A. *Angew. Chem. Int. Ed.* **2002**, *41*, 1162.
- [20] (a) Poblet, J. M.; López, X.; Bo, C. *Chem. Soc. Rev.* **2003**, *32*, 297. (b) López, X.; Carbó, J. J.; Bo, C.; Poblet, J. M. *Chem. Soc. Rev.* **2012**, *41*, 7537.
- [21] (a) Román, P.; Aranzabe, A.; Luque, A.; Gutiérrez-Zorrilla, J. M.; Martínez-Ripoll, M. *J. Chem. Soc., Dalton Trans.* **1995**, 2225. (b) Wéry, A. S. J.; Gutiérrez-Zorrilla, J. M.; Luque, A.; Román, P. *Polyhedron*, **1996**, *15*, 4555.
- [22] (a) Lindqvist, I. *Acta Crystallogr.* **1950**, *3*, 159. (b) Fuchs, J.; Freiwald, W.; Hartl, H. *Acta Crystallogr.* **1976**, *B32*, 740. (c) Fuchs, J.; Flindt, E. P. Z. *Naturforsch.* **1979**, *34b*, 412. (d) Chae, H. K.; Klemperer, W. G.; Day, V. W. *Inorg. Chem.* **1992**, *31*, 3187. (e) Rheingold, A. L.; White, C. B.; Haggerty, B. S.; Maatta, E. A. *Acta Crystallogr.* **1993**, *C49*, 756. (f) Gutiérrez-Zorrilla, J. M.; Yamase, Y.; Sugeta, M. *Acta Crystallogr.* **1994**, *C50*, 196.
- [23] Lindqvist, I. *Acta Crystallogr.* **1952**, *5*, 667.
- [24] (a) Román, P.; San José, A.; Luque, A.; Gutiérrez-Zorrilla, J. M. *Inorg. Chem.* **1993**, *32*, 775. (b) Wéry, A. S. J.; Gutiérrez-Zorrilla, J. M.; Luque, A.; Ugalde, M.; Román, P. *Chem. Mater.* **1996**, *8*, 408. (c) Müller, A.; Sessoli, R.; Krickemeyer, E.; Bögge, H.; Gatteschi, D.; Pardi, L.; Westphal, J.; Hovemeier, K.; Rohlfing, R.; Döring, J.; Hellweg, F.; Beugholt, C.; Schmidtman, M. *Inorg. Chem.* **1997**, *36*, 5239.
- [25] (a) Evans, H. T., Jr. *J. Am. Chem. Soc.* **1948**, *70*, 1291. (b) Evans, H. T., Jr. *Acta Crystallogr.* **1974**, *B30*, 2095. (c) Perloff, A. *Inorg. Chem.* **1970**, *9*, 2228. (d) Lee, U.; Ichida, H.; Kobayashi, A.; Sasaki, Y. *Acta Crystallogr.* **1984**, *C40*, 5.
- [26] Dawson, B. *Acta Crystallogr.* **1953**, *6*, 113.
- [27] Tézé, A.; Hervé, G. *Inorg. Synth.* **1990**, *27*, 85.
- [28] Casey, W. H. *Chem. Rev.* **2006**, *106*, 1.
- [29] (a) Mialane, P.; Dolbecq, A.; Lisnard, L.; Mallard, A.; Marrot, J.; Sécheresse, F. *Angew. Chem. Int. Ed.* **2002**, *41*, 2398. (b) El Moll, H.; Nohra, B.; Mialane, P.; Marrot, J.; Dupré, N.; Riflade, B.; Malacria, M.; Thorimbert, S.; Hasenknopf, B.; Lacôte, E.; Aparicio, P. A.; López, X.; Poblet, J. M.; Dolbecq, A. *Chem. Eur. J.* **2011**, *17*, 14138.
- [30] (a) Pope, M. T. *Handb. Phys. Chem. Rare Earths* **2007**, *38*, 337. (b) Bassil, B. S.; Kortz, U. *Z. Anorg. Allg. Chem.* **2010**, *636*, 2222. (c) Oms, O.; Dolbecq, A.; Mialane, P. *Chem. Soc. Rev.* **2012**, *41*, 7497. (d) Zheng, S.-T.; Yang, G.-Y. *Chem. Soc. Rev.* **2012**, *41*, 7623.
- [31] Bösing, M.; Loose, I.; Pohlmann, H.; Krebs, B. *Chem. Eur. J.* **1997**, *3*, 1232.
- [32] Weakley, T. J. R. *Polyhedron* **1987**, *6*, 931.
- [33] (a) Gouzerh, P.; Proust, A. *Chem. Rev.* **1998**, *98*, 77. (b) Proust, A.; Thouvenot, R.; Gouzerh, P. *Chem. Commun.* **2008**, 1837. (c) Dolbecq, A.; Dumas, E.; Mayer, C. R.; Mialane, P. *Chem. Rev.* **2010**, *110*, 6009. (d) Wang, Y.; Weinstock, I. A. *Chem.*

- Soc. Rev.* **2012**, *41*, 7479. (e) Rinfray, C.; Izzet, G.; Pinson, J.; Derouich, S. G.; Ganem, J.-J.; Combellas, C.; Kanoufi, F.; Proust, A. *Chem. Eur. J.* **2013**, *19*, 13838.
- [34] Proust, A.; Matt, B.; Villanneau, R.; Guillemot, G.; Gouzerh, P.; Izzet, G. *Chem. Soc. Rev.* **2012**, *41*, 7605.
- [35] (a) Bar-Nahum, I.; Neumann, R. *Chem. Commun.* **2003**, 2690 (b) Bar-Nahum, I.; Cohen, H. Neumann, R. *Inorg. Chem.* **2003**, *42*, 3677. (c) Ott, L. S.; Finke, R. G. *Coord. Chem. Rev.* **2007**, *251*, 1075. (d) Berardi, S.; Carraro, M.; Iglesias, M.; Sartorel, A.; Scorraro, G.; Albrecht, M.; Bonchio, M. *Chem. Eur. J.* **2010**, *16*, 10662. (e) Putaj, P.; Lefebvre, F. *Coord. Chem. Rev.* **2011**, *255*, 1642.
- [36] Witte, P. T.; Chowdhury, S. R.; ten Elshof, J. E.; Sloboda-Rozner, D.; Neumann, R.; Alsters, P. L. *Chem. Commun.* **2005**, 1206.
- [37] (a) Bonchio, M.; Carraro, M.; Scorraro, G.; Bagno, A. *Adv. Synth. Catal.* **2004**, *346*, 648. (b) Yokohama, A.; Kojima, T.; Ohkubo, K.; Fukuzumi, S. *Chem. Commun.* **2007**, 3997. (c) Odobel, F.; Severac, M.; Pellegrin, Y.; Blart, E.; Fosse, C.; Cannizzo, C.; Mayer, C. R.; Elliott, K. J.; Harriman, A. *Chem. Eur. J.* **2009**, *15*, 3130. (d) Matt, B.; Renaudineau, S.; Chamoreau, L.-M.; Afonso, C.; Izzet, G.; Proust, A. *J. Org. Chem.* **2011**, *76*, 3107.
- [38] Knoth, W. H. *J. Am. Chem. Soc.* **1979**, *101*, 759.
- [39] (a) Duffort, V.; Thouvenot, R.; Afonso, C.; Izzet, G.; Proust, A. *Chem. Commun.* **2009**, 6062. (b) Odobel, F.; Séverac, M.; Pellegrin, Y.; Blart, E.; Fosse, C.; Cannizzo, C.; Mayer, C. R.; Elliot, K. J.; Harriman, A. *Chem. Eur. J.* **2009**, *15*, 3130. (c) Aoki, S.; Kurashina, T.; Kasahara, Y.; Nishijima, T.; Nomiya, K. *Dalton Trans.* **2011**, *40*, 1243.
- [40] (a) Mazeaud, A.; Ammari, N.; Robert, F.; Thouvenot, R. *Angew. Chem. Int. Ed. Eng.* **1996**, *35*, 1961. (b) Mayer, C. R.; Fournier, I.; Thouvenot, R. *Chem. Eur. J.* **2000**, *6*, 105. (c) Agustin, D.; Coelho, C.; Mazeaud, A.; Herson, P.; Proust, A.; Thouvenot, R. *Z. Anorg. Allg. Chem.* **2004**, *630*, 2049.
- [41] (a) Mayer, C. R.; Cabuil, V.; Lalot, T.; Thouvenot, R. *Angew. Chem. Int. Ed.* **1999**, *38*, 3672. (b) Mayer, C. R.; Neveu, S.; Cabuil, V. *Angew. Chem. Int. Ed.* **2002**, *41*, 501. (c) Canizzo, C.; Mayer, C. R.; Sécherresse, F.; Larpent, C. *Adv. Mater.* **2005**, 2888.
- [42] (a) Sazani, G.; Pope, M. T. *Dalton Trans.* **2004**, 1989. (b) Joo, N.; Renaudineau, S.; Delapierre, G.; Bidan, G.; Chamoreau, L.-M.; Thouvenot, R.; Gouzerh, P.; Proust, A. *Chem. Eur. J.* **2010**, *16*, 5043. (c) Nomiya, K.; Togashi, Y.; Kasahara, Y.; Aoki, S.; Seki, H.; Noguchi, M.; Yoshida, S. *Inorg. Chem.* **2011**, *50*, 9606. (d) Deroich, S. G.; Rinfray, C.; Izzet, G.; Pinson, J.; Gallet, J.-J.; Kanoufi, F.; Proust, A.; Combellas, C. *Langmuir* **2014**, *30*, 2287.
- [43] (a) Kwak, W.; Pope, M. T.; Scully, T. F. *J. Am. Chem. Soc.* **1975**, *97*, 5735. (b) Kim, G.-S.; Hagen, K. S.; Hill, C. L. *Inorg. Chem.* **1992**, *31*, 5316. (c) Mayer, C. R.; Thouvenot, R. *Dalton. Trans.* **1998**, 7. (d) Mayer, C. R.; Herson, P.; Thouvenot, R. *Inorg. Chem.* **1999**, *38*, 6152. (e) Yamase, T.; Makino, H.; Naruke, H.; Wéry, A. M. S. *J. Chem. Lett.* **2000**, *12*, 1350. (f) Carraro, M.; Sartorel, A.; Scorrano, G.; Maccato, C.; Dickman, M. H.; Kortz, U.; Bonchio, M. *Angew. Chem. Int. Ed.* **2008**, *47*, 7275. (f) Breen, J. M.; Schmitt, W. *Angew. Chem. Int. Ed.* **2008**, *47*, 6904.
- [44] Hymann, D., Ed. *Curr. Pharm. Des.* **2010**, *16*, issue 27. (special issue)
- [45] Banerjee, A.; Bassil, B. S.; Röschenhaler, G.-V.; Kortz, U. *Chem. Soc. Rev.* **2012**, *41*, 7590.
- [46] (a) Bonavia, G.; Haushalter, R. C.; O'Connor, C. J.; Zubieta, J. *Inorg. Chem.* **1996**, *35*, 5603. (b) Dolbecq, A.; Compain, J. D.; Mialane, P.; Marrot, J.; Sécherresse, F.; Keita, B.; Holzle, L. R. B.; Miserque, F.; Nadjo, L. *Chem. Eur. J.* **2009**, *15*, 733. (c) Compain, J. C.; Mialane, P.; Marrot, J.; Sécherresse, F.; Zhu, W.; Oldfield, E.; Dolbecq, A. *Chem. Eur. J.* **2010**, *16*, 13741. (d) Banerjee, A.; Raad, F. S.; Vankova, N.; Bassil, B. S.; Heine, T.; Kortz, U. *Inorg. Chem.* **2011**, *50*, 11667. (e) El Moll, H.; Dolbecq, A.; Marrot, J.; Rousseau, G.; Haouas, M.; Taulelle, F.; Rogez, G.; Wernsdorfer, W.; Keita, B.; Mialane, P.; *Chem. Eur. J.* **2012**, *18*, 3845. (f) El Moll, H.; Rousseau, G.; Dolbecq, A.; Oms, O.; Marrot, J.; Haouas, M.; Taulelle, F.; Rivière, E.; Wernsdorfer, W.; Lachkar, D.; Lacôte, E.; Keita, B.; Mialane, P. *Chem Eur. J.* **2013**, *19*, 6753.
- [47] (a) Knoth, W. H. *J. Am. Chem. Soc.* **1979**, *101*, 2211. (b) Knoth, W. H.; Domaille, P. J.; Roe, D. C. *Inorg. Chem.* **1983**, *22*, 818. (c) Wang, X. H.; Dai, H. C.; Liu, J. F. *Polyhedron* **1999**, *18*, 2293. (d) Wang, X. H.; Liu, J. F. *J. Coord. Chem.* **2000**, *51*, 73.

[48] (a) Zonnevijlle, F.; Pope, M. T. *J. Am. Chem. Soc.* **1979**, *101*, 2211. (b) Xin, F.; Pope, M. T.; Long, G. J.; Russo, U. *Inorg. Chem.* **1996**, *35*, 1207. (c) Sazani, G.; Dickman, M. H.; Pope, M. T. *Inorg. Chem.* **2000**, *39*, 939. (d) Belai, N.; Pope, M. T. *Polyhedron* **2006**, *25*, 2015.

[49] (a) Bareyt, S.; Piligkos, S.; Hasenknopf, B.; Gouzerh, P.; Lacôte, E.; Thorimbert, S.; Malacria, M. *Angew. Chem. Int. Ed.* **2003**, *42*, 3404. (b) Bareyt, S.; Piligkos, S.; Hasenknopf, B.; Gouzerh, P.; Lacôte, E.; Thorimbert, S.; Malacria, M. *J. Am. Chem. Soc.* **2005**, *127*, 6788. (c) Boglio, C.; Micoine, K.; Derat, E.; Thouvenot, R.; Hasenknopf, B.; Thorimbert, S.; Lacôte, E.; Malacria, M. *J. Am. Chem. Soc.* **2008**, *130*, 4553. (d) Micoine, K.; Hasenknopf, B.; Thorimbert, S.; Lacôte, E.; Malacria, M. *Angew. Chem. Int. Ed.* **2009**, *48*, 3466.

[50] (a) Hussain, F.; Kortz, U.; Clark, R. J. *Inorg. Chem.* **2004**, *43*, 3237. (b) Hussain, F.; Kortz, U. *Chem. Commun.* **2005**, 1191. (c) Hussain, F.; Kortz, U.; Keita, B.; Nadjo, L.; Pope, M. T. *Inorg. Chem.* **2006**, *45*, 761.

[51] (a) Kortz, U.; Hussain, F.; Reicke, M. *Angew. Chem. Int. Ed.* **2005**, *44*, 3773. (b) Keita, B.; de Oliveira, P.; Nadjo, L.; Kortz, U. *Chem. Eur. J.* **2007**, *13*, 5480.

[52] (a) Reinoso, S.; Dickman, M. H.; Kortz, U. *Inorg. Chem.* **2006**, *45*, 10422. (b) Reinoso, S.; Dickman, M. H.; Reicke, M.; Kortz, U. *Inorg. Chem.* **2006**, *45*, 9014. (c) Piedra-Garza, L. F.; Reinoso, S.; Dickman, M. H.; Sanguinetti, M. M.; Kortz, U. *Dalton Trans.* **2009**, 6231. (d) Reinoso, S.; Dickman, M. H.; Kortz, U. *Eur. J. Inorg. Chem.* **2009**, 947.

[53] (a) Piedra-Garza, L. F.; Dickman, M. H.; Moldovan, O.; Breunig, H. J.; Kortz, U. *Inorg. Chem.* **2009**, *48*, 411. (b) Barsukova-Stuckart, M.; Piedra-Garza, L. F.; Gautam, B.; Alfaro-Espinoza, G.; Izarova, N. V.; Banerjee, A.; Bassil, B. S.; Ullrich, M. S.; Breuning, H. J.; Silvestru, C.; Kortz, U. *Inorg. Chem.* **2012**, *51*, 12015.

[54] (a) Marcoux, P. R.; Hasenknopf, B.; Vaissermann, J.; Gouzerh, P. *Eur. J. Inorg. Chem.* **2003**, 2406. (b) Song, Y.-F.; Long, D.-L.; Cronin, L. *Angew. Chem. Int. Ed.* **2007**, *46*, 3900. (c) Song, Y.-F.; McMillan, N.; Long, D.-L.; Thiel, J.; Ding, Y.; Chen, H.; Gadegaard, N.; Cronin, L. *Chem. Eur. J.* **2008**, *14*, 2349. (d) Song, Y.-F.; Long, D.-L.; Cronin, L. *CrystEngComm* **2010**, *12*, 109. (e) Santoni, M.-P.; Pal, A. K.; Hanan, G. S.; Proust, A.; Hasenknopf, B. *Inorg. Chem.* **2011**, *50*, 6737. (f) Thiel, J.; Yang, D.; Rosnes, M. H.; Liu, X.; Yvon, C.; Kelly, S. E.; Song, Y.-F.; Long, D.-L.; Cronin, L. *Angew. Chem. Int. Ed.* **2011**, *50*, 8871. (g) Hutin, M.; Yvon, C.; Yan, J.; Macdonell, A.; Long, D.-L.; Cronin, L. *CrystEngComm* **2013**, *15*, 4422. (h) Tong, US.; Chen, W.; Ritchie, C.; Wang, X.; Song, Y.-F. *Chem. Eur. J.* **2014**, *20*, 1500.

[55] (a) Favette, S.; Hasenknopf, B.; Vaissermann, J.; Gouzerh, P.; Roux, C. *Chem. Commun.* **2003**, 2664. (b) Allain, C.; Favette, S.; Chamoreau, L.-M.; Vaissermann, J.; Ruhlmann, L.; Hasenknopf, B. *Eur. J. Inorg. Chem.* **2008**, 3433. (c) Zhang, J.; Song, Y.-F.; Cronin, L.; Liu, T. *J. Am. Chem. Soc.* **2008**, *130*, 14409. (d) He, Z.; Yan, Y. Y.; Li, B.; Ai, H.; Wang, H.; Li, H.; Wu, L. *Dalton Trans.* **2012**, *41*, 10043. (e) Yue, L.; Ai, H.; Yang, Y.; Lu, W.; Wu, L. *Chem. Commun.* **2013**, *49*, 9770. (f) Tong, US.; Chen, W.; Ritchie, C.; Wang, X.; Song, Y.-F. *Chem. Eur. J.* **2014**, *20*, 1500.

[56] Hasenknopf, B.; Delmont, R.; Herson, P.; Gouzerh, P. *Eur. J. Inorg. Chem.* **2002**, 1081.

[57] (a) Song, Y.-F.; Long, D.-L.; Kelly, S. E.; Cronin, L. *Inorg. Chem.* **2008**, *47*, 9137. (b) Rosnes, M. H.; Musumeci, C.; Pradeep, C. P.; Mathieson, J. S.; Long, D.-L.; Song, Y.-F.; Pignataro, B.; Cogdell, R.; Cronin, L. *J. Am. Chem. Soc.* **2010**, *132*, 15490. (c) Wu, P.; Yin, P.; Zhang, J.; Hao, J.; Xiao, Z.; Wei, Y. *Chem. Eur. J.* **2011**, *17*, 12002. (d) Oms, O.; Hakouk, K.; Dessap, R.; Deniard, P.; Jobic, S.; Dolbecq, A.; Palacin, T.; Nadjo, L.; Keita, B.; Marrot, J.; Mialane, P. *Chem. Commun.* **2012**, *48*, 12103.

[58] (a) Chen, Q.; Goshorn, D. P.; Scholes, C. P.; Tan, X.-L.; Zubieta, J. *J. Am. Chem. Soc.* **1992**, *114*, 4667. (b) Han, J. W.; Hill, C. L. *J. Am. Chem. Soc.* **2007**, *129*, 15094. (c) Wu, P.; Xiao, Z.; Zhang, J.; Hao, J.; Chen, J.; Yin, P.; Wei, Y. *Chem. Commun.* **2011**, *47*, 5557. (d) Yin, P.; Wu, P.; Xiao, Z.; Li, D.; Bitterlich, E.; Zhang, J.; Cheng, P.; Vezenov, D. V.; Liu, T.; Wei, Y. *Angew. Chem. Int. Ed.* **2011**, *50*, 2521. (e) Li, D.; Song, J.; Yin, P.; Simotwo, S.; Bassler, A. J.; Aung, Y.; Roberts, J. E.; Hardcastle, K. I.; Hill, C. L.; Liu, T. *J. Am. Chem. Soc.* **2011**, *133*, 14010. (f) Santoni, M.-P.; Pal, A. K.; Hanan, G. S.; Tang, M.-C.; Venne, K.; Furtos, A.; Ménard-Tremblay, P.; Malveau, C.; Hasenknopf, B. *Chem. Commun.* **2012**, *48*, 200.

[59] Müller, A.; Meyer, J.; Mögge, H.; Stämmler, A.; Botar, A. Z. *Anorg. Allg. Chem.* **1995**, *621*, 1818.

[60] Pradeep, C. P.; Long, D.-L.; Newton, G. N.; Song, Y.-F.; Cronin, L. *Angew. Chem. Int. Ed.* **2008**, *47*, 4388.

- [61] (a) Pradeep, C. P.; Misdrahi, M. F.; Li, F.-Y.; Zhang, J.; Xu, L.; Long, D.-L.; Liu, T.; Cronin, L. *Angew. Chem. Int. Ed.* **2009**, *48*, 8309. (b) Yin, P.; Li, T.; Forgan, R. S.; Lydon, C.; Zuo, X.; Zheng, Z. N.; Lee, B.; Long, D.-L.; Cronin, L.; Liu, T. *J. Am. Chem. Soc.* **2013**, *135*, 13425.
- [62] (a) Zeng, H.; Newkome, G. R.; Hill, C. L. *Angew. Chem. Int. Ed.* **2000**, *39*, 1772. (b) Azcarate, I.; Ahmed, I.; Farha, R.; Goldmann, M.; Wang, X.; Xu, H.; Hasenknopf, B.; Lacôte, E.; Ruhlmann, L. *Dalton Trans.* **2013**, *42*, 12688. (c) Miao, W.-K.; Yan, Y.-K.; Wang, X.-L.; Xiao, Y.; Ren, L.-J.; Zheng, P.; Wang, C.-H.; Ren, L.-X.; Wang, W. *ACS Macro Lett.* **2014**, *3*, 211.
- [63] Li, J.; Huth, I.; Chamoreau, L.-M.; Hasenknopf, B.; Lacôte, E.; Thorimbert, S.; Malacria, M. *Angew. Chem. Int. Ed.* **2009**, *48*, 2035.
- [64] (a) Kortz, U.; Savelieff, M. G.; Ghali, F. Y. A.; Khalil, L. M.; Maalouf, S. A.; Sinno, D. I. *Angew. Chem. Int. Ed.* **2002**, *41*, 4070. (b) Chen Z.; An, H.; Zhang, H.; Hu, Y. *CrystEngComm* **2013**, *15*, 4711. (c) Yang, D.; Li, S.; Ma, P.; Wang, J.; Niu, J. *Inorg. Chem.* **2013**, *52*, 14034. (d) Yan, D.; Liang, Y.; Ma, P.; Li, S.; Wang, J.; Niu, J. *Inorg. Chem.* **2014**, *53*, 3048.
- [65] (a) Kang, H.; Zubieta, J. *J. Chem. Soc., Chem. Commun.* **1988**, 1192. (b) Du, Y.; Rheingold, A. L.; Maatta, E. A. *J. Am. Chem. Soc.* **1992**, *114*, 345.
- [66] Strong, J. B.; Yap, G. P.A.; Ostrander, R.; Liable-Sands, L. M.; Rheingold, A. L.; Thouvenot, R.; Gouzerh, P.; Maatta, E. A. *J. Am. Chem. Soc.* **2000**, *122*, 639.
- [67] Moore, A. R.; Kwen, H.; Beatty, A. M.; Maatta, E. A. *Chem. Commun.* **2000**, 1793.
- [68] (a) Wei, Y.; Xu, B.; Barnes, C. L.; Peng, Z. *J. Am. Chem. Soc.* **2001**, *123*, 4083. (b) Xu, B.; Wei, Y.; Barnes, C. L.; Peng, Z. *Angew. Chem. Int. Ed.* **2001**, *40*, 2290. (c) Xu, L.; Lu, M.; Xu, B.; Wei, Y.; Peng, Z.; Powell, D. R. *Angew. Chem. Int. Ed.* **2002**, *41*, 4129. (d) Lu, M.; Wei, Y.; Xu, B.; Cheung, C. F.-C.; Peng, Z.; Powell, D. R. *Angew. Chem. Int. Ed.* **2002**, *41*, 1566. (e) Kang, J.; Xu, B.; Peng, Z.; Zhu, X.; Wei, Y.; Powell, D. R. *Angew. Chem. Int. Ed.* **2005**, *44*, 6902. (f) Li, Q.; Wei, Y.; Hao, J.; Zhu, Y.; Wang L. *J. Am. Chem. Soc.* **2007**, *129*, 5810.
- [69] Hao, J.; Xia, Y.; Wang, L.; Ruhlmann, L.; Zhu, Y.; Li, Q.; Yin, P.; Wei, Y.; Guo, H. *Angew. Chem. Int. Ed.* **2008**, *47*, 2626.
- [70] (a) Xue, S.; Ke, S.; Yan, L.; Cai, Z.; Wei, Y. *J. Inorg. Biochem.* **2005**, *99*, 2276. (b) Xue, S.; Chai, A.; Cai, Z.; Wei, Y.; Xiang, C.; Bian, W.; Shen, J. *Dalton Trans.* **2008**, 4770. (c) Xue, S.; Xiang, C.; Wei, Y.; Tao, Z.; Chai, A.; Bian, W.; Xu, Z. *Cryst. Growth Des.* **2008**, *8*, 2437.
- [71] (a) Zhang, J.; Hao, J.; Wei, Y.; Xia, F.; Yin, P.; Wang, L. *J. Am. Chem. Soc.* **2010**, *132*, 14. (b) Zhang, J.; Yin, P.; Hao, J.; Xiao, F.; Chen, L.; Wei, Y. *Chem. Eur. J.* **2012**, *18*, 13596.
- [72] (a) Hsieh, T.-C.; Zubieta, J. *Inorg. Chem.* **1985**, *24*, 1287. (b) Kwen, H.; Young, V. G.; Maatta, E. A. *Angew. Chem. Int. Ed.* **1999**, *38*, 1145. (c) Bustos, C.; Hasenknopf, B.; Thouvenot, R.; Vaissermann, J.; Proust, A.; Gouzerh, P. *Eur. J. Inorg. Chem.* **2003**, 2757.
- [73] (a) Warren, C. J.; Haushalter, R. C.; Rose, D. J.; Zubieta, J. *Chem. Mater.* **1997**, *9*, 2694. (b) Zapf, P.; Haushalter, R. C.; Zubieta, J. *Chem. Mater.* **1997**, *9*, 2019. (c) Hagrman, D.; Zubieta, C.; Rose, D. J.; Zubieta, J.; Haushalter, R. C. *Angew. Chem. Int. Ed. Engl.* **1997**, *36*, 873. (d) Hagrman, P. L.; Hagrman, D.; Zubieta, J. *Angew. Chem. Int. Ed.* **1999**, *38*, 2638.
- [74] (a) Reinoso, S. *Complejos Dinucleares Cobre(II)-Carboxilato Puente Soportados Sobre Polioxometalatos Tipo Keggin*; Ph.D. Thesis, Universidad del País Vasco UPV/EHU, Leioa, Spain, May 2005. (b) Reinoso, S.; Vitoria, P.; San Felices, L.; Lezama, L.; Gutiérrez-Zorrilla, J. M. *Chem. Eur. J.* **2005**, *11*, 1538. (c) Reinoso, S.; Vitoria, P.; Gutiérrez-Zorrilla, J. M.; Lezama, L.; San Felices, L.; Beitia, J. I. *Inorg. Chem.* **2005**, *44*, 9731. (d) Reinoso, S.; Vitoria, P.; San Felices, L.; Lezama, L.; Gutiérrez-Zorrilla, J. M. *Inorg. Chem.* **2006**, *45*, 108. (e) Reinoso, S.; Vitoria, P.; Gutiérrez-Zorrilla, J.-M.; Lezama, L.; Madariaga, J. M.; San Felices, L.; Iturrospe, A. *Inorg. Chem.* **2007**, *46*, 4010. (f) Reinoso, S.; Vitoria, P.; San Felices, L.; Montero, A.; Lezama, L.; Gutiérrez-Zorrilla, J. M. *Inorg. Chem.* **2007**, *46*, 1237.
- [75] (a) San Felices, L. *Interacción de Heteropolianiones de Wolframio y Silicio, Germanio o Fósforo con Complejos de Cobre: Síntesis, Caracterización Química y Estructural y Estudio Topológico* Ph.D. Thesis, Universidad del País Vasco UPV/EHU, Leioa, October 2009. (b) San Felices, L.; Vitoria, P.; Gutiérrez-Zorrilla, J. M.; Lezama, L.; Reinoso, S. *Inorg. Chem.* **2006**, *45*,

7748. (c) Iturraspe, A. *Síntesis, Caracterización Química y Estudio Estructural de Sistemas Basados en Heteropolianiones de Wolframio y Silicio o Germanio y Complejos de Cobre con Ligandos N4-Tetradentados*. Ph.D. Thesis, Universidad del País Vasco UPV/EHU, Leioa, April 2013.

[76] (a) Iturraspe, A.; Artetxe, B.; Reinoso, S.; San Felices, L.; Vitoria, P.; Lezama, L.; Gutiérrez-Zorrilla, J. M. *Inorg. Chem.* **2013**, *52*, 3084. (b) Iturraspe, A.; Reinoso, S.; San Felices, L.; Artetxe, B.; Lezama, L.; Gutiérrez-Zorrilla, J. M. *Cryst. Growth Des.* **2014**, *14*, 2318.

[77] (a) Rhule, J. T.; Neiwert, W. A.; Hardcastle, K. I.; Do, T.; Hill, C. L. *J. Am. Chem. Soc.* **2001**, *123*, 12101. (b) Bi, L.; Hussain, F.; Kortz, U.; Sadakane, M.; Dickman, M. H. *Chem. Commun.* **2004**, 1420. (c) An, H.-Y.; Wang, E.-B.; Xiao, D.-R.; Li, Y.-G.; Su, Z.-M.; Xu, L. *Angew. Chem. Int. Ed.* **2006**, *45*, 904. (d) Streb, C.; Ritchie, C.; Long, D.-L.; Kögerler, P.; Cronin, L. *Angew. Chem. Int. Ed.* **2007**, *46*, 7579. (e) Yokoyama, A.; Kojima, T.; Ohkubo, K.; Fukuzumi, S. *Chem. Commun.* **2007**, 3997. (f) Uchida, S.; Mizuno, N. *Coord. Chem. Rev.* **2007**, *251*, 2537. (g) Gao, G.-G.; Cheng, P.-S.; Mak, T. C. W. *J. Am. Chem. Soc.* **2009**, *131*, 18257.

[78] (a) Baker, L. C. W.; Figgis, J. S. *J. Am. Chem. Soc.* **1970**, *92*, 3794. (b) Liu, H.; Gómez-García, C. J.; Peng, J.; Sha, J.; Li, Y.; Yan, Y. *Dalton Trans.* **2008**, 6211. (c) Liu, H.; Gómez-García, C. J.; Peng, J.; Sha, J.; Wang, L.; Yan, Y. *Inorg. Chim. Acta* **2009**, *362*, 1957.

[79] (a) Rong, C.; Pope, M. T. *J. Am. Chem. Soc.* **1992**, *114*, 2932. (b) Rong, C.; So, H.; Pope, M. T. *Eur. J. Inorg. Chem.* **2009**, 5211. (c) Lahootun, V. L.; Besson, C.; Villanneau, R.; Villain, F.; Chamoreau, L.-M.; Boubekeur, K.; Blanchard, S.; Thouvenot, R.; Proust, A. *J. Am. Chem. Soc.* **2007**, *129*, 7127.

[80] (a) Zheng, S.-T.; Wang, M.-H.; Yang, G.-Y. *Chem. Asian J.* **2007**, *2*, 1380. (b) Zhao, J.-W.; Li, B.; Zheng, S.-T.; Yang, G.-H. *Cryst. Growth Des.* **2007**, *7*, 2658. (c) Cui, R.-R.; Wang, H.-L.; Yang, X.-Y.; Ren, S.-H.; Hu, H.-M.; Fu, F.; Wang, J.-W.; Xue, G.-L. *Chin. J. Chem.* **2007**, *25*, 176. (e) Zheng, S.-T.; Wang, M.-H.; Yang, G.-Y. *Chem. Asian J.* **2007**, *2*, 1380. (f) Liu, H.; Qin, C.; Wei, Y.-G.; Xu, L.; Gao, G.-G.; Li, F.-Y.; Qu, X.-S. *Inorg. Chem.* **2008**, *47*, 4166.

[81] (a) Belai, N.; Pope, M. T. *Chem. Commun.* **2005**, 5760. (b) Belai, N.; Kapoor, P. N.; Dickman, M. H.; Butcher, R. J.; Pope, M. T. *Eur. J. Inorg. Chem.* **2009**, 5215.

[82] Shi, Q.; Zhang, Z.-M.; Li, Y.-G.; Wu, Q.; Yao, S.; Wang, E.-B. *Inorg. Chem. Commun.* **2009**, *12*, 293.

[83] Ritchie, C.; Boyd, T.; Long, D.-L.; Ditzel, E.; Cronin, L. *Dalton Trans.* **2009**, 1587.

[84] (a) Hasenknopf, B.; Micoine, K.; Lacôte, E.; Thorimbert, S.; Malacria, M.; Thouvenot, R. *Eur. J. Inorg. Chem.* **2008**, 5001. (b) Du, D.-Y.; Yan, L.-K.; Su, Z.-M.; Li, S.-L.; Lan, Y.-Q.; Wang, E.-B. *Coord. Chem. Rev.* **2013**, *257*, 702.

[85] (a) Fang, X.; Anderson, T. M.; Hill, C. L. *Angew. Chem. Int. Ed.* **2005**, *44*, 3540. (b) Fang, X.; Anderson, T. M.; Hou, Y.; Hill, C. L. *Chem. Commun.* **2005**, 5044.

[86] (a) Rousseau, G.; Oms, O.; Dolbecq, A.; Marrot, J.; Mialane, P. *Inorg. Chem.* **2011**, *50*, 7376. (b) Rousseau, G.; Rivière, E.; Dolbecq, A.; Marrot, J.; Oms, O.; Mialane, P. *Eur. J. Inorg. Chem.* **2013**, 1793.

[87] (a) Wassermann, K.; Lunk, H.-J.; Palm, R.; Fuchs, J.; Steinfeldt, N.; Stösser, R.; Pope, M. T. *Inorg. Chem.* **1996**, *35*, 3273. (b) Godin, B.; Chen, Y.-G.; Vaissermann, J.; Ruhlmann, L.; Verdaguer, M.; Gouzerh, P. *Angew. Chem. Int. Ed.* **2005**, *44*, 3072. (c) Botar, B.; Kögerler, P.; Hill, C. L. *Inorg. Chem.* **2007**, *46*, 5398. (d) Lisnard, L.; Mialane, P.; Dolbecq, A.; Marrot, J.; Clemente-Juan, J. M.; Coronado, E.; Keita, B.; de Oliveira, P.; Nadjó, L.; Sécheresse, F. *Chem. Eur. J.* **2007**, *13*, 3525. (e) Pichon, C.; Mialane, P.; Dolbecq, A.; Marrot, J.; Rivière, E.; Bassil, B. S.; Kortz, U.; Keita, B.; Nadjó, L.; Sécheresse, F. *Inorg. Chem.* **2008**, *47*, 11120. (f) Botar, B.; Ellern, A.; Kögerler, P. *Dalton Trans.* **2009**, 5606.

[88] (a) Errington, J. R.; Petkar, S. S.; Middleton, P. S.; McFarlane, W.; Clegg, W.; Coxall, R. A.; Harrington, R. W. *J. Am. Chem. Soc.* **2007**, *129*, 12181. (b) Errington, J. R.; Petkar, S. S.; Middleton, P. S.; McFarlane, W.; Clegg, W.; Coxall, R. A.; Harrington, R. W. *Dalton Trans.* **2007**, 5211. (c) Falber, A.; Burton-Pye, B. P.; Radivojevic, I.; Todaro, L.; Saleh, R.; Francesconi, L. C.; Drain, C. M. *Eur. J. Inorg. Chem.* **2009**, 2459. (d) Hirano, T.; Uehara, K.; Uchida, S.; Hibino, M.; Kamata, K.; Mizuno, N. *Inorg. Chem.* **2013**, *52*, 2662.

[89] (a) Zheng, S.-T.; Zhang, J.; Yang, G.-Y. *Angew. Chem. Int. Ed.* **2008**, *47*, 3909. (b) Zheng, S.-T.; Zhang, J.; Li, X.-X.; Fang, W.-H.; Yang, G.-Y. *J. Am. Chem. Soc.* **2010**, *132*, 15102. (c) Wang, X.; Liu, X.; Tian, A.; Ying, J.; Lin, H.; Liu, G.; Gao, Q. *Dalton Trans.* **2012**, *41*, 9587.

[90] (a) Zheng, S.-T.; Yuan, D.-Q.; Jia, H.-P.; Zhang, J.; Yang, G.-Y. *Chem. Commun.* **2007**, 1858. (b) Zhao, J.-W.; Jia, H.-P.; Zhang, J.; Zheng, S.-T.; Yang, G.-Y. *Chem. Eur. J.* **2007**, *13*, 10030. (c) Zhao, J.-W.; Wang, C.-M.; Zhang, J.; Zheng, S.-T.; Yang, G.-Y. *Chem. Eur. J.* **2008**, *14*, 9223. (d) Li, B.; Zhao, J.-W.; Zheng, S.-T.; Yang, G.-Y. *Inorg. Chem.* **2009**, *48*, 8294. (e) Zheng, S.-T.; Zhang, J.; Clemente-Juan, J. M.; Yuan, D.-Y.; Yang, G.-Y. *Angew. Chem. Int. Ed.* **2009**, *48*, 7176. (f) Zheng, Y.-Y.; Wen, R.; Kong, X.-J.; Long, L.-S.; Huang, R.-B.; Zheng, L.-S. *Dalton Trans.* **2012**, *41*, 9871.

Straightforward Organic Functionalization of Krebs-type Polyoxometalates

- 2.1. Introduction
- 2.2. Experimental section
- 2.3. Results and discussion
- 2.4. Conclusions
- 2.5. References

ABSTRACT: Reaction of 3d-metal disubstituted Krebs-type POMs with N,O-chelating ligands under mild conditions can result in the organic derivatization of the parent POM clusters via straightforward substitution of their labile aqua ligands. Carboxylate derivatives of aromatic, 5- or 6-membered N-heterocycles have been selected for performing systematic studies on the reactivity of disubstituted Krebs-type tungstoantimonates(III). These are 1H-imidazole-4-carboxylate (imc), 1H-pyrazole-3-carboxylate (pzc), picolinate (pic), pyridazine-3-carboxylate (pydc), pyrimidine-4-carboxylate (pymc) and pyrazine-2-carboxylate (pyzc). Nine hybrid derivatives have been synthesized as pure crystalline phases and characterized by elemental and thermal analyses, IR spectroscopy, and single-crystal X-ray diffraction (XRD). They all show the general formula $[\{ML(H_2O)_2(WO_2)_2(B-\beta-XW_9O_{33})_2\}]^{n-}$ and can be classified as follows: **1-SbM**, where L = imc, X = Sb, n = 12 and M = Mn, Co, Ni, Zn; **1-TeM**, where L = imc, X = Te, n = 10 and M = Mn, Co; **2-Ni**, where L = pzc, X = Sb, n = 12 and M = Ni; **3-M**, where L = pyzc, X = Sb, n = 12 and M = Co, Zn. All the reactions were monitored by IR spectroscopy because organic derivatization can be unequivocally determined using this technique prior to X-Ray diffraction studies. The solution stability of the frameworks was confirmed by 1H -NMR studies performed on the diamagnetic **1-SbZn** and **3-Zn**. Functionalization is strongly dependent on the nature of the ligand, in such a way that imc displays a "universal ligand" character, two of the ligands (pzc, pyzc) show selectivity toward specific 3d-metals, another two (pydc, pymc) promote partial decomposition of specific POM precursors to lead to $[ML_2(H_2O)_2]$ complexes, and pic showed to be inert under all conditions tested. Similarly, the results obtained from reactions carried out with some bridging ligands (pyrazine-2,3- (2,3- H_2 pyzdc) or 2,5-dicarboxylic acid (2,5- H_2 pyzdc) and 4,4'-bipyridine (4,4'-bpy)) are shown in the last part of this chapter. As observed for the N,O-chelating ligands, the organic functionalization is not trivial: 4,4'-bpy and 2,5-pyzdc are inert toward Krebs-type POMs, whereas 2,3-pyzdc showed selectivity toward the Ni-containing precursor. For the former ligand, a series of compounds containing pristine clusters and interstitial 4,4'-bpy molecules has been isolated as indicated by IR spectroscopy and X-ray analyses on the Mn-derivative (**4-Mn**). For the latter ligand, unexpected rearrangement of the POM framework takes place and the dimeric $[\mu-\{(2,3)\text{-pyzdc}\}_2\{Ni_2(H_2O)Sb_2W_{20}O_{70}\}_2]^{24-}$ (**5-Ni**) was obtained. The **5-Ni** hybrid is constituted by two novel $\{Ni_2Sb_2W_{20}O_{70}\}$ clusters bridged by two 2,3-pyrazinedicarboxylate ligands in ideal C_2 symmetry. The $\{Ni_2Sb_2W_{20}O_{70}\}$ cluster contains two $\{SbW_9O_{33}\}$ subunits connected by a $\{W_2O_{10}\}$ moiety whose linking mode transforms one of the rotated $\{W_3O_{13}\}$ trimers into an unprecedented $\{W_5O_{20}\}$ fragment. The magnetic properties and solution stability of **5-Ni** are discussed.

2.1. INTRODUCTION

Functionalization of POMs via covalent attachment of organic ligands to the inorganic metal-oxygen skeleton represents a suitable strategy to obtain hybrid derivatives with new properties and more selective applications.¹ As mentioned in the general introduction, the coordination of organic ligands to POM skeletons containing 3d- or 4f-metal centers with accessible positions in the coordination sphere is an efficient method for preparing functional POMs based materials with catalytically or magnetically active centers. Following this approach, 3d-metal substituted Krebs-type sandwich POMs could be ideal candidates for performing such ligand replacements because: i) they show 6 to 10 labile water molecules in accessible external positions; ii) they are stable in solution in a wide pH range and can be prepared in large amounts; iii) their structure allows to carry out systematic compositional variations.

In 1997, Krebs and co-workers reported the synthesis and structure of the parent $[\{WO_2(OH)\}_2(WO_2)_2(XW_9O_{33})_2]^{12-}$ anion composed of two $\{B-\beta-XW_9\}$ subunits linked by two inner *cis*- $\{WO_2\}$ and two outer *fac*- $\{WO_2(OH)\}$ octahedral groups, leading to a C_{2h} -symmetric assembly (Figure 2.1).² The latter groups are labile and can be easily exchanged for $\{M(H_2O)_3\}$ moieties, resulting in a large family of 3d-metal disubstituted species with general formula $[\{M(H_2O)_3\}_2(WO_2)_2(XW_9O_{33})_2]^{n-}$, where M can be Zn, Ni, Co^{II}, Fe^{III} or Mn^{II}, and X accounts for Sb^{III} or Bi^{III} (Figure 2.1.A).^{2,3} The inner positions have also been fully or partially exchanged for $\{M(H_2O)_2\}$ groups in several tri- and tetrasubstituted analogues (Figure 2.1.B),⁴ specially for certain heteroatoms (As^{III}, Te^{IV}, Se^{IV}) or metals (Fe^{III}, Cr^{III}, Al^{III}, In^{III}). Due to their interesting catalytic properties, Krebs-like clusters have been incorporated into functional materials in the formation of multilayer devices by layer-by-layer assembly techniques or polypyrrole films via POM immobilization.⁵ Highly efficient catalytic activity has been observed for tetra-iron-substituted Krebs POMs in the microwave-assisted oxygenation of cyclohexane and the bio-inspired oxidation of catechols, as well as for manganese-derivatives in the epoxidation of dienes.^{8b,6} The $[Al_4(H_2O)_{10}(X^{III}W_9O_{33})_2]^{6-}$ species (X=As, Sb) has been employed as Lewis acid catalyst in H₂O₂ based oxidations, whereas cobalt containing clusters have shown to be active in photosensitized water oxidation processes.^{3a,4e,7}

Despite their obvious potential as precursors in ligand replacement reactions, the organic functionalization of 3d-metal substituted Krebs-type POMs has remained largely unexplored as indicated by Dolbecq and coworkers in a recent review.^{1d} To our knowledge, only the oxalate derivatives of iron(III)-tetrasubstituted anions $[Fe^{III}_4(ox)_4(H_2O)_2(X^{III}W_9O_{33})_2]^{12-}$ can be found in the literature to date (X = As, Sb, Bi).⁸ Attempts for introducing some other functional groups at the external positions of the Krebs framework have also been reported in recent years. These include the catalytically active $\{Ru_4O_6(H_2O)_9\}$ group, the photoactive $\{M(CO)_3\}^{3+}$ (M^{III} = Re, Mn) moieties and different organo-ruthenium or -tin groups.⁹ Recently, mono- and di-lanthanide-containing clusters have been obtained for the smallest 4f-metals (Yb^{III}, Lu^{III}), which dispose in dimeric entities or one dimensional arrangements in the solid state, and show three coordinated water molecules on each 4f-metal center suitable for ligand substitution.¹⁰ Finally, it is also worth mentioning the DMSO-coordinated $[(W(dmsO)(OH))_2(XW_9O_{33})_2]^{8-}$ species, which show vacancies at external belt-sites.¹¹

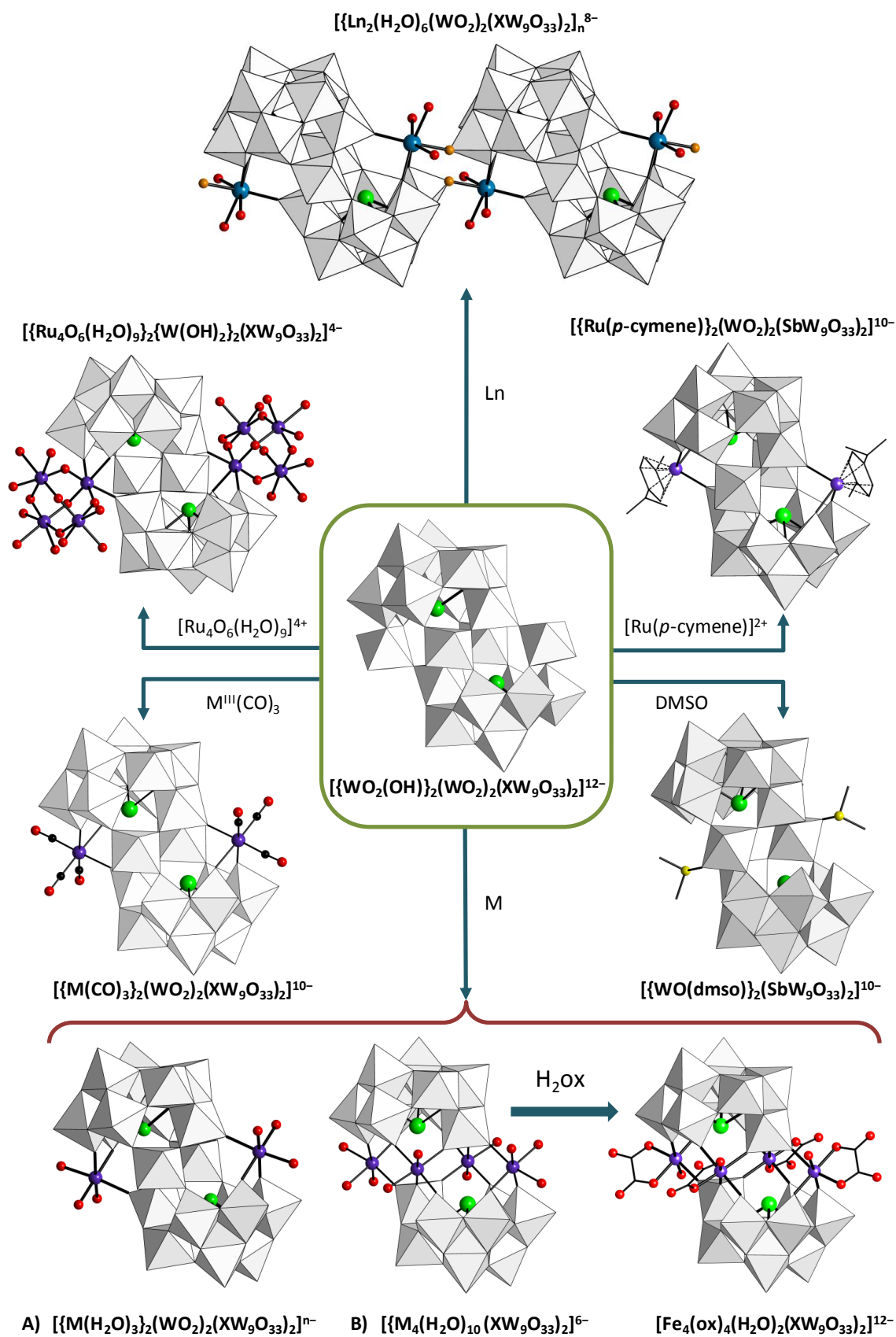
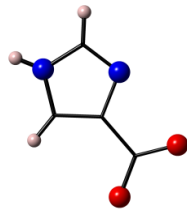
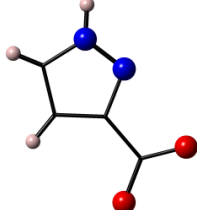
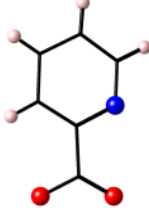
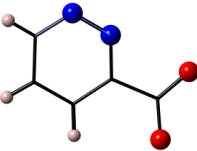
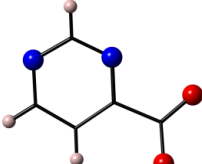
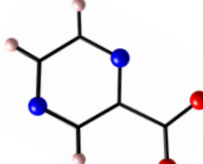
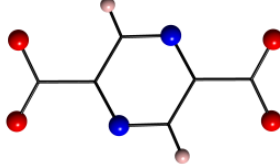
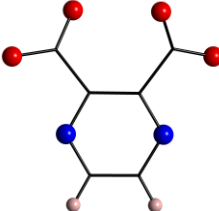
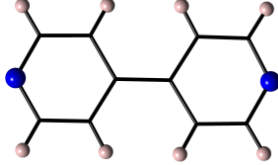


Figure 2.1. Structural diversity in Krebs-type POM derivatives.

Encouraged by the above, we decided to investigate the potential of 3d-metal disubstituted Krebs anions as precursors for preparing molecular hybrid clusters via replacement of their water molecules with organic ligands. Considering that previous reactions with aliphatic N,N-donor ligands like ethylenediamine did not prove to be successful,^{1b} we focused our studies on the reactivity of planar, aromatic O,N-chelating ligands (Table 2.1) toward Krebs type tungstoantimonates $[\{M(H_2O)_3\}_2(WO_2)_2(SbW_9O_{33})_2]^{10-}$ ($M = Mn^{II}, Co^{II}, Ni, Zn$). Carboxylate derivatives of 5- or 6-membered N-donor heterocycles were selected for this purpose, and more specifically, the diazolecarboxylates 1H-imidazole-4-carboxylic acid (Himc) and 1H-pyrazole-3-carboxylic acid (Hpzc); the picolinic acid (Hpic); and the diazinecarboxylates pyridazine-3-carboxylic acid (Hpydc), pyrimidine-4-carboxylic acid (Hpymc) and pyrazine-2-carboxylic acid (Hpyzc).

Table 2.1. Names, abbreviations and molecular structures of the organic ligands employed in this work.

<i>O,N-chelating ligands</i>		
<i>Diazolecarboxylates</i>		<i>Pyridinecarboxylate</i>
<i>imc</i>	<i>pzc</i>	<i>pic</i>
1H-Imidazole-4-carboxylate	1H-Pyrazole-3-carboxylate	Picolinate
		
<i>Diazinecarboxylates</i>		
<i>pydc</i>	<i>pymc</i>	<i>pyzc</i>
Pyridazine-3-carboxylate	Pyrimidine-4-carboxylate	Pyridazine-2-carboxylate
		
<i>Bridging ligands</i>		
<i>Pyrazinedicarboxylates</i>		<i>Bipyridine</i>
<i>2,5-pyzdc</i>	<i>2,3-pyzdc</i>	<i>4,4'-bpy</i>
Pyrazine-2,5-dicarboxylate	Pyrazine-2,3-dicarboxylate	4,4'-bipyridine
		

Three different synthetic approaches were initially evaluated using the imc ligand (methods 1, 2 and 3), whereas for the rest of organic molecules only methods 2 and 3 were tested after being identified as the most suitable. The imc ligand was also used to study the influence of the heteroatom on the reactivity of the Krebs-type anions by replacing Sb^{III} with Te^{IV}. This work has resulted in the isolation of nine hybrid derivatives of the Krebs-type structure, namely $[\{M(\text{imc})(\text{H}_2\text{O})\}_2(\text{WO}_2)_2(\text{XW}_9\text{O}_{33})_2]^{n-}$ (**1-XM**; X = Sb^{III} (n=12), M = Mn, Co, Ni, Zn; X = Te^{IV} (n=10), M = Mn, Co), $[\{\text{Ni}(\text{pzc})(\text{H}_2\text{O})\}_2(\text{WO}_2)_2(\text{SbW}_9\text{O}_{33})_2]^{12-}$ (**2-Ni**) and $[\{M(\text{pyzc})(\text{H}_2\text{O})\}_2(\text{WO}_2)_2(\text{SbW}_9\text{O}_{33})_2]^{12-}$ (**3-M**, M = Co, Zn). These compounds have been characterized by elemental analyses, infrared spectroscopy and thermogravimetry and their structures have been determined from single-crystal X-ray diffraction data. Their solution stability has also been analyzed by ¹H-NMR spectroscopy on the zinc-derivatives. Moreover, the transition metal complexes $[\text{Co}(\text{pzc})_2(\text{H}_2\text{O})_2]$ (**Co-pzc**), $[\text{M}(\text{pydc})_2(\text{H}_2\text{O})_2] \cdot 2\text{H}_2\text{O}$ (M = Co (**Co-pydc**), Ni (**Ni-pydc**)) and $[\text{Co}(\text{pymc})_2(\text{H}_2\text{O})_2] \cdot 2\text{H}_2\text{O}$ (**Co-pymc**) have also been isolated as crystalline products in the course of our systematic studies. A full characterization for these complexes is given in Appendix 1.

In the last section of this chapter, the results of some preliminary reactions of Krebs-type sandwich tungstoantimonates with the bridging organic ligands 4,4'-bipyridine (4,4'-bpy), 2,5-pyrazinedicarboxylic acid (2,5-H₂pyzdc) and 2,3-pyrazinedicarboxylic acid (2,3-H₂pyzdc) are compiled (Table 2.1). Compounds $\text{Na}_{10}[\text{Mn}_2(\text{H}_2\text{O})_6(\text{WO}_2)_2(\text{SbW}_9\text{O}_{33})_2] \cdot 2(4,4'\text{bpy}) \cdot 32\text{H}_2\text{O}$ (**4-Mn**) and $\text{Na}_{24}[\mu\text{-}\{(2,3)\text{pyzdc}\}_2\{\text{Ni}_2(\text{H}_2\text{O})\text{Sb}_2\text{W}_{20}\text{O}_{70}\}_2] \cdot 91\text{H}_2\text{O}$ (**5-Ni**) were obtained in those reactions. In addition to the techniques mentioned above, ESI mass spectrometric and magnetic studies have also been performed for **5-Ni**.

2.2. EXPERIMENTAL SECTION

2.2.1. Synthesis

Preparation of starting materials

The $[\text{B-}\alpha\text{-SbW}_9\text{O}_{33}]^{9-}$ POM precursor was synthesized according to reported procedures,² whereas all the 3d-metal disubstituted Krebs-type POMs were prepared as described for the Mn- or Zn-containing derivatives.^{3d} All the starting materials were identified by IR spectroscopy.

Na₉[B-α-SbW₉O₃₃]·20H₂O: Sb₂O₃ (1.96 g, 6.72 mmol) suspended in concentrated HCl (10 mL) was added dropwise to a solution of Na₂WO₄·2H₂O (40 g, 121.27 mmol) in water (80 mL) at 90 °C. The resulting mixture was refluxed for 1h, cooled to room temperature, filtered and left to evaporate. Crystals started forming immediately and were kept in their mother liquors for 6 days. Yield: 21 g, 55% based on W.

Na₁₀[M₂(H₂O)₆(WO₂)₂(B-β-SbW₉O₃₃)₂]·40H₂O, M^{II} = Mn, Co, Ni, Zn: The corresponding 3d metal salt (1.53 mmol; MnCl₂·4H₂O, 303 mg; CoCl₂·6H₂O, 364 mg; NiCl₂·6H₂O, 364 mg; or Zn(NO₃)₂·6H₂O, 456 mg) was added to a solution of Na₉[SbW₉O₃₃]·20H₂O (3 g, 1.02 mmol) in aqueous 1 M acetic acid/sodium acetate buffer (30 mL) at 40 °C. The reaction mixture was stirred at 40 °C for 1h and left to cool down to room temperature. Crystals were obtained by slow evaporation of the final solution after 10 days (Mn, orange; Co, purple; Ni, green, Zn, colorless). Yields: Mn, 2.1 g (37% based on W); Co, 1.1 g (19%); Ni, 1.7 g (30%); Zn, 1.5 g (26%).

General synthetic procedures

METHOD 1: To a hot solution of $\text{Na}_2\text{WO}_4 \cdot 2\text{H}_2\text{O}$ (1.32 g, 4.00 mmol) in aqueous 1 M acetic acid/sodium acetate buffer (40 mL), the heteroatomic source (0.40 mmol; SbCl_3 , 91 mg; TeO_2 , 64 mg) dissolved in 6M HCl (1 mL) and the corresponding 3d metal salt (0.40 mmol; $\text{MnCl}_2 \cdot 4\text{H}_2\text{O}$, 79 mg; $\text{CoCl}_2 \cdot 6\text{H}_2\text{O}$, 95 mg; $\text{NiCl}_2 \cdot 6\text{H}_2\text{O}$, 95 mg; or $\text{Zn}(\text{NO}_3)_2 \cdot 6\text{H}_2\text{O}$, 119 mg) were added successively. After stirring for 20 min at 90 °C, the organic ligand (0.40 mmol) was added and the resulting mixture was kept for 1 h at 90 °C.

METHOD 2: To a hot solution of $\text{Na}_{10}\{\text{M}(\text{H}_2\text{O})_3\}_2(\text{WO}_2)_2(\beta\text{-SbW}_9\text{O}_{33})_2 \cdot \sim 40\text{H}_2\text{O}$ (M = Mn, Co, Ni, Zn, 620 mg, 0.10 mmol) in aqueous 1 M acetic acid/sodium acetate buffer (30 mL) the organic ligand (0.20 mmol) was added. The resulting mixture was stirred for 1 h at 90 °C.

METHOD 3: To a hot solution of $\text{Na}_9[\alpha\text{-SbW}_9\text{O}_{33}] \cdot 20\text{H}_2\text{O}$ (251 mg, 0.10 mmol) in aqueous 1 M acetic acid/sodium acetate buffer (30 mL) the corresponding 3d metal salt (0.30 mmol; $\text{MnCl}_2 \cdot 4\text{H}_2\text{O}$, 59 mg; $\text{CoCl}_2 \cdot 6\text{H}_2\text{O}$, 71 mg; $\text{NiCl}_2 \cdot 6\text{H}_2\text{O}$, 71 mg; or $\text{Zn}(\text{NO}_3)_2 \cdot 6\text{H}_2\text{O}$, 89 mg) was added. After stirring for 10 min at 90 °C, the organic ligand (0.20 mmol) was added and the resulting mixture was kept for 1 h at 90 °C.

Hybrid Krebs-type POMs with N,O-chelating ligands**A) Functionalization with 1H-imidazole-4-carboxylate****i) Tungstoantimonates**

The hybrid compounds **1-SbM** (M = Mn, Co, Ni) can be prepared by following any of the three methods described above. Single crystals suitable for X-Ray diffraction were obtained by slow evaporation of the final solutions at room temperature. Best yields were obtained for method 3 with 1H-imidazole-4-carboxylic acid as ligand (22 mg).

$\text{Na}_{12}\{\text{Mn}(\text{imc})(\text{H}_2\text{O})\}_2(\text{WO}_2)_2(\text{SbW}_9\text{O}_{33})_2 \cdot 44\text{H}_2\text{O}$ (1-SbMn): orange, prismatic crystals were obtained after ca. 2 weeks (yield: 92 mg, 31% based on W). Anal. Calcd (found) for $\text{Na}_{12}\{\{\text{Mn}(\text{C}_4\text{H}_3\text{N}_2\text{O}_2)(\text{H}_2\text{O})\}_2\{\text{Mn}(\text{H}_2\text{O})_2\}_{0.4}(\text{WO}_2)_{1.6}(\text{SbW}_9\text{O}_{33})_2\} \cdot 44\text{H}_2\text{O}$, $\text{C}_8\text{H}_{99.6}\text{Mn}_{2.4}\text{N}_4\text{Na}_{12}\text{O}_{120}\text{Sb}_2\text{W}_{19.6}$: C, 1.50 (1.46); H, 1.56 (1.51); Mn, 2.05 (1.99); N, 0.87 (0.80); Na, 4.29 (4.51); Sb, 3.79 (4.14). IR (cm^{-1}): 1578 (m), 1501 (w), 1435 (w), 1389 (m), 1238 (w), 1223 (w), 1090 (w), 951 (s), 878 (s), 831 (vs), 808 (sh), 775 (sh), 658 (m), 521 (w).

$\text{Na}_{12}\{\text{Co}(\text{imc})(\text{H}_2\text{O})\}_2(\text{WO}_2)_2(\text{SbW}_9\text{O}_{33})_2 \cdot 44\text{H}_2\text{O}$ (1-SbCo): purple, prismatic crystals were obtained after ca. 2 weeks (yield: 70 mg, 25% based on W). Anal. Calcd (found) for $\text{Na}_{12}\{\{\text{Co}(\text{C}_4\text{H}_3\text{N}_2\text{O}_2)(\text{H}_2\text{O})\}_2\{\text{Co}(\text{H}_2\text{O})_2\}_{0.4}(\text{WO}_2)_{1.6}(\text{SbW}_9\text{O}_{33})_2\} \cdot 44\text{H}_2\text{O}$, $\text{C}_8\text{H}_{99.6}\text{Co}_{2.4}\text{N}_4\text{Na}_{12}\text{O}_{120}\text{Sb}_2\text{W}_{19.6}$: C, 1.49 (1.55); H, 1.56 (1.34); Co, 2.20 (2.03); N, 0.87 (0.86); Na, 4.29 (3.93); Sb, 3.78 (3.29). IR (cm^{-1}): 1578 (m), 1499 (w), 1431 (w), 1389 (m), 1236 (w), 1219 (w), 1088 (w), 949 (s), 872 (s), 833 (vs), 806 (sh), 770 (sh), 660 (m), 521 (w).

$\text{Na}_{12}\{\text{Ni}(\text{imc})(\text{H}_2\text{O})\}_2(\text{WO}_2)_2(\text{SbW}_9\text{O}_{33})_2 \cdot 44\text{H}_2\text{O}$ (1-SbNi): pale green, prismatic crystals were obtained after ca. 2 weeks (yield: 90 mg, 32% based on W). Anal. Calcd (found) for $\text{Na}_{12}\{\{\text{Ni}(\text{C}_4\text{H}_3\text{N}_2\text{O}_2)(\text{H}_2\text{O})\}_{1.8}\{\text{W}(\text{OH})\text{O}_2\}_{0.2}(\text{WO}_2)_2(\text{SbW}_9\text{O}_{33})_2\} \cdot 44\text{H}_2\text{O}$, $\text{C}_{7.2}\text{H}_{97.2}\text{N}_{3.6}\text{Na}_{12}\text{Ni}_{1.8}\text{O}_{120}\text{Sb}_2\text{W}_{20.2}$: C, 1.33 (1.50); H, 1.51 (1.35); N, 0.78 (0.81); Na, 4.25 (4.04); Ni, 1.63 (1.65); Sb, 3.75 (3.45). IR (cm^{-1}): 1576 (m), 1506 (w), 1431 (w), 1389 (m), 1238 (w), 1221 (w), 1088 (w), 949 (s), 872 (s), 832 (vs), 808 (sh), 775 (sh), 658 (m), 517 (w).

Na₁₂{[Zn(imc)(H₂O)]₂(WO₂)₂(SbW₉O₃₃)₂}.44H₂O (1-SbZn): colorless, prismatic crystals were obtained after ca. 2 weeks (yield: 118 mg, 41% based on W). Anal. Calcd (found) for Na₁₂{[Zn(C₄H₃N₂O₂)(H₂O)]_{1.8}{W(OH)O₂}_{0.2}(WO₂)₂(SbW₉O₃₃)₂}.44H₂O, C_{7.2}H_{97.2}N_{3.6}Na_{11.8}O₁₂₀Sb₂W_{20.2}Zn_{1.8}: C, 1.33 (1.45); H, 1.50 (1.32); N, 0.78 (0.83); Na, 4.24 (4.21); Sb, 3.74 (3.67); Zn, 1.81 (1.70). IR (cm⁻¹): 1578 (m), 1500 (w), 1433 (w), 1389 (m), 1240 (w), 1223 (w), 1090 (w), 949 (s), 876 (s), 839 (vs), 806 (sh), 773 (sh), 660 (m), 515 (w). ¹H-NMR (500 MHz, D₂O): δ 7.58 (s, 1H, N=CH-N), 8.30 (s, 1H, C=CH-N) ppm.

Thermal analyses (for the TGA/DTA curves, see Figure A2.9 in Appendix 2). Endothermic dehydration proceeds via continuous mass loss and it is completed at temperatures in the 360 – 390 °C range, involving release of ca. 46 water molecules for all compounds [calcd (found): **1-SbMn**, 12.80 (12.74); **1-SbCo**, 12.87 (12.70); **1-SbNi**, 12.53 (12.59); **1-SbZn**, 12.76 (12.66)]. Combustion of the ligand together with POM decomposition lead to final residues at temperatures in the 510 – 540°C range that increase when going from Mn to Zn [calcd (found): **1-SbMn**, 84.0 (84.7); **1-SbCo**, 84.2 (85.0); **1-SbNi**, 85.0 (85.2); **1-SbZn**, 85.0(85.4)].

ii) Tungstotellurates

Hybrid compounds **1-TeM** (M = Mn, Co) can be prepared following method 1 with TeO₂ as the heteroatomic source and 1H-imidazol-4-carboxylate as ligand (44 mg). Single crystals suitable for X-Ray diffraction were obtained by addition of aqueous 1M KCl (1 mL) to the final solution, followed by slow evaporation at room temperature.

Na₇K₃{[Mn(imc)(H₂O)]₂(WO₂)₂(TeW₉O₃₃)₂}.39H₂O (1-TeMn): orange, prismatic crystals were obtained after ca. 3 weeks (yield: 63 mg, 23% based on W). Anal. Calcd (found) for Na₇K₃{[Mn(C₄H₃N₂O₂)(H₂O)]₂(WO₂)₂(TeW₉O₃₃)₂}.39H₂O, C₈H₈₈K₃Mn₂N₄Na₇O₁₁₅Te₂W₂₀: C, 1.50 (1.56); H, 1.39 (1.21); K, 1.83 (1.66); Mn, 1.72 (1.73); N, 0.88 (0.81); Na, 2.51 (2.64); Te, 3.99 (3.88). IR (cm⁻¹): 1578 (m), 1501 (w), 1431 (w), 1391 (m), 1236 (w), 1221 (w), 1090 (w), 961 (s), 876 (s), 837 (vs), 783 (sh), 739 (sh), 691 (w), 658 (m), 509 (w).

Na₇K₃{[Co(imc)(H₂O)]₂(WO₂)₂(TeW₉O₃₃)₂}.39H₂O (1-TeCo): purple, plate-like crystals were obtained after ca. 3 weeks (yield: 42 mg, 15% based on W). Anal. Calcd (found) for Na₇K₃{[Co(C₄H₃N₂O₂)(H₂O)]₂{Co(H₂O)₂}_{0.2}(WO₂)_{1.8}(TeW₉O₃₃)₂}.39H₂O, C₈H_{88.8}Co_{2.2}K₃N₄Na₇O₁₁₅Te₂W_{19.8}: C, 1.50 (1.67); H, 1.40 (1.31); Co, 2.03 (1.96); K, 1.84 (1.66); N, 0.88 (0.82); Na, 2.53 (2.69); Te, 4.00 (4.08). IR (cm⁻¹): 1578 (m), 1501 (w), 1433 (w), 1383 (m), 1236 (w), 1221 (w), 1096 (w), 963 (s), 880 (s), 837 (vs), 791 (sh), 742 (w), 691 (w), 660 (m), 511 (w).

Thermal analyses (for the TGA/DTA curves, see Figure A2.9 in Appendix 2). Endothermic dehydration proceeds via continuous mass loss and it is completed at temperatures in the 320 – 330 °C range, involving release of ca. 41 water molecules for both compounds [calcd (found): **1-TeMn**, 11.54 (11.45); **1-TeCo**, 11.57 (11.56)]. Combustion of the ligand together with POM decomposition lead to final residues at temperatures in the 510 – 520 °C range [calcd (found): **1-TeMn**, 85.2 (84.6); **1-TeCo**, 85.1 (84.5)].

B) Functionalization with 1H-pyrazole-3-carboxylate

Compound **2-Ni** can be prepared by following either method 2 or 3 with 1H-pyrazole-3-carboxylic acid as ligand (22 mg). However, single crystals suitable for X-Ray diffraction could only be

obtained after the addition of aqueous 1M KCl (1 mL) to the final solution and consequent slow evaporation at room temperature. Method 3 afforded the best yields for this compound.

Na₈K₄{[Ni(pzc)(H₂O)]₂(WO₂)₂(SbW₉O₃₃)₂}]·36H₂O (2-Ni): green, block like single crystals were obtained after 1 month (yield: 178 mg, 61% based on W). Anal. Calcd (found) for Na₈K₄{[Ni(C₄H₃N₂O₂)(H₂O)]₂(WO₂)₂(SbW₉O₃₃)₂}]·36H₂O, C₈H₈₂K₄N₄Na₈Ni₂O₁₁₂Sb₂W₂₀: C, 1.50 (1.48); H, 1.29 (1.09); K, 2.44 (2.23); N, 0.87 (0.81); Na, 2.87 (2.68); Ni, 1.88 (1.83); Sb, 3.80 (3.62). IR (cm⁻¹): 1528 (w), 1503 (w), 1466 (w), 1385 (w), 1360 (m), 1246 (w), 1211 (w), 1119 (w), 1071 (w), 949 (s), 872 (s), 837 (vs), 807 (s), 775 (s), 664 (s), 509 (w). TGA (for the TGA/DTA curves, see Figure A2.10 in Appendix 2): The endothermic dehydration process is completed at around 320 °C and involves the release of 38 water molecules [calcd (found) 10.69 (10.78)]. This is followed by an exothermic mass loss stage comprising the combustion of the ligand and the POM decomposition, leading to the final residue at 550 °C [calcd (found) for K₄Na₈Ni₂O₇₃Sb₂W₂₀: 86.6 (86.6)].

C) Functionalization with pyrazinecarboxylate

The hybrid compounds 3-M (M = Zn, Co) can only be prepared by following method 3 with pyrazinecarboxylate as ligand (25 mg). Moreover, single crystals suitable for X-Ray diffraction are only obtained after addition of aqueous 1M KCl (1 mL) to the final solution and the consequent evaporation at room temperature.

Na₆K₆{[Co(pyzc)(H₂O)]₂(WO₂)₂(SbW₉O₃₃)₂}]·~32H₂O (3-Co): red, prismatic single crystals were obtained after ca. 3 weeks (yield: 84 mg, 29% based on W). Anal. Calcd (found) for Na₆K₆{[Co(C₅H₃N₂O₂)(H₂O)]_{1.8}{Co(H₂O)₂}_{0.2}{W(OH)O₂}_{0.2}(WO₂)_{1.8}(SbW₉O₃₃)₂}]·32H₂O, C₉H₇₄Co₂K₆N_{3.6}Na₆O₁₀₈Sb₂W₂₀: C, 1.70 (1.64); H, 1.17 (0.92); Co, 1.85 (1.91); K, 3.68 (3.77); N, 0.79 (0.83); Na, 2.16 (2.22); Sb, 3.82 (3.77). IR (cm⁻¹): 1589 (m), 1525 (w), 1478 (w), 1422 (w), 1370 (m), 1184 (w), 1169 (w), 1059 (w), 1044 (w), 951 (s), 876 (s), 833 (vs), 810 (s), 766 (m), 661 (m), 515 (w), 457(w). TGA (for the TGA/DTA curves, see Figure A2.10 in Appendix 2): The initial endothermic mass loss below 265 °C corresponds to dehydration and implies the release of 34 water molecules [calcd (found): 9.62 (9.60)]. The resulting amorphous anhydrous phase (according to powder X-ray diffraction analyses) is thermally stable up to 380 °C. It undergoes a highly exothermic mass loss stage originating from combustion of the ligand together with POM decomposition to lead to the final residue at 477 °C [calcd (found) for Co₂K₆Na₆O₇₃Sb₂W₂₀: 87.6 (87.3)].

Na₆K₆{[Zn(pyzc)(H₂O)]₂(WO₂)₂(SbW₉O₃₃)₂}]·~33H₂O (3-Zn): colorless prismatic single crystals were obtained after ca. 3 weeks (yield: 141 mg, 49% based on W). Anal. Calcd (found) for Na₆K₆{[Zn(C₅H₃N₂O₂)(H₂O)]_{1.6}{W(OH)O₂}_{0.4}(WO₂)₂(SbW₉O₃₃)₂}]·33H₂O, C₈H_{74.4}K₆N_{3.2}Na₆O₁₀₉Sb₂W_{20.4}Zn_{1.6}: C, 1.49 (1.54); H, 1.18 (1.21); K, 3.64 (3.79); N, 0.70 (0.81); Na, 2.14 (2.26); Sb, 3.78 (3.89); Zn, 1.63 (1.76). IR (cm⁻¹): 1589 (m), 1528 (w), 1478 (w), 1420 (w), 1375 (m), 1184 (w), 1169 (w), 1059 (w), 1044 (w), 951 (s), 874 (s), 837 (vs), 810 (s), 768 (m), 663 (m), 516 (w), 475 (w). TGA (for the TGA/DTA curves, see Figure A2.10 in Appendix 2): The initial endothermic dehydration process is completed at around 290 °C and involves the release of 35 water molecules [calcd (found): 9.81 (9.84)]. The anhydrous phase shows a thermal stability range up to about 380 °C, which is followed by a highly exothermic mass loss associated to the combustion of the ligand together with POM decomposition. The final residue is obtained at 580°C [calcd (found) for K₆Na₆O_{73.8}Sb₂W_{20.4}Zn_{1.6}: 87.9 (87.4)].

Hybrid Krebs-type POMs with bridging ligands**A) Functionalization with 4,4'-bipyridine**

Single crystals of **4-Mn** suitable for X-Ray diffraction were obtained by slow evaporation of the final solutions derived from either method 2 or 3 with 4,4'-bipyridine as ligand (31 mg). Best yields were observed for method 3.

Na₁₀[Mn₂(H₂O)₆(WO₂)₂(SbW₉O₃₃)₂]·2(4,4'-bpy)·32H₂O (4-Mn): orange prismatic single crystals were obtained after ca. 2 weeks (yield: 169 mg, 60% based on W). Anal. Calcd (found) for Na_{10.4}[[Mn(H₂O)₃]_{1.6}{W(OH)O₂]_{0.4}(WO₂)₂(SbW₉O₃₃)₂]·2(C₁₀H₈N₂)·32H₂O, C₂₀H₉₀Mn_{1.6}N₄Na_{10.4}O₁₀₈Sb₂W_{20.4}: C, 3.72 (3.47); H, 1.44 (1.49); Mn, 1.36 (1.45); N, 0.87 (0.89); Na, 3.70 (3.79); Sb, 3.78 (4.07). IR (cm⁻¹): 1487 (m), 1412 (w), 1379 (w), 1230 (w), 1207 (w), 953 (s), 887 (s), 826 (vs), 746 (v), 660 (s), 521 (w). TGA (for the TGA/DTA curves, see Figure A2.10 in Appendix 2): The endothermic dehydration process involving release of 38 water molecules is completed at around 370 °C [calcd (found): 10.62 (10.65)] and followed by the combustion of the organic molecules together with POM decomposition. The final residue is obtained at 695°C [calcd (found) for Mn_{1.6}Na_{10.4}O_{72.8}Sb₂W_{20.4}: 84.1 (83.9)].

B) Functionalization with pyrazine-2,3-dicarboxylate

Compound **5-Ni** can be prepared by following either method 2 or 3 with pyrazine-2,3-dicarboxylic acid as ligand (33 mg). Single crystals suitable for X-Ray diffraction were obtained by slow evaporation of the resulting solution at room temperature. Best quality crystals were observed for method 3.

Na₂₄[μ-((2,3)pyzdc)₂{Ni₂(H₂O)Sb₂W₂₀O₇₀}₂]·91H₂O (5-Ni): green, needle-like single crystals were obtained after ca. 1 month (yield: 167 mg, 58% based on W). Anal. Calcd (found) for Na₂₄[[Ni₂(H₂O)Sb₂W₂₀O₇₀]₂(C₆H₂N₂O₄)₂]·91H₂O, C₁₂H₁₉₀N₄Na₂₄Ni₄O₂₄₁Sb₄W₄₀: C, 1.12 (1.18); H, 1.49 (1.41); N, 0.44 (0.50); Na, 4.28 (4.14); Ni, 1.82 (1.76); Sb, 3.78 (3.64). IR (cm⁻¹): 1437 (w), 1373 (m), 1204 (w), 1175 (w), 1132 (w), 1082 (w), 949 (s), 881 (vs), 833 (s), 791 (vs), 733 (vs), 610 (m), 511 (w). TGA (for the TGA/DTA curves, see Figure A2.10 in Appendix 2): The endothermic dehydration process is completed at around 335 °C and involves the release of 93 water molecules [calcd (found): 13.09 (12.96)]. The thermal stability range up to 415 °C observed for the anhydrous phase is followed by the combustion of the ligand together with POM decomposition, leading to the final residue at 530°C [calcd (found) for Na₂₄Ni₄O₁₄₆Sb₄W₄₀: 85.2(84.9)].

2.2.2. X-Ray Crystallography

Crystal data for **1-XM** (X = Sb^{III}, Te^{IV}; M = Mn, Co, Ni, Zn), **2-Ni**, **3-M** (M = Co, Zn), **4-Mn** and **5-Ni** are summarized in Tables 2.2, 2.3 and 2.4. Thermal vibrations were treated anisotropically for heavy atoms (W, Sb, Te, K, 3d-metals). Hydrogen atoms on the organic ligands were placed in calculated positions and refined using standard SHELXL parameters.

Table 2.2. Crystallographic data for compounds **1-SbM** (M = Mn, Co, Ni, Zn).

	1-SbMn	1-SbCo	1-SbNi	1-SbZn
Formula	C ₈ H _{99.6} Mn _{2.4} N ₄ Na ₁₂ O ₁₂₀ Sb ₂ W _{19.6}	C ₈ H _{99.6} Co _{2.4} N ₄ Na ₁₂ O ₁₂₀ Sb ₂ W _{19.6}	C _{7.2} H _{97.2} N _{3.6} Na ₁₂ Ni _{1.8} O ₁₂₀ Sb ₂ W _{20.2}	C _{7.2} H _{97.2} N _{3.6} Na ₁₂ O ₁₂₀ Sb ₂ W _{20.2} Zn _{1.8}
FW (g mol ⁻¹)	6427.1	6436.8	6489.1	6501.1
Crystal system	triclinic	triclinic	monoclinic	triclinic
Space group	<i>P</i> -1	<i>P</i> -1	<i>P</i> 2 ₁ / <i>c</i>	<i>P</i> -1
<i>a</i> (Å)	13.8331(4)	13.6242(7)	16.2173(3)	13.8450(4)
<i>b</i> (Å)	14.6798(3)	14.7481(6)	27.2085(3)	14.6579(4)
<i>c</i> (Å)	15.7557(5)	15.6620(9)	13.0112(2)	15.7431(4)
α (°)	69.160(3)	68.763(5)	90	68.890(2)
β (°)	71.318(3)	71.840(5)	108.999(2)	70.831(2)
γ (°)	87.719(2)	87.406(4)	90	87.242(2)
<i>V</i> (Å ³)	2822.65(13)	2779.0(2)	5428.42(14)	2806.29(13)
<i>Z</i>	1	1	2	1
<i>D</i> _{calcd} (g cm ⁻³)	3.781	3.846	3.970	3.847
μ (mm ⁻¹)	20.781	44.529	22.278	21.630
Reflections				
Collected	14573	18695	22924	19508
Unique (<i>R</i> _{int})	9892 (0.037)	9901 (0.068)	10647 (0.022)	11630 (0.018)
Observed [<i>I</i> > 2 σ (<i>I</i>)]	9096	7585	9608	10873
Parameters	408	406	390	437
<i>R</i> (<i>F</i>) [<i>I</i> > 2 σ (<i>I</i>)]	0.047	0.049	0.034	0.025
<i>wR</i> (<i>F</i> ²) (all data)	0.126	0.134	0.073	0.056
GoF	1.051	0.990	1.091	1.086

In all cases tungsten and the corresponding 3d metal (M) were initially disordered over the four metal positions in the central belt of the polyoxometalate clusters (two internal and two external) and their population parameters were refined without restrictions. No M/W crystallographic disorder was found for **1-TeMn**, and **2-Ni**, whereas for **1-SbMn**, **1-SbCo** and **1-TeCo** negligible W populations (lower than 1%) were obtained for the external sites and partial M/W occupancies of 20/80 (**1-SbMn**), 18/82 (**1-SbCo**) and 12/88 (**1-TeCo**) were observed for the internal ones. The external positions were assigned as containing exclusively M in the final refinement cycle. In the case of **1-SbNi**, **1-SbZn**, **3-Zn** and **4-Mn**, the internal positions showed negligible M

populations, whereas partial M/W occupancies of 89/11 (**1-SbNi**), 94/6 (**1-SbZn**), 84/16 (**3-Zn**) and 80/20 (**4-Mn**) were found for the external ones. In the final step, the internal positions were refined as containing only tungsten and the occupancies of the ligand atoms were set equal to that of M. Finally, the external W population of about 5% was found to be equal to the cobalt population of the internal positions in **3-Co**.

Table 2.3. Crystallographic data for compounds **1-TeM** (M = Mn, Co, Ni, Zn) and **2-Ni**.

	1-TeMn	1-TeCo	2-Ni
Formula	C ₈ H ₈₈ K ₃ Mn ₂ N ₄ Na ₇ O ₁₁₅ Te ₂ W ₂₀	C ₈ Co _{2.2} H _{88.8} K ₃ N ₄ Na ₇ O ₁₁₅ Te ₂ W _{19.8}	C ₈ H ₈₂ K ₄ N ₄ Na ₈ Ni ₂ O ₁₁₂ Sb ₂ W ₂₀
FW (g mol ⁻¹)	6401.1	6384.9	6405.0
Crystal system	triclinic	triclinic	triclinic
Space group	<i>P</i> -1	<i>P</i> -1	<i>P</i> -1
<i>a</i> (Å)	12.2348(3)	12.1725(4)	12.2030(4)
<i>b</i> (Å)	13.6081(4)	13.5660(4)	13.3843(5)
<i>c</i> (Å)	17.2882(4)	17.1425(5)	17.3303(4)
α (°)	91.583(2)	91.535(3)	91.809(3)
β (°)	98.057(2)	98.099(3)	99.309(2)
γ (°)	106.723(2)	107.057(3)	104.266(3)
<i>V</i> (Å ³)	2722.39(11)	2672.34(14)	2699.56(15)
<i>Z</i>	1	1	1
<i>D</i> _{calcd} (g cm ⁻³)	3.904	3.967	3.940
μ (mm ⁻¹)	22.050	22.353	22.351
Reflections			
Collected	21395	17603	20516
Unique (<i>R</i> _{int})	10702 (0.052)	10479 (0.040)	10597 (0.047)
Observed [<i>I</i> > 2 σ (<i>I</i>)]	9672	9517	9386
Parameters	400	393	404
<i>R</i> (<i>F</i>) [<i>I</i> > 2 σ (<i>I</i>)]	0.052	0.048	0.059
<i>wR</i> (<i>F</i> ²) (all data)	0.137	0.129	0.168
GoF	1.089	1.080	1.077

Seven sites with appropriate geometries for a sodium cation were located in the Fourier maps of **1-SbMn** and **1-SbCo**. In the case of **1-SbNi** and **1-SbZn**, the number of potential sodium sites was six. The occupancies in these positions were initially refined without restrictions and this resulted in a total number of 5.8 (**1-SbMn**), 5.5 (**1-SbCo**), and 5.7 (**1-SbZn**) sodium atoms per asymmetric unit containing one half of the hybrid polyanion. For all of them, the sum of the sodium population factors was fixed to the expected number of six in the final refinement cycle. In the case of **1-SbNi**, only a total of 4.8 sodium atoms per asymmetric unit have been observed due to cation/solvent disorder.

Four sites with appropriate geometries for a sodium cation and two for potassium cations were located in the Fourier maps of **1-TeMn** and **1-TeCo**. The occupancies in these positions were initially refined without restrictions and this resulted in a total number of 1.5 K and 2.3 Na atoms for **1-TeMn** and 1.5 K and 2.8 Na atoms for **1-TeCo**. In both cases, the total number of 3.8 and 4.3 cations per half of the hybrid polyanion found in the crystal structures is significantly lower than that expected according to elemental analyses (5), due to cation/solvent disorder. In contrast, the 2 K and 4 Na atoms determined from elemental analyses for **2-Ni** were found in the crystal structure but disordered in three and five sites, respectively.

Table 2.4. Crystallographic data for compounds **3-M** (M = Co, Zn), **4-Mn** and **5-Ni**.

	3-Co	3-Zn	4-Mn	5-Ni
Formula	C ₉ H ₇₄ CO ₂ K ₆ N _{3.6} Na ₆ O ₁₀₈ Sb ₂ W ₂₀	C ₈ H _{74.4} K ₆ N _{3.2} Na ₆ O ₁₀₉ Sb ₂ W _{20.4} Zn _{1.6}	C ₁₀ H ₉₀ Mn _{1.6} N ₄ Na _{10.4} O ₁₀₈ Sb ₂ W _{20.4}	C ₁₂ H ₁₉₀ N ₄ Na ₂₄ Ni ₄ O ₂₄₁ Sb ₄ W ₄₀
FW (g mol ⁻¹)	6372.2	6431.1	6239.1	12802.6
Crystal system	triclinic	triclinic	triclinic	monoclinic
Space group	<i>P</i> -1	<i>P</i> -1	<i>P</i> -1	<i>C</i> 2/ <i>c</i>
<i>a</i> (Å)	12.2033(4)	12.2715(3)	12.8781(5)	43.6689(7)
<i>b</i> (Å)	15.0427(4)	15.9492(6)	12.9226(4)	19.2964(3)
<i>c</i> (Å)	15.8975(5)	16.0131(5)	17.5375(7)	26.5627(4)
α (°)	73.220(2)	65.534(3)	106.004(3)	90
β (°)	78.478(3)	67.844(3)	102.094(3)	94.788(2)
γ (°)	67.035(3)	78.232(2)	101.996(3)	90
<i>V</i> (Å ³)	2560.02(13)	2637.79(14)	2631.37(17)	22305.05(23)
<i>Z</i>	1	1	1	4
<i>D</i> _{calcd} (g cm ⁻³)	4.133	4.048	3.937	3.834
μ (mm ⁻¹)	23.593	23.383	23.007	42.745
Reflections				
Collected	20315	17726	18414	80184
Unique (<i>R</i> _{int})	10067 (0.029)	10357 (0.023)	10334 (0.036)	19886 (0.072)
Observed [<i>I</i> > 2 σ (<i>I</i>)]	9063	9486	8982	16628
Parameters	404	400	396	693
<i>R</i> (<i>F</i>) [<i>I</i> > 2 σ (<i>I</i>)]	0.035	0.038	0.052	0.063
<i>wR</i> (<i>F</i> ²) (all data)	0.083	0.097	0.104	0.180
GoF	1.052	1.058	1.073	1.087

For **3-Co**, two potassium and six sodium sites per asymmetric unit containing one half of the hybrid polyanion were located, and the free refinement of their occupancies resulted in a total number of 2.0 K and 3.0 Na atoms. Analogously, three potassium sites and only two sodium sites were located in the Fourier map of **3-Zn**, leading to a total number of 2.4 K and 2.0 Na atoms after

free refinement of their occupancies. These total numbers are significantly lower than the expected six alkaline cations determined from elemental analyses due to cation/solvent disorder.

Five sodium sites per half POM were located for **4-Mn**, and the free refinement of their occupancies resulted in a total number of 4.8 Na atoms out of the 5.7 calculated from elemental analyses. Eight of the expected twelve sodium sites per asymmetric unit containing one half of the hybrid POM were located in the Fourier map of **5-Ni**. Their populations were refined without restrictions giving a total number of only six sodium atoms. Similarly, sites suitable for 30 water molecules (out of the 46 calculated from thermogravimetric analyses) were found in the crystal structure and the free refinement of their occupancies resulted in a total number of 20. Calculations carried out using PLATON software revealed a Total Potential Solvent Area Volume of 4285 Å³/unit cell which accounts for almost the 20% of the unit cell volume and can host the sodium atoms (12) and water molecules (52) that could not be determined crystallographically. The two largest voids of 2052 Å³ each are located at $(x, y, z) = (1/4, 1/8, 0)$ and $(3/4, 2/3, 0)$.

2.3. RESULTS AND DISCUSSION

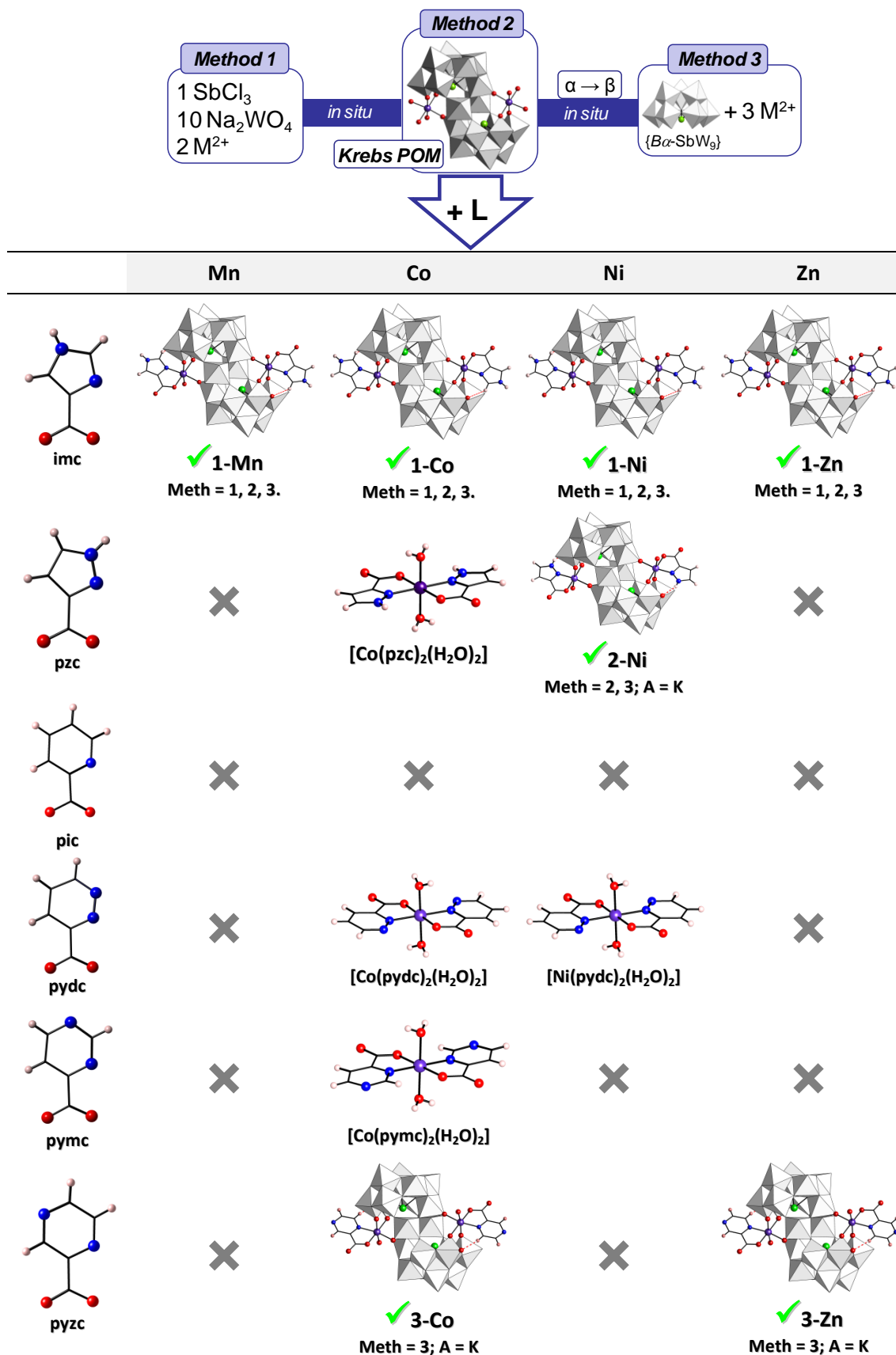
2.3.1. Reactions of Krebs type POMs with organic N,O-chelating ligands

General Synthetic Considerations

The reactivity toward different organic ligands of a series of 3d-metal substituted Krebs-type tungstoantimonates(III) has been evaluated to determine: i) whether Krebs-type clusters are suitable for organic derivatization via classical coordination chemistry on the external 3d-metal positions; ii) which ligand/s are the most appropriate for this purpose.

Planar, aromatic ligands with chelating capability have been selected for these studies, and more specifically, the following six carboxylate derivatives of N-donor heterocycles: the diazolcarboxylates imc and pzc, the pyridinecarboxylate pic; and the diazinecarboxylates pydc, pymc and pyzc. Three different synthetic approaches have been explored for the reaction between POMs and ligands in buffered medium under bench conditions. Method 1 consists in a one-pot synthesis involving the ligand and the most basic metallic reagents that can lead to the POM cluster (sodium tungstate, 3d-metal chloride or nitrate, and a heteroatomic source like SbCl₃). Method 2 is the direct reaction between the pre-formed $[\{M(H_2O)_3\}_2(WO_2)_2(SbW_9O_{33})_2]^{10-}$ (M = Mn^{II}, Co^{II}, Ni, Zn) POM precursor and the ligand in stoichiometric ratio, whereas in method 3 the POM precursor is generated *in situ* from the trilacunary $[B-\alpha-SbW_9O_{33}]^{9-}$ species and a 3d-metal salt. Reactions have been monitored by FT-IR spectroscopy on any solid material obtained by slow evaporation of the final solutions at room temperature until dryness. This technique has proven to be excellent for determining the success of our organic derivatization attempts. For the imc ligand, all the three synthetic methods were tested, whereas only methods 2 and 3 (as the most suitable) were evaluated for the rest of the ligands.

Scheme 2.1. Results obtained in the reactions between Krebs-type tungstoantimonates(III) and N,O-chelating ligands (color code: WO_6 , grey octahedra; X, green; M, purple; N, blue; O, red; H, pink; $\text{N/C-H}\cdots\text{O}_{\text{POM}}$, dashed red lines).



×: There is no reaction and the corresponding transition metal di-substituted Krebs type POM precursor is obtained as single-crystals. **Meth** = applied synthetic method. **A** = alkaline metal.

The use of four different $[\{M(H_2O)_3\}_2(WO_2)_2(SbW_9O_{33})_2]^{10-}$ Krebs-type POMs ($M = Mn^{II}, Co^{II}, Ni, Zn$), six different N,O-chelating ligands and three different synthetic approaches result in 52 possible combinations. All of them have been explored and the results are summarized in Scheme 2.1. Reaction between the Krebs-type POM and the ligand has been observed in 24 out of the 52 possible synthetic combinations. In the remaining 28, the only solid products isolated from the reaction mixtures were pristine Krebs-type POMs as shown by FT-IR spectroscopy. The 24 cases in which reaction took place can be divided into two groups according to the final product: in 16 of these reactions organic functionalization is successful and the corresponding hybrid POM is isolated, whereas in the remaining 8 combinations the initial Krebs-type species undergoes partial decomposition upon ligand attack and the corresponding neutral $[M(L)_2(H_2O)_2]$ complexes are obtained. As a result, 7 organic derivatives of Krebs-type POMs and four different monomeric complexes have been obtained in the course of our studies. These are:

Hybrid POMs

- 1) $[\{Mn(imc)(H_2O)\}_2(WO_2)_2(SbW_9O_{33})_2]^{12-}$ (**1-SbMn**)
- 2) $[\{Co(imc)(H_2O)\}_2(WO_2)_2(SbW_9O_{33})_2]^{12-}$ (**1-SbCo**)
- 3) $[\{Ni(imc)(H_2O)\}_2(WO_2)_2(SbW_9O_{33})_2]^{12-}$ (**1-SbNi**)
- 4) $[\{Zn(imc)(H_2O)\}_2(WO_2)_2(SbW_9O_{33})_2]^{12-}$ (**1-SbZn**)
- 5) $[\{Ni(pzc)(H_2O)\}_2(WO_2)_2(SbW_9O_{33})_2]^{12-}$ (**2-Ni**)
- 6) $[\{Co(pyzc)(H_2O)\}_2(WO_2)_2(SbW_9O_{33})_2]^{12-}$ (**3-Co**)
- 7) $[\{Zn(pyzc)(H_2O)\}_2(WO_2)_2(SbW_9O_{33})_2]^{12-}$ (**3-Zn**)

Transition metal complexes

- a) $[Co(pzc)_2(H_2O)_2]$ (**Co-pzc**)
- b) $[Co(pydc)_2(H_2O)_2] \cdot 2H_2O$ (**Co-pydc**)
- c) $[Ni(pydc)_2(H_2O)_2] \cdot 2H_2O$ (**Ni-pydc**)
- d) $[Co(pymc)_2(H_2O)_2] \cdot 2H_2O$ (**Co-pymc**)

Reactions with 1H-imidazole-4-carboxylic acid

Polyanions $[\{M(imc)(H_2O)\}_2(WO_2)_2(SbW_9O_{33})_2]^{12-}$ (**1-SbM**, $M = Mn, Co, Ni, Zn$) have been prepared following any of the above mentioned three different synthetic routes (Scheme 2.1) as indicated by IR spectroscopy. Single crystals were firstly obtained by addition of excess of Himc to solutions of the corresponding Krebs-type POM formed in situ from Na_2WO_4 and sources of Sb^{III} and M^{II} (10:1:1 ratio) in sodium acetate buffer (method 1). X-ray diffraction experiments performed on these crystals allowed us to locate the imc ligand coordinated to the Krebs-type POM framework, but unfortunately, a severe disorder in the outer positions with W populations of ca. 22% prevented the ligand from being satisfactorily modeled. As indicated by Krebs and coworkers,² the $[(WO_2)_2(SbW_9O_{33})_2]^{14-}$ intermediate in the formation of the target POM framework can be stabilized by addition of either two external $\{WO_2(OH)\}$ or $\{M^{II}(H_2O)_3\}$ groups, often leading to crystallographic disorder arising from co-crystallization of plenary and disubstituted species due to the similar charge, ionic radii and coordination geometry of both groups. We unsuccessfully tried to overcome this disorder by using an excess of M^{II} (10:1:2 ratio), so we decided to explore the other two synthetic approaches.

Following a more rational strategy, we reacted Himc with sodium salts of the preformed precursors $[\{M^{\text{II}}(\text{H}_2\text{O})_3\}_2(\text{WO}_2)_2(B-\beta\text{-SbW}_9\text{O}_{33})_2]^{10-}$ ($M = \text{Mn, Co, Ni, Zn}$). Reactions were carried out under the same conditions of method 1 but using the stoichiometric 2Himc:1POM ratio (method 2). Polyanions **1-SbM** could all be isolated as single crystals via this straightforward ligand substitution under mild conditions, but the W populations in the outer positions of these samples were also above 20% as for method 1. Fortunately, we could prepare the series **1-SbM** with trivial W populations in the outer positions by applying method 3. This method involves $\text{Na}_9[B-\alpha\text{-SbW}_9\text{O}_{33}]$ as precursor and consists in the addition of excess of Himc to solutions of Krebs-type POMs generated in situ with a twofold excess of 3d metal. Not surprisingly, the use of Cu^{II} in this method led to isolation of the well-known $[(B-\alpha\text{-SbW}_9\text{O}_{33})_2\{\text{Cu}(\text{H}_2\text{O})\}_3]^{12-}$ Hervé-type POM due to coordination requirements of this specific 3d-metal.¹²

Functionalization can be unequivocally determined by IR spectroscopy prior to single-crystal X-ray structural studies (Figure 2.2). The spectra of **1-SbM** ($M = \text{Mn, Co, Ni, Zn}$) show a series of weak to medium intensity peaks in the organic 1090 – 1620 cm^{-1} range that evidences the presence of the imc anion, whereas the POM domains below 1000 cm^{-1} are very similar to those of the 3d-metal disubstituted precursors with negligible variations in the band positions except for $\sim 10 \text{ cm}^{-1}$ red-shifts in the signals associated to $\nu(M^{\text{II}}-\text{O})$ modes ($\sim 670 \text{ cm}^{-1}$). However, the triplet of signals originating from the $M-\text{O}-M$ stretching (840 – 765 cm^{-1}) undergo a clear change in their relative intensities upon functionalization, in such a way that the central line becomes almost shadowed by an increase of intensity of the left line. These modifications are systematically observed for the whole **1-SbM** series, and therefore, they represent inherent signals of the Krebs-type POM derivatization with retention of the sandwich metal-oxo framework.

The diazocarboxylate ligand imc has shown up as a “universal” ligand towards Krebs-type tungstoantimonates(III) because its coordination to the external sites takes place regardless of the 3d-metal present with retention of the sandwich-type framework, and furthermore because functionalization is easily achieved in moderate to good yields regardless of the synthetic method applied. Taking advantage of the universality of imc as derivatizing agent, we also decided to explore the influence of a change in the charge of the heteroatom in the reactivity. For this purpose, we replaced SbCl_3 with TeO_2 as heteroatomic source in method 1 and performed an additional set of reactions. All of them led to the corresponding $[\{M^{\text{II}}(\text{H}_2\text{O})_3\}_2(\text{WO}_2)_2(B-\beta\text{-TeW}_9\text{O}_{33})_2]^{10-}$ hybrid analogues ($M = \text{Mn, Co, Ni, Zn}$) which represent the first observation of a transition-metal disubstituted Krebs-type framework with Te^{IV} as heteroatom. To date, only tri- and tetra-substituted tungstotellurate(IV) species have been reported in the literature.⁴ In contrast to the tungstoantimonate(III) compounds, single crystals suitable for X-ray experiments could only be obtained in the presence of potassium cation as counterion. Compounds **1-TeMn** and **1-TeCo** were isolated as pure crystalline phases, whereas for the Ni-derivative, mixtures of the hybrid **1-TeNi** with the corresponding POM precursor and $[\text{Ni}(\text{imc})_2(\text{H}_2\text{O})_2]$ complex were obtained as indicated by FT-IR spectroscopy (see Figure A2.2 in Appendix 2). Crystals of **1-TeNi** could be separated for X-ray diffraction experiments.¹³ In contrast, the corresponding POM precursor and transition metal complex were found as major phases for the reaction with Zn as identified again by FT-IR.

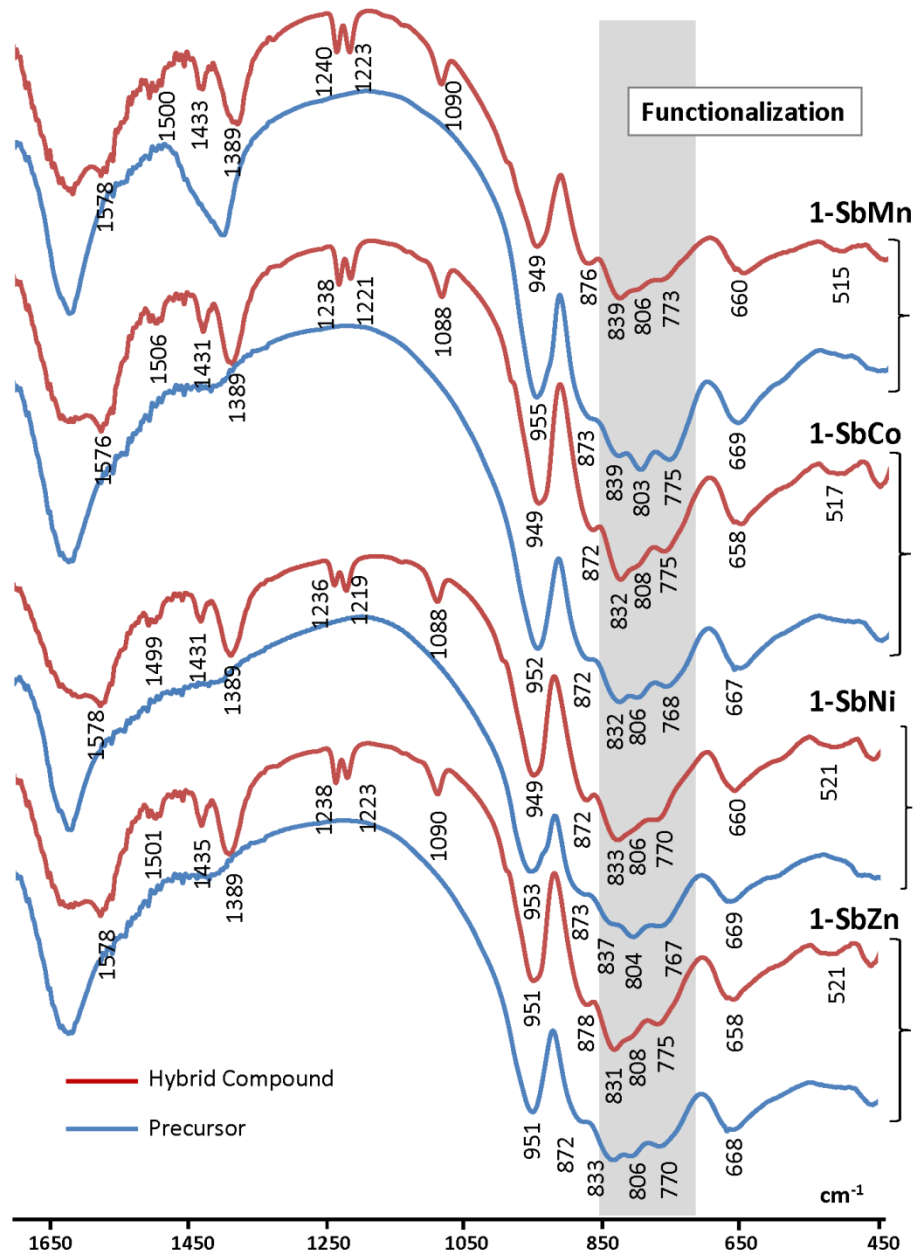


Figure 2.2. FT-IR spectra of 1-SbM (M = Mn, Co, Ni, Zn) compared to those of the corresponding Krebs-type POM precursors.

Reactions with the *pzc*, *pic*, *pydc*, *pymc* and *pyzc* ligands

Encouraged by the results obtained using the *imc* ligand, the study was extended to other aromatic N,O-chelating ligands (*pzc*, *pic*, *pydc*, *pymc*, *pyzc*) to achieve a better understanding about the reactivity of this POM family. However, the organic derivatization of Krebs type series did not show up to be a trivial issue, so that only three additional hybrid compounds were obtained. Different behaviors have been observed for each ligand:

i) Diazolcarboxylate ligands show completely different reactivity upon just modifying the relative positions of the two N atoms in the ring. In contrast to the “universal” character of *imc*, the *pzc* ligand has proven to be selective toward the functionalization of Ni-containing cluster regardless

of the synthetic method applied. The $[\{\text{Ni}(\text{pzc})(\text{H}_2\text{O})\}_2(\text{WO}_2)_2(\text{SbW}_9\text{O}_{33})_2]^{12-}$ hybrid species (**2-Ni**) has been obtained in all cases, but crystals suitable for X-ray diffraction could only be obtained in the presence of K^+ cations. The reactivity of pzc toward the rest of POM precursors is either non-existent (Mn, Zn) or implies partial decomposition of the Krebs-type framework (Co). In the latter case, mixtures of the POM precursor and the corresponding $[\text{Co}(\text{pzc})_2(\text{H}_2\text{O})_2]$ (**Co-pzc**) complex have been obtained as indicated by FT-IR and single-crystal X-ray diffraction. This compound represents the first structural characterization of a transition metal complex containing the pzc ligand. The full characterization of the complex is given in Appendix 1.

ii) The picolinate anion (pic) is completely inert toward Krebs-type tungstoantimonates(III).

iii) As observed for pzc, the diazincarboxylate ligands pydc and pymc promote the partial decomposition of the Krebs-type POMs leading to mixtures of the precursor and the corresponding monomeric complexes. More specifically, this fact takes place for the Co- and Ni-containing POMs in the case of pydc, and only for the Co-species in the case of pymc. All the three complexes $\text{M}(\text{pydc})_2(\text{H}_2\text{O})_2 \cdot 2\text{H}_2\text{O}$ (**M-pydc**, M = Co, Ni) and $[\text{Co}(\text{pymc})_2(\text{H}_2\text{O})_2] \cdot 2\text{H}_2\text{O}$ (**Co-pymc**) are isolated as crystalline products and a brief description, together with their full characterization, is compiled in Appendix 1.

iv) The remaining diazinecarboxylate ligand does not lead to complexes but it rather behaves as a selective agent for the derivatization of the Co- and Zn-clusters. However, the corresponding $[\{\text{M}(\text{pyzc})(\text{H}_2\text{O})\}_2(\text{WO}_2)_2(\text{SbW}_9\text{O}_{33})_2]^{12-}$ (**3-M**, M = Co, Zn) hybrid derivatives are exclusively obtained via method 3 in the presence of K^+ ions, that is, the direct stoichiometric reaction between pre-formed precursor and ligand is not operative.

From the point of view of the POM precursor, the stability of the parent transition metal disubstituted Krebs-type framework differs significantly from Mn to Zn. The Mn derivative appears to be the most stable precursor as it only reacts with the imc ligand to give the corresponding hybrid derivative. On the contrary, the Co substituted cluster can be considered as more labile than its analogues because it reacts with all ligands but for pic, resulting in the corresponding hybrid derivatives with imc and pyzc or in partial decomposition and consequent formation of mononuclear metal complexes with pzc, pymc and pydc.

Regarding synthetic aspects, it is worth mentioning that when the volume of several reaction mixtures was lowered to about 1-2 mL by slow evaporation and thus the concentration of reactants become high enough, a side-product consisting in chains of Krebs-like POMs was obtained for Mn and Zn derivatives, as identified by FT-IR spectroscopy and single-crystal X-ray diffraction.¹⁴ Linear one-dimensional arrangements of Krebs-type POMs in the solid state have been previously described,¹⁵ but in this case centrosymmetric POMs are linked through the coordination sphere of the transition metal atom via M—O—M bridges. The linear POM chains parallel to the [101] direction are related to each other by a twofold rotation axis located along the crystallographic *b* axis. Polymerization can be easily detected by FT-IR spectroscopy prior to X-Ray diffraction studies as shown in Figure 2.3, where a remarkable increase in the relative intensity of the central line of the $\nu(\text{M—O—M})$ triplet is observed with consequent vanishing of the two side signals.

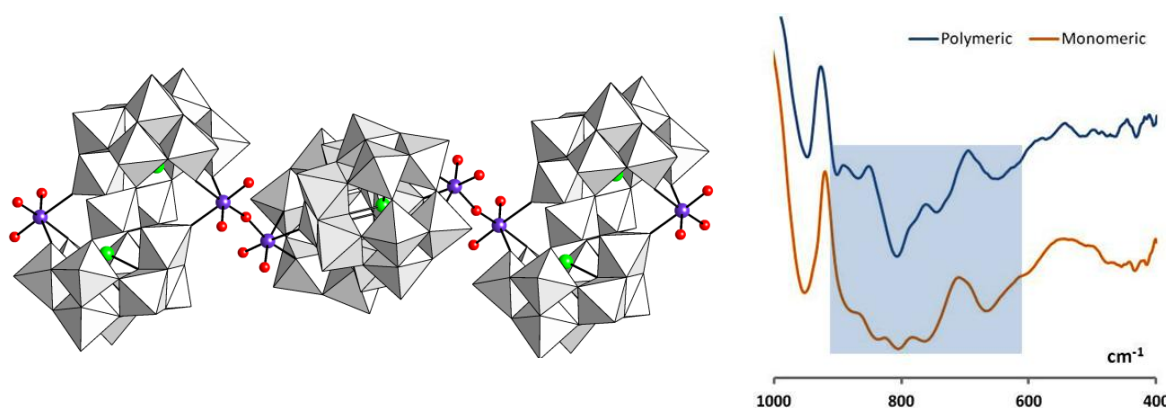


Figure 2.3. Solid state one-dimensional arrangement of Krebs-type anions running along the [101] direction (left) and FT-IR spectra of polymeric vs monomeric Krebs-like POMs (right).

As mentioned before, FT-IR spectroscopy represents an easy, cheap and very powerful technique to confirm the presence of hybrid POM-frameworks. Furthermore, it can also be used to undoubtedly differentiate a given hybrid POM from a solid sample consisting in a mixture of the pristine Krebs type POM precursor and the corresponding transition metal complex formed upon partial decomposition of the former. For the pzc ligand for example, the FT-IR spectrum of the solid product obtained in the reaction with the Co-precursor is simply the result of the combination of the individual spectra from the corresponding POM precursor and the transition metal complex as can be viewed in Figure 2.4. In contrast, the spectrum of **2-Ni** shows noticeable differences compared to the sum of the spectra from both components. Significant blue shifts for several bands located in the organic region (A band: ~ 10 cm⁻¹; B band: ~ 23 cm⁻¹; E band: ~ 30 cm⁻¹) besides the above mentioned variations in the relative intensities of the triplet of signals at 840 – 765 cm⁻¹. The bands A-F have been assigned in Table 2.5 to stretching and bending vibrations directly related to the coordinating N atom.¹⁶

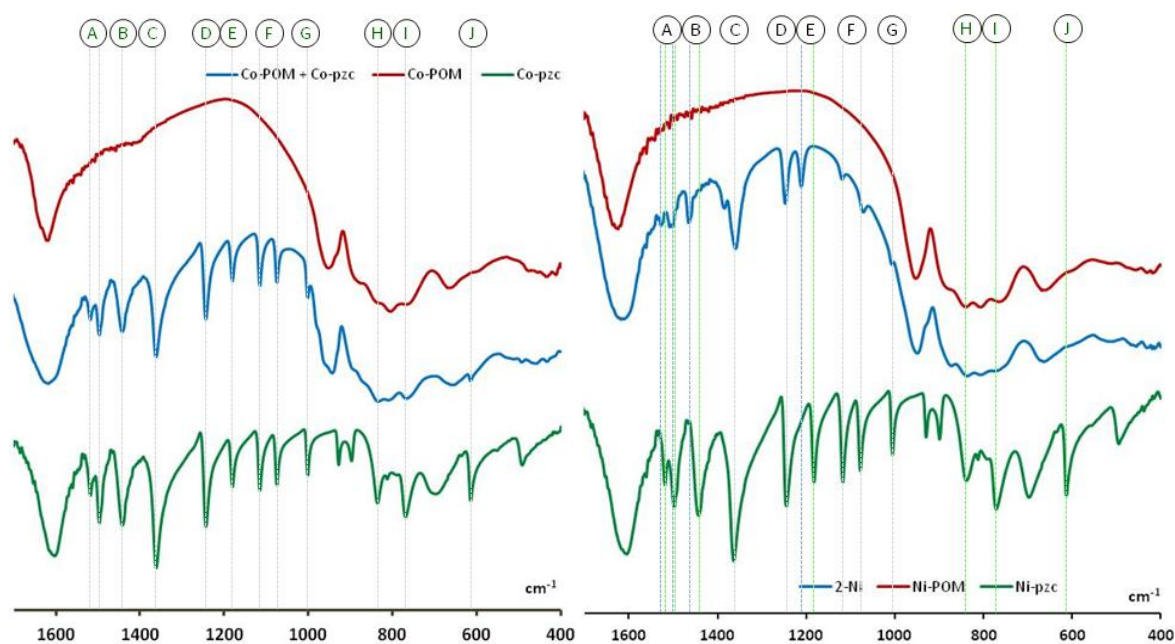


Figure 2.4. Left: FT-IR spectrum of a Co-POM/Co-pzc mixture and comparison to the individual spectra of compounds Co-POM and Co-pzc. Right: FT-IR spectrum of **2-Ni** compared to those Ni-POM and Ni-pzc.

Table 2.5 Representative bands (cm^{-1}) in the infrared spectra of compounds **Co-POM** and **Co-pzc**, Co-POM/Co-pzc mixture and compounds, **2-Ni**, Ni-POM and **Ni-pzc**.

	Assignment	Mixture	Co-POM	Co-pzc	2-Ni	Ni-POM	Ni-pzc
A	$\nu(\text{C}=\text{C})+$	1518w	-	1518m	1528w	-	1518m
	$\nu(\text{C}=\text{N})$	1497w		1497m	1503w		1497m
B	$\delta(\text{N-H})$	1443m	-	1442m	1466w	-	1443m
C	$\delta(\text{C-H}) +$	1362s	-	1362s	1360m	-	1364vs
D	$\nu(\text{C-O})$	1244m	-	1244m	1246w	-	1244m
E	$\nu(\text{C-C}) +$	1180m	-	1180m	1211w	-	1182m
F	$\nu(\text{C-N})$	1115m	-	1115m	1119w	-	1117m
		1074m		1074m	1071w		1078m
G	$\delta(\text{O-C-O})$	1001w	-	1001w	1008w	-	1005w
	$\nu(\text{W-O}_t)$	948s	952s	-	949s	953s	-
	$\nu(\text{O-W-O})$	875sh	872s	-	872s	873s	-
H	$\delta_{\text{ring}}+(\text{C-H})_{\text{oop}}$	897m	-	897m	-	-	899m
	$\nu(\text{O-W-O})$	833vs	832vs	-	837vs	837s	-
	$\nu(\text{O-W-O})$	810vs	806s	-	807s	804s	-
I	$\delta(\text{C-H})_{\text{oop}}$	769m	-	770m	-	-	771m
	$\nu(\text{O-W-O})$	767vs	768s	-	775s	767s	-
	$\nu(\text{M}^{\text{II}}-\text{O})$	666s	667s	-	664s	669s	-
J	$\delta(\text{N-H})+(\text{C-O})$	615m	-	613m	-	-	613m

ν = stretching; δ = bending; oop = out-of-plane.

w = weak; m = medium; s = strong; vs = very strong; sh = shoulder

Molecular structures of the 1-XM, 2-Ni and 3-M hybrid POMs

Single-crystal X-ray diffraction studies confirm the organic functionalization for the **1-XM** series, compound **2-Ni** and the **3-M** pair. All hybrid POMs reported in this section (Figure 2.5) show the well-known 3d-metal disubstituted Krebs-type skeleton of ideal C_{2h} symmetry composed of two trilacunary Keggin $[B-\beta\text{-Sb}^{\text{III}}\text{W}_9\text{O}_{33}]^{9-}$ subunits linked via corner-sharing by two internal WO_6 octahedra (each showing two *cis*-related terminal O atoms) and two M^{II} atoms coordinated at external positions (for a graphical representation of a di-substituted Krebs type POM see Figure 2.1.A). Polyanions **1-SbNi**, **1-SbZn** and **3-Zn** display relatively low W populations of only 11, 6 and 16% in their respective external positions. In the case of **1-SbMn**, **1-SbCo** and **1-TeCo** containing the more oxophilic 3d metals, there is no crystallographic W/ M^{II} external disorder, but we found noticeable M^{II} populations in the internal positions (20, 18 and 12% respectively). Analogously, trivial Co/W disorders (external 5% W and internal 6% Co) were detected in both internal and external sites for **3-Co**. For comparison, Krebs reported external W occupancies of 9 and 20% for the Mn and Zn POMs, respectively.^{3d} In contrast, Niu observed internal W/ M^{II} disorders for the Mn and Co POMs that compare well to ours.¹⁷

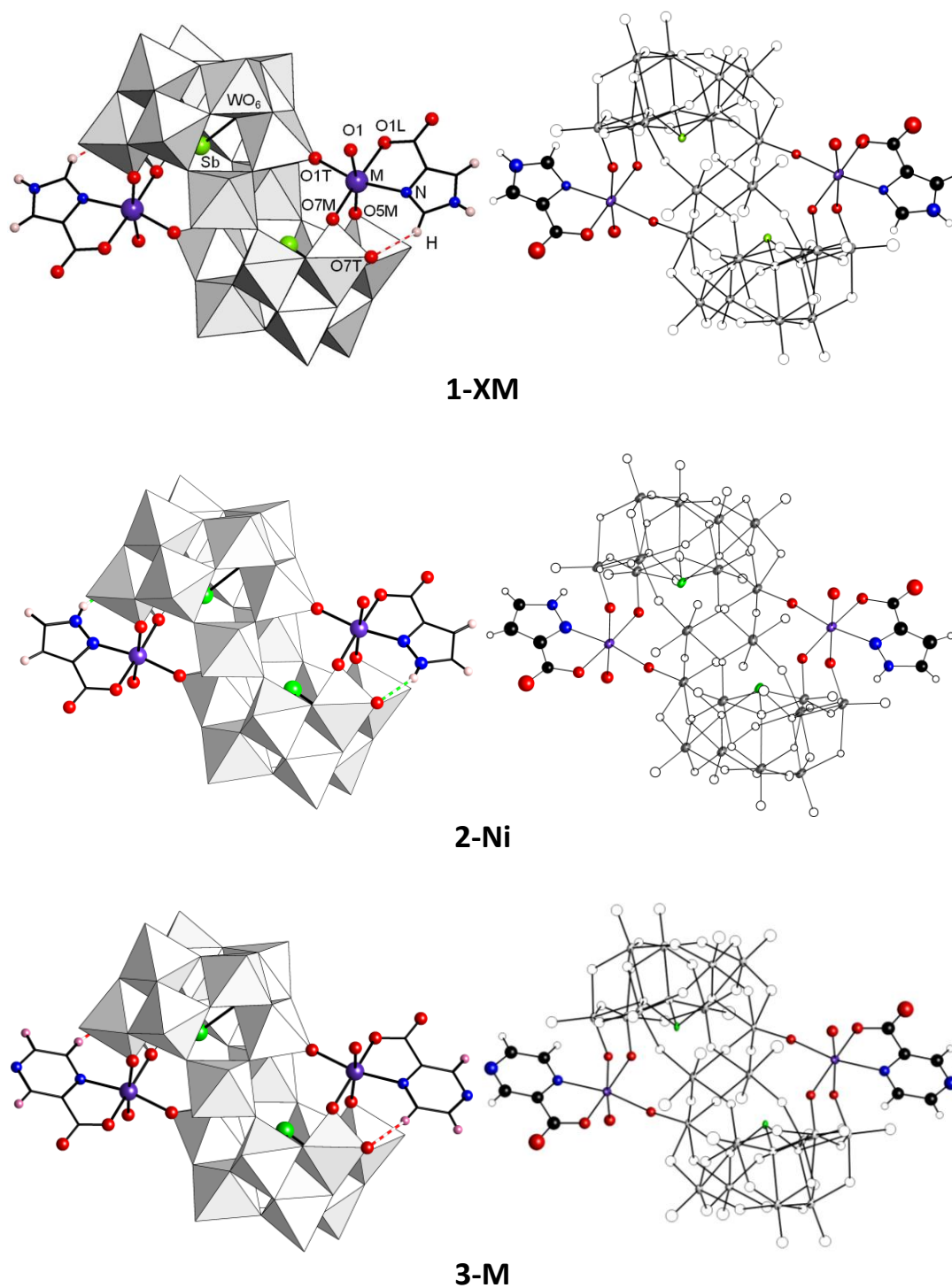


Figure 2.5. Left: Molecular structures for the centrosymmetric **1-XM**, **2-Ni** and **3-M** hybrid POMs with the general atom labeling for the transition metal coordination spheres. Right: ORTEP representations showing 50% probability ellipsoids for **1-SbZn**, **2-Ni** and **3-Zn** as representative examples. Intramolecular C—H...O_{POM} and N—H...O_{POM} bonds represented as dashed red and green lines, respectively.

CHAPTER 2

Three terminal O_{POM} atoms occupy *fac*-related positions in the octahedral coordination sphere of each M^{II} center: two belong to a $\{W_2O_{11}\}$ corner-shared fragment of one subunit (O5M/O7M) and the remaining one belongs to the 60° -rotated $\{W_3O_{13}\}$ trimer of the other subunit (O1T). The coordination spheres are completed with one water molecule (O1) and one anionic, O,N-chelating ligand (Table 2.6). BVS calculations¹⁸ confirm the O1 water molecule as the only protonation site, the relatively low values obtained for the terminal O atoms of the internal positions (1.39 – 1.51) being in agreement with the above mentioned W/ M^{II} disorder.

Table 2.6. Bond Lengths (Å) and values of the Continuous Shape Measures (CShM) with the ideal octahedron as reference shape (CShM = 0) for the $M^{\text{II}}L_6$ coordination spheres of **1-XM**, **2-Ni** and **3-M** compared to those of the $[ML_2(H_2O)_2]$ complexes and the Krebs-type $[\{M(H_2O)_3\}_2(WO_2)_2(SbW_9O_{33})_2]^{10-}$ precursors (M-POM, M = Mn, Co, Ni, and Zn). For the nomenclature see Figure 2.5.

	M–O1L	M–N	M–O1	M–O5M	M–O7M	M–O1T	CShM
Mn-POM ^{3d}	-	-	2.18(4)	2.10(4)	2.16(3)	2.18(4)	0.422
1-SbMn	2.194(9)	2.241(11)	2.236(12)	2.155(9)	2.122(9)	2.150(9)	1.015
1-TeMn	2.183(11)	2.204(11)	2.206(11)	2.149(10)	2.154(10)	2.148(9)	1.033
Co-POM ^{3c}	-	-	2.060(14)	2.065(10)	2.037(12)	2.106(12)	0.383
1-SbCo	2.095(12)	2.107(13)	2.137(13)	2.096(10)	2.068(10)	2.078(12)	0.627
1-TeCo	2.067(10)	2.117(11)	2.097(11)	2.099(9)	2.071(10)	2.087(10)	0.824
Co-imc ^{19c}	2.177(1)	2.076(2)	-	-	-	-	-
3-Co	2.029(8)	2.153(10)	2.107(7)	2.089(7)	2.060(6)	2.096(8)	1.130
Co-pyzc ²⁰	2.088(2)	2.095(2)	-	-	-	-	-
Ni-POM ²¹	-	-	2.07(2)	2.012(18)	2.004(17)	2.042(15)	0.224
1-SbNi	1.996(8)	2.022(10)	2.079(8)	2.069(7)	2.074(7)	2.074(7)	0.510
1-TeNi	2.090(8)	2.059(11)	2.090(8)	2.054(8)	2.054(8)	2.053(8)	0.573
Ni-imc ^{19a}	2.076(1)	2.050(2)	-	-	-	-	-
2-Ni	2.049(13)	2.028(16)	2.091(13)	2.057(12)	2.028(12)	2.047(12)	0.537
Ni-pzc ^[a]	2.074(1)	2.067(2)	-	-	-	-	-
Zn-POM ^{3d}	-	-	2.095(13)	2.052(12)	2.110(10)	2.107(10)	0.241
1-SbZn	2.098(6)	2.091(5)	2.110(6)	2.120(5)	2.043(5)	2.146(5)	0.815
Zn-imc ^{19b}	2.163(1)	2.075(2)	-	-	-	-	-
3-Zn	2.022(12)	2.066(12)	2.068(12)	2.112(9)	2.069(10)	2.127(9)	0.938
Zn-pyzc ²⁰	2.098(12)	2.080(2)	-	-	-	-	-

[a] See Appendix 1.

The organic ligand is arranged in such a way that the coordinating N atom and the O1T atom of the rotated trimer are *trans* to each other and the ring plane forms angles in the 51 – 58° range with the plane defined by the four W/ M^{II} metals of the central belt (**1-SbM**, 56 – 58° ; **1-TeM**, 51 – 53° ; **2-Ni**, 53° ; **3-M**, 52 – 55°). As shown in Figure 2.5, this ligand orientation allows for an intramolecular N–H \cdots O_{POM} (**2-Ni**) or C–H \cdots O_{POM} hydrogen-bond involving the proton located next to the coordinating N atom to be established (HN \cdots O_{POM} = $2.998(18)$ Å for **2-Ni**; HC \cdots O_{POM} = $3.125(10)$ – $3.218(16)$ Å for **1-SbM**; $3.182(18)$ – $3.293(18)$ Å for **1-TeM** and $3.256(17)$ – $3.273(2)$ Å for **3-M**). There

are no significant variations in the $M-O_{\text{POM}}$ bonding upon functionalization, and the $M-N$ and $M-O_L$ bond lengths also compare well to those reported for $[M(L)_2(H_2O)_2]$ complexes (Table 2.6). CShM calculations²² show that the distortion of the M^{II} coordination spheres from the ideal octahedral geometry increases with the ionic radius (ionic radii: 97 pm Mn, 88 pm Co, 83 pm Ni, 88 pm Zn)²³ and this trend is maintained and even stressed upon functionalization due to the introduction of a chelating ligand with nearly rigid bite angle.

Crystal packing of compounds 1-*XM*

Two different crystalline phases for the sodium salts of compounds **1-SbM** have been identified: triclinic (for Mn, Co, Zn) or monoclinic (for Ni). In all cases, polyanions are closely associated to each other via trifurcated hydrogen bonds that are established between the imidazole N-H groups and bridging O atoms of the tetrameric $\{W_4O_{18}\}$ faces ($\text{HN}\cdots\text{O}_{\text{POM}} = 2.839(18) - 3.322(16)$ Å). The tilting angle of the imc ligand with respect to the plane defined by the M^{II} and Sb atoms is more pronounced for the monoclinic **1-SbNi** (47°) than for the triclinic phases ($33 - 36^\circ$), and this slightly modifies the hydrogen-bonding network as shown in the details of Figure 2.6. Despite these subtle variations, compounds **1-SbM** show virtually the same type of one-dimensional POM arrangement for both triclinic and monoclinic phases (Figure 2.6). The hybrid POM chains stack following different structural patterns depending on the crystal system: the packing of the triclinic phase shows a brick-wall motif with chains parallel to the $[0-11]$ direction, whereas a herringbone pattern with chains propagating along the $[101]$ direction is observed for the monoclinic phase (Figure 2.7).

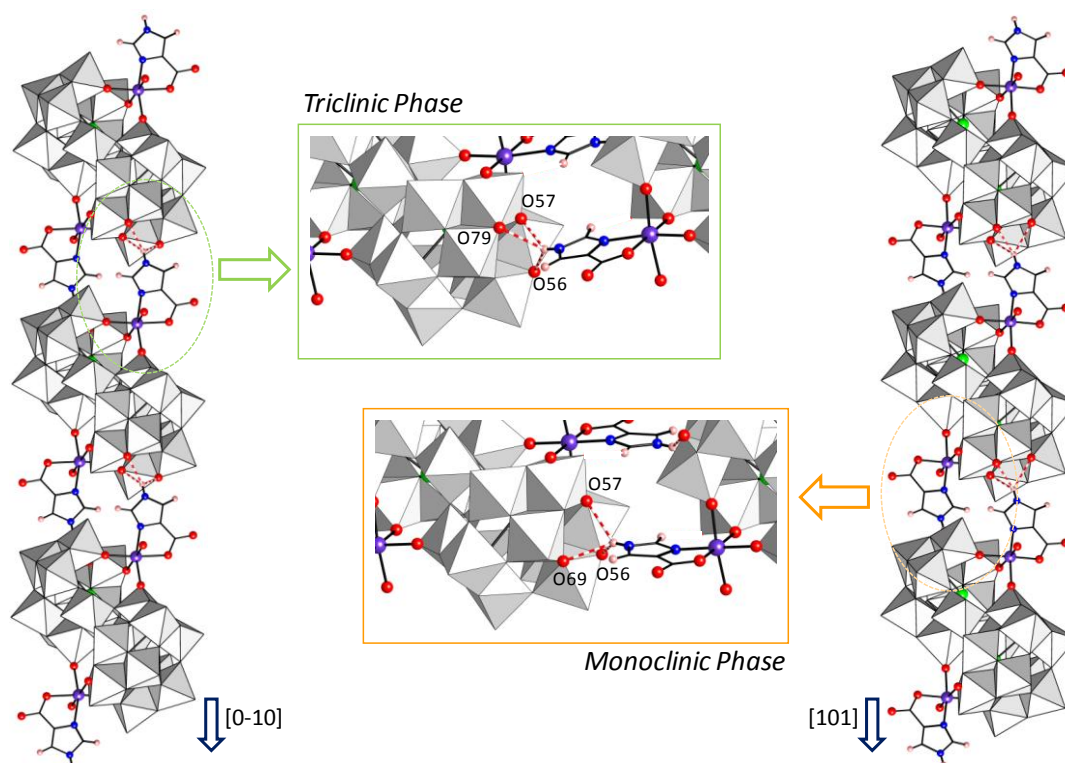


Figure 2.6. One-dimensional arrangement of hybrid POMs in the crystal packing of the triclinic (Mn, Co, Zn) and monoclinic (Ni) phases of **1-SbM** ($\text{N-H}\cdots\text{O}_{\text{POM}}$ hydrogen bonds represented as dashed red lines). Detail of the connectivity in both hydrogen-bonded chains.

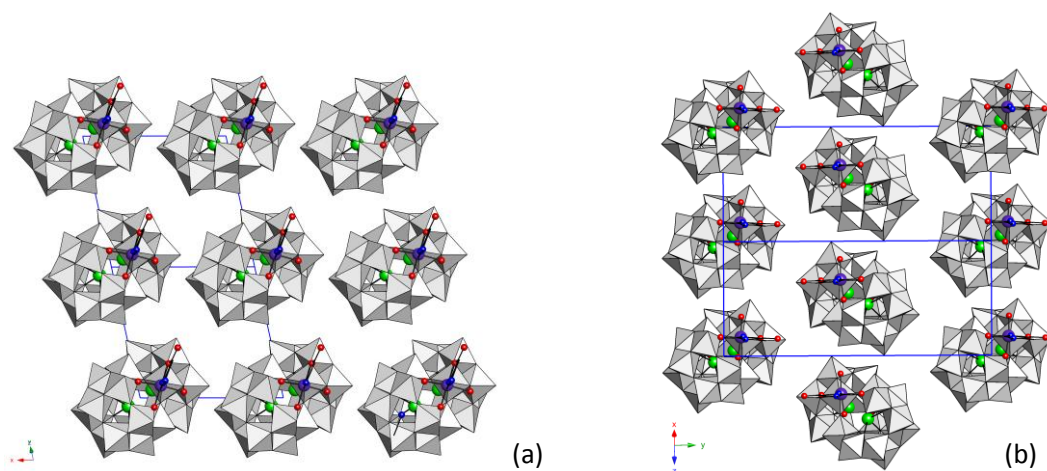


Figure 2.7. View of the crystal packing of (a) triclinic phases of **1-SbM** ($M = \text{Mn, Co, Zn}$) along the $[0-11]$ direction (b) the monoclinic phase **1-SbNi** along the $[101]$ direction (hydrogen atoms, sodium cations and hydration water molecules omitted for clarity).

Compounds **1-TeM** crystallize in two different triclinic phases. Phase A (**1-TeMn** and **1-TeCo**) shows a one-dimensional arrangement similar to that observed for the triclinic **1-SbM**, but with considerably longer $\text{HN}\cdots\text{O}_{\text{POM}}$ distances ($3.064(17) - 3.167(17) \text{ \AA}$). This lengthening of the $\text{HN}\cdots\text{O}$ distances is even more pronounced in phase B ($3.332(14) \text{ \AA}$ for **1-TeNi**), due to the 51° tilting angle of the imc ligand with respect to the plane defined by the M^{II} and Te atoms (Table 2.7). This results in the hybrid POMs being associated to each other via bifurcated $\text{N-H}\cdots\text{O}_{\text{POM}}$ hydrogen bonds instead of the trifurcated pattern described so far.

Crystal packing of compounds 2-Ni and 3-M

The arrangement of hybrid POMs in **2-Ni** is similar to those mentioned above. In this case, the interaction between two adjacent clusters is established by trifurcated $\text{C-H}\cdots\text{O}_{\text{POM}}$ interactions instead of $\text{N-H}\cdots\text{O}_{\text{POM}}$ hydrogen bonds ($\text{HC}\cdots\text{O}_{\text{POM}} = 3.24(2) - 3.32(2) \text{ \AA}$), resulting in chains running along the crystallographic c axis. The brick-wall type packing is strongly related to that found in triclinic **1-SbM** phases, despite the fact that the pyrazole ring shows a tilting angle of 47° with respect to the plane defined by the Ni^{II} and Sb atoms. This angle is similar to that observed for the monoclinic **1-SbNi**, so that the connectivity between contiguous POMs follows the same geometrical pattern (Figure 2.8).

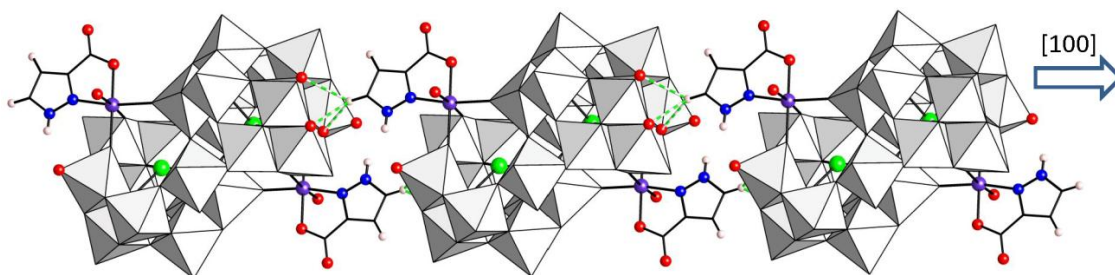


Figure 2.8. One-dimensional arrangement of hybrid POMs in the crystal packing of **2-Ni** running along the $[001]$ direction ($\text{C-H}\cdots\text{O}_{\text{POM}}$ interactions as dashed green lines).

Compounds **3-M** crystallize in two different triclinic groups. On the one hand, for **3-Zn**, the non-coordinated N4 atom from the ligand and the terminal O8T atom from the contiguous POM are connected through the coordination sphere of a sodium atom (Na1), which acts as a linker of hybrid adjacent POMs in a 1D-arrangement running along [0-11] direction. This linkage is reinforced by a weak intermolecular C5—H5···O9T_{POM} interaction (HC···O_{POM} = 3.24(2) Å; Figure 2.9). On the other hand, for **3-Co**, hybrid POMs are linked through the coordination sphere of the potassium atom K1 atom along the [100] direction. These chains are further connected by single weak intermolecular C—H···O_{POM} interactions into a 3D network (Figure 2.10). The tilting angle defined by the plane containing the ligand and the mirror plane of the POM is as low as 25° for both **3-Zn** and **3-Co**, so that the brick-wall type packing is present in the structures.

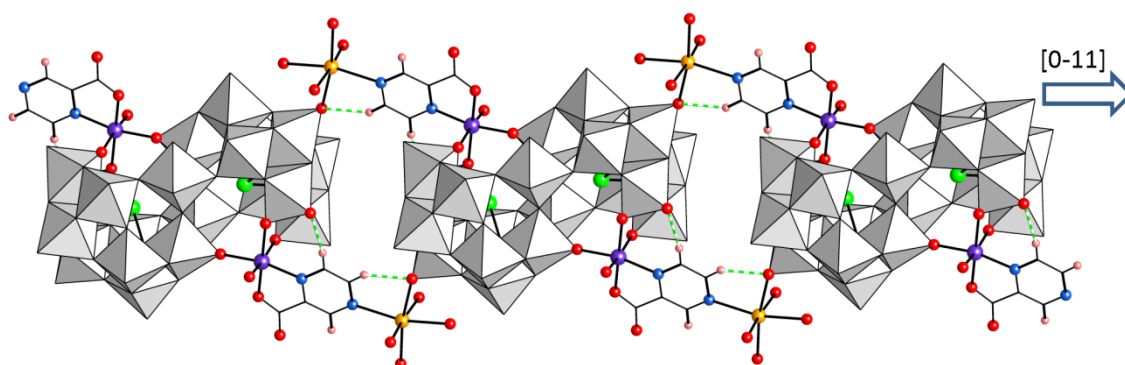


Figure 2.9. One-dimensional arrangement of hybrid POMs parallel to the [0-11] direction in the crystal packing of **3-Zn** (C—H···O_{POM} interactions as dashed green lines).

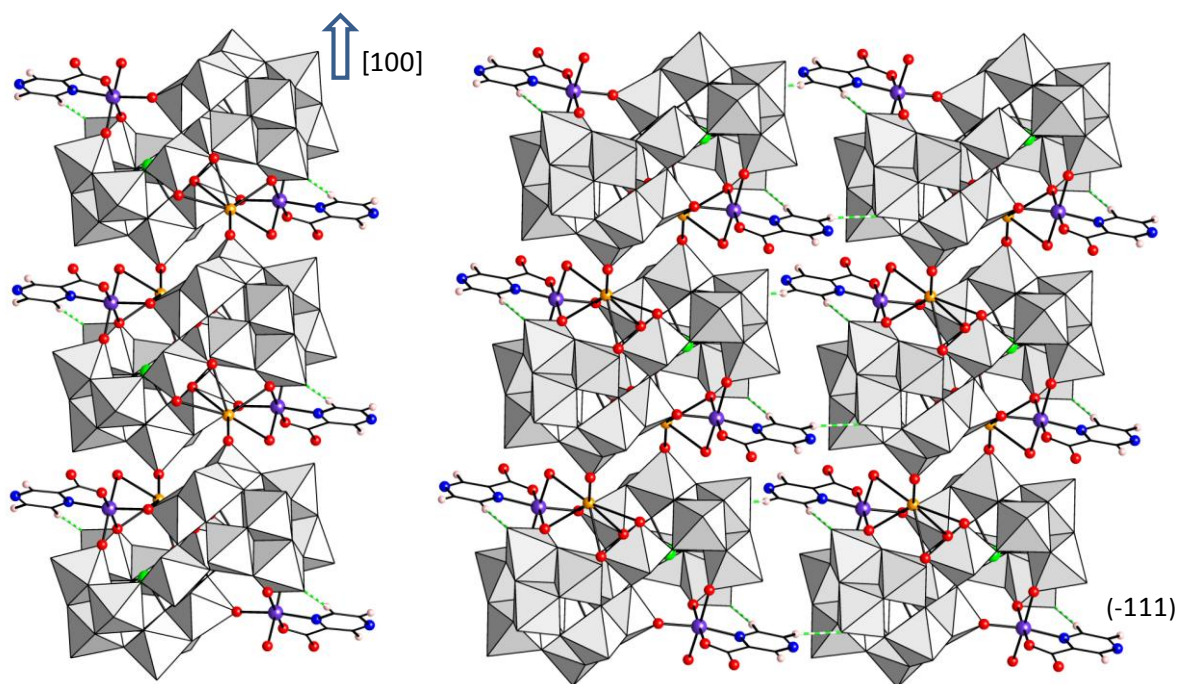


Figure 2.10. Left: One-dimensional arrangement of hybrid POMs parallel to the [100] direction in the crystal packing of **3-Co**. Right: Projection on the (-111) plane of the three-dimensional network formed by the connection of the K-bonded chains by C—H···O_{POM} interactions (represented as dashed green lines).

CHAPTER 2

Table 2.7. Geometrical parameters of the N-H...O_{POM} and C-H...O_{POM} interactions in the compounds reported in this section (Å, °).

	H...A	D...A	D-H...A
1-SbMn			
N2-H2...O56 ⁱ	2.42	3.103(14)	135
N2-H2...O57 ⁱ	2.19	2.894(14)	136
N2-H2...O79 ⁱ	2.57	2.976(15)	109
C1-H2...O7T (Intra)	2.39	3.199(17)	143
1-SbCo			
N2-H2...O56 ⁱ	2.50	3.141(17)	130
N2-H2...O57 ⁱ	2.08	2.839(18)	143
N2-H2...O79 ⁱ	2.55	3.01(2)	113
C1-H1...O7T (Intra)	2.33	3.15(2)	145
1-SbNi			
N2-H2...O56 ⁱⁱ	2.20	2.866(14)	132
N2-H2...O57 ⁱⁱ	2.59	3.322(16)	141
N2-H2...O69 ⁱⁱ	2.49	3.188(15)	137
C1-H1...O7T (Intra)	2.41	3.218(16)	143
1-SbZn			
N2-H2...O56 ⁱ	2.47	3.135(7)	132
N2-H2...O57 ⁱ	2.13	2.870(7)	142
N2-H2...O79 ⁱ	2.58	3.011(9)	111
C1-H1...O7T (Intra)	2.30	3.125(10)	144
1-TeMn			
N2-H2...O56 ⁱ	2.47	3.097(17)	130
N2-H2...O57 ⁱ	2.42	3.094(16)	135
N2-H2...O69 ⁱ	2.41	3.116(16)	140
C1-H1...O7T (Intra)	2.51	3.293(18)	142
1-TeCo			
N2-H2...O56 ⁱ	2.42	3.067(16)	133
N2-H2...O57 ⁱ	2.41	3.064(17)	133
N2-H2...O69 ⁱ	2.45	3.167(17)	141
C1-H1...O7T (Intra)	2.43	3.230(17)	145
1-TeNi			
N2-H2...O56 ⁱⁱ	2.18	2.885(16)	136
N2-H2...O69 ⁱⁱ	2.42	3.138(14)	139
C1-H1...O7T (Intra)	2.35	3.182(18)	146
2-Ni			
C5-H5...O56 ⁱⁱⁱ	2.59	3.33(2)	136
C5-H5...O57 ⁱⁱⁱ	2.46	3.28(2)	144
C5-H5...O79 ⁱⁱⁱ	2.49	3.24(2)	136
N1-H1...O5T (Intra)	2.18	2.998(18)	155
3-Co			
C3-H3...O4T ^{iv}	2.55	3.260(16)	132
C5-H5...O9T ^{iv}	2.38	3.186(15)	143
C6-H6...O7T (Intra)	2.32	3.256(15)	168
3-Zn			
C5-H5...O9T ⁱ	2.46	3.24(2)	139
C6-H6...O7T (Intra)	2.34	3.27(2)	166

Symmetry codes: (i) 1-x, -y, 1-z; (ii) -x, 1-y, 1-z; (iii) 1-x, 2-y, 1-z; (iv) -x, -y, 1-z.

Intra: intramolecular bond. D: donor. A: acceptor.

Stability in aqueous solution. $^1\text{H-NMR}$ spectroscopic studies for **1-SbZn and **3-Zn****

In order to investigate the stability in aqueous solution of the hybrid POMs reported in this chapter, $^1\text{H-NMR}$ studies were performed on **1-SbZn**. Figure 2.11 shows the comparison of the spectrum of **1-SbZn** compared to those of $[\text{Zn}(\text{imc})_2(\text{H}_2\text{O})_2]$ prepared as reported^{19b} and commercial Himc (Figure 2.11). The spectrum of the free ligand shows two singlets at δ 8.61 and 7.68 ppm that correspond to the protons located next to the coordinating N atom (H_A) and next to the carboxylate substituent (H_B), respectively. As shown by the complex spectrum, the signals of the two non-equivalent imidazole protons undergo upfield shift upon ligand coordination and this change in the chemical shift (δ) is significantly more pronounced for the H_A proton ($\Delta\delta(\text{H}_\text{A}) = 0.73$ vs. $\Delta\delta(\text{H}_\text{B}) = 0.05$ ppm). In the case of **1-SbZn**, the two-line spectrum shows analogous behavior with similar ΔH_B parameter (0.10 ppm), but the signal of H_A broadens and its δ value becomes considerably smaller ($\Delta\delta = 0.31$ ppm). This is probably due to the mentioned intramolecular $\text{C}-\text{H}\cdots\text{O}_{\text{POM}}$ interaction which confers a characteristic spectrum on the **1-SbZn** species. No evidence of the presence of the free ligand or the Zn-complex is observed. This indicates that **1-SbZn** keeps stable upon dissolution and that there is no ligand dissociation in the NMR time scale. The spectrum of **1-SbZn** remained virtually identical for 5 days, showing that this hybrid POM does not undergo any significant structural transformation to other species.

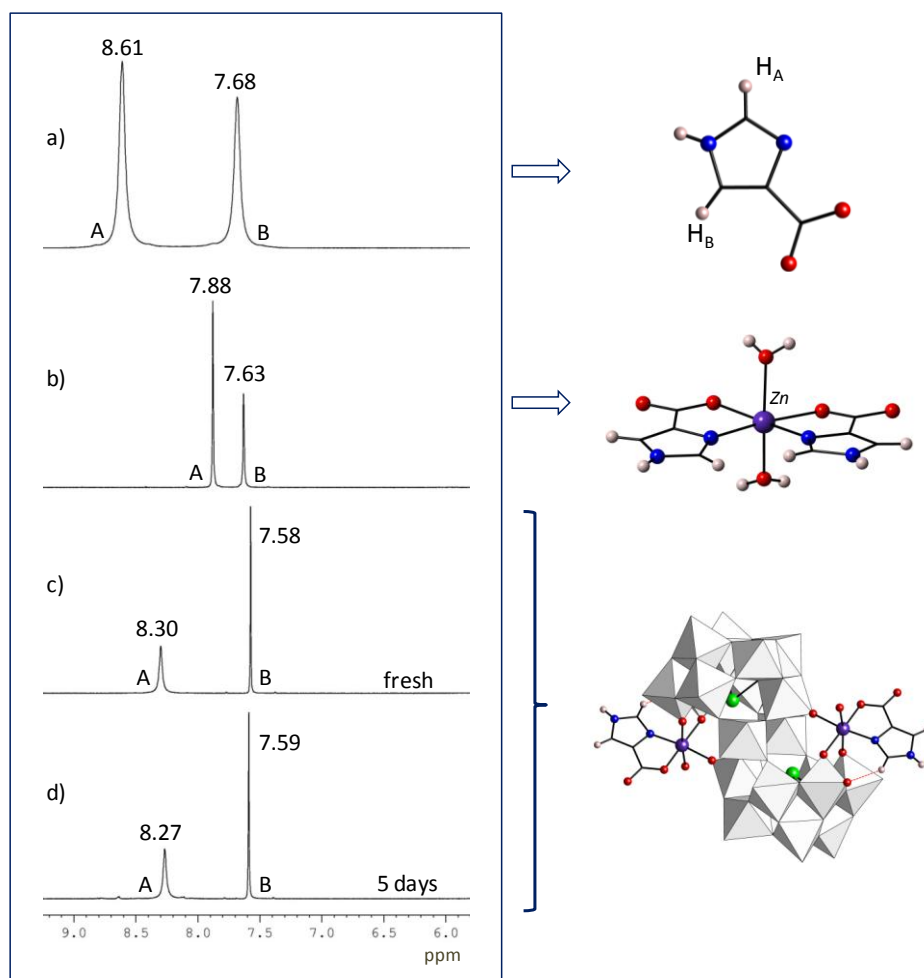


Figure 2.11. Comparison between the $^1\text{H-NMR}$ spectra of: a) free Himc ligand; b) $[\text{Zn}(\text{imc})_2(\text{H}_2\text{O})_2]$ complex; c) freshly dissolved polyanion **1-SbZn**; d) polyanion **1-SbZn** after 5 days.

Analogous studies have also been performed on the second diamagnetic hybrid POM obtained in this work, i.e. **3-Zn**. As shown in Figure 2.12, this species also shows a distinct $^1\text{H-NMR}$ spectrum which clearly differs from those of the free pyzc ligand and the $[\text{Zn}(\text{imc})_2(\text{H}_2\text{O})_2]$ complex. This spectrum remains unaltered for several days, confirming the stability of **3-Zn** in solution. These results demonstrate that $^1\text{H-NMR}$ spectroscopy is a suitable technique for analyzing the stability of diamagnetic organic derivatives of POM clusters. The ^1H nucleus affords clear advantages compared to the $^{183}\text{W-NMR}$ spectroscopy commonly used to evaluate the solution stability of polyoxotungstate frameworks because it is less time- and sample-consuming with consequent economic saving.

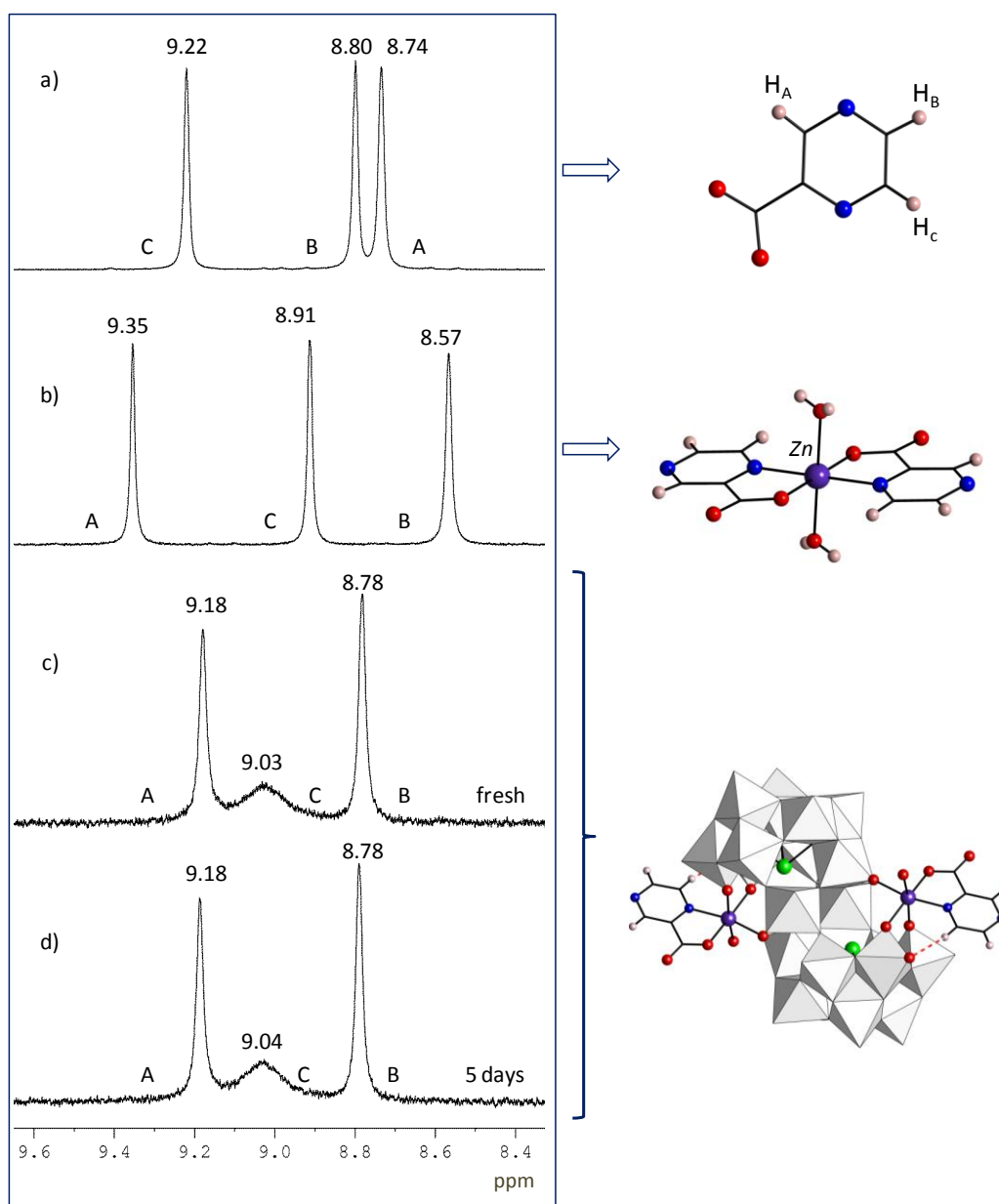
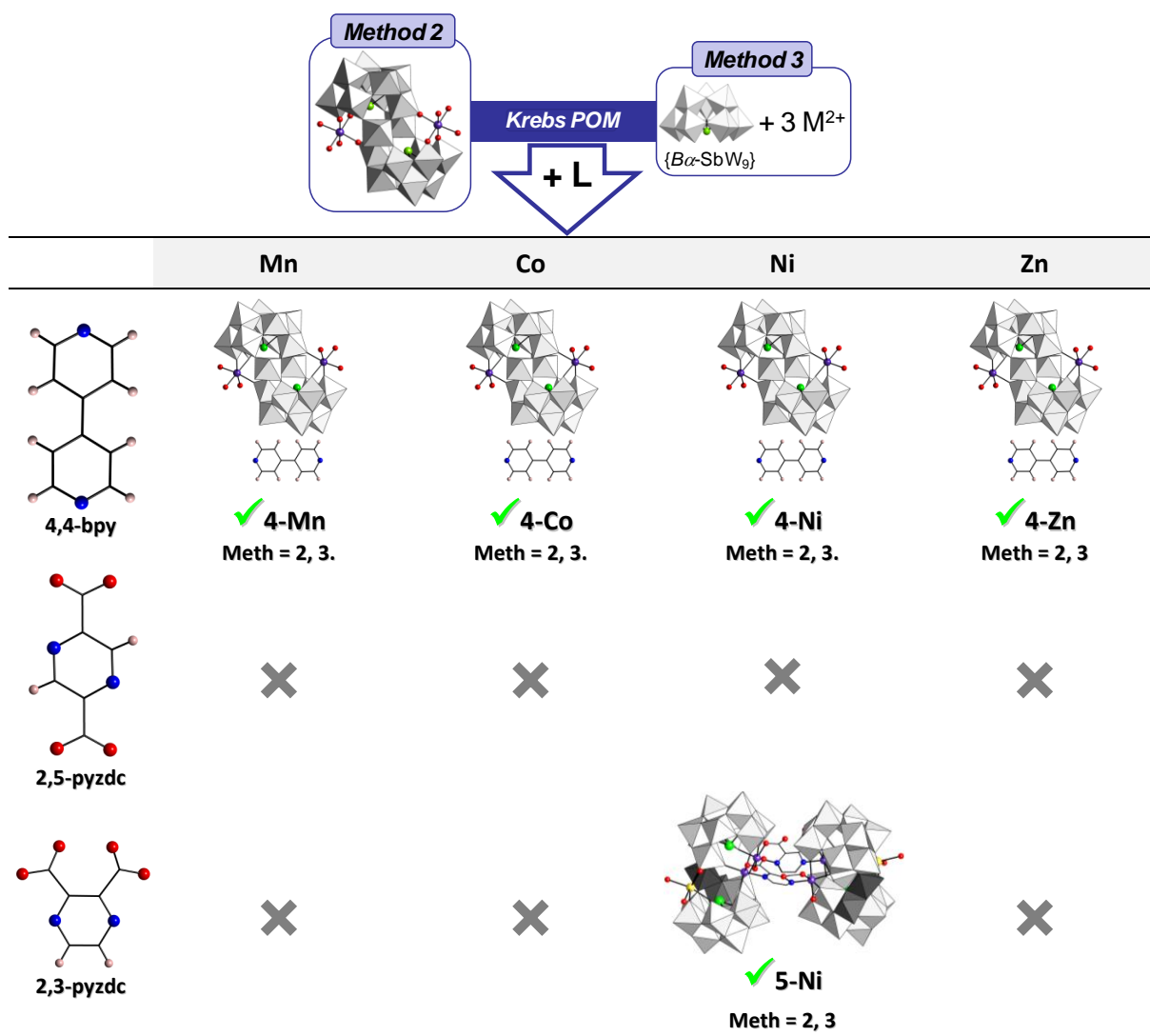


Figure 2.12. Comparison between the $^1\text{H-NMR}$ spectra of: a) free pyzc ligand; b) $[\text{Zn}(\text{pyzc})_2(\text{H}_2\text{O})_2]$ complex; c) freshly dissolved polyanion **3-Zn**; d) polyanion **3-Zn** after 5 days.

2.3.2. Reactions of Krebs type POMs with organic bridging ligands

Systematic studies analogous to those described in section 2.3.1 have also been performed for some organic molecules with demonstrated capability to act as bridging ligands between 3d-metal centers. Among the vast catalogue of commercial bridging ligands, we have selected the following three for a preliminary approach to the reactivity in this type of systems: the neutral 4,4'-bipyridine (4,4'-bpy) with bis(N-monodentate) bridging ability, and the diazinedicarboxylates pyrazine-2,5- and pyrazine-2,3-dicarboxylate (2,3-pyzdc and 2,5-pyzdc), which can coordinate 3d-metals in a bis(N,O-chelating) fashion. These three ligands have been reacted with the four $\text{Na}_{10}[\{\text{M}(\text{H}_2\text{O})_3\}_2(\text{WO}_2)_2(\text{B}\beta\text{-SbW}_9\text{O}_{33})_2\} \cdot 40\text{H}_2\text{O}$ tungstoantimonate(III) precursors ($\text{M} = \text{Mn, Co, Ni, Zn}$) following both synthetic methods 2 and 3. All reactions have been monitored by FT-IR spectroscopy. The results obtained from the 24 possible synthetic combinations are summarized in Scheme 2.2. As observed for the N,O-chelating ligands discussed in the previous section, the organic derivatization of Krebs-type POMs with bridging ligands is not trivial and reactivity has only been observed in one out of the 24 reactions evaluated.

Scheme 2.2. Results obtained in the reactions between Krebs-type tungstoantimonates(III) and organic bridging ligands



×: There is no reaction and the corresponding transition metal di-substituted Krebs type POM precursor is obtained as single-crystals. **Meth** = applied synthetic method.

i) Reaction of the 4,4'-bpy ligand with the 3d-metal disubstituted Krebs-type tungstoantimonates(III) following any of the two methods results in a series of compounds whose IR spectra are initially identical and show characteristic bands of the ligand in the region above 1000 cm^{-1} and the fingerprint of the Krebs-type cluster in the POM domain (Figure 2.13). However there is no alteration in the relative intensities of the triplet originating from the M—O—M stretching vibrations compared to the POM precursor. This indicates that, although present in the compound, the ligand is not coordinated to the POM skeleton. Single-crystal X-ray diffraction on the Mn derivative confirms this compound as $\text{Na}_{10}[\text{Mn}_2(\text{H}_2\text{O})_6(\text{WO}_2)_2(\text{SbW}_9\text{O}_{33})_2] \cdot 2(4,4'\text{bpy}) \cdot 32\text{H}_2\text{O}$ (**4-Mn**) formed by pristine $[\{\text{Mn}(\text{H}_2\text{O})_3\}_2(\text{WO}_2)_2(\text{B-}\beta\text{-SbW}_9\text{O}_{33})_2]^{10-}$ anions and interstitial 4,4'-bpy molecules. These results are in good agreement with those reported by Dolbecq et al.,^{8a} who tested the reactivity of ethylenediamine ligand toward iron-tetrasubstituted Krebs-type tungstoantimonates with the consequent isolation of POM-ethylenediammonium salts.

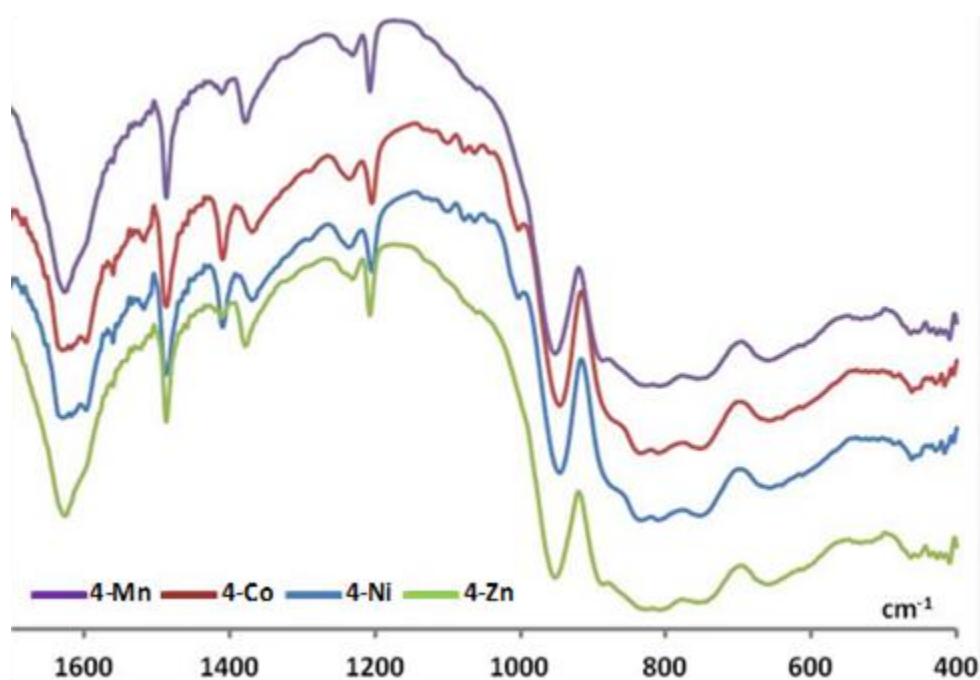


Figure 2.13. FT-IR spectra of the Mn, Co, Ni and Zn derivatives of **4-M**.

ii) The diazinedicarboxylate ligands tested show noticeably different reactivity toward Krebs-type anions. While the 2,5-pyzdc ligand is inert, 2,3-pyzdc showed to be selective toward the Ni-containing precursor regardless of the synthetic method. Unexpectedly, coordination of this ligand promotes the rearrangement of the polyoxotungstate framework into a completely different cluster as indicated by the remarkable variations in the IR spectrum compared to that of the precursor (Figure 2.14). Single-crystal X-ray diffraction confirms this compound as the sodium salt of the novel dimeric species $[\mu\text{-}\{(2,3)\text{-pyzdc}\}_2\{\text{Ni}_2(\text{H}_2\text{O})\text{Sb}_2\text{W}_{20}\text{O}_{70}\}_2]^{24-}$ (**5-Ni**). This result is a good indication of the fact that unprecedented POM frameworks might be obtained through ligand attack to Krebs-type clusters or other POM species containing exposed 3d-metal centers. The enormous variety of bridging ligands available from the literature will allow us to thoroughly extend this type of systematic studies in quest of novel POM architectures.

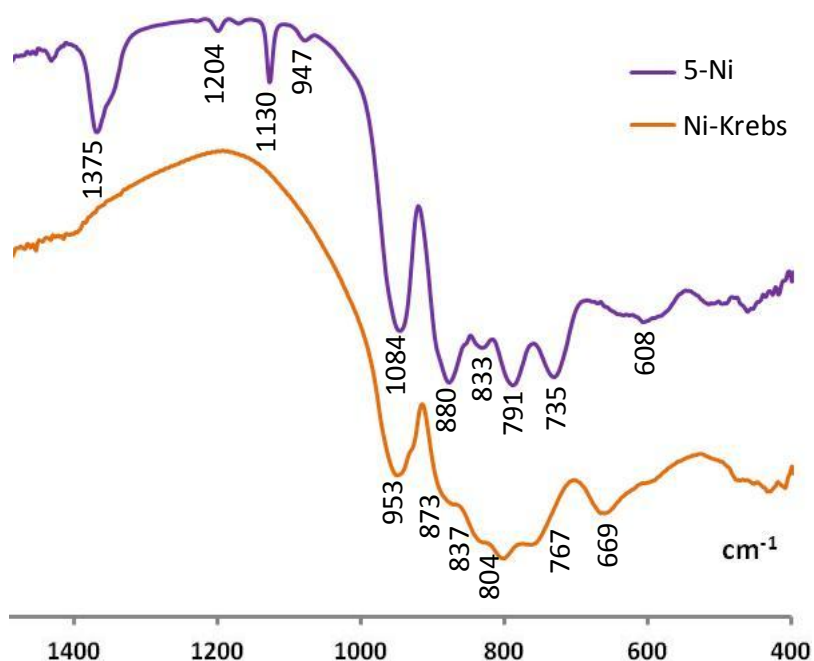


Figure 2.14. FT-IR spectra of 5-Ni and the Ni-disubstituted Krebs type POM precursor.

It is worth mentioning that the combination of the Zn-containing precursor and the 2,3-pydc ligand results in the $[C_2H_{10}Sb_2W_{31}O_{108}]^{14-}$ anion (Figure 2.15) when the final solution is left to evaporate until a volume of approx. 5 mL. Single crystal X-ray structural analysis²⁴ showed that this framework is closely related to the $[H_{10}Se_2W_{29}O_{103}]^{14-}$ tungstoselenite published in the literature.²⁵ The anion contains three main parts: one lacunary pentagonal unit $\{(WO_7)W_4\}$ capped by a dimeric $\{\mu-OAc(W_2O_3)\}$ moiety, two $B-\beta$ - $\{SbW_9O_{33}\}$ fragments and six $\{WO_6\}$ octahedra linking the above two parts together in a corner-sharing coordination mode. In the $\{(WO_7)W_4\}$ unit each W atom shows one terminal water ligand with $W-OH_2$ bond lengths longer than 2.2 Å. The vacant position of the $\{(WO_7)W_4\}$ unit is occupied by two K^+ cations, whereas, six extra K^+ atoms reinforce the linkage between trilacunary fragments and the pentagonal unit. As described by Cronin et al., the formation of this kind of clusters is strongly dependent on the presence of potassium cations and the high ionic strength of the aqueous solution. This is in full agreement with our observations. Optimization of this reaction, together with exploring the reactivity of the cluster $[C_2H_{10}Sb_2W_{31}O_{108}]^{14-}$ toward transition metals or lanthanides is planned for the near future.

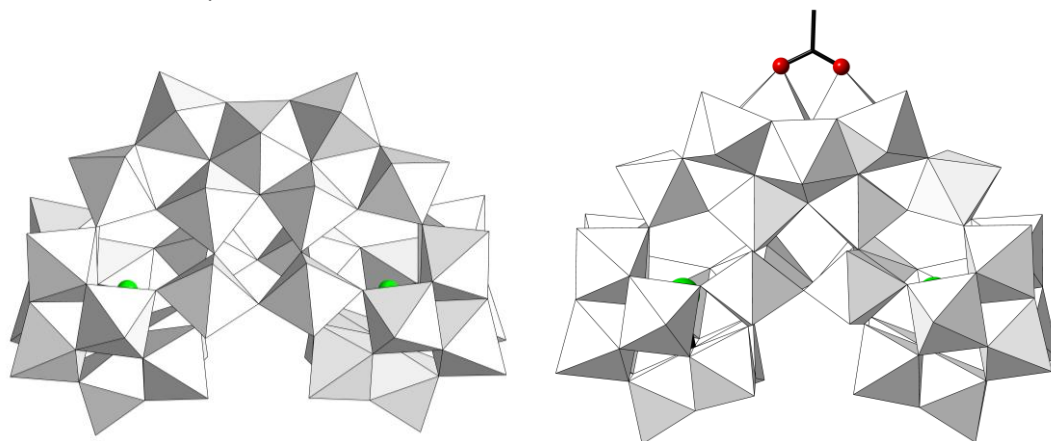


Figure 2.15. Structural relationship between $[H_{10}Se_2W_{29}O_{103}]^{14-}$ (left, ref. 25) and the $[(C_2H_3O_2)H_7Sb_2W_{31}O_{106}]^{14-}$ anion obtained in this work (right).

Crystal structure of 4-Mn

Single-crystal X-ray diffraction measurements carried out on the Mn^{II} derivative obtained from the reaction of Krebs-type precursor and 4,4'-bpy (**4-Mn**) confirms that the 4,4'-bpy molecules do not coordinate the transition metal centers at external positions. The structure is formed by pristine $[\{\text{Mn}(\text{H}_2\text{O})_3\}_2(\text{WO}_2)_2(\text{SbW}_9\text{O}_{33})_2]^{10-}$ clusters arranged in layers parallel to the (100) plane. The 4,4'-bpy molecules are located at interstitial positions (Figure 2.16) and interact with the tetrameric faces of the POMs via weak C—H \cdots O_{POM} hydrogen bonds. Two centrosymmetrically related 4,4'-bpy molecules are associated by π - π interactions and connect contiguous clusters in the [101] direction (Table 2.8).

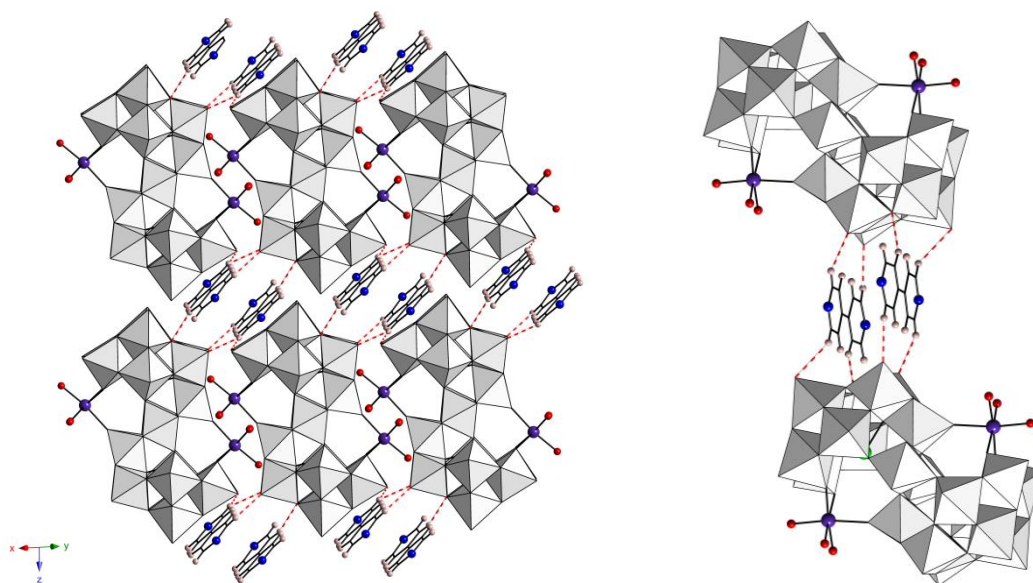


Figure 2.16. Left: View of the crystal packing of **4-Mn** along the [110] direction. Right: Detail of the C—H \cdots O_{POM} interactions between 4,4'-bpy molecules and the tetrameric faces of the POMs.

Table 2.8. Geometrical parameters of the C—H \cdots O bonds and π - π interactions (\AA , $^\circ$) in **4-Mn**.

	H \cdots A	D \cdots A	D—H \cdots A	
4-Mn				
C5—H5 \cdots O3T	2.31	3.047(19)	134	
C5—H5 \cdots O5T ⁱ	2.59	3.382(19)	141	
C12—H12 \cdots O39 ⁱ	2.42	3.32(2)	157	
C15—H15 \cdots O2T	2.43	3.11(2)	128	
	DZ	ANG	DC	DXY
CgN1—CgN2	3.383	3.412	3.699	1.558

Symmetry codes: (i) 1-x, 1-y, 1-z:

DZ: distance between one centroid and its projection in the plane; ANG: angle between planes; DC: distance between centroids; DXY: slippage. CgN1: ring defined by N1, C2, C3, C4, C5, C6 atoms. CgN2: ring defined by N11, C12, C13, C14, C15, C16 atoms.

Crystal structure of **5-Ni**

The dimeric hybrid **5-Ni** POM (Figure 2.17) is constituted by two unprecedented $\{\text{Ni}_2\text{Sb}_2\text{W}_{20}\text{O}_{70}\}$ clusters linked through two anionic 2,3-pyrazinedicarboxylate bridging ligands in a ideal C_2 symmetry. Each $\{\text{Ni}_2\text{Sb}_2\text{W}_{20}\text{O}_{70}\}$ cluster is formed by a novel 20-tungsto-2-antimonate(III) framework incorporating two octahedral Ni^{II} centers at the central belt. This framework can be rationalized as two trilacunary $\{B\text{-}\beta\text{-SbW}_9\text{O}_{33}\}$ subunits linked by one $\{\text{W}_2\text{O}_{10}\}$ dimeric moiety consisting in two edge-sharing WO_6 octahedra (Figure 2.18).

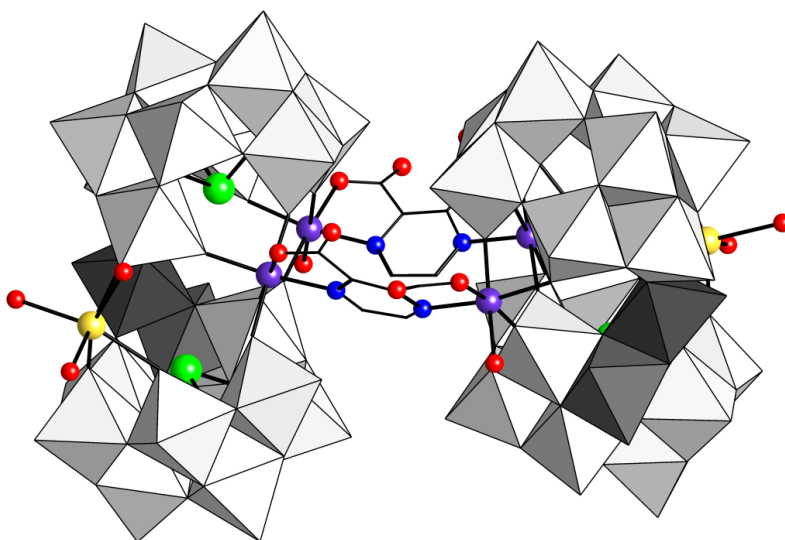


Figure 2.17. Combined ball & stick / polyhedral representation of the molecular structure of **5-Ni**. Na atoms in yellow.

The linking mode of the dimeric moiety is as follows: one of the W centers is incorporated into one of the trilacunary subunits by sharing edges with two octahedra of the 60° -rotated $\{\text{W}_3\text{O}_{13}\}$ trimer whereas the other W atom is placed over the hexameric ring and shares a corner with a non-rotated trimer. The second trilacunary subunit is then connected to the latter W center via corner-sharing involving two different $\{\text{W}_3\text{O}_{13}\}$ trimers, including the rotated one. As a result of the incorporation of the $\{\text{W}_2\text{O}_{10}\}$ moiety to one trilacunary subunit, this becomes a $\{\text{SbW}_{11}\text{O}_{39}\}$ type cluster where the rotated trimer is converted into a $\{\text{W}_5\text{O}_{20}\}$ fragment of edge-sharing WO_6 octahedra. Isopolyanion fragments have been widely reported as part of larger aggregates,²⁶ but to our knowledge, the $\{\text{W}_5\text{O}_{20}\}$ fragment in **5-Ni** has never been isolated as an independent isopolyanion. Nevertheless, it is closely related to the well-known $[\text{HW}_5\text{O}_{19}]^{7-}$ pentatungstate (Figure 2.19).²⁷ They both contain a rhombohedral $\{\text{W}_4\text{O}_{16}\}$ tetratungstate core and differ in the position of the fifth WO_6 octahedron. In $[\text{HW}_5\text{O}_{19}]^{7-}$, it is edge-shared to two octahedra (labeled as 1 and 3) and interacts with one of the internal O atoms, whereas in our $\{\text{W}_5\text{O}_{20}\}$ fragment it is connected to a single octahedron (4) by sharing an external edge.

Besides that occupied by a tungsten atom, the 20-tungsto-2-antimonate framework displays three additional coordination sites in its central belt. Two are occupied by the Ni centers and the third one is formally vacant. As observed for other 3d-metal containing defect POMs,²⁸ this vacant position is blocked by a Na cation, whose octahedral coordination sphere is formed by three O_{POM} atoms and three terminal water molecules. The presence of coordinated Na ions might be the key factor in stabilizing the unprecedented $\{\text{Ni}_2\text{Sb}_2\text{W}_{20}\text{O}_{70}\}$ cluster found in **5-Ni**. In close analogy to the defect 3d-metal containing POMs reported so far,²⁹ **5-Ni** could be a good candidate to incorporate

additional electrophilic groups in the Na-blocked vacant sites and therefore, we plan to study its reactivity toward different electrophiles (especially 3d and 4f metals) in the near future.

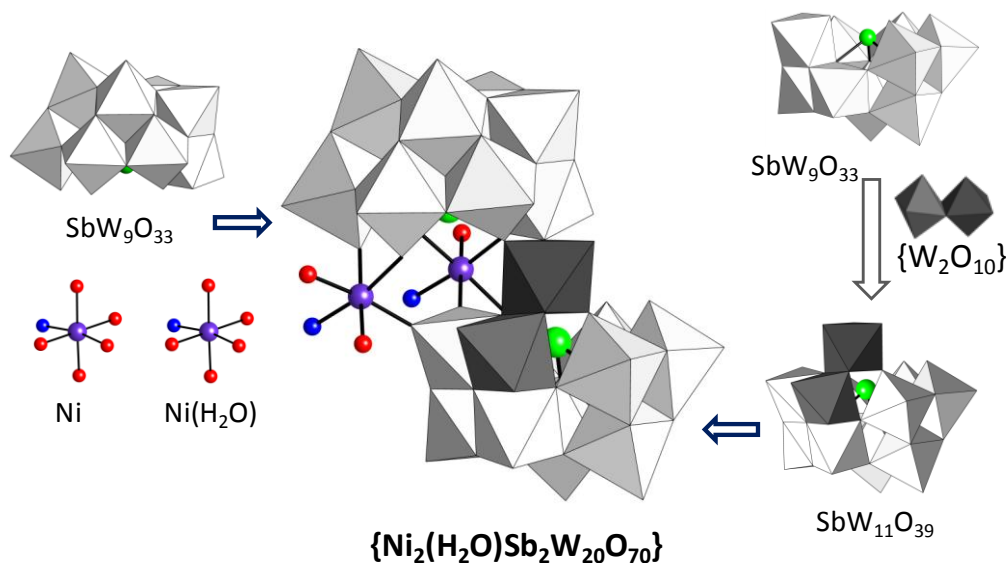


Figure 2.18. Schematic representation of the $\{\text{Ni}_2(\text{H}_2\text{O})\text{Sb}_2\text{W}_{20}\text{O}_{70}\}$ cluster from its basic structural components.

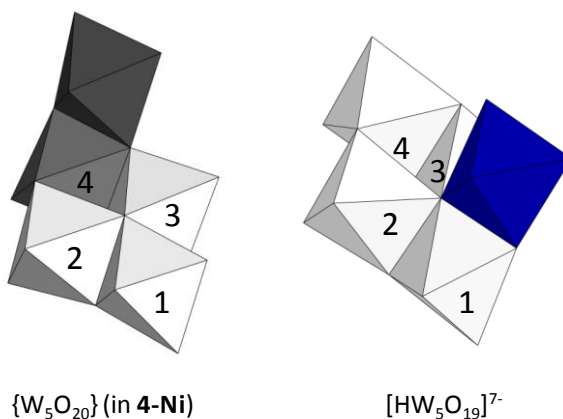


Figure 2.19. Left: $\{\text{W}_5\text{O}_{20}\}$ fragment in 5-Ni. Right: structure of the related $[\text{HW}_5\text{O}_{19}]^{7-}$ isopolytungstate. The octahedral units in the $\{\text{W}_4\text{O}_{16}\}$ cores are labeled as 1-4.

The structure of the $\{\text{Ni}_2\text{Sb}_2\text{W}_{20}\text{O}_{70}\}$ cluster is closely related to that of its Ni-disubstituted Krebs-type POM precursor and it appears to be formed upon a skeletal rearrangement promoted by 2,3-pyzdc ligands (Figure 2.20). Compared to the $[\{\text{Ni}(\text{H}_2\text{O})_3\}_2(\text{WO}_2)_2(\text{SbW}_9\text{O}_{33})_2]^{10-}$ parent POM, the $[\{\text{Na}(\text{H}_2\text{O})_3\}\{\text{Ni}(\text{H}_2\text{O})_3\}\{\text{Ni}(\text{H}_2\text{O})_2\}(\text{WO})(\text{SbW}_{10}\text{O}_{36})(\text{SbW}_9\text{O}_{33})]^{9-}$ cluster shows one $\{\text{Ni}(\text{H}_2\text{O})_2\}$ and one $\{\text{Na}(\text{H}_2\text{O})_3\}$ moiety replacing one of the internal (WO_2) groups and one of the external $\{\text{Ni}(\text{H}_2\text{O})_3\}$ moieties, respectively. Furthermore, one of the trilacunary units incorporates an additional $\{\text{WO}_6\}$ group in the 60° -rotated trimer via edge-sharing. Therefore, the $\{\text{Ni}_2\text{Sb}_2\text{W}_{20}\text{O}_{70}\}$ cluster could be seen as the product of the migration of one of the belt $\{\text{cis-WO}_2\}$ groups toward the space available in between the rotated trimer of one trilacunary subunit and the second $\{\text{WO}_2\}$ group. Consequently, the internal coordination position in the belt of the Krebs-type cluster left vacant by this migration is occupied by one of the external Ni atoms, which is in turn replaced with a Na ion from the medium to stabilize the resulting assembly.

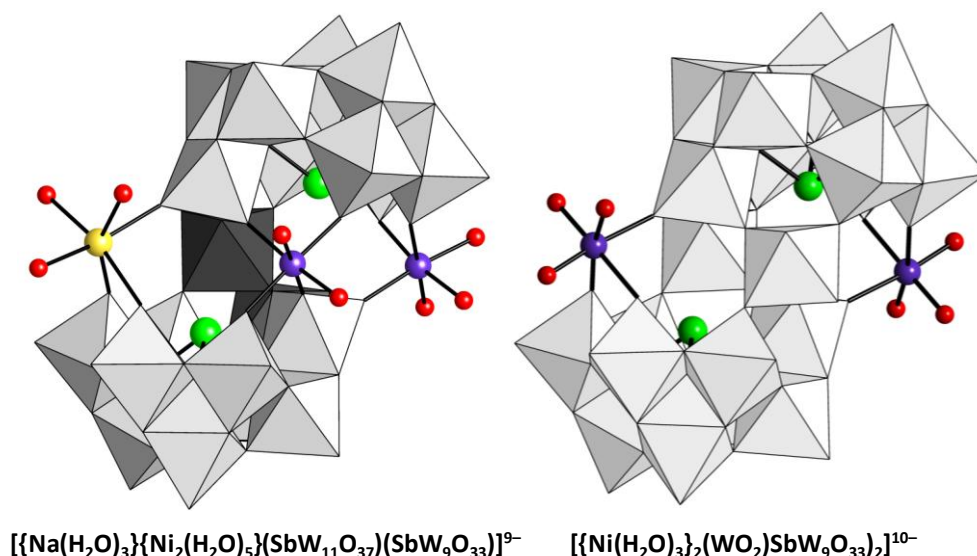


Figure 2.20. Structural relationship between the $[\{\text{Na}(\text{H}_2\text{O})_3\}\{\text{Ni}(\text{H}_2\text{O})_3\}\{\text{Ni}(\text{H}_2\text{O})_2\}(\text{WO})(\text{SbW}_{10}\text{O}_{36})(\text{SbW}_9\text{O}_{33})]^{9-}$ cluster $\{\text{Ni}_2\text{Sb}_2\text{W}_{20}\text{O}_{70}\}$ and the Ni-disubstituted Krebs type POM $[\{\text{Ni}(\text{H}_2\text{O})_3\}_2(\text{WO}_2)_2(\text{SbW}_9\text{O}_{33})_2]^{10-}$.

The two crystallographically independent Ni^{II} centers display octahedral NiO_5N chromophores. The coordination sphere of Ni1 is composed by four O atoms, two from each trilacunary subunit, and the O, N atoms from the anionic 2,3-pyzdc chelating ligand. The O_{POM} atoms belong to adjacent 60° -rotated and non-rotated trimers. Similarly, three terminal O_{POM} atoms occupy *fac*-related positions in the coordination sphere of the Ni2 center. Two belong to a $\{\text{W}_2\text{O}_{11}\}$ corner-shared fragment of one subunit and the remaining one to the rotated trimer of the other subunit. The coordination sphere of Ni2 is completed with one water molecule (O1) and the O, N atoms of one 2,3-pyzdc ligand in chelating fashion (Table 2.9). Therefore, the two 2,3-pyzdc molecules display a bis-(bidentate) coordination mode bridging one Ni atom from each cluster ($\text{Ni}\cdots\text{Ni} = 6.81 \text{ \AA}$) in such a way that the two carboxylate groups of each ligand undergo slight tilting with respect to the plane of the pyrazine ring (dihedral angle: 15° and 31°) due to the steric hydrance between both anionic groups. Non-coplanar configurations have been previously observed for this ligand in different coordination complexes.³⁰

Table 2.9. Bond Lengths (\AA) and values of the Continuous Shape Measures (CShM) calculations with the ideal octahedron as the reference shape ($\text{CShM} = 0$) for the Ni^{II} coordination spheres of **5-Ni** compared to those of the $[\text{Ni}(\text{pyzdcH})_2(\text{H}_2\text{O})_2]$ complex (Ni-pyzdc)³⁰ and the Krebs-type $[\{\text{Ni}(\text{H}_2\text{O})_3\}_2(\text{WO}_2)_2(\text{SbW}_9\text{O}_{33})_2]^{10-}$ precursor (Ni-POM).²¹

	M–O _{Ligand}	M–N	M–O1 _{POM}	M–O2 _{POM}	M–O3 _{POM}	M–O4 _{POM}	M–O1	CShM
Ni-POM	-	-	2.07(2)	2.012(18)	2.004(17)	-	2.07(2)	0.224
Ni1 (5-Ni)	2.043(12)	2.089(14)	1.999(13)	2.022(11)	2.029(13)	2.039(12)	-	0.375
Ni2 (5-Ni)	2.029(13)	2.069(14)	2.001(13)	2.045(12)	2.040(13)	-	2.080(15)	0.516
Ni-pyzdc	2.031(1)	2.074(3)	-	-	-	-	-	-

It is also worth mentioning that the two pyrazine rings are tilted 40° out of the plane defined by the four Ni atoms and this creates a central aromatic nest where one water molecule (O1W) is hosted (Figure 2.21) via $\text{O}_w\text{--H}\cdots\pi$ interactions.³¹ Based on electrostatic arguments, aromatic hydrogen bonds are expected to originate from the interaction between the LUMO orbitals of water

and the aromatic HOMO.³² Water molecules were identified as aromatic hydrogen-bonding donors in the late 70's, when O_w-H vectors pointing almost exactly at the center of the phenyl acceptor were observed.³³ The first X-ray diffraction evidences for aromatic hydrogen bonding to water were obtained for small, non-biological calixarene and tetraphenylborate salts,³⁴ but in spite of this, non conventional aromatic hydrogen-bonds have attracted enormous interest in structural biology because they are ubiquitous in macromolecules and they play a key role in the stabilization of local 3D structures.³⁵ Geometrical parameters of some compounds where a water molecule is trapped between two or more aromatic rings by $O-H \cdots \pi$ interactions are shown in Table 2.10, together with those observed in theoretical calculations for water-benzene aromatic hydrogen-bonds.³⁶ In our compound, the O1W water molecule might also be interacting with one bridging O_{POM} atom from each $\{Ni_2Sb_2W_{20}O_{70}\}$ cluster ($O_w \cdots O_{POM}$: 2.998(3)Å), although the bonding angle seems to be narrow enough for any efficient interaction to be hindered. The single-crystal X-Ray diffraction experiment carried out for **5-Ni** did not allow to locate any hydrogen atom in the water molecules and therefore, we cannot provide any structural confirmation for the hydrogen atoms of O1W to be pointing at the center of the pyrazine rings.

Table 2.10. Geometrical parameters (Å, °) of the $O_w-H \cdots \pi$ interactions between the O1W water molecule and the centroids of the aromatic rings in **5-Ni** and compared to some published results.

Compound	$O \cdots \pi$	$\pi \cdots O \cdots \pi$	Reference
5-Ni	3.217(2)	129	This work
Simulated (benzene-water)	3.11	-	36a
Calyx[4]arene sulphonate 13.5H ₂ O	3.16	133	34
	3.19		
[Ni ₂ (ox)(dien) ₂ (H ₂ O) ₂][B(Ph) ₄] ₂	3.168(3)	92	36b
[Ag ₂ (μ_2 -2-ap)(2-ap)(bnb)(H ₂ O)]	3.192(2)	135	36c
	3.267(2)		

ox = oxalate; dien=diethylenetriamine; Ph = phenyl; 2-ap=2-amino pyridine; bnb = 3,3-binitrobenzoate.

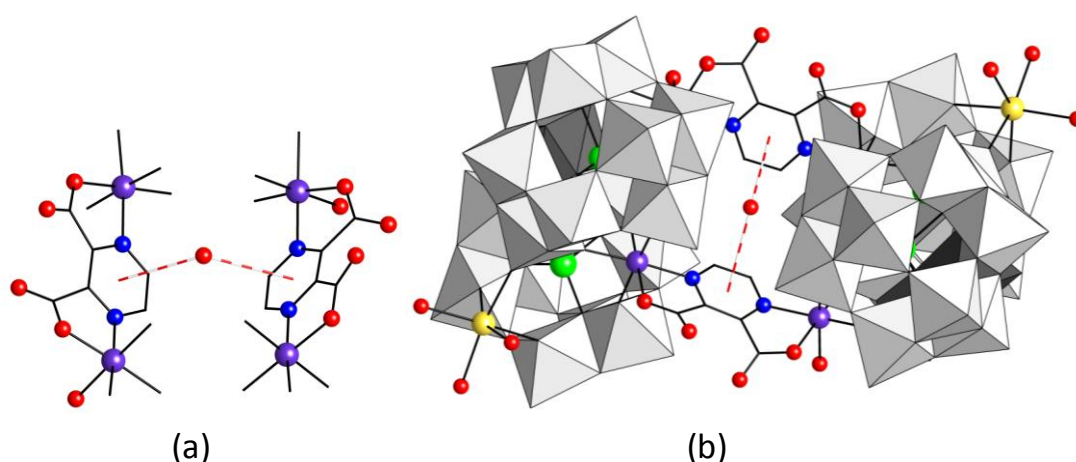


Figure 2.21. Combined ball & stick /polyhedral representation of the (a) detail of the coordination mode of 2,3-pydc ligands; (b) top view of **5-Ni** anion highlighting the aromatic hydrogen bonding interaction. ($O1W \cdots \pi$ bonds depicted as dashed red lines).

Magnetic properties of 5-Ni

Magnetic susceptibility (χ_m) studies for **5-Ni** were performed as detailed in Appendix 2. The temperature dependence of χ_m and the $\chi_m T$ product is depicted in Figure 2.22. The $\chi_m T$ product of **5-Ni** at room temperature is $5.065 \text{ cm}^3 \text{ K mol}^{-1}$, in good agreement with that expected for a magnetically diluted sample containing four non-interacting octahedral Ni^{II} ions considering $S = 1$ and $g = 2.25$ ($5.062 \text{ cm}^3 \text{ K mol}^{-1}$). The $\chi_m T$ curve remains nearly constant as the temperature decreases down to approximately 30K, below which it undergoes drastic decrease to reach a value of $4.15 \text{ cm}^3 \text{ K mol}^{-1}$ at 5K. Curie-Weiss behavior is observed for nearly the whole temperature range analyzed and the fit of the susceptibility data to the corresponding expression leads to C_m and θ values of $5.07 \text{ cm}^3 \text{ K mol}^{-1}$ and -0.4 K , respectively. The negative value of the Weiss temperature as well as the decrease of the $\chi_m T$ product below 30K could be indicative of the presence of weak antiferromagnetic (AF) interactions. The Ni^{II} centers on each $\{\text{Ni}_2(\text{H}_2\text{O})\text{Sb}_2\text{W}_{20}\text{O}_{70}\}$ clusters are connected through one WO_6 octahedron and one edge-sharing $\{\text{W}_2\text{O}_{10}\}$ fragment. It is known that O—W—O pathways leads to negligible magnetic exchange between paramagnetic centers,^{8a,37} and therefore, **5-Ni** could be described as two isolated $\{\text{Ni}_2(\mu\text{-}2,3\text{-pyzdc})\}$ dimers from a magnetic point of view. Following this assumption, magnetic susceptibility data were fitted by using Equation 1, which is the well-known expression for a dimeric $S = 1$ unit expressed per metal atom and multiplied by the four Ni^{2+} ions in our sample (Fit 1).³⁸

$$\chi_m = \frac{4 N g^2 \beta^2}{k T} \left[\frac{1 + 5 \exp(2x)}{3 + 5 \exp(2x) + \exp(-x)} \right] \quad \text{Eq. 1}$$

where $x = 2 J/kT$, N is the Avogadro's number, β is the Bohr magneton, k is the Boltzmann constant, g is the Landé factor and J is the intradimeric exchange coupling constant derived from the Heisenberg-van Vleck-Dirac spin Hamiltonian, $H = -2 J S_1 S_2$. The best fit results are $g = 2.25$ and $J = -0.35 \text{ cm}^{-1}$ (-0.5 K). These values are in good agreement with those observed for some 2,3-pyrazinedicarboxylate bridged Ni chains with extremely weak AF behavior.^{30a} However, this model does not reproduce the experimental data satisfactorily at temperatures below c.a. 130K, as shown in Figure 2.22. Therefore, we considered the zero-field splitting (ZFS) to be operative in our system, and consequently, the experimental data were fitted by the following expression considering four non-interacting $S = 1$ atoms showing single ion ZFS:³⁹

$$\chi_m = \frac{2 N g^2 \beta^2}{3 k T} \left[\frac{2/x - \frac{2 \exp(-x)}{x} + \exp(-x)}{1 + 2 \exp(-x)} \right] \quad \text{Eq. 2}$$

where $x = D/kT$; N , β , k and g have their usual meanings and D is the value of the zero-field splitting. Experimental data are very well reproduced with this equation and the best fit results are $D = 6.5 \text{ cm}^{-1}$ (9.3 K) and $g = 2.25$. The calculated D value is relatively large compared to that obtained for J , and therefore it can be concluded that the effect of the single ion anisotropy on the magnetic behavior of **5-Ni** is more pronounced than that due to the isotropic intradimeric exchange.

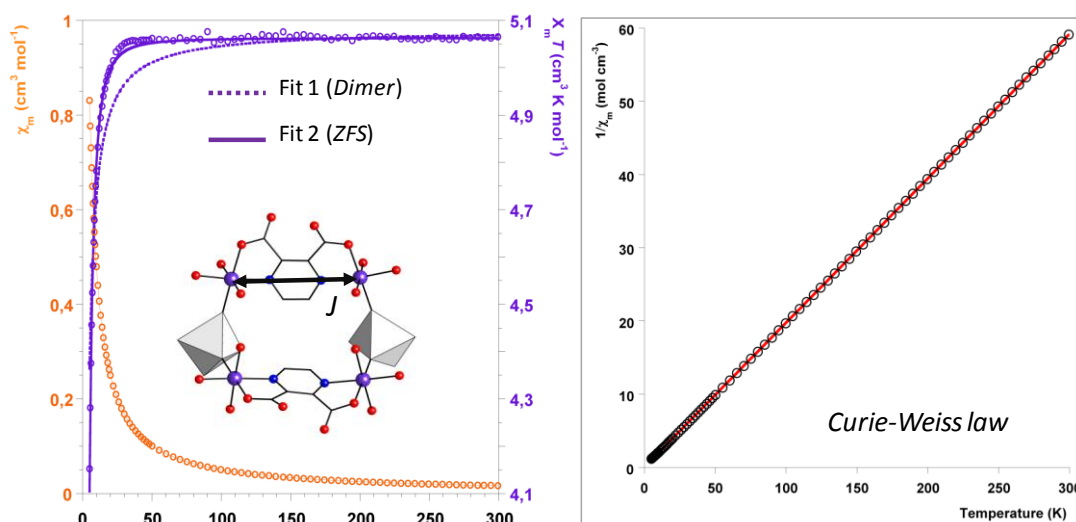


Figure 2.22. Left: Thermal evolution of χ_m and the $\chi_m T$ product for **5-Ni** (circles) and least-squares fit to the equation for dinuclear Ni^{2+} systems (Fit 1, dotted purple line) or for non-interacting Ni^{2+} centers with single-ion zero-field splitting (Fit 2, continuous purple line). Right: Fit of the magnetic susceptibility data (black circles) to the Curie-Weiss law (red line).

Stability in aqueous solution. Electrospray Ionization-Mass Spectrometry studies for 5-Ni.

In order to elucidate whether **5-Ni** is stable in solution or undergoes a decomposition process, electrospray ionization-mass spectrometry (ESI-MS) measurements were carried out as described in Appendix 2. The Ni^{II} centers of the cluster precluded us from using NMR spectroscopy as for **1-SbZn** and **3-Zn**, because the presence of paramagnetic centers usually results in wide chemical shift ranges and broadened signals that makes the interpretation of the spectra difficult.⁴⁰

Figure 2.23 shows the negative ESI mass spectrum of an aqueous solution of **5-Ni** recorded at low cone voltage. As can be observed in the spectrum, the dimeric **5-Ni** species dissociates into monomeric anions ($\{\text{M}\}^{n-}$) upon dissolution. Dissociation appears to be complete as no signals originating from dimeric species are observed in the spectrum. The monomeric anions are identified as three groups of signals spanning in the m/z 1000–1800 range. The isotopic pattern inspection, together with the m/z spacing between the groups of signals, indicate that the detected monomeric anions display similar composition with charge states of 5– (m/z 1043.7, $\{\text{M}\}^{5-}$), 4– (m/z 1310.7, $\{\text{M}\}^{4-}$) and 3– (m/z 1751.0, $\{\text{M}\}^{3-}$). These $\{\text{M}\}$ monomers are best described as pristine $\{\text{Ni}_2\text{Sb}_2\text{W}_{20}\text{O}_{70}\}$ clusters, and therefore, the 2,3-pyzdc ligand might be released during dissociation process. Because of the high charge state of the monomeric $\{\text{M}\}$ anion (10–), the gas-phase detected species in the negative ESI mass spectrum display different extent of protonation and counter-ion content, as well as the presence of loosely associated solvent molecules. This is commonly observed in negative ESI mass spectra of aqueous solutions of highly charged POMs.⁴¹ The most abundant group of signals is centered at m/z 1043.7 and formally corresponds to the series of anions of general formula $[\text{Ni}_2\text{Sb}_2\text{W}_{20}\text{O}_{70}+x\text{H}_2\text{O}+m\text{H}^++(5-m)\text{Na}^+]^{5-}$. Analogously, the group of signals at m/z 1310.7 and 1751.0 can be readily assigned to the $[\text{Ni}_2\text{Sb}_2\text{W}_{20}\text{O}_{70}+x\text{H}_2\text{O}+m\text{H}^++(6-m)\text{Na}^+]^{4-}$ and $[\text{Ni}_2\text{Sb}_2\text{W}_{20}\text{O}_{70}+x\text{H}_2\text{O}+m\text{H}^++(7-m)\text{Na}^+]^{3-}$ series, respectively.

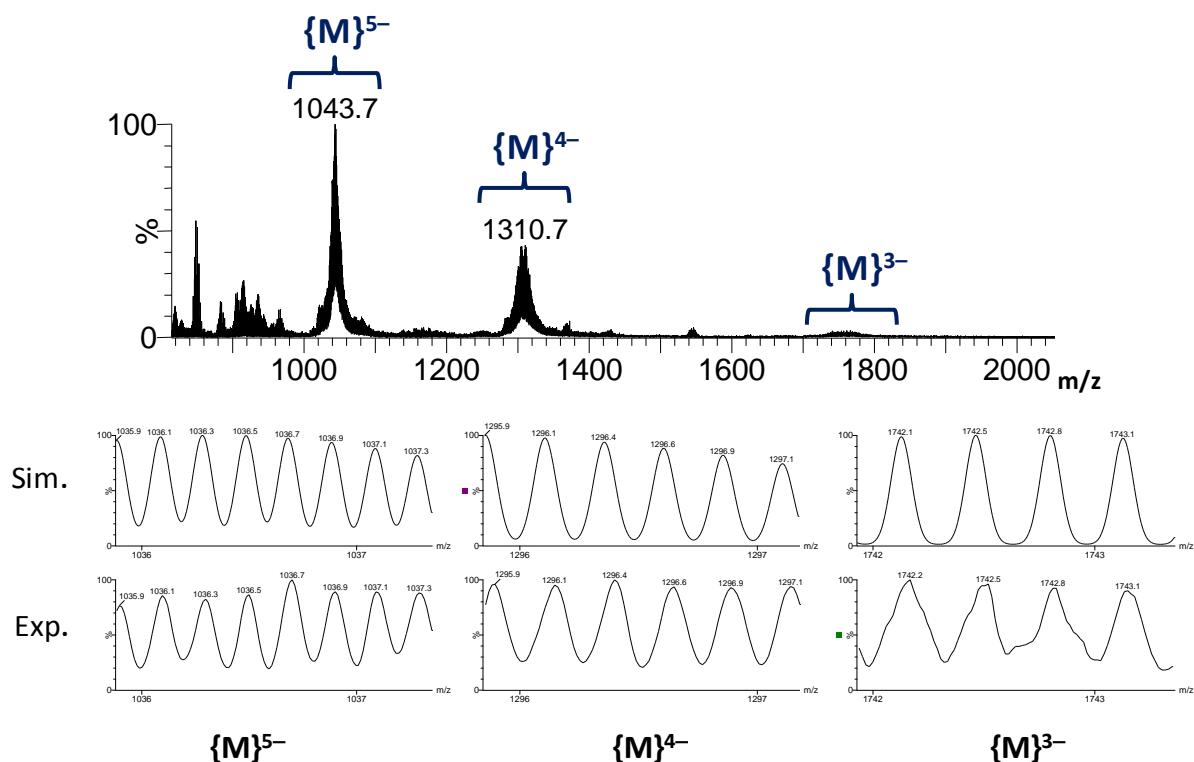


Figure 2.23. Top: Negative ESI mass spectrum ($U_c = 15$ V) of **5-Ni** in freshly prepared aqueous solution. $\{M\}^{(10-n)} = [Ni_2Sb_2W_{20}O_{70} + xH_2O + mH^+ + (n-m)Na^+]^{(10-n)-}$. Bottom: Expanded region of the group of signals observed in the ESI-MS for the 5-, 4- and 3- charge states compared to the simulated isotopic patterns.

2.4. CONCLUSIONS

This work nicely illustrates the potential of the well-known family of Krebs-type POMs as precursors for preparing molecular, hybrid POMs via straightforward ligand substitution of labile water molecules on pre-formed or in-situ prepared POM clusters under mild conditions. As a result, the first organic derivatives of 3d-metal disubstituted Krebs-type POMs are reported in this chapter. According to the ligand L, these seven compounds of general formula $[\{ML(H_2O)_2(WO_2)_2(B-\beta-SbW_9O_{33})_2\}^n]^{n-}$ can be classified in the following groups: **1-SbM**, where L = imc and M = Mn, Co, Ni, Zn; **2-Ni**, where L = pzc and M = Ni; and **3-M**, where L = pyzc and M = Co, Zn. In addition, reactions carried out with imc ligand but using Te^{IV} as heteroatom instead of Sb^{III} have resulted in the corresponding **1-TeM** analogues, from which only the compounds with M = Mn and Co have been isolated as pure crystalline phases. The series of **1-TeM** represents the first observation of a transition metal disubstituted Krebs-type tungstotellurate framework. Organic derivatization of 3d-metal disubstituted Krebs-type clusters has been shown up as extremely dependent on the exact ligand nature. The ligand imc has been identified as “universal ligand” because its coordination to the Krebs-type cluster takes place regardless of the external 3d-metal, reaction conditions or heteroatom. In contrast, the second pyrazole carboxylate ligand evaluated (pzc) appears to be selective toward the Ni-containing POM and promotes the partial decomposition of the Co-containing cluster, which leads to the first structurally characterized metal complex of the pzc ligand $[Co(pzc)_2(H_2O)_2]$. Selective behavior has also been observed for pyzc toward the Co- and Zn-disubstituted POM precursors, whereas the use of the pydc and pymc ligands resulted in the

complexes $[M(\text{pydc})_2(\text{H}_2\text{O})_2]$ ($M = \text{Co}, \text{Ni}$) and $[\text{Co}(\text{pydc})_2(\text{H}_2\text{O})_2]$, and the pic ligand showed to be inert toward any of the POM precursor selected. The cobalt derivative of the Krebs-type POM could be considered the most labile precursor because it reacts with most of the ligands evaluated, giving not only hybrid derivatives as the product, but also $[\text{CoL}_2(\text{H}_2\text{O})_2]$ complexes for some of the reactions explored as a result of partial decomposition. On the contrary, the manganese derivative appears to be the most stable because it can only be coordinated by the “universal” imc ligand. Functionalization can be efficiently monitored by IR spectroscopy, which represents a powerful, accessible and cheap technique to detect the organic derivatization of the parent metal-oxo framework prior to single-crystal X-Ray experiments. The resulting hybrid species are stable in aqueous solution according to $^1\text{H-NMR}$ studies performed on the diamagnetic derivatives.

Regarding the bridging ligands analyzed, 4,4'-bpy and 2,5-pyzdc have proven to be inert toward Krebs-type tungstoantimonates, although the former leads to a series of compounds with interstitial organic molecules as indicated by the X-ray analyses on **4-Mn**. On the contrary, 2,3-pyzdc shows selectivity toward the nickel-disubstituted Krebs-type POM and its coordination results in the rearrangement of the parent cluster to lead to the ligand-bridged **5-Ni** dimer. This dimeric species is constituted by two $\{\text{Ni}_2\text{Sb}_2\text{W}_{20}\text{O}_{70}\}$ clusters, which are novel and they show a $\{\text{W}_2\text{O}_{10}\}$ moiety incorporated into a $\{\text{SbW}_9\text{O}_{33}\}$ trilacunary unit in unprecedented manner. Furthermore, the assembly shows a water molecule nested between the pyrazine rings of the 2,3-pyzdc ligands via $\text{O}_w\text{-H}\cdots\pi$ interactions. ESI-MS studies show that the dimeric entity undergoes complete dissociation upon dissolution. The magnetic properties of **5-Ni** can be explained by the zero-field splitting of the Ni(II) centers.

2.5. REFERENCES

- [1] (a) Gouzerh, P.; Proust, A. *Chem. Rev.* **1998**, *98*, 77. (b) Proust, A.; Thouvenot, R.; Gouzerh, P. *Chem. Commun.* **2008**, 1837. (c) Long, D.-L.; Tsunashima, R.; Cronin, L. *Angew. Chem. Int. Ed.* **2010**, *49*, 1736. (d) Dolbecq, A.; Dumas, E.; Mayer, C. R.; Mialane P. *Chem. Rev.* **2010**, *110*, 6009.
- [2] Bösing, M.; Loose, I.; Pohlmann, H.; Krebs, B. *Chem. Eur. J.* **1997**, *3*, 1232
- [3] (a) Bösing, M.; Nöh, A.; Loose, I.; Krebs, B. *J. Am. Chem. Soc.* **1998**, *120*, 7252. (b) Rodewald, D.; Jeannin, Y. *C. R. Acad. Sci. Paris IIc* **1998**, *1*, 175. (c) Loose, I.; Droste, E.; Bösing, M.; Pohlmann, H.; Dickman, M. H.; Rosu, C.; Pope, M. T.; Krebs, B. *Inorg. Chem.* **1999**, *38*, 2688. (d) Piepenbrink, M.; Limanski, E. M.; Krebs, B. *Z. Anorg. Allg. Chem.* **2002**, *628*, 1187. (e) Liu, Y.-H.; Ma, P.-T.; Wang, J.-P. *J. Coord. Chem.* **2008**, *61*, 936.
- [4] (a) Kortz, U.; Savelieff, M. G.; Bassil, B. S.; Keita, B.; Nadjo, L. *Inorg. Chem.* **2002**, *41*, 783. (b) Limanski, E. M.; Drewes, D.; Droste, E.; Böhner, R.; Krebs, B. *J. Mol. Struct.* **2003**, *656*, 17. (c) Hussain, F.; Reicke, M.; Janowski, V.; de Silva, S.; Futuwi, J.; Kortz, U. *C. R. Chim.* **2005**, *8*, 1045. (d) Wang, J.-P.; Ma, P.-T.; Li, J.; Niu, H.-Y.; Niu, J.-Y. *Chem. Asian J.* **2008**, *3*, 822. (e) Carraro, M.; Bassil, B. S.; Sorarù, A.; Berardi, S.; Suchopar, A.; Kortz, U.; Bonchio, M. *Chem. Commun.* **2013**, *49*, 7914.
- [5] (a) Bi, L.-H.; McCormac, T.; Beloshapkin, S.; Dempsey, E. *Electroanalysis*, **2008**, *20*, 38. (b) Foster, K.; Bi, L.-H.; McCormac, T. *Electrochim. Acta* **2008**, *54*, 868.
- [6] (a) Bonchio, M.; Carraro, M.; Sartorel, A.; Scorrano, G.; Kortz U. *J. Mol. Catal. A: Chem.* **2006**, *251*, 93. (b) Bonchio, M.; Carraro, M.; Scorrano, G.; Kortz U. *Adv. Synth. Catal.* **2005**, *347*, 1909.
- [7] Evangelisti, F.; Car, P.-E.; Blacque, O.; Patzke, G. R. *Catal. Sci. Technol.* **2013**, *3*, 3117.

- [8] (a) Dolbecq, A.; Compain, J.-D.; Mialane P.; Marrot, J.; Rivière, E.; Sécheresse, F. *Inorg. Chem.* **2008**, *47*, 3371. (b) Sartorel, A.; Carraro, M.; Scorrano, G.; Bassil, B. S.; Dickman, M. H.; Keita, B.; Nadjo, L.; Kortz, U.; Bonchio, M. *Chem. Eur. J.* **2009**, *15*, 7854.
- [9] (a) Laurencin, D.; Villanneau, R.; Herson, P.; Thouvenot, R.; Jeannin, Y.; Proust, A. *Chem. Commun.* **2005**, 5524. (b) Bi, L.-H.; Al-Kadamany, G.; Chubarova, E. V.; Dickman, M. H.; Chen, L.; Gopala, D. S.; Richards, R. M.; Keita, B.; Nadjo, L.; Jaensch, H.; Mathys, G.; Kortz, U. *Inorg. Chem.* **2009**, *48*, 10068. (c) Zhang, L.-C.; Xue, H.; Zhu, Z.-M.; Wang, Q.-X.; You W.-S.; Li, Y.-G.; Wang, E.-B. *Inorg. Chem. Commun.* **2010**, *13*, 609. (d) Kalinina, I. V.; Izarova, N. V.; Kortz, U. *Inorg. Chem.* **2012**, *51*, 7442. (e) Zhao, C.; Kambara, C. S.; Yang, Y.; Kaledin, A. L.; Musaev, D. G.; Lian, T.; Hill, C. L. *Inorg. Chem.* **2013**, *52*, 671.
- [10] Ismail, A. H.; Bassil, B. S.; Römer, I.; Kortz, U. *Z. Anorg. Allg. Chem.* **2013**, *639*, 2510.
- [11] (a) Bi, L.-H.; Li, B.; Wu, L.-X. *Inorg. Chem. Commun.* **2008**, *11*, 1184. (b) Bi, L.-H.; Hou, G.-F.; Bao, Y.-Y.; Li, B.; Wu, L.-X.; Gao, Z.-M.; McCormac, T.; Mal, S. S.; Dickman, M. H.; Kortz, U. *Eur. J. Inorg. Chem.* **2009**, 5259.
- [12] Kortz, U.; Al-Kassem, N. K.; Savelieff, M. G.; Al Kadi, N. A.; Sadakane, M. *Inorg. Chem.* **2001**, *40*, 4742.
- [13] Crystal data of $\text{Na}_8\text{K}_2[\{\text{Ni}(\text{imc})(\text{H}_2\text{O})\}_2(\text{WO}_2)_2(\text{TeW}_9\text{O}_{33})_2] \cdot 40\text{H}_2\text{O}$ (1-TeNi): $\text{C}_8\text{H}_{90}\text{K}_2\text{N}_4\text{Na}_8\text{Ni}_2\text{O}_{116}\text{Te}_2\text{W}_{20}$, FW = 6410.7 g mol⁻¹, triclinic *P*-1, $a = 12.9079(4)$, $b = 15.4074(5)$, $c = 16.0861(5)$ Å, $\alpha = 63.706(3)$, $\beta = 71.705(3)$, $\gamma = 77.412(3)^\circ$, $V = 2711.5(2)$ Å³, $T = 100(2)$ K, $Z = 1$, $2\theta_{\text{max}} = 52.0^\circ$, 18192 reflections, 10634 unique ($R_{\text{int}} = 0.033$), 9555 observed ($I > 2\sigma(I)$), 396 parameters, $R(F) = 0.042$ ($I > 2\sigma(I)$), $wR(F^2) = 0.106$ (all data), GoF = 1.065, max./min. electron densities 4.132/-4.020 e Å⁻³, green plate. Agilent SuperNova (Eos CCD detector, monochromated MoK α radiation, $\lambda = 0.71073$ Å).
- [14] Crystal data of $\text{Na}_6\text{K}_4[\{\text{Zn}(\text{H}_2\text{O})\}_3(\text{WO}_2)_3(\text{SbW}_9\text{O}_{33})_2] \cdot 70\text{H}_2\text{O}$: $\text{H}_{146}\text{K}_4\text{Na}_6\text{O}_{145}\text{Sb}_2\text{W}_{20}\text{Zn}_2$, FW = 6946.2 g mol⁻¹, monoclinic *C2/c*, $a = 23.7929(2)$, $b = 22.7751(3)$, $c = 19.6239(3)$ Å, $\beta = 110.799(2)^\circ$, $V = 9940.9(3)$ Å³, $T = 100(2)$ K, $Z = 4$, $2\theta_{\text{max}} = 52.0^\circ$, 27292 reflections, 9774 unique ($R_{\text{int}} = 0.040$), 8799 observed ($I > 2\sigma(I)$), 370 parameters, $R(F) = 0.039$ ($I > 2\sigma(I)$), $wR(F^2) = 0.098$ (all data), GoF = 1.059, max./min. electron densities 3.320/-3.340 e Å⁻³, colorless plate. Agilent SuperNova (Eos CCD detector, monochromated MoK α radiation, $\lambda = 0.71073$ Å).
- [15] Chen, B.-W.; Chen, W.-L.; Li, Y.-G.; Wang, E.-B. *J. Cluster Sci.* **2011**, *22*, 73.
- [16] (a) Ibrahim, M.; Nada, A.; Kamal, D. E. *Indian J. Pure Appl. Phys.* **2005**, *43*, 911. (b) Morzyk-Ociepa, B.; Rózycka-Sokolowska, E.; Michalska, D. *J. Mol. Struct.* **2012**, *1028*, 49.
- [17] Wang, J.-P.; Ma, P.-T.; Li, J.; Niu, H.-Y.; Niu, J.-Y. *Chem. Asian J.* **2008**, *3*, 822.
- [18] BVSumCalc program as a courtesy of Dr. M. H. Dickman.
- [19] (a) Zheng, S.; Cai, S.; Fan, J.; Zhang, W. *Acta Crystallogr.* **2011**, *E67*, m865. (b) Shuai, W.; Cai, S.; Zheng, S. *Acta Crystallogr.* **2011**, *E67*, m897. (c) Artetxe, B.; San Felices, L.; Reinoso, S.; Pache, A.; Gutiérrez-Zorrilla, J. M. *Acta Crystallogr.* **2013**, *E69*, m94.
- [20] Ptasiwicz-Bak, H.; Leciejewicz, J.; Zachara, J. *J. Coord. Chem.* **1995**, *36*, 317.
- [21] Liu, Y.-H.; Ma, P.-T.; Wang, J.-P. *J. Coord. Chem.* **2008**, *61*, 936.
- [22] Alvarez, S.; Alemany, P.; Casanova, D.; Cirera, J.; Llunell, M.; Avnir, D. *Coord. Chem. Rev.* **2005**, *249*, 1693.
- [23] (a) Shanon, R. D.; Prewitt, C. T. *Acta Crystallogr.* **1969**, *B25*, 925. (b) Shanon, R. D. *Acta Crystallogr.* **1976**, *A32*, 751.
- [24] Crystal data of $\text{K}_8\text{Na}_6[\text{C}_2\text{H}_{10}\text{Sb}_2\text{W}_{31}\text{O}_{108}] \cdot 32\text{H}_2\text{O}$: Estimated formula $\text{C}_2\text{H}_{48}\text{K}_8\text{Na}_6\text{O}_{142}\text{Sb}_2\text{W}_{31}$, FW = 8737.7 g mol⁻¹, triclinic *P*-1, $a = 18.453(2)$, $b = 21.968(2)$, $c = 22.362(8)$ Å, $\alpha = 1118.70(1)$, $\beta = 92.17(1)$, $\gamma = 109.06(1)^\circ$, $V = 7393.2(6)$ Å³, $T = 100(2)$ K, $Z = 2$, $2\theta_{\text{max}} = 134.0^\circ$, 47991 reflections, 37663 unique ($R_{\text{int}} = 0.078$), 15134 observed ($I > 2\sigma(I)$), 1004 parameters, $R(F) = 0.110$ ($I > 2\sigma(I)$), $wR(F^2) = 0.229$ (all data), GoF = 1.048, max./min. electron densities 5.930/-5.010 e Å⁻³, colorless plate. Agilent SuperNova (Atlas CCD detector, monochromated CuK α radiation, $\lambda = 1.54184$ Å).
- [25] Gao, J.; Yan, J.; Beeg, S.; Long, D.-L.; Cronin, L. *J. Am. Chem. Soc.* **2013**, *135*, 1796.

- [26] (a) Reinoso, S.; Dickman, M. H.; Kortz, U. *Inorg. Chem.* **2006**, *45*, 10422. (b) Zheng, S.-T.; Zhang, J.; Clemente-Juan, J.-M.; Yuan, D.-Q.; Yang, G.-Y. *Angew. Chem. Int. Ed.* **2009**, *48*, 7176. (c) Fang, X.; Luban, M. *Chem. Commun.* **2011**, *47*, 3066.
- [27] Fuchs, J.; Palm, R.; Hartl, H. *Angew. Chem. Int. Ed. Engl.* **1996**, *35*, 2651.
- [28] See for example: (a) Zhang, X.; Anderson, T. M.; Chen Q.; Hill, C. L. *Inorg. Chem.* **2001**, *40*, 418. (b) Kortz, U.; Mbomekalle, I. M.; Keita, B.; Nadjó L.; Berthet, P. *Inorg. Chem.* **2002**, *41*, 6412. (c) Ruhlmann, L.; Canny, J.; Contant, R.; Thouvenot, R. *Inorg. Chem.* **2002**, *41*, 3811. (d) Hou, Y.; Xu, L.; Cichon, M. J.; Lense, S.; Hardcastle, K. I.; Hill, C. L. *Inorg. Chem.* **2010**, *49*, 4125.
- [29] (a) Anderson, T. M.; Zhang, X.; Hardcastle, K. I.; Hill, C. L. *Inorg. Chem.* **2002**, *41*, 2477. (b) Mbomekalle, I. M.; Keita, B.; Nadjó, L.; Neiwert, W. A.; Zhang, L.; Hardcastle, K. I.; Hill, C. L.; Anderson, T. M. *Eur. J. Inorg. Chem.* **2003**, 3924. (f) Ruhlmann, L.; Costa-Coquelard, C.; Canny, J.; Thouvenot, R. *Eur. J. Inorg. Chem.* **2007**, 1493. (g) Mbomekalle, I. M.; Mialane, P.; Dolbecq, A.; Marrot, J.; Sécheresse, F.; Berthet, P.; Keita, B.; Nadjó, L. *Eur. J. Inorg. Chem.* **2009**, 5194.
- [30] (a) Mao, L.; Rettig, S. J.; Thompson, R. C.; Trotter, J.; Xia, S. *Can. J. Chem.* **1996**, *74*, 433. (b) Beobide, G.; Castillo, O.; García-Couceiro, U.; García-Terán, J. P.; Román, P. *Inorg. Chem.* **2006**, *45*, 5367.
- [31] Steiner, T.; Schreurs, A. M. M.; Kanters, J. A.; Kroon, J. *Acta Crystallogr.* **1998**, *D54*, 25.
- [32] Egli, M.; Sarkhel, S. *Acc. Chem. Res.* **2007**, *40*, 197.
- [33] Aubry, A.; Protas, J.; Moreno-Gonzales, E.; Marraud, M. *Acta Crystallogr.* **1977**, *B33*, 2572.
- [34] Atwood, J. L.; Hamada, F.; Robinson, K. D.; Orr, G. W.; Vincent, R. L. *Nature* **1991**, *349*, 683.
- [35] (a) Steiner, T.; Koellner, G. *J. Mol. Biol.* **2001**, *305*, 535. (b) Sarkhel, S.; Rich, A.; Egli, M. *J. Am. Chem. Soc.* **2003**, *125*, 8998.
- [36] (a) Jorgensen, W. L.; Severance, D. L. *J. Am. Chem. Soc.* **1990**, *112*, 4768. (b) Callejo, L. M.; Muga, I.; Vitoria, P.; Reinoso, S.; Román, P.; Gutiérrez-Zorrilla, J. M. *Acta Crystallogr.* **2003**, *E59*, m684. (c) Li, Y.-G.; Jiang, Q.-B.; Cheng, K.; Yan, H.; Zhu, H.-L. *Z. Anorg. Allg. Chem.* **2009**, *635*, 2572.
- [37] See for example: (a) Kortz, U.; Nellutla, S.; Stowe, A. C.; Dalal, N. S.; van Tol, J.; Bassil, B. S. *Inorg. Chem.* **2004**, *43*, 144. (b) Mialane, P.; Dolbecq, A.; Marrot, J.; Rivière, E.; Sécheresse, F. *Chem. Eur. J.* **2005**, *11*, 1771.
- [38] Santana, M. D.; García, G.; Vicente-Hernández, C.; García, L.; Pérez, J.; Rojo, T.; Lezama, L. *J. Organomet. Chem.* **2008**, *693*, 2009.
- [39] (a) Landee, C. P.; Mudgett, D. M.; Foxman, B. M. *Inorg. Chim. Acta* **1991**, *186*, 45. (b) López-Banet, L.; Santana, M. D.; García, G.; García, L.; Pérez, J.; Rojo, T.; Lezama, L.; Costes, J. P. *Inorg. Chem.* **2011**, *50*, 437.
- [40] Mitchell, T. N.; Costisella, B. *NMR-From Spectra to Structures*; Springer: New York, NY, USA, 2007.
- [41] (a) Bonchio, M.; Bortolini, O.; Conte, V.; Sartorel, A. *Eur. J. Inorg. Chem.* **2003**, 699. (b) Mayer, C. R.; Roch-Marchal, C.; Lavanant, H.; Thouvenot, R.; Sellier, N.; Blais, J.-C.; Sécheresse, F. *Chem. Eur. J.* **2004**, *10*, 5517. (c) Miras, H. N.; Zang, H. Y.; Long, D.-L.; Cronin, L. *Eur. J. Inorg. Chem.* **2011**, 5105. (d) Korenev, V. S.; Abramov, P. A.; Vicent, C.; Mainichev, D. A.; Floquet, S.; Cadot, E.; Sokolov, M. N.; Fedin, V. P. *Dalton Trans.* **2012**, *41*, 14484.

Structural diversity in lanthanide-containing tungstogermanate assemblies

3.1. Introduction

3.2. General synthetic aspects

3.3. POM assemblies containing early lanthanides

3.3.1. Experimental section

3.3.2. Results and discussion

3.4. POM assemblies containing mid-to-late lanthanides

3.4.1. Experimental section

3.4.2. Results and discussion

3.5. Conclusions

3.6. References

ABSTRACT: Reaction of lanthanide(III) ions with Ni(II), GeO₂ and Na₂WO₄ in NaOAc buffer at room temperature results in a library of [Ln₂(GeW₁₀O₃₈)]⁶⁻ isomers, which consist of dilacunary Keggin fragments stabilized by coordination of 4f-metal atoms to the vacant sites and show the ability to undergo cation-directed assembly processes. For early lanthanides (Ce to Sm), hexameric crown-shaped [Na₄Ln₁₂Ge₆W₆₀O₂₂₈(H₂O)₂₄]³⁵⁻ (**6-Ln**, Ln = Pr, Nd) architectures were obtained in the presence of Na⁺, whereas the addition of K⁺ leads to an analogous [K₄Sm₁₂Ge₆W₆₀O₂₂₈(H₂O)₂₂]³⁵⁻ (**7-Sm**) cluster for Sm and to giant dodecameric [K₇Ln₂₄Ge₁₂W₁₂₀O₄₄₄(OH)₁₂(H₂O)₆₄]⁵²⁻ (**8-Ln**, Ln = Ce, Pr, Nd) structures for Ce, Pr and Nd. Anions **8-Ln** dissociate upon dissolution in water into hexameric and monomeric entities, as identified by conductivity and electrospray ionization mass spectrometry (ESI-MS) studies. The former species self-assemble into spherical, hollow, single-layered and stable vesicle-like blackberry type structures, as monitored by laser light scattering techniques (LLS). Similar studies in water-acetone mixtures showed that **8-Nd** remains stable and forms blackberries with sizes increasing with the acetone concentration. On the contrary, rod-like [Ln₄(H₂O)₆(GeW₁₀O₃₈)₂]¹²⁻ (**9-Ln**, Ln = Gd, Tb, Dy, Ho, Er, Tm, Yb, Lu) dimers and diamond-shaped [Ln₄(H₂O)₅(GeW₁₀O₃₈)₂]²⁴⁻ (**10-Ln**, Ln = Ho, Er, Tm, Yb, Lu) tetramers were formed for mid-to-late lanthanides (Gd to Lu) in the exclusive presence of Na⁺ or upon the addition of Cs⁺, respectively. Combination of ESI-MS and ¹⁸³W-NMR experiments indicates that **10-Ln** tetramers fragment into **9-Ln** like dimers upon dissolution, which undergo partial dissociation into monomeric anions. The compounds obtained were characterized by means of elemental and thermal analyses, IR spectroscopy and single-crystal X-ray diffraction. Photoluminescence of **7-Sm**, **9-Tb** and **9-Dy** and magnetic properties in the **9-Ln** series are also discussed.

3.1. INTRODUCTION

Lanthanide containing POMs could be considered as ideal precursors for direct organic derivatization because they usually show several water molecules coordinated to accessible 4f-metal centers. Combination of lacunary POMs with 4f-metals constitutes a powerful tool to obtain complex architectures because the large size, oxophilic character and high coordination numbers (usually higher than 7) make lanthanides ideal candidates for linking POM fragments in a large variety of assemblies. The chemistry of these compounds is dominated by polyoxotungstates as a large number of lacunary species are available, in such a way that structures ranging from dimeric entities to giant assemblies included among the largest polyoxotungstates to date are known. Extensive work has been carried out for several years in this field due to the interesting structural and physicochemical properties that lanthanide containing POMs might show, including luminescence, magnetism or their role as Lewis acid catalysts.¹ Recently some detailed structural reviews on lanthanide containing POMs have been published.^{1,2}

3.1.1. Lanthanide containing isopolyoxotungstates

Peacock and Weakley described the first family of lanthanide-containing POMs in 1971, namely the series $[\text{Ln}(\text{W}_5\text{O}_{18})_2]^{9-}$ ($\text{Ln}^{\text{III}} = \text{La} - \text{Sm}, \text{Ho}, \text{Yb}$) and the $[\text{Ce}^{\text{IV}}(\text{W}_5\text{O}_{18})_2]^{8-}$ POM.³ These species consist of two monolacunary Lindqvist type POMs encapsulating a 4f-metal ion in an eight-coordinated square-antiprismatic $\text{LnO}_4(\text{O}_4')$ fashion (Figure 3.2). Since then, a large number of derivatives have been prepared by using different lanthanides salts.⁴ Subsequently, all the sandwich-type clusters formed by a lanthanide ion trapped between two monolacunary fragments have been known as Peacock-Weakley type anions.

Besides the decatungstate sandwich-type anions, structural characterizations of only three other types of lanthanide containing iso-POMs have been reported to date. Cao's $[\text{Ce}_2(\text{H}_2\text{O})\text{Cl}(\text{H}_6\text{W}_{15}\text{O}_{54})]^{7-}$ comprises one Ce^{III} dimer surrounded by a cyclic $\{\text{H}_6\text{W}_{15}\text{O}_{54}\}$ structure composed of three $\{\text{W}_3\text{O}_{14}\}$ units linked to each other *via* corner sharing with three $\{\text{W}_2\text{O}_{10}\}$ moieties. Each Ce atom in this POM is capped by one water molecule or one Cl atom.⁵ On the other hand, Kortz's $[\text{Ln}_2(\text{H}_2\text{O})_{10}\text{W}_{22}\text{O}_{72}(\text{OH})_2]^{8-}$ dimer ($\text{Ln} = \text{La}, \text{Ce}, \text{Tb} - \text{Lu}$)⁶ and $[\text{Ln}_2(\text{H}_2\text{O})_{10}\text{W}_{28}\text{O}_{93}(\text{OH})_2]^{14-}$ V-shaped trimer ($\text{Ln} = \text{La} - \text{Eu}$)⁷ are related to the $[\text{H}_4\text{W}_{11}\text{O}_{38}]^{6-}$ undecatungstate⁸ unit. The former is composed of two corner sharing undecatungstate subunits stabilized by the coordination of two lanthanide atoms and shows a 1D arrangement in the solid state, whereas the latter is formed by two undecatungstate subunits and one hexatungstate fragment linked by two nine-coordinated lanthanide ions (Figure 3.1).

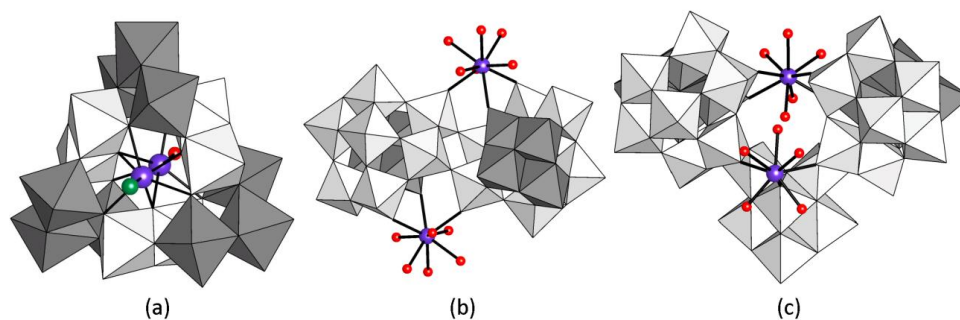


Figure 3.1. Structure of: (a) the $[\text{Ce}_2(\text{H}_2\text{O})\text{Cl}(\text{H}_6\text{W}_{15}\text{O}_{54})]^{7-}$ anion (Cl atom depicted in dark green and $\{\text{W}_3\text{O}_{14}\}$ moieties in dark grey); (b) the $[\text{Ln}_2(\text{H}_2\text{O})_{10}\text{W}_{22}\text{O}_{72}(\text{OH})_2]^{8-}$ framework; (c) the $[\text{Ln}_2(\text{H}_2\text{O})_{10}\text{W}_{28}\text{O}_{93}(\text{OH})_2]^{14-}$ assembly ($\{\text{W}_4\text{O}_{16}\}$ moieties of the undecatungstate units depicted in dark grey).

3.1.2. Lanthanide containing heteropolyoxotungstates

Compounds based on monolacunary fragments

A wide range of Peacock-Weakley-type POMs³ containing Keggin or Wells-Dawson monolacunary units have been reported to date, including the $\{\text{Ln}(\alpha\text{-XW}_{11}\text{O}_{39})_2\}$ ($\text{X} = \text{Si}^{\text{IV}}, \text{P}^{\text{V}}, \text{As}^{\text{V}}$),⁹ $\{\text{Ln}(\beta_2\text{-SiW}_{11}\text{O}_{39})_2\}$ ¹⁰ or $\{\text{Ln}(\alpha\text{-P}_2\text{W}_{17}\text{O}_{61})_2\}$ ($\alpha = \alpha_1, \alpha_2$)¹¹ families (Figure 3.2). The chiral POMs derived from the assembly of α -Keggin units show two enantiomeric forms depending on the clockwise (D) or counter clockwise (L) 45° twisting of one of the Keggin fragments with respect to the other. Among the anions containing intrinsically chiral β_2 -isomers, two configurations are found: (A) showing the same enantiomer and (B) with different ones. The former isomer is favored for early lanthanides, whereas the latter is gradually preferred for mid- to late 4f-metal ions. In the case of structures containing Wells-Dawson anions, an extensive work was carried out in terms of lanthanide speciation studies in solution. Furthermore, the mixed iso/hetero Peacock-Weakley type $\{\text{Ln}(\alpha\text{-BW}_{11}\text{O}_{39})(\text{W}_5\text{O}_{18})\}$ mixed assembly was also obtained by Yamase.¹²

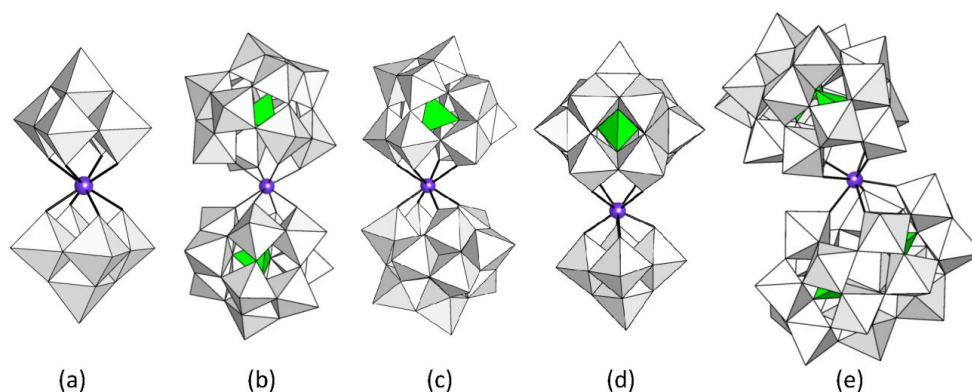


Figure 3.2. Molecular structures of representative Peacock-Weakley type POMs. (a) $\{\text{Ln}(\text{W}_5\text{O}_{18})_2\}$; (b) $\text{L}\{-\{\text{Ln}(\alpha\text{-XW}_{11}\text{O}_{39})_2\}$; (c) $\text{A}\{-\{\text{Ln}(\beta_2\text{-SiW}_{11}\text{O}_{39})_2\}$; (d) $\{\text{Ln}(\alpha\text{-BW}_{11}\text{O}_{39})(\text{W}_5\text{O}_{18})\}$; (e) $\{\text{Ln}(\alpha_2\text{-P}_2\text{W}_{17}\text{O}_{61})_2\}$.

Although lanthanide substituted monomeric species were identified in solution by Peacock & Weakley in their early works, self assembled derivatives forming chains¹³ or dimers^{11,14} and showing accessible coordination water molecules, have only been isolated in the solid state (Figure 3.3). While Keggin subunits usually lead to one-dimensional architectures or dimeric assemblies, a variety of dimers showing *cap-to-cap*, *belt-to-belt* and *cap-to-belt* coordination modes have been observed for Wells-Dawson fragments depending on the size of the employed lanthanide.

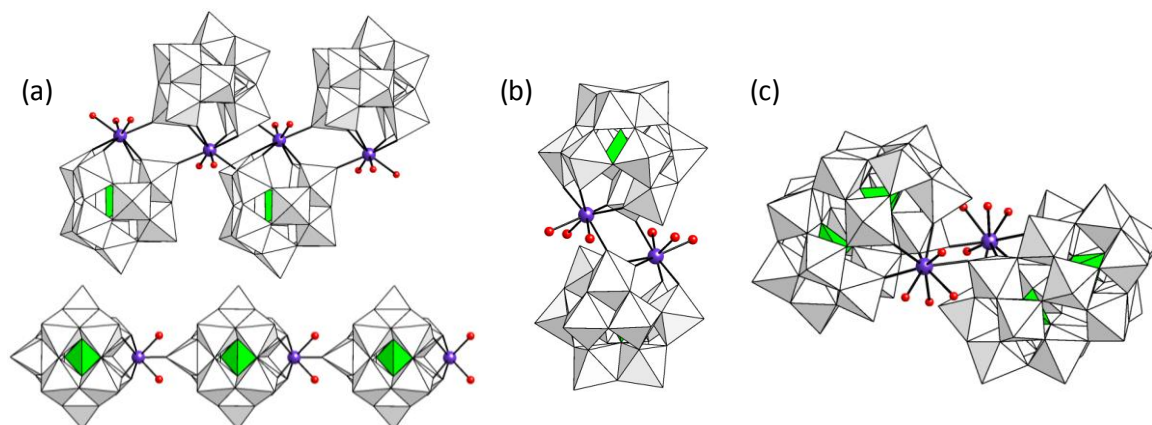


Figure 3.3. Structures of: (a) zig-zag and linear $\{\text{Ln}(\text{H}_2\text{O})_2(\alpha\text{-XW}_{11}\text{O}_{39})\}_n$ chains. (b) $[\{\text{Ln}(\text{H}_2\text{O})_3(\alpha\text{-PW}_{11}\text{O}_{39})\}_2]^{6-}$ dimer (c) *belt-to-belt* linkage in the $[\{\text{Ln}(\text{H}_2\text{O})_4(\alpha_2\text{-P}_2\text{W}_{17}\text{O}_{61})\}_2]^{14-}$ dimer.

Compounds based on polylacunary fragments

Besides Peacock-Weakley species, some other lanthanide containing dimeric POMs are known. These are based on trilacunary Keggin units and include Krebs- and Knoth-type POMs incorporating 4f-metals, the so-called open Wells-Dawson anions, or lanthanide substituted $[\text{As}_2\text{W}_{19}\text{O}_{67}]^{14-}$ clusters formed by two $[\text{B}-\alpha\text{-AsW}_9\text{O}_{33}]^{9-}$ subunits linked *via* one $\{\text{WO}_6\}$ moiety.¹⁵ Alternatively, polylacunary Wells-Dawson fragments have been observed to encapsulate a central rhomblike cerium cluster, a $\{\text{Yb}_6\text{O}_6\}$ hexamer, or to lead to the insertion of lanthanide ions in more complex architectures like the Preyssler $[\text{P}_5\text{W}_{30}\text{O}_{110}]^{15-}$ or the wheel-shaped $[\text{P}_8\text{W}_{48}\text{O}_{184}]^{40-}$ polyanions.¹⁶

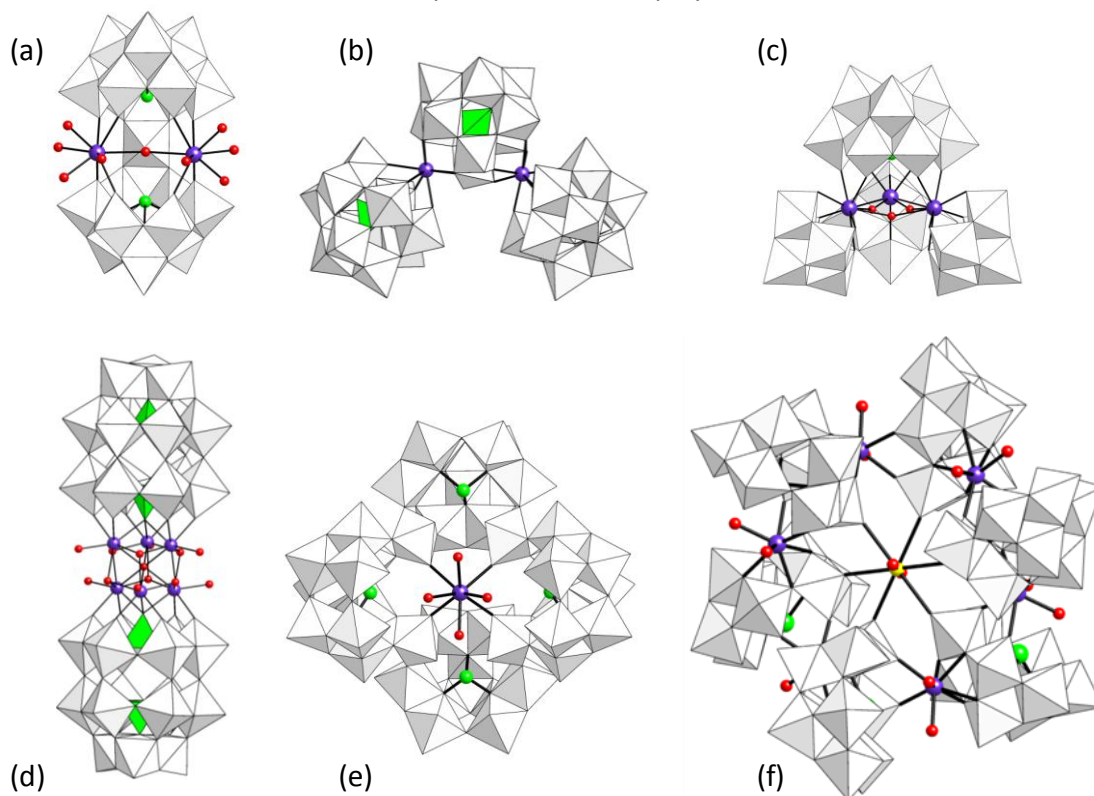


Figure 3.4. Molecular structures of some lanthanopolyoxotungstates based on polylacunary units: (a) $[\text{La}_2(\text{H}_2\text{O})_6\text{As}_2\text{W}_{19}\text{O}_{67}(\text{H}_2\text{O})]^{8-}$. (b) $[\text{Ce}_2(\text{PW}_{10}\text{O}_{38})(\text{PW}_{11}\text{O}_{39})_2]^{10-}$. (c) $[\text{Ce}_3(\text{CO}_3)(\text{SbW}_9\text{O}_{33})(\text{W}_5\text{O}_{18})_3]^{20-}$. (d) $[\{\text{Yb}_6(\text{OH})_6(\text{H}_2\text{O})_6\}(\text{P}_2\text{W}_{15}\text{O}_{56})_2]^{14-}$. (e) $[\text{Ce}(\text{H}_2\text{O})_5(\text{As}_4\text{W}_{40}\text{O}_{140})]^{25-}$. (f) $[\text{Kc}\{\text{Eu}(\text{H}_2\text{O})_2(\text{AsW}_9\text{O}_{33})\}_6]^{35-}$.

Only a few examples of trimeric lanthanopolyoxotungstates are found in the literature, whereas tetrameric species represent a large group where almost all members display dilacunary Keggin type POMs or trilacunary units with lone-pair containing heteroatoms like As^{III} or Sb^{III} . Nogueira's $[\text{Ce}^{\text{IV}}_2(\text{PW}_{10}\text{O}_{38})(\text{PW}_{11}\text{O}_{39})_2]^{17-}$ ceriopolyoxotungstate containing dilacunary α -Keggin type subunits is an illustrating example of the first group.¹⁷ Yamase's $[\text{Ln}_3(\alpha\text{-SbW}_9\text{O}_{33})(\text{W}_5\text{O}_{18})_3]^{18-}$, the $[\text{Ce}_3(\text{H}_2\text{O})_8\{\text{Sb}_4\text{O}_4\}\{\text{WO}_2(\text{H}_2\text{O})_2\}(\alpha\text{-SbW}_9\text{O}_{33})_4]^{19-}$ anion trapping the unusual $\{\text{Sb}_4\text{O}_4\}$ cluster, the $[(\text{BiW}_9\text{O}_{33})_4(\text{WO}_3)\{\text{Bi}_6(\mu^3\text{-O})_4(\mu^2\text{-OH})_3\}(\text{Ln}_3(\text{H}_2\text{O})_6\text{CO}_3)]^{22-}$ assembly showing the central $\{\text{Bi}_6(\mu^3\text{-O})_4(\mu^2\text{-OH})_3\}$ moiety, Francesconi's $[(\text{Eu}_2\text{PW}_{10}\text{O}_{38})_4(\text{W}_3\text{O}_{14})]^{30-}$ anions and some others prepared by the derivatization of the tetrameric $\{\text{As}_4\text{W}_{40}\text{O}_{140}\}$ POM cryptate could be considered as representative examples of the second group.¹⁸ Higher nuclearity has also been observed in crown-shaped $\{\text{M}\{\text{Eu}(\text{H}_2\text{O})_2(\alpha\text{-AsW}_9\text{O}_{33})\}_n\}$ tetra- or hexameric assemblies (where $\text{M} = \text{K}$, $n = 6$; $\text{M} = \text{Cs}$, $n = 4$) or the hexameric $[\text{Cs}\{\text{Ln}_6\text{As}_6\text{W}_{63}\text{O}_{218}(\text{H}_2\text{O})_{14}(\text{OH})_4\}]^{25-}$ and $[\text{Ho}_5(\text{H}_2\text{O})_{16}(\text{OH})_2\text{As}_6\text{W}_{64}\text{O}_{220}]^{25-}$ anions¹⁹ (Figure 3.4).

3.1.3. Organically derivatized lanthanide-containing POMs

Except for Peacock-Weakley type clusters, lanthanide centers incorporated to POM clusters usually show several accessible water molecules suitable for further organic derivatization. However, direct organic ligand replacement on those 4f-metal centers can be more challenging than *a priori* expected. The oxo-philic nature of lanthanide centers make carboxylic acids suitable ligands for such functionalization, but the negative charge of both lanthanide-containing POMs and carboxylate groups, as well as the steric hindrance that a given POM could produce, are the main difficulties for the reaction to take place. These drawbacks have been overcome by using small ligands in a large excess, chelating ligands or even positively charged POMs.

Figure 3.5 displays some representative examples of organically derivatized lanthanide containing POMs. Bridging acetates have been incorporated to monomeric $\{\text{Ln}(\text{POM})\}$ species to lead to dimeric $[\{\text{Ln}(\text{H}_2\text{O})_3(\text{POM})\}_2]$ assemblies constituted by monolacunary α -Keggin^{14,20} or α_2 -Wells-Dawson fragments²¹. Oligomerization of late-lanthanide monosubstituted Wells-Dawson or Keggin anions takes place when the oxalate (ox) bridging ligand is employed.²² Similar reaction results in hybrid $[\text{Yb}_2(\text{H}_2\text{O})_2(\text{ox})\{\alpha\text{-}(1,11)\text{-PW}_{10}\text{O}_{38}\}]_n^{3-}$ chains when Yb^{III} is used as lanthanide source. Using the N,O-chelating picolinic acid, Boskovic and co-workers succeeded in preparing organically functionalized Tb or Eu derivatives of the $[\text{As}_2\text{W}_{19}\text{O}_{67}(\text{H}_2\text{O})]^{14-}$ lacunary polyanion, which show interesting photoluminescent properties.²³ Starting from the trilacunary $[\text{A-}\alpha\text{-AsW}_9\text{O}_{34}]^{9-}$ anion, Xu et al. recently obtained a Dy^{III} disubstituted Keggin cluster showing one citrate ligand completing the coordination sphere of each lanthanide center, namely $[\text{Dy}_2\{\text{COH}(\text{COO})(\text{CH}_2\text{COO})_2\}_2\text{AsW}_{10}\text{O}_{38}]^{11-}$.²⁴ The citrate ligands are coordinated to the Dy centers in a tridentate fashion through two carboxylate O atoms and one OH group.

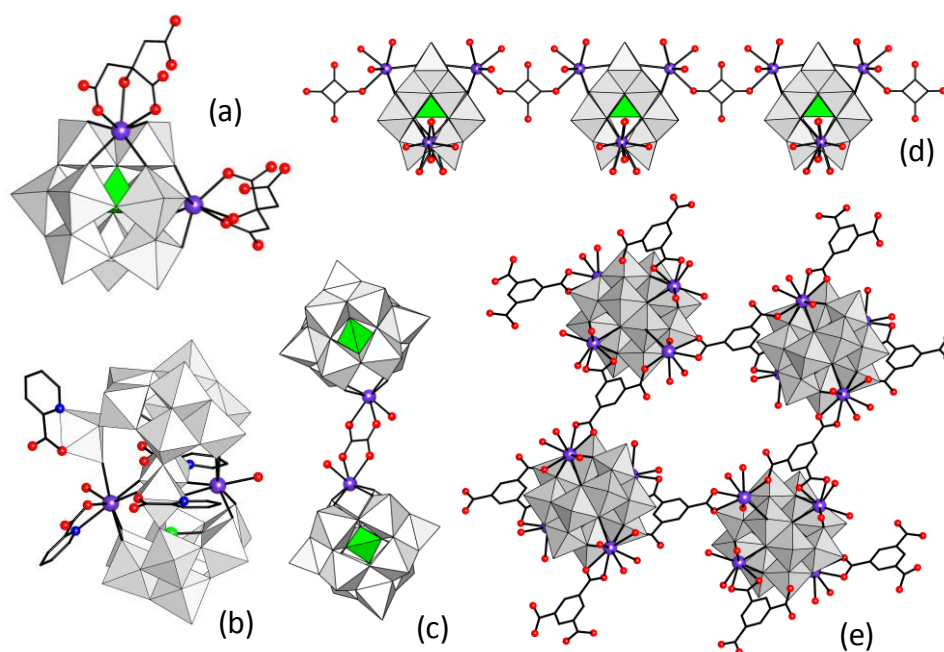


Figure 3.5. Representative examples of organically derivatized lanthanide-containing POMs: (a) Monomeric $[\text{Dy}_2\{\text{COH}(\text{COO})(\text{CH}_2\text{COO})_2\}_2(\text{AsW}_{10}\text{O}_{38})]^{11-}$. (b) $[\text{Ln}_2(\text{pic})(\text{H}_2\text{O})_2(\text{B-AsW}_8\text{O}_{30})_2\{\text{WO}_2(\text{pic})\}_3]^{10-}$. (c) Dimeric $[(\mu\text{-ox})\{\text{Ln}(\text{H}_2\text{O})(\text{PW}_{11}\text{O}_{39})\}_2]^{10-}$. (d) chains of $[\{\epsilon\text{-PMo}_{12}\text{O}_{39}(\text{OH})\}\text{La}_4(\text{H}_2\text{O})_{22}(\text{C}_4\text{O}_4)]$. (e) Three-dimensional network in $[\{\epsilon\text{-PMo}_{12}\text{O}_{35}(\text{OH})_5\}\text{La}_4(\text{H}_2\text{O})_{10}(\text{C}_9\text{H}_3\text{O}_6)_2]$.

The mixed-valence $[\{\epsilon\text{-PMo}^{\text{V}}_8\text{Mo}^{\text{VI}}_4\text{O}_{36}(\text{OH})_4\}\{\text{La}(\text{H}_2\text{O})_4\}]^{5+}$ polyoxomolybdate cation with an ϵ -Keggin type core capped with four lanthanum ions²⁵ has been used as building block for the design of extended hybrid organic-inorganic frameworks. The lability of the terminal water molecules on the 4f-metal center allows for the reaction of the polyoxomolybdate precursor with bidentate bridging ligands leading to one, two or three dimensional arrangements in the solid state. Polycarboxylic ligands like acetate, glutarate, squarate and di-, tri- or tetra-substituted benzenecarboxylates have been used for constructing such type of arrangements.²⁶ The cationic nature of the cluster makes the functionalization easier in such a way that it takes place even at room temperature and under mild conditions. (Figure 3.5)

3.1.4. Properties and applications of lanthanide-containing POMs

Among the vast POM family, 4f-metal containing species constitute one of the largest and currently most active groups because combination of POM building-blocks with rare-earth metals has been shown up as a suitable method for introducing additional properties (catalytic, optical, magnetic) to the POM system.

Lanthanide containing POMs as Lewis acid catalysts

The usual accessible and labile coordination sites on the metal centers make 4f-metal containing POMs effective Lewis acid catalysts for the activation of organic substrates. 4f-metal monosubstituted Keggin $\{\text{XW}_{11}\text{O}_{39}\}$ or Wells-Dawson $\{\text{P}_2\text{W}_{17}\text{O}_{61}\}$ polyoxotungstates have been used as selective and recoverable catalysts for C–C bond formation with enhanced chemo- and diastereoselectivity in Diels-Alder, Mannich and Mukaiyama type reactions or even employed for the aerobic oxidation of formaldehyde.²⁷ Moreover, combination of Lewis acid lanthanide sites and nucleophilic POM surfaces with Lewis base character can result in bifunctional catalysts suitable for cyanosilylation or oximation reactions owing to their ability to simultaneously activate complementary substrates, as well as in artificial proteases for the selective cleavage of peptide bonds under mild conditions because of the enzyme-like molecular recognition that POMs can undergo toward positively charged regions on proteins.²⁸ Similarly, lanthanide capped ϵ -Keggin type POMs have also been tested as the first example of polyoxocations with catalytic activity.²⁹

Magnetism: Single Molecule Magnets (SMM)

From a magnetic point of view, combination of the intrinsic large magnetic anisotropy and large ground-state spin values displayed by rare-earth metal ions under certain ligand fields with the rigidity and insulating ability of POMs as ligands (which hinder possible alterations in the ligand field or intermolecular magnetic interactions from taking place) have been proved to result in molecular systems showing slow relaxation of the magnetization. Different 4f-containing POMs have been reported to behave as effective single-ion or single-molecule magnets (SIMs or SMMs) or spin qubits in recent years, even with chemically-controlled reversible switching of the SMM behavior, and this may pave their way for being applied in high density memory-storage/sensor devices, spintronics or quantum computing.³⁰

For example, Peacock-Weakley iso- or hetero-polyanions comprising a single lanthanide atom in D_{4d} square-antiprismatic environment^{10b, 31} and Preyssler type POMs showing a 4f-metal center in unusual 5 fold symmetry³² have been identified as part of the growing family of SIMs. The former can

be seen as inorganic analogues of Ishikawa's phthalocyaninato-lanthanide $[\text{LnPc}_2]^-$ complexes with a "double-decker" structure.³³ These systems represent the limit in the miniaturization of a nanomagnet since a single magnetic center has been shown to be enough to behave as a SMM.

Photoluminescent properties

Lanthanide ions have been widely used in technological applications (e.g. photovoltaic cells, optical transistors, lasers, light-emitting diodes) or biomedical analyses and imaging because of their photophysical properties.³⁴ Trivalent lanthanide ions show characteristic photoluminescent properties, which result in weak emission because of the forbidden f-f transitions. However, effective emission can be observed by employing suitable "antenna" ligands that allows efficient energy transfer to the lanthanoid center, populating the metal excited states. It is well known that POMs can act as multidentate antenna ligands because the photoexcitation of the O→M (M = Nb, Mo, W) ligand to metal charge transfer (LMCT) bands sensitize the emitting centers as a result of the cited intramolecular energy transfer.³⁵ Owing to their multidentate character, they can also block coordination sites against aqua ligands responsible for emission quenching. These facts can lead to sharp and monochromatic emission bands and relatively long luminescence lifetimes for Sm, Eu, Tb and Dy species in the visible region or for Nd, Er and Yb in the near infrared.

It is worth mentioning that polyoxometaloeuropates exhibit the highest photoluminescence quantum yield among all the luminescent POMs described in the literature because the intermolecular energy transfer from O→M LMCT to Eu^{3+} centers is more efficient compared to that from any other 4f-metal POM. The $[\text{Eu}(\text{W}_5\text{O}_{18})_2]^{9-}$ anion reported by Yamase is certainly one of the most applied POMs in the construction of functional materials.³⁶ This cluster has been incorporated into multi-wavelength core/shell nanoparticles and Langmuir-Blodgett or layer-by-layer thin films containing different types of matrices (e.g. surfactants, agarose, polysaccharides, layered double hydroxides) and showing color-tuning or chemically-controlled switching of the emission.³⁷ Efficient sensitization of some other 4f-containing POMs has also been achieved by the coordination of organic antenna ligands to the emitting centers.²³

3.1.5. Giant POMs

Giant polyoxomolybdates showing more than 100 Mo atoms and sizes comparable to proteins have been thoroughly obtained by the group of Müller who has reported a variety of $\{\text{Mo}_{72}\text{M}_{30}\}$ Keplerates or $\{\text{Mo}_{154}\}$, $\{\text{Mo}_{176}\}$ and $\{\text{Mo}_{248}\}$ type "big wheels" based on mixed valence molybdenum ("Molybdenum Blues"). All have pentagonal $\{(\text{Mo})\text{Mo}_5\}$ moieties containing a central Mo atom in a pentagonal bipyramidal environment as a common structural feature.³⁸ In addition, lanthanide atoms have also been incorporated to those frameworks.³⁹ The potential of these systems to form large assemblies is so high that the $\{\text{Mo}_{368}\}$ hedgehog or "blue lemon" structure still represents the largest POM obtained to date.⁴⁰ The pentagonal bipyramidal $\{\text{Mo}_7\}$ unit has also been observed for tungsten as part of Keplerate-type polyoxotungstates or even as part of a "defect" pentagonal $\{(\text{W})\text{W}_4\}$ core in hexameric selenotungstates.⁴¹ However, the lower lability and much slower assembly processes of tungstates compared to molybdates has made the search of tungsten analogues of "molybdenum blues" an almost unexplored field.

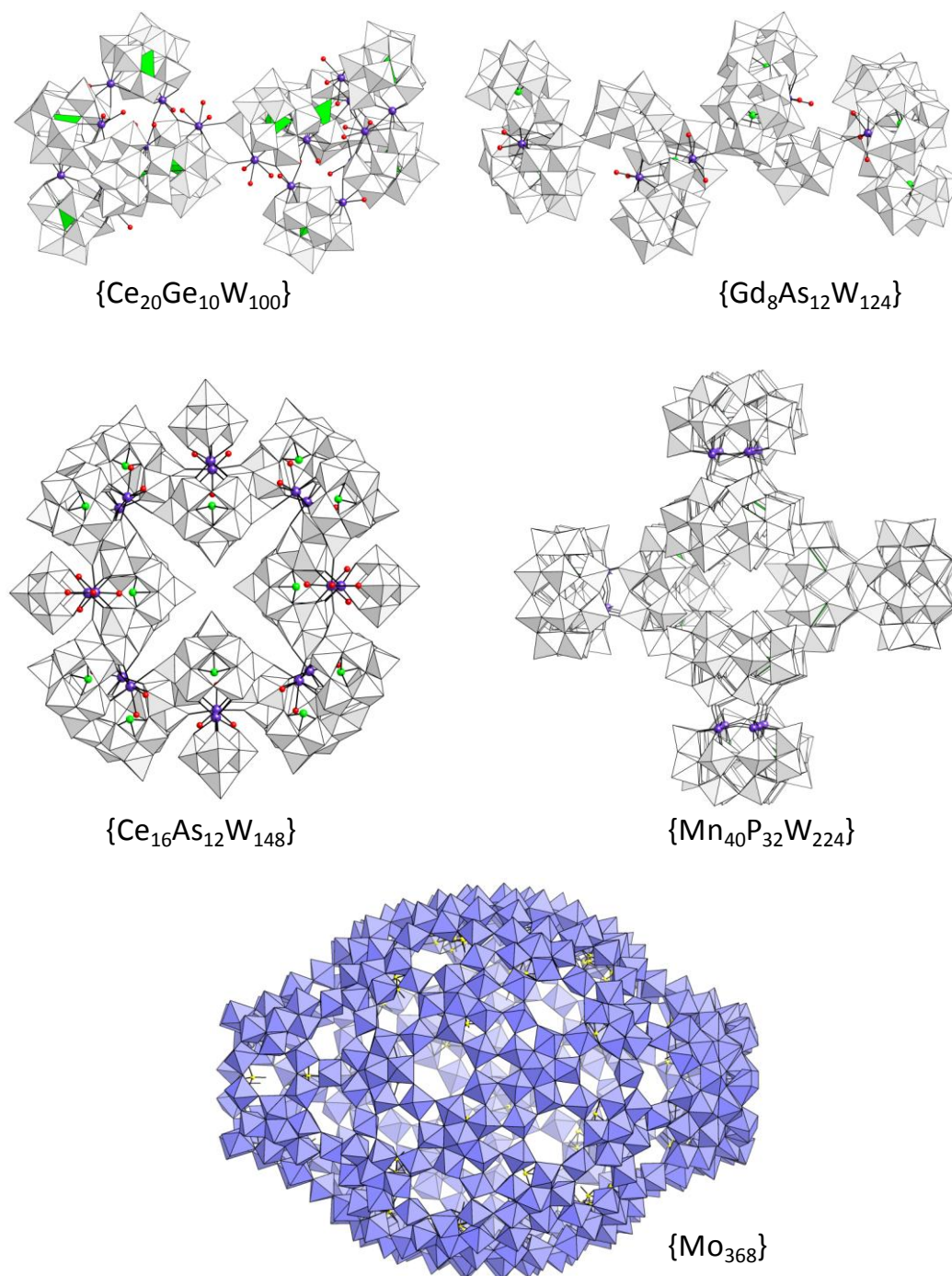


Figure 3.6. Molecular structures of some giant POMs showing more than 100 addenda metal atoms.

Regarding classical polyoxotungstates, the use of 4f-metal ions represents a powerful strategy to construct large, novel architectures due to their ability to link lacunary polyoxotungstates because of their high oxophilicity and coordination numbers. The larger size of 4f ions compared to 3d metals usually prevents their full incorporation in lacunary frameworks as addenda atoms, and therefore, additional sites are available in the coordination sphere of the lanthanide center for further derivatization. Among the nine structures containing more than 100 metal atoms, five belong to the family of lanthanide containing POMs and four of them show more than 100 W atoms. The largest polyoxotungstate architectures known in terms of the number of tungsten atoms have been obtained by employing first row transition metal linkers, such as the $\{\text{W}_{200}\text{Co}_8\text{O}_{660}\}$ cluster assembly containing isopolyoxotungstate fragments derived from the pentagonal $\{\text{W}(\text{W}_5)\}$ subunit or the

$[\text{Mn}_{40}\text{P}_{32}\text{W}_{224}\text{O}_{888}]^{144-}$ species based on $\{\text{P}_8\text{W}_{48}\}$ anions which is considered the largest polyoxotungstate to date.⁴² Nevertheless, the combination of lanthanide atoms with dilacunary $\{\text{GeW}_{10}\text{O}_{38}\}$ or trilacunary $\{\text{B-As}^{\text{III}}\text{W}_9\text{O}_{33}\}$ units has also led to several gigantic metal-oxo frameworks. The $[\text{As}_{12}\text{Ce}_{16}(\text{H}_2\text{O})_{36}\text{W}_{148}\text{O}_{524}]^{76-}$ anion synthesized by Pope and co-workers in 1997 was the largest polyoxotungstate known until 2010. This anion incorporates twelve $\{\text{B-}\alpha\text{-AsW}_9\text{O}_{33}\}$ subunits, four monolacunary Lindqvist-type $\{\text{W}_5\text{O}_{18}\}$ subunits and sixteen Ce centers linked by extra tungstate groups in a disc-shaped assembly with ideal D_{2d} symmetry.⁴³ The POMs $[\text{Ce}_{20}\text{Ge}_{10}\text{W}_{100}\text{O}_{376}(\text{OH})_4(\text{H}_2\text{O})_{30}]^{56-}$ and $[\text{Gd}_8\text{As}_{12}\text{W}_{124}\text{O}_{432}(\text{H}_2\text{O})_{22}]^{60-}$ can be both described as dimeric entities composed of two halves related by an inversion center. The pentameric half of the former dumbbell-shaped POM comprises five $\{\beta\text{-Ce}_2\text{GeW}_{10}\text{O}_{38}\}$ subunits linked to each other by the coordination sphere of Ce atoms in such a way that chiral R and S halves are present in the dimeric species. Hexameric halves in the latter POM are composed of six $\{\text{AsW}_9\text{O}_{33}\}$ and two $\{\text{Gd}_2\text{W}_4\}$ building blocks.⁴⁴ Similarly, the series of $[\text{Ln}_{16}\text{As}_{16}\text{W}_{164}\text{O}_{576}(\text{OH})_8(\text{H}_2\text{O})_{42}]^{80-}$ isomeric macroanions (Ln = Eu, Gd, Tb, Dy, Ho) synthesized by Hussain et al. from the $[\text{As}_2\text{W}_{19}\text{O}_{67}(\text{H}_2\text{O})]^{14-}$ POM precursor can also be considered as representative examples of the potential of 4f-metals in the construction of these outstanding polyoxotungstates. In spite of containing less than 100 W atoms, it is also worth mentioning the asymmetric $[\text{Yb}_{10}\text{As}_{10}\text{W}_{88}\text{O}_{308}(\text{OH})_8(\text{H}_2\text{O})_{28}(\text{OAc})_4]^{40-}$ anion reported by the same authors, which shows a decanuclear 4f-metal magnetic core stabilized by four $\{\text{B-}\alpha\text{-AsW}_9\text{O}_{33}\}$ and two $\{\text{B-}\beta\text{-As}^{\text{III}}\text{W}_9\text{O}_{33}\}$ fragments linked by extra tungstate units.⁴⁵ The last member of the family of giant lanthanide-containing polyoxometalates is the crown-shaped $[\text{K}_7\text{Ce}_{24}\text{Ge}_{12}\text{W}_{120}\text{O}_{444}(\text{OH})_{12}(\text{H}_2\text{O})_{64}]^{52-}$ POM, which was published in 2010 by Reinoso et al. and it is going to be discussed later during this chapter.⁴⁶

Self-assembly of large polyoxoanions in solution

Polyanions are suitable models to understand the gap in the solution behavior between simple ionic solutions (small ions that can be considered as point charges) and unstable colloidal suspensions. Polyoxometalates cannot be treated as point charges because of their big size, but opposite to colloidal suspensions, they form stable “real solutions”. Due to their well-defined molecular structure, high negative charge and high solubility in polar solvents, large POMs with sizes ranging from *ca.* 2 nm to 6 nm (e.g. giant Mo-rings, Keplerates, 3d- or 4f-containing polyoxotungstates, Figure 3.7) can show unusual behaviors in solution. More specifically, clusters can slowly self-assemble into spherical, hollow, single-layered and stable vesicle-like supramolecular entities, the so-called “blackberry” type structures.⁴⁷ To date, $\{\text{Cu}_{20}\text{P}_8\text{W}_{48}\}$ has been identified as the smallest polyanion to be able to self-assemble into blackberries in solution.⁴⁸ Laser light scattering (LLS), traditionally used for polymers, represents an ideal technique to monitor this type of self-assembly processes in diluted POM solutions (more details are given in Appendix 2).

Despite the fact that slow formation of spherical structures in aqueous solution by large POMs was previously observed in giant polyoxomolybdates by Müller⁴⁹ and Liu,⁵⁰ the publication of a complete study on the formation of blackberries in 2003 was the starting point for the development of this intriguing field.⁵¹ Size disparity between the macroions and their counterions leads to the counterion mediated attraction, which is considered as the main driving force in the self-assembly process. This theory has been proved by the determination of the counterion association around discrete polyanions in solution using small-angle X-ray scattering techniques (SAXS).⁵² When the effective charge of the POM is either too high or too low, no blackberries are formed in solution. The single-ion blackberry transition driven by the counterion association is not strong enough to

overcome the repulsion between POMs with very high charges, whereas POMs with very low charges are not able to hold counterions as ion-pairing structures, which will largely reduce the attractive force among them.⁵³

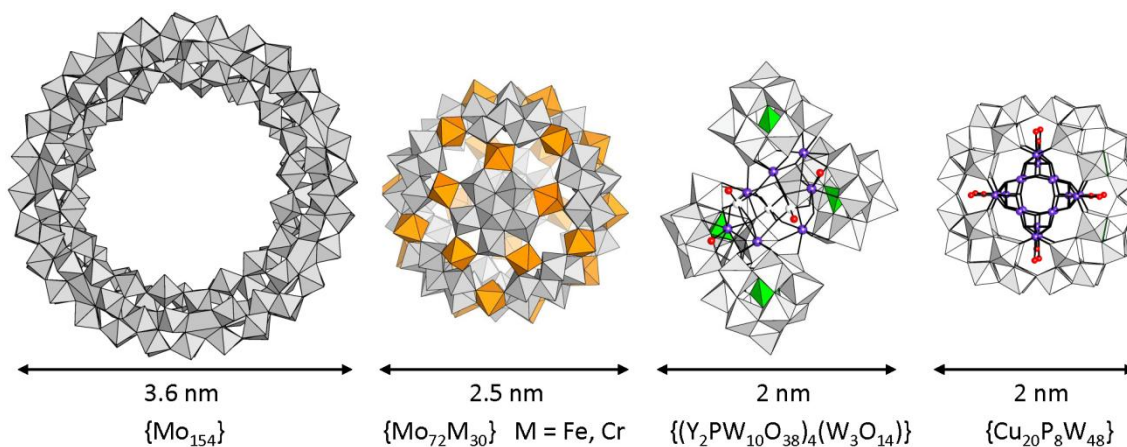


Figure 3.7. Size and molecular structure of some typical large POMs that can form blackberries in aqueous solutions. Color code: MoO_x polyhedra, grey; MO_6 ($M = \text{Fe}, \text{Cr}$) octahedra, orange.

Due to the importance of the charge regulated mechanism, the assembly/disassembly of the blackberries, as well as their size, can be adjusted by modifying different parameters like the solvent polarity (the blackberry size shows linear relationship with the inverse of the dielectric constant of the solvent);⁵⁴ the effective charge of the POM (which might be modulated by changing the pH)⁵⁵; and the addition of extra salts⁵⁶ or cationic surfactants⁵⁷ to the media. Sometimes, hydrogen bonding also plays an important role in the formation of the assemblies. Recently, rod-like assemblies were also observed for certain POMs showing anisotropic distribution of the charge density in the surface.⁵⁸

Blackberry-type structures can be found not only in macroanionic solutions, but also with macrocations such as metal-organic nanocages,⁵⁹ and therefore, they could be seen as a universal kind of self-assembly for soluble macroions. Moreover, hollow vesicles show certain similarities with some biomolecular systems, including the general structure of the spherical virus capsid and the kinetics of their formation process, or even the interaction between DNA and proteins.⁶⁰ Some fascinating biological behaviors such as the self-recognition among molecules take place during the blackberry formation. Two types of almost identical POM macroions can self-recognize each other in a mixed solution during their self-assembly process, resulting in two types of homogenous blackberries instead of mixed assemblies. This behavior has been explained by slightly different charge distributions of the macroions which are sensitive for long-range counterion-mediated electrostatic attraction.⁶¹

3.1.6. Aim of the work

In 2010, the largest tungstogermanate to date was published in *Angewandte Chemie International Edition* by Reinoso et al., namely $[\text{K}_7\text{Ce}_{24}\text{Ge}_{12}\text{W}_{120}\text{O}_{444}(\text{OH})_{12}(\text{H}_2\text{O})_{64}]^{52-}$ (**8-Ce**).⁴⁶ This compound was described as containing the largest number of 4f-metal ions in a POM so far, and it was considered as the first giant POM with a crown shape, that is, displaying a central cavity available for ion encapsulation in an inorganic analogue of crown ethers. This POM was obtained upon addition of K^+ to a one-pot reaction involving $\text{NiCl}_2 \cdot 6\text{H}_2\text{O}$, $\text{Ce}(\text{NO}_3)_3 \cdot 6\text{H}_2\text{O}$, GeO_2 and $\text{Na}_2\text{WO}_4 \cdot 2\text{H}_2\text{O}$ in sodium acetate buffered medium at room temperature. According to preliminary results, **8-Ce**

appears to undergo a blackberry-type aggregation in aqueous solution. Encouraged by these findings and taking into account the potential properties that lanthanides might confer on the new POMs, a systematic study on the influence of different synthetic variables (e.g. lanthanide, alkaline counterion) of the one-pot procedure in the final products has been carried out as it will be explained later in this chapter. The POMs obtained are summarized in Figure 3.8 and they will be discussed in two different sections. By using early lanthanides (Ce to Sm), large assemblies containing 6 (**6-Ln**, **7-Sm**) or 12 (**8-Ln**) lanthanide disubstituted Keggin-type dilacunary $[\text{Ln}_2\text{GeW}_{10}\text{O}_{38}]^{6-}$ subunits ($\{\text{Ln}_2\text{GeW}_{10}\}$) were obtained, whereas smaller assemblies based on 2 (**9-Ln**) or 4 (**10-Ln**) $\{\text{Ln}_2\text{GeW}_{10}\}$ subunits were found for mid-to-late 4f-metals (Gd to Lu). As a result, here we report on the synthesis and full characterization in terms of solid state properties and solution behavior of 18 lanthanide containing tungstogermanates, namely $\text{Na}_{31}\text{Ni}_2[\text{Na}\langle\text{Ln}_{12}\text{Ge}_6\text{W}_{60}\text{O}_{228}(\text{H}_2\text{O})_{24}\rangle] \cdot \sim 145\text{H}_2\text{O}$ (**6-Ln**, Ln = Pr, Nd), $\text{Na}_{27}\text{K}_4\text{Ni}_2[\text{K}\langle\text{Sm}_{12}\text{Ge}_6\text{W}_{60}\text{O}_{228}(\text{H}_2\text{O})_{22}\rangle] \cdot \sim 123\text{H}_2\text{O}$ (**7-Sm**), $\text{Na}_{40}\text{K}_6\text{Ni}_3[\text{K}\langle\text{K}_7\text{Ln}_{24}\text{Ge}_{12}\text{W}_{120}\text{O}_{444}(\text{OH})_{12}(\text{H}_2\text{O})_{64}\rangle] \cdot \sim 280\text{H}_2\text{O}$ (**8-Ln**, Ln = Ce, Pr, Nd), $\text{Na}_{12}[\text{Ln}_4(\text{H}_2\text{O})_6(\beta\text{-GeW}_{10}\text{O}_{38})_2] \cdot n\text{H}_2\text{O}$ (**9-Ln**, Ln = Gd, Tb, Dy, Ho, Er, Tm, Yb, Lu; n = 40-44) and $\text{Cs}_y\text{Na}_{24-y}[\{\text{Ln}_4(\text{H}_2\text{O})_5(\text{GeW}_{10}\text{O}_{38})_2\}_2] \cdot n\text{H}_2\text{O}$ (**10-Ln**, Ln = Ho, Er, Tm, Yb, Lu; y = 5-7; n = 63-66). Compounds containing early lanthanides (**6-Ln**, **7-Sm** and **8-Ln**) will be discussed in Section 3.3, whereas those derived from mid-to-late lanthanides (**9-Ln** and **10-Ln**) will be described in Section 3.4.

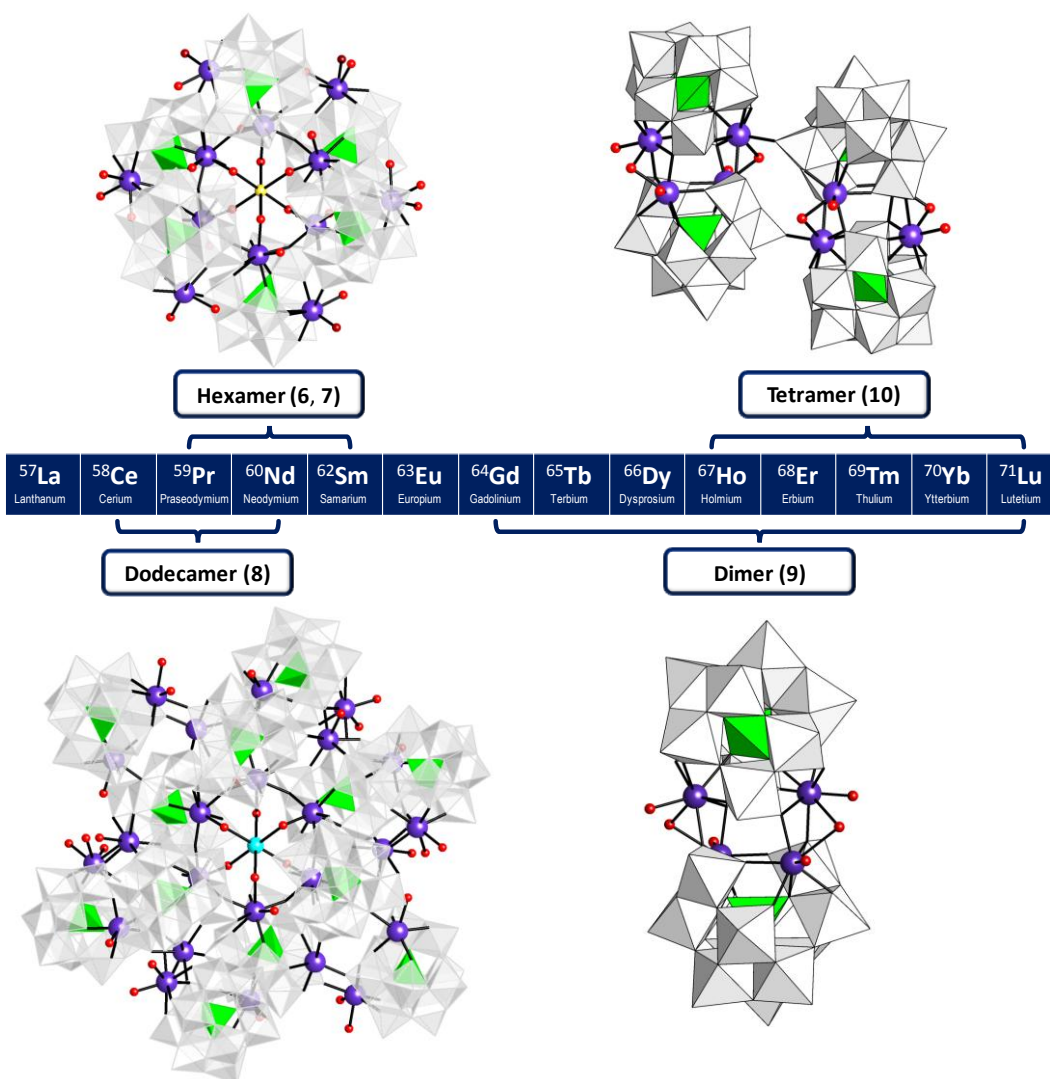


Figure 3.8. Schematic representation of the compounds included in Chapter 3.

3.2. GENERAL SYNTHETIC ASPECTS

The corresponding $1.1\text{Ni}^{2+}:1.1\text{Ln}^{3+}:1\text{GeO}_2:9\text{WO}_4^{2-}$ or $1.1\text{Ln}^{3+}:1\text{GeO}_2:9\text{WO}_4^{2-}$ reactions were carried out in 0.5M NaOAc buffer solution at room temperature. The use of 14 different lanthanide ions in the presence or absence of Ni^{2+} , together with the addition of K^+ or Cs^+ cations as crystallizing agents results in a total number of 84 possible reactions. All of them were performed and the results obtained are summarized in Table 3.1.

Table 3.1. Summary of the main results derived from the systematic studies included in Chapter 3.

	$1.1 \text{M}^{2+} : 1.1 \text{Ln}^{3+} : 1 \text{GeO}_2 : 9 \text{WO}_4^{2-}$					
	M = Ni			M = \emptyset		
	Na	K	Cs	Na	K	Cs
⁵⁷ La Lanthanum	×	<i>a</i>	×	×	<i>e</i>	×
⁵⁸ Ce Cerium	×	✓ 8-Ce*	<i>b</i>	×	8-CeB	<i>f</i>
⁵⁹ Pr Praseodymium	✓ 6-Pr	✓ 8-Pr	<i>c</i>	<i>g</i>	<i>h</i>	<i>i</i>
⁶⁰ Nd Neodymium	✓ 6-Nd	✓ 8-Nd	<i>d</i>	<i>j</i>	<i>k</i>	<i>l</i>
⁶² Sm Samarium	×	✓ 7-Sm	×	×	<i>m</i>	×
⁶³ Eu Europium	×	×	×	×	×	×
⁶⁴ Gd Gadolinium	×	×	×	✓ 9-Gd	×	×
⁶⁵ Tb Terbium	×	×	×	✓ 9-Tb	×	×
⁶⁶ Dy Dysprosium	×	×	×	✓ 9-Dy	×	×
⁶⁷ Ho Holmium	×	×	×	✓ 9-Ho	×	✓ 10-Ho
⁶⁸ Er Erbium	×	×	×	✓ 9-Er	×	✓ 10-Er
⁶⁹ Tm Thulium	×	×	×	✓ 9-Tm	×	✓ 10-Tm
⁷⁰ Yb Ytterbium	×	×	×	✓ 9-Yb	×	✓ 10-Yb
⁷¹ Lu Lutetium	×	×	×	✓ 9-Lu	×	✓ 10-Lu

*previously published (see reference 46).

8-CeB: a crystal structure was obtained from this reaction.

c, d, g, i, j, l: the IR spectra of these solids are similar to those of 6-Ln and 7-Sm.

a, b, e, f, h, k, m: the IR spectra of these solids are similar to those of 8-Ln.

Only 32 out of the 84 possible synthetic combinations have resulted in identifiable solid products. These can be classified into two groups: compounds whose structure was determined by single-crystal X-ray diffraction and those identified only by IR spectroscopy. As part of the former group, three types of compounds have been obtained for early lanthanides (Ce to Sm) and with the help of Ni^{2+} cations. The hexameric, crown-shaped $[\text{Na}\{\text{Ln}_{12}\text{Ge}_6\text{W}_{60}\text{O}_{228}(\text{H}_2\text{O})_{24}\}]^{35-}$ architectures (**6-Ln**, Ln = Pr, Nd) were obtained in the exclusive presence of Na^+ , whereas the addition of K^+ lead to a similar kind of cluster for Sm $[\text{K}\{\text{Sm}_{12}\text{Ge}_6\text{W}_{60}\text{O}_{228}(\text{H}_2\text{O})_{22}\}]^{35-}$ (**7-Sm**) and giant dodecameric $[\text{K}\{\text{K}_7\text{Ln}_{24}\text{Ge}_{12}\text{W}_{120}\text{O}_{444}(\text{OH})_{12}(\text{H}_2\text{O})_{64}\}]^{52-}$ structures (**8-Ln**) for Ce, Pr and Nd. Besides, another two types of architectures have been obtained for mid-to-late lanthanides in the absence of Ni^{2+} cations (Gd to Lu): rod-like dimeric $[\text{Ln}_4(\text{H}_2\text{O})_6(\beta\text{-GeW}_{10}\text{O}_{38})_2]^{12-}$ (**9-Ln**, Ln = Tb to Lu) and diamond-shaped tetrameric $[\{\text{Ln}_4(\text{H}_2\text{O})_5(\text{GeW}_{10}\text{O}_{38})_2\}]^{24-}$ (**10-Ln**, Ln = Ho to Lu) assemblies, which were formed in the exclusive presence of Na^+ cations or upon addition of Cs^+ ions, respectively. All these results account for the 16 new structures reported in this chapter. As mentioned before, the synthesis and crystal structure of **8-Ce** was reported previously,⁴⁶ but a full study of its solution behavior by means of Laser Light Scattering techniques will be given in this chapter.

On the contrary, the second group is composed by the solid phases isolated from the reactions performed for early-lanthanides with La^{III} as the rare earth source, Cs^+ as counterion or those carried out in the absence of Ni^{2+} cations. The dimeric compound **9-Gd** can also be classified in this group because it could only be characterized by elemental and thermal analyses, IR spectroscopy and magnetic measurements. For the Cs^+ containing procedures, the solid product isolated from the reaction carried out with Ce^{III} displays an IR spectrum comparable to those of **6-Ln** and **7-Sm**, whereas those of the products obtained with Pr^{III} or Nd^{III} are identical to the spectrum of **8-Ln**. Moreover, the compounds isolated in the presence of K^+ or only Na^+ exhibit similar IR spectra to those observed for **8-Ln** and **6-Ln/7-Sm**, respectively. In the case of Ce^{III} , when the organic chelating ligand 2,6-pyridinedicarboxylic acid was used as structure directing agent, we were able to isolate crystals suitable for X-Ray Diffraction experiments and the structure of a dodecameric assembly was determined (**8-CeB**). Unfortunately, we cannot give further proof of this structure to be representative of the almost amorphous bulk phase.

3.3. POM ASSEMBLIES CONTAINING EARLY LANTHANIDES

3.3.1. Experimental section

General synthetic procedure. Solid $\text{NiCl}_2 \cdot 6\text{H}_2\text{O}$ (233 mg, 0.98 mmol), $\text{Ln}(\text{NO}_3)_3 \cdot 6\text{H}_2\text{O}$ (0.98 mmol, Ln = Pr, Nd, Sm), GeO_2 (93 mg, 0.89 mmol), and $\text{Na}_2\text{WO}_4 \cdot 2\text{H}_2\text{O}$ (2.64 g, 8.00 mmol) were successively added to a 0.5M NaOAc/AcOH buffer solution (40 mL). The reaction mixture was stirred for 1 h at room temperature. After filtering any solid off, the resulting solution was left to evaporate. $\text{Na}_{31}\text{Ni}_2[\text{Na}\{\text{Ln}_2(\text{H}_2\text{O})_4(\beta\text{-GeW}_{10}\text{O}_{38})\}_6] \cdot \sim 145\text{H}_2\text{O}$ (**6-Ln**; Ln = Pr, Nd) was isolated as small prismatic X-ray quality single crystals by slow evaporation after four days. $\text{Na}_{27}\text{K}_4\text{Ni}_2[\text{K}\{\text{Sm}_2(\text{H}_2\text{O})_4(\beta\text{-GeW}_{10}\text{O}_{38})\}_6] \cdot \sim 121\text{H}_2\text{O}$ (**7-Sm**) and $\text{Na}_{40}\text{K}_8\text{Ni}_2[\text{K}\{\text{K}_7\text{Ln}_{24}\text{Ge}_{12}\text{W}_{120}\text{O}_{444}(\text{OH})_{12}(\text{H}_2\text{O})_{56}\}] \cdot \sim 288\text{H}_2\text{O}$ (**8-Ln**, Ln = Pr, Nd) were obtained as prismatic plates by addition of aqueous 1M KCl (~ 1 mL) to the final solution, followed by slow evaporation at room temperature for three days.

$\text{Na}_{31}\text{Ni}_2[\text{Na}\{\text{Pr}_{12}\text{Ge}_6\text{W}_{60}\text{O}_{228}(\text{H}_2\text{O})_{24}\}] \cdot \sim 145\text{H}_2\text{O}$ (6-Pr): $\text{Pr}(\text{NO}_3)_3 \cdot 6\text{H}_2\text{O}$ (426 mg) was used as the lanthanide source. Yield: 70 mg, 5 % based on Pr. Anal. Calcd (found) for $\text{Ge}_6\text{H}_{314}\text{Na}_{32}\text{Ni}_2\text{O}_{385}\text{Pr}_{12}\text{W}_{60}$:

Ge, 2.13 (2.18); Na, 3.59 (3.64); Ni, 0.57 (0.61); Pr, 8.25 (8.16). IR (cm^{-1}): 936 (m), 870 (sh), 827 (s), 783 (s), 729 (m), 517 (w), 480 (w), 424 (m).

Na₃₁Ni₂[Na<Nd₁₂Ge₆W₆₀O₂₂₈(H₂O)₂₄] \cdot ~145H₂O (6-Nd): Nd(NO₃)₃·6H₂O (430 mg) was used as the lanthanide source. Yield: 90 mg, 6 % based on Nd. Anal. Calcd (found) for Ge₆H₃₁₄Na₃₂Nd₁₂Ni₂O₃₈₅W₆₀: Ge, 2.17 (2.09); Na, 3.58 (3.51); Nd, 8.43 (8.29); Ni, 0.57 (0.62). IR (cm^{-1}): 936 (m), 872 (sh), 826 (s), 783 (s), 731 (m), 513 (w), 480 (w), 428 (m).

Na₂₇K₄Ni₂[K<Sm₁₂Ge₆W₆₀O₂₂₈(H₂O)₂₂] \cdot ~123H₂O (7-Sm): Sm(NO₃)₃·6H₂O (436 mg) was used as the lanthanide source. Yield: 290 mg, 11 % based on Sm. Anal. Calcd (found) for Ge₆H₂₉₀K₄Na₂₇Ni₂O₃₇₃Sm₁₂W₆₀: Ge, 2.13 (1.97); K, 0.96 (0.99); Na, 2.13 (2.33); Ni, 0.57 (0.53); Sm, 8.82 (8.68). IR (cm^{-1}): 934 (m), 875 (sh), 827 (s), 785 (s), 733 (m), 513 (w), 476 (w), 432 (m). TGA/DTA: Dehydration process is completed at around 490 °C. [calcd (found) for 145H₂O: 12.77 (12.71)] and followed by the decomposition of the POM resulting in the final residue at 650 °C.

Na₄₀K₆Ni₃[K<K₇Pr₂₄Ge₁₂W₁₂₀O₄₄₄(OH)₁₂(H₂O)₆₄] \cdot ~280H₂O (8-Pr): Pr(NO₃)₃·6H₂O (426 mg) was used as the lanthanide source. Yield 340 mg, 14 % based on Pr. Anal. Calcd (found) for Ge₁₂H₇₀₀K₁₄Na₄₀Ni₃O₈₀₀Pr₂₄W₁₂₀: Ge, 2.10 (2.14); K, 1.32 (1.47); Na, 2.22 (2.30); Ni, 0.43 (0.44); Pr, 8.16 (7.94). IR (cm^{-1}): 941 (m), 856 (sh), 820 (s), 789 (s), 731 (m), 700 (m), 530 (w), 426 (m).

Na₄₀K₆Ni₃[K<K₇Nd₂₄Ge₁₂W₁₂₀O₄₄₄(OH)₁₂(H₂O)₆₄] \cdot ~280H₂O (8-Nd): Nd(NO₃)₃·6H₂O (430 mg) was used as the lanthanide source. Yield 390 mg, 16 % based on Nd. Anal. Calcd (found) for Ge₁₂H₇₀₀K₁₄Na₄₀Nd₂₄Ni₃O₈₀₀W₁₂₀: Ge, 2.10 (2.23); K, 1.32 (1.43); Na, 2.21 (2.27); Nd, 8.33 (8.49); Ni, 0.42 (0.41). IR (cm^{-1}): 943 (m), 856 (sh), 826 (s), 786 (s), 729 (m), 698 (m), 524 (w), 428 (m).

Thermal analyses: The TGA/DTA curves for compounds **6-Ln** (Ln = Pr, Nd), **7-Sm** and **8-Ln** (Ln = Pr, Nd) are shown in Figure A2.11 in Appendix 2. In all cases, the dehydration process is observed as an endothermic mass loss that extends continuously up to temperatures in the 455-520 °C range, above which the POM framework starts decomposing as indicated by a set of overlapped exothermic signals. Table 3.2 displays the experimental mass losses observed (Δm) compared to the calculated values, together with the temperature ranges at which POM decomposition takes place (T_d).

Table 3.2. Thermal data of compounds **6-Ln**, **7-Sm** and **8-Ln**.

	Δm_{exp} (%)	Δm_{calcd} (%), $n\text{H}_2\text{O}$	T_d (°C)
6-Pr	13.75	13.81 for $n = 157$	530
6-Nd	13.81	13.78 for $n = 157$	540
7-Sm	12.71	12.77 for $n = 145$	650
8-Pr	14.95	14.95 for $n = 344$	630
8-Nd	14.98	14.92 for $n = 344$	640

Single-crystal X-ray diffraction

Crystal data for **6-Ln** (Ln = Pr, Nd), **7-Sm** and **8-Ln** (Ln = Pr, Nd) are summarized in Table 3.3. Thermal vibrations were treated anisotropically for heavy atoms (W, Ge, K, lanthanides). All compounds display significant disorder between counterions and lattice water molecules. For the isostructural **6-Ln**, 14 (Nd) and 16 (Pr) sites with appropriate geometries for a sodium cation were

located in the Fourier maps. The occupancies in these positions were initially refined without restrictions and rounded to the first decimal in the last cycle. The same procedure was followed with the 2 nickel sites located for both compounds. This resulted in the following total number of Na/Ni atoms per asymmetric unit containing half of the polyanion: 10.5/1.0 for **6-Pr** and 9.3/0.7 for **6-Nd**. For **7-Sm**, the lower quality of the data only allowed us to locate 12 sodium, 2 potassium and 2 nickel sites. The free refinement of the population factors of these sites and consequent round to the first decimal resulted in a total number of 7.0 Na, 1.0 K and 0.7 Ni atoms respectively.

In the case of the isostructural **8-Ln** (Ln = Pr, Nd), the low quality of the data together with a heavy disorder between counterions and solvent molecules result in a final structural solution with large voids accounting for about 10% of the unit cell (1046 \AA^3 at $x,y,z = 0, 0, 1/2$ for **8-Pr** and 1864 \AA^3 at $x,y,z = 0, 0, 0$ for **8-Nd**). Because of this, we could only find a total Na/K/Ni number of 13.0/6.0/0.7 (**8-Pr**) and 11/6/0 (**8-Nd**) cations per asymmetric unit containing one half of the polyanion. The presence of the three Ni^{II} ions in **8-Nd** was unequivocally determined by elemental analyses.

Table 3.3. Crystallographic data for **6-Ln** (Ln = Pr, Nd), **7-Sm** and **8-Ln** (Ln = Pr, Nd).

Compound	6-Pr	6-Nd	7-Sm	8-Pr	8-Nd
Formula	Ge ₆ H ₃₁₄ Na ₃₂ Ni ₂ O ₃₈₅ Pr ₁₂ W ₆₀	Ge ₆ H ₃₁₄ Na ₃₂ Nd ₁₂ Ni ₂ O ₃₈₅ W ₆₀	Ge ₆ H ₂₉₀ K ₄ Na ₂₇ Ni ₂ O ₃₇₃ Sm ₁₂ W ₆₀	Ge ₁₂ H ₇₀₀ K ₁₄ Na ₄₀ Ni ₃ O ₈₀₀ Pr ₂₄ W ₁₂₀	Ge ₁₂ H ₇₀₀ K ₁₄ Na ₄₀ Nd ₂₄ Ni ₃ O ₈₀₀ W ₁₂₀
FW (g mol ⁻¹)	20487.1	20527.0	20425.61	41462.4	41542.4
Crystal system	triclinic	triclinic	triclinic	triclinic	triclinic
Space group	<i>P</i> -1	<i>P</i> -1	<i>P</i> -1	<i>P</i> -1	<i>P</i> -1
<i>a</i> (Å)	17.3447(3)	17.3446(3)	17.0643(3)	23.3793(3)	23.5166(3)
<i>b</i> (Å)	22.7515(4)	22.7465(3)	22.8140(4)	27.1546(5)	27.1213(3)
<i>c</i> (Å)	23.5880(4)	23.5557(4)	23.0050(4)	28.4780(6)	27.8711(3)
α (°)	112.0901(17)	112.090(10)	112.158(2)	70.9537(18)	75.2772(10)
β (°)	111.3416(17)	111.255(2)	109.021(2)	79.8520(14)	78.0106(10)
γ (°)	94.7239(15)	94.7110(10)	96.241(2)	64.7253(15)	64.3650(11)
<i>V</i> (Å ³)	7770.1(2)	7764.4(2)	7562.3(3)	15439.3(5)	15402.5(3)
<i>Z</i>	1	1	1	1	1
<i>D</i> _{calcd} (g cm ⁻³)	4.378	4.390	4.485	4.460	4.479
μ (mm ⁻¹)	56.43	57.34	61.022	25.038	58.514
Reflections					
Collected	46061	55364	55455	113913	111285
Unique (<i>R</i> _{int})	27405 (0.052)	27695 (0.049)	26967 (0.044)	54385 (0.049)	54817 (0.057)
Observed [<i>I</i> > 2 σ (<i>I</i>)]	22115	22656	22298	39239	42039
Parameters	1133	1132	1122	2169	2095
<i>R</i> (<i>F</i>) [<i>I</i> > 2 σ (<i>I</i>)]	0.052	0.049	0.056	0.064	0.064
<i>wR</i> (<i>F</i> ²) (all data)	0.146	0.136	0.156	0.169	0.189
GoF	1.055	1.009	1.026	1.050	1.025

Polyoxometalates can be described as the product of the alkaline-metal ion (Na for **6-Ln**, K for **7-Sm** and **8-Ln**) directed assembly of six (**6-Ln**, **7-Sm**) or twelve (**8-Ln**) dilacunary Keggin POM $[\text{Ln}_2\text{GeW}_{10}\text{O}_{38}]^{6-}$ subunits ($\{\text{Ln}_2\text{GeW}_{10}\}$), which consist in a dilacunary Keggin-type POM fragment stabilized by the incorporation of two lanthanide ions onto the vacant site. The nuclearity of the final assembly is strongly dependent on the size of the lanthanide and nature of the employed counterion. For Pr^{III} and Nd^{III} , the smaller size of the sodium cation only allows the formation of the hexameric $\{\text{Na} \subset (\beta\text{-Ln}_2\text{GeW}_{10})_6\}$ assembly (**6-Pr**, **6-Nd**), whereas six additional $\{\text{Ln}_2\text{GeW}_{10}\}$ subunits can be accommodated by using the larger potassium because this ion acts not only as template for the formation of the central hexameric crown, but also links six external units to the central core to lead to a dodecameric structure (**8-Pr**, **8-Nd**). For cerium, a dodecameric entity was obtained upon addition of K^+ (**8-Ce**), but in contrast, no identifiable solids were isolated in the exclusive presence of sodium. No crystals suitable for X-ray diffraction were obtained for lanthanum upon addition of K^+ , but the IR spectrum of the final product closely resembles that of a dodecameric assembly. However, a crown-shaped $\{\text{K} \subset (\beta\text{-Ln}_2\text{GeW}_{10})_6\}$ hexamer, similar to that observed for **6-Pr** and **6-Nd**, was obtained for samarium (**7-Sm**) in the presence of potassium cations instead of the expected dodecamer. The smaller size of the Sm^{III} ion as a result of the well-known lanthanide contraction effect might not allow the external subunits to be stabilized, avoiding their linkage to the central cluster and consequent formation of larger clusters.

The solids obtained from reactions involving the addition of Cs^+ to Pr or Nd mixtures show virtually identical spectra to those of **6-Ln** ($\text{Ln} = \text{Pr}, \text{Nd}$), and this suggests that the same kind of hexameric assembly is formed. However, the spectrum registered for the final product of the Ce containing mixture is similar to those of **8-Ln** ($\text{Ln} = \text{Ce}, \text{Pr}, \text{Nd}$), and therefore, a larger assembly related to the dodecameric cluster could be expected. Unfortunately, we cannot confirm this by standard X-Ray diffraction experiments because these crystals show diffraction spots only at very low 2θ angles, suggesting a short-range order in the structure. We tried to improve the crystallization of these species and some other different cations were used in an attempt to grow crystals suitable for single-crystal structural analyses, but without any success. No crystalline products were obtained by adding Rb^+ , Ca^{2+} , NH_4^+ , or organic cations (guanidinium, ethylenediammonium, tetramethylammonium, tetrabutylammonium) to the media, confirming the essential structural role of the counterions. Modifications in the acetic acid/acetate buffer solutions by changing its counterion (K^+ , NH_4^+) or concentration (0.5M, 2M), as well as in the total concentration of the reactants, did neither give any product suitable for further characterization.

As reported for **8-Ce**, $[\text{Ni}(\text{H}_2\text{O})_6]^{2+}$ counterions also play a crucial structural role as crystallizing species through the establishment of an extensive hydrogen-bonding network with the POM surface. The use of other 3d-metals like Co^{II} or Mn^{II} resulted in the same kind of assembly, and therefore we did not perform any systematic study on the nature of 3d-metal but rather kept Ni^{2+} as a fixed synthetic parameter. Reactions performed without any first row transition metal ion under the same synthetic conditions lead to solid products with the appearance of single-crystals. Even though their IR spectra compare very well to those of the 3d-metal containing analogues, powder X-ray diffraction patterns of these samples did not show any clear, well-defined diffraction maxima (Figure 3.10), suggesting extremely short-range crystalline order in these “glassy crystals”. Only in the case of Ce^{III} , we were able to perform X-Ray diffraction experiments on a single-crystal obtained when the organic 2,6-pyridinedicarboxylic acid chelating ligand was included in the reaction as structure directing

agent (**8-CeB**). The use of organic multidentate O-donor ligands as structure directing agents has been previously reported by Wang's group. These authors claimed that these ligands might play an important role in the preparation of certain lanthanotungstates despite not being present in the final structure.⁶³ In our case, the crystal structure of **8-CeB** shows molecular dodecameric assemblies analogous to those obtained for **8-Ln** (Ln = Ce, Pr, Nd) but for the fact that they are isolated instead of forming chains in the solid state.⁶⁴ Unfortunately, we could not get further unequivocal proof of this structure being representative of the bulk sample because its PXRD pattern corresponds to an almost amorphous phase (inset in Figure 3.10), showing the "glassy" nature of the crystals.

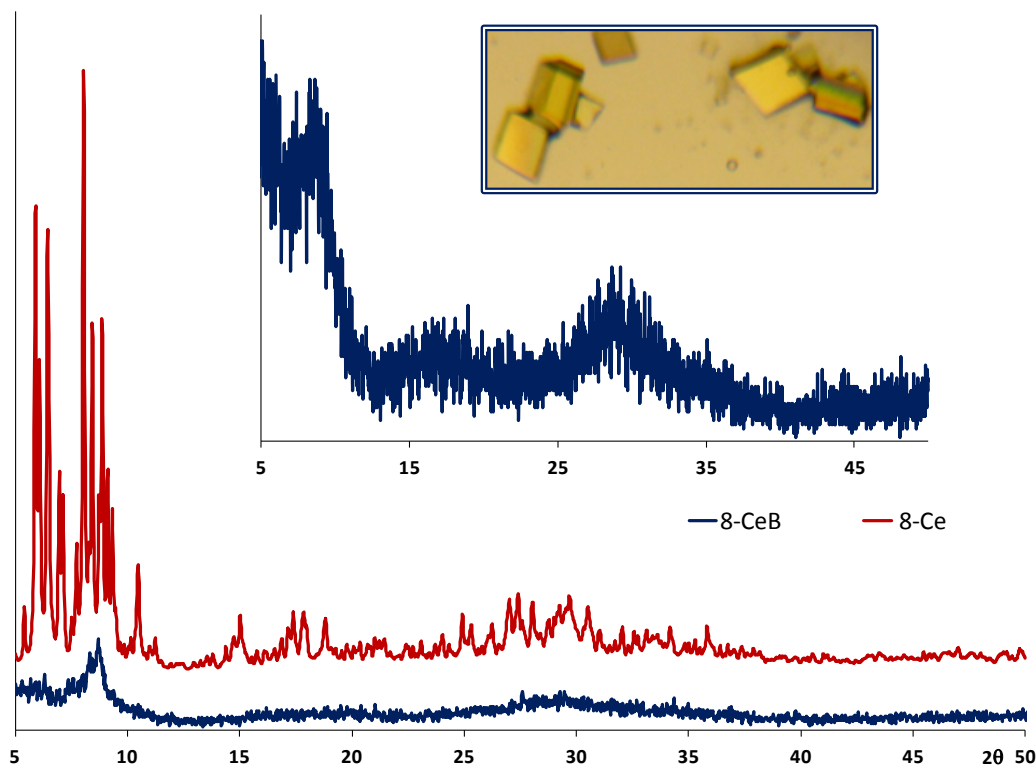


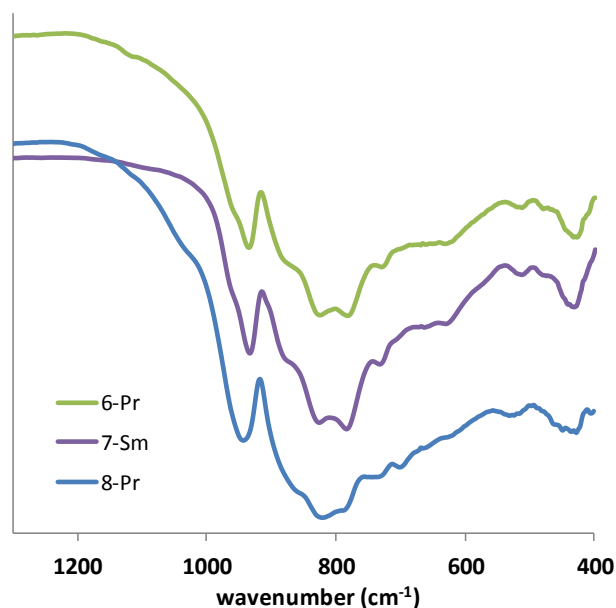
Figure 3.10. Experimental powder X-Ray diffraction pattern for the solid sample obtained from the $1.1\text{Ce}^{3+} : 1\text{GeO}_2 : 9\text{WO}_4^{2-}$ reaction upon addition of K^+ (blue) and comparison to that of **8-Ce** (red). Inset: Detail of the diffraction pattern of **8-CeB** highlighting its low crystallinity and photograph of the 'glassy crystals' of **8-CeB** taken in an optical microscope.

Both types of crown-shaped hexameric or dodecameric structures can be unambiguously distinguished by IR spectroscopy (Figure 3.11). The spectra of **8-Ln** are very similar to that reported for the **8-Ce** derivative⁴⁶ and clearly differ from those of **6-Ln** or **7-Sm**, which are almost identical to each other. Besides the fact that the signal associated to the $\nu_{\text{as}}(\text{W}-\text{O}_i)$ mode is sharpened and red-shifted when going from **8-Ln** (above 940 cm^{-1}) to **6-Ln** or **7-Sm** (below 940 cm^{-1}), the main difference between the spectra of dodecamers and hexamers lays on the signals originating from the M–O–M stretching vibration. These go from a single broad band centered at about $820\text{--}825\text{ cm}^{-1}$ for the former to a doublet located at ~ 825 and $\sim 785\text{ cm}^{-1}$ for the latter (Table 3.4). These modifications are systematically observed, confirming the viability of the IR spectroscopy for determining the hexameric or dodecameric nature of the compound.

Table 3.4. Most representative IR bands (cm^{-1}) for **6-Pr**, **7-Sm**, **8-Pr**.

6-Pr	7-Sm	8-Pr
935 (s)	934 (s)	942 (s)
883 (m)	880 (m)	868 (m)
827 (vs)	827 (vs)	825 (vs)
783 (vs)	785 (vs)	789 (vs)
729 (s)	732 (s)	730 (s)
625 (m)	630 (m)	700 (m)
517 (w)	513 (w)	525 (w)
480 (w)	475 (w)	448 (w)
424 (w)	431 (w)	426 (w)

w=weak, m = medium, s =strong, vs =very strong.

**Figure 3.11.** IR spectra for **6-Pr**, **7-Sm** and **8-Pr**.

Crystal structure of compounds **6-Ln**, **7-Sm** and **8-Ln**

Polyanions **6-Ln**, **7-Sm** and **8-Ln** all exhibit $[\text{Ln}_2\text{GeW}_{10}\text{O}_{38}]^{6-}$ subunits ($\{\text{Ln}_2\text{GeW}_{10}\}$) as a common structural feature. These subunits consist in a dilacunary Keggin-type tungstogermanate fragment stabilized by coordination of Ln atoms onto the vacant sites. Three different anti-Lipscomb-type⁶⁵ isomers of the dilacunary Keggin fragment are present in these compounds, namely the enantiomeric $\beta(1,5)$ and $\beta(1,8)$ pair and the $\gamma(3,4)$ form. Figure 3.12 displays a representation of all $\{\text{Ln}_2\text{GeW}_{10}\}$ subunits included in this work which have been named following IUPAC rules as explained in Appendix 3.⁶⁶ The vacant sites of the enantiomeric $\beta(1,5)$ and $\beta(1,8)$ isomers are located at the corner-sharing $\{\text{W}_3\text{O}_{15}\}$ unit (position 1) and the central belt (positions 5 or 8). In the case of the $\gamma(3,4)$ forms, each lacunae reside in one of the 60° -rotated $\{\text{W}_3\text{O}_{13}\}$ trimers. The diversity of $\{\text{GeW}_{10}\}$ isomers present in the structures of **6-Ln** (Ln = Pr, Nd), **7-Sm** and **8-Ln** (Ln = Ce to Nd) suggests that different species may be formed at a similar acidic pH (4.5-5.5), which might probably be exchangeable and highly reactive intermediates in the formation of the predominant $[\text{GeW}_{11}\text{O}_{39}]^{8-}$ anion. To date, only the $\gamma(1,2)$ - $[\text{XW}_{10}\text{O}_{36}]^{8-}$ dilacunary anion (X = Si⁶⁷, Ge⁶⁸, P⁶⁹) has been isolated in the solid state as independent POM precursor. However, it has been thoroughly demonstrated that the incorporation of lanthanide or transition metal atoms can stabilize several other types of dilacunary units.^{17b, 18d, 45a, 71} In spite of the fact that a variety of α or β forms can be found in literature,⁷⁰ only one of the β forms displays vacancies at the belt and the corner-sharing triad, namely the $\beta(1,9)$ isomer.⁷¹ On the other hand, a single γ -dilacunary species is known to date, the above mentioned C_{2v} -symmetric $\gamma(1,2)$ with vacancies at the two edge-sharing octahedra of the rotated trimers. Therefore, all the three $\{\text{GeW}_{10}\}$ fragments found in this family of compounds represent interesting building blocks in POM chemistry and were unprecedented until the publication of **8-Ce** in 2010.

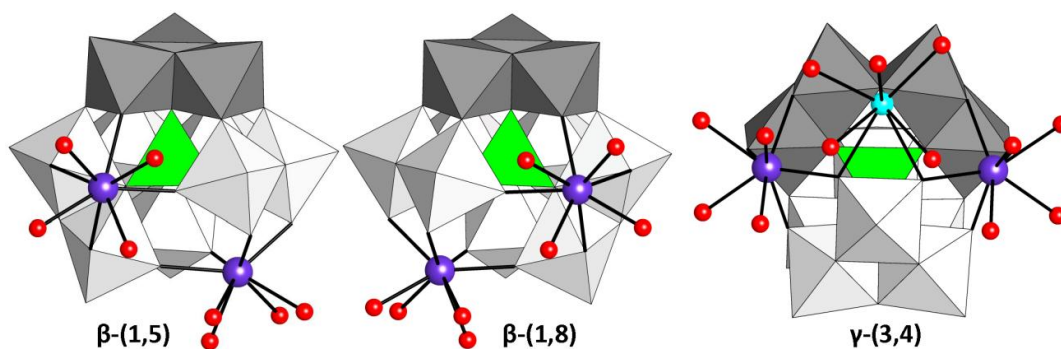


Figure 3.12. Representation of the β -(1,5), β -(1,8) and γ -(3,4)- $\{\text{Ln}_2\text{GeW}_{10}\}$ building blocks found in the compounds included in this section. Rotated $\{\text{W}_3\text{O}_{13}\}$ trimers depicted in dark grey and potassium atom as light blue ball.

Polyanions **6-Ln** (Ln = Pr, Nd) are constructed by the Na^+ -directed assembly of six lanthanide-stabilized $\{\text{Ln}_2\text{GeW}_{10}\}$ dilacunary Keggin subunits formed *in situ*. The crown-shaped centrosymmetric assembly is formed by three β (1,5) and three β (1,8) subunits alternately arranged, in a similar way to that observed for the hexameric core of the previously reported **8-Ce** species.⁴⁶ Neighboring subunits are linked by coordination of Ln^{3+} ions in position 1 (located at the corner-sharing triad) to two *cis*-related O atoms from the belt WO_6 octahedron adjacent to both vacancies, in such a way that it results in a six membered Ln_6O_6 ring of LnO_8 polyhedra connected by $\text{Ln}-\text{O}_b-\text{Ln}$ bridges and showing a chair-like conformation. Each of these internal lanthanide centers displays two water molecules, one of which is directed to the inner part of the ring to create a central pocket where a Na^+ ion in a distorted octahedral geometry is hosted (Figure 3.13).

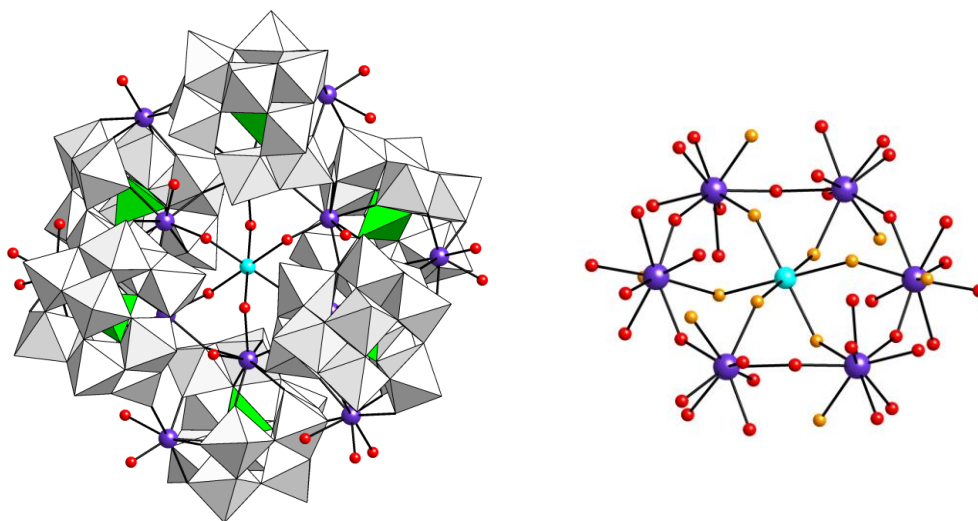


Figure 3.13. Mixed polyhedral / ball & stick representations of the molecular **6-Ln** (Ln = Pr, Nd) POM (left) and the internal $\{\text{Na}\langle\text{Ln}_6\text{O}_{30}(\text{H}_2\text{O})_{12}\rangle$ ring (right). Sodium atoms depicted as light blue balls and water molecules as orange balls.

Lanthanide centers in the belt 5/8 positions display additional $\text{Ln}-\text{O}_t-\text{W}$ bridges with the $\{\text{LnW}_2\}$ fragments of the neighboring $\{\beta\text{-Ln}_2\text{GeW}_{10}\}$ subunits, reinforcing the cyclic arrangement. Furthermore, these lanthanides located at the external part of the cluster link contiguous hexameric POMs, resulting in a two dimensional arrangement in the solid state (Figure 3.14). The connectivity along the [001] direction is established through the coordination of the O22B terminal oxygen atom from the 60° rotated trimer to the Ln25 center, whereas the linkage in the [010] direction is formed between the O13B atom and the Ln18 center. This linkage is reinforced by coordination of the nickel

atom Ni1 to the terminal O3T and O20T atoms from adjacent hexameric POMs. The resulting layers are parallel to the (011) plane and stack in such a way that they interact via interlayer hydrogen-bonding involving coordination water molecules associated to the Ln8 center ($\text{O3F}\cdots\text{O78} = 2.662(3)$ Å and $\text{O2F}\cdots\text{O78} = 2.835(5)$ Å).

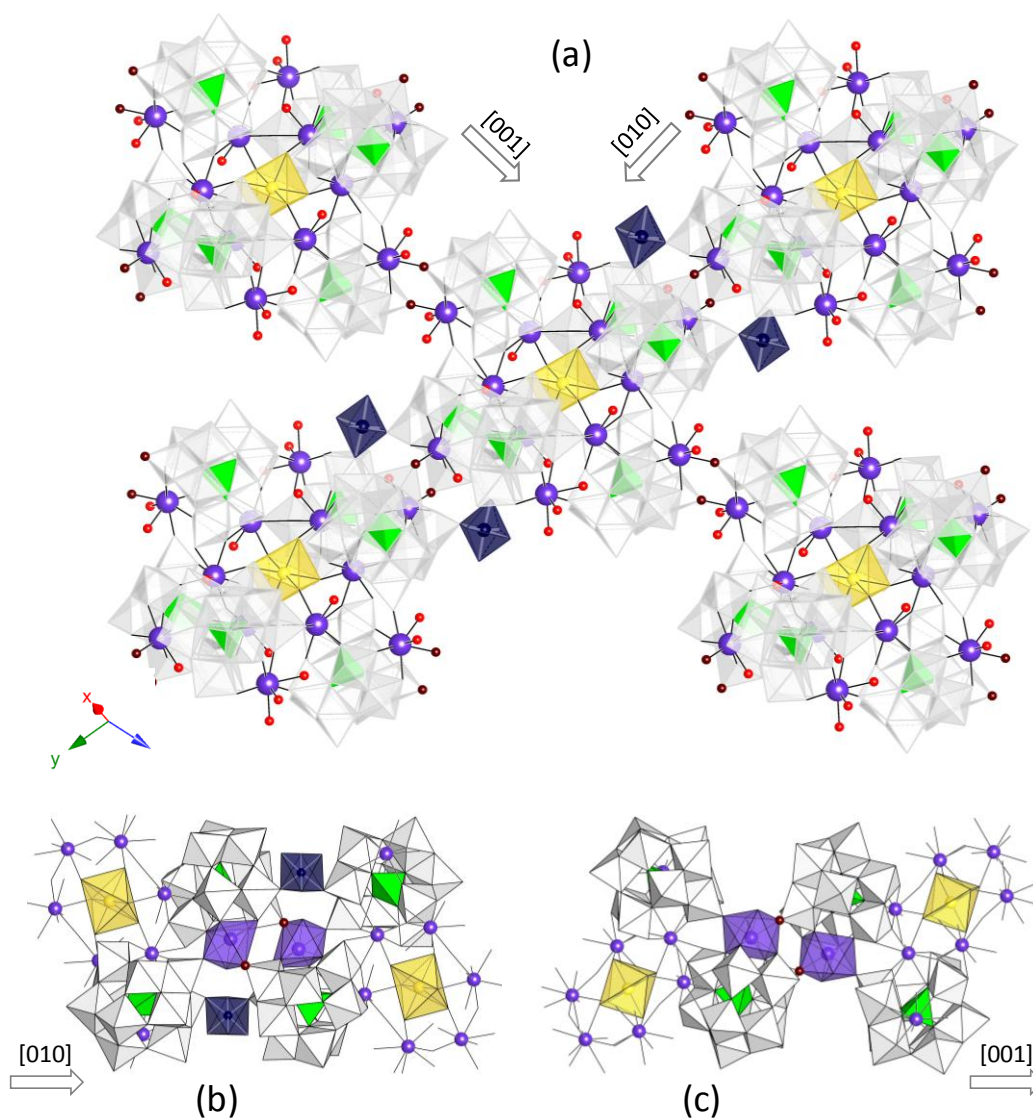


Figure 3.14. (a) Two-dimensional arrangement of hexameric assemblies for **6-Ln** (bridging O atoms depicted in brown). (b) and (c) Details of the connectivity between $\{\text{Na}\langle\text{Ln}_2\text{GeW}_{10}\rangle_6\}$ units along the [010] and [001] direction (bridging lanthanide ions represented as translucent polyhedra and Keggin subunits not involved in the linkage omitted for clarity).

Polyanion **7-Sm** is strongly related to **6-Ln**, but the former shows one K^+ ion acting as template in the central cavity instead of Na^+ . Considering the smaller ionic radius of Sm^{III} compared to those of Pr^{III} and Nd^{III} a smaller central pocket in the Sm_6O_6 ring could be *a priori* expected; however, the flexibility of the hexameric assembly allows for the insertion of the larger K^+ compared to Na^+ , resulting in clusters with diameters of ca. 2.5 nm in both cases. Bond-Valence Sum (BVS) calculations do not indicate any clear protonation site in the structures, with the exception of the water molecules coordinated to lanthanide centers. The crystal packing is very much alike to that described for compounds **6-Ln**, but in this case, we have located $[\{\text{Ni}(\text{H}_2\text{O})_5\}_2]^{4+}$ dimers occupying the space

between the layers of hexameric POMs. These dimers establish an extensive network of hydrogen bonds with the POMS surfaces as illustrated in Figure 3.15.

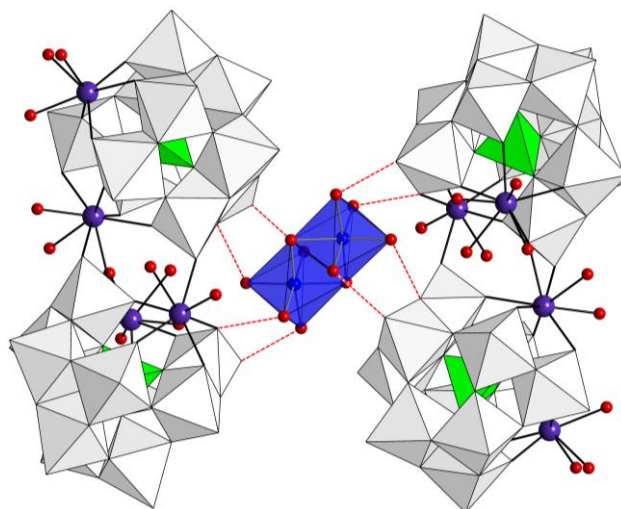


Figure 3.15. $\text{O}_{\text{Ni}}-\text{H}\cdots\text{O}_{\text{POM}}$ hydrogen bonding pattern of a $[\text{Ni}_2(\text{H}_2\text{O})_{10}]^{4+}$ dimer (dark blue octahedron) buried between two layers of hexameric POMs in the crystal packing of **7-Sm** (hydrogen-bonds represented as dotted red lines).

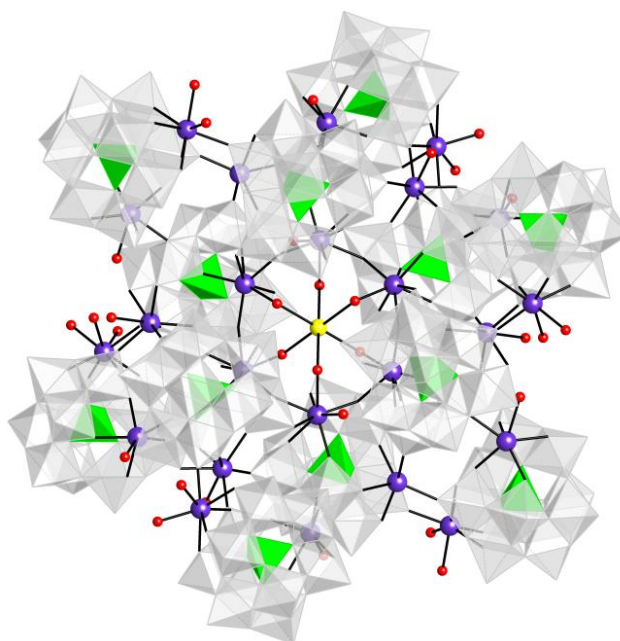


Figure 3.16. Mixed polyhedral/ball & stick representation of **8-Ln** (Ln = Pr, Nd).

Polyanions **8-Ln** (Ln = Pr, Nd) show the same molecular structure as that displayed for the previously reported **8-Ce** analogue. These polyanions display a hexameric crown-shaped $\text{Kc}\{(\beta\text{-Ln}_2\text{GeW}_{10})_6\}$ moiety, which is virtually identical to that described for **7-Sm** and acts as a central core to which six external $\{\gamma\text{-Ln}_2\text{GeW}_{10}\}$ are linked. Each γ subunit is connected to two adjacent β units through the coordination of the lanthanide atoms to terminal oxygen atoms of the $\{\text{LnW}_2\}$ fragments and the rotated $\{\text{W}_3\text{O}_{13}\}$ cap, together with Ln—O bonding between the $\gamma\text{-WO}_6$ octahedron adjacent to both vacant sites and belt $\beta\text{-Ln}$ centers. The whole assembly results in a dodecameric POM architecture with C_3 symmetry and about 4 nm diameter (Figure 3.16). The six-coordinated geometry of the $\{\text{K}(\text{H}_2\text{O})_6\}$ fragment is printed to the whole architecture, in such a way that it can be described

as an arrangement of $\{\gamma\text{-Ln}_2\text{GeW}_{10}\}$ subunits with the Ge atoms at the vertices of a trigonally compressed octahedron, which in turn encloses an analogous and even more compressed octahedron of $\{\beta\text{-Ln}_2\text{GeW}_{10}\}$ subunits containing the central $\{\text{K}(\text{H}_2\text{O})_6\}$ fragment (Figure 3.17). BVS calculations indicate diprotonation in the outer γ -subunits, and more specifically on the Ln-coordinated O atoms of the addenda metal positions 9 or 10 (O349, OX32) and on the bridging O atom from the edge-sharing W_2O_{10} unit not linked to the K^+ (OX12) (BVS values: 1.04-1.39) (Figure 3.18). Diprotonation in each γ -subunit of **8-Ln** polyanions is in full agreement with the number of cations determined by elemental analyses. Each dodecamer is linked to two neighbors via two pairs of $\gamma\text{-Ln}-\text{O}_t-\beta\text{-W}$ bridges involving the terminal oxygen atom O6T and this results in one-dimensional chains that run along the [010] direction. These chains are arranged in layers parallel to the (110) plane and the $[\text{Ni}(\text{H}_2\text{O})_6]^{2+}$ cations, located at the center of the unit cell (1/2, 1/2, 1/2), occupy interlamellar spaces, in such a way that they result closely embraced by two β and two γ subunits of $[\mathbf{8}]_\infty$ chains from contiguous layers through strong $\text{O}_{\text{Ni}}-\text{H}\cdots\text{O}_{\text{POM}}$ hydrogen bonding (Figure 3.19).

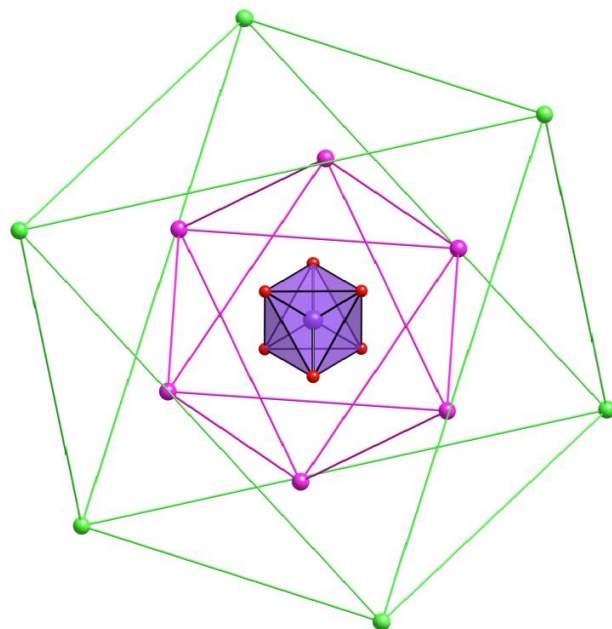


Figure 3.17. Representation of the polyhedra described by the Ge atoms in **8-Ln**. Color code: Ge atoms in $\{\gamma\text{-Ln}_2\text{GeW}_{10}\}$ subunits, green; Ge atoms in $\{\beta\text{-Ln}_2\text{GeW}_{10}\}$ subunits, pink; central $\{\text{K}(\text{H}_2\text{O})_6\}^+$ fragment, lilac.

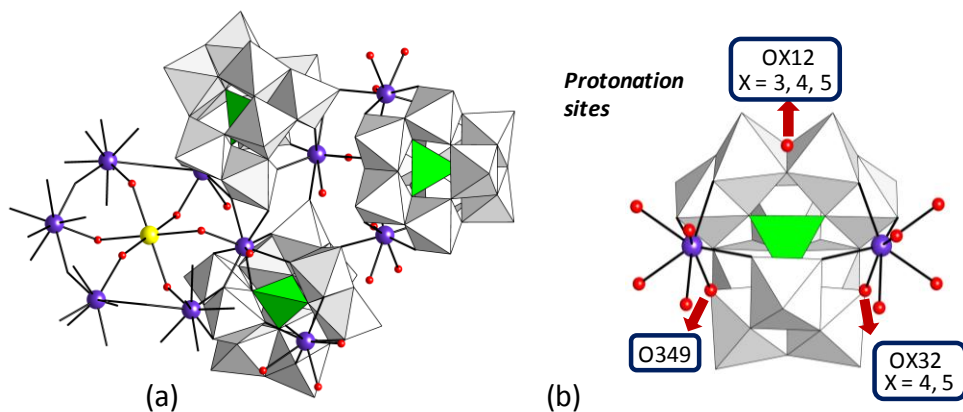


Figure 3.18. Polyhedral/ball & stick representation of: (a) $\text{KLn}_6\text{O}_{42}$ ring and the connectivity between two β - and one $\{\gamma\text{-Ln}_2\text{GeW}_{10}\}$ subunits; (b) protonation sites in $\{\gamma\text{-Ln}_2\text{GeW}_{10}\}$ subunits. The atom labeling corresponds to that based on IUPAC rules as explained in Appendix 3 and X indicates the subunit number.

All the lanthanide centers display out-of-pocket coordination modes toward the divacant $\{\text{GeW}_{10}\text{O}_{38}\}$ skeletons. In addition to the four O atoms delimiting each vacant site (O_L), the 4f ions in the β -subunits also coordinate to the corresponding $\{\beta\text{-GeW}_{10}\text{O}_{38}\}$ neighbors in the crown-shaped architecture (O_R). The three external coordination sites are occupied either by aqua ligands (O_w) or by O atoms from adjacent hexamers in the two-dimensional arrangement of **6-Ln** and **7-Sm** or from neighboring subunits (O_b) in the case of compound **8-Ln**. Besides, the water molecules of coordination can be divided into two groups: terminal aqua ligands and those bridging the lanthanide atoms of the Ln_6O_6 ring (position 1) with the central alkaline ion. For the 4f ions in the γ -subunits of compounds **8-Ln**, the coordination spheres are formed by the four O atoms delimiting the lacunae (O_L), one O atom from the hexameric core (O_R) and three terminal water molecules (O_w) with the exception of the Ln33 and Ln 34 centers for which one water molecule is replaced with an O atom from an adjacent dodecamer in the one-dimensional arrangement (O_b).

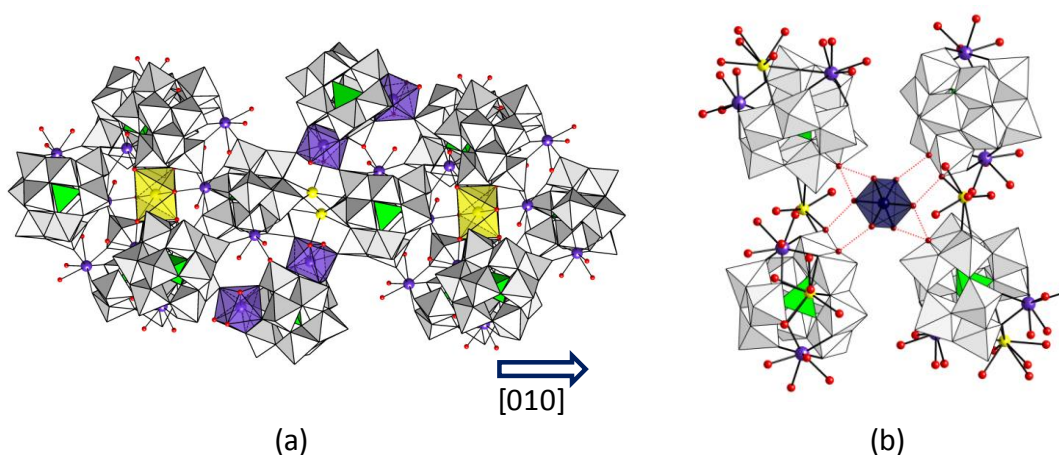


Figure 3.19. (a) One-dimensional $[\mathbf{8}]_{\infty}$ assembly in **8-Ln** (for clarity, only the central $\text{K} \subset \{(\beta\text{-Ln}_2\text{GeW}_{10})_6\}$ core and the $\gamma\text{-}\{\text{Ln}_2\text{GeW}_{10}\}$ subunits taking part in the connectivity between adjacent POMs are represented). Central K1 atom is depicted as a yellow octahedron and the lanthanide atoms of the connecting $\gamma\text{-}\{\text{Ln}_2\text{GeW}_{10}\}$ subunits as purple polyhedra. (b) $\text{O}_{\text{Ni}}\text{—H}\cdots\text{O}_{\text{POM}}$ hydrogen bonding pattern of a $[\text{Ni}(\text{H}_2\text{O})_6]^{2+}$ cation (dark blue octahedron) buried between two $[\mathbf{8}]_{\infty}$ chains (hydrogen-bonds represented as dotted red lines).

For compounds **6-Ln** and **7-Sm**, the Ln–O bond lengths follow the order $\text{Ln}\text{—}\text{O}_L < \text{Ln}\text{—}\text{O}_b < \text{Ln}\text{—}\text{O}_R < \text{Ln}\text{—}\text{O}_w$, that is, the bridging Ln– O_b bonds between adjacent hexamers in the layers are shorter than those established between neighboring subunits in the crown-shaped assembly (Ln– O_R). This suggests strong association in the two-dimensional network found in the solid state, which might well explain their insolubility in water, a fact that did not allow us to perform solution studies on these compounds. As expected from the lanthanide contraction effect, the Ln–O bond lengths decrease when going from the Pr to the Sm derivatives, resulting in an average shortening of about 0.05 Å (Table 3.5). Nevertheless, mean Ln \cdots Ln distances in the inner Ln_6O_6 rings increase from 4.665 Å for **6-Pr** to the 4.785 Å for **7-Sm** as the larger K^+ counterion is hosted in the central cavity. In the case of the lanthanide atoms in the hexameric cores of compounds **8-Ln**, the presence of the larger K^+ ion in their central cavity results in a subtle increase of the Ln– O_R bond lengths established between β -subunits compared to those in **6-Ln**. The $\gamma\text{-Ln}\text{—}\text{O}$ bond lengths in **8-Ln** are comparable to those of lanthanides in β -subunits (Table 3.6).

Lanthanide atoms present in **6-Ln** (Ln = Pr, Nd), **7-Sm** and **8-Ln** (Ln = Pr, Nd) display highly distorted coordination geometries that have been analyzed through Continuous Shape Measures

(CShM).⁷² In the case of **6-Ln**, all the 4f centers are eight-coordinated except those taking part in the connection between adjacent POMs along the [010] direction (Ln18). Due to the smaller size of Sm, the two 4f-metals linking contiguous clusters in the 2D-arrangement of **7-Sm** (Sm18 and Sm25) are seven-coordinated. The geometry of these seven coordinated centers can be viewed as slightly distorted capped trigonal prisms (CShM values < 1.2).

Table 3.5. Ranges and mean lanthanide–oxygen bond lengths (Å) for eight-coordinated centers in compounds **6-Ln** (Ln = Pr, Nd), **7-Sm** and **8-Ln** (Ln = Pr, Nd).^[a]

	Ln–O _L	Ln–O _b	Ln–O _R	Ln–O _w
6-Pr	2.287(12)–2.464(12)	2.449(14)–2.455(13)	2.477(12)–2.574(10)	2.525(16)–2.689(11)
	2.408	2.452	2.525	2.589
6-Nd	2.285(11)–2.435(10)	2.412(11)–2.460(12)	2.465(11)–2.576(10)	2.492(13)–2.646(9)
	2.387	2.436	2.515	2.563
7-Sm	2.233(13)–2.412(13)	2.373(13)–2.375(13)	2.401(12)–2.654(12)	2.504(13)–2.590(12)
	2.352	2.374	2.501	2.534
8-Pr	2.347(17)–2.517(18)	2.43(2)–2.45(2)	2.460(17)–2.632(15)	2.56(2)–2.677(19)
	2.423	2.439	2.536	2.618
8-Nd	2.345(14)–2.461(15)	2.382(16)–2.421(15)	2.450(12)–2.621(13)	2.536(16)–2.653(15)
	2.403	2.397	2.520	2.579

[a] *Abbreviations.* O_L: O atoms delimiting the vacant site onto which the 4f ion is coordinated; O_R: bridging O_{POM} atom between Keggin subunits in the [C₂{Ln₂(H₂O)₄(β-GeW₁₀O₃₈)₆}] ring; O_b: bridging O_{POM} atom between adjacent POMs in the two-dimensional arrangement of **6-Ln** and **7-Sm**, and between adjacent β- and γ-subunits for **8-Ln**; O_w: O atom from terminal aqua ligands.

Table 3.6. Ranges and mean lanthanide–oxygen bond lengths (Å) for eight-coordinated centers of γ-subunits in compounds **8-Ln** (Ln = Pr, Nd).^[a]

	Ln–O _L	Ln–O _b	Ln–O _w
8-Pr	2.359(18)–2.49(2)	2.39(2)–2.502(17)	2.45(3)–2.66(2)
	2.422	2.456	2.565
8-Nd	2.331(15)–2.49(2)	2.419(14)–2.482(15)	2.422(18)–2.65(2)
	2.405	2.451	2.557

[a] *Abbreviations.* O_L: O atoms delimiting the vacant site onto which the 4f ion is coordinated; O_b: bridging O_{POM} atom between adjacent γ- and β-subunits; O_w: O atom from terminal aqua ligands.

The most representative CShM values (lower than 10) obtained for the eight-coordinated lanthanide atoms are compiled in Table 3.7. In the case of **8-Ln**, the lanthanide atoms located at the γ-subunits and the belt positions of β-subunits (X5/X8) exhibit CShM values in the 0.26–1.06 range when compared with the ideal square antiprism (SAPR) as the reference shape. These relatively low CShM values, together with the significantly higher numbers (above 2) obtained upon comparison with any other reference polyhedron, indicate that the coordination geometry of these 4f ions in best described as square antiprismatic, though slightly distorted from ideality. On the contrary, low CShM values (< 1) relative to the spherical bicaugmented trigonal prism (s-BTP) are observed for the lanthanide atoms in the bottom-triad position (LnX1) and for a few exceptions regarding γ-subunits. However, close values are also observed for SAPR and the Johnson- bicaugmented trigonal prism (J-BTP) shapes, and therefore, the geometry in these Ln centers would represent intermediate stages

between those three ideal states. The SAPR vs. s-BTP shape map (Figure 3.20) shows that some of these 4f ions scatter from the ideal SAPR geometry toward the s-BTP one following the trend marked by the minimal distortion pathway between the two reference polyhedra with path deviation values (P) in the 0.27–0.39 range (around the upper limit of 0.3 selected by Casanova et al.). In contrast, most of the lanthanides in X1 position deviate significantly from this path ($p > 0.48$). This confirms that the best description for the geometry of the first group of lanthanides is bicapped trigonal prismatic distorted toward square antiprismatic, whereas the remaining 4f-metal centers (LnX1) can be best described as distorted spherical biaugmented trigonal prisms with more than one type of distortion operating simultaneously. It is worth noting that in these cases, the CShM values for the SAPR and J-BTP shapes (>1.53) are relatively higher than those obtained for s-BTP (0.77–0.98), although non-negligible.

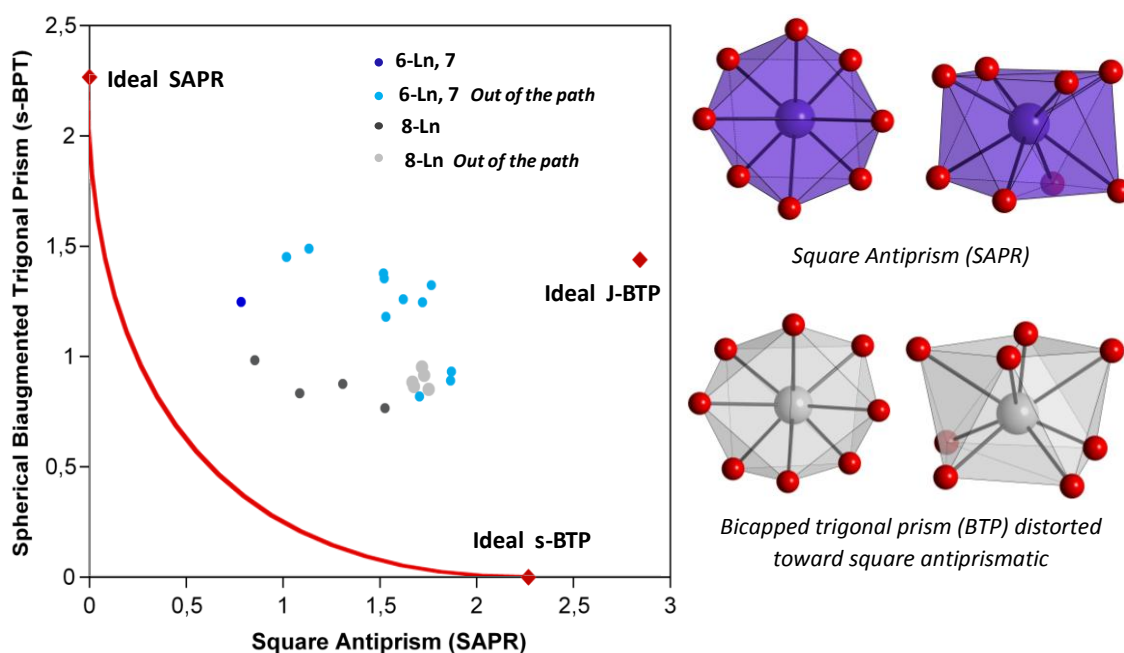


Figure 3.20. Left: Spherical biaugmented trigonal prism (s-BTP) vs. square antiprism (SAPR) shape map for the eight-coordinated 4f ions in compounds **6-Ln**, **7-Sm** and **8-Ln** (solid line: minimal distortion pathway between the reference shapes). Right: Top and side view of the less distorted square-antiprismatic coordination polyhedron and the bicapped trigonal prismatic geometry distorted toward square antiprismatic.

For compounds **6-Ln** and **7-Ln**, CShM values significantly lower than 2 are obtained upon comparison to the SAPR and s-BTP ideal shapes. In the case of the 4f-metals in belt positions (LnX5/LnX8), the lowest values are obtained for the former shape (SAPR: 0.61–1.13), whereas shape measurements of the lanthanide centers in the bottom triad (LnX1) fit better with the latter model (s-BTP: 0.82–1.38). However, only Pr8 and Sm8 can be undoubtedly described as slightly distorted square antiprismatic because the difference between both SAPR and BTP values is around 1. For the remaining lanthanide atoms, the SAPR and s-BTP values are comparable. The representation of the SAPR vs. BTP shape map (Figure 3.20), indicates that only the belt Nd8 ion can be considered close to the trend marked by the minimal distortion pathway between the two reference polyhedra ($p = 0.33$). The rest of belt 4f-metals and those located at bottom triads lie out from this path and can be respectively best described as distorted square antiprisms or spherical biaugmented trigonal prisms with more than one distortion operating simultaneously.

Table 3.7. Continuous Shape Measures for the eight-coordinated spheres of the lanthanide atoms in compounds **6-Ln** (Ln = Pr, Nd), **7-Sm** and **8-Ln** (Ln = Pr, Nd)^[a].

		SD	s-BTP	J-BTP	DD	SAPR
6-Pr	Pr1	5.108	1.324	2.377	2.629	1.765
	Pr8	4.626	1.309	2.115	2.360	0.741
	Pr11	5.415	1.378	2.490	2.421	1.518
	Pr21	5.354	1.261	2.382	2.521	1.620
	Pr25	5.098	1.490	2.584	2.138	1.133
6-Nd	Nd1	5.028	1.247	2.241	2.551	1.719
	Nd8	4.645	1.249	2.056	2.281	0.783
	Nd11	5.290	1.355	2.347	2.446	1.522
	Nd21	5.152	1.181	2.204	2.384	1.531
	Nd25	4.980	1.452	2.497	2.066	1.017
7-Sm	Sm1	4.386	0.932	1.617	2.593	1.869
	Sm8	5.035	1.517	2.363	2.599	0.614
	Sm11	4.509	0.892	1.766	2.634	1.865
	Sm21	4.410	0.820	1.526	2.784	1.704
8-Pr	Pr1	4.460	0.915	1.679	2.503	1.728
	Pr8	4.365	1.878	2.237	2.098	0.807
	Pr11	4.702	0.954	1.783	2.560	1.717
	Pr15	4.176	1.893	2.124	2.285	0.857
	Pr21	4.491	0.767	1.559	2.398	1.526
	Pr25	4.287	1.872	2.229	2.026	0.952
	Pr33	3.891	0.877	1.247	1.441	1.307
	Pr34	5.313	2.011	2.746	2.462	0.405
	Pr43	5.121	2.009	2.795	1.939	0.981
	Pr44	4.932	1.518	2.097	2.452	0.255
8-Nd	Nd1	4.294	1.484	1.991	1.745	0.564
	Nd1	4.622	0.865	1.657	2.430	1.676
	Nd5	4.764	2.103	2.510	2.184	0.782
	Nd11	4.620	0.852	1.663	2.511	1.751
	Nd18	4.814	2.244	2.648	2.517	0.590
	Nd21	4.452	0.884	1.667	2.561	1.668
	Nd28	4.110	2.075	2.452	2.191	1.060
	Nd33	5.256	2.112	2.750	2.465	0.489
	Nd34	3.807	0.835	1.147	1.792	1.085
	Nd43	4.097	0.984	1.512	1.553	0.854
Nd44	4.866	1.931	2.611	1.748	0.800	
Nd53	4.337	1.219	1.862	1.789	0.429	

[a] *Abbreviations.* **SD**: snub disphenoid (D_{2d}); **s-BTP**: Spherical biaugmented trigonal prism (C_{2v}); **J-BTP**: Johnson biaugmented trigonal prism (C_{2v}); **DD**: triangular dodecahedron (D_{2d}); **SAPR**: square antiprism (D_{4d}). For a graphical representation of these polyhedra, see Figure A2.17 in Appendix 2. Values highlighted in grey correspond to the best geometry.

Photoluminescent properties of **7-Sm**

According to Yamase's pioneering work,⁷³ the luminescence of weak-emitting lanthanides can be sensitized by POMs acting as antenna ligands via intramolecular energy transfer from O→W ligand-to-metal charge transfer bands (LMCT) upon photoexcitation. This can result in sharp emission bands in the visible region and relatively long lifetimes for lanthanide-containing POMs with Ln^{III} = Sm, Eu, Tb and Dy, although low quantum yields are usually obtained for Tb-, Sm- and Dy-derivatives due to radiationless deactivation *via* Tb^{IV}-W^V charge transfer states for the former and to cross-relaxation for the latter species.

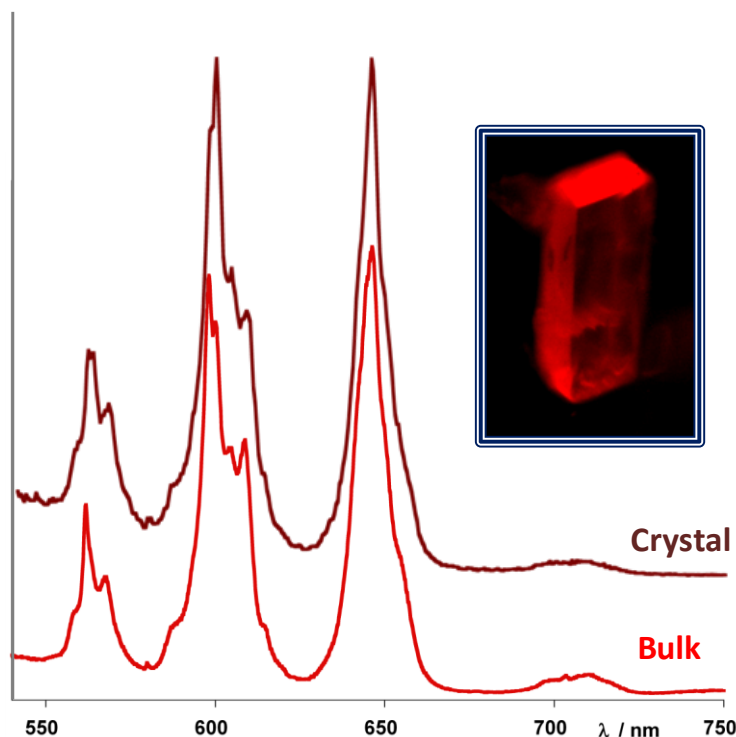


Figure 3.21. Room-temperature photoluminescence emission spectra ($\lambda_{\text{exc}} = 325 \text{ nm}$) for a bulk sample and for a single-crystal of **7-Sm**. Inset: Photograph of an orange-reddish emitting crystal.

Room-temperature emission spectra for a bulk solid sample of **7-Sm** (Figure 3.21) displays the characteristic profile of a Sm^{III} center. Compound **7-Sm** emits orange-reddish luminescence and its spectrum shows four peaks with maxima at c.a. 562, 598, 646, 710 nm that correspond to well-known transitions from the ⁴G_{5/2} excited state to the ⁶H_J manifold, where J = 11/2, 9/2, 7/2, and 5/2, respectively.⁷⁴ The fact that most of the peaks are split in the spectrum indicates the low symmetry and lack of inversion center of the emitting Sm^{III} centers, in good agreement with the structural data.⁷⁵ As shown in Figure 3.21, the emission spectra recorded for a crystal is virtually identical to that of the bulk solid sample.

As observed for Eu^{III}-containing POMs,⁷³ quenching of the emission can occur by thermal deactivation of the LMCT states via hopping of d¹ electrons to the lanthanide site as a result of $f\pi$ - $p\pi$ - $d\pi$ orbital mixing. This mixing is operative when Ln-O-W angles are around 150°, i.e. when LnO_x polyhedra share corners with WO₆ octahedra. On the contrary, orbital mixing and consequent electron delocalization is not favored when edge-sharing takes place; hence 4f luminescence is less efficiently quenched when Ln-O-W angles are about 100°. In our case, two types of metal centers

can be clearly distinguished; external Sm ions and internal centers belonging to the Ln_6O_6 rings. Each metal center located in outer positions of the crown-shaped anion ($\text{SmX5}/\text{SmX8}$) is sharing corners with the $\{\text{W}_2\text{O}_{10}\}$ unit ($\text{Sm}-\text{O}-\text{W} = 120-125^\circ$) and three adjacent $\{\text{W}_3\text{O}_{13}\}$ trimers ($\text{Sm}-\text{O}-\text{W} = 149-169^\circ$). The coordination spheres are completed with two or three aqua ligands. In the former case (2 aqua ligands), the eighth coordination position is occupied by a terminal O atom from neighboring crown-shaped anions in the 2D arrangement. Based on the structural data and the role of water molecules responsible for non-radiative deactivation due to coupling with high frequency OH oscillators, we can assume that the luminescence should be effectively quenched in those Sm centers. However, neighboring SmO_8 polyhedra at the internal Sm_6O_6 ring (SmX1) are linked to each other by sharing two *cis*-related O atoms from the belt WO_6 octahedron adjacent to both vacant sites ($\text{Sm}-\text{O}-\text{W} = 95-106^\circ$). The presence of two water molecules, in addition to the $\{\text{W}_2\text{O}_{10}\}$ fragment ($\text{Sm}-\text{O}-\text{W} = 117-124^\circ$) and two adjacent trimeric corner-sharing units ($\text{Sm}-\text{O}-\text{W} = 153-164^\circ$), seems to be insufficient to quench the Sm^{III} emitting centers, and therefore, we can infer that the Sm atoms in the Sm_6O_6 ring delimiting the central cavity of the POM are the only efficient emitting centers in **7-Sm** (Figure 3.22).

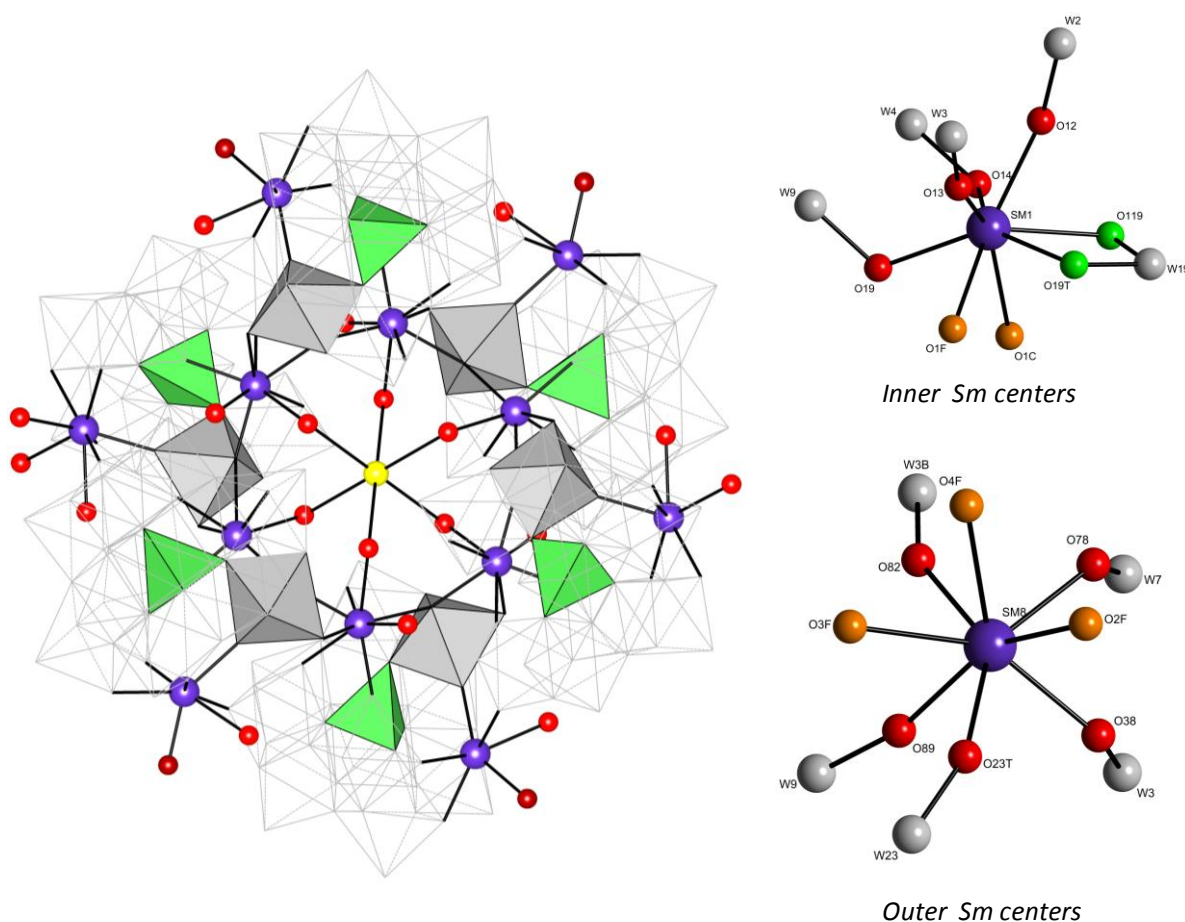


Figure 3.22 Left: Molecular structure of **7-Sm** highlighting the two types of Sm^{III} emitting centers: inner SmO_8 units sharing edges with $\{\text{WO}_6\}$ octahedra (represented as grey polyhedra) and outer Sm^{III} centers sharing corners with all the neighboring $\{\text{WO}_6\}$ octahedra. Right: Details of the coordination spheres of both types of Sm^{III} centers, together with the atom labeling scheme (O_{water} atoms depicted as orange balls and O atoms taking part in the edge sharing linkage as green balls).

Solution behavior. Laser Light Scattering studies on compounds **8-Ln**

Encouraged by their size, high charge and solubility in water, solution behavior of polyanions **8-Ln** ($\text{Ln} = \text{Pr}, \text{Nd}$) was studied in detail. Compounds **6-Ln** and **7-Sm** are not suitable for this type of study, because they are almost insoluble in water due to the two-dimensional network they show in the crystal structure. The great similarity for all the $\text{Ln}-\text{O}_{\text{POM}}$ bond lengths in **8-Ln** make difficult to infer from the structure which species could be present in solution after fragmentation of $[\mathbf{8}]_{\infty}$ chains. After considering the presence of paramagnetic Ni^{2+} and Ln^{3+} centers and the high number of independent tungsten atoms as major handicaps for performing ^{183}W -NMR spectroscopic studies, we decided to make use of Laser Light Scattering techniques (LLS). Preliminary Dynamic Light Scattering (DLS) experiments performed on **8-Ce** suggested that the dodecameric assembly most likely dissociates upon dissolution into $\{\gamma\text{-Ce}_2\text{GeW}_{10}\}$ monomers and $\{\text{K}(\beta\text{-Ce}_2\text{GeW}_{10})_6\}$ hexamers, which appear to undergo a blackberry-type aggregation. Further investigations were needed to confirm this hypothesis, and therefore, a complete study based on LLS techniques was carried out on the whole family of compounds **8-Ln** (**8-Ce**, **8-Pr** and **8-Nd**).

Dissolution of **8-Ln** in water involves chemical bond cleavage in the one-dimensional arrangement $[\mathbf{8}]_{\infty}$ observed in the solid state. Thus, two different large species could be expected to be present in solution: the dodecameric **8-Ln** (size 4 nm; 53 negative charges) and/or its hexameric central core $[\text{K}(\text{Ln}_2(\text{H}_2\text{O})_2(\beta\text{-GeW}_{10}\text{O}_{38}))_6]^{35-}$ (diameter ca. 2.5 nm) originating from the release of the external $\{\gamma\text{-Ln}_2\text{GeW}_{10}\text{O}_{36}\}$ subunits (Figure 3.23).

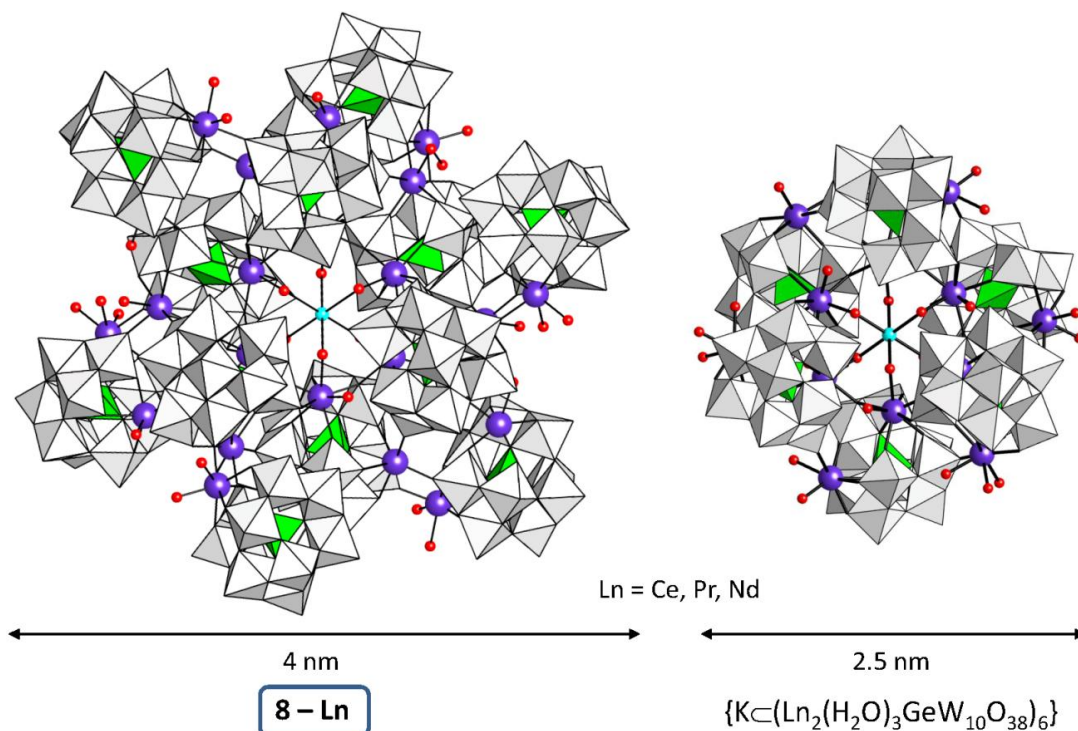


Figure 3.23. Large species suggested to be present in aqueous solution of **8-Ln**.

The pH measurements on aqueous **8-Ln** solutions obtained by dissolution of solid samples ($\text{pH} = 7.0 - 7.6$) indicate that the protons are not released when the clusters are dissolved in water. On the other hand, time resolved conductivity measurements on 1 mg mL^{-1} solutions of **8-Ln** show similar trends for the three samples: the conductivity undergoes drastic increase in the first 10 hours,

after which it slows down until it is nearly stabilized after approximately two days. This behavior suggests a dissociation process (Figure 3.24).

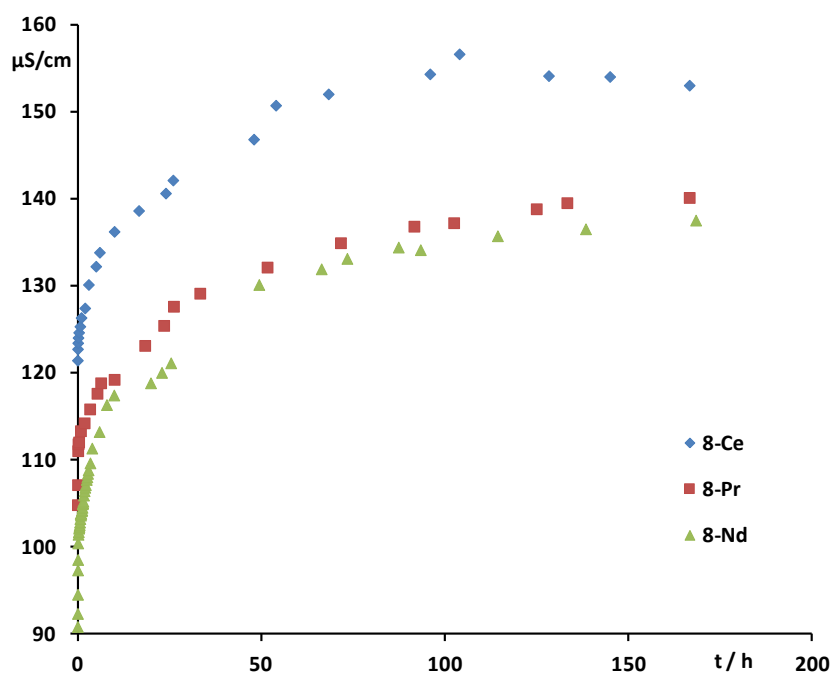


Figure 3.24. Time resolved conductivity measurements for **8-Ce**, **8-Pr** and **8-Nd** in 1 mg mL⁻¹ aqueous solutions.

The contribution of all the 40 Na, 14 K and 3 Ni counterions to the solution conductance was calculated using tabulated equivalent molar conductivities⁷⁶ to be 50.1 μS cm⁻¹, 25.7 μS cm⁻¹ and 7.5 μS cm⁻¹, respectively. The total conductance observed experimentally at the final stage (>130 μS cm⁻¹) is much higher than that calculated by considering the release of all counterions (83.3 μS cm⁻¹). This suggests further dissociation of the dodecameric cluster. A simple literature approach based on the Hückel equation was used to calculate the contribution of the potential larger species in the total conductivity.⁷⁷ The equivalent molar conductivity per charge (EMC) was estimated from the simple tungstate anion, which can be viewed as a building block of the larger clusters (Equation 1).

$$\frac{\text{EMC}_{\text{Large-Anion}}}{\text{EMC}_{\text{WO}_4^{2-}}} = \frac{R_{\text{WO}_4^{2-}}}{R_{\text{Large-Anion}}} \quad (\text{Eq. 1})$$

Using $R_{\text{WO}_4^{2-}} = 0.19$ nm and the radius of the smallest spheres that could contain the monomeric $\{\text{Ln}_2\text{GeW}_{10}\}$ and the hexameric $\{\text{K}(\text{Ln}_2\text{GeW}_{10})_6\}$ ring ($R_{\text{monomer}} = 0.50$ nm and $R_{\text{hexamer}} = 1.2$ nm), the contribution of these species should be around 23.1 μS cm⁻¹ (for six monomers) and 9.4 μS cm⁻¹, respectively. The experimental conductivity value (above 130 μS cm⁻¹ in all cases) is even higher than that calculated taking into account all counterions and the contribution of six released $\{\gamma\text{-Ln}_2\text{GeW}_{10}\}$ monomers and the hexameric $\{\text{K}(\text{Ln}_2\text{GeW}_{10})_6\}$ subunit (about 116 μS cm⁻¹), and this confirms the dissociation of the dodecamer in solution. The difference between the calculated and experimental values at the final stage might originate from the rough approach used for the estimation, or even from further decomposition processes involving the monomeric $\{\gamma\text{-Ln}_2\text{GeW}_{10}\}$ subunits. These observations are in good agreement with the DLS results reported previously for **8-Ce**.⁴⁶ As shown in Figure 3.23, the dissociation process is much faster for **8-Ce** than for **8-Pr** or **8-Nd**, suggesting that, the hexamer becomes the dominant species in solution almost immediately upon dissolution. Besides, dissociation of **8-Pr** appears to be faster than that of **8-Nd** because its

conductivity values in the first hours after dissolution are consistently higher than those of the Nd derivative, although they tend to balance to similar values in the stability range observed after ca. 2 days.

The presence of multiple species in water prevents the characterization by Small Angle X-Ray Scattering (SAXS) of the initial state where the clusters should exist as discrete macroions, so that Electrospray Ionization-Mass Spectrometry (ESI-MS) was chosen to confirm the presence of hexameric species in solution. Figure 3.25 shows the negative ESI mass spectrum of an aqueous solution of **8-Pr** recorded at low cone voltage (similar spectra were obtained for the Ce and Nd derivatives, which are given in Figure A2.14 and A2.15 in Appendix 2). The expected hexameric anion can be clearly identified as five groups of signals spanning from m/z 1700 to 3000.

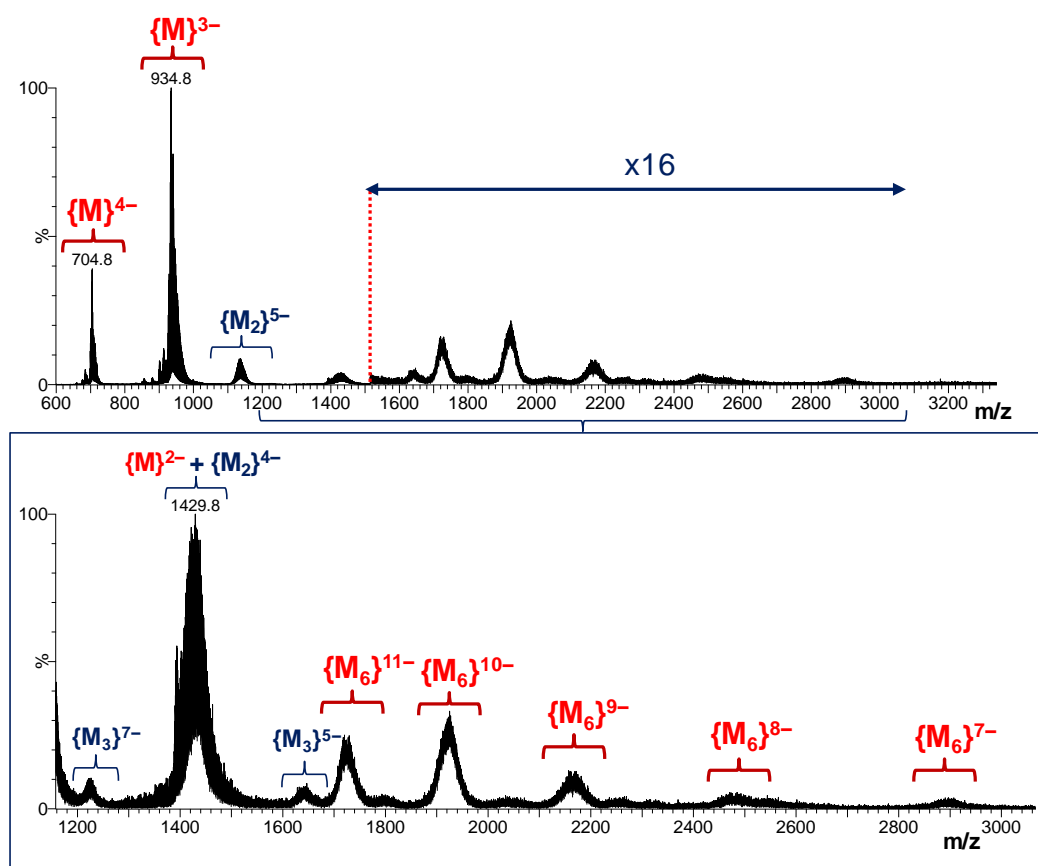


Figure 3.25. Top: Negative ESI mass spectrum of aqueous solution of **8-Pr** ($U_c = 15$ V). The intensity of the m/z 1500-3300 range is increased (x16) for a better visualization. Bottom: Expanded m/z 1150-3100 region (note that dimeric and monomeric species are overlapped in the m/z 1400-1500 range). $\{M\}^{(6-n)-} = [\text{Pr}_2\text{GeW}_{10}\text{O}_{38} + x\text{H}_2\text{O} + m\text{K}^+ + (n-m)\text{Na}^+]^{(6-n)-}$; $\{M_2\}^{(12-n)-} = [(\text{Pr}_2\text{GeW}_{10}\text{O}_{38})_2 + x\text{H}_2\text{O} + m\text{K}^+ + (n-m)\text{Na}^+]^{(12-n)-}$; $\{M_3\}^{(18-n)-} = [(\text{Pr}_2\text{GeW}_{10}\text{O}_{38})_3 + x\text{H}_2\text{O} + m\text{K}^+ + (n-m)\text{Na}^+]^{(18-n)-}$; $\{M_6\}^{(36-n)-} = [(\text{Pr}_2\text{GeW}_{10}\text{O}_{38})_6 + x\text{H}_2\text{O} + m\text{K}^+ + (n-m)\text{Na}^+]^{(36-n)-}$.

The isotopic pattern inspection is not possible in this case, because the molecular weight of the hexameric species is beyond the resolution of the instrument. Nevertheless, the m/z spacing between the groups of signals indicates that the detected anionic species display similar composition, which corresponds to the hexameric ($\{M_6\}$) entity with charge states of 11- (m/z 1727.3, $\{M_6\}^{11-}$), 10- (m/z 1926.4, $\{M_6\}^{10-}$), 9- (m/z 2165.7, $\{M_6\}^{9-}$), 8- (m/z 2474.0, $\{M_6\}^{8-}$) and 7- (m/z 2896.9, $\{M_6\}^{7-}$). The gas-phase detected species in the negative ESI mass spectrum display different extent of protonation and counter-ion content, as well as the presence of a variable number of loosely associated solvent molecules, because of the high charge state of the hexameric

anion (36⁻). This is commonly observed in negative ESI mass spectra of aqueous solutions of highly charged POMs.⁷⁸ However, the most abundant group of signals is centered at m/z 934.8 and formally corresponds to the series of monomeric anions ($\{M\}$) of general formula $[\text{Pr}_2\text{GeW}_{10}\text{O}_{38}+x\text{H}_2\text{O}+m\text{K}^++(6-m)\text{Na}^+]^{3-}$. Analogously, the group of signals at m/z 704.8 and 1429.8 can be readily assigned to the $[\text{Pr}_2\text{GeW}_{10}\text{O}_{38}+x\text{H}_2\text{O}+m\text{K}^++(7-m)\text{Na}^+]^{4-}$ and $[\text{Pr}_2\text{GeW}_{10}\text{O}_{38}+x\text{H}_2\text{O}+m\text{K}^++(9-m)\text{Na}^+]^{2-}$ series, respectively. The presence monomeric anions and the higher intensity of their signals in comparison to those of the hexamer could be explained by the fact that six $\{\gamma\text{-Ln}_2\text{GeW}_{10}\}$ subunits should be released from each central core in the dissociation process of the **8-Ln** dodecamer. In addition to the $\{M\}$ and $\{M_6\}$ forms, low intensity peaks corresponding to dimeric and trimeric species can also be found in the spectrum. The dimers ($\{M_2\}$) can be identified as two groups of signals centered at m/z 1181.2 and 1429.8 that correspond to the 5⁻ and 4⁻ charge states, respectively. The latter appears highly overlapped with the signals attributed to the $\{M\}^{2-}$ species. In the case of the trimers ($\{M_3\}$), these are observed as the $\{M_3\}^{7-}$ and $\{M_3\}^{5-}$ species at average m/z values of 1227.4 and 1623.8, respectively. This suggests that further aggregation of monomeric species takes place in solution. The ESI-MS spectra of the freshly prepared sample and that recorded after 3 days show a virtually identical pattern, confirming the stability of the hexamer in aqueous solution (Figure 3.26).

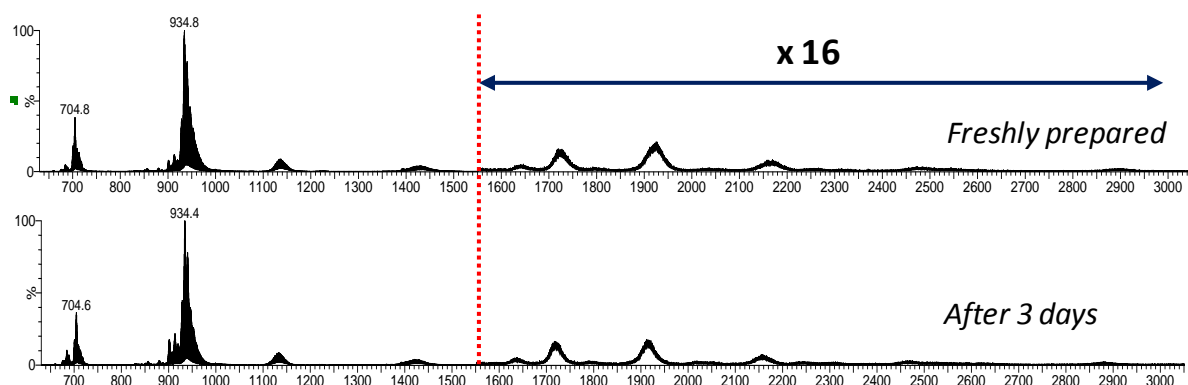


Figure 3.26. Negative ESI mass spectrum of **8-Pr** in aqueous solution for a freshly prepared sample (top) and for the same sample after 3 days (bottom). The intensity of the m/z 1550-3050 range is increased (x16) for a better visualization.

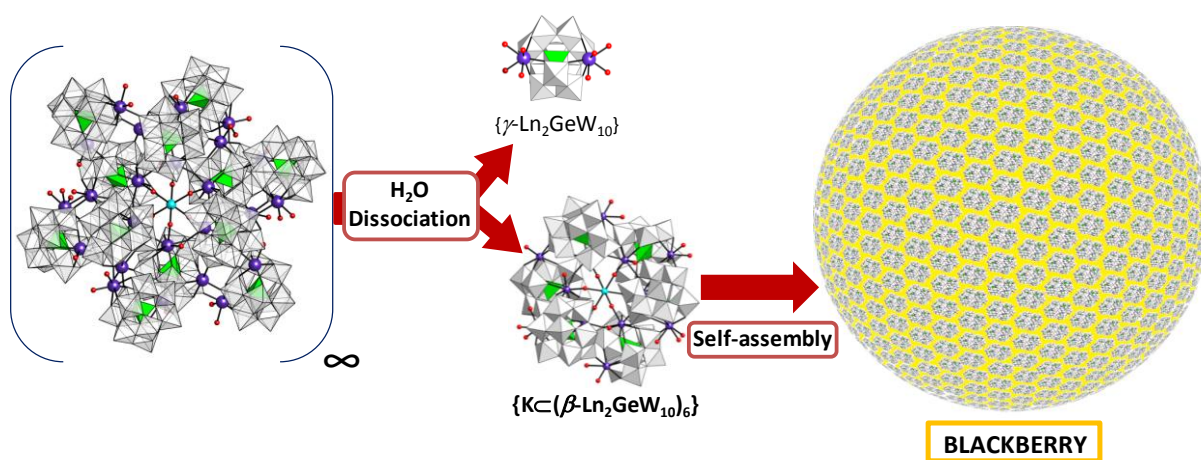


Figure 3.27. Schematic representation for the blackberry formation in aqueous solutions of **8-Ln**.

Compounds **8-Pr** and **8-Nd** self-assemble into spherical, hollow and single-walled vesicle-like blackberry-type structures in aqueous solutions with concentrations of 0.1 mg mL^{-1} (Figure 3.27), as confirmed by Dynamic and Static Light Scattering (DLS and SLS) studies and TEM experiments. The association process occurs slowly as monitored by using DLS and SLS. Time resolved scattering intensity plots for **8-Pr** and **8-Nd** are shown in Figure 3.27. After a significant lag period⁷⁹ of 4 (**8-Pr**) and 11 (**8-Nd**) days induced by the presence of extra electrolytes in solution originated from the dissociation process, the kinetics of the self-assembly follows the expected sigmoidal curve. This type of behavior has also been reported for other two-step association processes like vesicle or nanoparticle formation, where the slow formation of oligomeric nucleus reaches a critical value during the lag period, and it is followed by the addition of monomers or oligomers to the growing assemblies until they are completed.⁸⁰ The kinetics of the association processes in **8-Pr** and **8-Nd** are considerably different. Blackberries are obtained in a period of time of 10 days for **8-Pr**, whereas formation of this structure takes much longer for **8-Nd** (more than 30 days). CONTIN analysis from the DLS study of individual solutions reveals large aggregates showing no angular dependence and narrow distributions with hydrodynamic radius ($R_{h,0}$) of 73 nm for **8-Pr** and 74 nm for **8-Nd** (Figure 3.28). SLS studies by partial Zimm plots (Figure 3.29) shows average radii of gyration (R_g) of $72.7 \pm 0.7 \text{ nm}$ for **8-Pr** and $74.6 \pm 0.5 \text{ nm}$ for **8-Nd**. The $R_h/R_g \approx 1$ ratio indicates the hollow spherical nature of the assemblies for both compounds as confirmed by preliminary TEM images (Figure 3.30). More TEM micrographs, together with EDS studies will be provided in a near future.

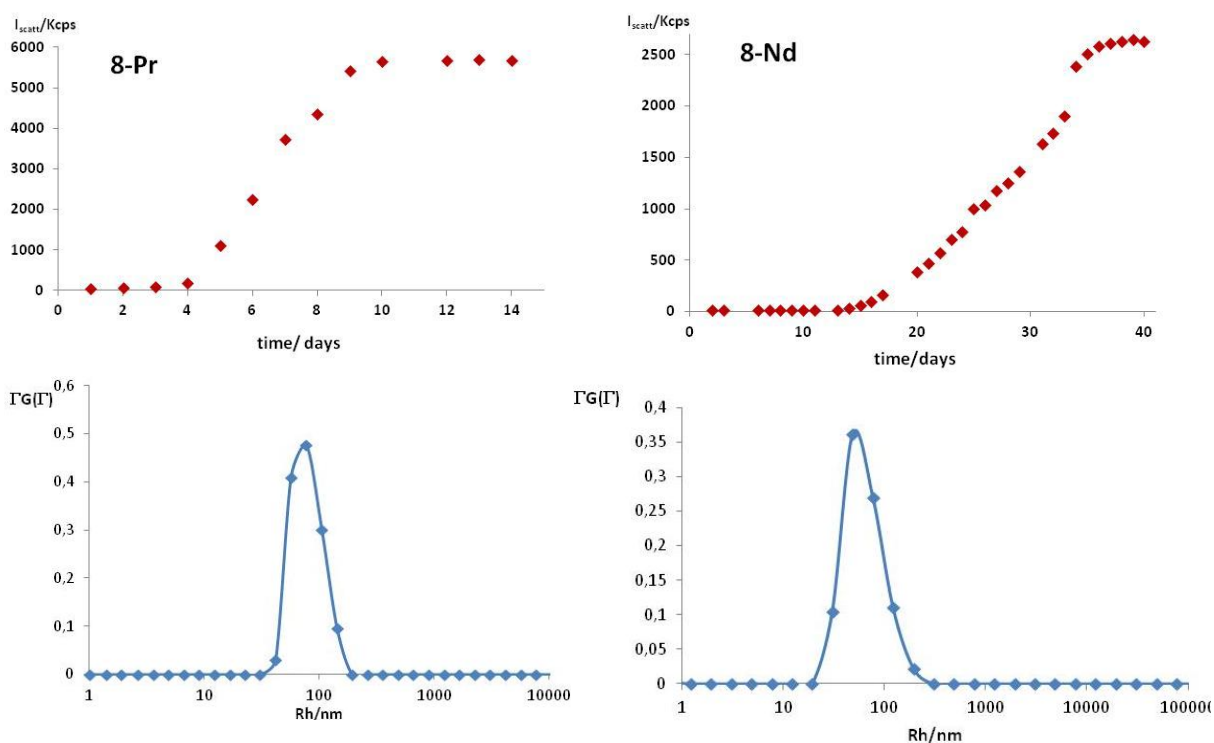


Figure 3.28. Time-resolved scattering intensity plots (top) and CONTIN analysis (bottom) from the DLS data for **8-Pr** and **8-Nd**.

The almost identical size of both **8-Pr** and **8-Nd** spherical assemblies makes self-recognition to be operative in our systems *a priori* difficult. Nevertheless, we believe that testing the self-recognition of these almost identical molecules (only the lanthanide atom is different) showing

similar intermolecular interactions (the size of both blackberries is almost the same) could be certainly interesting to check whether the assembly process can distinguish between both species on the basis of their rather different kinetics. This work is still in progress.

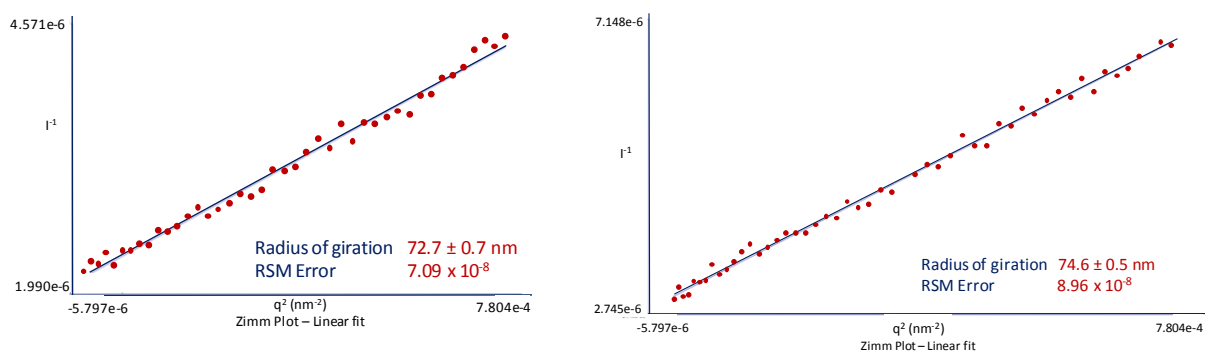


Figure 3.29. Partial Zimm plots from the SLS study in aqueous solution of **8-Pr** (left) and **8-Nd** (right).

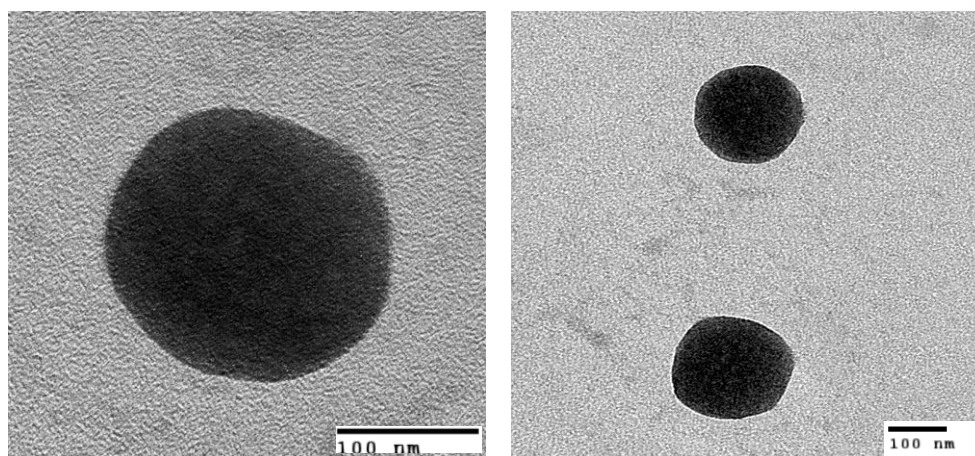


Figure 3.30. TEM images of the spherical and uniform blackberry-type aggregates for the aqueous solution of **8-Pr**.

In contrast to **8-Pr** and **8-Nd**, aqueous solution of **8-Ce** with concentration in the 0.1–1 mg mL⁻¹ range did not afford large blackberry-type assemblies. For much more concentrated solutions (5 or 10 mg mL⁻¹), precipitation was observed after monitoring the increasing light scattering intensity for about 8 days. These solutions were filtered and relatively stable scattering intensity values were recorded on the filtrate for the following 5 days. Considering that $R_{h,90^\circ}$ was nearly identical before and after precipitation, this process was attributed to the effect of the high concentration employed. As observed in Figure 3.31, a sigmoidal time resolved scattering intensity plot was initially obtained until precipitation, when a severe drop in the scattering intensity value was observed. A typical CONTIN analysis from the DLS study reveals large assemblies showing no angular dependence and average values for the hydrodynamic radius of $R_{h,0} = 85$ nm. SLS study by Berry plot indicates an average radius of gyration of $R_g = 81.9 \pm 0.4$ nm. As mentioned above for **8-Pr** and **8-Nd**, the $R_h/R_g \approx 1$ ratio constitutes a good indication of the hollow spherical nature of the assemblies. The low scattering intensity values obtained for such a high POM concentration suggest that only a small portion of the hexameric cluster is being self-assembled into blackberries, and this lead us to conclude that the Critical Micelle Concentration defined as the lowest concentration for finding large associations (CMC) is much higher in **8-Ce** than those observed for **8-Pr** and **8-Nd**.

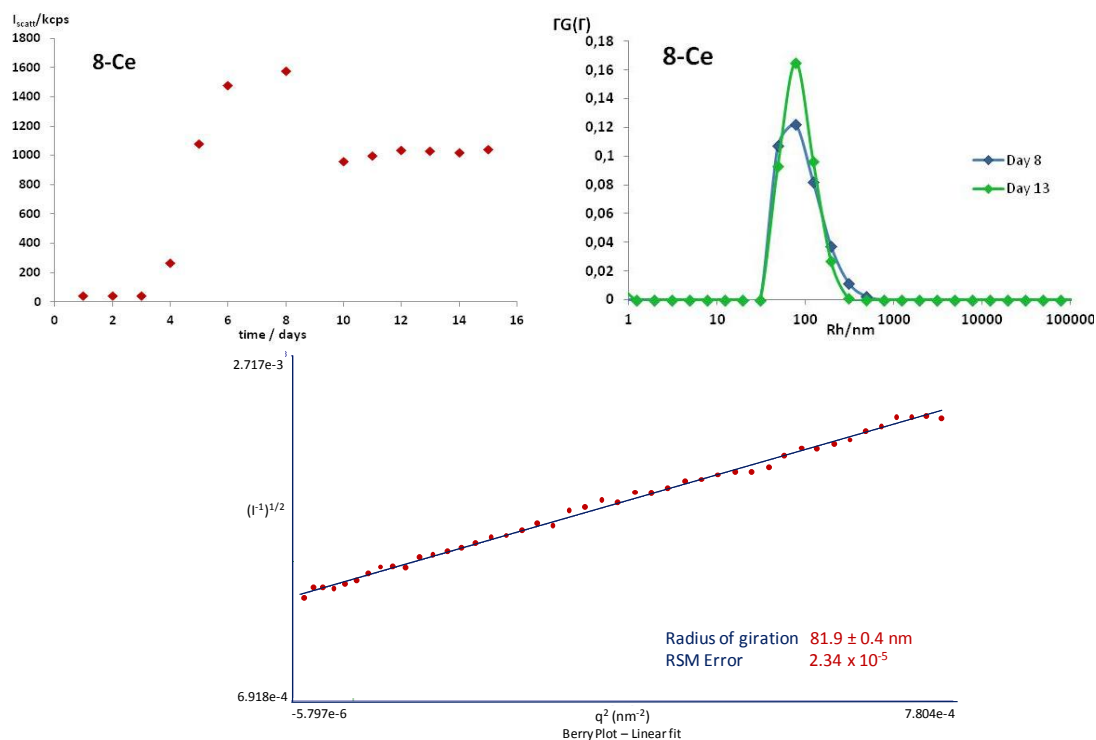


Figure 3.31. Top: Time resolved scattering intensity plot (left) and time resolved CONTIN analysis (right) for **8-Ce**. Bottom: SLS Berry plot for **8-Ce** in water.

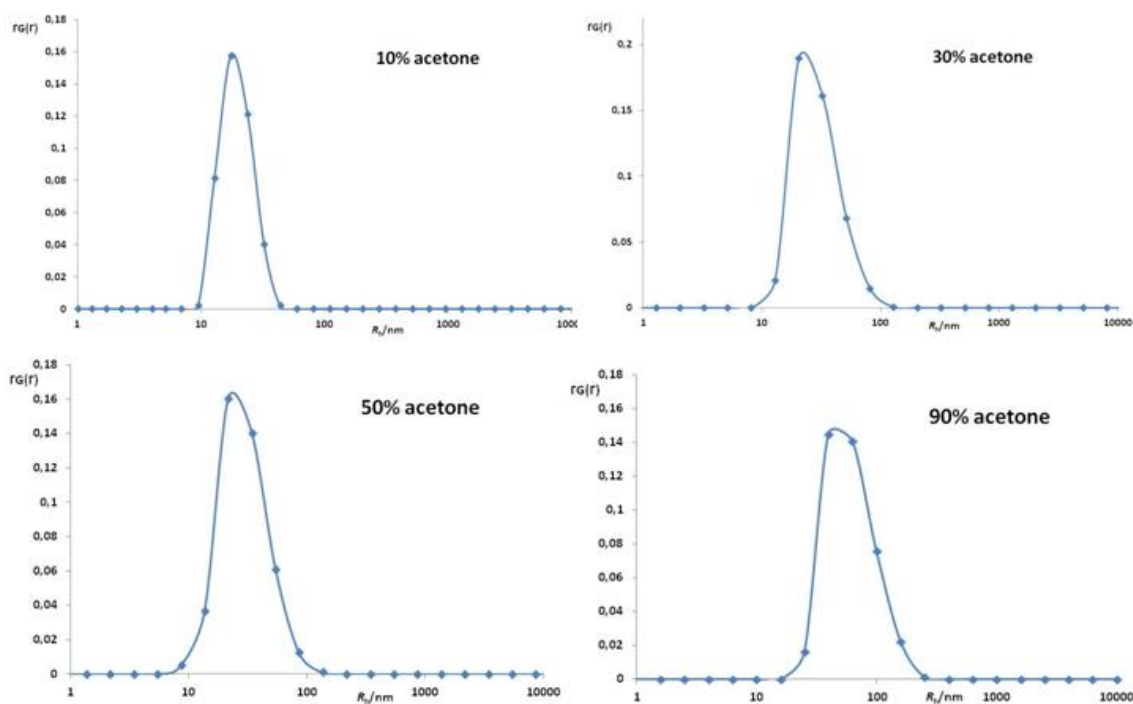


Figure 3.32. CONTIN analysis from the DLS data for **8-Nd** dissolved in water/acetone mixtures (0.1 mg mL^{-1} concentration). The acetone volume percentage is indicated for each plot.

It is well known that the blackberry size increases with decreasing solvent polarity because the charge density on each macroion drops, in such a way that the electrostatic repulsion becomes weaker and makes the attraction between them easier.⁵⁴ This trend is observed for solutions of **8-Nd** in water/acetone mixtures with different acetone concentration. The radii of the blackberry-type assemblies go from ca. 25 nm in a 10% vol. acetone solution to 50 nm in a 90% vol. acetone sample,

as shown in CONTIN plots (Figure 3.32). All the collected time resolved scattering intensity plots (at 90°) and partial Zimm plots resulting from SLS studies for **8-Nd** samples in water/acetone solutions are gathered in Figures A2.18-A2.22 in Appendix 2 (the solid sample is not soluble in pure acetone). As shown in Figure 3.33, the size of the blackberry-type assemblies displays a clear linear relationship with $1/\epsilon$ (ϵ being the dielectric constant of the solvent mixture) which is represented in the plot as the content of acetone.

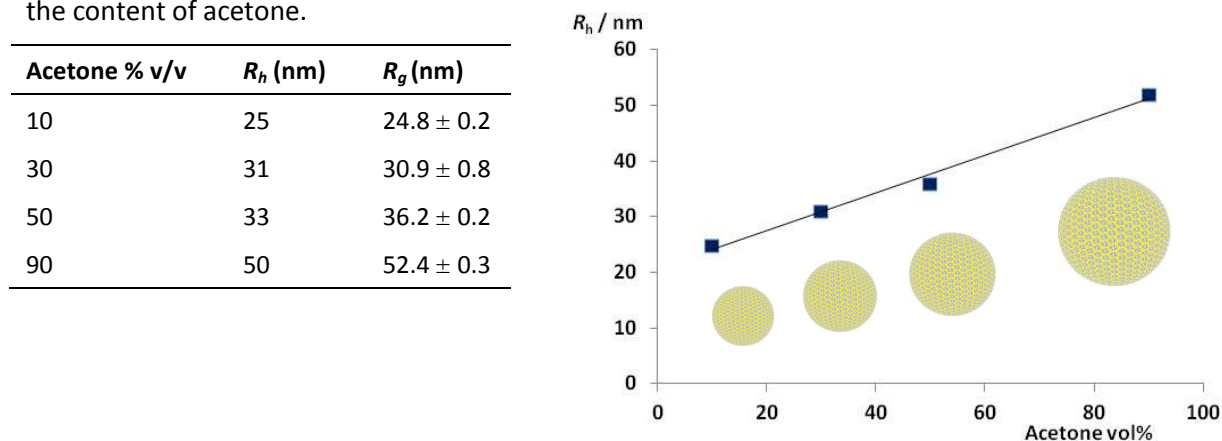


Figure 3.33. Left: R_h and R_g values for different water/acetone mixture solutions of **8-Nd**. Right: Linear relationship between the size of the assembly and the acetone volume percentage.

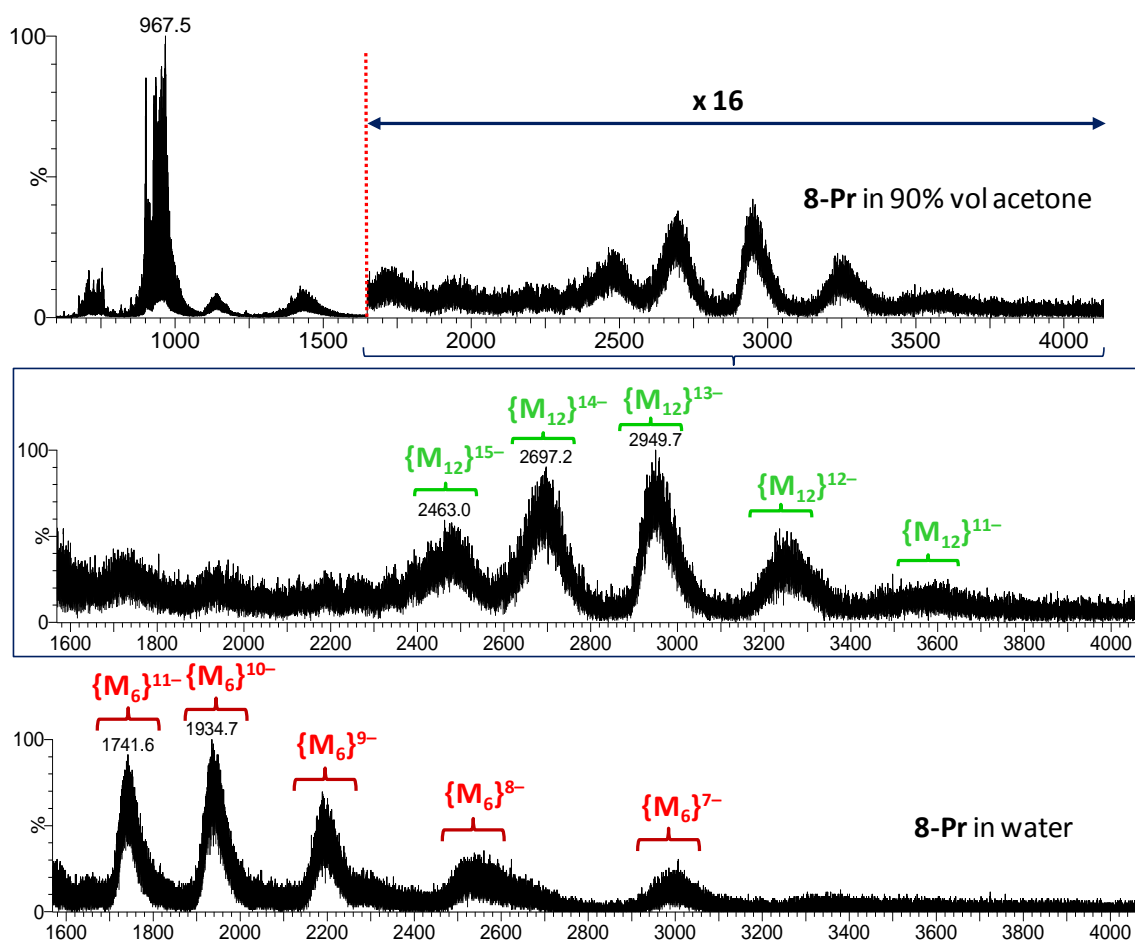


Figure 3.34. Top: Negative ESI-mass spectrum of **8-Pr** dissolved in 90% vol. acetone solution. Note that the intensity of the m/z 1650-4150 range is increased (x16) for a better visualization. Middle: Expanded m/z 1600-4050 region of **8-Pr** in 90% vol. acetone. Bottom: Expanded m/z 1600-4050 region of **8-Pr** in aqueous solution.

Unexpectedly, the sizes of the assemblies in water/acetone mixtures ($R = 25\text{--}50\text{ nm}$) are remarkably smaller than that observed for a pure water sample ($R = 75\text{ nm}$). This feature strongly suggests that the addition of acetone as co-solvent delays or even stops the dissociation of dodecamers into hexamers, in such a way that the former becomes the main species undergoing blackberry-type association in water/acetone mixtures. This fact was confirmed by ESI-MS experiments. The negative ESI-MS spectrum of a 90 % vol. acetone solution of **8-Pr** exhibits a series of five groups of signals in the m/z 2400–3800 range that correspond to high charge states (signals are close to each other) and molecular weights of about 40000 g mol^{-1} and can easily ascribed to the presence of dodecameric species in solution ($\{M_{12}\}^{(52-n)-} = [(\text{Pr}_2\text{GeW}_{10}\text{O}_{38})_{12} + x\text{H}_2\text{O} + m\text{K}^+ + (n-m)\text{Na}^+]^{(52-n)-}$; m/z 2480.5, $\{M_{12}\}^{15-}$; 2680.4 $\{M_{12}\}^{14-}$; 2949.7, $\{M_{12}\}^{13-}$; 3248.4, $\{M_{12}\}^{12-}$ and 3568.4, $\{M_{12}\}^{11-}$). A similar spectrum is obtained for **8-Nd** derivative as shown in Figure A2.16 (see Appendix 2). Compared to the ESI-mass spectrum carried out on aqueous samples, the $m/z < 1600$ region indicates that the dominant signals in both spectra correspond to $\{\text{Pr}_2\text{GeW}_{10}\text{O}_{38}\}$ monomers and their association into dimeric species. However, close inspection of the m/z 1600–3800 range clearly shows the presence of hexameric $\{\text{Pr}_2\text{GeW}_{10}\}_6$ anions in pure water, whereas the main large species in the 90% vol. acetone solution was found to be the dodecameric $\{\text{Pr}_2\text{GeW}_{10}\}_{12}$ anion (Figure 3.34). Stabilization of POM clusters in solution by the addition of organic solvents was already observed by Tézé and co-workers for the γ -decatungstosilicate anion.⁸¹

3.4. POM ASSEMBLIES CONTAINING MID-TO-LATE LANTHANIDES

3.4.1. Experimental section

General Synthetic Procedure. To a solution of the corresponding lanthanide(III) salt (0.98 mmol) in aqueous 0.5 M sodium acetate buffer (40 mL) solid GeO_2 (0.093 g, 0.89 mmol) and $\text{Na}_2\text{WO}_4 \cdot 2\text{H}_2\text{O}$ (2.640 g, 8.00 mmol) were successively added and a precipitate was formed. The reaction mixture was stirred at room temperature for 1h, resulting in a limpid solution. Compounds $\text{Na}_{12}[\text{Ln}_4(\text{H}_2\text{O})_6(\beta\text{-GeW}_{10}\text{O}_{38})_2] \cdot x\text{H}_2\text{O}$ (**9-Ln**, Ln = Gd, Tb, Dy, Ho, Er, Tm, Yb, Lu) were isolated as cottony solids formed by highly gathered needles (except for the non-crystalline **9-Gd**) from slow evaporation of the final solution at room temperature for ca. 3 weeks (final volume 20–30 mL). Compounds $\text{Cs}_y\text{Na}_{24-y}[\{\text{Ln}_4(\text{H}_2\text{O})_5(\text{GeW}_{10}\text{O}_{38})_2\}_2] \cdot x\text{H}_2\text{O}$ (**10-Ln**, Ln = Ho, Er, Tm, Yb, Lu) were obtained as prismatic plates by addition of aqueous 1M CsCl (~0.3 mL) to the final solution, followed by slow evaporation at room temperature for a few days.

$\text{Na}_{12}[\text{Gd}_4(\text{H}_2\text{O})_6(\beta\text{-GeW}_{10}\text{O}_{38})_2] \cdot \sim 44\text{H}_2\text{O}$ (9-Gd**).** $\text{Gd}(\text{NO}_3)_3 \cdot 6\text{H}_2\text{O}$ (0.442 g) was used as the lanthanide source. Yield: 0.20 g, 12% based on Gd. Anal. Calcd (found) for $\text{Gd}_4\text{Ge}_2\text{H}_{100}\text{Na}_{12}\text{O}_{126}\text{W}_{20}$: Gd, 9.19 (8.88); Ge, 2.12 (2.14); Na, 4.03 (4.30). IR (cm^{-1}): 936 (s), 874 (s), 822 (vs), 760 (s), 683 (s), 509 (m), 440 (m).

$\text{Na}_{12}[\text{Tb}_4(\text{H}_2\text{O})_6(\beta\text{-GeW}_{10}\text{O}_{38})_2] \cdot \sim 44\text{H}_2\text{O}$ (9-Tb**).** $\text{Tb}(\text{NO}_3)_3 \cdot 5\text{H}_2\text{O}$ (0.426 g) was used as the lanthanide source. Yield: 0.25 g, 15% based on Tb. Anal. Calcd (found) for $\text{Ge}_2\text{H}_{100}\text{Na}_{12}\text{O}_{126}\text{Tb}_4\text{W}_{20}$: Ge, 2.12 (2.13); Na, 4.03 (4.17); Tb, 9.28 (9.26). IR (cm^{-1}): 936 (s), 876 (s), 822 (vs), 760 (s), 683 (s), 509 (m), 438 (m). Unit cell parameters (single-crystal, 100 K): triclinic $P\bar{1}$, $a = 12.766(10)$, $b = 18.883(14)$, $c = 22.130(16)$ Å, $\alpha = 87.40(6)$, $\beta = 87.72(6)$, $\gamma = 81.82(6)^\circ$, $V = 5272(7)$ Å³.

Na₁₂[Dy₄(H₂O)₆(β-GeW₁₀O₃₈)₂]·~44H₂O (9-Dy). DyCl₃·6H₂O (0.369 g) was used as the lanthanide source. Yield: 0.27 g, 16% based on Dy. Anal. Calcd (found) for Dy₄Ge₂H₁₀₀Na₁₂O₁₂₆W₂₀: Dy, 9.47 (9.46); Ge, 2.12 (2.11); Na, 4.02 (4.04). IR (cm⁻¹): 937 (s), 878 (s), 818 (vs), 760 (s), 683 (s), 513 (m), 438 (m).

Na₁₂[Ho₄(H₂O)₆(β-GeW₁₀O₃₈)₂]·~44H₂O (9-Ho) and **Cs₇Na₁₇[{Ho₄(H₂O)₅(GeW₁₀O₃₈)₂]₂]·~66H₂O (10-Ho).** HoCl₃·6H₂O (0.372 g) was used as the lanthanide source. **9-Ho.** Yield: 0.36 g, 21% based on Ho. Anal. Calcd (found) for Ge₂H₁₀₀Ho₄Na₁₂O₁₂₆W₂₀: Ge, 2.11 (2.10); Ho, 9.60 (9.69); Na, 4.01 (3.96). IR (cm⁻¹): 937 (s), 876 (s), 816 (vs), 757 (s), 685 (s), 511 (m), 444 (m). **10-Ho.** Yield: 0.30 g, 17% based on Ho. Anal. Calcd (found) for Cs₇Ge₄H₁₅₂Ho₈Na₁₇O₂₂₈W₄₀: Cs, 6.60 (6.53); Ge, 2.06 (2.06); Ho, 9.37 (9.08); Na, 2.78 (3.01). IR (cm⁻¹): 936 (s), 871 (s), 802 (vs), 746 (s), 681 (s), 509 (m), 442 (m).

Na₁₂[Er₄(H₂O)₆(β-GeW₁₀O₃₈)₂]·~44H₂O (9-Er) and **Cs₆Na₁₈[{Er₄(H₂O)₅(GeW₁₀O₃₈)₂]₂]·~66H₂O (10-Er).** ErCl₃·6H₂O (0.374 g) was used as the lanthanide source. **9-Er.** Yield: 0.45 g, 27% based on Er. Anal. Calcd (found) for Er₄Ge₂H₁₀₀Na₁₂O₁₂₆W₂₀: Er, 9.72 (9.53); Ge, 2.11 (2.10); Na, 4.01 (4.06). IR (cm⁻¹): 936(s), 876 (s), 822 (vs), 764 (s), 681 (s), 513 (m), 444 (m). **10-Er.** Yield: 0.26 g, 15% based on Er. Anal. Calcd (found) for Cs₆Er₈Ge₄H₁₅₂Na₁₈O₂₂₈W₄₀: Cs, 5.70 (5.87); Er, 9.56 (9.54); Ge, 2.08 (2.10); Na, 2.96 (3.26). IR (cm⁻¹): 936 (s), 872 (s), 802(vs), 748 (s), 679(s), 509(m), 440(m).

Na₁₂[Tm₄(H₂O)₆(β-GeW₁₀O₃₈)₂]·~41H₂O (9-Tm) and **Cs₅Na₁₉[{Tm₄(H₂O)₅(GeW₁₀O₃₈)₂]₂]·~63H₂O (10-Tm).** TmCl₃·6H₂O (0.376 g) was used as the lanthanide source. **9-Tm.** Yield: 0.25 g, 15% based on Tm. Anal. Calcd (found) for Ge₂H₉₄Na₁₂O₁₂₃Tm₄W₂₀: Ge, 2.12 (2.11); Na, 4.04 (4.43); Tm, 9.88 (9.84). IR (cm⁻¹): 936 (s), 876 (s), 822 (vs), 764 (s), 683 (s), 511 (m), 448 (m). **10-Tm.** Yield: 0.48 g, 28% based on Tm. Anal. Calcd (found) for Cs_{5.3}Ge₄H₁₄₆Na_{18.7}O₂₂₅Tm₈W₄₀: Cs, 5.08 (5.16); Ge, 2.09 (2.15); Na, 3.10 (3.50); Tm, 9.74 (9.84). IR (cm⁻¹): 936 (s), 872 (s), 806 (vs), 754 (s), 681 (s), 509 (m), 440 (m).

Na₁₂[Yb₄(H₂O)₆(β-GeW₁₀O₃₈)₂]·~41H₂O (9-Yb) and **Cs₆Na₁₈[{Yb₄(H₂O)₅(GeW₁₀O₃₈)₂]₂]·~63H₂O (10-Yb).** YbCl₃·6H₂O (0.380 g) was used as the lanthanide source. **9-Yb.** Yield: 0.23 g, 14% based on Yb. Anal. Calcd (found) for Ge₂H₉₄Na₁₂O₁₂₃W₂₀Yb₄: Ge, 2.12 (2.14); Na, 4.03 (4.30); Yb, 10.10 (10.45). IR (cm⁻¹): 937 (s), 874 (s), 818 (vs), 762 (s), 685 (s), 511 (m), 446 (m). **10-Yb.** Yield: 0.30 mg, 18% based on Yb. Anal. Calcd (found) for Cs_{5.5}Ge₄H₁₄₆Na_{18.5}O₂₂₅W₄₀Yb₈: Cs, 5.25 (5.26); Ge, 2.08 (2.06); Na, 3.05 (3.14); Yb, 9.94 (9.96). IR (cm⁻¹): 936 (s), 876 (s), 810 (vs), 758 (s), 683 (s), 513 (m), 440 (m).

Na₁₂[Lu₄(H₂O)₆(β-GeW₁₀O₃₈)₂]·~41H₂O (9-Lu) and **Cs₅Na₁₉[{Lu₄(H₂O)₅(GeW₁₀O₃₈)₂]₂]·~63H₂O (10-Lu).** LuCl₃·6H₂O (0.382 g) was used as the lanthanide source. **9-Lu.** Yield: 0.31 g, 18% based on Lu. Anal. Calcd (found) for Ge₂H₉₄Lu₄Na₁₂O₁₂₃W₂₀: Ge, 2.12 (2.10); Lu, 10.20 (10.20); Na, 4.02 (4.41). IR (cm⁻¹): 939 (s), 876 (s), 818 (vs), 764 (s), 690 (s), 513 (m), 448 (m). **10-Lu.** Yield: 0.26 g, 15% based on Lu. Anal. Calcd (found) for Cs₅Ge₄H₁₄₆Lu₈Na₁₉O₂₂₅W₄₀: Cs, 4.78 (4.99); Ge, 2.09 (2.11); Lu, 10.08 (10.12); Na, 3.14 (3.35). IR (cm⁻¹): 937 (s), 868 (s), 806 (vs), 754 (s), 683 (s), 507 (m), 444 (m).

Thermal Analyses. All compounds **9-Ln** and **10-Ln** show TGA/DTA curves with similar profiles (see Figure A2.12 in Appendix 2). Dehydration is observed as an endothermic mass loss that extends continuously to temperatures around 500 °C, at which the POM framework starts decomposing as indicated by a set of overlapped exothermic signals. Table 3.8 displays the experimental and calculated mass losses (Δm) for the dehydration, together with the decomposition temperatures (T_d).

Table 3.8. Thermal data of compounds **9-Ln** and **10-Ln**.

	Δm_{exp} (%)	Δm_{calcd} (%), $n\text{H}_2\text{O}$	T_d (°C)		Δm_{exp} (%)	Δm_{calcd} (%), $n\text{H}_2\text{O}$	T_d (°C)
9-Gd	13.87	13.16 for $n = 50$	475				
9-Tb	13.38	13.15 for $n = 50$	475				
9-Dy	13.19	13.12 for $n = 50$	485				
9-Ho	13.05	13.10 for $n = 50$	485	10-Ho	9.63	9.63 for $n = 76$	500
9-Er	12.98	13.08 for $n = 50$	485	10-Er	9.74	9.63 for $n = 76$	500
9-Tm	12.50	12.39 for $n = 47$	490	10-Tm	9.30	9.48 for $n = 73$	495
9-Yb	12.13	12.36 for $n = 47$	490	10-Yb	9.45	9.44 for $n = 73$	500
9-Lu	12.45	12.34 for $n = 47$	495	10-Lu	9.45	9.47 for $n = 73$	500

X-ray crystallography

Crystal data for **9-Ln** (Ln = Dy to Lu) and **10-Ln** (Ln = Ho to Lu) are summarized in Tables 3.9 and 3.10, respectively. Thermal vibrations were treated anisotropically for heavy atoms (W, Ge, Cs, lanthanides). In compounds **9-Ln**, both $\{\text{Ln}_2(\beta\text{-GeW}_{10}\text{O}_{38})\}$ fragments in the asymmetric unit showed disorder in the rotated W_3O_{13} trimers formed by the W10/W11/W12 and the W30/W31/W32 octahedra. This disorder originates from contribution of the corresponding $\{\text{Ln}_2(\alpha\text{-GeW}_{10}\text{O}_{38})\}$ isomer with the W_3O_{13} trimer back-rotated by 60° . Only the W atoms of the back-rotated trimers could be located from successive Fourier maps and they were included in the refinement with isotropic thermal parameters. The three W atoms on each β -trimer, together with their associated terminal and bridging O atoms, were refined with the same occupancies and the sum of the population factors for each β -W/ α -W pair (e.g. W10/W10A) was restricted to 1, resulting in contributions in the 2 – 13% range of the α -form (Dy, 2.3/7.7; Ho, 5.9/8.2; Er, 5.1/7.0; Tm, 6.4/12.9; Yb, 3.6/8.5; Lu, 8.2/8.6).

For compounds **10-Ln**, one of the two $\{\text{Ln}_2(\beta\text{-GeW}_{10}\text{O}_{38})\}$ fragments in the asymmetric unit showed similar disorder in the W30/W31/W32 rotated trimer. This disorder was modeled analogously (except for **10-Er**, for which the low quality of the available data precluded any treatment), resulting in contributions of c.a. 5% for the α -form (Ho, 4.4; Tm, 5.9; Yb, 4.7; Lu, 5.8). The second $\{\text{Ln}_2(\text{GeW}_{10}\text{O}_{38})\}$ fragment displayed a much more pronounced α/β disorder for all the five **10-Ln** compounds. In this case, all terminal and bridging O atoms of the α -trimer defined by the W10A/W11A/W12A octahedra could also be located from successive Fourier cycles. Treatment of the W atoms, together with their associated O atoms, was as explained above for both α - and β -trimers. Final results indicate that both α - and β -forms of the $\{\text{Ln}_2(\text{GeW}_{10}\text{O}_{38})\}$ fragment coexist in the structure with the following α/β population factors: 42.0/58.0 for Ho, 39.1/60.9 for Er, 52.8/47.2 for Tm, 53.5/46.5 for Yb; and 60.8/39.2 for Lu.

All compounds display significant disorder between counterions and lattice water molecules. For **9-Ln**, 11 to 14 sites with appropriate geometries for a Na cation were located in the Fourier maps. The occupancies in these positions were initially refined without restrictions and rounded to the first decimal in the last cycle. This resulted in a total number of 8.5 (**9-Dy**), 8.4 (**9-Ho**), 8.3 (**9-Er**),

9.3 (**9-Tm**), 9.3 (**9-Yb**) and 8.8 (**9-Lu**) Na atoms per asymmetric unit containing one polyanion. In **10**, the disorder observed was much more severe because the coexistence of α/β forms for one of the $\{\text{Ln}_2(\text{GeW}_{10}\text{O}_{38})\}$ fragments in the asymmetric unit with population factors ranging from 40 to 60% led us to observe overlapping of two different cation/solvent networks around these fragments with consequent impossibility to discriminate most of the atomic positions. The occupancies of those Cs/Na sites identified in the Fourier maps were refined as explained above, resulting in a total number of 2.0/3.1 (**10-Ho**), 2.6/2.4 (**10-Er**), 1.6/4.9 (**10-Tm**), 1.9/5.0 (**10-Yb**), 1.8/5.0 (**10-Lu**) Cs/Na cations per asymmetric unit containing one half of the polyanion.

Table 3.9. Crystal data of compounds **9-Ln**.

	9-Dy	9-Ho	9-Er	9-Tm	9-Yb	9-Lu
Formula	Dy ₄ Ge ₂ H ₁₀₀ Na ₁₂ O ₁₂₆ W ₂₀	Ge ₂ H ₁₀₀ Ho ₄ Na ₁₂ O ₁₂₆ W ₂₀	Er ₄ Ge ₂ H ₁₀₀ Na ₁₂ O ₁₂₆ W ₂₀	Ge ₂ H ₉₄ Na ₁₂ O ₁₂₃ Tm ₄ W ₂₀	Ge ₂ H ₉₄ Na ₁₂ O ₁₂₃ W ₂₀ Yb ₄	Ge ₂ H ₉₄ Lu ₄ Na ₁₂ O ₁₂₃ W ₂₀
FW (g mol ⁻¹)	6864.9	6874.6	6883.9	6836.5	6853.0	6860.7
Crystal system	triclinic	triclinic	triclinic	triclinic	triclinic	triclinic
Space group	<i>P</i> -1	<i>P</i> -1	<i>P</i> -1	<i>P</i> -1	<i>P</i> -1	<i>P</i> -1
<i>a</i> (Å)	12.7056(2)	12.7152(2)	12.7079(5)	12.7042(2)	12.70257(14)	12.6836(3)
<i>b</i> (Å)	18.8410(5)	18.8144(4)	18.7881(7)	19.7803(4)	19.8138(7)	19.7846(4)
<i>c</i> (Å)	22.0984(4)	22.0744(4)	22.0649(7)	22.3835(3)	22.4348(3)	22.3822(4)
α (°)	87.696(2)	87.758(2)	87.988(3)	90.4070(10)	90.4473(17)	90.430(2)
β (°)	87.5400(10)	87.7140(10)	87.905(3)	93.5870(10)	93.8195(10)	93.807(2)
γ (°)	81.850(2)	81.656(2)	81.488(3)	90.398(2)	90.8531(17)	90.766(2)
<i>V</i> (Å ³)	5228.69(19)	5217.81(17)	5204.3(3)	5613.50(16)	5633.1(2)	5603.5(2)
<i>Z</i>	2	2	2	2	2	2
<i>D</i> _{calcd} (g cm ⁻³)	4.360	4.376	4.400	4.045	4.040	4.066
μ (mm ⁻¹)	25.471	25.693	25.986	24.220	24.306	24.621
Reflections						
Collected	35458	34970	32970	36700	40683	36560
Unique (<i>R</i> _{int})	18384 (0.029)	18360 (0.037)	18275 (0.079)	19752 (0.025)	19839 (0.030)	19715 (0.046)
Observed [<i>I</i> > 2 σ (<i>I</i>)]	15239	15632	12171	17643	17639	16902
Parameters	817	814	790	825	817	813
<i>R</i> (<i>F</i>) [<i>I</i> > 2 σ (<i>I</i>)]	0.045	0.042	0.082	0.036	0.046	0.047
<i>wR</i> (<i>F</i> ²) (all data)	0.103	0.097	0.215	0.084	0.115	0.133
GoF	1.044	1.039	1.054	1.082	1.064	1.043

Crystals of both Er derivatives **9-Er** and **10-Er** were systematically of much poorer quality than their analogues, as evidenced by the significantly higher values of the *R*_{int} parameter and agreement factors. We made measurements on several crystals from several different batches in quest of a better set of crystallographic data for both compounds but without any success. For **10-Er**, low

quality data together with the coexistence of α - and β - $\{\text{Ln}_2\text{GeW}_{10}\text{O}_{38}\}$ forms made impossible to refine most of the Na ions and lattice water molecules, resulting in a final structural solution with large voids accounting for the 15% of the unit cell (voids of 587 and 208 Å³ voids at $x,y,z = 0, 1/2, 0$ and $1/2, 1/2, 1/2$ respectively). We tried to apply the SQUEEZE routine from PLATON to overcome this but we did not observe any improvement in the agreement factors.

Table 3.10. Crystal data of compounds **10-Ln**.

	10-Ho	10-Er	10-Tm	10-Yb	10-Lu
Formula	Cs ₇ Ge ₄ H ₁₅₂ Ho ₄ Na ₁₇ O ₂₂₈ W ₄₀	Cs ₆ Er ₄ Ge ₄ H ₁₅₂ Na ₁₈ O ₂₂₈ W ₄₀	Cs ₅ Ge ₄ H ₁₄₆ Na ₁₇ O ₂₂₅ Tm ₈ W ₄₀	Cs ₆ Ge ₄ H ₁₄₆ Na ₁₈ O ₂₂₅ W ₄₀ Yb ₈	Cs ₅ Ge ₄ H ₁₄₆ Lu ₈ Na ₁₉ O ₂₂₅ W ₄₀
FW (g mol ⁻¹)	14086.2	13994.9	13844.3	13987.1	13892.6
Crystal system	triclinic	triclinic	triclinic	triclinic	triclinic
Space group	<i>P</i> -1	<i>P</i> -1	<i>P</i> -1	<i>P</i> -1	<i>P</i> -1
<i>a</i> (Å)	14.0737(2)	13.3091(6)	14.0721(3)	14.0508(3)	14.0465(3)
<i>b</i> (Å)	19.6092(4)	21.4625(10)	19.6282(5)	19.6071(5)	19.5799(4)
<i>c</i> (Å)	21.3394(4)	22.0117(9)	21.3640(5)	21.3326(6)	21.3288(5)
α (°)	103.083(2)	112.719(4)	103.070(2)	102.930(2)	102.864(2)
β (°)	107.118(2)	101.933(4)	107.216(2)	107.185(2)	107.325(2)
γ (°)	103.786(2)	104.460(4)	103.875(2)	103.942(2)	103.957(2)
<i>V</i> (Å ³)	5179.69(16)	5282.5(4)	5183.6(2)	5166.2(2)	5152.76(19)
<i>Z</i>	1	1	1	1	1
<i>D</i> _{calcd} (g cm ⁻³)	4.516	4.399	4.435	4.496	4.477
μ (mm ⁻¹)	27.064	26.552	27.070	27.519	27.621
Reflections					
Collected	38139	34136	32754	32702	38034
Unique (<i>R</i> _{int})	18252 (0.044)	18591 (0.085)	18257 (0.026)	18193 (0.025)	18132 (0.027)
Observed [<i>I</i> > 2 σ (<i>I</i>)]	15711	12414	15788	15538	16301
Parameters	828	716	843	851	851
<i>R</i> (<i>F</i>) [<i>I</i> > 2 σ (<i>I</i>)]	0.054	0.118	0.042	0.043	0.041
<i>wR</i> (<i>F</i> ²) (all data)	0.146	0.321	0.106	0.106	0.101
GoF	1.022	1.024	1.025	1.045	1.034

3.4.2. Results and discussion

Synthesis

After studying the early lanthanides, mid to late 4*f*-metals (Ln^{III} = from Gd to Lu) were selected to extend our systematic studies. It is known that POM assemblies are highly sensitive to the exact nature of the employed lanthanide, in such a way that the architectures obtained for small lanthanides after the Gd break are often different to those of the larger ions due to the lanthanide

contraction effect and consequent decrease in the number of coordination sites around the 4f ion.⁸² Unfortunately, we did not obtain any crystalline product suitable for structural characterization when the corresponding $1.1\text{Ln}^{3+}:1.1\text{GeO}_2:9\text{WO}_4^{2-}$ reactions were performed under the same synthetic conditions (including addition of K^+ or Cs^+ cations) as for early lanthanides.

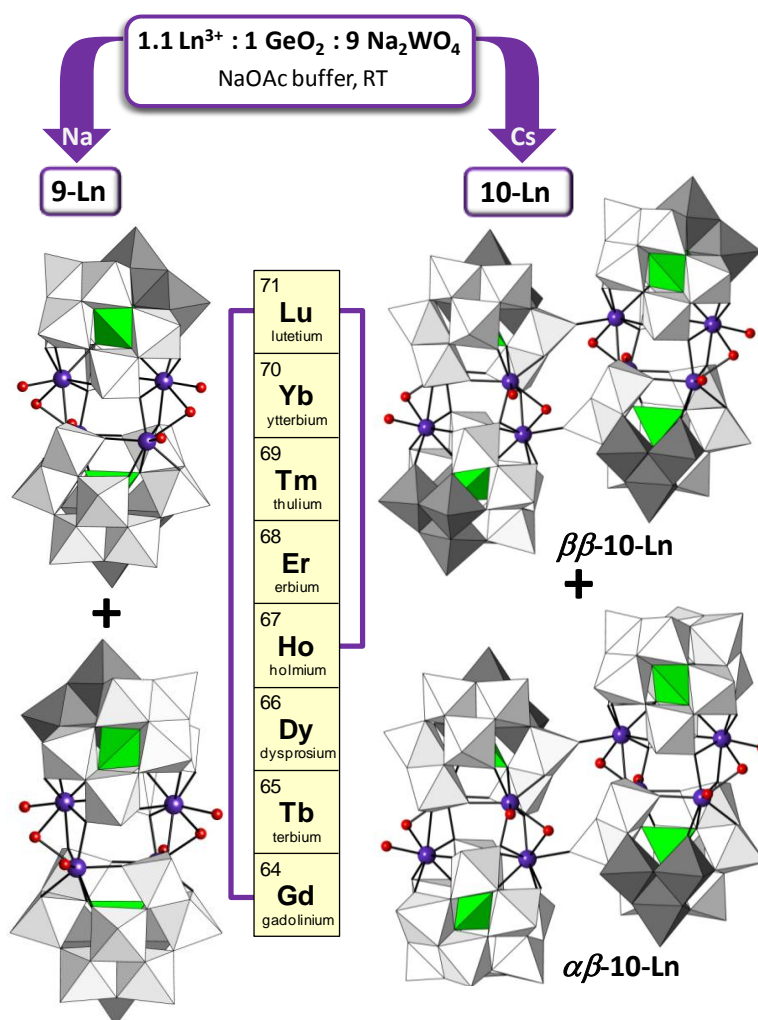


Figure 3.35. Synthetic approach for compounds **9-Ln** (Ln = Gd to Lu) and **10-Ln** (Ln = Ho to Lu). Rotated W_3O_{13} trimers are highlighted in dark grey.

Taking into account the structural role played by the $[\text{M}(\text{H}_2\text{O})_6]^{2+}$ cations for **6-Ln**, **7-Sm** and **8-Ln**, it appears that these species are not appropriate crystallizing agents when mid to late lanthanides are used, and therefore, we decided to simplify the system to $1.1\text{Ln}^{3+}:1\text{GeO}_2:9\text{Na}_2\text{WO}_4$ mixtures (Figure 3.35). When no alkaline cations were added and the reactions were carried out in the presence of exclusively sodium coming from the buffer, the dimeric POMs $[\text{Ln}_4(\text{H}_2\text{O})_6(\beta\text{-GeW}_{10}\text{O}_{38})_2]^{12-}$ (**9-Ln**) were obtained for the whole series from Ln = Gd to Lu, whereas tetrameric assemblies $[\{\text{Ln}_4(\text{H}_2\text{O})_5(\text{GeW}_{10}\text{O}_{38})_2\}_2]^{24-}$ (**10-Ln**) were isolated when CsCl (aq) was added to the reaction mixture, but only for the latest lanthanides from Ln = Ho to Lu. Non-crystalline, fine powders were formed in the case of Ln = Gd, Tb and Dy, but their identity as tetrameric POMs could not be unequivocally established on the basis of IR spectroscopy.

Regarding synthetic aspects, it is worth mentioning the following: i) **9** and **10** can be prepared starting from the corresponding $2\text{Ln}^{3+}:\text{1GeO}_2:\text{10Na}_2\text{WO}_4$ stoichiometric mixtures, but the initial precipitates formed in the reactions did not dissolve completely, resulting in significantly lower yields of final crystalline products; ii) no identifiable compounds were obtained when Eu^{3+} salts were used as lanthanide sources, and hence there is an structural break in the system between the series $\text{Ln} = \text{Gd}$ to Lu and earlier, larger 4f ions from La to Sm ; iii) in contrast to the template role of cyclic structural motifs observed for K^+ in **7-Sm** and **8-Ln**, addition of this alkaline cation to the present reaction mixtures resulted in the appearance of colloidal precipitates or even jellification of the final solutions upon evaporation.

Molecular structure of the 9-Ln anions

Polyanions $[\text{Ln}_4(\text{H}_2\text{O})_6(\beta\text{-GeW}_{10}\text{O}_{38})_2]^{12-}$ (**9-Ln**, $\text{Ln} = \text{Gd}$ to Lu) are composed of two $[\text{Ln}_2(\beta\text{-GeW}_{10}\text{O}_{38})]^{6-}$ subunits ($\{\beta\text{-Ln}_2\text{GeW}_{10}\}$) associated in a face-to-face manner via two pairs of $\text{Ln}-\text{O}(\text{WO}_5)-\text{Ln}$ bridges, resulting in a chiral dimeric assembly with ideal C_2 point symmetry broken down to C_1 as a result of the asymmetric coordination of bridging water molecules between lanthanide centers (Figure 3.36). These subunits contain dilacunary $\{\text{GeW}_{10}\text{O}_{38}\}^{12-}$ skeletons derived from the β -Keggin cluster, which is usually described as formed by a 60° -rotated $\{\text{M}_3\text{O}_{13}\}$ cap, a central hexameric belt and a bottom $\{\text{M}_3\text{O}_{15}\}$ triad. In this case, the vacant sites are located in non-adjacent positions of the belt and the bottom triad, resulting in anti-Lipscomb type⁶⁵ frameworks with two WO_6 octahedra common to both vacant sites that show three unshared O atoms each. These skeletons are formed in situ during the reaction and further stabilized by coordination of a 4f ion to the four O atoms delimiting each lacuna and the corresponding central O atom, in such a way that the two mentioned WO_6 octahedra and the $\{\text{GeO}_4\}$ group connect the two 4f ions via one $\text{O}-\text{Ge}-\text{O}$ and two $\text{O}-\text{W}-\text{O}$ bridges (Figure 3.37). Closely related dimeric assemblies were reported a few years ago by Li et al. for $\text{Ln} = \text{Dy}, \text{Er}$.⁸³ These POMs with C_2 point symmetry were obtained from reaction of the $[\gamma\text{-GeW}_{10}\text{O}_{36}]^{8-}$ precursor with a lanthanide source in warm water at $\text{pH} = 4$ and their constituent $\{\alpha\text{-Ln}_2\text{GeW}_{10}\}$ subunits show dilacunary Keggin skeletons of the $\alpha(1,4)$ type according to the Pope & Scully notation.⁸⁴

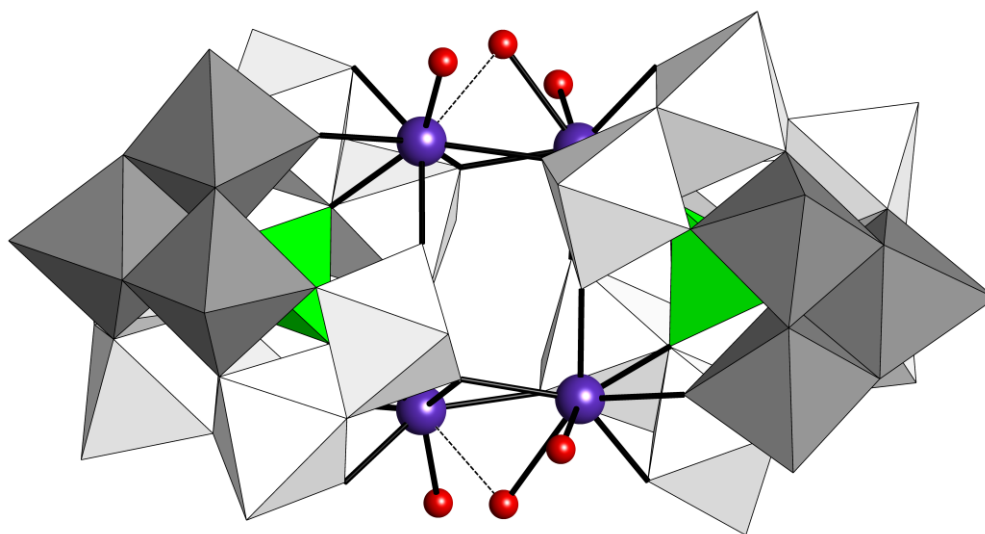


Figure 3.36. View of a **9-Ln** POM along the ideal C_2 axis broken by the asymmetric bridging of the water molecules. Long $\text{Ln}-\text{O}_w$ bonds depicted as dashed lines.

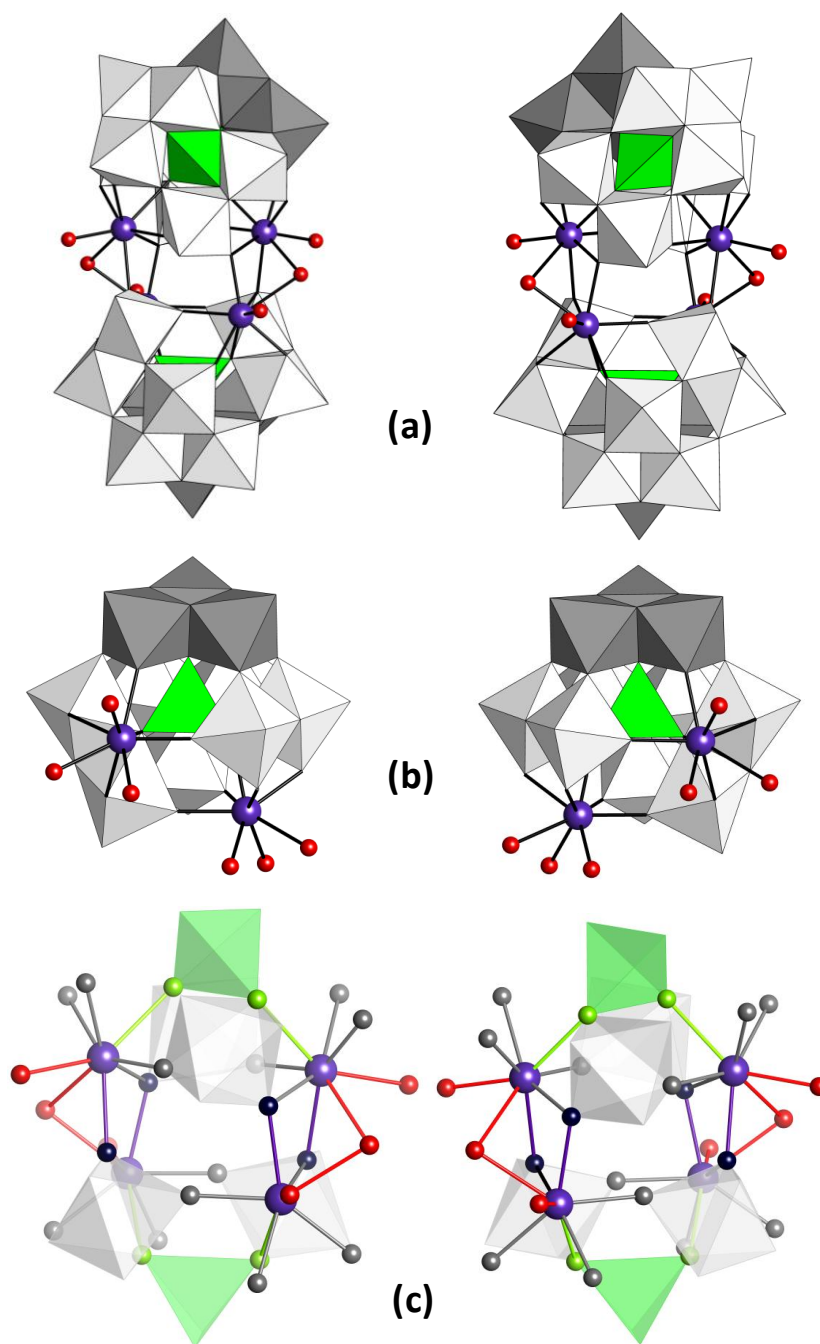


Figure 3.37. (a) Dimeric $[\text{Ln}_4(\text{H}_2\text{O})_6(\beta\text{-GeW}_{10}\text{O}_{38})_2]^{12-}$ POMs found in the asymmetric units of **9-Tm**, **-Yb**, **-Lu** (phase A, left) and **9-Tb**, **-Dy**, **-Ho**, **-Er** (phase B, right). (b) Details of their $[\beta\text{-Ln}_2\text{GeW}_{10}\text{O}_{38}]^{6-}$ subunits [left: $\beta(1,5)$; right: $\beta(1,8)$] and (c) Details of the central $\{\text{Ln}_4\}$ cores (left: clockwise; right: anti-clockwise orientation). Note the enantiomeric relation between both **9-Ln** dimers and both $\{\beta\text{-Ln}_2\text{GeW}_{10}\}$ subunits. Bonding and oxygen atom color code: Ln–O_L, grey; Ln–O_b, violet; Ln–O_{wt} and Ln–O_{wb}, red; Ln–O_c, green (for the abbreviations O_L, O_b, O_{wt}, O_c, O_{wb}, see the footnote in Table 3.12).

Two different crystalline phases have been identified by single-crystal X-ray diffraction for compounds **9-Ln**: phase A in crystals with Ln = Tm to Lu and phase B in those samples where Ln = Dy to Er. Both phases crystallize in the triclinic space group $P\bar{1}$ as highly gathered needles. Powder X-ray diffractograms, together with their comparison to the simulated patterns for **9-Lu** and **9-Dy** as phase A and B representatives (Figure 3.38), show that solid samples for all compounds **9-Ln** are

mixtures of both phases (Figure 3.39). The relative contribution of phase A to the mixture decreases when going from Ln = Dy to heavier lanthanides, in such a way that it is almost imperceptible for Ln = Yb and Lu (but not negligible, note that the structural determination for these two derivatives has been performed on single crystals from phase A). Powder X-ray diffraction also evidences the poor crystallinity of **9-Tb** compared to the rest of compounds; this fact did not allow us to obtain a complete set of single-crystal X-ray data, but only to determine its unit-cell parameters, which correspond to those of phase B (see Experimental Section 3.3.1). In the case of the non-crystalline **9-Gd**, its identity as the $[\text{Gd}_4(\text{H}_2\text{O})_6(\beta\text{-GeW}_{10}\text{O}_{38})_2]^{12-}$ POM is unequivocally established by IR spectroscopy (see Figure A2.7 in Appendix 2).

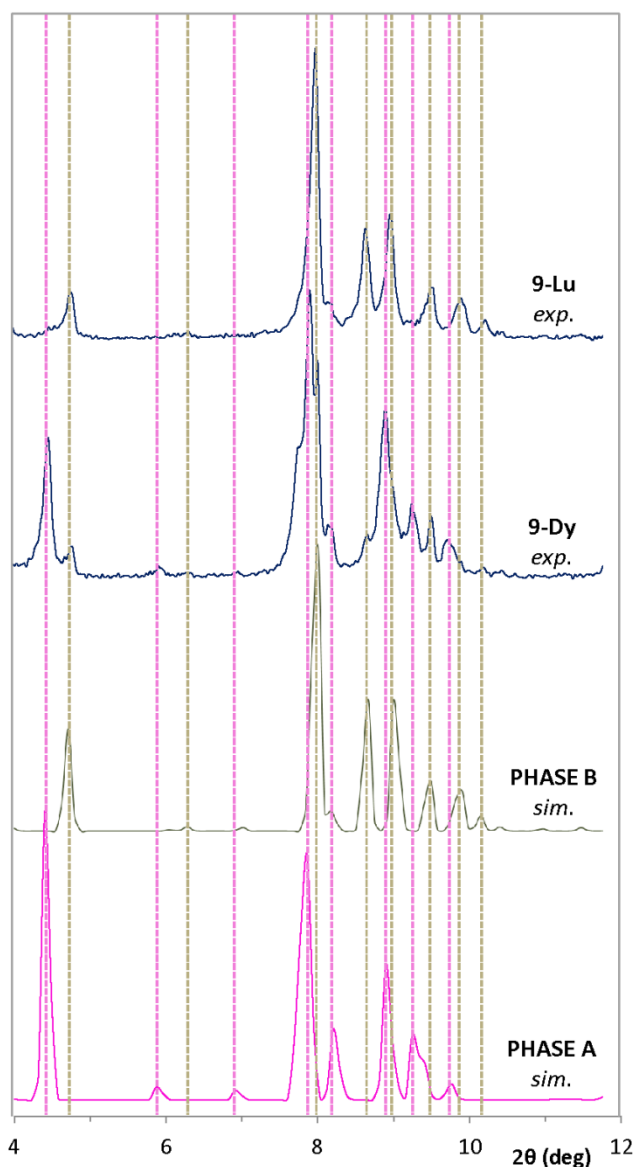


Figure 3.38. Comparison between the experimental powder X-ray diffractograms of **9-Lu** and **9-Dy** and the simulated patterns (from single-crystal X-ray diffraction data) for phases A and B.

The **9-Ln** POM in the asymmetric unit of phase A contains two $\{\beta\text{-Ln}_2\text{GeW}_{10}\}$ subunits with the 4f ions located in relative positions 1 (bottom triad) and 5 (belt) according to the IUPAC notation⁶⁶ ($\beta(1,5)$ isomer), whereas relative positions 1 and 8 ($\beta(1,8)$ isomer) are observed for the two subunits

of the POM contained in the asymmetric unit of phase B. In both cases, the Ln–O(WO₅)–Ln bridges are established between belt and bottom-triad lanthanides and they involve the two WO₆ octahedra common to both vacant sites. As a result, the {Ln₄} central core displays two Ln₂(μ-OWO₅)₂(μ-OH₂) dinuclear fragments arranged in clockwise orientation for phase A and anti-clockwise fashion for phase B (Figure 3.37). Subunits β(1,5) and β(1,8) constitute an enantiomeric pair and both dimeric POMs found in phases A and B are also enantiomerically related, hence all analyzed samples consist in racemic crystals containing equal amounts of both right- and left-handed **9-Ln** forms regardless of the phase.

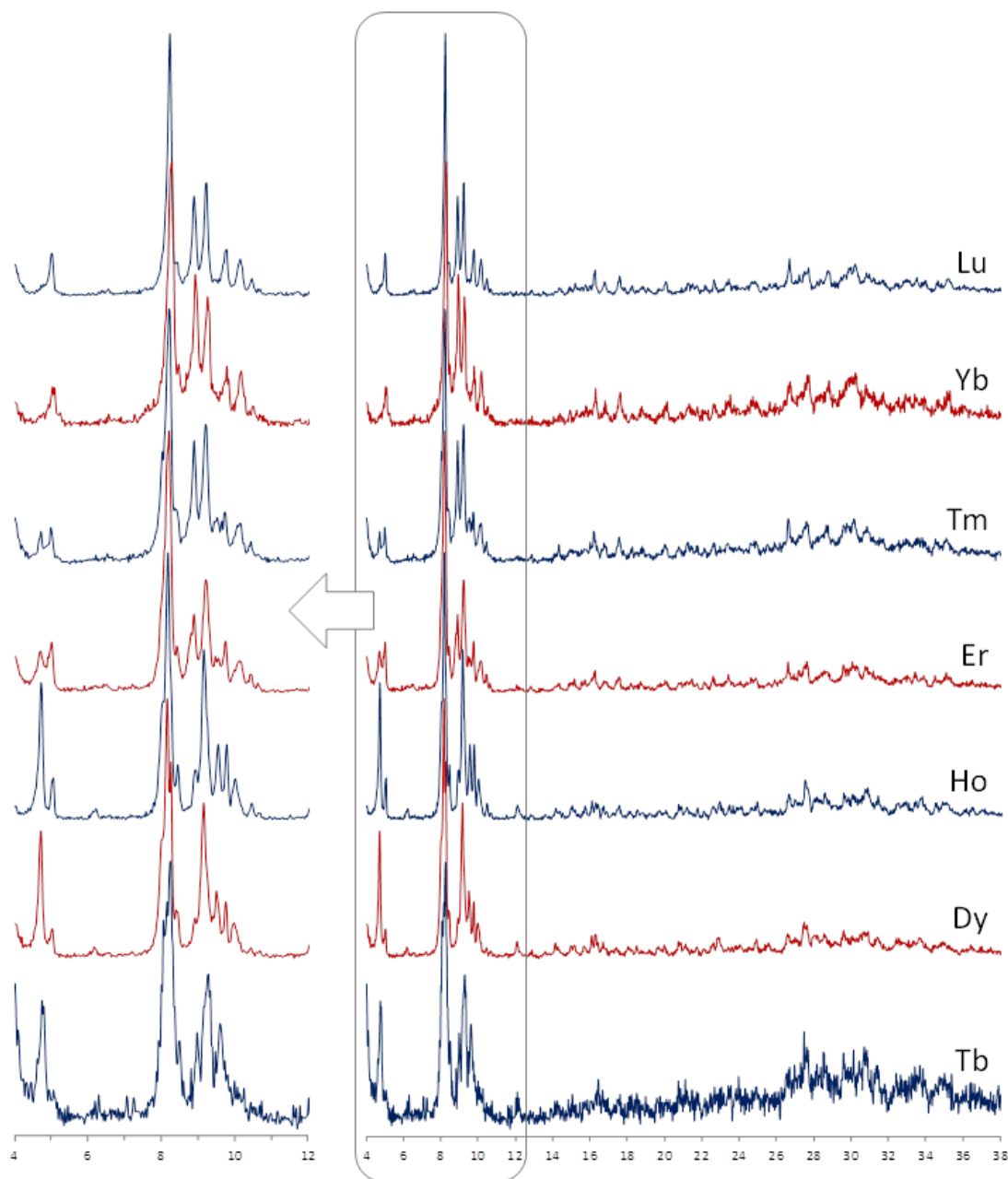


Figure 3.39. Powder X-ray diffractograms of compounds **9-Ln** (Ln = Tb to Lu).

The β(1,5)/β(1,8) enantiomeric pair was firstly described in the central cyclic motif of the the **8-Ce** dodecamer and has been repeatedly observed for the rest of **8-Ln** compounds and the **6-Ln** and **7-Sm** hexamers.⁴⁶ Beyond the cyclic vs. rod-like arrangement, the assembly pattern of {β-Ln₂GeW₁₀}

subunits in compound **6-Ln**, **7-Sm** (hexamers) or **8-Ln** (dodecamers) shows other noticeable differences compared to that observed in **9-Ln** (dimers): i) compounds **6-Ln**, **7-Sm** and **8-Ln** contain both $\beta(1,5)$ and $\beta(1,8)$ isomers arranged alternately, whereas the **9** species display a single type of $\{\beta\text{-Ln}_2\text{GeW}_{10}\}$ subunit [either $\beta(1,5)$ or $\beta(1,8)$]; ii) the Ln–O(WO₅)–Ln bridges in the formers involve lanthanide atoms placed only in the bottom triad, whereas belt and bottom-triad 4f ions participate from this linkages in the **9-Ln** species.

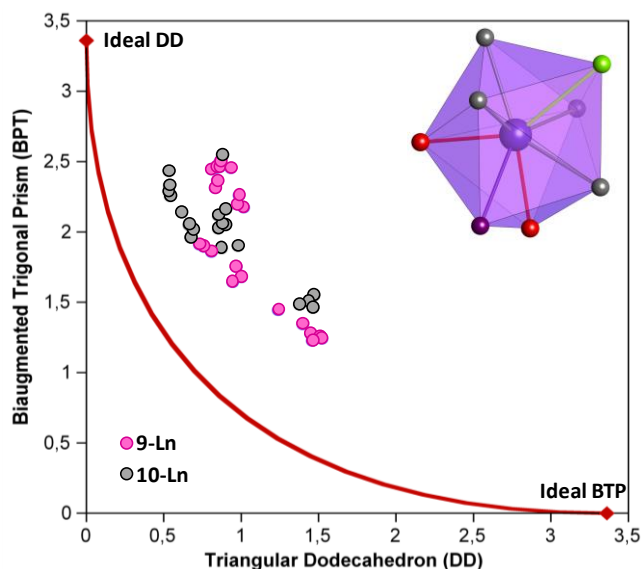


Figure 3.40. Biaugmented trigonal prism (BTP) vs. triangular dodecahedron (DD) shape map for the 4f ions in compounds **9-Ln** and **10-Ln** (solid line : minimal distortion pathway between the reference shapes). Inset: detail of the lanthanide coordination geometry (bonding color code same as Figure 3.37).

The four lanthanide atoms in each **9-Ln** anion display highly distorted eight-coordinated geometries that have been analyzed through Continuous Shape Measures (CShM).⁷² For the lanthanide atoms located in belt positions (5/25, 8/28), CShM values in the 0.81–1.02 range have been obtained with the triangular dodecahedron (DD) as the reference shape, while comparison with any other eight-coordinated reference polyhedron results in significantly higher values (above 2.00, Table 3.11). This indicates that the coordination geometry of these 4f ions is best described as triangular dodecahedral, though certainly distorted from ideality. On the contrary, close CShM values relative to the DD and the biaugmented trigonal prism (BTP) shapes are observed for the lanthanide atoms in the bottom-triad position 21, precluding initial discrimination between both geometries (1.24–1.52 vs. 1.23–1.44, CShM values with other reference shapes being above 2.32). Lanthanides in position 1 would represent an intermediate stage. Nevertheless, the DD vs. BTP shape map (Figure 3.40) shows that the mid-to late 4f ions in **9-Ln** and **10-Ln** scatter from the ideal DD geometry toward the BTP one following the trend marked by the minimal distortion pathway between the two reference polyhedra with path deviation values in the 0.22–0.38 range (around the upper limit of 0.3 selected by Casanova et al.). This confirms that the best description for the mid-to late lanthanide coordination geometries in **9-Ln** and **10-Ln** is triangular dodecahedral distorted toward bicapped trigonal prismatic.

Table 3.11. Continuous Shape Measures for the eight-coordinated spheres of the lanthanide atoms in compounds **9-Ln** (Ln = Dy to Lu) and **10-Ln** (Ln = Ho to Lu)^[a]

9-Ln					10-Ln				
	SD	J-BTP	DD	SAPR		SD	J-BTP	DD	SAPR
Dy1	2.720	1.677	0.999	2.687					
Dy8	2.082	2.468	0.842	2.368					
Dy21	2.835	1.255	1.506	2.359					
Dy28	2.136	2.502	0.864	3.069					
Ho1	2.644	1.643	0.946	2.637	Ho1	2.739	1.547	1.470	2.964
Ho8	2.090	2.445	0.808	2.404	Ho5	2.153	2.140	0.616	3.340
Ho21	2.718	1.226	1.458	2.316	Ho21	2.265	2.286	0.532	3.066
Ho28	2.098	2.366	0.845	3.194	Ho25	2.049	2.059	0.881	3.466
Er1	2.800	1.752	0.969	2.558	Er1	2.307	1.883	0.872	3.219
Er8	2.873	2.313	0.830	2.638	Er8	2.139	2.547	0.879	2.444
Er21	2.455	1.444	1.238	2.609	Er21	2.476	1.900	0.978	2.877
Er28	2.360	2.454	0.932	3.180	Er28	2.110	2.159	0.898	3.592
Tm1	2.331	1.859	0.808	2.958	Tm1	2.663	1.459	1.464	2.913
Tm5	2.164	2.462	0.859	2.133	Tm5	2.100	2.050	0.660	3.249
Tm21	2.728	1.241	1.520	2.386	Tm21	2.242	2.432	0.532	3.235
Tm25	2.005	2.196	0.972	3.503	Tm25	2.007	2.046	0.895	3.408
Yb1	2.352	1.896	0.758	2.918	Yb1	2.673	1.504	1.438	2.911
Yb5	2.218	2.453	0.837	2.126	Yb5	2.148	2.015	0.686	3.255
Yb21	2.700	1.274	1.449	2.459	Yb21	2.198	2.328	0.535	3.104
Yb25	2.045	2.262	0.985	3.428	Yb25	1.988	2.116	0.850	3.320
Lu1	2.344	1.911	0.730	2.952	Lu1	2.568	1.483	1.375	2.914
Lu5	2.146	2.456	0.831	2.197	Lu5	2.063	1.960	0.672	3.146
Lu21	2.512	1.344	1.397	2.466	Lu21	2.185	2.255	0.541	3.060
Lu25	2.009	2.174	1.015	3.566	Lu25	1.912	2.023	0.850	3.387

[a] *Abbreviations.* **SD**: snub disphenoid (D_{2d}); **J-BTP**: Johnson biaugmented trigonal prism (C_{2v}); **DD**: triangular dodecahedron (D_{2d}); **SAPR**: square antiprism (D_{4d}). For a graphical representation of these polyhedra, see Figure A2.17 in Appendix 2. Values highlighted in grey correspond to the best geometry.

This type of geometry originates from in-pocket coordination modes of the 4f ions toward the divacant $\{\beta\text{-GeW}_{10}\text{O}_{38}\}$ skeleton. In addition to the four O atoms delimiting each vacant site (O_L), the 4f ions also coordinate to the corresponding central O atom from the GeO_4 group (O_C), resulting in mean Ln...W distances inside the mixed $\{\text{LnW}_2\}$ edge-sharing trimers that decrease from 3.554 Å for **9-Dy** to 3.512 Å for **9-Lu**. For comparison, the analogous mean Ce...W distance is 3.749 Å in **8-Ce** showing out-of-pocket coordinated Ce atoms with square-antiprismatic geometries. Therefore, the lanthanide atoms could be seen as incorporated into the β -Keggin framework with three external coordination sites occupied by the bridging O atom from the neighboring subunit (O_b), one terminal aqua ligand (O_{wt}) and one loosely bound water molecule acting as additional linkage between lanthanides (O_{wb}). Considering the latter as an effective bridge, the dinuclear lanthanide fragments in the $\{\text{Ln}_4\}$ central cores should then be described as formed by two face-sharing LnO_8 triangular dodecahedra. Bond Valence Sum calculations⁸⁵ indicate that the identified terminal and bridging water molecules are the only protonation sites and this is fully consistent with the number of Na cations determined from elemental analyses.

Table 3.12. Ranges and mean lanthanide–oxygen bond lengths (Å) in compounds **9-Ln** and **10-Ln**^[a]

	Ln–O _L	Ln–O _b	Ln–O _{wt}	Ln–O _c	Ln–O _{wb}
9-Lu	2.180(11)–2.297(12)	2.279(11)–2.306(11)	2.279(11)–2.321(11)	2.509(10)–2.542(10)	2.505(12)–2.728(11)
	2.246	2.292	2.297	2.526	2.624
10-Lu	2.166(9)–2.285(9)	2.273(8)–2.323(9)	2.256(10)–2.314(10)	2.515(8)–2.554(8)	2.465(9)–2.675(9)
	2.239	2.300	2.281	2.538	2.570
9-Yb	2.184(9)–2.294(11)	2.272(9)–2.311(10)	2.304(11)–2.239(10)	2.517(10)–2.553(10)	2.520(11)–2.724(10)
	2.249	2.289	2.318	2.536	2.628
10-Yb	2.178(10)–2.295(10)	2.281(9)–2.318(10)	2.289(9)–2.345(11)	2.517(9)–2.558(11)	2.475(10)–2.681(10)
	2.247	2.306	2.313	2.542	2.583
9-Tm	2.200(8)–2.300(8)	2.292(8)–2.323(8)	2.313(9)–2.347(8)	2.529(8)–2.571(8)	2.536(9)–2.729(8)
	2.257	2.310	2.326	2.554	2.634
10-Tm	2.193(9)–2.306(10)	2.281(9)–2.336(9)	2.277(11)–2.355(11)	2.539(9)–2.561(10)	2.476(9)–2.688(9)
	2.257	2.310	2.310	2.553	2.588
9-Er	2.15(2)–2.34(2)	2.34(3)–2.36(3)	2.31(2)–2.35(2)	2.51(2)–2.52(2)	2.52(2)–2.69(2)
	2.29	2.30	2.33	2.51	2.62
10-Er	2.19(3)–2.32(3)	2.34(3)–2.36(3)	2.30(3)–2.39(4)	2.52(3)–2.59(3)	2.56(3)–2.72(3)
	2.27	2.35	2.34	2.55	2.62
9-Ho	2.218(9)–2.340(10)	2.304(9)–2.359(9)	2.328(10)–2.374(9)	2.514(9)–2.594(9)	2.579(10)–2.704(10)
	2.281	2.323	2.350	2.554	2.642
10-Ho	2.209(12)–2.327(12)	2.297(11)–2.354(12)	2.280(12)–2.383(14)	2.534(11)–2.565(12)	2.505(11)–2.698(12)
	2.276	2.329	2.327	2.554	2.600
9-Dy	2.241(10)–2.362(10)	2.312(10)–2.362(11)	2.356(11)–2.380(10)	2.534(10)–2.601(10)	2.576(11)–2.694(10)
	2.291	2.339	2.370	2.570	2.638

[a] *Abbreviations.* O_L: O atoms delimiting the vacant site to which the 4f ion is incorporated; O_b: bridging O_{POM} atom between lanthanides; O_{wt}: O atom from a terminal aqua ligand (or an adjacent WO₆ octahedron for **10-Ln**); O_c: central O atom from the {GeO₄} group; O_{wb}: bridging water molecule between lanthanides.

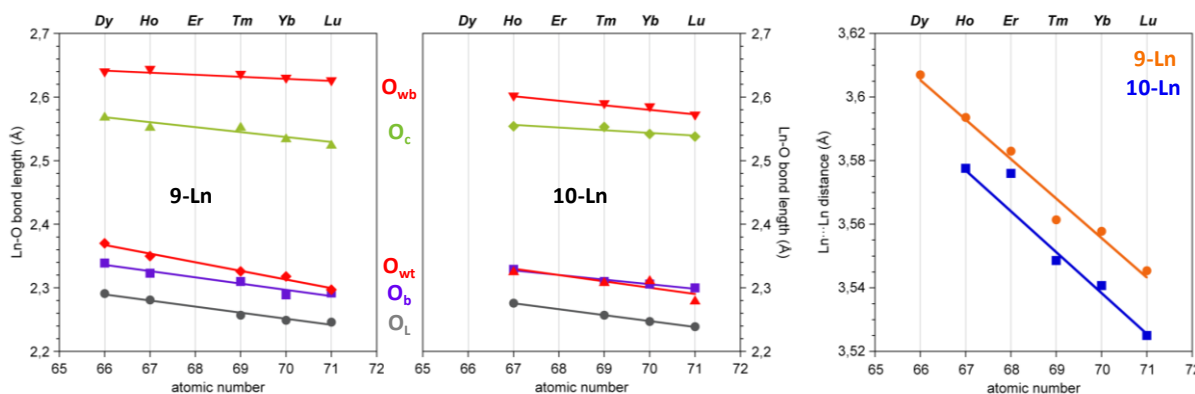


Figure 3.41. Variation of the mean lanthanide–oxygen bond lengths (Er derivatives not represented due to the low precision of the data) and lanthanide–lanthanide distances between adjacent $\{\beta\text{-Ln}_2\text{GeW}_{10}\}$ subunits (see Appendix 3) with the atomic number for compounds **9-Ln** and **10-Ln**. For the abbreviations O_L, O_b, O_{wt}, O_c, O_{wb}, see the footnote in Table 3.12.

The Ln–O bonding (Table 3.12. and Appendix 3) is composed of six short bonds with O_{POM} atoms (O_L and O_b) and the terminal aqua ligand, one long bond with the central O atom and one long or very long bond with the bridging water molecule. The linkage mode of this molecule is

asymmetrical, being more closely coordinated to one of the 4f ions than to the other at distances of c.a. 2.50 vs. 2.70 Å, respectively. The Ln–O bond lengths follow the order $\text{Ln–O}_L < \text{–O}_b < \text{–O}_{wt} \ll \text{–O}_c < \text{–O}_{wb}$ as shown in Figure 3.37, though differences between the three types of short bonds are subtle. As pointed out for other series of lanthanide-containing anions like Peacock-Weakley sandwich-type species,¹⁰ the Ln–O bond lengths tend to linearly decrease with increasing the lanthanide atomic number due to the well-known contraction effect in rare-earth metals, but variations in this series do not exceed 0.1 Å. It is worth mentioning that while those bonds involving O atoms of $\{\beta\text{-GeW}_{10}\text{O}_{38}\}$ skeletons (O_L , O_b , O_c) show parallel decreasing trends when going from Dy to Lu, the Ln– O_{wt} bonds undergo more pronounced shortening and the Ln– O_{wb} bonds remain nearly constant through the series.

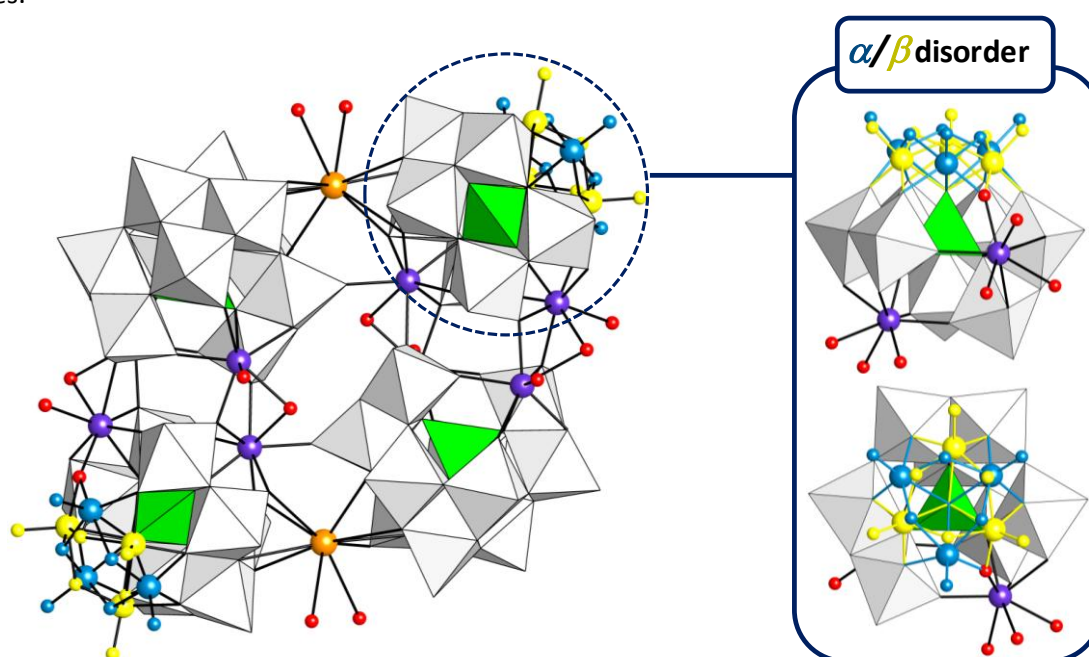


Figure 3.42. Centrosymmetric $[\{\text{Ln}_4(\text{H}_2\text{O})_5(\text{GeW}_{10}\text{O}_{38})_2\}_2]^{24-}$ tetrameric POM as determined from single-crystal X-ray diffraction data for compounds **10-Ln** (Ln = Ho to Lu), together with a detail in ball & stick model of the α/β disorder observed for one of the $\{\text{Lu}_2\text{GeW}_{10}\}$ subunits in **10-Lu** (50% probability displacement ellipsoids). Color code: Tungsten atoms, W–O bonds and WO_6 octahedra of the disordered $\{\text{W}_3\text{O}_{13}\}$ cap are depicted in blue for the $\{\alpha\text{-Ln}_2\text{GeW}_{10}\}$ form and in yellow for the corresponding β -form.

Molecular structure of the **10-Ln** anions

The tetrameric polyanions $[\{\text{Ln}_4(\text{H}_2\text{O})_5(\text{GeW}_{10}\text{O}_{38})_2\}_2]^{24-}$ (**10-Ln**, Ln = Ho to Lu) can be seen as the product of the Cs-directed assembly of two dimeric $[\text{Ln}_4(\text{H}_2\text{O})_6(\text{GeW}_{10}\text{O}_{38})_2]^{12-}$ entities, resulting in a centrosymmetric architecture with diamond-like shape and diagonals of c.a. 2.5×2.1 nm (Figure 3.42). The dimeric halves are closely related to the **9-Ln** anions and they assemble via two Ln–O=W linkages formed by replacement of one terminal aqua ligand on each half with the terminal O atom of a belt- WO_6 octahedron from the adjacent dimer. This association is reinforced by two Cs ions inserted in the clefts formed between the assembled dimers.

There are some remarkable differences between the dimeric halves of **10-Ln** and the dimeric **9-Ln** anions. Despite containing $\{\beta\text{-Ln}_2\text{GeW}_{10}\}$ subunits like in **9-Ln**, one of the two crystallographically independent subunits in all **10-Ln** compounds displays significant disorder in the rotated $\{\text{W}_3\text{O}_{13}\}$ cap (Figure 3.42). This crystallographic disorder arises from contribution of a $\{\text{W}_3\text{O}_{13}\}$ trimer back-rotated

by 60° , i.e. from contribution of the corresponding α -isomer for the $\{\text{GeW}_{10}\text{O}_{38}\}$ skeleton. Back-rotation of the cap for the $\beta(1,5)$ and $\beta(1,8)$ subunits results in the $\alpha(1,5)/\alpha(1,8)$ pair of C_2 -symmetric enantiomers following the IUPAC rule, which is commonly encompassed in Pope & Scully's $\alpha(1,4)$ notation.

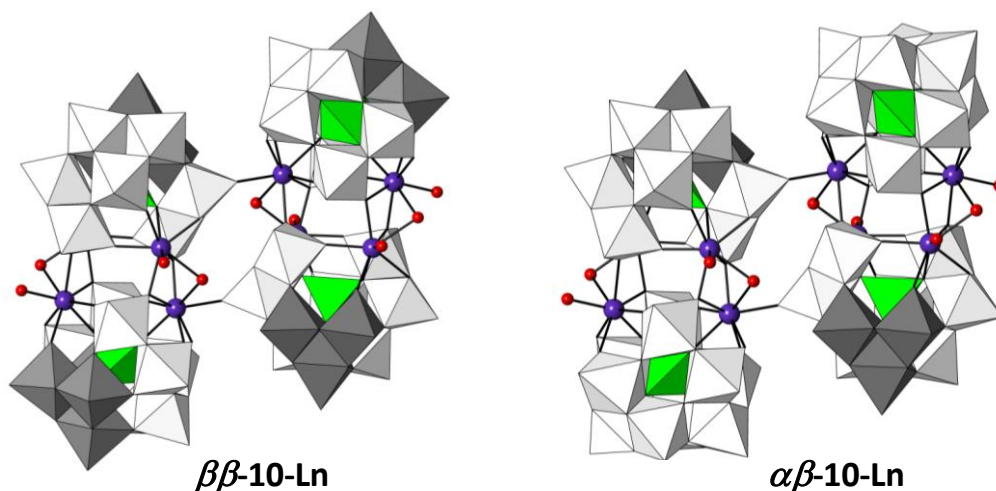


Figure 3.43. Individual representations of the two types of tetrameric POMs coexisting in each **10-Ln** crystal.

According to the structural data, there is no clear predominance of one of the isomers in this α/β disorder, but the population factors observed for the α - and β -caps indicate that the α form tends to be favored over the β -one when going from Ho to Lu. The α -form represents the minor fraction for Ln = Ho and Er (α/β ratio of c.a. 40/60) but becomes the major one for Ln = Lu (c.a. 60/40), the compounds where Ln = Tm and Yb exemplifying the situation where contributions of both isomeric forms are nearly equivalent. This disorder evidences that two types of tetrameric assemblies of $\{\text{Ln}_2\text{GeW}_{10}\}$ subunits coexist in each **10-Ln** crystal: one is a full $\beta\beta$ -**10-Ln** architecture with dimeric halves composed of either $\beta(1,5)$ or $\beta(1,8)$ clusters, whereas the other one is a mixed $\alpha\beta$ -**10-Ln** assembly where each half contains one of these β -subunits linked to its corresponding $\{\alpha\text{-Ln}_2\text{GeW}_{10}\}$ derivative (Figure 3.43).

Another significant difference between the dimeric halves in the architecture of **10-Ln** and the **9-Ln** anions is that the Ln–O(WO₅)–Ln bridges in the former are established between two lanthanides located either in the belt or in the bottom-triad, whereas both types of 4f centers are involved in each of these linkages for the latter. As a result, the subunits assemble with the rotated $\{\text{W}_3\text{O}_{13}\}$ caps facing opposite sides of the dimeric half in **10-Ln** POMs, whereas for the **9-Ln** species both caps reside in the same side of the assembly. Nevertheless, the $\{\text{Ln}_4\}$ central cores for both $\beta\beta$ - and $\alpha\beta$ -**10-Ln** architectures are virtually identical to those observed for **9-Ln** anions regardless of the differences in isomeric forms and their linkages. Overall, the Ln–O bonding follows the same trends as the ones described for **9-Ln** anions with nearly equivalent Ln–O_{wt} and Ln–O_b bonds and a more efficient bridging role of the loosely bound water molecule. Moreover, face-to-face association between subunits in **10-Ln** appears to be stronger than in **9-Ln** as indicated by the systematically shorter intradimeric Ln...Ln distances observed for the whole series (Appendix 4). As expected, these distances tend to decrease linearly as the lanthanide becomes heavier, so that parallel trends have been found for dimeric and tetrameric species (Figure 3.41).

Solution stability of 9-Ln and 10-Ln anions

Structural analysis of **9-Ln** anions reveals that the four Ln–O_b bonds linking the two Ln₂ subunits in a dimeric species are very similar in length to the Ln–O_l bonds involving the 4f ions and the { β -GeW₁₀O₃₈} skeleton to which they are incorporated. This might indicate that the association between subunits in **9-Ln** anions is strong, hence it could be expected that the dimeric assembly maintains its integrity in solution. On the contrary, only two Ln–O=W linkages bring the two **9-Ln**-like dimeric halves together in the **10-Ln** anions, in such a way that fragmentation of the tetrameric assembly upon dissolution seems plausible unless coordination of the Cs⁺ ions in the clefts plays an effective stabilizing role. To ascertain the accuracy of these preliminary appreciations, we decided to explore the stability of **9-Ln** and **10-Ln** anions in solution by a combination of ESI-MS and ¹⁸³W-NMR experiments and selected the Ho-derivatives as representative members of the whole series for this purpose.

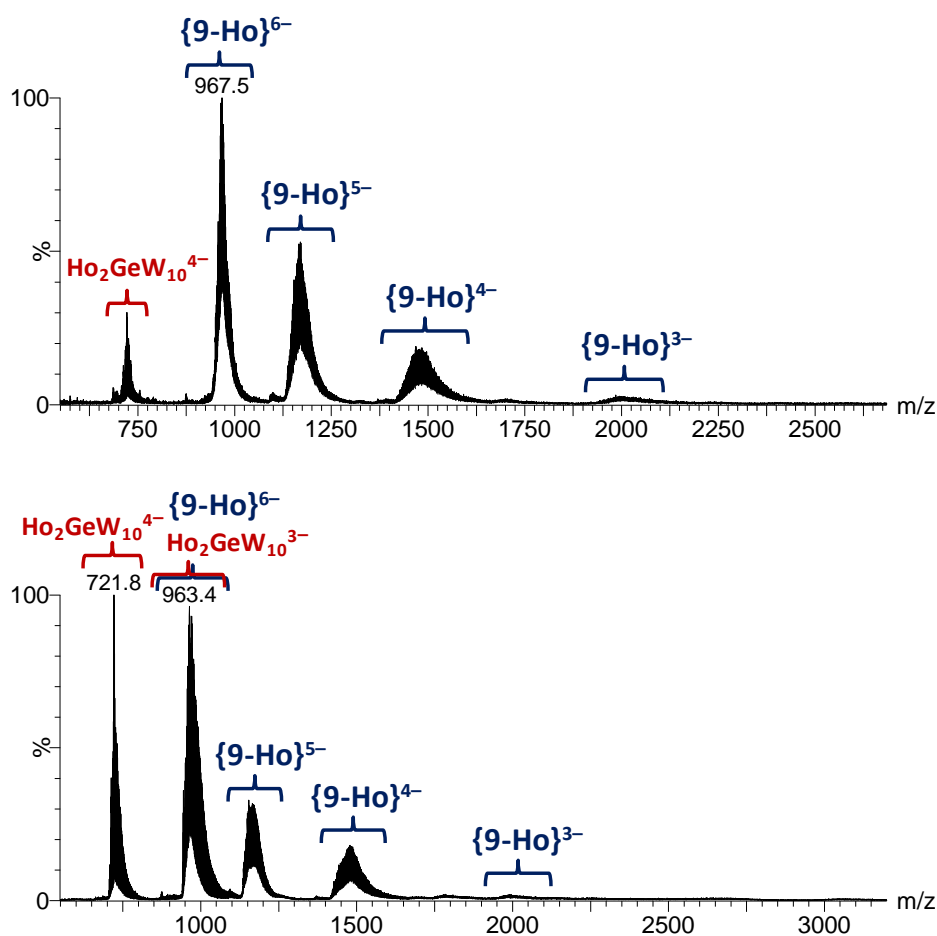


Figure 3.44. Negative ESI mass spectrum of H₂O:CH₃CN (1:1) solutions of **9-Ho** ($U_c = 15$ V). Top: freshly prepared sample. Bottom: solution aged 5 days in air (note that dimeric **9-Ho** and monomeric {Ho₂GeW₁₀} species are overlapped in the m/z 940–995 range). {Ho₂GeW₁₀}⁽⁶⁻ⁿ⁾⁻ = [Ho₂GeW₁₀O₃₈+xH₂O+mH⁺+(n-m)Na⁺]⁽⁶⁻ⁿ⁾⁻; {**9-Ho**}⁽¹²⁻ⁿ⁾⁻ = [Ho₄(GeW₁₀O₃₈)₂+xH₂O+mH⁺+(n-m)Na⁺]⁽¹²⁻ⁿ⁾⁻.

Figure 3.44 shows the negative ESI mass spectra of a H₂O:CH₃CN (1:1) solution of **9-Ho** recorded at low cone voltage. For the freshly prepared sample (top), the intact dimeric **9-Ho** anion can be clearly identified as four groups of signals spanning in the m/z 900–2150 range. The isotopic pattern inspection (Figure 3.45), together with the m/z spacing between the groups of signals, indicate that the detected anionic species display similar composition with charge states of 6– (m/z

967.5, {**9-Ho**}⁶⁻, 5- (m/z 1170.6, {**9-Ho**}⁵⁻, 4- (m/z 1477.2, {**9-Ho**}⁴⁻) and 3- (m/z 1997.6, {**9-Ho**}³⁻). The most abundant group of signals is centered at m/z 967.5 and formally corresponds to the series of anions of general formula $[\text{Ho}_4(\text{GeW}_{10}\text{O}_{38})_2 + x\text{H}_2\text{O} + m\text{H}^+ + (6-m)\text{Na}^+]^{6-}$. Analogously, the group of signals at m/z 1170.6, 1477.2 and 1997.6 can be readily assigned to the $[\text{Ho}_4(\text{GeW}_{10}\text{O}_{38})_2 + x\text{H}_2\text{O} + m\text{H}^+ + (7-m)\text{Na}^+]^{5-}$, $[\text{Ho}_4(\text{GeW}_{10}\text{O}_{38})_2 + x\text{H}_2\text{O} + m\text{H}^+ + (8-m)\text{Na}^+]^{4-}$ and $[\text{Ho}_4(\text{GeW}_{10}\text{O}_{38})_2 + x\text{H}_2\text{O} + m\text{H}^+ + (9-m)\text{Na}^+]^{3-}$ series, respectively.

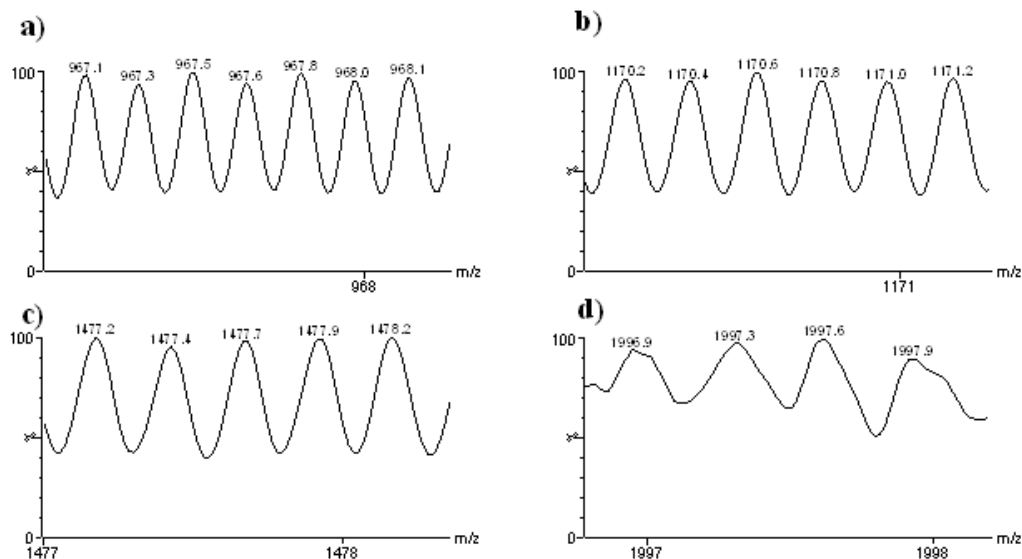


Figure 3.45. Expanded region of the group of signals observed in the negative ESI mass spectrum of **9-Ho** illustrating the 6- charge state in a), 5- in b), 4- in c) and 3- in d).

Compound **10-Ho** was investigated at identical concentration and mass spectrometric conditions (Figure 3.46). The negative ESI mass spectrum of **10-Ho** is very much alike to that observed for **9-Ho**, except that the groups of signals are slightly shifted to higher m/z values because of the presence of Cs^+ ions in addition to Na^+ . No experimental evidence of species larger than a dimer was obtained. These observations strongly suggests that the tetrameric **10-Ho** assembly determined by single crystal X-ray diffraction is not preserved in solution and fragments to the corresponding **9-Ho**-like dimeric halves upon dissolution. We also performed additional ESI-MS experiments using more concentrated **10-Ho** samples (up to 5×10^{-4} M), lower desolvation temperatures and lower cone voltages to rule out that the tetramer to dimer dissociation occurs during the ESI process, but the presence of tetrameric anions was not detected in any case.

The spectra of both **9-Ho** and **10-Ho** also show an additional set of signals of weak intensity in the m/z 675–775 range that were assigned to the contribution of a small fraction of monomeric $\{\text{Ho}_2\text{GeW}_{10}\}$ anions. Such species might originate from the ESI process, but could also be indicative of slow fragmentation of the dimeric species present in solution. Taking advantage of the versatility of ESI-MS for solution studies in POM chemistry,⁸⁶ we tracked the stability of the {**9-Ho**} species for a period of time of three weeks. For this purpose, 10^{-3} M aqueous solutions of **9-Ho** and **10-Ho** were allowed to stand in air and aliquots of these stock solutions were extracted every 24 hours, diluted with a $\text{H}_2\text{O}:\text{CH}_3\text{CN}$ (1:1) mixture of solvents and analyzed by ESI-MS as described above. In both cases, we observed a significant increase in the intensity of the above signal after 5 days, together with the appearance of a second group of signals at m/z values near those of the {**9-Ho**}⁶⁻ series. For

example, the ESI mass spectrum of **9-Ho** revealed two groups of signals that correspond to the anions $[\text{Ho}_2(\text{GeW}_{10}\text{O}_{38})+x\text{H}_2\text{O}+m\text{H}^++(2-m)\text{Na}^+]^{4-}$ ($\{\text{Ho}_2\}^{4-}$, m/z 721.8) and $[\text{Ho}_2(\text{GeW}_{10}\text{O}_{38})+x\text{H}_2\text{O}+m\text{H}^++(3-m)\text{Na}^+]^{3-}$ ($\{\text{Ho}_2\text{GeW}_{10}\}^{3-}$, m/z 964) as shown in Figure 3.46. After 3 weeks, both **9-Ho** and **10-Ho** solutions remained stable in terms of the relative ratio of monomeric and dimeric species. These observations indicate that $\{\text{Ho}_4\}$ anions undergo partial dissociation to $\{\text{Ho}_2\text{GeW}_{10}\}$ species in solution and that slow dimer to monomer equilibration is achieved after a few days.

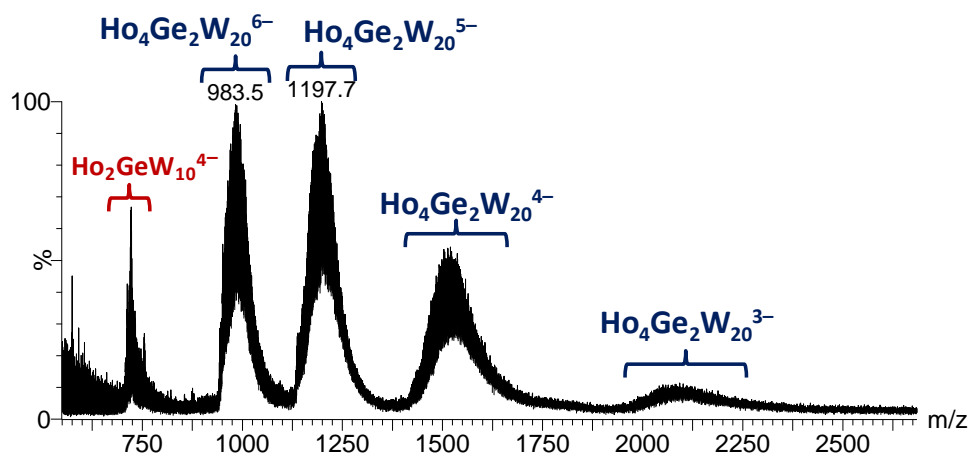


Figure 3.46. Negative ESI mass spectrum ($U_c = 15$ V) of freshly prepared $\text{H}_2\text{O}:\text{CH}_3\text{CN}$ (1:1) solutions of **10-Ho**. $\{\text{Ho}_2\text{GeW}_{10}\}^{(6-n)-} = [\text{Ho}_2(\text{GeW}_{10}\text{O}_{38})+x\text{H}_2\text{O}+m\text{H}^++(n-m)\text{Cs}^+/\text{Na}^+]^{(6-n)-}$; $\{\text{Ho}_4\text{Ge}_2\text{W}_{20}\}^{(12-n)-} = [\text{Ho}_4(\text{GeW}_{10}\text{O}_{38})_2+x\text{H}_2\text{O}+m\text{H}^++(n-m)\text{Cs}^+/\text{Na}^+]^{(12-n)-}$.

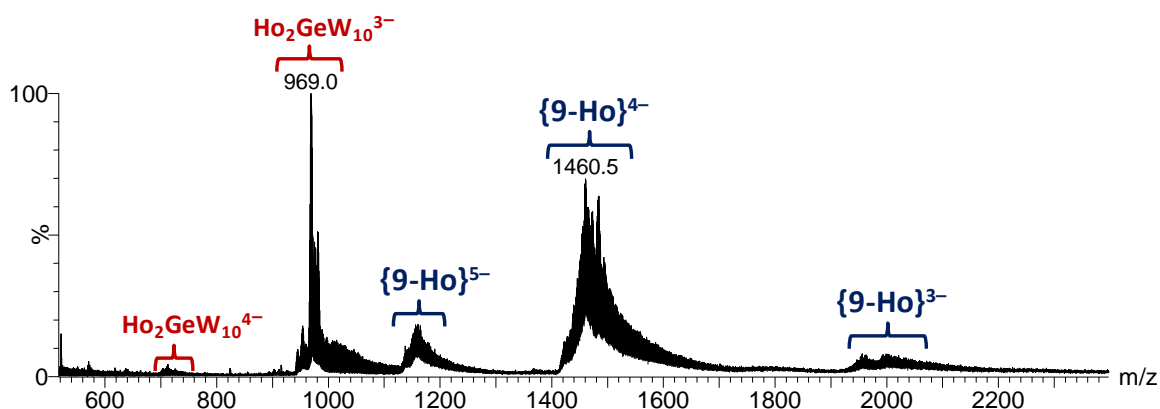


Figure 3.47. Negative ESI mass spectrum ($U_c = 15$ V) of $\text{H}_2\text{O}:\text{CH}_3\text{CN}$ (1:1) solutions of **9-Ho** prepared from an aqueous 10^{-3} M stock solution allowed to stand in air for 3 weeks. $\{\text{Ho}_2\text{GeW}_{10}\}^{(6-n)-} = [\text{Ho}_2(\text{GeW}_{10}\text{O}_{38})+x\text{H}_2\text{O}+m\text{H}^++(n-m)\text{Na}^+]^{(6-n)-}$; $\{\mathbf{9-Ho}\}^{(12-n)-} = [\text{Ho}_4(\text{GeW}_{10}\text{O}_{38})_2+x\text{H}_2\text{O}+m\text{H}^++(n-m)\text{Na}^+]^{(12-n)-}$.

It is also worth highlighting that a change in the relative intensities of the signals associated to both $\{\text{Ho}_2\text{GeW}_{10}\}$ and $\{\mathbf{9-Ho}\}$ anions is observed after 3 weeks, in such a way that those corresponding to the series $\{\mathbf{9-Ho}\}^{4-}$ and $\{\text{Ho}_2\text{GeW}_{10}\}^{3-}$ become the most intense to the detriment of the formerly predominant $\{\mathbf{9-Ho}\}^{6-}$ and $\{\text{Ho}_2\text{GeW}_{10}\}^{4-}$ (Figure 3.47). We speculate that this could be related to a second process taking place in solution, and more specifically, to β to α isomerization of $\{\text{Ho}_2\text{GeW}_{10}\}$ clusters followed by reassembly in $\alpha\alpha$ -derivatives of the **9-Ho** dimers similar to those reported by Li et al.⁸³ In fact, we were able to observe the co-crystallization of $\alpha\alpha$ -**9-Ln** derivatives as thick prisms when needle-like crystals of compounds **9-Ln** (Ln = Er, Tm, Yb) were stored in their mother liquors for 2–3 months. The $\alpha\alpha$ -**9-Ln** nature of these POMs has been established by single-

crystal X-ray diffraction⁸⁷ (Figure 3.48), but unfortunately, we could not isolate these phases with sufficient reproducibility to report them as a third series of lanthanide-containing POMs. It must be noted that: i) in contrast to the monoclinic $P2_1/n$ space group reported by Li et al., our $\alpha\alpha$ -**9-Ln** anions crystallize in the triclinic $P\bar{1}$ space group and this could be related to the fact that the asymmetric unit of our compounds contain $\alpha(1,5)$ - $\{\text{Ho}_2\text{GeW}_{10}\}$ subunits instead of the $\alpha(1,8)$ clusters (according to the IUPAC notation) observed by Li; ii) compared to the $\beta\beta$ -**9-Ln** anions, one of the Ln–O_{wb} bonds in the $\alpha\alpha$ -**9-Ln** derivatives is lengthened up to c.a. 3.0 Å, in such a way that one of the water molecules loses its bridging role forcing the 4f ions in position 1 to become seven-coordinated with monocapped trigonal prismatic geometry.

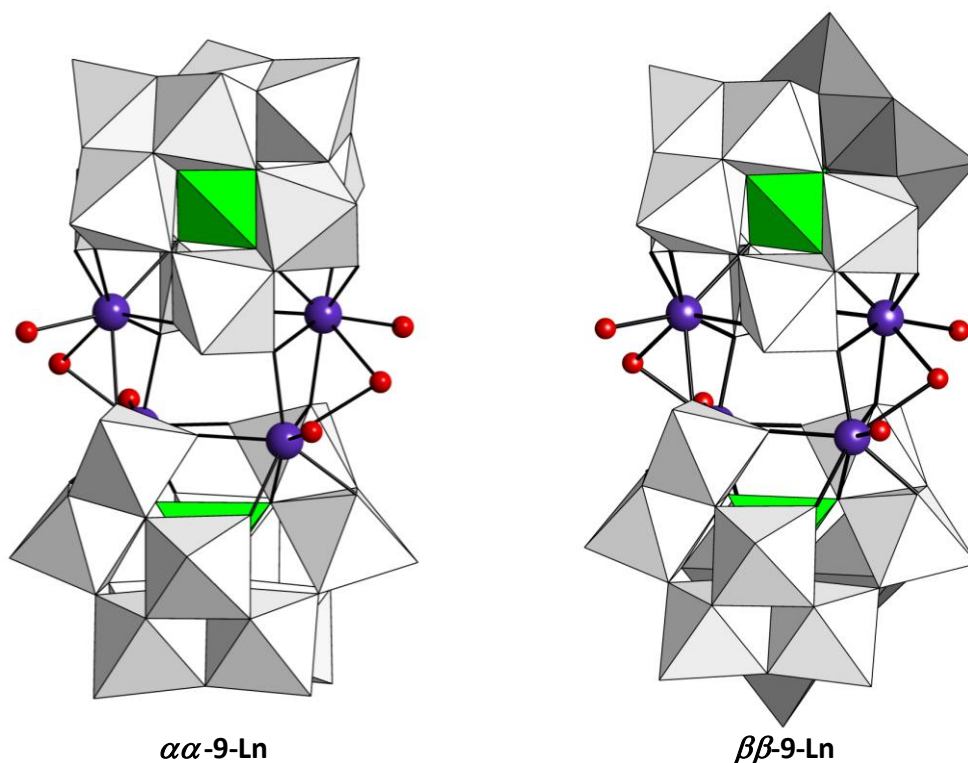


Figure 3.48. Representation of the $[\text{Ln}_2(\text{H}_2\text{O})_6(\alpha\text{-GeW}_{10}\text{O}_{38})_2]^{12-}$ POM derivatives ($\alpha\alpha$ -**9-Ln**, Ln = Er, Tm, Yb) and structural relationship between $\alpha\alpha$ - and $\beta\beta$ -**9-Ln** dimeric assemblies.

To get further insight on the solution stability of **9-Ln** dimers, we also performed ^{183}W -NMR studies on the diamagnetic **9-Lu** derivative (Figure 3.49). After c.a. 2 days of acquisition time, the spectrum shows a 10-line pattern spanning from δ –80 to –230 ppm (δ –79.9, –91.2, –113.9, –138.8, –146.0, –148.3, –161.1, –163.3, –221.1, –230.4 ppm). Assuming negligible influence on the NMR time scale of the asymmetrically bridging water molecules, this pattern would be consistent with the ten unique W centers in a **9-Lu** framework of ideal C_2 symmetry containing two equivalent $\{\beta\text{-Lu}_2\text{GeW}_{10}\}$ subunits. The spectrum also shows a poorly resolved signal (probably a doublet) of low intensity at δ –52.8 ppm, which might be attributed to the presence of a minor fraction of $\{\beta\text{-Lu}_2\text{GeW}_{10}\}$ monomers. As shown in Figure 3.37, only two of the ten unique WO_6 octahedra of a $\{\beta\text{-Ln}_2\text{GeW}_{10}\}$ subunit are involved in the face-to-face association into **9-Ln** dimers, i.e. positions 2/22 in the bottom-triad and 4/24 in the belt. The remaining octahedra would not be affected by dimerization, hence the environments of these W atoms in the $\{\beta\text{-Ln}_2\text{GeW}_{10}\}$ monomer should be almost identical to those in the **9-Ln** dimer. It is then plausible that the ^{183}W -NMR signals of eight out of the ten W atoms of the $\{\beta\text{-Lu}_2\text{GeW}_{10}\}$ monomer appear at δ values very similar to those of the corresponding W

centers in the **9-Ln** dimer, and consequently, they should be hidden in our spectrum. Only the signals of tungstens 2/22 and 4/24 should undergo significant shift when going from the **9-Lu** to the $\{\beta\text{-Lu}_2\text{GeW}_{10}\}$ species, and therefore, the poorly resolved doublet could be tentatively assigned to these atoms in the $\{\beta\text{-Lu}_2\text{GeW}_{10}\}$ monomer. This could also explain the differences in the relative intensities observed in the 10-line pattern because only two signals should exclusively originate from the **9-Lu** dimer, whereas the remaining eight should be due to contributions from both species. We have observed two weaker signals at δ -161.1 and -230.4 ppm that could be tentatively assigned to tungstens 2/22 and 4/24 in the **9-Lu** dimer.

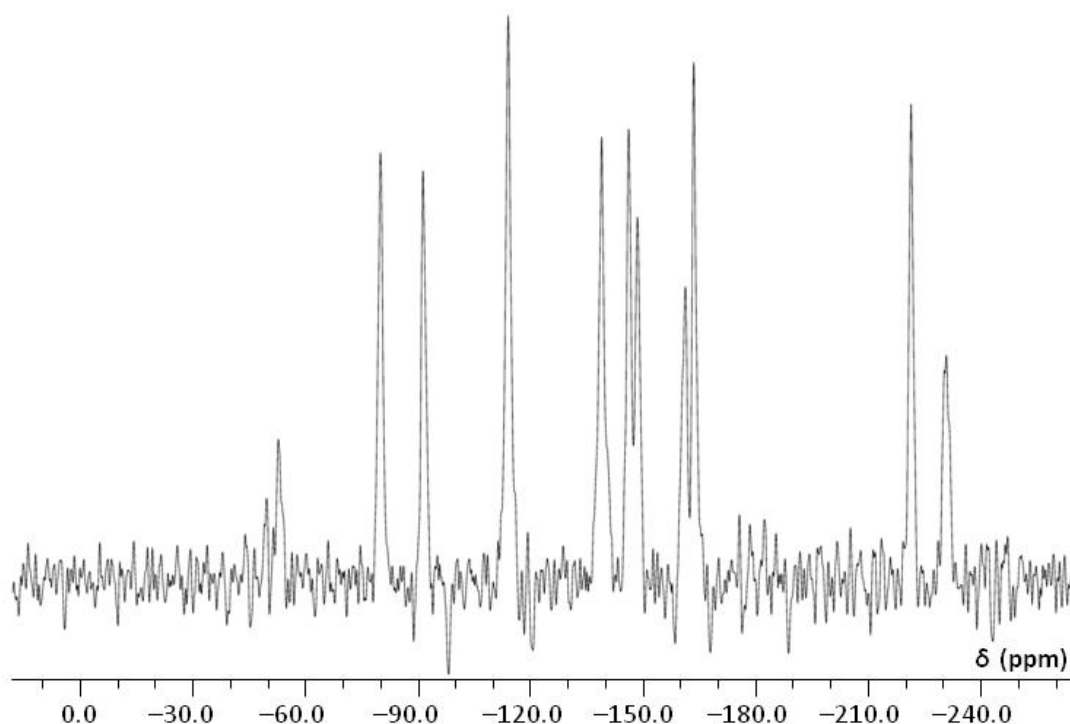


Figure 3.49. ^{183}W -NMR spectrum of **9-Lu** recorded on crystalline samples dissolved in NaOAc buffer solution (pH 4.8).

Magnetic properties of compounds 9-Ln

From a magnetic point of view, the $\{\text{Ln}_4\}$ cores in compounds **9-Ln** and **10-Ln** can be rationalized as two isolated $\text{Ln}_2(\mu\text{-OWO}_5)_2(\mu\text{-OH}_2)$ dinuclear moieties after assuming negligible magnetic exchange between lanthanide centers through the long O–W–O and O–Ge–O pathways^{15d} (Figure 3.37). Both dinuclear moieties in a $\{\text{Ln}_4\}$ core can be considered as magnetically equivalent according to the almost identical bonding geometry around the lanthanide atoms (see Appendix 4). Figure 3.50 shows the thermal dependence of the magnetic molar susceptibility (χ_m) and the $\chi_m T$ product for **9-Gd**, the only compound in the whole series whose magnetic properties can be analyzed through an isotropic spin Hamiltonian due to the absence of spin-orbit coupling in Gd^{3+} ions. The χ_m curve increases continuously when going from room temperature down to 5 K with no apparent maxima. This thermal variation of the susceptibility data obeys the Curie-Weiss law in the whole temperature range analyzed and the fit to the corresponding expression affords values of the Curie constant and Weiss temperature of $C_m = 31.31 \text{ cm}^3 \text{ K mol}^{-1}$ and $\theta = -1.00 \text{ K}$, the latter being indicative of weak antiferromagnetism in **9-Gd**.

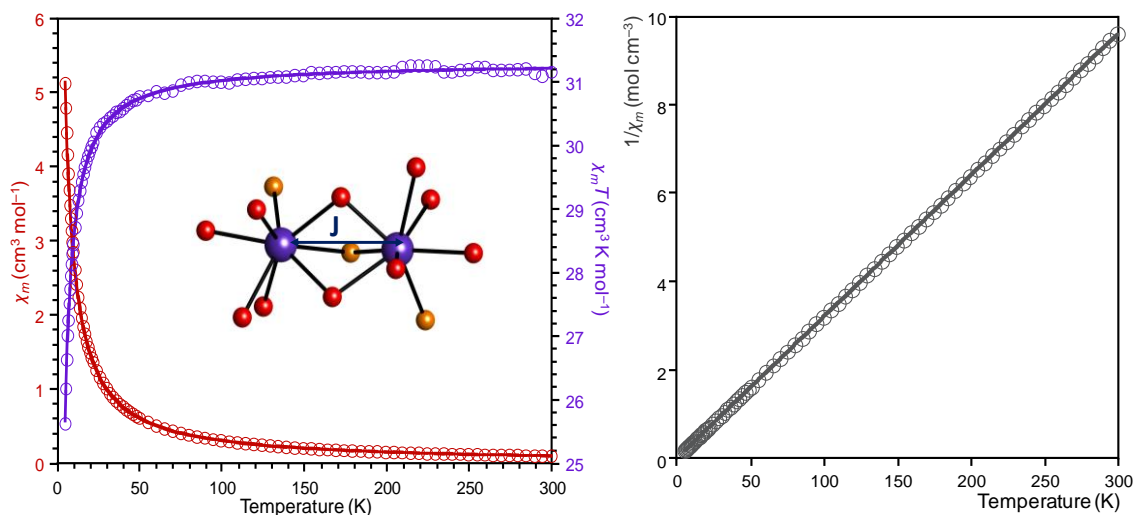


Figure 3.50. Left: Thermal evolution of χ_m and the $\chi_m T$ product for **9-Gd** (circles) and least-squares fit to the equation for dinuclear Gd^{3+} systems (continuous lines). Inset: Schematic representation of dinuclear $\text{Gd}_2(\mu\text{-OWO}_5)_2(\mu\text{-OH}_2)$ moieties. O_{POM} atoms in red. O atoms from water molecules in orange. Right: Fit of the magnetic susceptibility data to the Curie-Weiss law.

The $\chi_m T$ product at room temperature ($31.16 \text{ cm}^3 \text{ K mol}^{-1}$) is almost identical to that expected for four non-interacting Gd^{3+} ions per formula unit considering $S = 7/2$ and $g = 2.00$ ($31.52 \text{ cm}^3 \text{ K mol}^{-1}$). The $\chi_m T$ curve remains nearly constant down to temperatures around 50 K, below which undergoes drastic decrease to reach a value of $25.63 \text{ cm}^3 \text{ K mol}^{-1}$ at 5 K. Experimental data have been analyzed using the well-known equation for dinuclear gadolinium systems,⁸⁸ which expressed per metal atom and multiplied by the four Gd^{3+} ions in **9-Gd** is as follows,

$$\chi_m = 4 \left(\frac{N\beta^2 g^2}{kT} \right) \left(\frac{e^x + 5e^{3x} + 14e^{6x} + 30e^{10x} + 55e^{15x} + 91e^{21x} + 140e^{18x}}{1 + 3e^x + 5e^{3x} + 7e^{6x} + 9e^{10x} + 11e^{15x} + 13e^{21x} + 15e^{18x}} \right) \quad (\text{Eq. 3})$$

In this equation, x accounts for J/kT , N is the Avogadro number, β is the Bohr magneton, k is the Boltzmann constant, g is the Landé factor and J is the exchange coupling constant, which is defined by the Hamiltonian $H = -J S_{\text{Gd1}} S_{\text{Gd2}}$ ($S_{\text{Gd1}} = S_{\text{Gd2}} = 7/2$). Experimental data are very well reproduced with this equation and the best fit results are $J = -0.118 \text{ cm}^{-1}$ and $g = 1.993$, confirming the presence of weak antiferromagnetic interaction in the $\text{Gd}_2(\mu\text{-OWO}_5)_2(\mu\text{-OH}_2)$ dinuclear moieties of the $\{\text{Gd}_4\}$ core. To our knowledge, there is a lack in the literature of magnetic studies on POMs containing polynuclear moieties of $\text{O}(\text{WO}_5)$ -bridged Gd atoms, and therefore, comparison of our results to related magnetostructural models has been unfortunately not possible. Nevertheless, the magnitude of the calculated coupling constant is fully consistent with those observed for a number of dimeric complexes containing Gd^{3+} centers bridged by carboxylato or phenoxo ligands in different coordination modes.⁸⁹

The magnetic curves of the remaining **9-Ln** compounds ($\text{Ln} = \text{Tb}$ to Yb) are shown in Figure 3.51. Experimental values of the $\chi_m T$ product at room temperature are compared in Table 3.13 to those calculated using the formulae in Appendix 2, section A2.2.VII. Although the magnetic properties in this series of POMs are dominated by strong spin-orbit coupling, the values of the $\chi_m T$ product at room temperature are in general terms very close to those expected for four non-

interacting Ln^{3+} ions, as observed for **9-Gd** derivative. The $\chi_m T$ product undergoes continuous decrease with the temperature mainly due to the single-ion anisotropy, which precludes reliable identification of the exchange interactions. However, a significant increase is observed for the **9-Dy** and **9-Yb** derivatives at very low temperatures, suggesting the presence of ferromagnetic interactions.

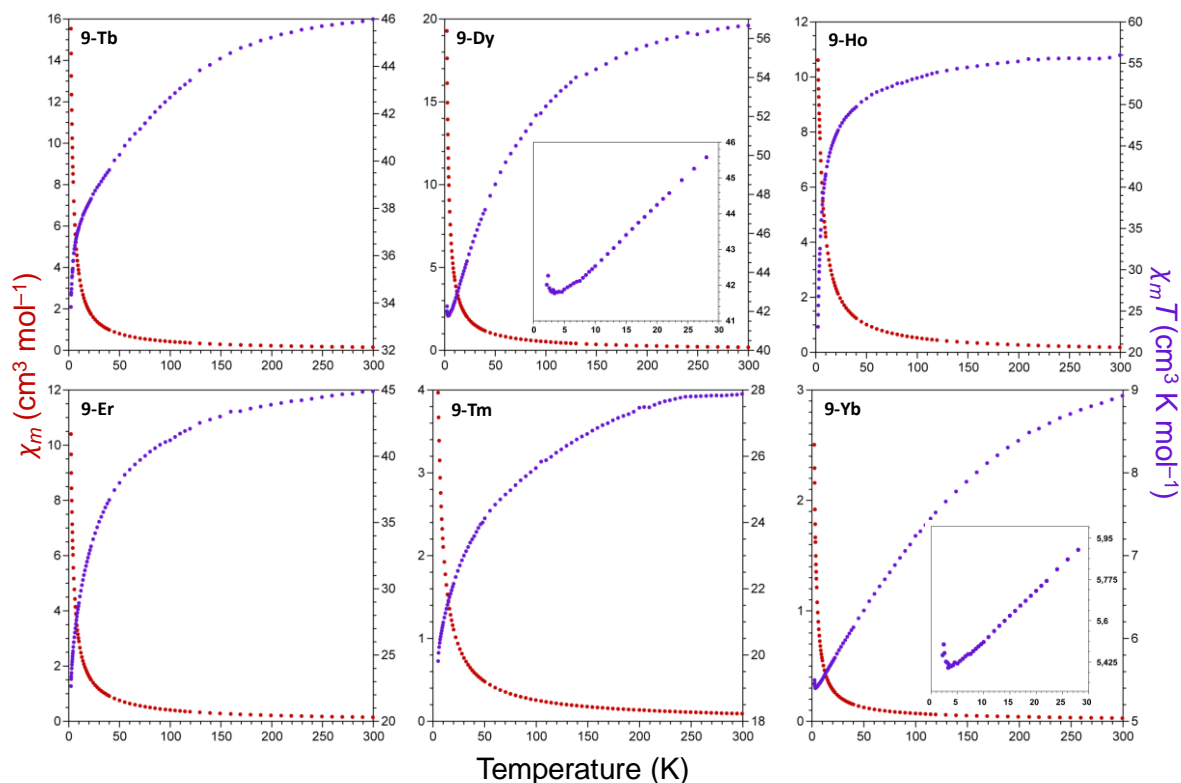


Figure 3.51. Thermal evolution of χ_m and the $\chi_m T$ product for compounds **9-Ln** ($\text{Ln} = \text{Tb}$ to Yb).

Table 3.13. Experimental and calculated $\chi_m T$ values at room temperature for **9-Ln** ($\text{Ln} = \text{Tb}$ to Yb).

	9-Tb	9-Dy	9-Ho	9-Er	9-Tm	9-Yb
$\chi_m T$ (300 K)						
Experimental	45.99	56.67	55.97	45.92	27.88	8.93
Calculated	47.28	56.72	56.28	44.90	28.65	10.29

Photoluminescent properties of 9-Tb and 9-Dy

As mentioned before for early-lanthanides, low photoluminescence quantum yields are usually obtained for Tb^{III} -, Sm^{III} - and Dy^{III} -containing POMs due to radiationless deactivation *via* Tb^{IV} - W^{V} charge transfer states for the former and to cross-relaxation for the latter, respectively. Room-temperature emission spectra for bulk solid samples of **9-Tb** and **9-Dy** are shown in Figure 3.45 and both display the characteristic profile of the corresponding Ln^{III} center. Compound **9-Tb** emits green luminescence and its spectrum shows four peaks with maxima at c.a. 489, 546, 590, 622 nm that correspond to well-known transitions from the $^5\text{D}_4$ excited state to the $^7\text{F}_J$ manifold, where $J = 6, 5, 4,$ and $3,$ respectively.²³ The spectrum of the yellow-emitting **9-Dy** displays three bands at 485, 573 and

663 nm that can be assigned to ${}^4F_{9/2} \rightarrow {}^6H_J$ transitions, where $J = 15/2, 13/2$ and $11/2$, respectively.^{15d,90} The fact that the peak originating from the hypersensitive ${}^4F_{9/2} \rightarrow {}^6H_{15/2}$ transition is not the principal in our spectrum indicates non-centrosymmetrical coordination geometries for the Dy centers, in good agreement with the structural data.⁹¹

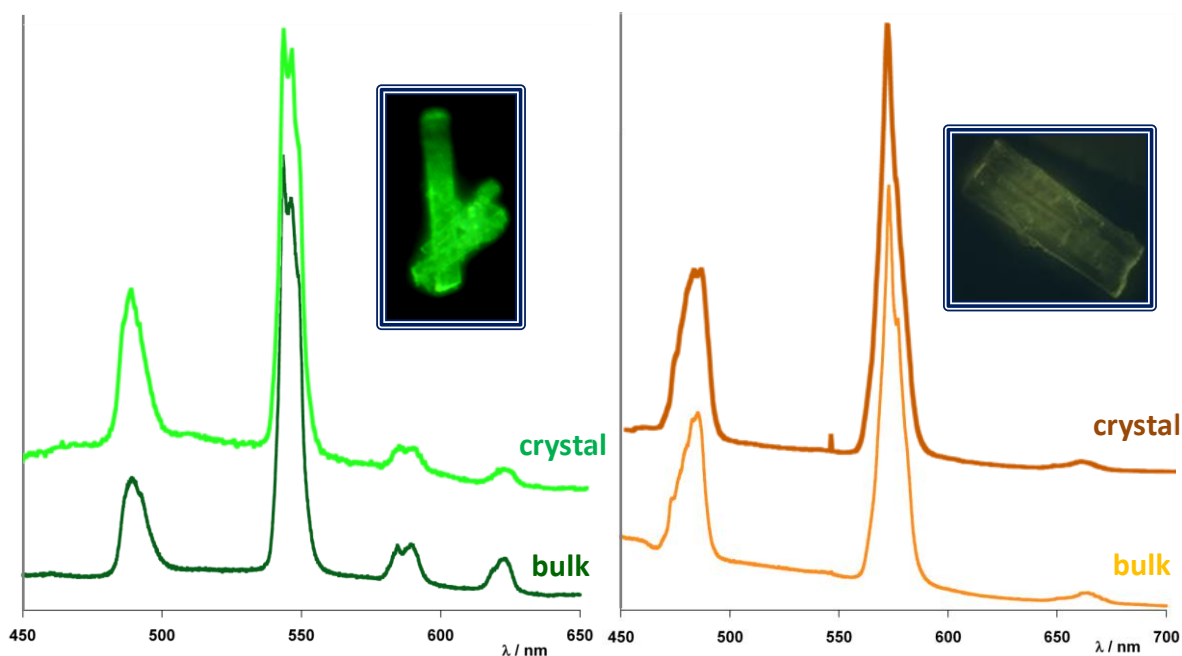


Figure 3.52. Room-temperature photoluminescence emission spectra ($\lambda_{\text{exc}} = 325$ nm) for bulk samples and specific crystals of **9-Tb** (left) and **9-Dy** (right). Insets: Photographs of green- and yellow-emitting crystals of **9-Tb** and **9-Dy**, respectively.

Emission spectra recorded for a specific group of crystals are virtually identical to those of the bulk solid for both compounds (Figure 3.52). The in-pocket coordination mode observed for the 4f ions in **9-Ln** anions allows Tb and Dy to become part of mixed $\{\text{LnW}_2\}$ trimers in the Keggin skeleton of the $\{\beta\text{-Ln}_2\text{GeW}_{10}\}$ subunits. Thus, each LnO_8 triangular dodecahedron shares edges with two WO_6 octahedra with $\text{Ln-O}_c\text{-W}$ and $\text{Ln-O}_l\text{-W}$ angles in the 92–94 and 118–120° ranges for **9-Dy** (similar values should be expected for the isostructural **9-Tb**). Corner-sharing with adjacent $\{\text{LnW}_2\}$ and $\{\text{W}_3\text{O}_{13}\}$ trimers ($\text{Ln-O}_l\text{-W} = 147\text{--}168^\circ$) and one WO_6 octahedron from the second $\{\beta\text{-Ln}_2\text{GeW}_{10}\}$ subunit ($\text{Ln-O}_b\text{-W} = 134\text{--}138^\circ$), together with the presence of two aqua ligands in the coordination sphere (responsible for nonradiative deactivation due to coupling with OH oscillators), appears to be insufficient to quench the Tb^{III} and Dy^{III} emitting centers in **9-Dy** and **9-Tb** anions.

3.5. CONCLUSIONS

This work nicely illustrates the potential of lanthanide-heteroatom-tungstate synthetic systems as dynamic libraries of building-blocks with the ability to undergo cation-directed self-assembly processes for constructing new POM architectures.

One-pot reactions carried out with early lanthanides (Ce to Sm) have resulted in a series of $[\beta\text{-Ln}_2\text{GeW}_{10}\text{O}_{38}]^{6-}$ or $[\gamma\text{-Ln}_2\text{GeW}_{10}\text{O}_{38}]^{6-}$ clusters, which consist of anti-Lipscomb type dilacunary Keggin fragments stabilized by the coordination of 4f ions to the vacant sites. In the presence of exclusively Na^+ as counterion, three $\beta(1,5)$ and three $\beta(1,8)$ enantiomerically-related subunits arrange

alternatively in a crown shaped $[\text{Na}\{\text{Ln}_2(\text{H}_2\text{O})_4(\beta\text{-GeW}_{10}\text{O}_{38})\}_6]^{35-}$ architecture (**6-Ln**, Ln = Pr, Nd). A similar assembly is obtained for Sm^{III} upon addition of K^+ , namely $[\text{K}\{\text{Sm}_2(\text{H}_2\text{O})_4(\beta\text{-GeW}_{10}\text{O}_{38})\}_6]^{35-}$ (**7-Sm**). In the case of Ln = Ce, Pr, Nd addition of K^+ results in giant dodecameric $[\text{K}\{\text{K}_7\text{Ln}_{24}\text{Ge}_{12}\text{W}_{120}\text{O}_{444}(\text{OH})_{12}(\text{H}_2\text{O})_{56}\}]^{52-}$ POMs (**8-Ln**), constructed by the incorporation via Ln–O–W bonds of six external $\gamma(3,4)$ subunits to a central K^+ -templated hexameric core analogous to that obtained for Sm. In all the structures, neighboring β -subunits are linked by 4f-metal atoms through Ln–O–Ln and Ln–O–W bridges, resulting in an internal Ln_6O_6 ring with a central cavity where one alkaline cation is trapped. The $[\text{Ni}^{\text{II}}(\text{H}_2\text{O})_6]^{2+}$ cation plays an essential role as crystallizing agent by establishing networks of $\text{O}_W\text{—H}\cdots\text{O}_{\text{POM}}$ hydrogen bonds. Regarding their solution behavior, compounds **8-Ln** dissociate upon dissolution in water into hexameric and monomeric entities, as identified by ESI-MS experiments. The former species can further self-assemble into supramolecular vesicle-like blackberry type nanostructures, as monitored by DLS and SLS techniques. Similar studies in water-acetone mixtures showed that the dodecameric **8-Nd** remains stable in solution and forms blackberries with sizes increasing with the acetone concentration.

The use of mid-to-late lanthanides (Gd to Lu) results in a series of $[\beta\text{-Ln}_2\text{GeW}_{10}\text{O}_{38}]^{6-}$ clusters stabilized by insertion of 4f ions in the vacant sites. In the presence of Na^+ , two β -subunits of either the $\beta(1,5)$ or the $\beta(1,8)$ type assemble via Ln–O(WO₅)–Ln bridges to form the chiral, dimeric $[\text{Ln}_4(\text{H}_2\text{O})_6(\beta\text{-GeW}_{10}\text{O}_{38})_2]^{12-}$ polyanions (**9-Ln**, Ln = Gd to Lu). When Cs^+ is added as crystallizing cation, two dimeric entities further assemble via Ln–O=W linkages to give the diamond-shaped $[\{\text{Ln}_4(\text{H}_2\text{O})_5(\text{GeW}_{10}\text{O}_{38})_2\}_2]^{24-}$ tetrameric assemblies (**10-Ln**, Ln = Ho to Lu). Two types of tetramers coexist in the solid state: one species shows a full $\beta\beta$ -**10-Ln** architecture based on the enantiomeric $\beta(1,5)/\beta(1,8)$ pair, whereas the other one is a $\alpha\beta$ -**10-Ln** mixed assembly where each of these β -subunits is linked to its corresponding α -derivative. Combination of ESI mass spectrometry and ^{183}W -NMR experiments indicates that **10-Ln** tetramers fragment into **9-Ln**-like dimers upon dissolution, which undergo partial dissociation into monomeric $\{\text{Ln}_2\text{GeW}_{10}\}$ anions and slow dimer to monomer equilibration. This is most likely followed by β to α isomerization of monomeric clusters and consequent reassembly in $\alpha\alpha$ -**9-Ln** dimers, as indicated by isolation of three additional $\alpha\alpha$ -**9-Ln** derivatives (Ln = Er to Yb). Regardless of differences in isomeric forms and relative arrangements, $\{\text{Ln}_2\text{GeW}_{10}\}$ subunits in all anions assemble to give virtually identical $\{\text{Ln}_4\}$ cores containing $\text{Ln}_2(\mu\text{-OWO}_5)_2(\mu\text{-OH}_2)$ moieties with antiferromagnetic exchange for **9-Gd**. According to Continuous Shape Measures, the *out-of-pocket* coordination mode of eight-coordinated early lanthanides in **6-Ln**, **7-Sm** and **8-Ln** results in 4f-metals centers with distorted square-antiprismatic geometry, whereas the *in-pocket* mode for mid-to-late lanthanides leads to geometries close to triangular dodecahedral.

The weak-emitting 4f ions are sensitized in the POM assemblies, in such a way that orange-red, green and yellow emission is observed for the **7-Sm**, **9-Tb** and **9-Dy** derivatives, respectively. In the case of **7-Sm**, only the inner 4f metals of the crown shaped-architecture are identified as efficient emitting centers due to their geometrical features.

3.6. REFERENCES

- [1] (a) Pope, M. T. *Handb. Phys. Chem. Rare Earths*; **2007**, *38*, 337. (b) Bassil, B. S.; Kortz, U. *Z. Anorg. Allg. Chem.* **2010**, *636*, 2222. (c) Granadeiro, C. M.; de Castro, B.; Balula, S. S.; Cunha-Silva, L. *Polyhedron* **2013**, *52*, 10.
- [2] Reinoso, S.; San Felices, L.; Gutiérrez-Zorrilla, J. M. in *Cerium. Molecular structure, technological applications and health effects*; Izyumov, A., Plaksin, G. Eds.; Nova Science Publishers: New York, NY, USA, 2013; 1-42.
- [3] (a) Peacock, R. D.; Weakley, T. J. R. *J. Chem. Soc. A* **1971**, 1836. (b) Iball, J.; Low, J. N.; Weakley, T. J. R. *J. Chem. Soc., Dalton Trans.* **1974**, 2021.
- [4] (a) Ozeki, T.; Takahashi, M.; Yamase, T. *Acta Crystallogr., Sect. C* **1992**, *48*, 1370. (b) Yamase, T.; Ozeki, T. *Acta Crystallogr.* **1993**, *C49*, 1577. (c) Ozeki, T.; Yamase, T. *Acta Crystallogr.* **1994**, *B50*, 128. (d) Yamase, T.; Ozeki, T.; Tosaka, M.; *Acta Crystallogr.* **1994**, *C50*, 1849.
- [5] Li, T.; Li, F.; Jian, L.; Lü, J.; Guo, Z.; Gao, S.; Cao, R. *Inorg. Chem.* **2008**, *47*, 5612.
- [6] Ismail, A. H.; Dickman, M. H.; Kortz, U. *Inorg. Chem.* **2009**, *48*, 1559.
- [7] Ismail, A. H.; Bassil, B. S.; Suchopar, A.; Kortz, U. *Eur. J. Inorg. Chem.* **2009**, 5247.
- [8] Lehmann, T.; Fuchs, J. *Z. Naturforsch.* **1988**, *43b*, 89.
- [9] (a) Shan, Y. K.; Liu, Z. X. *Sci. China Ser. B* **1991**, *34*, 313; *Acta Chim. Sin.* **1992**, 364. (b) Niu, J.; Wang, Z.; Wang, J. *J. Coord. Chem.* **2003**, *56*, 895. (c) Chen, W.; Chen, B.; Li, Y.; Wang, Y.; Wang, E. *Inorg. Chim. Acta* **2009**, *362*, 5043. (d) Iijima, J.; Ishikawa, E.; Nakamura, Y.; Naruke, H. *Inorg. Chim. Acta* **2010**, *363*, 1500.
- [10] (a) Bassil, B. S.; Dickman, M. H.; von der Kammer, B.; Kortz, U. *Inorg. Chem.* **2007**, *46*, 2452. (b) AlDamen, M. A.; Cardona-Serra, S.; Clemente-Juan, J. M.; Coronado, E.; Gaita-Ariño, A.; Martí-Gastaldo, C.; Luis, F.; Montero, O. *Inorg. Chem.* **2009**, *48*, 3467.
- [11] (a) Luo, Q.; Howell, R. C.; Dankova, M.; Bartis, J.; Williams, C. W.; DeW. Horrocks, W., Jr.; Young, V. G., Jr.; Rheingold, A. L.; Francesconi, L. C.; Antonio, M. R. *Inorg. Chem.* **2001**, *40*, 1894. (b) Luo, Q.; Howell, R. C.; Dankova, M.; Bartis, J.; Williams, C. W.; DeW. Horrocks, W., Jr.; Rheingold, A. L.; Francesconi, L. C. *Inorg. Chem.* **2002**, *41*, 6112. (c) Belai, N.; Dickman, M. H.; Pope, M. T.; Contant, R.; Keita, B.; Mbomekalle, I. M.; Nadjó, L. *Inorg. Chem.* **2005**, *44*, 169. (d) Jing, J.; Burton-Pye, B. P.; Francesconi, L. C.; Antonio, M. R. *Inorg. Chem.* **2008**, *47*, 6889. (e) Burton-Pye, B. P.; Francesconi, L. C. *Dalton Trans.* **2011**, *40*, 4421.
- [12] Naruke, H.; Yamase, T. *Bull. Chem. Soc. Jpn.* **2000**, *73*, 375.
- [13] (a) Sadakane, M.; Dickman, M. H.; Pope, M. T. *Angew. Chem. Int. Ed.* **2000**, *39*, 2914. (b) Mialane, P.; Lisnard, L.; Mallard, A.; Marrot, J.; Antic-Fidancev, E.; Aschehoug, P.; Vivien, D.; Sécheresse, F. *Inorg. Chem.* **2003**, *42*, 2102. (c) Wang, J.; Duan, X.; Du, X.; Niu, J. *Cryst. Growth Des.* **2006**, *6*, 2266. (d) Lu, Y.; Xu, Y.; Li, Y.; Wang, E.; Xu, X.; Ma, Y. *Inorg. Chem.* **2006**, *45*, 2055.
- [14] (a) Sadakane, M.; Ostuni, A.; Pope, M. T. *J. Chem. Soc., Dalton Trans.* **2002**, 63. (b) Zhao, X.-Y.; Liu, S.-X.; Ren, Y.-H.; Cao, J.-F.; Cao, R.-G.; Shao, K.-Z. *J. Solid State Chem.* **2008**, *181*, 2488. (c) Niu, J.; Wang, K.; Chen, H.; Zhao, J.; Ma, P.; Wang, J.; Li, M.; Bai, Y.; Dang, D. *Cryst. Growth Des.* **2009**, *9*, 4362.
- [15] (a) Knoth, W. H.; Domaille, P. J.; Harlow, R. L. *Inorg. Chem.* **1986**, *25*, 1577. (b) Chen, W.; Li, Y.; Wang, Y.; Wang, E.; Su, Z. *Dalton Trans.* **2007**, 4293. (c) Ismail, A. H.; Bassil, B. S.; Römer, I.; Redeker, N. C. Kortz, U. *Z. Naturforsch.* **2010**, *65b*, 383. (d) Ni, L.; Hussain, F.; Spingler, B.; Weyeneth, W.; Patzke, G. R. *Inorg. Chem.* **2011**, *50*, 4944. (e) Ismail, A. H.; Bassil, B. S.; Römer, I.; Kortz, U. *Z. Anorg. Allg. Chem.* **2013**, *639*, 2510.
- [16] (a) Creaser, I.; Heckel, M. C.; Neitz, R. J.; Pope, M. T. *Inorg. Chem.* **1993**, *32*, 1573. (b) Ostuni, A.; Pope, M. T. *C. R. Acad. Sci. Paris, Sér. IIc.* **2000**, *3*, 199. (c) Fang, X.; Anderson, T. M.; Benelli, C.; Hill, C. L. *Chem. Eur. J.* **2005**, *11*, 712. (d) Zimmermann, M.; Belai, N.; Butcher, R. J.; Pope, M. T.; Chubarova, E. V.; Dickman, M. H.; Kortz, U. *Inorg. Chem.* **2007**, *46*, 1737.

- [17] (a) Sousa, F. L.; Almeida Paz, F. A.; Cavaleiro, A. M. V.; Klinowski, J.; Nogueira, H. I. S. *Chem. Commun.* **2004**, 2656.
- [18] (a) Yamase, T.; Naruke, H.; Sasaki, Y. *J. Chem. Soc., Dalton Trans.* **1990**, 1687. (b) Naruke, H.; Yamase, T. *Bull. Chem. Soc. Jpn.* **2001**, *74*, 1289. (c) Wassermann, K.; Pope, M. T. *Inorg. Chem.* **2001**, *40*, 2766. (d) Howell, R. C.; Perez, F. G.; Jain, S.; DeW. Horrocks, W., Jr.; Rheingold, A. L.; Francesconi, L. C. *Angew. Chem. Int. Ed.* **2001**, *40*, 4031. (e) Xuie, G.; Vaissermann, J.; Gouzerh, P. *J. Cluster Sci.* **2002**, *13*, 409. (f) Cui, K.; Li, F.; Xu, L.; Xu, B.; Jiang, N.; Wang, Y.; Zhang, J. *Dalton Trans.* **2012**, *41*, 4871.
- [19] (a) Fukaya, K.; Yamase, T. *Angew. Chem. Int. Ed.* **2003**, *42*, 654. (b) Drewes, D.; Piepenbrink, M.; Krebs, B. Z. *Anorg. Allg. Chem.* **2006**, *632*, 534. (c) Hussain, F.; Spingler, B.; Conrad, F.; Speldrich, M.; Kögerler, P.; Boskovic, C.; Patzke, G. R. *Dalton Trans.* **2009**, 4423.
- [20] (a) Mialane, P.; Dolbecq, A.; Rivière, E.; Marrot, J.; Sécheresse, F. *Eur. J. Inorg. Chem.* **2004**, *33*. (b) Zhang, D.; Zhang, C.; Chen, D.; Ma, P.; Wang, J.; Niu, J. *Inorg. Chim. Acta* **2012**, *391*, 218.
- [21] Kortz, U. *J. Clust. Sci.* **2003**, *14*, 205.
- [22] (a) Mialane, P.; Dolbecq, A.; Marrot, J.; Sécheresse, F. *Inorg. Chem. Commun.* **2005**, *8*, 740. (b) Zhang, S.; Wang, Y.; Zhao, J.; Ma, P.; Wang, J.; Niu, J. *Dalton Trans.* **2012**, *541*, 3764.
- [23] (a) Ritchie, C.; Moore, E. G.; Speldrich, M.; Kögerler, P.; Boskovic, C. *Angew. Chem. Int. Ed.* **2010**, *49*, 7702. (b) Ritchie, C.; Baslon, V.; Moore, E. G.; Reber, C.; Boskovic, C. *Inorg. Chem.* **2012**, *51*, 1142.
- [24] Li, F.; Guo, W.; Xu, L.; Ma, L.; Wang, Y. *Dalton Trans.* **2012**, *41*, 9220.
- [25] Mialane, P.; Dolbecq, A.; Lisnard, L.; Mallard, A.; Marrot, J.; Sécheresse, F. *Angew. Chem. Int. Ed.* **2002**, *41*, 2398.
- [26] (a) Dolbecq, A.; Mialane, P.; Lisnard, L.; Marrot, J.; Sécheresse, F. *Chem. Eur. J.* **2003**, *9*, 2914. (b) Dolbecq, A.; Mellot-Draznieks, C.; Mialane, P.; Marrot, J.; Férey, G.; Sécheresse, F. *Eur. J. Inorg. Chem.* **2005**, 3009.
- [27] (a) Kholdeeva, O. A.; Timofeeva, M. N.; Maksimov, G. M.; Maksimovskaya, R. I.; Neiwert, W. A.; Hill, C. L. *Inorg. Chem.* **2005**, *44*, 666. (b) Boglio, C.; Lemièrre, G.; Hasenknopf, B.; Thorimbert, S.; Lacôte, E.; Malacria, M. *Angew. Chem. Int. Ed.* **2006**, *45*, 3324. (b) Dupré, N.; Rémy, P.; Micoine, K.; Boglio, C.; Thorimbert, S.; Lacôte, E.; Hasenknopf, B.; Malacria, M. *Chem. Eur. J.* **2010**, *16*, 7256.
- [28] (a) Suzuki, K.; Sugawa, M.; Kikukawa, Y.; Kamata, K.; Yamaguchi, K.; Mizuno, N. *Inorg. Chem.* **2012**, *51*, 6953. (b) Zhao, S.; Huang, L.; Song, Y.-F. *Eur. J. Inorg. Chem.* **2013**, 1659. (c) Stroobants, K.; Moelants, E.; Ly, H. G. T.; Proost, P.; Bartik, K.; Parac-Vogt, T. N. *Chem. Eur. J.* **2013**, *19*, 2848.
- [29] El Moll, H.; Nohra, B.; Mialane, P.; Marrot, J.; Dupré, N.; Riflade, B.; Malacria, M.; Thorimbert, S.; Hasenknopf, B.; Lacôte, E.; Aparicio, P. A.; López, X.; Poblet, J. M.; Dolbecq, A. *Chem. Eur. J.* **2011**, *17*, 14129.
- [30] (a) Clemente-Juan, J. M.; Coronado, E.; Gaita-Ariño, A. *Chem. Soc. Rev.* **2012**, *41*, 7464. (b) Sato, R.; Suzuki, K.; Sugawa, M.; Mizuno, N. *Chem. Eur. J.* **2013**, *19*, 12982. (c) Suzuki, K.; Sato, R.; Mizuno, N. *Chem. Sci.* **2013**, *4*, 596.
- [31] AlDamen, M. A.; Clemente-Juan, J. M.; Coronado, E.; Martí-Gastaldo, C.; Gaita-Ariño, A. *J. Am. Chem. Soc.*, **2008**, *130*, 8874.
- [32] Cardona-Serra, S.; Clemente-Juan, J. M.; Coronado, E.; Gaita-Ariño, A.; Camón, A.; Evangelisti, M.; Luis, F.; Martínez-Pérez, M. J.; Sesé, J. *J. Am. Chem. Soc.* **2012**, *134*, 14982.
- [33] Ishikawa, N.; Sugita, M.; Ishikawa, T.; Koshihara, S.; Kaizu, Y. *J. Am. Chem. Soc.* **2003**, *125*, 8694.
- [34] (a) Bünzli, J.-C. G.; Piguet, C. *Chem. Soc. Rev.* **2005**, *34*, 1048. (b) Binnemans, K. *Chem. Rev.* **2009**, *109*, 4283. (c) Armelao, L.; Quici, S.; Barigelletti, F.; Accorsi, G.; Bottaro, M.; Cavazzini, M.; Tondello, E. *Coord. Chem. Rev.* **2010**, *254*, 1681. (d) Bünzli, J.-C. G. *Chem. Rev.* **2010**, *110*, 2729.
- [35] (a) Yamase, T. in *Polyoxometalates: From Platonic Solids to Anti-Retroviral Activity*; Pope, M. T.; Müller, A., Eds.; Kluwer: Dordrecht, The Netherlands, 1994. (b) Yamase, T. *Handb. Phys. Chem. Rare Earths* **2009**, *39*, 297.

- [36] (a) Yamase, T.; Ozeki, T.; Ueda, K. *Acta Crystallogr.*, **1993**, *C49*, 1572. (b) Yamase, T.; Kobayashi, T.; Sugeta, M.; Naruke, H. *J. Phys. Chem. A* **1997**, *101*, 5046. (c) Zhang, H.; Lin, X.; Yan, Y.; L. Wu *Chem. Commun.* **2006**, 4575. (d) Qi, W.; Li, H.; Wu, L. *Adv. Mater.* **2007**, *19*, 1983.
- [37] (a) Liu, S.; Kurth, D. G.; Bredenkötter, B.; Volkmer, D. *J. Am. Chem. Soc.* **2002**, *124*, 12279. (b) Bu, W.; Li, H.; Sun, S.; Yin, L.; Wu, L. *J. Am. Chem. Soc.* **2005**, *127*, 8016. (c) Li, H.; Qi, W.; Li, W.; Sun, H.; Bu, W.; Wu, L. *Adv. Mater.* **2005**, *17*, 2688. (d) Granadeiro, C. M.; Ferreira, R. A. S.; Soares-Santos, P. C. R.; Carlos, L. D.; Trindade, T.; Nogueira, H. I. S. *J. Mater. Chem.* **2010**, *20*, 3313. (e) Clemente-León, M.; Coronado, E.; López-Muñoz, A.; Repetto, D.; Ito, T.; Konya, T.; Yamase, T.; Constable, E. C.; Housecroft, C. E.; Doyle, K.; Graber, S. *Langmuir* **2010**, *26*, 1316. (f) Xu, J.; Zhao, S.; Han, Z.; Wang, X.; Song, Y.-F. *Chem. Eur. J.* **2011**, *17*, 10365. (g) Han, Z.; Guo, Y.; Tsunashima, R.; Song, Y.-F. *Eur. J. Inorg. Chem.* **2013**, 1475. (h) Pinto, R. J. B.; Granadeiro, C. M.; Freire, C. S. R.; Silvestre, A. J. D.; Neto, C. P.; Ferreira, R. A. S.; Carlos, L. D.; Cavaleiro, A. M. V.; Trindade, T.; Nogueira, H. I. S. *Eur. J. Inorg. Chem.* **2013**, 1890.
- [38] (a) Müller, A.; Krickemeyer, E.; Meyer, J.; Bögge, H.; Peters, F.; Plass, W.; Diemann, E.; Dillinger, S.; Nonnenbruch, F.; Randerath, M.; Menke, C. *Angew. Chem. Int. Ed. Eng.* **1995**, *34*, 2122. (b) Müller, A.; Krickemeyer, E.; Bögge, H.; Schmidtman, M. *Angew. Chem. Int. Ed.* **1998**, *37*, 3360. (c) Müller, A.; Shahs, S. Q. N.; Bögge, H.; Schmidtman, M. *Nature*, **1999**, 397, 48. (d) Müller, A.; Gouzerh, P. *Chem. Soc. Rev.* **2012**, *41*, 7431.
- [39] (a) Cronin, L.; Beugholt, C.; Krickemeyer, E.; Schmidtman, M.; Bögge, H.; Kögerler, P.; Luong, T. K. T.; Müller, A. *Angew. Chem. Int. Ed.* **2002**, *41*, 2805. (b) Müller, A.; Bögge, H.; Sousa, F. L.; Schmidtman, M.; Kurth, D. G.; Volkmer, D.; van Slageren, J.; Dressel, M.; Kistler, M. L.; Liu, T. *Small* **2007**, *6*, 986.
- [40] Müller, A.; Beckmann, E.; Bögge, H.; Schmidtman, M.; Dress, A. *Angew. Chem. Int. Ed.* **2002**, *41*, 1162.
- [41] (a) Scäffer, C.; Merca, A.; Bögge, H.; Todea, A. M.; Kistler, M. L.; Liu, T.; Thouvenot, R.; Gouzerh, P.; Müller, A. *Angew. Chem. Int. Ed.* **2009**, *48*, 149. (b) Todea, A. M.; Merca, A.; Bögge, H.; Glaser, T.; Pigga, J. M.; Langston, M. L. K.; Liu, T.; Prozorov, R.; Luban, M.; Schröder, C.; Casey, W. H.; Müller, A. *Angew. Chem. Int. Ed.* **2010**, *49*, 514. (c) Gao, J.; Yan, J.; Beeg, S.; Long, D.-L.; Cronin, L. *J. Am. Chem. Soc.* **2013**, *135*, 1796.
- [42] (a) Fang, X.; Kögerler, P.; Furukawa, Y.; Speldrich, M.; Luban, M. *Angew. Chem. Int. Ed.* **2011**, *50*, 5212. (b) Ruiz de la Oliva, A.; Sans, V.; Miras, H. N.; Yan, J.; Zang, H.; Richmond, C. J.; Long, D.-L.; Cronin, L. *Angew. Chem. Int. Ed.* **2012**, *51*, 12759.
- [43] Wassermann, K.; Dickman, M. H.; Pope, M. T. *Angew. Chem. Int. Ed.* **1997**, *36*, 1445.
- [44] (a) Bassil, B. S.; Dickman, M. H.; Römer, I.; von der Kammer, B.; Kortz, U. *Angew. Chem. Int. Ed.* **2007**, *46*, 6192. (b) Hussain, F.; Conrad, F.; Patzke, G. R. *Angew. Chem. Int. Ed.* **2009**, *48*, 9088.
- [45] (a) Hussain, F.; Gable, R. W.; Speldrich, M.; Kögerler, P.; Bosovic, C. *Chem. Commun.* **2009**, 328. (b) Hussain, F.; Patzke, G. R. *CrystEngComm* **2011**, *13*, 530.
- [46] Reinoso, S.; Giménez-Marqués, M.; Galán-Mascarós, J. R.; Vitoria, P.; Gutiérrez-Zorrilla, J. M. *Angew. Chem. Int. Ed.* **2010**, *49*, 8384.
- [47] (a) Li, D.; Yin, P.; Liu, T. in *Polyoxometalate Chemistry: Some Recent Trends*; Sécheresse, F., Ed.; World Scientific: Singapore, 2013; pp.49-99. (b) Yin, P.; Li, D.; Liu, T. *Chem. Soc. Rev.* **2012**, *41*, 7368. (c) Liu, T. *Langmuir* **2010**, *26*, 9202.
- [48] Liu, G.; Liu, T.; Mal, S. S.; Kortz, U. *J. Am. Chem. Soc.* **2006**, *128*, 10103.
- [49] Müller, A.; Diemann, E.; Kuhlmann, C.; Eimer, W.; Serain, C.; Tak, T.; Knöchel, A.; Pranzas, P. K. *Chem. Commun.* **2001**, 1928.
- [50] Liu, T. *J. Am. Chem. Soc.* **2002**, *124*, 10942; *J. Am. Chem. Soc.*, **2003**, *125*, 312.
- [51] Liu, T.; Diemann, E.; Li, H.; Dress, A. W. M.; Müller, A. *Nature* **2003**, 426, 59.
- [52] Pigga, J. M.; Kistler, M. L.; Shew, C.-Y.; Antonio, M. R.; Liu, T. *Angew. Chem. Int. Ed.* **2009**, *48*, 6538.

- [53] Liu, G.; Liu, T. *J. Am. Chem. Soc.* **2005**, *127*, 6942.
- [54] Kistler, M. L.; Bhatt, A.; Liu, G.; Casa, D.; Liu, T. *J. Am. Chem. Soc.* **2007**, *129*, 6453.
- [55] (a) Liu, T.; Imber, B.; Diemann, E.; Liu, G.; Cokleski, K.; Li, H.; Chen, Z.; Müller, A. *J. Am. Chem. Soc.* **2006**, *128*, 15914. (b) Mishra, P. P.; Jing, J.; Francesconi, L. C.; Liu, T. *Langmuir* **2008**, *24*, 9308.
- [56] Pigga, J. M.; Teprovich, J. A.; Flowers, R. A.; Antonio, M. R.; Liu, T. *Langmuir* **2010**, *26*, 9449.
- [57] Kistler, M. L.; Patel, K. G.; Liu, T. *Langmuir* **2009**, *25*, 7328.
- [58] Haso, F.; Fang, X.; Yin, P.; Li, D.; Ross, J. L.; Liu, T. *Chem. Commun.* **2013**, *49*, 609.
- [59] (a) Li, D.; Zhang, J.; Landskron, K.; Liu, T. *J. Am. Chem. Soc.* **2008**, *130*, 4226. (b) Li, D.; Zhou, W.; Landskron, K.; Sato, S.; Kiely, C. J.; Fujita, M.; Liu, T. *Angew. Chem. Int. Ed.* **2011**, *50*, 5182.
- [60] (a) Johnson, J. E.; Speir, J. A. *J. Mol. Biol.* **1997**, *269*, 665. (b) Zlotnik, A.; Johnson, J. M.; Wingfield, P. W.; Stahl, S. J.; Endres, D. T. *Biochemistry* **1999**, *38*, 14644.
- [61] (a) Liu, T.; Langston, M. L. K.; Li, D.; Pigga, J. M.; Pichon, C.; Todea, A. M.; Müller, A. *Science* **2011**, *331*, 1590. (b) Yin, P.; Zhang, J.; Li, T.; Zuo, X.; Hao, J.; Warner, A. M.; Chattopadhyay, S.; Shibata, T.; Wei, Y.; Liu, T. *J. Am. Chem. Soc.* **2013**, *135*, 4529.
- [62] Kortz, U.; Nellutla, S.; Stowe, A. C.; Dalal, N. S.; Rauwald, Y.; Danquah, W.; Ravot, D. *Inorg. Chem.* **2004**, *43*, 2308.
- [63] (a) Chen, W.; Li, Y.; Wang, Y.; Wang, E. *Eur. J. Inorg. Chem.* **2007**, 2216. (b) Chen, W.; Li, Y.; Wang, Y.; Wang, E.; Su, Z. *Dalton Trans.* **2007**, 4293. (c) Chen, W.-L.; Chen, B.-W.; Li, Y.-G.; Wang, Y.-H.; Wang, E.-B. *Inorg. Chim. Acta* **2009**, *362*, 5043. (d) Du, D.-Y.; Qin, J.-S.; Li, S.-L.; Wang, X.-L.; Yang, G.-S.; Li, Y.-G.; Shao, K.-Z.; Su, Z.-M. *Inorg. Chim. Acta* **2010**, *363*, 3823.
- [64] Crystal data of $\text{Na}_{53-x}\text{K}_x[\text{K}_6\text{Ce}_6\text{Ge}_{12}\text{W}_{120}\text{O}_{444}(\text{OH})_{12}(\text{H}_2\text{O})_{56}] \cdot n\text{H}_2\text{O}$ (**8-Ce-b**). $\text{Ce}_{24}\text{Ge}_{12}\text{H}_{324}\text{K}_{23}\text{Na}_{38}\text{O}_{612}\text{W}_{120}$, $M_w = 38265.7 \text{ g mol}^{-1}$, triclinic crystal system, $P\bar{1}$ space group, $a = 23.9330(4)$, $b = 27.5898(4)$, $c = 28.7336(5) \text{ \AA}$, $\alpha = 76.008(1)$, $\beta = 69.300(2)$, $\gamma = 76.541(1)^\circ$, $V = 16993.3(5) \text{ \AA}^3$, $T = 100(2) \text{ K}$, $Z = 1$, $\rho_{\text{calcd}} = 3.739 \text{ g cm}^{-3}$, $\mu = 22.584 \text{ mm}^{-1}$, 109619 reflections collected, 59842 unique ($R_{\text{int}} = 0.042$), 15716 observed [$I > 2\sigma(I)$], 2307 parameters, $R(F) = 0.063$ [$I > 2\sigma(I)$], $wR(F^2) = 0.151$ (all data), GoF 1.075.
- [65] Lipscomb, W. N. *Inorg. Chem.* **1965**, *4*, 132.
- [66] Jeannin, Y. P. *Chem. Rev.* **1998**, *98*, 51.
- [67] Canny, J.; Teze, A.; Thouvenot, R.; Herve, G. *Inorg. Chem.* **1986**, *25*, 2114.
- [68] Nsouli, N. H.; Bassil, B. S.; Dickman, M. H.; Kortz, U.; Keita, B.; Nadjo, L. *Inorg. Chem.* **2006**, *45*, 3858.
- [69] Knoth, W. H.; Harlow, R. L. *J. Am. Chem. Soc.* **1981**, *103*, 1865.
- [70] See for example: (a) Kortz, U.; Jeannin, Y. P.; Tézé, A.; Hervé, G.; Isber, S. *Inorg. Chem.* **1999**, *38*, 3670. (b) Nsouli, N. H.; Mal, S. S.; Dickman, M. H.; Kortz, U.; Keita, B.; Nadjo, L.; Clemente-Juan, J. M. *Inorg. Chem.* **2007**, *46*, 8763. (c) Assran, A. S.; Mal, S. S.; Izarova, N. V.; Banerjee, A.; Suchopar, A.; Sadakane, M.; Kortz, U. *Dalton Trans.* **2011**, *40*, 2920.
- [71] Bassil, B. S.; Dickman, M. H.; Kortz, U. *Inorg. Chem.* **2006**, *45*, 2394.
- [72] (a) Casanova, D.; Alemany, P.; Boffil, J. M.; Alvarez, S. *Chem. Eur. J.* **2003**, *9*, 1281. (b) Casanova, D.; Llunell, M.; Alemany, P.; Alvarez, S. *Chem. Eur. J.* **2005**, *11*, 1479.
- [73] Yamase, T. *Chem. Rev.* **1998**, *98*, 307.
- [74] (a) Zhao, X.-Y.; Liu, S.-X.; Ren, Y.-H.; Cao, J.-F.; Cao, R.-G.; Shao, K.-Z. *J. Solid. State Chem.* **2008**, *181*, 2488. (b) Zhu, Y.-Y.; Sun, Z.-G.; Chen, H.; Zhang, J.; Zhao, Y.; Zhang, N.; Liu, L.; Lu, X.; Wang, W.-N.; Tong, F.; Zhang, L.-C. *Cryst. Growth Des.* **2009**, *9*, 3228.
- [75] Yan, B.; Bai, Y.-Y. *J. Fluoresc.* **2005**, *15*, 606.

- [76] "Ionic conductivity and diffusion at infinite dilution", in *CRC Handbook of Chemistry and Physics*; Lide, D. R., Ed. CRC Press: Boca Raton, FL, 2005.
- [77] (a) Liu, G.; Kistler, M. L.; Li, T.; Bhatt, A.; Liu, T. *J. Cluster Sci.* **2006**, *17*, 427. (b) Roy, K. I.; Lucy, C. A. *Electrophoresis* **2003**, *24*, 370.
- [78] (a) Bonchio, M.; Bortolini, O.; Conte, V.; Sartorel, A. *Eur. J. Inorg. Chem.* **2003**, 699. (b) Mayer, C. R.; Roch-Marchal, C.; Lavanant, H.; Thouvenot, R.; Sellier, N.; Blais, J.-C.; Sécheresse, F. *Chem. Eur. J.* **2004**, *10*, 5517. (c) Miras, H. N.; Zang, H. Y.; Long, D.-L.; Cronin, L. *Eur. J. Inorg. Chem.* **2011**, 5105. (d) Korenev, V. S.; Abramov, P. A.; Vicent, C.; Mainichev, D. A.; Floquet, S.; Cadot, E.; Sokolov, M. N.; Fedin, V. P. *Dalton Trans.* **2012**, *41*, 14484.
- [79] Liu, G.; Liu, T. *Langmuir* **2005**, *21*, 2713.
- [80] Zhang, J.; Li, D.; Liu, G.; Glover, K. J.; Liu, T. *J. Am. Chem. Soc.* **2009**, *131*, 15152.
- [81] Tézé, A.; Canny, J.; Gurban, L.; Thouvenot, R.; Hervé, G. *Inorg. Chem.* **1996**, *35*, 1001.
- [82] Mialane, P.; Lisnard, L.; Mallard, A.; Marrot, J.; Antic-Fidancev, E.; Aschehoug, P.; Vivien, D.; Sécheresse, F. *Inorg. Chem.* **2003**, *42*, 2102.
- [83] Li, Y.G.; Xu, L.; Gao, G.G.; Jiang, N.; Liu, H.; Li, F.Y.; Yang, Y.Y. *CrystEngComm* **2009**, *11*, 1512.
- [84] Pope, M. T.; Scully, T. F. *Inorg. Chem.* **1975**, *14*, 953.
- [85] Brown, I. D.; Altermatt, D. *Acta Crystallogr.* **1985**, *B41*, 244.
- [86] (a) Miras, H. N.; Wilson, E. F.; Cronin, L. *Chem. Commun.* **2009**, 1297. (b) Sokolov, M. N.; Adonin, S. A.; Sinkevich, P. L.; Vicent, C.; Mainichev, D. A.; Fedin, V. P. *Dalton Trans.* **2012**, *41*, 9889. (c) Ohlin, C. A. *Chem. Asian J.* **2012**, *7*, 262. (d) Xu, C.; Fan, Y.; Fan, L.; Cao, J.; Hu, C. *Prog. Chem.* **2013**, *25*, 809.
- [87] Crystal data of: (a) $\text{Na}_{12}[\text{Er}_4(\text{H}_2\text{O})_6(\alpha\text{-GeW}_{10}\text{O}_{38})_2]\cdot\sim 30\text{H}_2\text{O}$ ($\alpha\alpha\text{-9-Er}$). $\text{Er}_4\text{Ge}_2\text{H}_{72}\text{Na}_{12}\text{O}_{112}\text{W}_{20}$, $M_w = 6631.7 \text{ g mol}^{-1}$, triclinic crystal system, $P\bar{1}$ space group, $a = 11.6480(3)$, $b = 20.8918(7)$, $c = 21.3495(4) \text{ \AA}$, $\alpha = 81.659(2)$, $\beta = 87.806(2)$, $\gamma = 79.100(2)^\circ$, $V = 5047.3(2) \text{ \AA}^3$, $T = 100(2) \text{ K}$, $Z = 2$, $\rho_{\text{calcd}} = 4.364 \text{ g cm}^{-3}$, $\mu = 26.732 \text{ mm}^{-1}$, 31755 reflections collected, 17750 unique ($R_{\text{int}} = 0.043$), 15716 observed [$I > 2\sigma(I)$], 751 parameters, $R(F) = 0.058$ [$I > 2\sigma(I)$], $wR(F^2) = 0.148$ (all data), GoF 1.082. (b) $\text{Na}_{12}[\text{Tm}_4(\text{H}_2\text{O})_6(\alpha\text{-GeW}_{10}\text{O}_{38})_2]\cdot\sim 30\text{H}_2\text{O}$ ($\alpha\alpha\text{-9-Tm}$). $\text{Ge}_2\text{H}_{72}\text{Na}_{12}\text{O}_{112}\text{Tm}_4\text{W}_{20}$, $M_w = 6638.4 \text{ g mol}^{-1}$, triclinic crystal system, $P\bar{1}$ space group, $a = 11.6502(2)$, $b = 20.8536(6)$, $c = 21.3197(3) \text{ \AA}$, $\alpha = 81.724(2)$, $\beta = 87.8640(10)$, $\gamma = 79.014(2)^\circ$, $V = 5031.46(18) \text{ \AA}^3$, $T = 100(2) \text{ K}$, $Z = 2$, $\rho_{\text{calcd}} = 4.382 \text{ g cm}^{-3}$, $\mu = 27.008 \text{ mm}^{-1}$, 26614 reflections collected, 17600 unique ($R_{\text{int}} = 0.032$), 15449 observed [$I > 2\sigma(I)$], 759 parameters, $R(F) = 0.049$ [$I > 2\sigma(I)$], $wR(F^2) = 0.121$ (all data), GoF 1.053. (c) $\text{Na}_{12}[\text{Yb}_4(\text{H}_2\text{O})_6(\alpha\text{-GeW}_{10}\text{O}_{38})_2]\cdot\sim 30\text{H}_2\text{O}$ ($\alpha\alpha\text{-9-Yb}$). $\text{Ge}_2\text{H}_{72}\text{Na}_{12}\text{O}_{112}\text{W}_{20}\text{Yb}_4$, $M_w = 6654.8 \text{ g mol}^{-1}$, triclinic crystal system, $P\bar{1}$ space group, $a = 11.6784(3)$, $b = 20.8898(5)$, $c = 21.3588(5) \text{ \AA}$, $\alpha = 81.660(2)$, $\beta = 87.889(10)$, $\gamma = 78.912(2)^\circ$, $V = 5059.1(2) \text{ \AA}^3$, $T = 100(2) \text{ K}$, $Z = 2$, $\rho_{\text{calcd}} = 4.369 \text{ g cm}^{-3}$, $\mu = 27.050 \text{ mm}^{-1}$, 64242 reflections collected, 17782 unique ($R_{\text{int}} = 0.064$), 14487 observed [$I > 2\sigma(I)$], 759 parameters, $R(F) = 0.050$ [$I > 2\sigma(I)$], $wR(F^2) = 0.126$ (all data), GoF 1.018.
- [88] Panagiotopoulos, A.; Zafiropoulos, T. F.; Perlepes, S. P.; Bakalbassis, E.; Masson-Ramade, I.; Kahn, O.; Terzis, A.; Raptopoulou, C. P. *Inorg. Chem.* **1995**, *34*, 4918.
- [89] (a) Avecilla, F.; Platas-Iglesias, C.; Rodríguez-Cortiñas, R.; Guillemot, G.; Bünzli, J.-C. G.; Brondino, C. D.; Geraldès, C. F. G. C.; de Blas, A.; Rodríguez-Blas, T. *J. Chem. Soc., Dalton Trans.* **2002**, 4658. (b) Lam, A. W.-H.; Wong, W.-T.; Gao, S.; Wen, G.; Zhang, X.-X. *Eur. J. Inorg. Chem.* **2003**, 149. (c) Rohde, A.; Urland, W. *Dalton Trans.* **2006**, 2974. (d) John, D.; Urland, W. *Eur. J. Inorg. Chem.* **2006**, 3503.
- [90] Zhao, J.; Shi, D.; Chen, L.; Li, Y.; Ma, P.; Wang, J.; Niu, J. *Dalton Trans.* **2012**, *41*, 10740.
- [91] Lai, H.; Bao, A.; Yang, Y.; Xu, W.; Tao, Y.; Yan, H. *J. Lumin.* **2008**, *128*, 521.

Heterometallic 3d-4f polyoxometalates derived from the 3d-metal disubstituted Krebs-type framework

4.1. Introduction

4.2. Experimental section

4.3. Results and discussion

4.4. Conclusions

4.5. References

ABSTRACT: The combination of early lanthanide(III) ions with pre-formed or in situ generated 3d-metal disubstituted $\{[M(H_2O)_3]_2(WO_2)_2(B-\beta-SbW_9O_{33})_2\}^{10-}$ ($M = Co, Ni, Zn$) Krebs-type POMs in NaOAc buffer promotes the rearrangement of the parent anion to lead to the formation of heterometallic $\{[B-\alpha-SbW_9O_{32}(OH)]_3\{(WO_2)_3(M^II W_6O_{24})\}Ln^{III}_3(H_2O)_7M(OAc)(Sb_4O_4)\}^{19-}$ clusters **11-LnM** ($Ln^{III} = La$ to Gd , $M^{II} = Co$; $Ln^{III} = Ce$, $M^{II} = Ni, Zn$). Compounds **11-LnM** have been characterized by means of elemental and thermal analyses and infrared spectroscopy. According to single-crystal X-ray diffraction studies, the molecular structure of the **11-LnM** anions can be viewed as a tetrameric assembly of three Keggin-type $\{B-\alpha-SbW_9O_{33}\}$ trilacunary subunits linked to each other by two nine-coordinated 4f-metal atoms and one $\{LnM(\mu-OAc)\}$ dimer capped with a $\{MW_6O_{24}\}$ Anderson-Evans-type fragment, that is connected to the trilacunary subunits via three additional $\{WO_2\}$ centers. This POM framework encapsulates the unusual $\{Sb_4O_4\}$ cluster, which confers chirality on the **11-LnM** anions by arranging in left- or right-handed orientations as a result of this cluster pivoting on one of its Sb centers. The **11-LnM** cluster is stable in aqueous solution, as confirmed by electrospray ionization mass spectrometric studies carried out for the **11-CeCo** derivative. The **11-CeCo** anion undergoes a self-assembly process in diluted solutions to form spherical, hollow and single-layered vesicle-like blackberry type structures, as monitored by static- and dynamic-light scattering experiments and confirmed by transmission electron microscopy. The electron paramagnetic resonance spectra of **11-CeCo** and **11-GdCo** are in good agreement with the arrangement of the clusters in the crystal structure.

4.1. INTRODUCTION

A systematic study on the organic derivatization of well-known POM clusters with exposed 3d-metal centers is described in Chapter 2, whereas POM assemblies containing 4f-metals and suitable for the organic functionalization are reported in Chapter 3. While 3d-substituted clusters form the largest POM family¹ and the field of 4f-containing POMs has been significantly expanding during the last decades,² little work has been dedicated to heterometallic 3d-4f POMs as indicated by a recent review.³ This fact is even more surprising considering the high interest of 3d-4f-metal complexes in molecular magnetism and in the preparation of bifunctional optical-magnetic compounds. Large magnetic anisotropy, together with high ground-state spin values as a consequence of strong spin-orbit coupling, make heavy 4f-metal ions (Dy^{III} , Tb^{III} , Ho^{III} , and Er^{III}) ideal candidates for the design of Single Molecule Magnets (SMMs). As mentioned in Chapter 3, some 4f-metal containing POMs have exhibited slow relaxation of magnetization.⁴ The magnetic coupling of heavy lanthanides with first row transition metal ions is often ferromagnetic, and this could lead to ground states with even larger magnetic moments. Therefore, the combination of 3d and 4f metals represents a suitable strategy to improve the magnetic properties.

Synthetic aspects could be considered the reason why the field of 3d-4f POMs did not undergo significant expansion until very recent years. Even for the more traditional heterometallic coordination complexes, the mixture of 3d- and 4f-metal salts with an organic ligand does not usually lead to the formation of the desired mixed-metal compounds, but mostly to pure 3d compounds. To overcome these difficulties, new effective synthetic approaches have been applied which involve the design of organic ligands with specific coordination sites for both types of metals or the use of pre-formed 3d-metal polynuclear complexes in the reaction with lanthanides.⁵

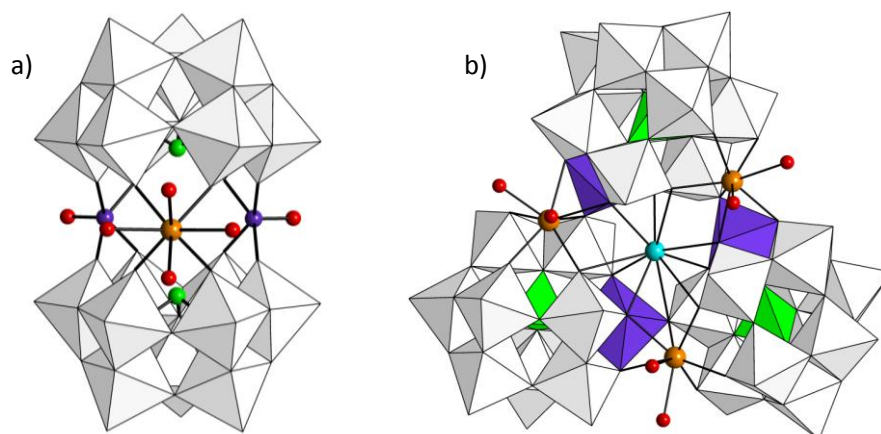


Figure 4.1. Structures of: a) $[(\text{VO})_2\{\text{Dy}(\text{H}_2\text{O})_4\}\{\text{B-}\alpha\text{-AsW}_9\text{O}_{33}\}_2]^{11-}$ Hervé-like POM; b) $[\text{K}\{\text{Ce}(\text{H}_2\text{O})_2(\text{AsW}_{10}\text{FeO}_{38})\}_3]^{14-}$ trimeric aggregate. (Color code: WO_6 , grey; heteroatom, green; 4f ion, orange; 3d metal, purple; K, light blue; O, red).

Besides some multidimensional compounds based on 4f-metal containing POMs with 3d-metal linkers (or *vice versa*),⁶ to date only ten structures of heterometallic 3d-4f-polyoxometalates showing both types of metals as part of the inorganic skeleton have been reported. Merca et al. prepared the $[(\text{VO})_2\text{Dy}(\text{H}_2\text{O})_4(\text{AsW}_9\text{O}_{33})_2]^{11-}$ Hervé-like sandwich POM composed of two trilacunary $[\text{B-}\alpha\text{-As}^{\text{III}}\text{W}_9\text{O}_{33}]^{9-}$ Keggin subunits trapping two square pyramidal VO^{2+} groups and one square-antiprismatic Dy^{3+} ion.⁷ On the other hand, Wang and coworkers synthesized the

$[K\{\text{Ce}(\text{H}_2\text{O})_2(\text{AsW}_{10}\text{FeO}_{38})\}_3]^{14-}$ cluster comprising a K^+ -templated cyclic aggregate of three metal substituted dilacunary $[\alpha\text{-As}^{\text{V}}\text{W}_{10}\text{O}_{38}]^{11-}$ Keggin subunits. Each unit shows one vacant position filled by a Fe^{3+} and one square-antiprismatic Ce^{3+} placed over the second vacancy.⁸ Both reactions were carried out starting from the most basic metallic reagents that can lead to the POM cluster (3d- and 4f-metal salts, heteroatomic source and sodium tungstate) at acidic aqueous media and in the presence of K^+ cation (Figure 4.1). Alternatively, reaction of the pre-formed ring shaped $[\text{H}_7\text{P}_8\text{W}_{48}\text{O}_{184}]^{33-}$ superlacunary POM precursor with Fe^{III} and Ln^{III} ($\text{Ln} = \text{Eu}, \text{Gd}$) salts in a LiOAc solution led to the corresponding heterometallic derivative as a results of a ring opening process. The horseshoe-shaped cluster represents the first observation of a rupture of the very stable $\{\text{P}_8\text{W}_{48}\}$ wheel in aqueous solution. The $[\{\text{Gd}(\text{H}_2\text{O})_5\}\{\text{Ni}(\text{H}_2\text{O})_2\}(\text{As}_4\text{W}_{40}\text{O}_{140})]^{21-}$ POM reported by Xue et al. was prepared analogously, using the well-known multivacant $\{\text{As}_4\text{W}_{40}\}$ cryptate as starting material (Figure 4.2).⁹

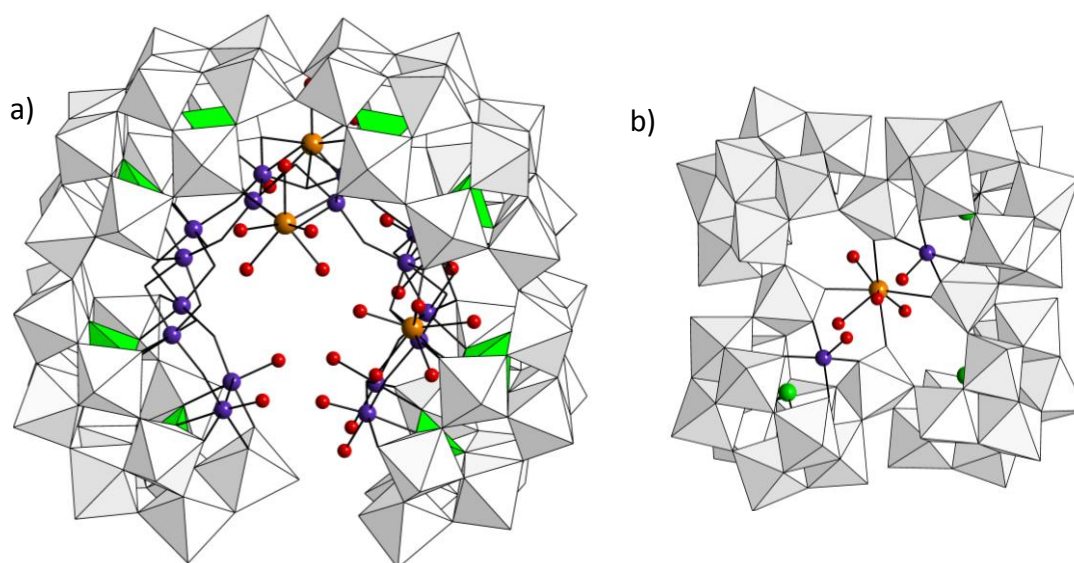


Figure 4.2. Structure of: a) $[\text{Fe}_{16}\text{O}_2(\text{OH})_{23}(\text{H}_2\text{O})_9(\text{P}_8\text{W}_{49}\text{O}_{189})\text{Ln}_4(\text{H}_2\text{O})_{20}]^{11-}$ ($\text{Ln} = \text{Eu}, \text{Gd}$) horseshoe-shaped cluster; b) $[\{\text{Gd}(\text{H}_2\text{O})_5\}\{\text{Ni}(\text{H}_2\text{O})_2\}(\text{As}_4\text{W}_{40}\text{O}_{140})]^{21-}$ POM (water molecules in red).

Different synthetic approaches have been applied to overcome the reaction competitions in 3d/4f/POM systems. The first route is based on the use of preformed oxo- or hydroxo-bridged 3d-4f-heterometallic complexes. Fang and Kögerler were able to graft the $[\text{Ce}^{\text{IV}}\text{Mn}^{\text{IV}}_6\text{O}_9(\text{OAc})_9(\text{NO}_3)(\text{H}_2\text{O})_2]$ complex in a dilacunary $[\text{P}_2\text{W}_{16}\text{O}_{57}(\text{OH})_2]^{12-}$ Wells-Dawson type anion. On the contrary, a hexameric architecture buried on 3d-4f complexes sandwiched between two trilacunary $[\alpha\text{-P}_2\text{W}_{15}\text{O}_{46}]^{12-}$ fragments was obtained using the $[\text{Ce}^{\text{IV}}_3\text{Mn}^{\text{IV}}_2\text{O}_6(\text{OAc})_5(\text{NO}_3)_3]$ complex. Formation of this hexameric aggregate is templated by a central, encapsulated PO_4^{3-} group, which acts as a bridging ligand between the three heterometallic complexes (Figure 4.3).¹⁰

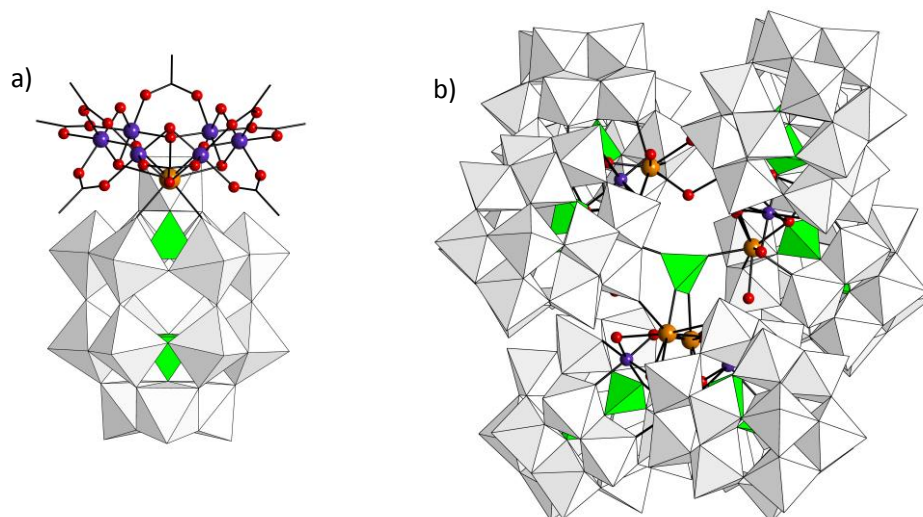


Figure 4.3. Structures of: a) $[\{P_2W_{16}O_{57}(OH)_2\}\{Ce^{IV}Mn^{IV}_6O_9(OAc)_8\}]^{8-}$ hybrid POM; b) $[\{P_2W_{15}O_{56}\}_6\{Ce^{IV}_3Mn^{IV}_2O_4(OH)_2\}_3(OH)_2(H_2O)_2(PO_4)]^{47-}$ hexameric assembly.

Another strategy involves the use of external organic ligands as stabilizing agents. Stoichiometric mixtures of Cu^{2+} , Ln^{3+} , ethylenediamine (en) and Keggin-type trilacunary $[A-\alpha-XW_9O_{34}]^{8-}$ ($X = Si, Ge$) anions result in the dimeric $[\{(Cu(en)(OH))_3Ln(H_2O)(\alpha-XW_{11}O_{39})\}_2]^{4-}$ ($X = Si, Ln = Gd, Eu; X = Ge, Ln = Eu, Tb, Dy$) clusters under hydrothermal conditions.¹¹ Each $\{(Cu(en)(OH))_3Ln(\alpha-XW_{11}O_{39})\}$ subunit is formed by a $\{(Cu(en)(OH))_3Ln(H_2O)\}$ cubane grafted at the monolacunary Keggin fragment through the coordination of the lanthanide to the vacant site. These 4f-metal centers act as intradimeric linkers through the formation of $Ln-O$ bonds. The same synthetic approach was followed by Su and coworkers to incorporate one Mn^{2+} and two Gd^{3+} atoms in the lacunary $[P_6W_{39}O_{147}(H_2O)_3]^{30-}$ POM making use of the tartrate ligand (tart), which links the 3d and 4f-metals to each other (Figure 4.4).¹²

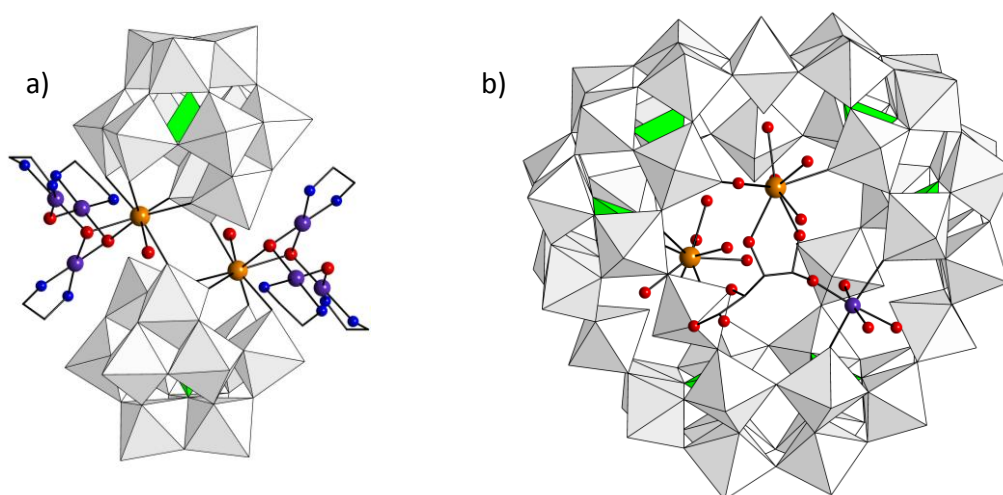


Figure 4.4. Structures of: a) Dimeric $[\{(Cu(en)(OH))_3Ln(H_2O)(\alpha-XW_{11}O_{39})\}_2]^{4-}$ ($X = Si, Ln = Gd, Eu; X = Ge, Ln = Eu, Tb, Dy$) (N, blue); b) Cyclic $[\{HMnGd_2(tart)O_2(H_2O)_{15}\}\{P_6W_{42}O_{151}(H_2O)_7\}]^{19-}$ assembly.

The last synthetic approach that will be commented in this section is based on the reaction of 4f-metal ions with 3d-substituted POM precursors. This strategy was applied by Reinoso et al. for incorporating one or two square-antiprismatic 4f-metal centers into Weakley-type $[M_4(H_2O)_2(B-\alpha-GeW_9O_{34})_2]^{12-}$ POMs. Weakley-like sandwich-type species are composed of two trilacunary $B-\alpha$ -Keggin or α -Wells-Dawson fragments and a central $\{M_4O_{16}\}$ rhomblike core of four edge sharing MO_6 octahedra where the outer 3d metals display a terminal aqua ligand.¹³ These outer $M(H_2O)$ groups are relatively labile as indicated by the isolation of defect di- and trisubstituted derivatives,¹⁴ which can act as lacunary species to incorporate M' ions in their vacancies.¹⁵ The $[\{Ce^{III}(H_2O)_2\}_2Mn^{III}_2(B-\alpha-GeW_9O_{34})_2]^{8-}$ anion was prepared by stoichiometric reaction of Ce^{IV} with $[Mn^{II}_4(H_2O)_2(B-\alpha-GeW_9O_{34})_2]^{12-}$ in water (pH = 1), whereas the reaction carried out in a NaOAc buffer with the Cu^{II} containing Weakley-like derivative led to the monosubstituted $[\{Ce^{IV}(C_2H_3O_2)\}Cu^{II}_3(H_2O)(B-\alpha-GeW_9O_{34})_2]^{11-}$ species (Figure 4.5).¹⁶ Since reactions with several trivalent ions were unsuccessful, the authors suggested that the formation of the cerium disubstituted POM could take place via release of outer $\{Mn(H_2O)\}$ groups as a result of Mn^{II} to Mn^{III} oxidation by Ce^{IV} and consequent cerium quenching of the disubstituted Weakley-type species. However, the use of the non-oxidizable Cu -derivative shows that the incorporation of cerium can take place regardless to the oxidizable nature of the 3d centers. In both cases, the sandwich skeleton undergoes an isomerization process.

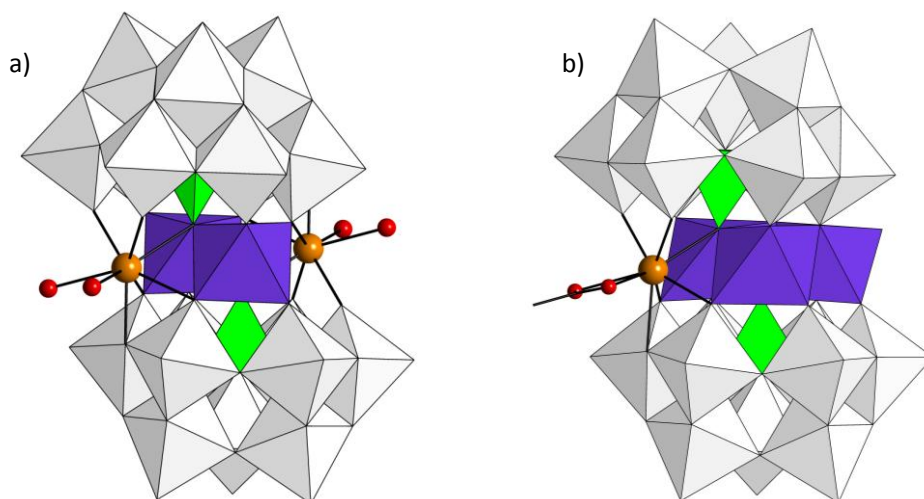


Figure 4.5. Structures of the sandwich type heterometallic POMs: a) $[\{Ce^{III}(H_2O)_2\}_2Mn^{III}_2(B-\alpha-GeW_9O_{34})_2]^{8-}$ and b) $[\{Ce^{IV}(C_2H_3O_2)\}Cu^{II}_3(H_2O)(B-\alpha-GeW_9O_{34})_2]^{11-}$.

Besides Weakley-type anions, Krebs-like sandwich POMs might also be seen as a suitable 3d-substituted clusters for applying the above mentioned synthetic approach. As indicated by Krebs, the defect $[(WO_2)_2(B-\beta-SbW_9O_{33})_2]^{14-}$ intermediate can be formed at slightly acidic conditions from the parent $[\{WO_2(OH)\}_2(WO_2)_2(B-\beta-Sb^{III}W_9O_{33})_2]^{12-}$ cluster and this intermediate that can be stabilized by the incorporation of different electrophiles at external vacant positions. In fact, the closely related $[(W(dmsO)(OH))_2(B-\beta-SbW_9O_{33})_2]^{8-}$ species, showing DMSO coordinated internal tungsten atoms and vacancies at external belt-sites, has been reported a few years ago.¹⁷ The variety of electrophiles that can occupy external positions in Krebs-type fragments include $\{WO_2(OH)\}$, $\{M(H_2O)_3\}$ and $\{M(CO)_3\}$ groups¹⁸ or even lanthanide ions. Very recently, 4f-metals have been incorporated in the external positions of Krebs-type POM skeletons by reacting late-lanthanides ($Ln^{III} = Yb, Lu$) with the $[B-\alpha-SbW_9O_{33}]^{9-}$ trilacunary unit in acidic aqueous media,¹⁹ in such a way that mono- and di-substituted species were obtained depending on the pH of the final solution. The tetrasubstituted

CHAPTER 4

$[M_4(H_2O)_{10}(X^{III}W_9O_{33})_2]^{6-}$ Krebs-type POMs²⁰ are likely to show analogous behavior, and as a consequence Krebs-type species with heterometallic 3d-4f central belts could be *a priori* designed. Moreover, we have shown in Chapter 2 that Krebs-type POMs can undergo skeletal rearrangement under specific conditions to lead to novel POM architectures, and therefore, reaction with 4f ions might result in novel types of heterometallic 3d-4f clusters.

The aim of this chapter is to systematically test the reactivity of 3d-metal disubstituted Krebs-type tungstoantimonate(III) $[\{M^{II}(H_2O)_3\}_2(WO_2)_2(B-\beta-SbW_9O_{33})_2]^{10-}$ (M = Co, Ni, Zn) precursors toward 4f-metals in quest for novel 3d-4f POM architectures derived from this well-known family of sandwich species. The insertion of 4f-metal centers into 3d-metal containing POMs could lead not only to new heterometallic magnetic clusters, but might also confer additional coordination sites on the POM system potentially available for further coordination of organic ligands due to the larger coordination spheres of the lanthanide atoms. As a result of our systematic studies, here we report on the series of heterometallic $[Sb_7W_{36}O_{130}(OH)_3Ln_3M_2(OAc)(H_2O)_8]^{14-}$ (**11-LnM**) POMs, which include the cobalt-containing species **11-LnCo** with Ln = La to Gd, and also the cerium containing clusters **11-CeM** where M = Ni and Zn. All compounds have been characterized by elemental and thermal analyses, infrared and electronic spin resonance spectroscopy and single-crystal X-ray diffraction. The solution stability of these POMs has been studied by a combination of ESI-MS, Laser Light Scattering techniques and TEM studies carried out on **11-CeCo** species.

4.2. EXPERIMENTAL SECTION

4.2.1. Synthesis

Preparation of starting materials

The $[B-\alpha-SbW_9O_{33}]^{9-}$ POM precursor was synthesized according to reported procedures,^{18a} whereas all the 3d-metal disubstituted Krebs-type POMs were prepared as described for the Mn- or Zn-containing derivatives.¹⁸ All the starting materials were identified by IR spectroscopy (for the experimental procedures and reaction yields see Chapter 2, section 2.2.1).

General synthetic procedures

METHOD 1. To a solution of $Na_{10}[\{M(H_2O)_3\}_2(WO_2)_2(SbW_9O_{33})_2] \cdot \sim 40H_2O$ (M = Co, Ni, Zn; 0.20 mmol, 1.24 g) in aqueous 1 M acetic acid/sodium acetate buffer (30 mL), the corresponding lanthanide salt (0.20 mmol) was added. The mixture was heated for 1 h at 90 °C and then cooled down to room temperature. After filtering any solid off, the resulting solution was left to evaporate.

METHOD 2. To a solution of $Na_9[\alpha-SbW_9O_{33}] \cdot 20H_2O$ (502 mg, 0.20 mmol) in aqueous 1 M acetic acid/sodium acetate buffer (40 mL), the corresponding transition metal (0.40 mmol) and lanthanide salts (0.40 mmol) were added. The mixture was heated for 1 h at 90 °C and then cooled down to room temperature. After filtering any solid off, the resulting solution was left to evaporate.

Synthesis of 11-LnM

In all cases, crystalline solid products are obtained as a mixture of the corresponding 3d-metal disubstituted Krebs-type POM precursor as the major component and the desired compound **11-**

LnM. Crystals of **11-LnM** were manually separated under an optical microscope for full characterization and structural determination. Best yields for all transition metal/lanthanide combinations analyzed were obtained by applying method 2.

Na₁₄[Sb₇W₃₆O₁₃₀(OH)₃La₃Co₂(OAc)(H₂O)₈] \cdot ~62H₂O (11-LaCo): CoCl₂·6H₂O (95 mg) and La(NO₃)₃·6H₂O (173 mg) were used and a mixture of light pink (**11-LaCo**) and purple (Krebs-type POM) prismatic X-ray quality single crystals was obtained by slow evaporation of the final solution for ca. two months. Yield: 24 mg, 30% based on Sb. Anal. Calcd (found) for C₂H₁₄₈Co₂La₃Na₁₄O₂₀₆Sb₇W₃₆: C, 0.20 (0.25); H, 1.25 (1.33); Co, 1.00 (1.04); La, 3.53 (3.60); Na, 2.73 (2.94); Sb, 7.24 (7.18). IR (cm⁻¹): 1412 (m), 943 (s), 860 (vs), 808 (vs), 712 (vs), 683 (sh), 613 (w), 516 (w), 450 (m). Unit cell parameters (single-crystal, 100 K): orthorhombic *Pnma*, *a* = 30.746(2) *b* = 33.309(3), *c* = 19.901(2) Å, *V* = 20379.8(3) Å³.

Na₁₄[Sb₇W₃₆O₁₃₀(OH)₃Ce₃Co₂(OAc)(H₂O)₈] \cdot ~62H₂O (11-CeCo): CoCl₂·6H₂O (95 mg) and Ce(NO₃)₃·6H₂O (174 mg) were used and a mixture of orange (**11-CeCo**) and purple (Krebs-type POM) prismatic X-ray quality single crystals were obtained by slow evaporation of the final solution for ca. two months. Yield: 40 mg, 50% based on Sb. Anal. Calcd (found) for C₂H₁₄₈Ce₃Co₂Na₁₄O₂₀₆Sb₇W₃₆: C, 0.20 (0.24); H, 1.25 (1.19); Ce, 3.57 (3.56); Co, 1.00 (1.08); Na, 2.73 (3.01); Sb, 7.23 (6.98). IR (cm⁻¹): 1412 (m), 945 (s), 860 (vs), 806 (vs), 712 (vs), 687 (sh), 613 (w), 509 (w), 453 (m).

Na₁₄[Sb₇W₃₆O₁₃₀(OH)₃Pr₃Co₂(OAc)(H₂O)₈] \cdot ~62H₂O (11-PrCo): CoCl₂·6H₂O (95 mg) and Pr(NO₃)₃·6H₂O (174 mg) were used and a mixture of light pink (**11-PrCo**) and purple (Krebs-type POM) prismatic X-ray quality single crystals were obtained by slow evaporation of the final solution for ca. two months. Yield: 28 mg, 32% based on Sb. Anal. Calcd (found) for C₂H₁₄₈Co₂Na₁₄O₂₀₆Pr₃Sb₇W₃₆: C, 0.20 (0.26); H, 1.25 (1.28); Co, 1.00 (1.11); Na, 2.73 (2.98); Pr, 3.59 (3.61); Sb, 7.23 (7.14). IR (cm⁻¹): 1412 (m), 943 (s), 860 (vs), 808 (vs), 712 (vs), 683 (sh), 613 (w), 509 (w), 453 (m).

Na₁₄[Sb₇W₃₆O₁₃₀(OH)₃Nd₃Co₂(OAc)(H₂O)₈] \cdot ~62H₂O (11-NdCo): CoCl₂·6H₂O (95 mg) and Nd(NO₃)₃·6H₂O (175 mg) were used and a mixture of light pink (**11-NdCo**) and purple (Krebs-type POM) prismatic X-ray quality single crystals were obtained by slow evaporation of the final solution for ca. two months. Yield: 26 mg, 31% based on Sb. Anal. Calcd (found) for C₂H₁₄₈Co₂Na₁₄Nd₃O₂₀₆Sb₇W₃₆: C, 0.20 (0.19); H, 1.25 (1.15); Co, 1.00 (1.03); Na, 2.73 (2.69); Nd, 3.67 (3.71); Sb, 7.23 (7.29). IR (cm⁻¹): 1420 (m), 945 (s), 860 (vs), 810 (vs), 714 (vs), 687 (sh), 625 (w), 517 (w), 451 (m).

Na₁₄[Sb₇W₃₆O₁₃₀(OH)₃Sm₃Co₂(OAc)(H₂O)₈] \cdot ~62H₂O (11-SmCo): CoCl₂·6H₂O (95 mg) and Sm(NO₃)₃·6H₂O (178 mg) were used and a mixture of light pink (**11-SmCo**) and purple (Krebs-type POM) prismatic X-ray quality single crystals were obtained by slow evaporation of the final solution for ca. two months. Yield: 22 mg, 28% based on Sb. Anal. Calcd (found) for C₂H₁₄₈Co₂Na₁₄O₂₀₆Sb₇Sm₃W₃₆: C, 0.20 (0.18); H, 1.25 (1.10); Co, 1.00 (0.96); Na, 2.72 (2.62); Sb, 7.22 (7.12); Sm, 3.82 (3.93). IR (cm⁻¹): 1400 (m), 945 (s), 862 (vs), 810 (vs), 712 (vs), 685 (sh), 619 (w), 507 (w), 449 (m).

Na₁₄[Sb₇W₃₆O₁₃₀(OH)₃Eu₃Co₂(OAc)(H₂O)₈] \cdot ~62H₂O (11-EuCo): CoCl₂·6H₂O (95 mg) and Eu(NO₃)₃·5H₂O (171 mg) were used and a mixture of light pink (**11-EuCo**) and purple (Krebs-type POM) prismatic X-ray quality single crystals were obtained by slow evaporation of the final solution for ca. two months. Yield: 22 mg, 28% based on Sb. Anal. Calcd (found) for C₂H₁₄₈Co₂Eu₃Na₁₄O₂₀₆Sb₇W₃₆: C, 0.20 (0.31); H,

CHAPTER 4

1.24 (1.01); Co, 1.00 (1.11); Eu, 3.86 (3.95); Na, 2.72 (2.84); Sb, 7.21 (7.33). IR (cm^{-1}): 1402 (m), 945 (s), 862 (vs), 810 (vs), 712 (vs), 685 (sh), 619 (w), 507 (w), 449 (m).

Na₁₄[Sb₇W₃₆O₁₃₀(OH)₃Gd₃Co₂(OAc)(H₂O)₈] \cdot ~62H₂O (11-GdCo): CoCl₂·6H₂O (95 mg) and Gd(NO₃)₃·6H₂O (180 mg) were used and a mixture of light pink (11-GdCo) and purple (Krebs-type POM) prismatic X-ray quality single crystals were obtained by slow evaporation of the final solution for ca. two months. Yield: 30 mg, 33% based on Sb. Anal. Calcd (found) for C₂H₁₄₈Co₂Gd₃Na₁₄O₂₀₆Sb₇W₃₆: C, 0.20 (0.19); H, 1.24 (1.23); Co, 1.00 (0.98); Gd, 3.99 (4.02); Na, 2.72 (2.77); Sb, 7.20 (7.16). IR (cm^{-1}): 1410 (m), 940 (s), 862 (vs), 808 (vs), 712 (vs), 686 (sh), 617 (w), 508 (w), 449 (m).

Na₁₄[Sb₇W₃₆O₁₃₀(OH)₃Ce₃Ni₂(OAc)(H₂O)₈] \cdot ~62H₂O (11-CeNi): NiCl₂·6H₂O (95 mg) and Ce(NO₃)₃·6H₂O (174 mg) were used and a mixture of yellow (11-CeNi) and green (Krebs-type POM) prismatic X-ray quality single crystals were obtained by slow evaporation of the final solution for ca. two months. Yield: 10 mg, 8% based on Sb. Anal. Calcd (found) for C₂H₁₄₈Ce₃Na₁₄Ni₂O₂₀₆Sb₇W₃₆: C, 0.20 (0.24); H, 1.25 (1.22); Ce, 3.57 (3.63); Na, 2.73 (2.90); Ni, 1.00 (0.99); Sb, 7.23 (7.18). IR (cm^{-1}): 1425 (m), 945 (s), 862 (vs), 808 (vs), 710 (vs), 679 (sh), 619 (w), 513 (w), 442 (m). Unit cell parameters (single-crystal, 100 K): orthorhombic *Pnma*, *a* = 30.699(4), *b* = 33.231(5), *c* = 19.620(6) Å, *V* = 20015.6(7) Å³.

Na₁₄[Sb₇W₃₆O₁₃₀(OH)₃Ce₃Zn₂(OAc)(H₂O)₈] \cdot ~62H₂O (11-CeZn): Zn(NO₃)₂·6H₂O (119 mg) and Ce(NO₃)₃·6H₂O (174 mg) were used and a mixture of pale yellow (11-CeZn) and colorless (Krebs-type POM) prismatic X-ray quality single crystals were obtained by slow evaporation of the final solution for ca. two months. Yield: 9 mg, 6% based on Sb. Anal. Calcd (found) for C₂H₁₄₈Ce₃Na₁₄O₂₀₆Sb₇W₃₆Zn₂: C, 0.20 (0.15); H, 1.25 (1.18); Ce, 3.56 (3.49); Na, 2.73 (2.81); Sb, 7.23 (7.19); Zn, 1.11 (1.10). IR (cm^{-1}): 1416 (m), 945 (s), 861 (vs), 807 (vs), 711 (vs), 685 (sh), 614 (w), 510 (w), 449 (m). Unit cell parameters (single-crystal, 100 K): orthorhombic *Pnma*, *a* = 30.736(5), *b* = 33.414(6), *c* = 19.815(4) Å, *V* = 20350.2(6) Å³.

Thermal analyses. TGA/DTA analyses in the 11-LnM series have only been carried out for the 11-LaCo, 11-CeCo and 11-EuCo derivatives so far, because the combination of long crystallization times and relatively low yields of the reactions did not allow us to isolate enough amounts of solid samples before finishing this report. Studies will be completed in due course. All 11-LnCo compounds studied show TGA/DTA curves with similar profiles (see Figure A2.13 in Appendix 2). Dehydration is observed as an endothermic mass loss that extends continuously up to temperatures in the 290-320 °C range [calcd (found) for 70H₂O: 11-LaCo, 10.71 (10.64); 11-CeCo, 10.71 (10.80); 11-EuCo, 10.67 (10.56)] and it is immediately followed by combustion of the acetate ligand as indicated by an exothermic mass loss of 0.3-0.6% [calcd (found) for C₂H₃O₂: 11-LaCo, 0.50 (0.62); 11-CeCo, 0.50 (0.47); 11-EuCo, 0.50 (0.31)]. Loss of acetate is followed by a thermal stability range up to temperatures in the 469-471 °C range, above which the POM frameworks undergoes decomposition. Decomposition of the POM results in the final residue at about 540-550 °C [calcd (found) for Na₁₇Ln₃Co₂Sb₇W₃₆O_{131.5}: 11-LaCo 89.08 (87.79); 11-CeCo, 89.08 (87.76); 11-EuCo, 89.11 (87.40)].

4.2.2. X-ray Crystallography

Crystal data for compounds **11-LnM** (Ln = Ce to Gd, M = Co) are summarized in Table 4.1. Thermal vibrations were treated anisotropically for heavy atoms (W, Sb, 3d-/4f- metals). Hydrogen atoms on the acetate groups were placed in calculated positions and refined using a riding model with standard SHELXL parameters. In compounds **11-CeCo**, **11-PrCo** and **11-SmCo**, the central {Sb₄O₄} cluster located at the mirror plane was disordered over to positions with the same occupancies. More specifically, the Sb₄ atom was split into two positions (Sb4A and Sb4B) as this was the only {Sb₄O₄} metal atom in the asymmetric units that was not contained in the mirror plane. Disorder of the {Sb₄O₄} cluster is in good agreement with Gouzerh's results, who found the thermal ellipsoid of the equivalent Sb atom in his analogous cluster "flattened".²¹ The crystallographic disorder of the antimony cluster makes the trilacunary {SbW₉O₃₃} fragment located at the mirror plane to be disordered over two positions related by a 60° rotation. Consequently, three W atoms per asymmetric unit containing half of the polyanion, were positioned in the {W₃O₁₅} triad (W21, W22, W23) and refined with population factors of 0.5. The bridging and terminal O atoms of the two disordered {W₃O₁₅} triads could also be located and refined with occupancies of 0.5. The bridging O atoms connecting the top triad and the central belt of the trilacunary unit were also located over two positions. Unfortunately we were not able to model the disorder for the belt atoms, so that only 6W atoms with their respective terminal and bridging O atoms were positioned. This type of disorder in a trilacunary {SbW₉O₃₃} subunits was also observed by Gouzerh in the related [(α-SbW₉O₃₃)₄{WO₂(H₂O)}₂Ce₃(H₂O)₈(Sb₄O₄)]¹⁹⁻ POM.

All compounds display significant disorder between counterions and lattice water molecules. Six to ten sites with appropriate geometries for a Na cation were located in the Fourier maps of **11-CeCo**, **11-PrCo** and **11-SmCo**. The occupancies in these positions were initially refined without restrictions and rounded to the first decimal in the last cycle. This resulted in a total number of 4.6 (**11-CeCo**), 3.5 (**11-PrCo**) and 6 (**11-SmCo**) Na atoms per asymmetric unit containing half a polyanion. These numbers are significantly lower than the 7 Na ions determined by elemental analyses. These facts can be explained by the crystallographic disorder present in one of the trilacunary units, which led us to observe severe overlapping of two different cation/solvent networks around these fragments with consequent impossibility to discriminate most of the atomic positions. Therefore, only 22 and 21 positions for hydration water molecules were found in the asymmetric units of **11-CeCo** and **11-PrCo**, respectively. Refinement of their occupancies resulted in a total number of 16 and 15, out of the 31 water molecules determined by thermogravimetric analyses. Calculations carried out using PLATON software revealed Total Potential Solvent Area Volumes of 4375 (Ce) and 4870 (Pr) Å³ per unit cell located at $x, y, z = (0, 0, 1/2)$. These voids account for almost the 25% of the unit cell volumes and can host the remaining sodium atoms and water molecules that could not be determined crystallographically. In the case of **11-SmCo** 35 positions were located for the water molecules, resulting in a total number of 21 after free refinement of the population factors. Calculations carried out using PLATON revealed two relatively small voids of 350 Å³ per unit cell centered at $x, y, z = (0, 0, 1/2)$ and $(0, 1/2, 1/2)$.

Table 4.1. Crystallographic data for compounds **11-LnM** (Ln = Ce, Pr, Nd, Sm, Eu, Gd and M = Co).

	11-CeCo	11-PrCo	11-NdCo	11-SmCo	11-EuCo	11-GdCo
Formula	C ₂ H ₁₄₈ Ce ₃ Co ₂ Na ₁₄ O ₂₀₆ Sb ₇ W ₃₆	C ₂ H ₁₄₈ Co ₂ Na ₁₄ O ₂₀₆ Pr ₃ Sb ₇ W ₃₆	C ₂ H ₁₄₈ Co ₂ Na ₁₄ Nd ₃ O ₂₀₆ Sb ₇ W ₃₆	C ₂ H ₁₄₈ Co ₂ Na ₁₄ O ₂₀₆ Sb ₇ Sm ₃ W ₃₆	C ₂ H ₁₄₈ Co ₂ Eu ₃ Na ₁₄ O ₂₀₆ Sb ₇ W ₃₆	C ₂ H ₁₄₈ Co ₂ Gd ₃ Na ₁₄ O ₂₀₆ Sb ₇ W ₃₆
FW (g mol ⁻¹)	11800.1	11802.5	11812.2	11830.8	11835.3	11851.2
Crystal system	orthorhombic	orthorhombic	orthorhombic	orthorhombic	orthorhombic	orthorhombic
Space group	<i>Pnma</i>	<i>Pnma</i>	<i>Pnma</i>	<i>Pnma</i>	<i>Pnma</i>	<i>Pnma</i>
<i>a</i> (Å)	30.8307(2)	30.7459(2)	30.8367(3)	30.7879(2)	31.1149(8)	30.6734(4)
<i>b</i> (Å)	33.4407(3)	33.3087(3)	33.3068(4)	33.2012(4)	33.3259(7)	33.0436(4)
<i>c</i> (Å)	19.9377(2)	19.9013(2)	19.9251(2)	19.8855(2)	19.3634(8)	19.7445(5)
<i>V</i> (Å ³)	20555.8(3)	20379.8(3)	20464.5(4)	20326.8(4)	20078.5(11)	20012.3(6)
<i>Z</i>	4	4	4	4	4	4
<i>D</i> _{calcd} (g cm ⁻³)	3.813	3.847	3.834	3.866	3.915	3.934
μ (mm ⁻¹)	21.905	22.141	51.726	22.347	22.683	22.512
Reflections						
Collected	148281	143100	131578	147760	136027	146096
Unique (<i>R</i> _{int})	20556 (0.075)	18278 (0.075)	19778 (0.117)	20344 (0.057)	20091 (0.240)	23972 (0.122)
Observed ^[a]	17297	15646	17377	17532	11535	17203
Parameters	712	701	679	760	595	689
<i>R</i> (<i>F</i>) ^[a]	0.059	0.070	0.082	0.055	0.172	0.098
<i>wR</i> (<i>F</i> ²) (all)	0.142	0.169	0.210	0.126	0.338	0.235
GoF	1.134	1.129	1.074	1.156	1.082	1.046

*for [*I* > 2σ(*I*)]

Crystals of **11-NdCo**, **11-EuCo** and **11-GdCo** were systematically of much poorer quality than their analogues, as evidenced by the significantly higher values of the *R*_{int} parameter and agreement factors. The X-ray diffraction experiments resulted in very low intensity data, and therefore, we were only able to locate **11-LnM** POMs upon structural resolution. New single-crystal X-ray experiments are planned in the near future for these derivatives, together with the full data acquisition for the **11-LaCo**, **11-CeNi** and **11-CeZn** derivatives.

4.3. RESULTS AND DISCUSSION

4.3.1. Synthesis

In order to perform systematical studies on the incorporation of lanthanides in the Krebs-type framework of transition metal disubstituted $[\{M^{II}(\text{H}_2\text{O})_3\}_2(\text{WO}_2)_2(\text{SbW}_9\text{O}_{33})_2]^{10-}$ tungstoantimonates(III), we first explored the reactivity of the Co^{II}-derivative toward the complete series of rare earth metals. The Co-containing species was selected as POM precursor in a first stage because it appears to be the most labile cluster among the 3d-metal disubstituted Krebs-type tungstoantimonates(III), as shown in Chapter 2. Two different synthetic methods were applied: Method 1 is the direct reaction of the pre-formed $[\{\text{Co}^{II}(\text{H}_2\text{O})_3\}_2(\text{WO}_2)_2(\text{SbW}_9\text{O}_{33})_2]^{10-}$ POM precursor

and the lanthanide source (1:1 ratio) in 1M NaOAc buffer at 90 °C, whereas in Method 2 the precursor is generated in situ from $[\text{SbW}_9\text{O}_{33}]^{9-}$ and a Co^{2+} salt and subsequently reacted with 0.4 equivalents of the lanthanide source under the same conditions. Both methods afforded analogous results, which are summarized in Scheme 4.1. Unexpectedly, the combination of early-to-mid 4f-metals ($\text{Ln} = \text{La}–\text{Gd}$) with the Co^{II} di-substituted Krebs-type tungstoantimonate(III) (Co-POM) precursor did not result in the incorporation of lanthanide centers to the Krebs-type framework, but in decompositions and consequent reassembly of different POM fragments in the tetrameric anion $[\text{Sb}_7\text{W}_{36}\text{O}_{130}(\text{OH})_3\text{Ln}_3\text{Co}_2(\text{OAc})(\text{H}_2\text{O})_8]^{14-}$ (**11-LnCo**). On the contrary, we did not observe any reaction for late lanthanides (Tb to Lu) and the pristine Co-POM reactant was the only product isolated in the solid state as identified by IR spectroscopy.

Scheme 4.1. Results obtained in the reactions between Krebs-type tungstoantimonates(III) and lanthanides. Inset: synthetic approaches for compounds **11-LnM** (both methods afforded analogous results).

	⁵⁷ La	⁵⁸ Ce	⁵⁹ Pr	⁶⁰ Nd	⁶² Sm	⁶³ Eu	⁶⁴ Gd	⁶⁵ Tb	⁶⁶ Dy	⁶⁷ Ho	⁶⁸ Er	⁶⁹ Tm	⁷⁰ Yb	⁷¹ Lu
Co	✓ 11-LaCo	✓ 11-CeCo	✓ 11-PrCo	✓ 11-NdCo	✓ 11-SmCo	✓ 11-EuCo	✓ 11-GdCo	✗	✗	✗	✗	✗	✗	✗
Ni		✓ 11-CeNi												
Zn		✓ 11-CeZn												

Method 1

preformed

Method 2

in situ

Krebs POM

Ln³⁺

✗ : There is no reaction and the corresponding 3d-metal disubstituted Krebs-type POM precursor is obtained as single-crystals. Blank cells indicate that reactions based on those combinations will be tested in due course.

The first reaction in the series was carried out by applying method 1 with Ce^{III} as the lanthanide source. The final product of this reaction was a mixture of a few orange plates of **11-CeCo** and purple prisms of the Co-POM precursor. Similar reactions carried out in water (pH = 5) or 0.5 M NaOAc buffer did not result in the desired compound, but in the Co-POM precursor. Following method 2, purity and yields were notably improved in such a way that **11-CeCo** could be obtained as a pure crystalline phase by fractional crystallization. The first product to crystallize in this specific system is the Co-POM, and removal of these crystals allows for the **11-CeCo** compounds to be isolated as a pure batch of crystals from the mother liquors. However, this requires an extremely precise control of the crystallization time and volume of solution. Although increasing of the yield was also observed for the rest of early 4f metals (La, Pr, Nd, Sm, Eu, Gd) by applying method 2, fractional crystallization did not show to be operative and the final products were in all cases identified as mixtures of **11-LnCo** and the Co-POM precursor as the major component. Attempts for

optimizing the synthetic process in terms of yield and purity by modifying the 3d:4f:SbW₉ ratio or by changing the reaction media were unsuccessful. In fact, no identifiable solid products were obtained when similar reactions were carried out in water at pH = 5. Optimization of this synthetic work is still in progress.

The availability of a large variety of M²⁺ or M³⁺ di-, tri- and tetrasubstituted Krebs-type POMs (for more details see Chapter 2),^{18,20,22} encouraged us to extend the systematic study to some other 3d-metal containing POMs. More specifically, we decided to explore the influence of changing the 3d-metal atom in the disubstituted Krebs-type tungstoantimonates(III) and reacted the Ni and Zn derivatives with Ce^{III}. Cerium was selected as the reference lanthanide because it led to the best results in terms of yield and purity when reacted with the Co-containing POM (see above). Our observations show that reaction of Ce^{III} with the $[\{M(H_2O)_3\}_2(WO_2)_2(XW_9O_{33})_2]^{10-}$ (M = Ni, Zn) precursors also leads to the corresponding Ni (**11-CeNi**) and Zn (**11-CeZn**) analogues of **11-CeCo** by following either methods 1 or 2. However, compounds **11-CeNi** and **11-CeZn** were obtained in very low yields and always mixed together with their corresponding Krebs-type POM precursor. Completion of the synthetic system illustrated in Scheme 4.1, improvement of the yields if possible and reactions changing the charge of the heteroatom (i.e. As^{III}, Bi^{III}, Se^{IV}, Te^{IV}) are planned for the near future.

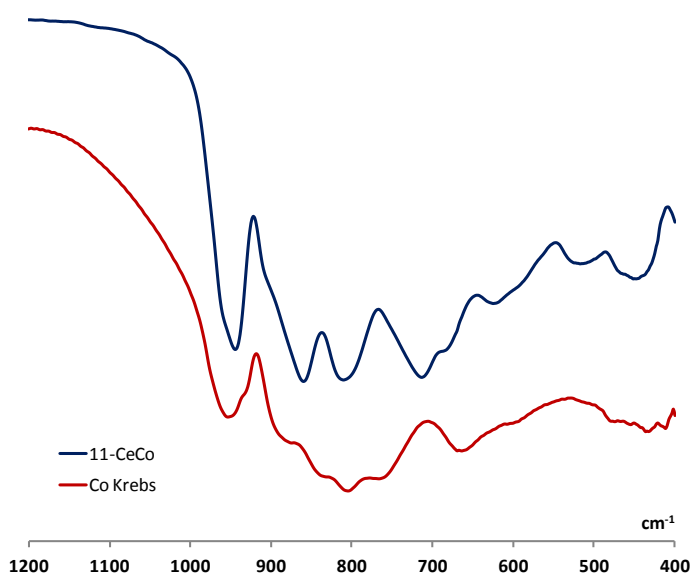


Figure 4.6. FT-IR spectra of **11-CeCo** and Co-Krebs precursor.

Table 4.2. Most representative IR bands (cm⁻¹) for **11-CeCo** compared to those of the Co-POM precursor.

11-CeCo	Co-Krebs
945	952
860	872
806	832
712	806
687	768
613	667
509	515
453	

w = weak; m = medium; s = strong; vs = very strong; sh = shoulder

All the FT-IR spectra of the **11-LnM** series are nearly identical to each other and no significant shifts are observed as a result of the change in the lanthanide or the transition metal atoms (see Appendix 2, Figure A2.8). As shown in Figure 4.6 and Table 4.2, the transformation of the POM skeleton when going from the Krebs-type structure to the final $[Sb_7W_{36}O_{130}(OH)_3 Ln_3M_2(OAc)(H_2O)_8]^{14-}$ assembly can be clearly noticed by IR spectroscopy, and therefore, this technique allows to unequivocally distinguishing compounds **11-LnM** from the 3d-metal disubstituted Krebs-type tungstoantimonate(III) precursors.

4.3.2. Molecular structure of 11-LnM

All compounds included in the **11-LnM** family are isostructural to each other. Polyanion $[\{\alpha\text{-SbW}_9\text{O}_{32}(\text{OH})\}_3\{(\text{WO}_2)_3(\text{M}^{\text{II}}\text{W}_6\text{O}_{24})\}\text{Ln}^{\text{III}}_3(\text{H}_2\text{O})_7\text{M}(\text{OAc})(\text{Sb}_4\text{O}_4)]^{19-}$ ($\text{M} = \text{Co}$, $\text{Ln} = \text{La}$ to Gd ; $\text{M} = \text{Ni}$ or Zn , $\text{Ln} = \text{Ce}$) can be viewed as a unique dissymmetric assembly of three Keggin-type trilacunary $\{\alpha\text{-SbW}_9\text{O}_{33}\}$ subunits and one Anderson-Evens-type $\{\text{MW}_6\text{O}_{24}\}$ capping cluster linked to each other via three Ln^{III} atoms, three additional *cis*- $\{\text{WO}_2\}$ groups, one $\{\text{M}^{\text{II}}(\text{OAc})\}$ moiety and the encapsulated $\{\text{Sb}_4\text{O}_4\}$ unit (Figure 4.7). The formation of **11-LnM** from the 3d-metal disubstituted Krebs-type $[\{\text{M}(\text{H}_2\text{O})_3\}_2(\text{WO}_2)_2(\text{B-}\beta\text{-SbW}_9\text{O}_{33})_2]^{10-}$ ($\text{M} = \text{Co}$, Ni , Zn) POM precursor upon reaction with lanthanides implies not only the decomposition of the Krebs-type framework, but also the transformation of the $[\text{B-}\beta\text{-SbW}_9\text{O}_{33}]^9$ units to the corresponding α -isomers and the formation of new POM fragments like the Anderson-Evens cluster.

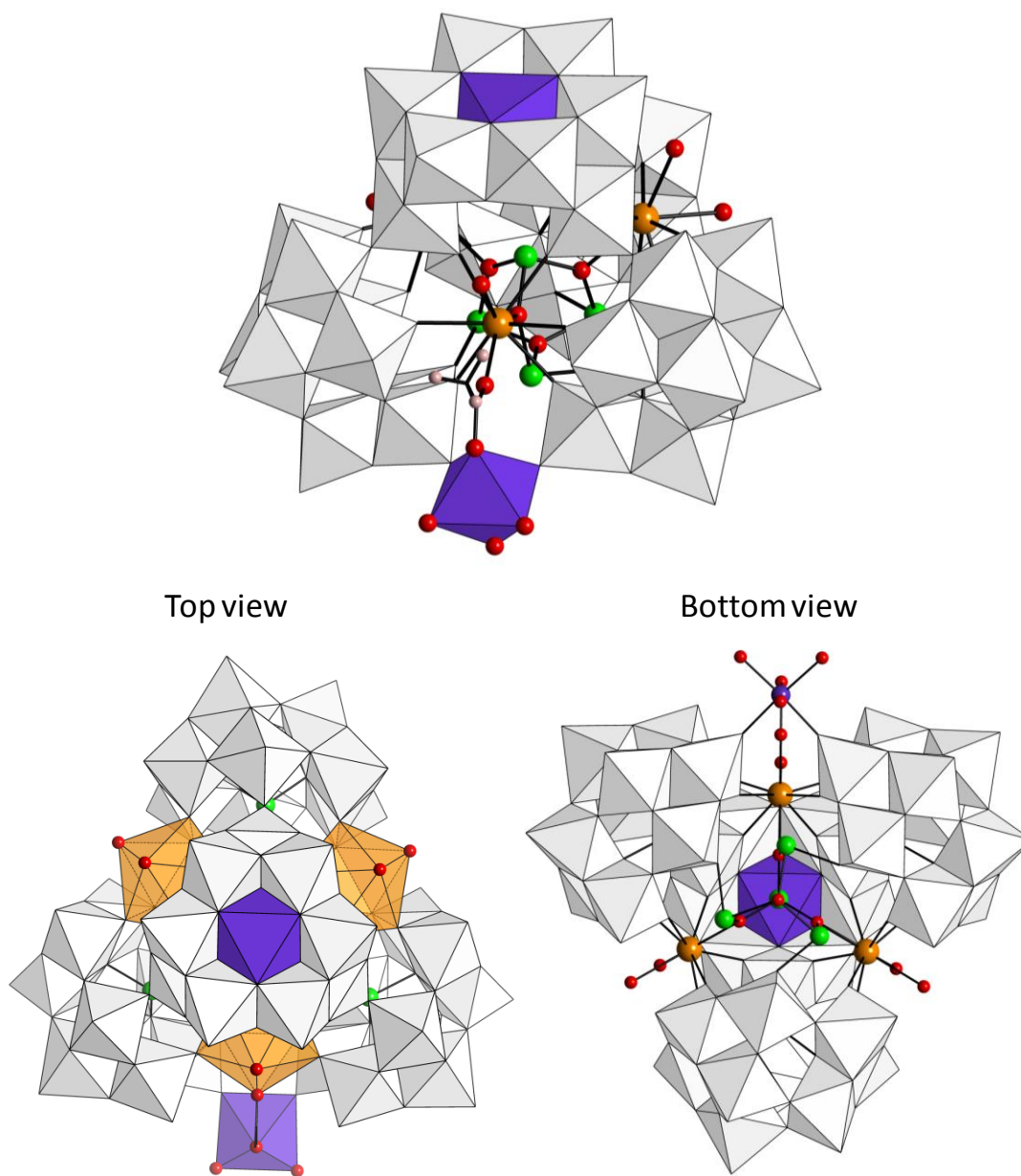


Figure 4.7. Side, top and bottom views of the combined polyhedral / ball & stick representation of **11-LnM**.

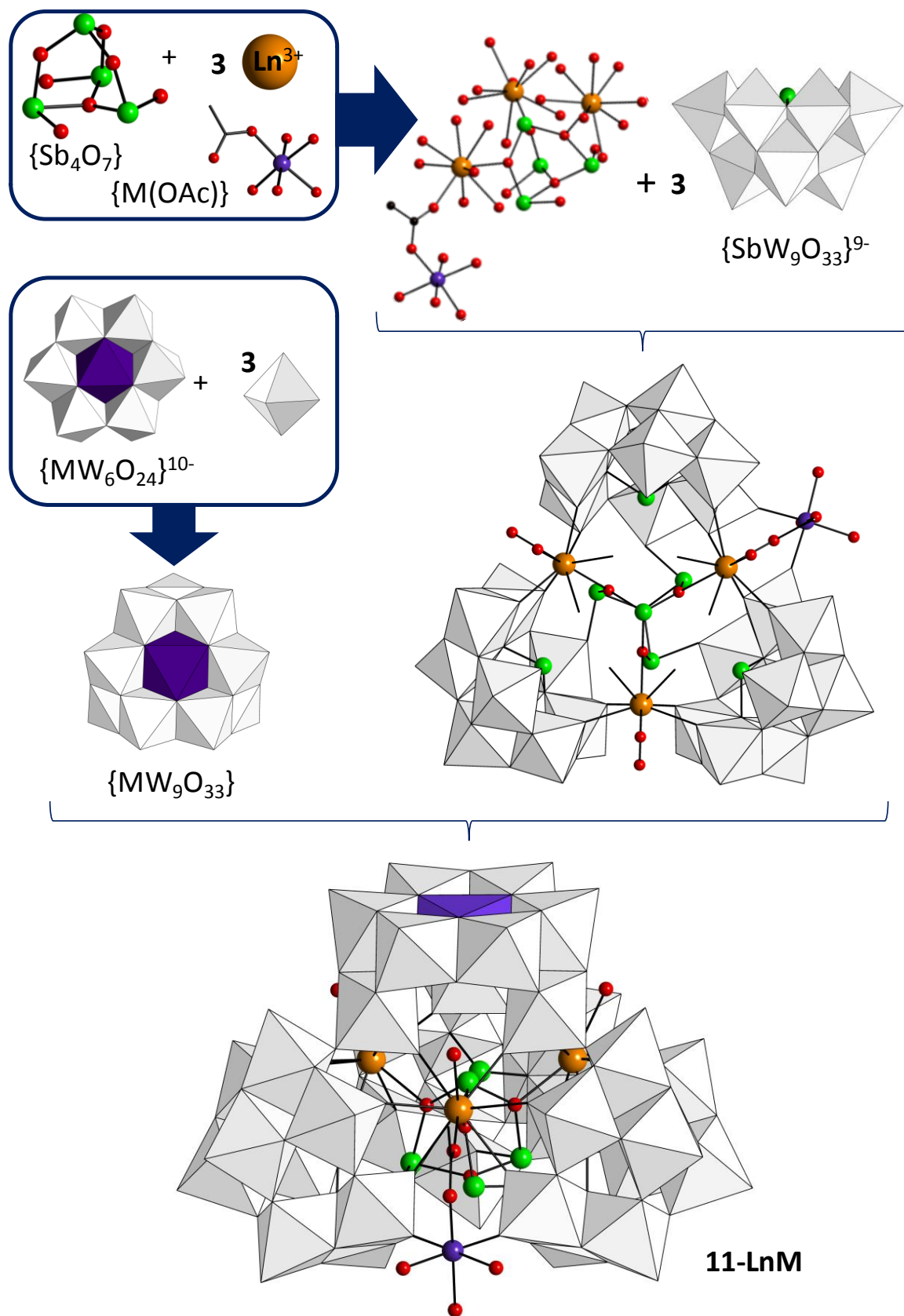


Figure 4.8. Schematic representation of the 11-LnM assemblies from their basic structural components.

The three $\{\alpha\text{-SbW}_9\text{O}_{33}\}$ fragments are linked together through the coordination spheres of three lanthanide atoms. The 4f-metal atoms are bound to two terminal oxo groups from each adjacent trilacunary unit, but three different configurations are observed. Each lanthanide coordinates either to i) two edge-sharing $\{\text{W}_3\text{O}_{13}\}$ trimers; ii) two corner sharing $\{\text{W}_2\text{O}_{11}\}$ units; or iii) one $\{\text{W}_3\text{O}_{13}\}$ unit and one $\{\text{W}_2\text{O}_{11}\}$ moiety. The 4f-metal center coordinated to two $\{\text{W}_2\text{O}_{11}\}$ units is also connected to a 3d metal center through an acetate bridging ligand in bis(monodentate) fashion, leading to a $\{\text{LnM}(\mu\text{-OAc})\}$ dimeric moiety. This 3d-metal center (M2) reinforces the linkage between adjacent trilacunary units by further coordinating to two terminal oxo atoms from each POM subunit (Figure 4.8).

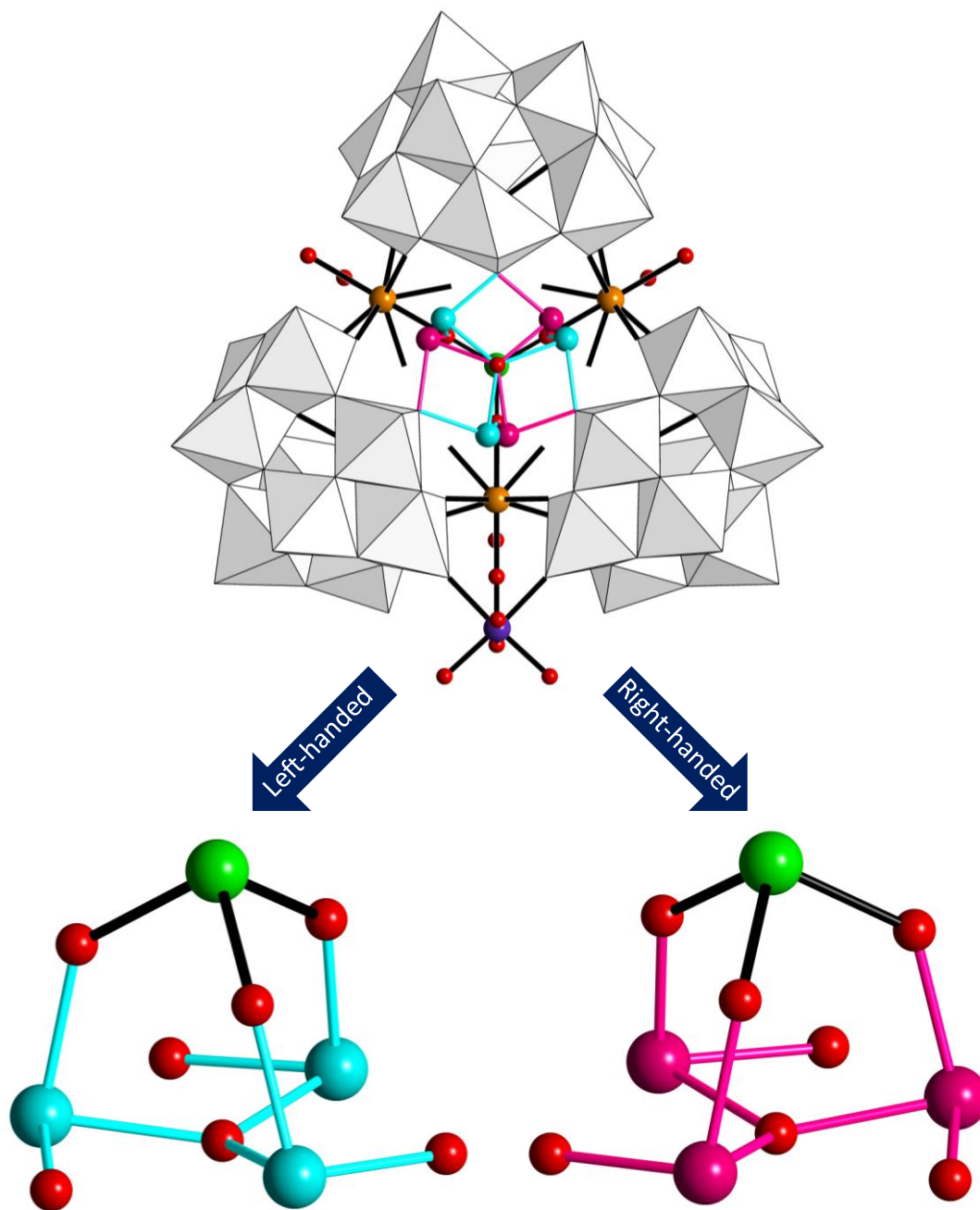


Figure 4.9. Left-handed (left) and right-handed (right) orientations of the $\{\text{Sb}_4\text{O}_3(\mu_3\text{-O})(\mu_2\text{-O})_3\}$ cluster in **11-LnM**.

The assembly of three trilacunary subunits linked by three 4f ions encapsulates a central $\{\text{Sb}_4\text{O}_4\}$ antimony cluster. This unusual cluster is formed by a $\{\text{Sb}_3(\mu_3\text{-O})\}$ triangle capped by a SbO_3 pyramid, which also links the three lanthanide centers. The four antimony atoms are located at the corners of a distorted tetrahedra (Sb...Sb distances: 3.60–3.65 Å), and each of the Sb centers of the $\{\text{Sb}_3(\mu_3\text{-O})\}$ triangle complete their coordination sphere with a terminal O atom of a different trilacunary subunit, thus, reinforcing the POM assembly. In the resulting $\{\text{Sb}_4\text{O}_3(\mu_3\text{-O})(\mu_2\text{-O})_3\}$ fragment, the Sb-O bond lengths are in the expected range (1.843(4)–2.164(3) Å) and the Sb atoms of the triangle display *fac*-trivacat octahedral coordination as indicated by CShM values ranging from 0.2 to 1.5. It is worth mentioning that POM assemblies containing antimony based oxo-clusters were rarely reported before.²³ According to single-crystal X-ray diffraction studies, the antimony cluster is disordered over two different positions: the $\{\text{Sb}_4\text{O}_4\}$ fragment appears to pivot on the SbO_3 capping pyramid in such a way that it can undergo twisting of ca. 20° with respect to the $\text{O}_3\text{Sb}-(\mu_3\text{-O})$ axis. As a result of this twisting each Sb atom of the triangle results linked either to the O atom of the nearest trilacunary subunit in clockwise direction or to that of the nearest subunit in counterclockwise one.

This pivoting of the $\{\text{Sb}_4\text{O}_4\}$ unit confers chirality to the overall assembly, in such a way that the **11-Ln** POMs can show two enantiomerically related forms: left-handed with the antimony cluster in counterclockwise orientation and right-handed showing the cluster oriented clockwise (Figure 4.9). Compounds **11-LnM** crystallize in the orthorhombic *Pnma* group with the POM located on a mirror plane including the $\{\text{LnM}(\mu\text{-OAc})\}$ moiety, the capping SbO_3 pyramid and the bridging $(\mu_3\text{-O})$ ligand, and therefore, each crystal must contain equal amounts of both left- and right-handed forms. The two possible orientations of the central antimony cluster most likely induce the crystallographic disorder observed for the trilacunary subunit lying on the mirror plane. To rule out that these crystallographic disorders originate from a superimposed symmetry, the structures of **11-LnM** have also been solved in the triclinic *P1* space group and similar results have been observed. This confirms that disorders are inherent to the compounds, and more specifically, to their crystallization as racemates.

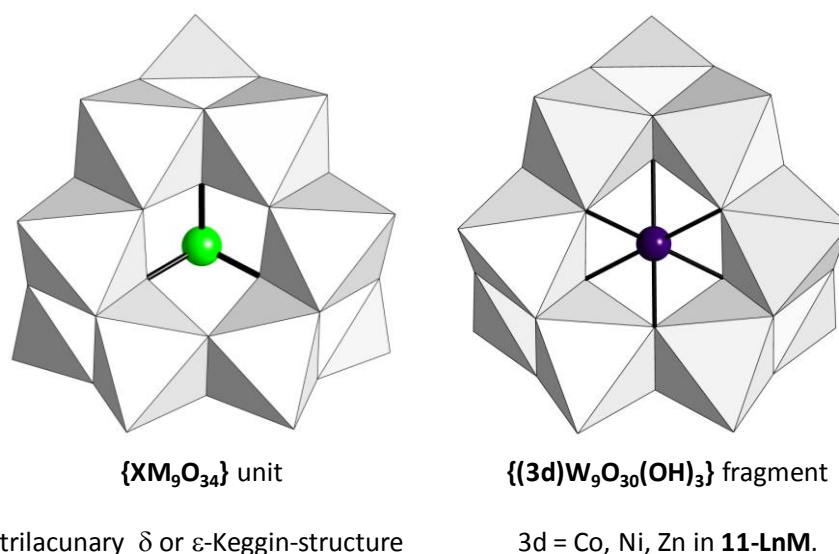


Figure 4.10. Structure of the trilacunary $\{\text{XM}_9\text{O}_{34}\}$ unit derived from the δ or ε Keggin-type structure compared to the $\{(3d)\text{W}_9\text{O}_{30}(\text{OH})_3\}$ subunit in **11-LnM** POMs (3d = Co, Ni, Zn).

The structure of the **11-LnM** anion is completed with the capping Anderson-Evans-type $\{M^II W_6 O_{24}\}$ POM fragment via three extra *cis*- $\{WO_2\}$ groups. Although the incorporation of different heteroatoms into molecular α -Anderson-Evans-type polyoxomolybdates has been extensively studied,²⁴ polyoxotungstate analogues are less abundant, especially when considering those containing 3d-metals. In fact, the $[NiW_6O_{18}(OH)_6]^{4-}$ derivative represents the only example to date of a structurally characterized Anderson-Evans-type polyoxotungstate containing a divalent first-row transition metal in the central position of the $\{W_6O_{24}\}$ ring.²⁵ Therefore, the $\{MW_6O_{24}\}^{10-}$ ($M = Co, Zn$) fragments observed in the **11-LnM** series are completely unprecedented. In the tetrameric **11-LnM** assemblies, each additional *cis*- $\{WO_2\}$ group is linked to the Anderson-Evans cap by sharing edges with a $\{W_2O_{10}\}$ dimer of the tungstate ring, in such a way that these dimers are converted into well-known $\{W_3O_{13}\}$ trimers. Thus, the Anderson-Evans becomes $\{MW_9O_{33}\}$ subunit with a polyoxotungstate shell composed of three $\{W_3O_{13}\}$ trimers sharing edges. This shell is virtually identical to that of a hypothetical trilacunary derivative of the δ or ε -Keggin cluster and represent a novel building block in POM chemistry (Figure 4.10).

The $\{MW_9O_{33}\}$ subunit caps the $\{Sb_4O_4\}$ -encapsulated basal assembly of three $\{\alpha\text{-SbW}_9O_{33}\}$ subunits connected by lanthanide atoms through W—O—W corner sharing (Figure 4.11). To our knowledge, this is the first example in the literature where an Anderson-type POM acts as a building-block of a larger cluster by establishing W—O—W linkages. Bond Valence Sum (BVS) calculations²⁶ indicate protonation of the bridging O in the W—O—W linkages between trilacunary $\{SbW_9O_{33}\}$ units and the capping $\{MW_9O_{33}\}$ subunit (BVS values, 1.027-1.060). These results are in full agreement with the number of Na ions found by elemental analyses

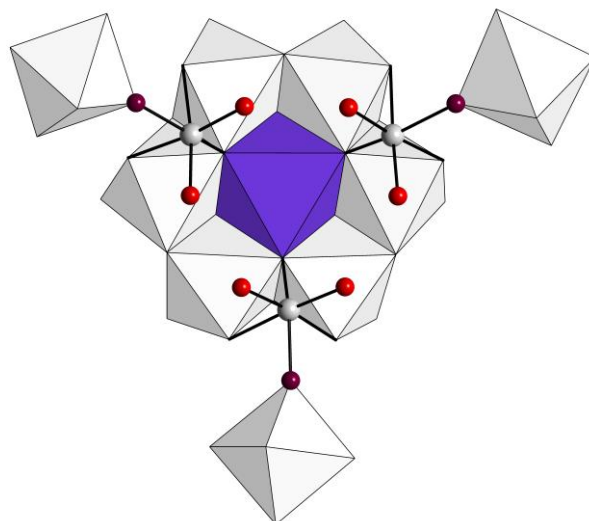


Figure 4.11. Schematic representation of the linkage between trilacunary units and the Anderson-type POM via three additional *cis*- $\{WO_2\}$ groups. Protonation sites (OH units) depicted as brown balls.

A similar tetrameric assembly containing the same $\{Sb_4O_4\}$ antimony cluster was previously observed by Gouzerh in his $[(\alpha\text{-SbW}_9O_{33})_4\{WO_2(H_2O)\}_2Ce_3(H_2O)_8(Sb_4O_4)]^{19-}$ anion.²¹ For comparison, the trimeric $\{(\alpha\text{-SbW}_9O_{33})_3Ln_3(H_2O)_8(Sb_4O_4)\}$ unit is virtually identical for both structures, but for the addition of one $\{M(OAc)\}$ moiety linked to one of the lanthanide centers in **11-LnM**. However, the capping unit in Gouzerh's POM is a trilacunary $\{SbW_9O_{33}\}$ fragment connected by two additional $\{WO_2(H_2O)\}$ groups to the trimeric basal assembly, whereas **11-LnM** is capped by a novel POM building block formed by condensation of an Anderson-Evans-type $\{M^II W_6 O_{24}\}$ POM fragment with

the three extra $\{\text{WO}_2\}$ units (Figure 4.12). Related tetrameric $[(\text{BiW}_9\text{O}_{33})_4(\text{WO}_3)\{\text{Bi}_6(\mu_3\text{-O})_4(\mu_2\text{-OH})_3\}(\text{Ln}_3(\text{H}_2\text{O})_6\text{CO}_3)]^{22-}$ ($\text{Ln} = \text{La}, \text{Pr}, \text{Nd}$) structures showing an hexameric central bismuth-oxo-cluster have also been reported recently.²⁷

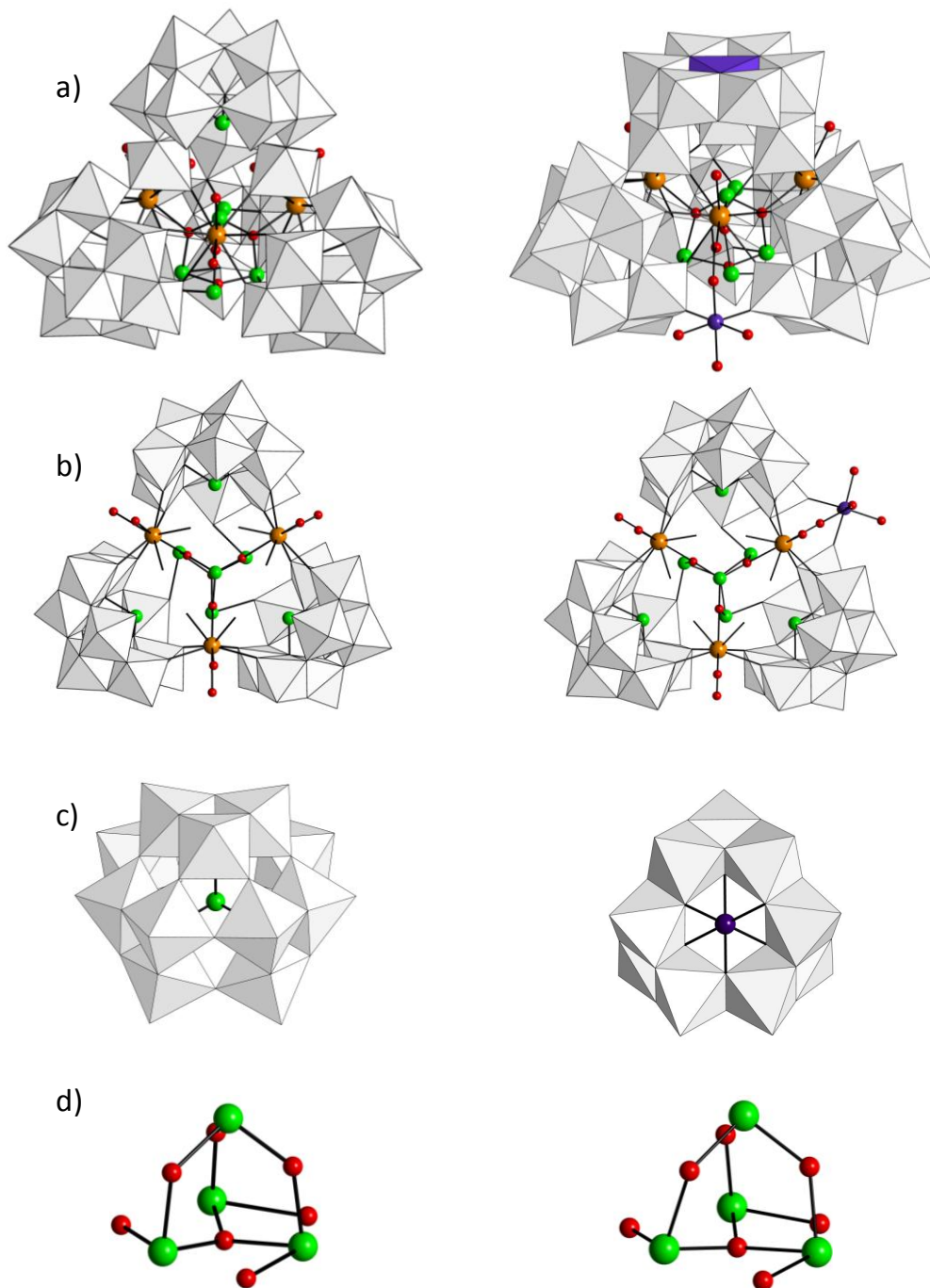


Figure 4.12. Structural comparison between Gouzerh's $[(\alpha\text{-SbW}_9\text{O}_{33})_4\{\text{WO}_2(\text{H}_2\text{O})\}_2\text{Ce}_3(\text{H}_2\text{O})_8(\text{Sb}_4\text{O}_4)]^{19-}$ anion (left) and **11-LnM** (right) regarding: (a) molecular structure, (b) trimeric basal unit, (c) capping unit; (d) right-handed orientation of the central $\{\text{Sb}_4\text{O}_3(\mu_3\text{-O})(\mu_2\text{-O})\}^{2-}$ cluster.

Both 3d-metal ions in **11-LnM** structures display octahedral MO_6 geometries. The six O atoms of the M1 sphere belong to the Anderson-Evans $\{\text{W}_6\text{O}_{24}\}$ ring, whereas the coordination geometry for M2 is defined by two O_{POM} atoms from neighboring $\{\alpha\text{-SbW}_9\text{O}_{33}\}$ subunits, one O atom from the acetate bridging ligand and three water molecules. The Co—O bond lengths for the **11-LnCo** ($\text{Ln} = \text{Ce}$ to Gd) derivatives are compiled in Table 4.3, together with the Continuous Shape Measures (CShM)

for the cobalt(II) centers in comparison to the ideal octahedral reference polyhedron. The Co—O bond lengths are similar for both Co1 and Co2 centers in all the **11-LnCo** derivatives. The values observed indicate that the Co1 centers in the Anderson-Evans type fragments are displaced toward the triangular face located at the inner part of the cluster. This results in a considerably distorted octahedron, which is in good agreement with the calculated CShM values. In the case of the Co2 centers, the octahedral geometry is quiet more regular.

Table 4.3. 3d- and 4f-metal –oxygen bond lengths (Å) and values of the Continuous Shape Measures (CShM) with the ideal octahedron as reference shape (CShM = 0) in compounds **11-LnCo** (Ln = Ce to Gd, M =Co).

	11-CeCo	11-PrCo	11-NdCo	11-SmCo	11-EuCo	11-GdCo	
3d-metals	Co1–O1M	2.058(12)	2.049(15)	2.025(13)	2.042(11)	2.04(3)	2.046(12)
	Co1–O1M ⁱ	2.058(12)	2.049(15)	2.025(13)	2.042(11)	2.04(4)	2.05(2)
	Co1–O3M	2.108(12)	2.109(15)	2.124(13)	2.099(11)	2.11(4)	2.08(2)
	Co1–O3M	2.108(12)	2.109(15)	2.124(13)	2.099(11)	2.11(5)	2.08(2)
	Co1–O11M	2.091(18)	2.08(2)	2.08(2)	2.098(15)	2.07(5)	2.11(3)
	Co1–O33F	2.063(17)	2.04(2)	2.057(19)	2.042(15)	2.03(6)	2.02(3)
	CShM (OC) ^b	0.946	0.966	0.882	0.856	0.893	0.867
	Co2–O15T	2.054(13)	2.030(16)	2.053(15)	2.043(12)	2.08(4)	2.05(2)
	Co2–O15T ⁱ	2.054(13)	2.030(16)	2.053(15)	2.043(12)	2.08(5)	2.05(2)
	Co2–O1L	2.06(2)	2.07(3)	2.05(2)	2.069(18)	2.07(5)	2.09(4)
	Co2–O1MW	2.082(14)	2.085(18)	2.051(18)	2.069(13)	2.11(4)	2.08(2)
	Co2–O1MW	2.082(14)	2.085(18)	2.051(18)	2.069(13)	2.11(5)	2.08(2)
	Co2–O2MW	2.123(19)	2.12(2)	2.13(2)	2.114(16)	2.20(7)	2.13(3)
	CShM (OC) ^b	0.338	0.301	0.245	0.383	0.494	0.503
4f-metals	Ln1–O5F	2.534(11)	2.511(14)	2.564(17)	2.498(10)	2.45(4)	2.489(19)
	Ln1–O5F ⁱ	2.534(11)	2.511(14)	2.564(17)	2.498(10)	2.45(4)	2.489(19)
	Ln1–O14F	2.462(12)	2.464(16)	2.447(19)	2.416(11)	2.43(4)	2.431(19)
	Ln1–O14F ⁱ	2.462(12)	2.464(16)	2.447(19)	2.416(11)	2.43(4)	2.43(2)
	Ln1–O15F	2.585(11)	2.577(15)	2.514(17)	2.542(11)	2.52(4)	2.516(19)
	Ln1–O15F ⁱ	2.585(11)	2.577(15)	2.514(17)	2.542(11)	2.52(4)	2.516(19)
	Ln1–O3SS	2.558(19)	2.56(2)	2.48(3)	2.488(16)	2.34(6)	2.51(3)
	Ln1–O2L	2.381(19)	2.37(2)	2.36(3)	2.329(15)	2.30(6)	2.35(3)
	Ln1–O1FW	2.54(2)	2.53(3)	2.48(3)	2.454(16)	2.48(7)	2.44(3)
	Ln2–O4F	2.524(12)	2.507(15)	2.505(18)	2.476(11)	2.44(5)	2.45(2)
	Ln2–O5F2	2.523(13)	2.492(15)	2.47(2)	2.472(11)	2.47(4)	2.45(2)
	Ln2–O17F	2.581(13)	2.579(17)	2.578(14)	2.550(12)	2.53(5)	2.55(2)
	Ln2–O18F	2.463(13)	2.449(17)	2.44(2)	2.424(12)	2.37(4)	2.39(2)
	Ln2–O25F	2.561(14)	2.537(17)	2.534(15)	2.530(13)	2.48(5)	2.50(2)
	Ln2–O26F	2.457(14)	2.431(17)	2.447(17)	2.415(12)	2.32(4)	2.40(2)
	Ln2–O2SS	2.501(14)	2.491(19)	2.45(2)	2.445(14)	2.43(4)	2.41(2)
	Ln2–O2FW	2.589(15)	2.574(18)	2.536(18)	2.523(13)	2.48(4)	2.49(2)
	Ln2–O3FW	2.556(13)	2.543(16)	2.498(18)	2.481(12)	2.48(4)	2.46(2)

Symmetry Codes. i: x, -y+3/2, z

The three lanthanide atoms in each **11-LnCo** (Ln = Ce to Gd) anion display distorted nine-coordinated geometries. Besides the O_{POM} atoms from the $\{\text{SbW}_9\text{O}_{33}\}$ subunits, the coordination spheres are completed by two oxo groups from contiguous $\{\text{WO}_2\}$ centers, one oxo ligand from the central antimony cluster (O_s) and two water molecules (O_w). Regarding the Ln—O bond lengths (Table 4.3), no clear trend originating from the lanthanide contraction effect is observed. This fact might be due to a low flexibility in the **11-LnM** assembly when incorporating different Ln atoms in the structure. This fact could explain why small, late lanthanide atoms are not suitable for being part of the **11-LnM** assembly as indicated by our experimental results. Nevertheless, the poor quality of the crystal data for **11-NdCo**, **11-EuCo** and **11-GdCo** also prevent us from observing any clear trend.

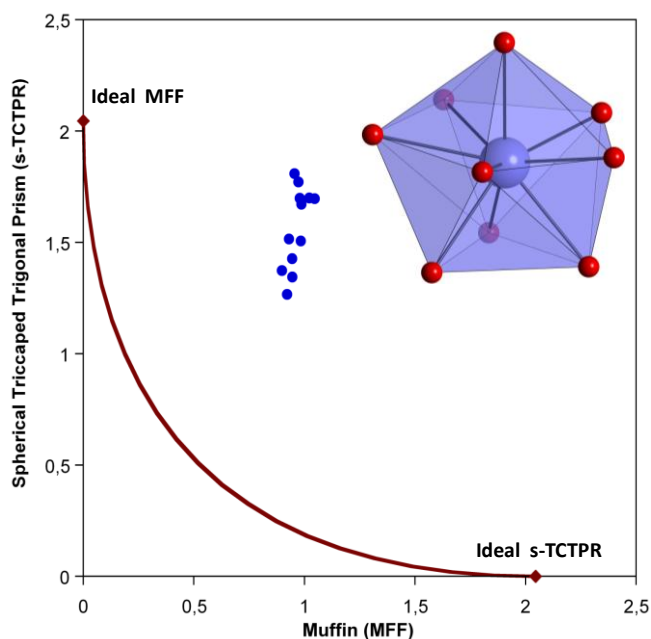


Figure 4.13. Spherical bicapped trigonal prism (s-TCTPR) vs. muffin (MFF) shape map for the 4f ions in compounds **11-LnM** (solid line : minimal distortion pathway between the reference shapes). Inset: detail of the lanthanide coordination geometry.

The distorted nine-coordinated geometries have been analyzed through CShM (Table 4.4).²⁸ For all the lanthanide atoms, close CShM values relative to the C_s -symmetric Muffin (MFF, 0.898–1.046), spherical tricapped trigonal prism (s-TCTPR, 1.267–1.772) and spherical capped square antiprism s-CSAPR, 1.226–1.435) shapes are observed. The lower CShM values are in all cases obtained by comparison to the ideal MFF shape. This, together with the high deviations observed in the minimal distortion pathway between the MFF and s-CSAPR reference polyhedra (1.28–1.44, much higher than the upper limit of 0.3 selected by Casanova et al.) suggested that the geometry of the lanthanide centers could fall in the pathway between the MFF and s-TCTPR shapes. The MFF vs s-TCTPR shape map (Figure 4.13) shows that the coordination polyhedra of the 4f-metal centers in **11-LnCo** scatter from the ideal MFF geometry toward the s-TCTPR one close to the trend marked by the minimal distortion pathway between the two reference polyhedra. The path deviation values in the 0.45–0.62 range are still above those expected for an intermediate geometry, but close enough considering that Casanova et al. define the limit of 0.3 as “somewhat arbitrary”. Therefore, the lanthanide centers in **11-LnCo** can be best described as muffin-like distorted toward spherical tricapped trigonal prisms.

Table 4.4. Continuous Shape Measures for the nine-coordinated spheres of the lanthanide atoms in compounds **11-LnM** (Ln = Ce to Gd, M =Co)

	11-CeCo	11-PrCo	11-NdCo	11-SmCo	11-EuCo	11-GdCo
MFF	0.930	0.898	0.979	0.945	0.983	0.921
	0.955	0.973	0.944	0.986	1.022	1.046
TCTPR	1.515	1.374	1.699	1.345	1.700	1.267
	1.809	1.772	1.427	1.671	1.506	1.697
JTCTPR	3.915	3.681	4.116	3.799	4.187	3.509
	4.174	4.171	3.965	4.051	3.924	4.123
CSAPR	1.402	1.317	1.349	1.310	1.246	1.226
	1.409	1.435	1.383	1.351	1.379	1.396
JCSAPR	2.681	2.540	2.574	2.548	2.607	2.385
	2.738	2.771	2.620	2.606	2.677	2.625

[a] *Abbreviations.* **MFF**: muffin (C_3); **TCTPR**: spherical tricapped trigonal prism (D_{3h}); **JTCTPR**: Johnson tricapped trigonal prism (D_{3h}); **CSAPR**: capped square antiprism (C_{4v}); **JCSAPR**: Johnson capped square antiprism (C_{4v}). For a graphical representation of these polyhedra, see: Appendix 2, Figure A2.17. Values highlighted in grey correspond to the best geometry.

Table 4.5. Donor-acceptor distances of the O-H...O_{POM} hydrogen-bonds and Co1...Co2 distances in the crystal packing of **11-LnCo** (Ln= Ce to Gd) (Å).

	O_W-H...O_{POM}		Intermolecular Co1...Co2	
11-CeCo	O1MW...O3M ⁱ	2.669(18)	Co1...Co2 ⁱⁱⁱ	4.959(4)
	O1MW...O3M ⁱⁱ	2.669(18)		
	O2MW ...O11M ⁱⁱⁱ	2.68(2)		
11-PrCo	O1MW...O3M ⁱ	2.66(2)	Co1...Co2 ⁱⁱⁱ	4.943(6)
	O1MW...O3M ⁱⁱ	2.66(2)		
	O2MW ...O11M ⁱⁱⁱ	2.69(3)		
11-NdCo	O1MW...O3M ⁱ	2.68(5)	Co1...Co2 ⁱⁱⁱ	4.943(17)
	O1MW...O3M ⁱⁱ	2.68(5)		
	O2MW ...O11M ⁱⁱⁱ	2.69(9)		
11-SmCo	O1MW...O3M ⁱ	2.682(16)	Co1...Co2 ⁱⁱⁱ	4.943(3)
	O1MW...O3M ⁱⁱ	2.682(16)		
	O2MW ...O11M ⁱⁱⁱ	2.69(2)		
11-EuCo	O1MW...O3M ⁱ	2.57(5)	Co1...Co2 ⁱⁱⁱ	4.942(17)
	O1MW...O3M ⁱⁱ	2.57(5)		
	O2MW ...O11M ⁱⁱⁱ	2.67(9)		
11-GdCo	O1MW...O3M ⁱ	2.69(3)	Co1...Co2 ⁱⁱⁱ	4.909(7)
	O1MW...O3M ⁱⁱ	2.69(3)		
	O2MW ...O11M ⁱⁱⁱ	2.70(4)		

Symmetry codes: (i) 1/2+x, y, 3/2-z (ii) -1/2+x, y, 3/2-z (iii) -1/2+x, 3/2-y, 3/2-z

4.3.3. Crystal packing of **11-LnM**

The crystal packing of **11-LnM** is dominated by the face-to-face interaction between the octahedral M1 and M2 centers from adjacent POMs. Three strong hydrogen bonds are established between the O atoms delimiting the external face of the M1 center buried into the Anderson-type structure and the three *fac*-arranged water molecules from the M2 center embedded between two trilacunary POMs and linked to the lanthanide (III) center through a bridging acetate anion. These interactions result in zigzagging chains of **11-LnM** anions running along the [100] direction (Figure 4.14). Geometrical parameters of the hydrogen bonding interactions for the **11-LnCo** derivatives (Ln = Ce to Gd) are summarized in Table 4.5.

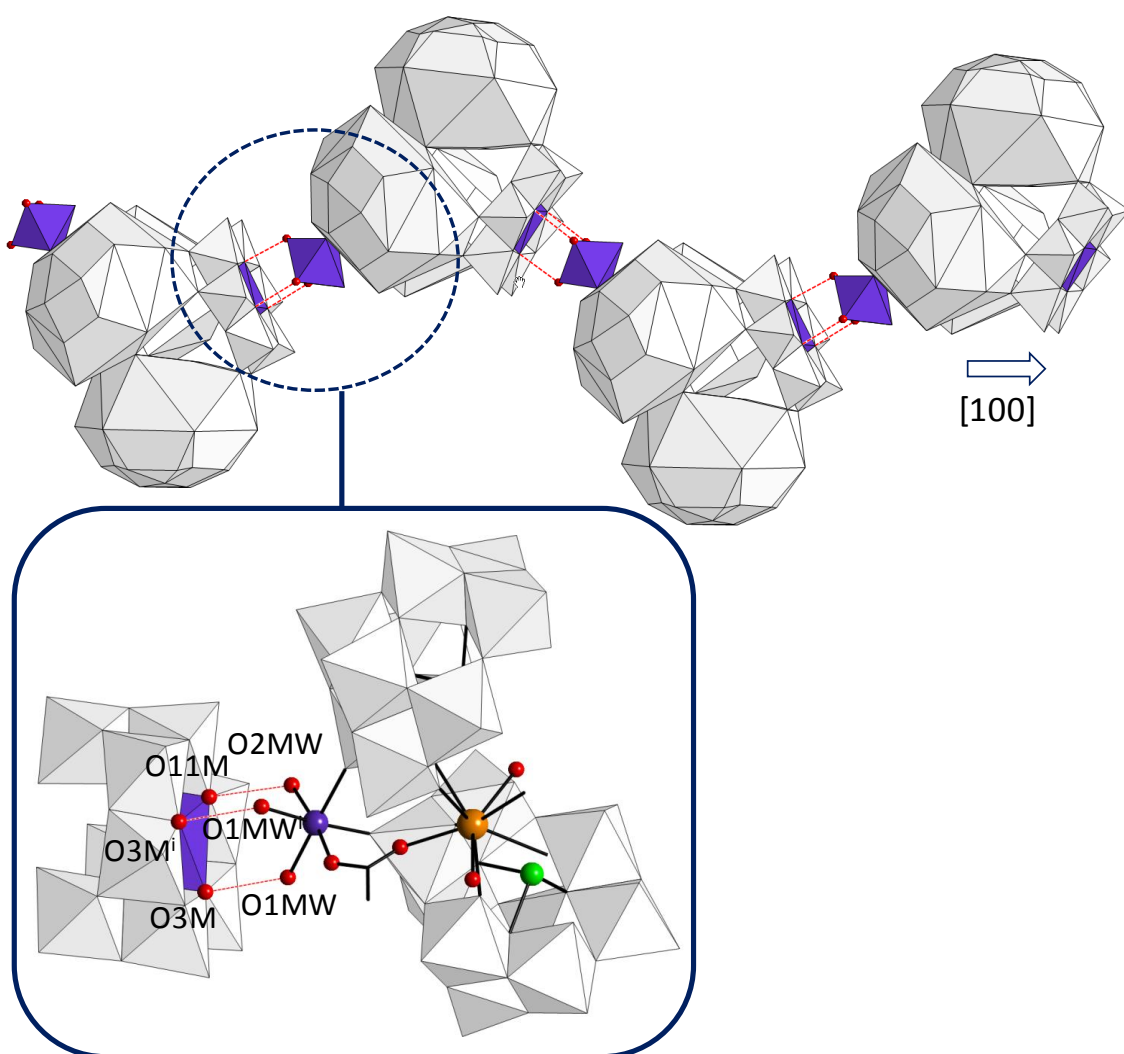


Figure 4.14. Hydrogen-bonded one-dimensional POM arrangement in the crystal structure of **11-LnM**. Detail of the hydrogen bonding interactions together with atom labeling.

4.3.4. Solution behavior. Laser Light Scattering studies on 11-CeCo

Compound **11-CeCo** self-assembles into spherical, hollow and single-layered blackberry-type structures in 0.1 mg mL^{-1} water solution, as confirmed by a combination of DLS, SLS and TEM studies. Time resolved scattering intensity plot recorded at 90° consists on the expected sigmoidal curve showing a relatively long lag period of almost 15 days. CONTIN analysis from the DLS study reveals the presence in solution of large assemblies with no angular dependence, which show narrow distribution and average values for hydrodynamic radius of $R_{h,0} = 39 \text{ nm}$. SLS study by partial Zimm plot indicates an average radius of gyration of $R_g = 37.8 \pm 0.8 \text{ nm}$ for the assemblies. The hollow spherical nature of the assemblies inferred from the $R_h/R_g \approx 1$ ratio was confirmed by TEM images taken for a diluted solution of **11-CeCo** aged for 3 weeks (Figure 4.15).

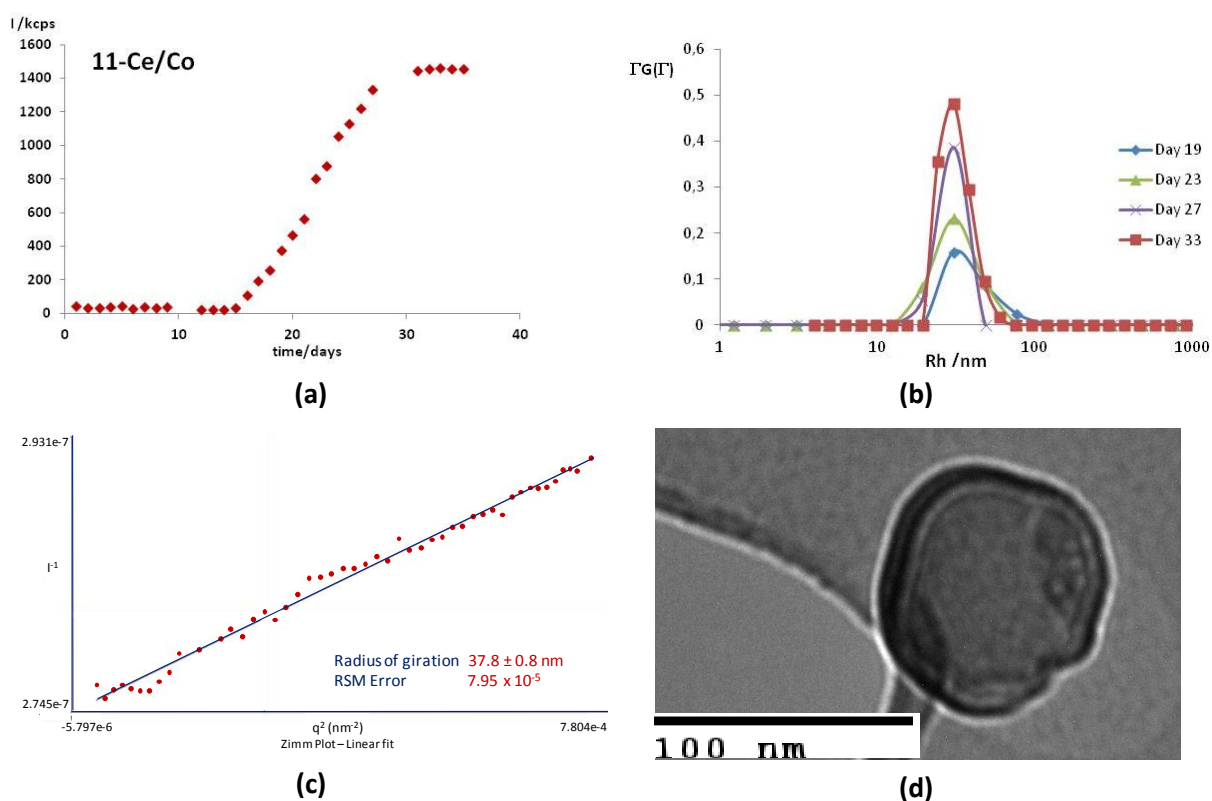


Figure 4.15. (a) Time-resolved scattering intensity plot; (b) CONTIN analysis from the DLS data at different stages; (c) partial Zimm plot from the SLS data; and (d) TEM image of a blackberry-type structure for a 0.1 mg mL^{-1} aqueous solution of **11-CeCo**.

The fact that the **11-CeCo** species can undergo formation of blackberry-type structures strongly suggests that this type of POM architecture is stable in solution and does not dissociate in any of its basic building blocks because no clusters smaller than 2 nm have been found to be able to form blackberries to date.²⁹ This feature was confirmed by ESI-MS as shown in Figure 4.16. The negative ESI mass spectra recorded at low cone voltage displays the intact $[\text{Sb}_7\text{W}_{36}\text{O}_{130}(\text{OH})_3\text{Ce}_3\text{Co}_2(\text{OAc})(\text{H}_2\text{O})_8]^{14-}$ anion as four groups of signals spanning from m/z 1450 to 2650. The isotopic pattern inspection, together with the m/z spacing between signals, indicate that the detected main species can be attributed to the $\{\text{M}\}^n$ series with 7- (m/z 1458.8, $\{\text{M}\}^{7-}$), 6- (m/z 1711.8, $\{\text{M}\}^{6-}$), 5- (m/z 2076.7, $\{\text{M}\}^{5-}$) and 4- (m/z 2633.3, $\{\text{M}\}^{4-}$) charge states, where $\{\text{M}\}^{(14-n)-} =$

$[\text{Sb}_7\text{W}_{36}\text{O}_{130}(\text{OH})_3\text{Ce}_3\text{Co}_2(\text{OAc})+x\text{H}_2\text{O}+m\text{H}^++(n-m)\text{Na}^+]^{(14-n)-}$. As observed in the ESI-MS experiments carried out earlier in this work (Chapter 3), each species displays different extent of protonation and counter-ion content, as well as the presence of loosely associated solvent molecules. Low intensity peaks located between those corresponding to the $\{\text{M}\}^{n-}$ anions could be ascribed to impurities, as crystals of **11-CeCo** for the solution studies were selected manually from the mixture of crystals obtained as the reaction product. The ESI mass spectrum of the two-day aged sample is virtually identical to that observed for the freshly prepared sample, confirming the stability of the POM framework in solution.

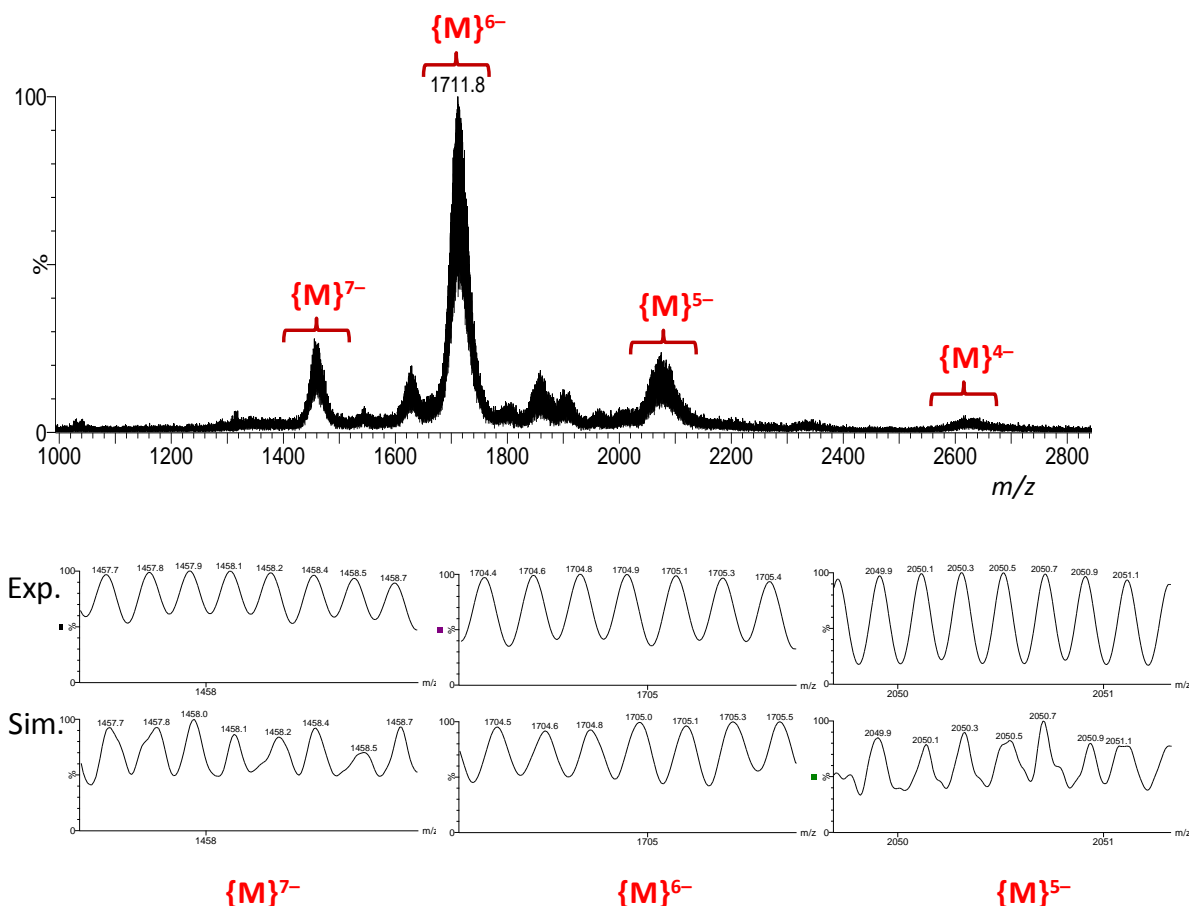


Figure 4.16. Top: Negative ESI mass spectrum of **11-CeCo** ($U_c = 15$ V). Bottom: Experimental (top) vs simulated (bottom) isotopic patterns for the $\{\text{M}\}^{7-}$, $\{\text{M}\}^{6-}$ and $\{\text{M}\}^{5-}$ charge states. $\{\text{M}\}^{(14-n)-} = [\text{Sb}_7\text{W}_{36}\text{O}_{130}(\text{OH})_3\text{Ce}_3\text{Co}_2(\text{OAc})+x\text{H}_2\text{O}+m\text{H}^++(n-m)\text{Na}^+]^{(14-n)-}$

4.3.5. ESR spectroscopy studies on **11-CeCo** and **11-GdCo**

Variable temperature (4.2 — 100 K) electronic spin resonance (ESR) spectra recorded in X-band for the **11-CeCo** derivative are illustrated in Figure 4.17. All the spectra display an anisotropic broad resonance centered at c.a. 1550 G that can be described in terms of spin doublet $S = 1/2$ interacting with a single ^{59}Co nucleus ($I = 7/2$). This effective spin doublet arises from the splitting of the 4T1 term through spin-orbit coupling and local distortion of the octahedral atoms.³⁰ The intensity of the signal increases considerably as the system is cooled, in such a way that it disappears above 100 K. The absence of hyperfine structure indicates that the paramagnetic ions are not magnetically isolated in the structure. This is in good agreement with the structural features found for the Ce1 and

Co2 centers, which are linked by a bridging acetate anion in a $\{\text{CeCo}(\mu\text{-OAc})\}$ moiety. The Co1 center could *a priori* be expected to remain magnetically isolated thanks to the shielding provided by the Anderson-Evans type $\{\text{W}_6\text{O}_{24}\}$ ring in which this atom is inserted. However, Co1 and Co2 centers of contiguous **11-CeCo** POMs are closely associated via strong $\text{O}_w\text{-H}\cdots\text{O}_{\text{POM}}$ hydrogen bonding, as discussed in section 4.3.2. Thus, this type of strong face-to-face interaction between the CoO_6 chromophores of Co1 and Co2 seems to be operative for allowing magnetic exchange between both centers.

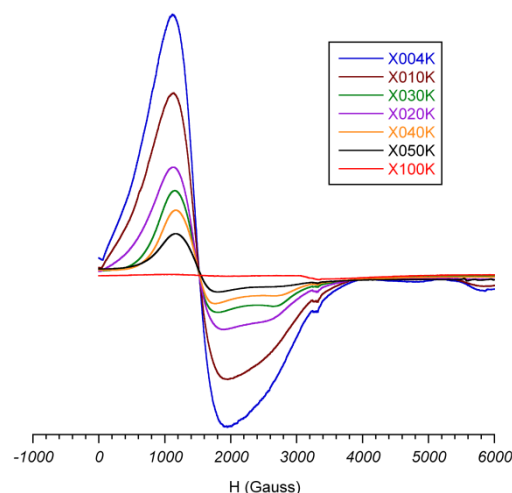


Figure 4.17. Thermal variation of the X band ESR spectra for compound **11-CeCo**.

Table 4.6. Components and average value of the exchange tensor in **11-CeCo** obtained from the fitting of the ESR spectra at different temperatures.

	4 K	20 K	40 K
g_1	6.05	6.05	5.92
g_2	4.55	4.52	4.40
g_3	2.61	2.55	2.42
$\langle g \rangle$	4.40	4.37	4.25
Σg	13.21	13.12	12.74

In spite of the two Co^{II} centers present in the molecular structure of **11-CeCo**, the spectrum at 40K could be fitted to a single anisotropic signal whose g values compare well with those expected for a octahedral $\text{Co}^{\text{II}}\text{O}_6$ chromophore.³¹ Moreover, the total sum of the three components gives a value near 13, in good agreement with that proposed by Abragam and Pryce for the sum of the three orthogonal g -values.³² The fact that the spectra is fitted to a single signal could be explained on the basis of the following effects: i) the two crystallographically independent cobalt(II) atoms show similar CoO_6 geometry as deduced from the CShM values and similar orientation in the crystal packing, hence their contributions could well average in a single signal; ii) the signal from the Co2 center is expected to undergo broadening due to magnetic exchange with the Ce^{III} center in the $\{\text{Co}^{\text{II}}(\mu\text{-OAc})\text{Ce}^{\text{III}}\}$ dimer. Below 30K, the signal is broadened and its resolution becomes noticeably poorer. This behavior could be attributed to the magnetic interaction present at low temperatures between the Co1 and Co2 centers from contiguous **11-CeCo** anions through the three $\text{O}_w\text{-H}\cdots\text{O}_{\text{POM}}$ pathways (Figure 4.14). Alternatively, the contribution of the Ce^{III} atom to the spectra could also lead

to broadening of ESR signals. These effects result in slightly different g values below and above 30K, as can be observed in Table 4.6.

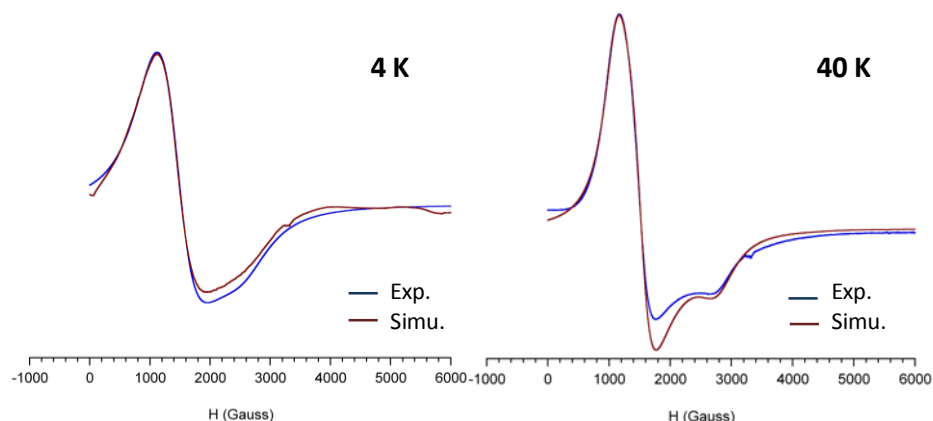


Figure 4.18. Experimental and simulated curves for the X band ESR spectra in compound **11-CeCo** at 4 K(left) and 40 K (right).

Variable temperature X-band ESR studies carried out for the **11-GdCo** derivative show that the signal remains unaltered from room temperature to 4,2 K (Figure 4.19) in spite of the fact that the intensity and resolution, together with the narrowing of the signal are improved with lowering the temperature. The resonance centered at 2450 G ($g \approx 2$) is formed by the overlapping of different signals. The main contribution to the overall spectrum originates from the Gd^{III} ion, and more specifically, from its zero-field splitting and magnetic coupling to the Co_2 atom in the $Co^{II}(\mu-OAc)Ce^{III}$ dimer. The absence of temperature dependence in the signal suggests that the $Gd \cdots Co$ exchange is operative in whole temperature range studied. The ESR studies on the **11-LaCo** derivative will allow us to achieve more insight in this type of magnetic system. Due to the diamagnetic nature of the La^{III} ion the hyperfine structures of both Co_1 and Co_2 centers are expected to be observed at higher temperatures, whereas magnetic coupling between both centers may well take place below 30 K. These studies are still in progress.

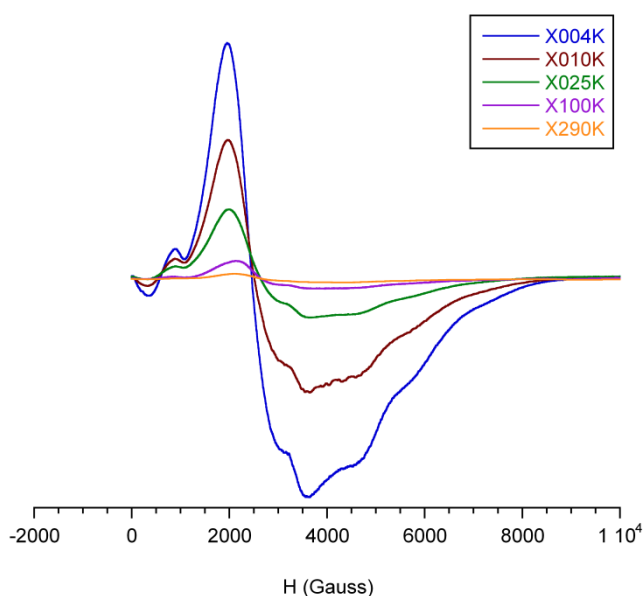


Figure 4.19. Thermal variation of the X band ESR spectra for compound **11-GdCo**.

4.4. CONCLUSIONS

This work nicely illustrates how reaction of lanthanide ions with 3d-metal containing POMs can promote the rearrangement of a given metal-oxo cluster to generate novel heterometallic 3d/4f-POM structures. In this particular case, the combination of early lanthanide(III) ions with pre-formed or in situ generated 3d-metal disubstituted Krebs-type POMs in NaOAc buffer results in the formation of a family of $[\{B-\alpha\text{-SbW}_9\text{O}_{32}(\text{OH})\}_3\{(\text{WO}_2)_3(\text{M}^{\text{II}}\text{W}_6\text{O}_{24})\}\text{Ln}^{\text{III}}_3(\text{H}_2\text{O})_7\text{M}(\text{OAc})(\text{Sb}_4\text{O}_4)]^{19-}$ (**11-LnM**) clusters. For $\text{M} = \text{Co}$, we have been able to isolate a complete series of compounds for early-to-mid lanthanides $\text{Ln} = \text{La}$ to Gd . When Ce is selected as the lanthanide atom and M^{II} is varied, the **11-CeNi** and **11-CeZn** are obtained. The **11-LnM** anions can be viewed as a dissymmetric assembly of three Keggin-type $\{B-\alpha\text{-SbW}_9\text{O}_{33}\}$ trilacunary subunits linked to each other by two nine-coordinated 4f-metal atoms and one $\{\text{Ln}(\mu\text{-OAc})\text{M}\}$ dimer, with a capping $\{\text{MW}_6\text{O}_{24}\}$ Anderson-Evans-type POM fragment connected to the former subunits via three additional $\{\text{WO}_2\}$ groups. This tetrameric framework encapsulates the unusual $\{\text{Sb}_4\text{O}_4\}$ cluster that confers chirality on the assembly by adopting left- or right-handed orientations depending on which trilacunary subunits their basal atoms link to. The condensation between the Anderson-Evans fragment and the three additional *cis*- $\{\text{WO}_2\}$ linkers leads to a $\{\text{MW}_9\text{O}_{33}\}$ subunit which represent a novel building block in POM chemistry. To our knowledge, the **11-LnM** series represents the first example in the literature where an Anderson-type POM acts as a fragment of a larger cluster through the establishment of $\text{W}-\text{O}-\text{W}$ bonds. Furthermore, the $\{\text{CoW}_6\text{O}_{24}\}$ and $\{\text{ZnW}_6\text{O}_{24}\}$ polyoxotungstate fragments are completely unprecedented. ESI-MS experiments carried out for the **11-CeCo** derivative indicates that the POM cluster is stable in aqueous solution. Moreover, **11-CeCo** undergoes a self-assembly process in diluted aqueous solution to form spherical, hollow and single-layered vesicle-like blackberry type structures as monitored by DLS and SLS techniques. The hollow nature of the blackberry-type assemblies was confirmed by TEM images. ESR spectroscopic studies for **11-CeCo** and **11-GdCo** indicate that the cobalt (II) centers are magnetically coupled at low temperature. These observations are in good agreement with the hydrogen-bonded one-dimensional arrangement of the **11-LnM** clusters in the crystal packing.

4.5. REFERENCES

- [1] (a) Oms, O.; Dolbecq, A.; Mialane, P. *Chem. Soc. Rev.* **2012**, *41*, 7497. (b) Zheng, S.-T.; Yang, G.-Y. *Chem. Soc. Rev.* **2012**, *41*, 7623.
- [2] (a) Pope, M. T. *Handb. Phys. Chem. Rare Earths* **2007**, *38*, 337. (b) Bassil, B. S.; Kortz, U. Z. *Anorg. Allg. Chem.* **2010**, *636*, 2222. (c) Granadeiro, C. M.; de Castro, B.; Balula, S. S.; Cunha-Silva, L. *Polyhedron* **2013**, *52*, 10.
- [3] Reinoso, S. *Dalton Trans.* **2011**, *40*, 6610.
- [4] Clemente-Juan, J. M.; Coronado, E.; Gaita-Ariño, A. *Chem. Soc. Rev.* **2012**, *41*, 7464.
- [5] Sessoli, R.; Powell, A. K. *Coord. Chem. Rev.* **2009**, *253*, 2328. (b) Andruh, M.; Costes, J. P.; Diaz, C.; Gao, S. *Inorg. Chem.* **2009**, *48*, 3342.
- [6] (a) Chen, W.; Li, Y.; Wang, Y.; Wang, E. *Eur. J. Inorg. Chem.* **2007**, 2216. (b) Cao, J.; Liu, S.; Cao, R.; Xie, L.; Ren, Y.; Gao, C.; Xu, L. *Dalton Trans.* **2008**, 115. (c) Zhang, S.; Zhao, J.; Ma, P.; Chen, H.; Niu, J.; Wang, J. *Cryst. Growth Des.* **2012**, *12*, 1263. (d) Zhao, J.; Luo, J.; Chen, L.; Yuan, J.; Li, H.; Ma, P.; Wang, J.; Niu, J. *CrystEngComm* **2012**, *14*, 7981. (e) Zhang, J.; Li, J.; Li, L.; Zhao, H.; Ma, P.; Zhao, J.; Chen, L. *Spectrochim. Acta, Part A* **2013**, *114*, 360.

- [7] Merca, A.; Müller, A.; van Slageren, J.; Läge, M.; Krebs, B. *J. Cluster Sci.* **2007**, *18*, 711.
- [8] Chen, W.; Li, Y.; Wang, Y.; Wang, E.; Zhang, Z. *Dalton Trans.* **2008**, 865.
- [9] (a) Xue, G.; Liu, B.; Hu, H.; Yang, J.; Wang, J.; Fu, F. *J. Mol. Struct.* **2004**, *690*, 95. (b) Ismail, A. H.; Bassil, B. S.; Yassin, G. H.; Keita, B.; Kortz, U. *Chem. Eur. J.* **2012**, *18*, 6163.
- [10] (a) Fang, X.; Kögerler, P. *Chem. Commun.* **2008**, 3396. (b) Fang, X.; Kögerler, P. *Angew. Chem. Int. Ed.* **2008**, *47*, 8123.
- [11] (a) Nohra, B.; Mialane, P.; Dolbecq, A.; Rivière, E.; Marrot, J.; Sécheresse, F. *Chem. Commun.* **2009**, 2703. (b) Zhao, J.; Shi, D.; Chen, L.; Li, Y.; Ma, P.; Wang, J.; Niu, J. *Dalton Trans.* **2012**, *41*, 10740.
- [12] Yao, S.; Zhang, Z.; Li, Y.; Lu, Y.; Wang, E.; Su, Z. *Cryst. Growth Des.* **2010**, *10*, 135.
- [13] See for example: (a) Weakley, T. J. R.; Evans, H. T., Jr.; Showell, J. S.; Tourné, G.; Tourné, C. M. *J. Chem. Soc., Chem. Commun.* **1973**, 139. (b) Finke, R. G.; Droege, M. W. *Inorg. Chem.* **1983**, *22*, 1006. (c) Gómez-García, C. J.; Borrás-Almenar, J. J.; Coronado, E.; Ouahab, L. *Inorg. Chem.* **1994**, *33*, 4016. (d) Bi, L.-H.; Wang, E.-B.; Peng, J.; Huang, R.-D.; Xu, L.; Hu, C.-W. *Inorg. Chem.* **2000**, *39*, 671. (e) Kortz, U.; Nellutla, S.; Stowe, A. C.; Dalal, N. S.; Rauwald, U.; Danquah, W.; Ravot, D. *Inorg. Chem.* **2004**, *43*, 2308.
- [14] See for example: (a) Zhang, X.; Anderson, T. M.; Chen, Q.; Hill, C. L. *Inorg. Chem.* **2001**, *40*, 418. (b) Kortz, U.; Mbomekalle, I. M.; Keita, B.; Nadjjo, L.; Berthet, P. *Inorg. Chem.* **2002**, *41*, 6412. (c) Ruhlmann, L.; Canny, J.; Contant, R.; Thouvenot, R. *Inorg. Chem.* **2002**, *41*, 3811. (d) Hou, Y.; Xu, L.; Cichon, M. J.; Lense, S.; Hardcastle, K. I.; Hill, C. L. *Inorg. Chem.* **2010**, *49*, 4125.
- [15] (a) Anderson, T. M.; Zhang, X.; Hardcastle, K. I.; Hill, C. L. *Inorg. Chem.* **2002**, *41*, 2477. (b) Mbomekalle, I. M.; Keita, B.; Nadjjo, L.; Neiwert, W. A.; Zhang, L.; Hardcastle, K. I.; Hill, C. L.; Anderson, T. M. *Eur. J. Inorg. Chem.* **2003**, 3924. (f) Ruhlmann, L.; Costa-Coquelard, C.; Canny, J.; Thouvenot, R. *Eur. J. Inorg. Chem.* **2007**, 1493. (g) Mbomekalle, I. M.; Mialane, P.; Dolbecq, A.; Marrot, J.; Sécheresse, F.; Berthet, P.; Keita, B.; Nadjjo, L. *Eur. J. Inorg. Chem.* **2009**, 5194.
- [16] (a) Reinoso, S.; Galán-Mascarós, J. R. *Inorg. Chem.* **2010**, *49*, 377. (b) Reinoso, S.; Galán-Mascarós, J. R.; Lezama, L. *Inorg. Chem.* **2011**, *50*, 9587.
- [17] Bi, L.-H.; Li, B.; Wu, L.-X. *Inorg. Chem. Commun.* **2008**, *11*, 1184.
- [18] (a) Bösing, M.; Loose, I.; Pohlmann, H.; Krebs, B. *Chem. Eur. J.* **1997**, *3*, 1232. (b) Bösing, M.; Nöh, A.; Loose, I.; Krebs, B. *J. Am. Chem. Soc.* **1998**, *120*, 7252. (c) Loose, I.; Droste, E.; Bösing, M.; Pohlmann, H.; Dickman, M. H.; Rosu, C.; Pope, M. T.; Krebs, B. *Inorg. Chem.* **1999**, *38*, 2688. (d) Piepenbrink, M.; Limanski, E. M.; Krebs, B. *Z. Anorg. Allg. Chem.* **2002**, *628*, 1187. (e) Zhao, C.; Kambara, C. S.; Yang, Y.; Kaledin, A. L.; Musaev, D. G.; Lian, T.; Hill, C. L. *Inorg. Chem.* **2013**, *52*, 671.
- [19] Ismail, A. H.; Bassil, B. S.; Römer, I.; Kortz, U. *Z. Anorg. Allg. Chem.* **2013**, *639*, 2510.
- [20] Kortz, U.; Savelieff, M. G.; Bassil, B. S.; Keita, B.; Nadjjo, L. *Inorg. Chem.* **2002**, *41*, 783
- [21] Xue, G.; Vaissermann, J.; Gouzerh, P. *J. Cluster Sci.* **2002**, *13*, 409.
- [22] (a) Hussain, F.; Reicke, M.; Janowski, V.; de Silva, S.; Futuwil, J.; Kortz, U. *C. R. Chim.* **2005**, *8*, 1045. (b) Wang, J.-P.; Ma, P.-T.; Li, J.; Niu, H.-Y.; Niu, J.-Y. *Chem. Asian J.* **2008**, *3*, 822. (c) Carraro, M.; Bassil, B. S.; Sorarù, A.; Berardi, S.; Suchopar, A.; Kortz, U.; Bonchio, M. *Chem. Commun.* **2013**, *49*, 7914.
- [23] Fischer, J.; Ricard, L.; Weiss, R. J. *J. Am. Chem. Soc.* **1976**, *98*, 3050.
- [24] See for example: (a) Ito, F.; Ozeki, T.; Ichida, H.; Miyamae, H.; Sasaki, Y. *Acta Crystallogr.* **1989**, *C45*, 946. (b) Allen, C. C.; Burns, R. C.; Lawrance, G. A.; Turner, P.; Hambley, T. W. *Acta Crystallogr.* **1997**, *C53*, 7. (c) Nolan, A. L.; Allen, C. C.; Burns, R. C.; Craig, D. C.; Lawrance, G. A. *Aust. J. Chem.* **1998**, *51*, 825. (d) Wéry, A. S. J.; Gutiérrez-Zorrilla, J. M.; Luque, A.; Ugalde, M.; Román, P.; Lezama, L.; Rojo, T. *Acta Chem. Scand.* **1998**, *52*, 1247. (e) Lee, U.; Joo, H.-C.; Kwon, J.-S. *Acta Crystallogr.* **2002**, *E58*, i6.
- [25] Polyakov, E. V.; Denisova, T. A.; Maksimova, L. G.; Gyrdasova, O. I.; Manakova, L. I. *Inorg. Mater.* **2002**, *38*, 956.

- [26] Brown, I. D.; Alternatt, D. *Acta Crystallogr.* **1985**, *B41*, 244.
- [27] Cui, K.; Li, F.; Xu, B.; Jiang, N.; Wang, Y.; Zhang, J. *Dalton Trans.* **2012**, *41*, 4871.
- [28] (a) Casanova, D.; Cirera, J.; Llunell, M.; Alemany, P.; Avnir, D.; Alvarez, S. *J. Am. Chem. Soc.* **2004**, *126*, 1755. (b) Ruiz-Martínez, A.; Casanova, D.; Alvarez, S. *Chem. Eur. J.* **2008**, *14*, 1291.
- [29] (a) Li, D.; Yin, P.; Liu, T. in *Polyoxometalate Chemistry: Some Recent Trends*; Sécheresse, F., Ed.; World Scientific: Singapore, 2013; pp.49-99. (b) Yin, P.; Li, D.; Liu, T. *Chem. Soc. Rev.* **2012**, *41*, 7368. (c) Liu, T. *Langmuir* **2010**, *26*, 9202.
- [30] Carling, R. L. *Magnetochemistry*; Springer: Berlin, 1986.
- [31] Goñi, A.; Lezama, L.; Barberis, G. E.; Pizarro, J. L.; Arriortua, M. I.; Rojo, T. *J. Magn. Magn. Mater.* **1996**, *164*, 251.
- [32] Abragam, A.; Pryce, M. H. L. *Proc. R. Soc. London A* **1951**, *206*, 173.

Final remarks and future perspectives

- 5.1.** Final remarks
- 5.2.** Future perspectives

5.1. FINAL REMARKS

The following general conclusions can be deduced from this work:

CHAPTER 2:

1) The family of transition metal disubstituted Krebs-type tungstoantimonates(III) are suitable precursors for preparing hybrid POMs via straightforward ligand substitution of labile water molecules on preformed or *in-situ* prepared POM clusters under mild conditions.

2) Organic derivatization of the 3d-metal disubstituted Krebs-type clusters is extremely dependent on the exact nature of the ligand. The imc ligand has been identified as a “universal ligand” because its coordination to the cluster takes place regardless of the external 3d-metal, reaction conditions or heteroatom as indicated by the **1-XM** series. In contrast, the pzc and pyzc ligands are selective toward some of the transition metal containing clusters leading to the compounds **2-Ni** and **3-M**. The use of the pydc and pymc ligands promote the partial decomposition of some of the precursors, resulting in the corresponding monomeric $[ML_2(H_2O)_2]$ transition metal complex, whereas the pic ligand showed to be inert toward any of the four POM precursors selected.

3) The hybrids obtained (**1-SbM**, **2-Ni**, **3-M**) constitute the first organic derivatives of 3d-metal disubstituted Krebs-type tungstoantimonates(III), and what is more, the related tungstotellurates(IV), **1-TeM**, represent the first observation of a transition metal disubstituted Krebs-type framework containing tellurium as heteroatom. Similarly, the compounds $[M(pzc)_2(H_2O)_2]$ (M = Co, Ni) are the first structurally characterized metal complexes of the pzc ligand

4) The FT-IR spectroscopy represents a powerful, accessible and cheap technique to detect the organic derivatization of the parent metal-oxo framework prior to single-crystal X-Ray experiments.

5) The prepared hybrid species are stable in aqueous solution according to 1H -NMR studies performed on diamagnetic derivatives.

6) Studies with bridging ligands have showed that 4,4'-bpy and 2,5-pydc are inert toward Krebs-type tungstoantimonates, although the former leads to a series of compounds with interstitial 4,4'-bipyridine molecules (**4-M**). On the contrary, 2,3-pydc shows selectivity toward the nickel-disubstituted Krebs-type POM and its coordination results in the rearrangement of the parent cluster to lead to the ligand-bridged **5-Ni** dimer.

7) The $\{Ni_2Sb_2W_{20}O_{70}\}$ subunits in **5-Ni** showing a $\{W_{20}O_{70}\}$ moiety incorporated into a $\{SbW_9O_{33}\}$ trilacunary unit are completely unprecedented in POM chemistry. The ESI-MS studies show that the dimeric **5-Ni** entity undergoes complete dissociation into these subunits upon dissolution in water.

CHAPTER 3:

9) Lanthanide-heteroatom-tungstate synthetic systems are potential dynamic libraries of building-blocks with the ability to undergo cation-directed self-assembly processes for constructing new POM architectures. This fact is exemplified by the enantiomerically related $\beta(1,5)$ - and $\beta(1,8)$ - $[Ln_2(GeW_{10}O_{38})]^{6-}$ and the $\gamma(3,4)$ - $[Ln_2(GeW_{10}O_{38})]^{6-}$ clusters obtained in these studies, which are composed of anti-Lipscomb type dilacunary Keggin fragments stabilized by the coordination of 4f ions to the vacant sites.

CHAPTER 5

10) One-pot reactions carried out with early lanthanides (Ce to Sm) have resulted in crown shaped $[\text{Na}\{\beta\text{-Ln}_2(\text{H}_2\text{O})_4(\text{GeW}_{10}\text{O}_{38})\}_6]^{35-}$ architectures (**6-Ln**, Ln = Pr, Nd) in the presence of exclusively Na^+ as counterion, whereas the addition of K^+ has led to a similar $[\text{K}\{\beta\text{-Sm}_2(\text{H}_2\text{O})_4(\text{GeW}_{10}\text{O}_{38})\}_6]^{35-}$ assembly for Sm^{III} (**7-Sm**) and giant dodecameric $[\text{K}\{\text{K}_7\text{Ln}_{24}\text{Ge}_{12}\text{W}_{120}\text{O}_{444}(\text{OH})_{12}(\text{H}_2\text{O})_{56}\}]^{52-}$ POMs for Ce, Pr and Nd (**8-Ln**). The dodecamers are constructed by the aggregation via Ln–O–W bonds of six external $\gamma(3,4)$ subunits to a central hexameric core analogous to that obtained for Sm.

11) The $[\text{Ni}^{\text{II}}(\text{H}_2\text{O})_6]^{2+}$ cation plays an essential role as crystallizing agent in the isolation of these lanthanide containing tungstogermanates by establishing networks of $\text{O}_W\text{—H}\cdots\text{O}_{\text{POM}}$ hydrogen bonds. Crystals with extreme short-range order (glassy crystals) are obtained in absence of nickel.

12) Compounds **8-Ln** dissociate upon dissolution in water into hexameric and monomeric entities, as identified by ESI-MS experiments. The former self-assemble into supramolecular vesicle-like blackberry-type nanostructures, as monitored by DLS and SLS techniques and confirmed by TEM images. Similar studies in water-acetone mixtures showed that the dodecameric **8-Nd** remains stable in solution and forms blackberries with sizes increasing with the acetone concentration.

13) For mid-to-late lanthanides (Gd to Lu), the *in-pocket* coordination mode of the 4f-metals in the formation of $[\beta\text{-Ln}_2(\text{GeW}_{10}\text{O}_{38})]^{6-}$ subunits has led to chiral, rod-like $[\text{Ln}_4(\text{H}_2\text{O})_6(\beta\text{-GeW}_{10}\text{O}_{38})_2]^{12-}$ dimeric polyanions in the presence of Na^+ (**9-Ln**, Ln = Gd to Lu). When Cs^+ is added as crystallizing cation, two dimeric entities further assemble via Ln–O=W linkages to give the diamond-shaped $[\{\text{Ln}_4(\text{H}_2\text{O})_5(\text{GeW}_{10}\text{O}_{38})_2\}_2]^{24-}$ tetrameric assemblies (**10-Ln**, Ln = Ho to Lu), where $\alpha\beta$ and $\beta\beta$ -type species are coexisting in each single crystal.

14) Combination of ESI-MS and ^{183}W -NMR experiments indicates that **10-Ln** tetramers fragment into **9-Ln**-like dimers upon dissolution, which undergo partial dissociation into monomeric $\{\text{Ln}_2\text{GeW}_{10}\}$ anions and slow dimer to monomer equilibration. This is most likely followed by β to α isomerization of monomeric clusters and consequent reassembly in $\alpha\alpha$ -**9-Ln** dimers, as indicated by isolation of three additional $\alpha\alpha$ -**9-Ln** derivatives (Ln = Er to Yb) in the solid state.

15) The weak-emitting 4f ions are sensitized in the POM assemblies, in such a way that orange-red, green and yellow emission is observed for the **7-Sm**, **9-Tb** and **9-Dy** derivatives, respectively. In the case of **7-Sm**, only the inner 4f metals of the crown shaped-architecture are identified as efficient emitting centers due to their geometrical features.

CHAPTER 4:

17) Reaction of lanthanide ions with 3d-metal containing POMs can promote the rearrangement of a given metal-oxo cluster to generate novel heterometallic 3d/4f-POM structures. In this particular case, the combination of early lanthanide(III) ions with pre-formed or in situ generated 3d-metal disubstituted Krebs-type POMs in NaOAc buffer results in the formation of a family of $[\{\beta\text{-}\alpha\text{-SbW}_9\text{O}_{32}(\text{OH})\}_3\{(\text{WO}_2)_3(\text{M}^{\text{II}}\text{W}_6\text{O}_{24})\}\text{Ln}^{\text{III}}_3(\text{H}_2\text{O})_7\text{M}(\text{OAc})(\text{Sb}_4\text{O}_4)]^{19-}$ clusters (**11-LnM**).

18) The **11-LnM** anions can be viewed as a dissymmetric assembly of three Keggin-type $\{\beta\text{-}\alpha\text{-SbW}_9\text{O}_{33}\}$ trilacunary subunits linked to each other by two nine-coordinated 4f-metal atoms and one

{Ln(μ -OAc)M} dimer, with a capping {MW₆O₂₄} Anderson-Evans-type POM fragment connected to the trilacunary subunits via three additional {WO₂} groups. This tetrameric framework encapsulates the unusual {Sb₄O₄} cluster, which confers chirality on the assembly by adopting left- or right-handed orientations depending on which trilacunary subunits its basal Sb atoms link to.

19) The condensation between the Anderson-Evans fragment and the three additional *cis*-{WO₂} linkers leads to a {MW₉O₃₃} subunit which represent a novel building block in POM chemistry. Moreover, the **11-LnM** series represents the first example in the literature where an Anderson-type POM acts as a fragment of a larger cluster through the establishment of W—O—W bonds. It is also worth highlighting that the {CoW₆O₂₄} and {ZnW₆O₂₄} polyoxotungstate fragments are completely unprecedented.

20) The **11-CeCo** derivative is stable in aqueous solution according to in ESI-MS experiments and self-assembles into single-layered vesicle-like blackberry type structures as monitored by DLS and SLS techniques. The hollow nature of the blackberry-type assemblies was confirmed by TEM images.

21) ESR spectroscopic studies for **11-CeCo** and **11-GdCo** indicate that the cobalt (II) centers are magnetically coupled at low temperature, in good agreement with the hydrogen-bonded one-dimensional arrangement of the **11-LnM** clusters in the crystal packing.

5.2. FUTURE PERSPECTIVES

New experiments are planned for the near future to complete or even improve this work. Furthermore, new research lines have been identified in the course of the studies described in this dissertation. All these considerations are compiled in this section.

CHAPTER 2:

1) The unexpected rearrangement of the parent nickel(II) disubstituted Krebs-type tungstoantimonate(III) anion upon reaction with 2,3-pyzd represents an encouraging fact to extend these studies to some other bis(chelating) bridging ligands. Furthermore, some different experiments are intended to be carried out for **5-Ni**. As mentioned in Chapter 2, a formally vacant site blocked by a Na⁺ ion is present in the molecular structure of the {Ni₂Sb₂W₂₀O₇₀} clusters, and therefore, **5-Ni** could be a good candidate to incorporate additional electrophilic groups in these vacant sites. Thus, we plan to study its reactivity toward different electrophiles (especially 3d and 4f metals) in the near future. ESI-MS studies have shown that dimeric **5-Ni** dissociates into its monomeric halves upon dissolution in water. As a consequence, we could try to isolate the monomeric halves by dissolving the dimeric compound and adding different alkaline metal cations. Moreover, promising results are being obtained in solution studies of **5-Ni** in water/organic-solvent mixtures by LLS techniques. For example, the dimeric anion seems to self-assemble into blackberry-type structures in water/acetone mixtures with high acetone concentration.

2) Hybrid compounds obtained in the reactions of transition metal disubstituted Krebs-type POMs with N,O-chelating ligands could be considered as model systems for these clusters to be incorporated into polymeric surfaces. As part of a new research line implemented in this group,

polymeric films bearing antenna imc groups will be synthesized, and used to incorporate transition metal disubstituted Krebs-type POMs to their surface via classical coordination chemistry. This approach could lead to the formation of new multifunctional materials.

3) The isolation of the $[\text{C}_2\text{H}_{10}\text{Sb}_2\text{W}_{31}\text{O}_{108}]^{14-}$ anion as a byproduct paves the way for a new research line. This cluster contains the defect $(\text{WO}_7)\text{W}_4$ pentagonal fragment containing the pentagonal bipyramidal $\{\text{WO}_7\}$ unit. The potential of this type of fragments in the formation of giant structures based on molybdenum, together with the scarce examples reported for polyoxotungstates, make the cluster interesting. Therefore, attempts to optimize its synthesis are planned in the first stage.

CHAPTERS 3 and 4:

4) The organic functionalization of the clusters prepared in Chapters 3 and 4 by replacing the aqua ligands of the exposed 4f-centers by organic ligands will be tested. The use of blocking organic ligands could lead to the isolation of the dilacunary $\beta(1,5)$ -, $\beta(1,8)$ - and $\gamma(3,4)$ - $\{\text{Ln}_2\text{GeW}_{10}\text{O}_{38}\}$ fragments as monomers.

5) Regarding Chapter 3, the effect of the media will be evaluated in the $1,1\text{Ni}:1,1\text{Ln}:1\text{GeO}_2:9\text{WO}_4^{2-}$ reaction by using aqueous solutions at different pHs, NaCl solutions of various concentrations, etc.

6) Additional TEM images for **8-Nd** in water and water/acetone mixtures and for **8-Ce** in water are needed to confirm the hollow and spherical nature of all the blackberry-type structures detected. Furthermore, EDS will allow us to confirm that the major element in all those aggregates is tungsten. As indicated in the main text, we also intend to test the self-recognition behavior between **8-Nd** and **8-Pr** samples in water.

8) The reactions described in Chapter 4 between lanthanides and Krebs-type POMs need to be optimized in terms of yields and purity of the final product. After optimizing the synthetic process, transition metal containing Krebs-type POMs with other lone-pair containing heteroatoms (As^{III} , Bi^{III} , Te^{IV} , Se^{IV}) are planned to be tested in reactions with lanthanides under the same conditions. In a final stage, reactions with trisalkoxo ligands will also be performed with the aim of obtaining hybrid derivatives of **11-LnM** by replacing the shell O atoms from the Anderson-Evans-type fragment. Although this reaction is very usual among polyoxomolybdates, no organic derivatization of Anderson-Evans-type polyoxotungstate can be found in the literature.

Synthesis and characterization of transition metal complexes with N,O-chelating ligands

A1.1. $[\text{Co}(\text{imc})_2(\text{H}_2\text{O})_2]$ (**Co-imc**)

A1.2. $[\text{M}(\text{pzc})_2(\text{H}_2\text{O})_2]$, M = Co, Ni (**Co-pzc** and **Ni-pzc**)

A1.3. $[\text{M}(\text{pydc})_2(\text{H}_2\text{O})_2] \cdot 2\text{H}_2\text{O}$, M = Co, Ni (**Co-pydc** and **Ni-pydc**)

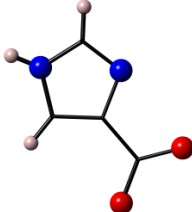
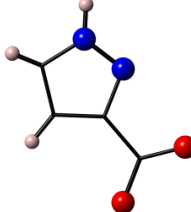
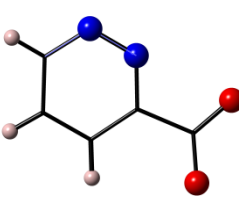
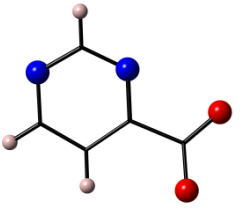
A1.4. $[\text{Co}(\text{pymc})_2(\text{H}_2\text{O})_2] \cdot 2\text{H}_2\text{O}$ (**Co-pymc**)

A1.5. References

ABSTRACT: The synthesis, chemical characterization and structure of the transition metal complexes with N,O-chelating ligands obtained in Chapter 2 are summarized in this appendix. Compounds $[\text{Co}(\text{imc})_2(\text{H}_2\text{O})_2]$ (**Co-imc**), $[\text{M}(\text{pzc})_2(\text{H}_2\text{O})_2]$ where M = Co (**Co-pzc**) or Ni (**Ni-pzc**), $[\text{M}(\text{pydc})_2(\text{H}_2\text{O})_2] \cdot 2\text{H}_2\text{O}$ where M = Co (**Co-pydc**) or Ni (**Ni-pydc**), and $[\text{Co}(\text{pymc})_2(\text{H}_2\text{O})_2] \cdot 2\text{H}_2\text{O}$ (**Co-pymc**) (imc = 1H-imidazole-4-carboxylate, pzc = 1H-pyrazole-3-carboxylate, pydc = pyridazine-3-carboxylate, , pymc = pyrimidine-4-carboxylate) have been analyzed by means of elemental and thermal analyses, infrared spectroscopy and single-crystal X-ray diffraction. All the complexes are isostructural with the analogues found in the CSD database, except for **M-pzc** (M = Co, Ni) which represent the first examples of transition metal complexes containing the 1H-pyrazole-3-carboxylate ligand.

Compounds $[\text{Co}(\text{pzc})_2(\text{H}_2\text{O})_2]$ (**Co-pzc**), $[\text{M}(\text{pydc})_2(\text{H}_2\text{O})_2] \cdot 2\text{H}_2\text{O}$ (pydc = pyridazine-3-carboxylate, M = Co (**Co-pydc**) or Ni (**Ni-pydc**)) and $[\text{Co}(\text{pymc})_2(\text{H}_2\text{O})_2] \cdot 2\text{H}_2\text{O}$ (pymc = pyrimidine-4-carboxylate, **Co-pymc**) were firstly obtained in an attempted synthesis of the corresponding organic derivative of the transition metal disubstituted Krebs-type polyanion (see Chapter 2). All four complexes were later prepared on purpose for their full characterization. In the case of complexes $[\text{Co}(\text{imc})_2(\text{H}_2\text{O})_2]$ (imc = 1H-imidazole-4-carboxylate, **Co-imc**) and $[\text{Ni}(\text{pzc})_2(\text{H}_2\text{O})_2]$ (pzc = 1H-pyrazole-3-carboxylate, **Ni-pzc**), they were synthesized with the aim of comparing their bond lengths and angles in the metal coordination sphere to those of the corresponding Krebs-type hybrid POMs (compounds **1-Co** and **2-Ni**) (Table A1.1).

Table A1.1. Summary of the transition metal complexes described in Appendix 1.

	Co-imc	Co-pzc, Ni-pzc	Co-pydc, Ni-pydc	Co-pymc
<i>Complex</i>	$[\text{CoL}_2(\text{H}_2\text{O})_2]$	$[\text{ML}_2(\text{H}_2\text{O})_2]$	$[\text{ML}_2(\text{H}_2\text{O})_2] \cdot 2\text{H}_2\text{O}$	$[\text{CoL}_2(\text{H}_2\text{O})_2] \cdot 2\text{H}_2\text{O}$
<i>Ligand</i>	1H-Imidazole-4-carboxylate	1H-Pyrazole-3-carboxylate	Pyridazine-3-carboxylate	Pyrimidine-4-carboxylate
				

A1.1. $[\text{Co}(\text{imc})_2(\text{H}_2\text{O})_2]$ (**Co-imc**)

Experimental: To a solution of $\text{CoCl}_2 \cdot 6\text{H}_2\text{O}$ (12 mg, 0.05 mmol) in water (15 mL) 1H-imidazole-4-carboxylic acid (12 mg, 0.10 mmol) was added and the resulting solution was stirred for 30 min at room temperature. Prismatic red crystals were obtained by slow evaporation after several days (12 mg; yield 76%). Anal. Calcd. (found) for $\text{C}_8\text{H}_{10}\text{CoN}_4\text{O}_6$: C, 30.30 (30.55); H, 3.18 (3.26); N, 17.67 (17.27). IR (cm^{-1} , Figure A1.1a): 3148 (s), 2934 (s), 1685 (m), 1588 (vs), 1555 (vs), 1528 (s), 1462 (s), 1406 (vs), 1333 (m), 1234 (s), 1177 (m), 1101 (m), 1005 (m), 930 (m), 845 (m), 820 (m), 791 (m), 658 (s), 610 (m), 492 (m). TGA/DTA (Figure A1.1b): In spite of showing axially coordinated water molecules, **Co-imc** is thermally stable up to a temperature as high as $\sim 140^\circ\text{C}$ because of the effective hydrogen-bonding network described below. The complex undergoes an endothermic dehydration process, which is completed at c.a. 220°C [calcd (found) for 2 H_2O : 11.36 (11.54)] and followed by a two-step, highly exothermic ligand combustion. The final residue is obtained above 405°C [calcd (found) for CoO : 23.62 (24.10)].

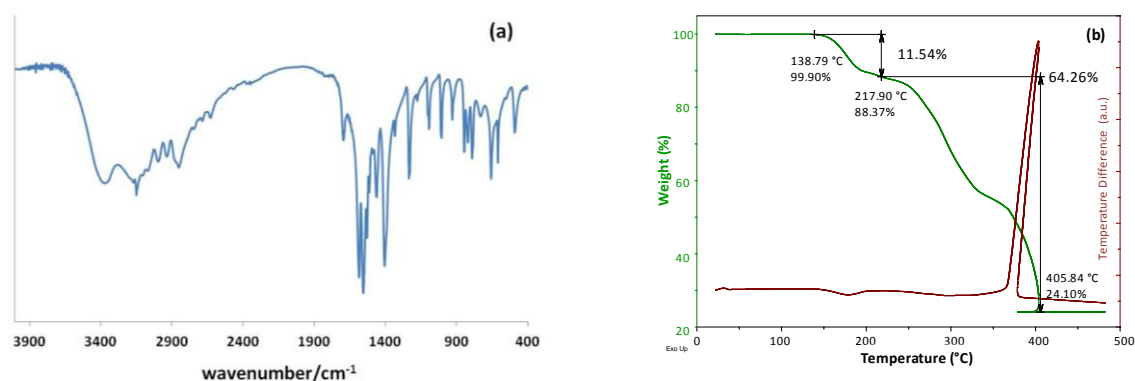


Figure A1.1. FT-IR spectrum (a) and TGA/DTA curves (b) for **Co-imc**.

Crystal Structure: *cis*-[Co(imc)₂(H₂O)₂] crystallizes in the orthorhombic *Pccn* space group¹ (Table A1.2) and is isostructural with the Zn and Cd analogues reported previously.² The complex contains one Co^{II} cation on a twofold rotation axis, exhibiting a distorted octahedral coordination geometry. The equatorial plane is formed by two O,N-bidentate 1H-imidazole-4-carboxylate ligands and the axial positions are occupied by water molecules. As expected, the Co—O (2.177(1) Å) and Co—N bond lengths (2.076(2) Å) are similar to those of the Zn^{II} analogue. The crystal packing consists in a three-dimensional network stabilized by strong O—H···O and N—H···O hydrogen bonds involving the N—H group from the imidazole ring, the non-coordinating carboxylate O atom and the coordinating water molecule. Weak π – π interactions between the imidazole rings also contribute to the stabilization of the crystal packing (Figure A1.2).

Table A1.2. Crystallographic data for **Co-imc**

Formula	C ₈ H ₁₀ CoN ₄ O ₆
FW (g mol ⁻¹)	317.13
Crystal system	orthorhombic
Space group	<i>Pccn</i>
<i>a</i> (Å)	7.1236(16)
<i>b</i> (Å)	11.6305(2)
<i>c</i> (Å)	13.5496(4)
<i>V</i> (Å ³)	1122.6(3)
<i>Z</i>	4
<i>D</i> _{calcd} (g cm ⁻³)	1.876
μ (mm ⁻¹)	1.561
Reflections	
Collected	2396
Unique (<i>R</i> _{int})	1162 (0.018)
Observed [<i>I</i> > 2 σ (<i>I</i>)]	1025
Parameters	95
<i>R</i> (<i>F</i>) [<i>I</i> > 2 σ (<i>I</i>)]	0.027
<i>wR</i> (<i>F</i> ²) (all)	0.063
GoF	1.084

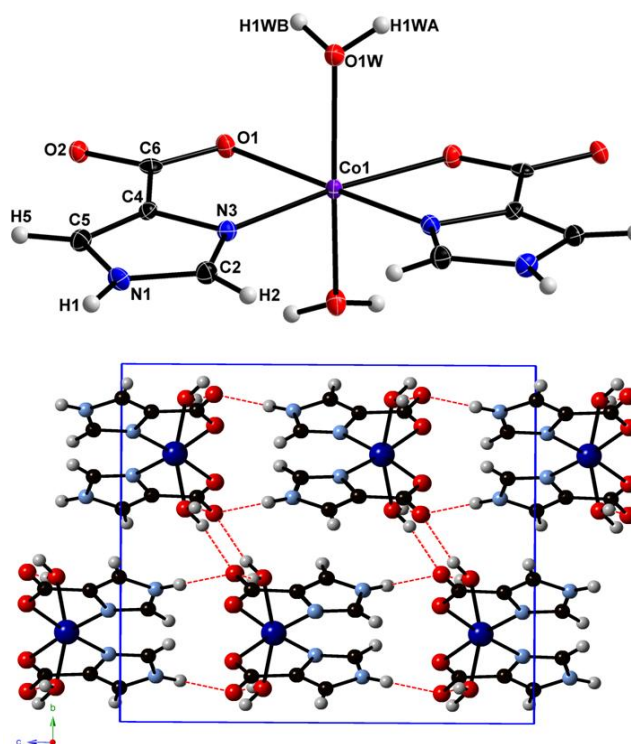


Figure A1.2. Top: ORTEP view of **Co-imc** showing atom labels for the asymmetric unit and 50% probability displacement ellipsoids. Bottom: View of the crystal packing along the crystallographic *a* axis (hydrogen bonds represented as dashed lines).

A1.2. [M(pzc)₂(H₂O)₂]; M = Co (Co-pzc), Ni (Ni-pzc)

Experimental: To a solution of MCl₂·6H₂O (M = Co, Ni; 71 mg; 0.30 mmol) in hot water (15 mL) 1H-pyrazole-3-carboxylic acid (74 mg, 0.60 mmol) dissolved in hot water (10 mL) was added dropwise and the resulting solution was stirred for 30 min at 90 °C. Prismatic crystals (Co: orange; Ni: blue) were obtained by slow evaporation after several days. **Co-pzc:** 51 mg, yield 54 %. Anal. Calcd. (found) for C₈H₁₀CoN₄O₆: C, 30.30 (30.86); H, 3.18 (3.21); N, 17.67 (17.39). IR (cm⁻¹, Figure A1.3): 3273 (s), 3200 (s), 1604 (vs), 1518 (m), 1497 (m), 1442 (m), 1362 (vs), 1244 (s), 1180 (m), 1115 (m), 1074(m), 1001 (m), 928 (m), 897 (m), 835 (m), 770 (m), 698 (m), 613 (m), 492 (m). **Ni-pzc:** 63 mg, yield 66 %. Anal. Calcd. (found) for C₈H₁₀N₄NiO₆: C, 30.32 (29.40); H, 3.18 (3.35); N, 17.68 (16.99) IR (cm⁻¹, Figure

A.3): 3293 (s), 3204 (s), 3140 (s), 1616 (s), 1518 (m), 1497 (m), 1443 (m), 1364 (s), 1244 (m), 1182 (m), 1117 (m), 1078 (m), 1005 (w), 930 (w), 899 (w), 851 (m), 839 (m), 772 (m), 693 (m), 613 (m), 494 (w).

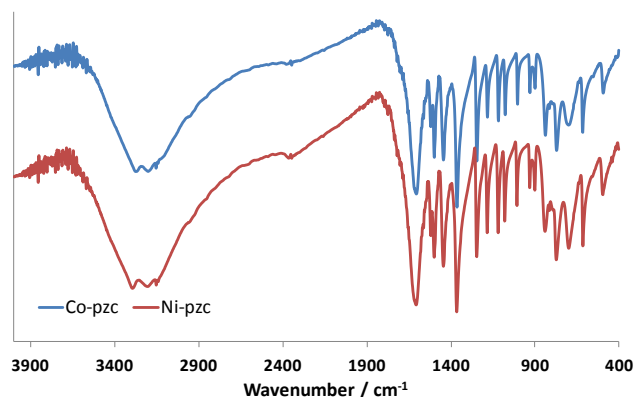


Figure A1.3. FT-IR spectra of **Co-pzc** and **Ni-pzc**.

TGA/DTA (Figure A1.4): Complexes **M-pzc** (M = Co, Ni) are thermally stable up to ~175 °C (**Co-pzc**) and 195 °C (**Ni-pzc**) due to the effective hydrogen-bonding network described below. The endothermic dehydration process, which is completed at ~250 °C for **Co-pzc** [calcd (found) for 2 H₂O: 11.36 (12.06)], is followed by a two step, highly exothermic ligand combustion, resulting in the final residue above 430 °C [calcd (found) for Co₂O₃: 26.15 (25.53)]. In the case of **Ni-pzc** both dehydration and combustion mass loss stages are noticeably overlapped, in such a way that it was not possible to calculate the water content. Nevertheless, the weight percentage of the final residue obtained at ~410 °C is in full agreement with the expected value [calcd (found) for NiO: 23.57 (23.50)].

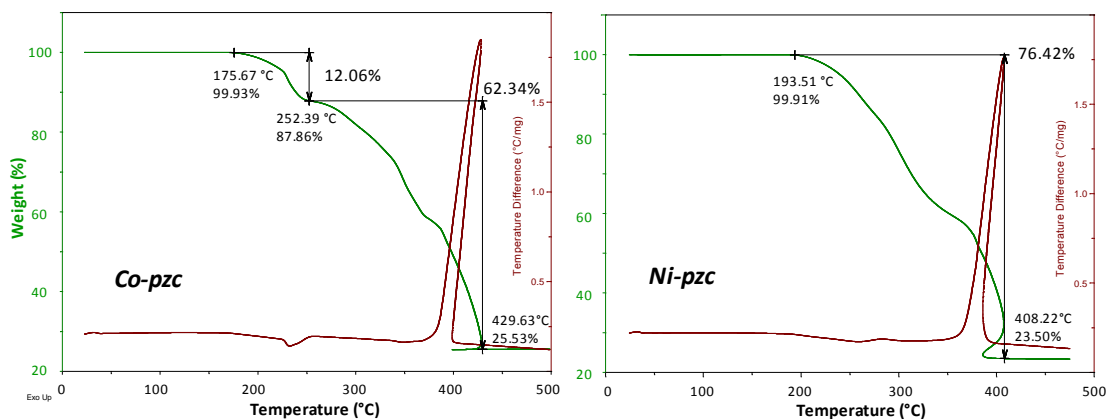


Figure A1.4. TGA/DTA curves for **Co-pzc** and **Ni-pzc**.

Crystal Structure: Compounds **M-pzc** (M = Co, Ni) crystallize in the monoclinic $P2_1/c$ space group (Table A1.3) and represent the first examples of transition metal complexes containing the 1H-pyrazole-3-carboxylate ligand. Both complexes display the metal atom on an inversion center, showing an octahedral coordination geometry. The equatorial plane is formed by two *trans*-related N,O-bidentate ligands and the axial positions are occupied by water molecules (Figure A1.5). The complexes are stacked in columns along the crystallographic *a* axis by O—H...O hydrogen bonds established between the coordinating carboxylate O atom and the coordination water molecule. These columns are further connected into a three dimensional network by additional hydrogen bonds involving the non-coordinating carboxylate O atoms, the coordination water molecules, and

the N-H groups from the pyrazole rings. The hydrogen bonding network is reinforced by additional C—H···O interactions. (Figure A1.6).

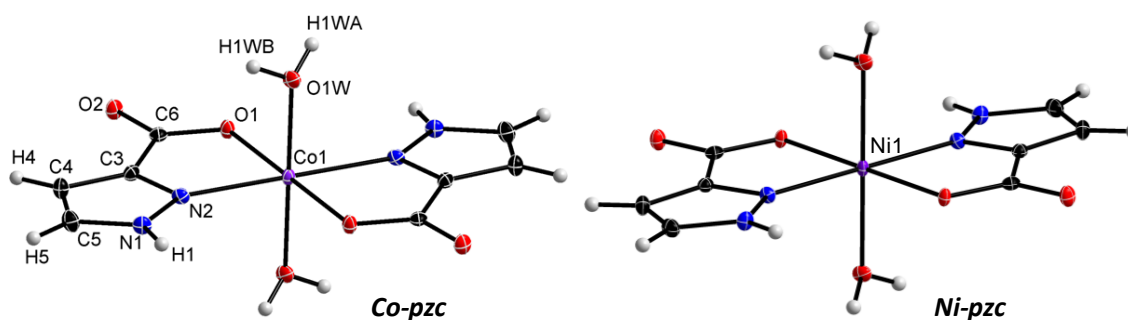


Figure A1.5 ORTEP view of **Co-pzc** and **Ni-pzc** showing atom labels for the asymmetric unit and 50% probability displacement ellipsoids.

Table A1.3. Crystallographic data for **M-pzc** (**M** = **Co**, **Ni**)

Formula	$C_8H_{10}CoN_4O_6$	$C_8H_{10}NiN_4O_6$
FW ($g\ mol^{-1}$)	317.13	316.91
Crystal system	monoclinic	monoclinic
Space group	$P2_1/c$	$P2_1/c$
a (Å)	5.0874(1)	5.0879(3)
b (Å)	11.4002(3)	11.2855(6)
c (Å)	9.2880(4)	9.2686(6)
β (°)	96.932(2)	97.216(6)
V (Å ³)	534.74(2)	527.99(6)
Z	2	2
D_{calcd} ($g\ cm^{-3}$)	1.970	1.993
μ (mm^{-1})	1.639	3.031
Reflections		
Collected	4004	2552
Unique (R_{int})	1110 (0.024)	893 (0.024)
Observed [$I > 2\sigma(I)$]	1025	791
Parameters	94	96
$R(F)$ [$I > 2\sigma(I)$]	0.023	0.024
$wR(F^2)$ (all)	0.056	0.063
GoF	1.079	1.077

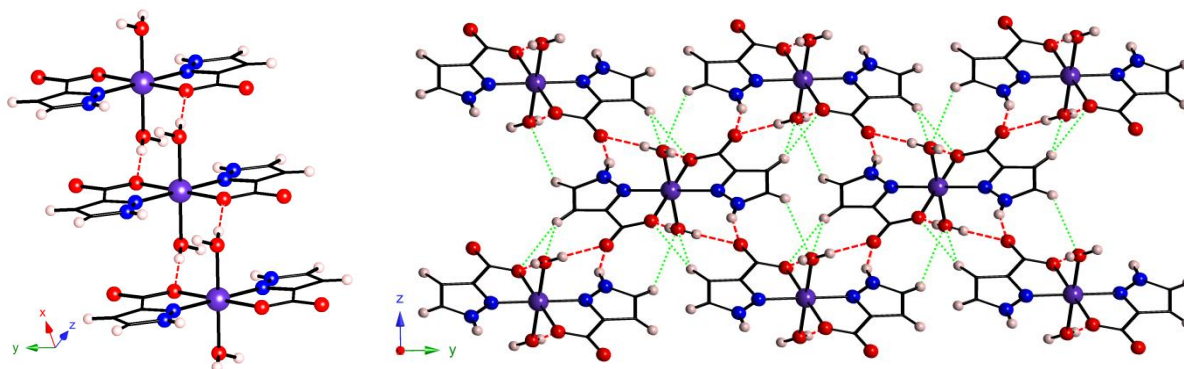


Figure A1.6. Hydrogen bonded chain of **M-pzc** complexes running along the crystallographic *a* axis (left). View of the crystal packing along the [100] direction (right). O—H...O and N—H...O hydrogen bonds represented as dashed red lines. C—H...O interactions as green lines.

A1.3. $[M(\text{pydc})_2(\text{H}_2\text{O})_2] \cdot 2\text{H}_2\text{O}$, $M = \text{Co}$ (**Co-pydc**), Ni (**Ni-pydc**)

Experimental: To a solution of $\text{MCl}_2 \cdot 6\text{H}_2\text{O}$ ($M = \text{Co}, \text{Ni}$, 71 mg; 0.30 mmol) in hot water (15 mL) pyridazine-3-carboxylic acid (74 mg, 0.60 mmol) dissolved in hot water (10 mL) was added dropwise and the resulting solution was stirred for 30 min at 90 °C. Prismatic crystals (Co : orange; Ni : green) were obtained by slow evaporation after several days. **Co-pydc:** 97 mg; yield 86 %. Anal. Calcd. (found) for $\text{C}_{10}\text{H}_{14}\text{CoN}_4\text{O}_8$: C, 31.84 (31.35); H, 3.74 (3.48); N, 14.85 (14.41). IR (cm^{-1} , Figure A1.7): 3500 (s), 3320 (s), 3229 (s), 3075 (s), 1626 (s), 1580 (m), 1559 (s), 1451 (w), 1385 (w), 1163 (w), 1090 (w), 1074 (w), 988 (m), 851 (m), 783 (m), 721 (m), 675 (m). **Ni-pydc:** 81 mg; yield 72 %. Anal. Calcd. (found) for $\text{C}_{10}\text{H}_{14}\text{N}_4\text{NiO}_8$: C, 31.86 (32.27); H, 3.74 (3.64); N, 14.86 (14.94) IR (cm^{-1} , Figure A1.7): 3505 (s), 3318 (s), 3074 (s), 1628 (s), 1580 (m), 1560 (s), 1454 (w), 1385 (w), 1163 (w), 1092 (w), 1078 (w), 988 (m), 851 (m), 783 (m), 725 (m), 669 (m).

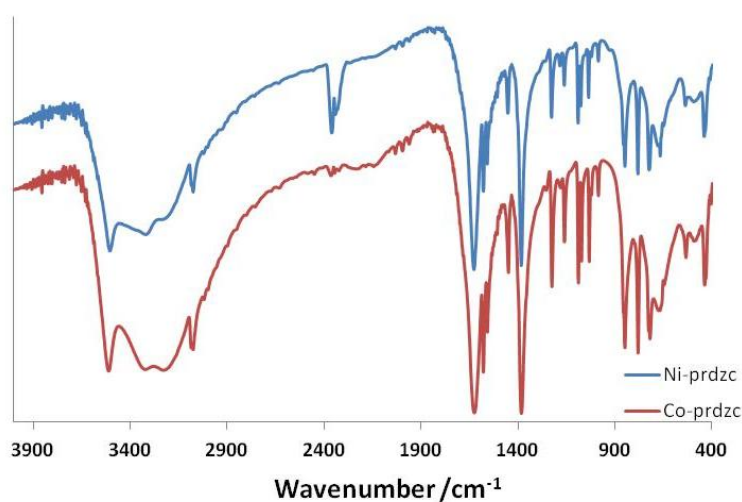
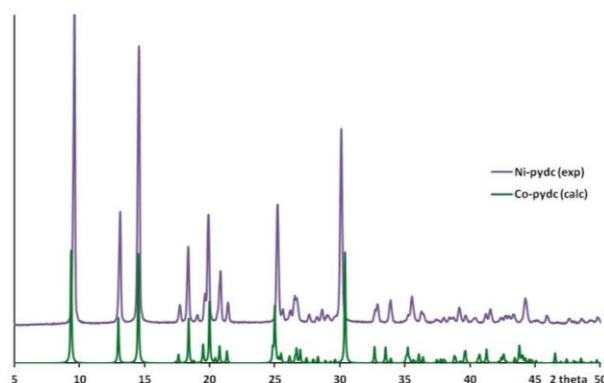
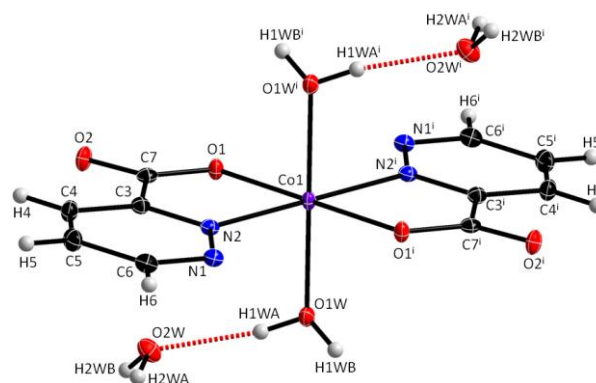


Figure A1.7. FT-IR spectra for **M-pydc** ($M = \text{Co}, \text{Ni}$).

Table A.4. Crystallographic data for **Co-pydc**.

Co-pydc	
Formula	C ₁₀ H ₁₄ CoN ₄ O ₈
FW (g mol ⁻¹)	377.18
Crystal system	triclinic
Space group	<i>P</i> -1
<i>a</i> (Å)	5.2934(4)
<i>b</i> (Å)	7.2817(8)
<i>c</i> (Å)	9.6196(9)
α (°)	79.673(8)
β (°)	89.875(7)
γ (°)	72.321(8)
<i>V</i> (Å ³)	347.01(6)
<i>Z</i>	1
<i>D</i> _{calcd} (g cm ⁻³)	1.805
μ (mm ⁻¹)	1.289
Reflections	
Collected	2202
Unique (<i>R</i> _{int})	1369 (0.018)
Observed [<i>I</i> > 2 σ (<i>I</i>)]	1309
Parameters	122
<i>R</i> (<i>F</i>) [<i>I</i> > 2 σ (<i>I</i>)]	0.026
<i>wR</i> (<i>F</i> ²) (all)	0.058
GoF	1.084

**Figure A1.8.** Comparison between the experimental powder XRD pattern of **Ni-pydc** and that calculated from the single-crystal data of **Co-pydc**.**Figure A1.9.** ORTEP view of **Co-pydc** showing atom labels and 50% probability displacement ellipsoids (symmetry code: (i) 1 - *x*, 1 - *y*, 1 - *z*). Hydrogen bonds represented as dotted red lines.

Crystal Structure: *trans*-**Co-pydc**³ and **Ni-pydc** (isostructural with the Co²⁺ analogue according to the powder X-ray diffraction patterns shown in Figure A1.8) crystallize in the triclinic *P*-1 space group (Table A1.4). They are isostructural with the published Zn and Mn complexes.⁴ Both compounds contain a M^{II} ion on an inversion center, exhibiting an octahedral coordination geometry. The equatorial plane is formed by two *trans*-related N,O-bidentate pyridazine-3-carboxylate ligands and the axial positions are occupied by two water molecules (Figure A1.9). The M—O (Co: 2.069(1) Å) and M—N (Co: 2.102(1) Å) bond lengths are similar to those of the previously reported analogues. The complexes are stacked in columns along the crystallographic *a* axis by O—H⋯N hydrogen bonds between the non-coordinating pyridazine N atoms and the coordinating water molecules. These columns are further connected into layers parallel to the *ac* plane by additional hydrogen bonds involving the coordinating and non-coordinating water molecules, and the non-coordinating carboxylate O atoms. The crystal packing is completed by interlayer, weak C—H⋯O interactions (Figure A1.10).

APPENDIX 1

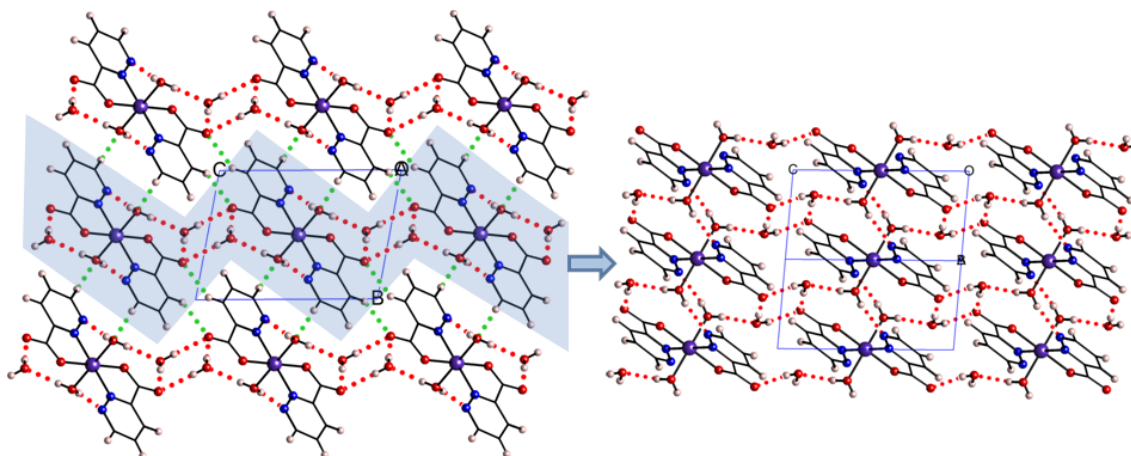


Figure A1.10. View of the crystal packing of **Co-pydc** along the crystallographic a axis (left) and projection of a layer along the $[110]$ direction (right). $O-H\cdots O$ and $O-H\cdots N$ hydrogen bonds represented as dotted red lines and $C-H\cdots O$ weak interactions as dotted green.

TGA/DTA: According to the TGA/DTA analysis (Figure A1.11), **Ni-pydc** is thermally stable up to 50 °C whereas the decomposition of **Co-pydc** starts at room temperature. In both complexes, the endothermic dehydration process takes place in two separate mass loss stages. First, the release of the two hydration water molecules takes place and it is completed at 92 °C for **Co-pydc** and 101 °C for **Ni-pydc** [calcd (found) for 2 H₂O: **Co-pydc**, 9.56 (9.39); **Ni-pydc**, 9.56 (9.71)] resulting in $[M(\text{pydc})_2(\text{H}_2\text{O})_2]$ species. The release of the two coordination water molecules proceeds in the second step [calcd (found) for 2 H₂O: **Co-pydc**, 9.56 (9.16); **Ni-pydc**, 9.56 (9.21)], leading to the corresponding anhydrous $[M(\text{pydc})_2]$ phases above c.a. 160 °C for **Co-pydc** and 170 °C for **Ni-pydc**. Narrow thermal stability ranges are observed between both dehydration stages (**Co-pydc**: 90-120 °C; **Ni-pydc**: 100-120 °C). The anhydrous phases are thermally stable up to ~255°C, above which they undergo highly exothermic ligand combustion. The final residues are obtained at 375 °C for **Co-pydc** and 370 °C for **Ni-pydc** [calcd (found) for Co₂O₃: 21.98 (22.20); NiO: 19.79 (18.80)].

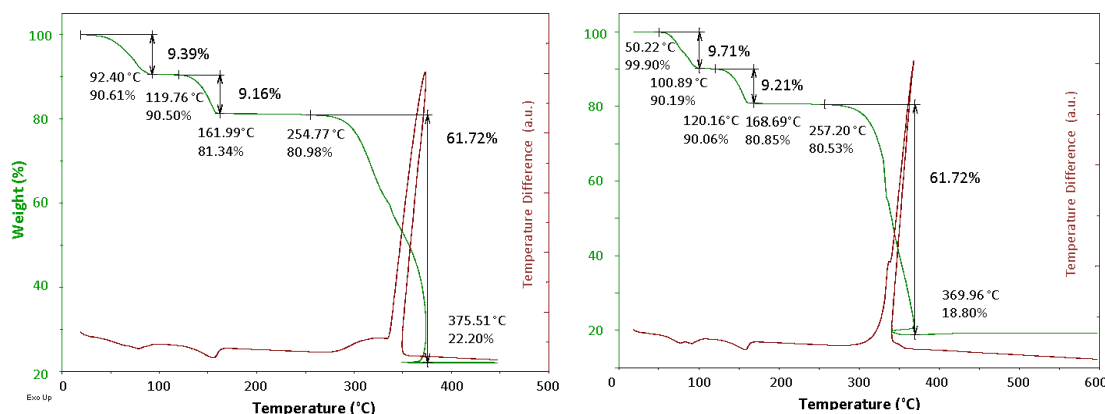


Figure A1.11. TGA/DTA curves for **Co-** (left) and **Ni-pydc** (right).

In order to determine whether the above thermally stable phases retain crystallinity or undergo amorphisation, variable temperature powder X-ray diffraction experiments were carried out for **Co-pydc** between room temperature and 450 °C (Figure A1.12, left). The $[\text{Co}(\text{pydc})_2(\text{H}_2\text{O})_2]$ phase ($T = 110$ °C) displays a well-defined diffraction pattern with noticeable variations in the number and positions of the diffraction maxima. This indicates substantial structural modifications upon the release of the lattice water molecules. Full-profile refinement of the diffractogram using the unit cell parameters of the closely related $[\text{Zn}(\text{pydc})_2(\text{H}_2\text{O})_2]$ ⁵ complex found in the CSD database did not

result in satisfactory agreement factors (Figure A1.12, right), revealing that the non-hydrated phase is not isostructural with this compound. On the contrary, the anhydrous $[\text{Co}(\text{pydc})_2]$ phase ($T = 175^\circ\text{C}$) is amorphous.

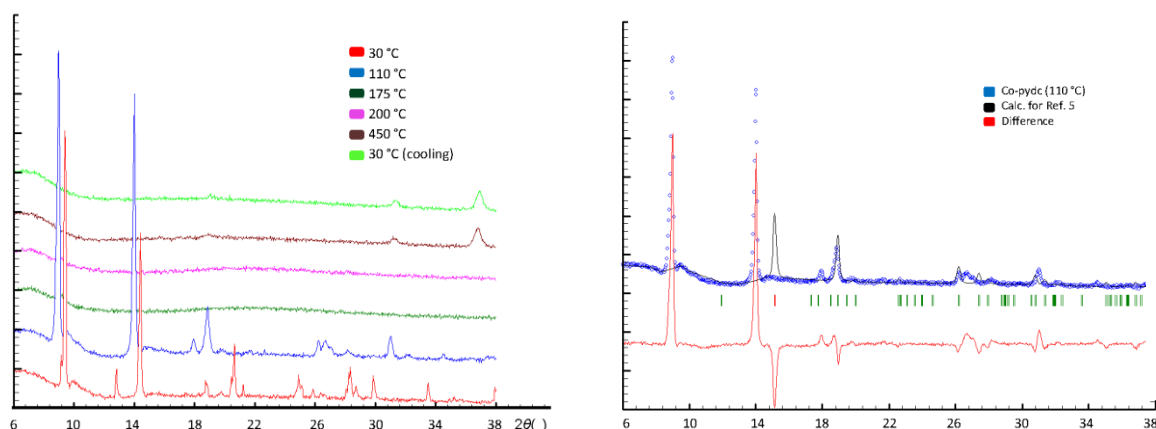


Figure A1.12. Left: Powder XRD patterns at different temperatures for **Co-pydc**. Right: Full-profile X-ray refinements of **Co-pydc** at 110°C and $[\text{Zn}(\text{pydc})_2(\text{H}_2\text{O})_2]$.⁵ The experimental and calculated intensity data are plotted as dotted and solid lines, respectively, and the difference ($I_{\text{exp}} - I_{\text{cal}}$) is shown as the lower solid line.

A1.4. $[\text{Co}(\text{pymc})_2(\text{H}_2\text{O})_2] \cdot 2\text{H}_2\text{O}$ (**Co-pymc**)

Experimental: To a solution of $\text{CoCl}_2 \cdot 6\text{H}_2\text{O}$ (71 mg, 0.30 mmol) in hot water (15 mL) pyrimidine-4-carboxylic acid (74 mg, 0.60 mmol) dissolved in hot water (10 mL) was added and the resulting solution was stirred for 30 min at 90°C . Prismatic orange crystals were obtained by slow evaporation after several days (58 mg, yield 51 %). Anal. Calcd. (found) for $\text{C}_{10}\text{H}_{14}\text{CoN}_4\text{O}_8$: C, 31.84 (31.70); H, 3.74 (3.68); N, 14.85 (14.73). IR (cm^{-1} , Figure A1.13): 3495 (s), 3323 (s), 3150 (s), 3104 (s), 3044 (s), 1626 (s), 1595 (s), 1557 (s), 1402 (s), 1383 (s), 1304 (m), 1207 (w), 1173 (w), 1155 (w), 1074 (m), 1026 (m), 860 (m), 810 (m), 712 (m), 619 (w), 542 (w), 436 (w).

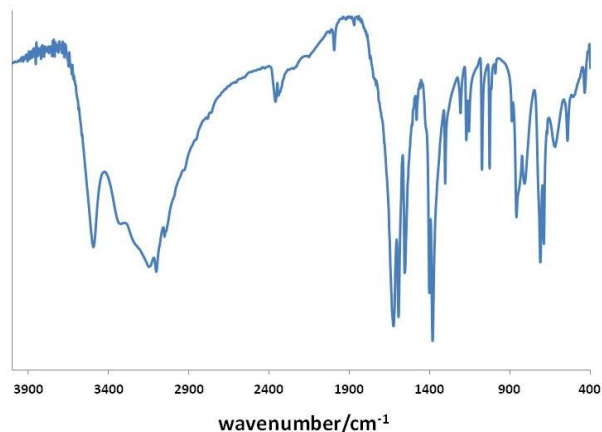
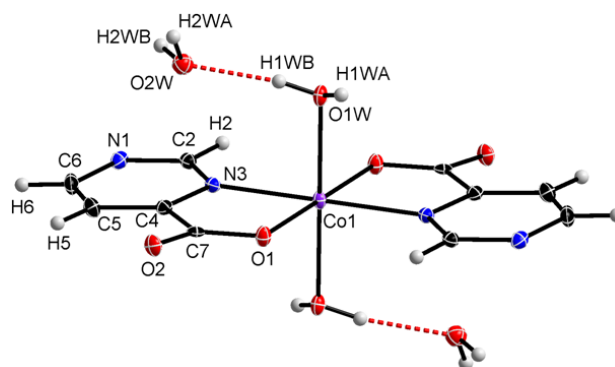
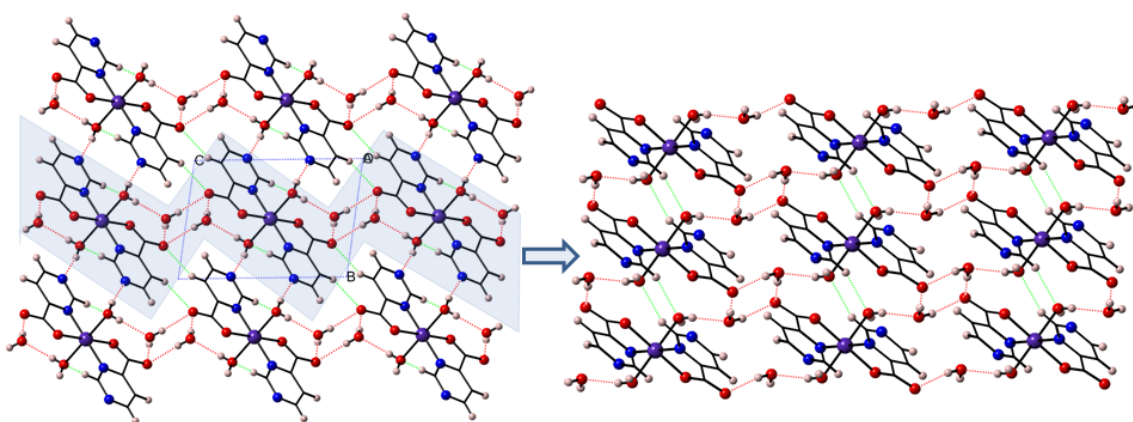
Crystal Structure: Compound **Co-pymc** crystallizes in the triclinic $P-1$ space group (Table A1.5) and is isostructural with the reported Zn and Ni analogues.⁶ The complex contains a Co^{II} ion on an inversion center, exhibiting an octahedral coordination geometry. The equatorial plane is formed by two *trans*-related N,O-bidentate pyrimidine-4-carboxylate ligands and the axial positions are occupied by two water molecules (Figure A1.14). The Co—O (2.071(2) Å) and Co—N (2.106(2) Å) bond lengths are similar to those reported for the Zn and Ni analogues.

The crystal packing closely resembles that of **Co-pydc** (Figure A1.10), but the connectivity is slightly different due to the change in the relative position of the non-coordinating N atom in the diazine ring. As for **Co-pydc**, the complexes are stacked in columns *via* O—H \cdots N hydrogen bonds, but in this case, the columns run along the $[1-10]$ direction instead of the $[100]$ direction observed for **Co-pydc**. These columns are not further connected into layers as in **Co-pydc**, but into a three dimensional network by additional hydrogen bonds involving the coordination and hydration water molecules and the non-coordinating carboxylate O atoms (Figure A1.15).

APPENDIX 1

Table A.5. Crystallographic data for **Co-pymc**

Formula	$C_{10}H_{14}CoN_4O_8$
FW ($g\ mol^{-1}$)	377.18
Crystal system	triclinic
Space group	$P-1$
a (Å)	5.5524(5)
b (Å)	7.1608(8)
c (Å)	9.4616(9)
α (°)	81.680(9)
β (°)	88.202(8)
γ (°)	70.571(9)
V (Å ³)	350.98(6)
Z	1
D_{calcd} ($g\ cm^{-3}$)	1.785
μ (mm^{-1})	1.274
Reflections	
Collected	2166
Unique (R_{int})	1380 (0.024)
Observed [$I > 2\sigma(I)$]	1241
Parameters	117
$R(F)$ [$I > 2\sigma(I)$]	0.032
$wR(F^2)$ (all)	0.068
GoF	1.024

**Figure A1.13.** IR spectrum for **Co-pymc**.**Figure A1.14.** ORTEP view of **Co-pymc** showing atom labels for the asymmetric unit and 50% probability displacement ellipsoids. O—H...O hydrogen bonds represented as dotted red lines.**Figure A1.15.** View of the crystal packing along the crystallographic a axis (left) and projection of a layer along the $[1-10]$ direction (right). O—H...O and O—H...N hydrogen bonds represented as dotted red lines and C—H...O weak interactions as dotted green.

TGA/DTA: Thermal properties of **Co-pymc** are similar to those of **Co-pydc**. Thermal decomposition starts at 52 °C and it is followed by two mass-loss stages corresponding to endothermic dehydration processes where the lattice [calcd (found) for 2 H₂O: 9.56 (9.61)] and coordination [calcd (found) for 2 H₂O: 9.56 (9.17)] water molecules are released below 105 °C and 160 °C, respectively (Figure A1.16, left). In contrast to **Co-pydc**, no stability range is observed between the two well-defined mass losses associated to dehydrations, whereas that of the anhydrous phase extends to higher temperatures (270 °C). The highly endothermic ligand combustion results in the final residue at 405 °C [calcd (found) for Co₂O₃, 21.98 (22.19)]. Variable temperature powder X-ray diffraction between room temperature and 450 °C (Figure A.16, right) shows a well-defined diffraction pattern for the [Co(pymc)₂(H₂O)₂] without lattice water molecules, whereas the anhydrous phase is amorphous.

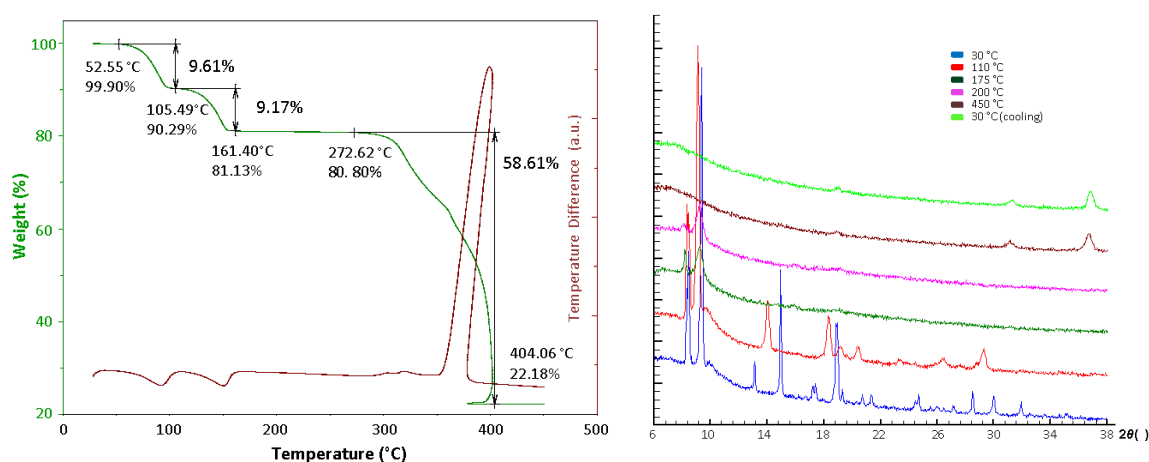


Figure A1.16. TGA/DTA curves (left) and variable temperature powder XRD patterns (right) for **Co-pymc**.

A1.5. REFERENCES

- [1] Artetxe, B.; San Felices, L.; Reinoso, S.; Pache, A.; Gutiérrez-Zorrilla, J. M. *Acta Crystallogr.* **2013**, *E69*, m94.
- [2] (a) Shuai, W.; Cai, S.; Zheng, S. *Acta Crystallogr.* **2011**, *E67*, m897. (b) Yin, W.-P.; Li, Y.-G.; Mei, X.-L.; Yao, J.-C. *Chin. J. Struct. Chem.* **2009**, *28*, 1155.
- [3] Artetxe, B.; Reinoso, S.; San Felices, L.; Martín-Caballero, J.; Gutiérrez-Zorrilla, J. M. *Acta Crystallogr.* **2013**, *E69*, m420.
- [4] (a) Gryz, M.; Starosta, W.; Ptasiewicz, H.; Leciejewicz, J. *J. Coord. Chem.* **2003**, *56*, 1505. (b) Ardiwlnata, E. S.; Craig, C. D.; Phillips, D. J. *Inorg. Chim. Acta* **1989**, *166*, 233.
- [5] Gryz, M.; Starosta, W.; Ptasiewicz, H.; Leciejewicz, J. *Acta Crystallogr.* **2004**, *E60*, m1481.
- [6] Aakeröy, C. B.; Desper, J.; Levin, B.; Valdés-Martínez, J. *Inorg. Chim. Acta* **2006**, *359*, 1255.

Materials and methods

A.2.1. Reagents

A.2.2. Instrumental techniques

A.2.3. X-ray Crystallography

A.2.4. Laser Light Scattering

A.2.5. References

A2.1. REAGENTS

All the chemicals employed in this work were purchased from commercial sources and used without further purification. Their name, formula, purity, chemical company (CC) and CAS number are compiled in Tables A2.1 and A2.2. Figure A2.1 shows the Electrostatic Potential Surfaces of the organic ligands used in Chapter 2.

Table A2.1. Employed commercial chemicals.

Compound	Formula	Purity	CC	CAS
Buffers				
Sodium hydroxide	NaOH	≥97%	Sigma-Aldrich	1310-73-2
Acetic acid	CH ₃ COOH	≥99%	Sigma-Aldrich	64-19-7
POM precursors				
Sodium tungstate dihydrate	Na ₂ WO ₄ ·2H ₂ O	99%	Sigma-Aldrich	10213-10-2
Hydrochloric acid	HCl	37%	Sigma-Aldrich	7647-01-0
Antimony(III) oxide	Sb ₂ O ₃	≥98%	Fluka	1309-64-4
Antimony(III) chloride	SbCl ₃	≥99%	Sigma-Aldrich	10025-91-9
Germanium oxide	GeO ₂	99.9%	Aldrich	1310-53-8
Metal salts				
Potassium chloride	KCl	≥99%	Sigma-Aldrich	7447-40-7
Cesium chloride	CsCl	≥98%	Sigma	7647-17-8
Manganese(II) chloride tetrahydrate	MnCl ₂ ·4H ₂ O	≥98%	Sigma-Aldrich	13446-34-9
Cobalt(II) chloride hexahydrate	CoCl ₂ ·6H ₂ O	≥98%	Sigma-Aldrich	7791-13-1
Nickel(II) chloride hexahydrate	NiCl ₂ ·6H ₂ O	≥98%	Sigma-Aldrich	7791-20-0
Zinc nitrate hexahydrate	Zn(NO ₃) ₂ ·6H ₂ O	98%	Sigma-Aldrich	10196-18-6
Lanthanum(III) nitrate hexahydrate	La(NO ₃) ₃ ·6H ₂ O	≥99%	Aldrich	10277-43-7
Cerium(III) nitrate hexahydrate	Ce(NO ₃) ₃ ·6H ₂ O	≥99%	Aldrich	10294-41-4
Praseodymium(III) nitrate hexahydrate	Pr(NO ₃) ₃ ·6H ₂ O	≥99%	Aldrich	15878-77-0
Neodymium(III) nitrate hexahydrate	Nd(NO ₃) ₃ ·6H ₂ O	≥99%	Aldrich	16454-60-7
Samarium(III) nitrate hexahydrate	Sm(NO ₃) ₃ ·6H ₂ O	≥99%	Aldrich	13759-83-6
Europium(III) nitrate pentahydrate	Eu(NO ₃) ₃ ·5H ₂ O	≥99%	Aldrich	63026-01-7
Gadolinium(III) nitrate hexahydrate	Gd(NO ₃) ₃ ·6H ₂ O	≥99%	Aldrich	19598-90-4
Terbium(III) nitrate pentahydrate	Tb(NO ₃) ₃ ·5H ₂ O	≥99%	Aldrich	57584-27-7
Dysprosium(III) chloride hexahydrate	DyCl ₃ ·6H ₂ O	≥99%	Aldrich	15059-52-6
Holmium(III) chloride hexahydrate	HoCl ₃ ·6H ₂ O	≥99%	Aldrich	14914-84-2
Erbium(III) chloride hexahydrate	ErCl ₃ ·6H ₂ O	99.9%	Aldrich	10025-75-9
Thulium(III) chloride hexahydrate	TmCl ₃ ·6H ₂ O	99.99%	Aldrich	1331-74-4
Ytterbium(III) chloride hexahydrate	YbCl ₃ ·6H ₂ O	99.9%	Aldrich	10035-01-5
Lutetium(III) chloride hexahydrate	LuCl ₃ ·6H ₂ O	99.9%	Aldrich	15230-79-2

APPENDIX 2

Table A2.2. Commercial organic ligands employed in Chapter 2.

Compound	Formula	Purity	CC	CAS
1H-imidazole-4-carboxylic acid	C ₄ H ₄ N ₂ O ₂	98%	Aldrich	1072-84-0
1H-pyrazole-3-carboxylic acid	C ₄ H ₄ N ₂ O ₂	97%	Aldrich	1621-91-6
Picolinic acid	C ₆ H ₅ NO ₂	99%	Aldrich	98-98-6
Pyridazine-3-carboxylic acid	C ₅ H ₄ N ₂ O ₂	97%	Aldrich	2164-61-6
Pyrimidine-4-carboxylic acid	C ₅ H ₄ N ₂ O ₂	97%	Aldrich	819850-18-5
Pyrazine-2-carboxylic acid	C ₅ H ₄ N ₂ O ₂	99%	Aldrich	98-97-5
4,4'-bipyridine	C ₁₀ H ₈ N ₂	98%	Aldrich	533-26-4
2,5-pyrazinedicarboxylic acid	C ₆ H ₄ N ₂ O ₄	96%	Aldrich	205692-63-3
2,3-pyrazinedicarboxylic acid	C ₆ H ₄ N ₂ O ₄	97%	Aldrich	89-01-0

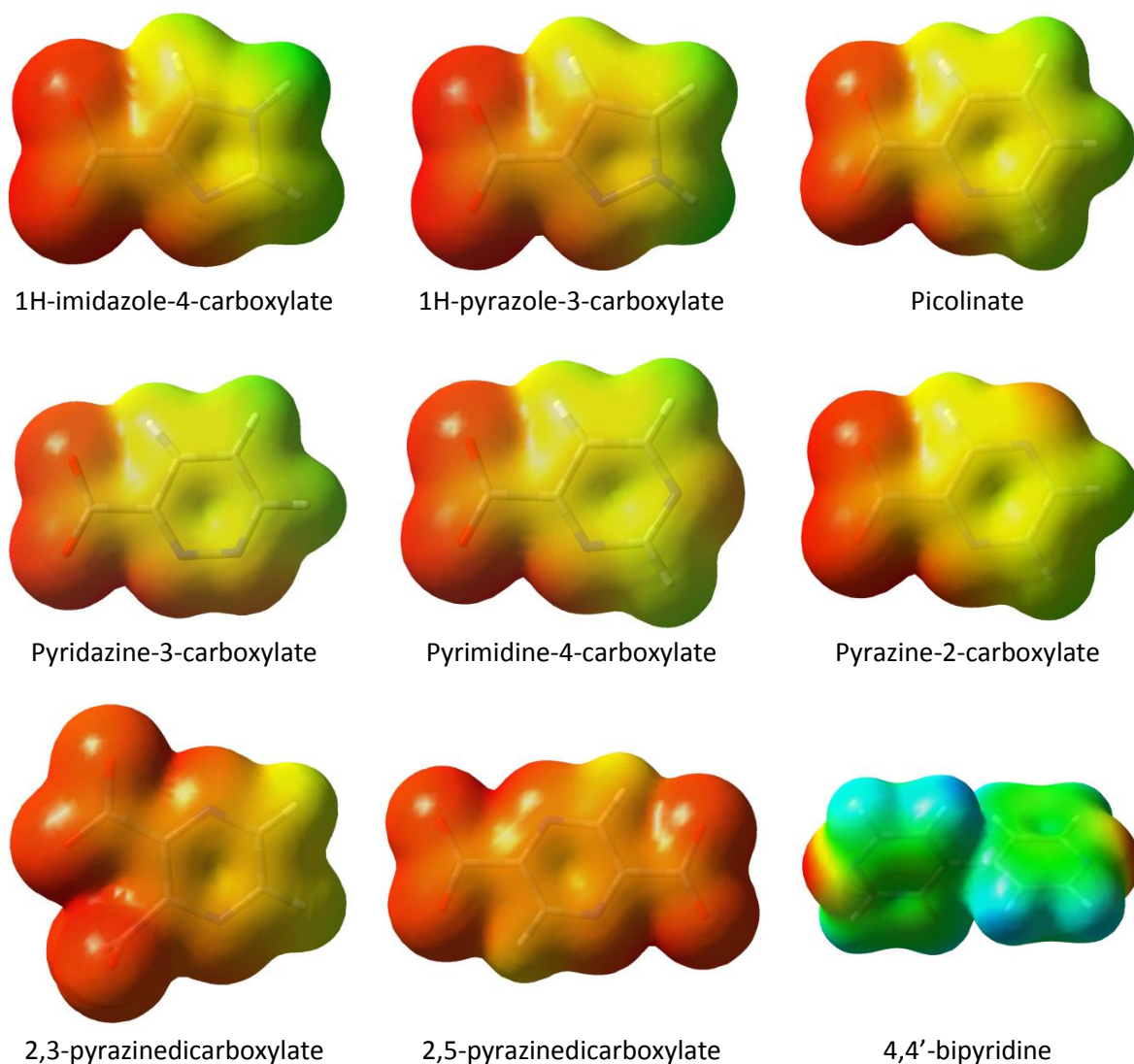


Figure A2.1. Electrostatic potential surfaces of the anionic ligands used in Chapter 2.

A2.2. INSTRUMENTAL TECHNIQUES

All the experimental conditions applied for the characterization methods are described in this section. Thermal analyses and FT-IR measurements were performed at Departamento de Química Inorgánica (UPV/EHU), whereas the following studies were carried out at Servicios Generales de Investigación (SGIker) de la UPV/EHU: powder and single-crystal X-ray diffraction studies (Servicios Generales de rayos X), elemental analyses (metals: IBERCRON; CHN: SCAB), ^1H -NMR experiments (Servicios Generales de RMN) and magnetic susceptibility measurements (Servicio General de Medidas Magnéticas). Luminescence measurements were performed at Departamento de Física Aplicada II (UPV/EHU) under the supervision of Prof. Jose Angel García. Laser Light Scattering studies were carried out during a three-month stay at the Department of Polymer Science of the University of Akron (Akron, OH, USA) under the supervision of Prof. Tianbo Liu. The ESI-MS spectra were recorded at Universitat Jaume I (Castellón, Spain) by Dr. Cristian Vicent. ^{183}W -NMR spectroscopy was performed at Jacobs University (Bremen, Germany) by Ali Haider and Prof. Ulrich Kortz.

A2.2.I. Elemental analysis

The C, H and N content of compounds **1-SbM**, **1-TeM**, **2-Ni**, **3-M**, **4-Mn**, **5-Ni** and **11-LnM** was determined in a Perkin-Elmer 2400 CHN elemental analyzer employing about 5 mg of powdered crystalline samples. Metal contents (lanthanides, transition metals, heteroatoms and alkaline metals) were analyzed using a Q-ICP-MS Thermo XSeries2 inductively coupled plasma-mass spectrometry device. Samples (50 mg) were digested in 25 mL of ultra-high purity Milli-Q water.

A2.2.II. FT-IR spectroscopy

The infrared spectra (IR) were recorded in the $400\text{--}4000\text{ cm}^{-1}$ region (4 cm^{-1} resolution) on a Shimadzu FT-IR 4800S spectrophotometer as KBr (Aldrich, FT-IR grade) pellets. The IR spectra of all compounds reported in this work are displayed in Figures A2.2 to A2.8.

APPENDIX 2

CHAPTER 2: Krebs-type hybrid POMs

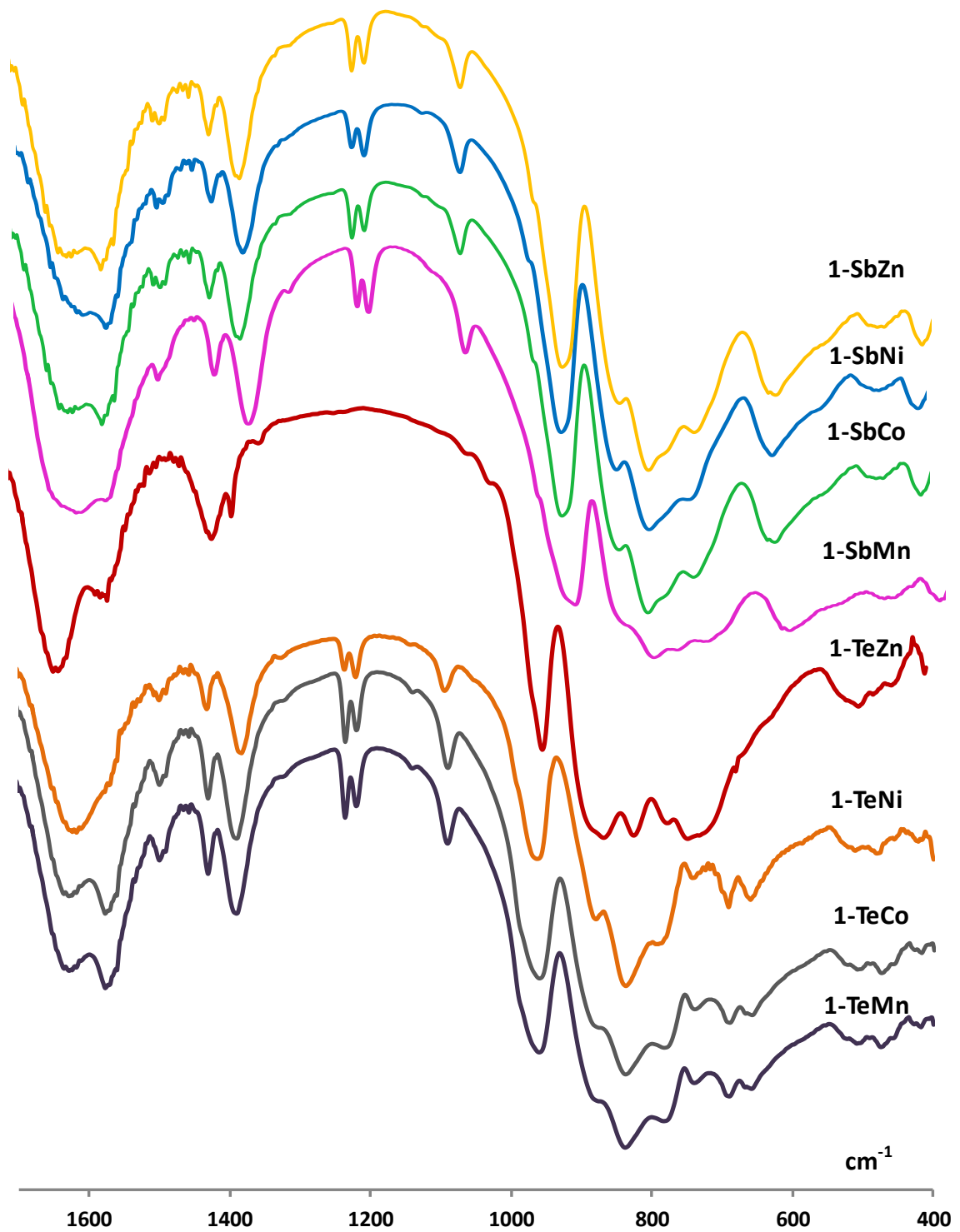


Figure A2.2. FT-IR spectra of compounds **1-SbM** and **1-TeM**. Note that **1-TeZn** cannot be obtained as pure phase.

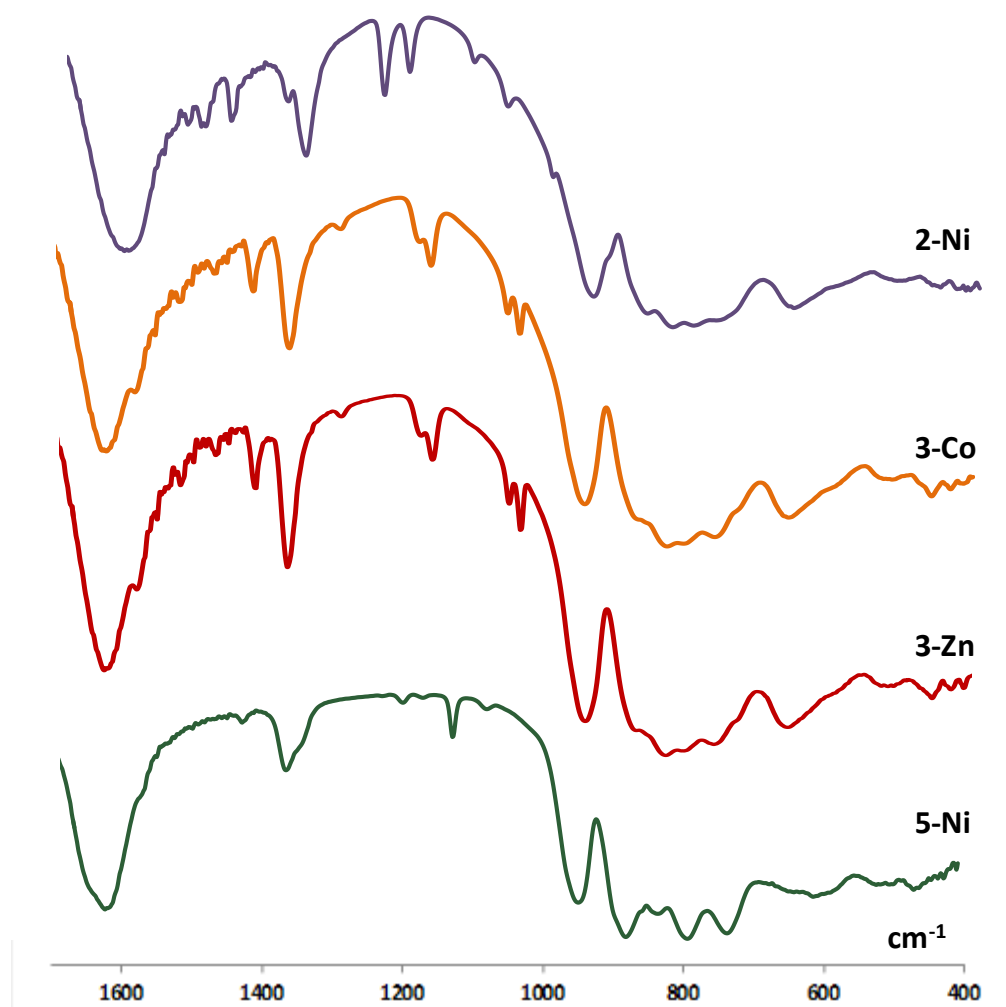


Figure A2.3. FT-IR spectra of compounds 2-Ni, 3-Co, 3-Zn and 5-Ni.

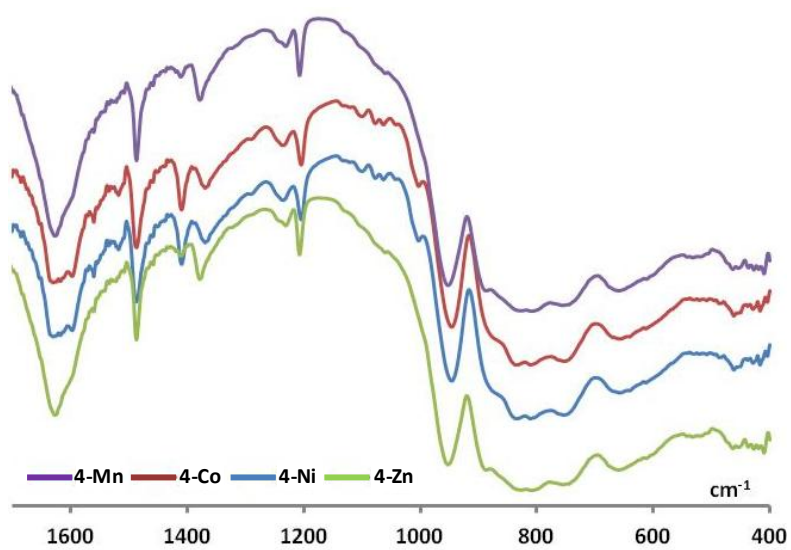


Figure A2.4. FT-IR spectra of compounds 4-M.

CHAPTER 3. Lanthanide containing tungstogermanates

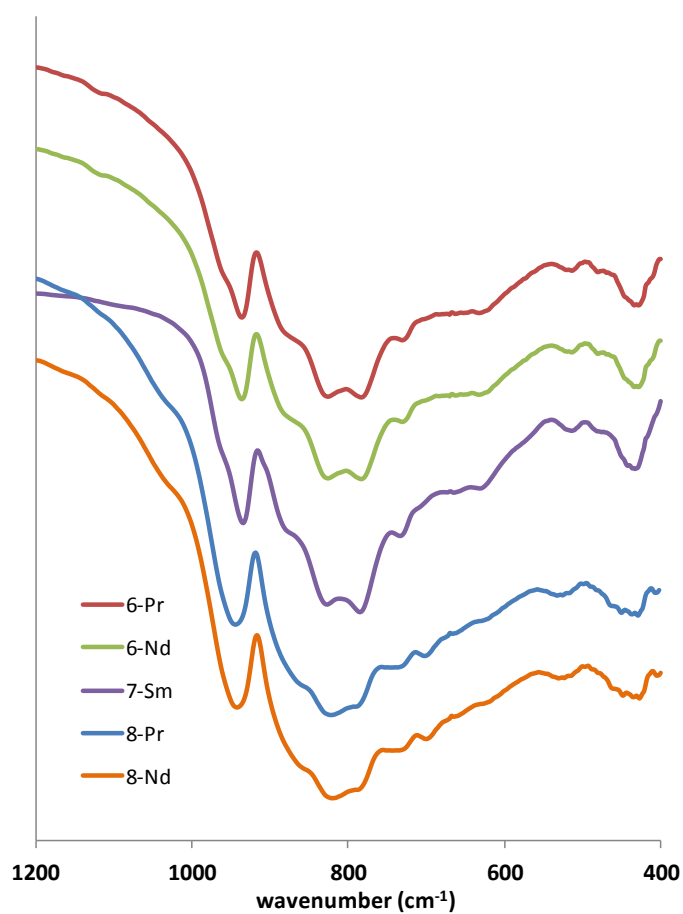
Assemblies containing early lanthanides

Figure A2.5. FT-IR spectra of **6-Ln** (Ln = Pr, Nd), **7-Sm** and **8-Ln** (Ln = Pr, Nd).

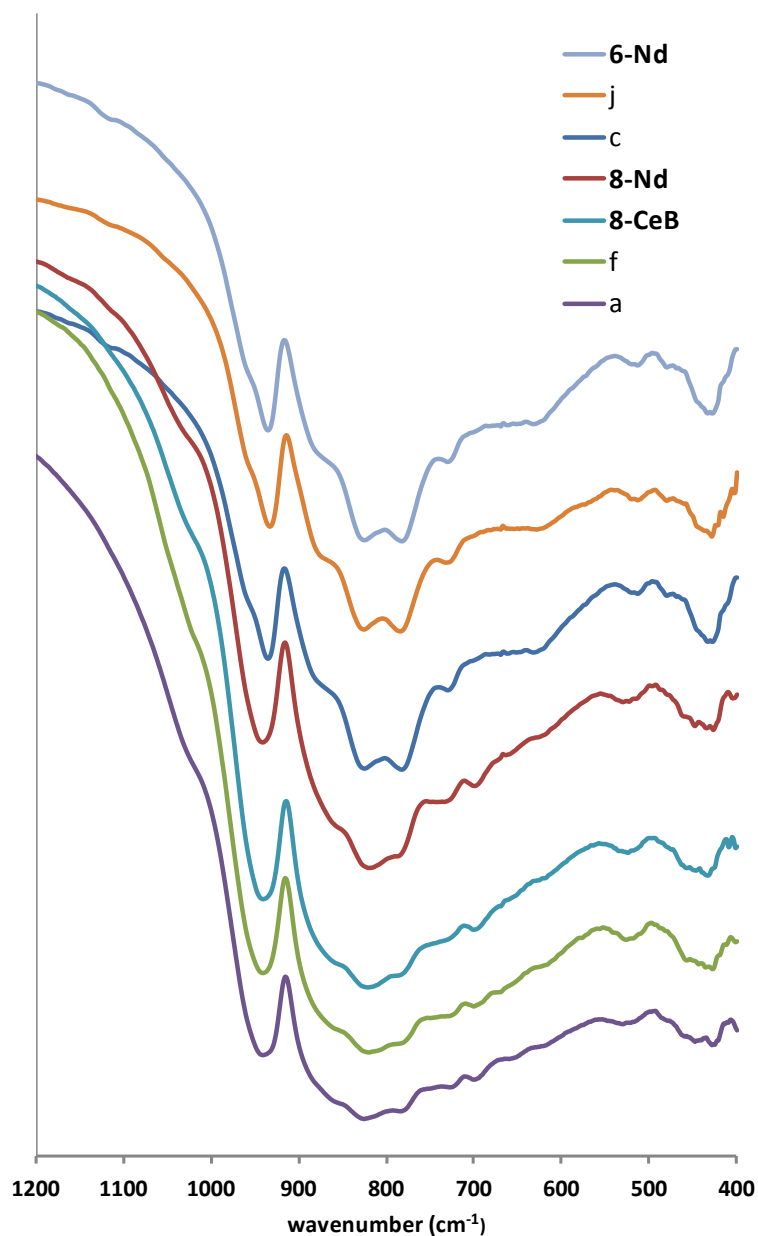
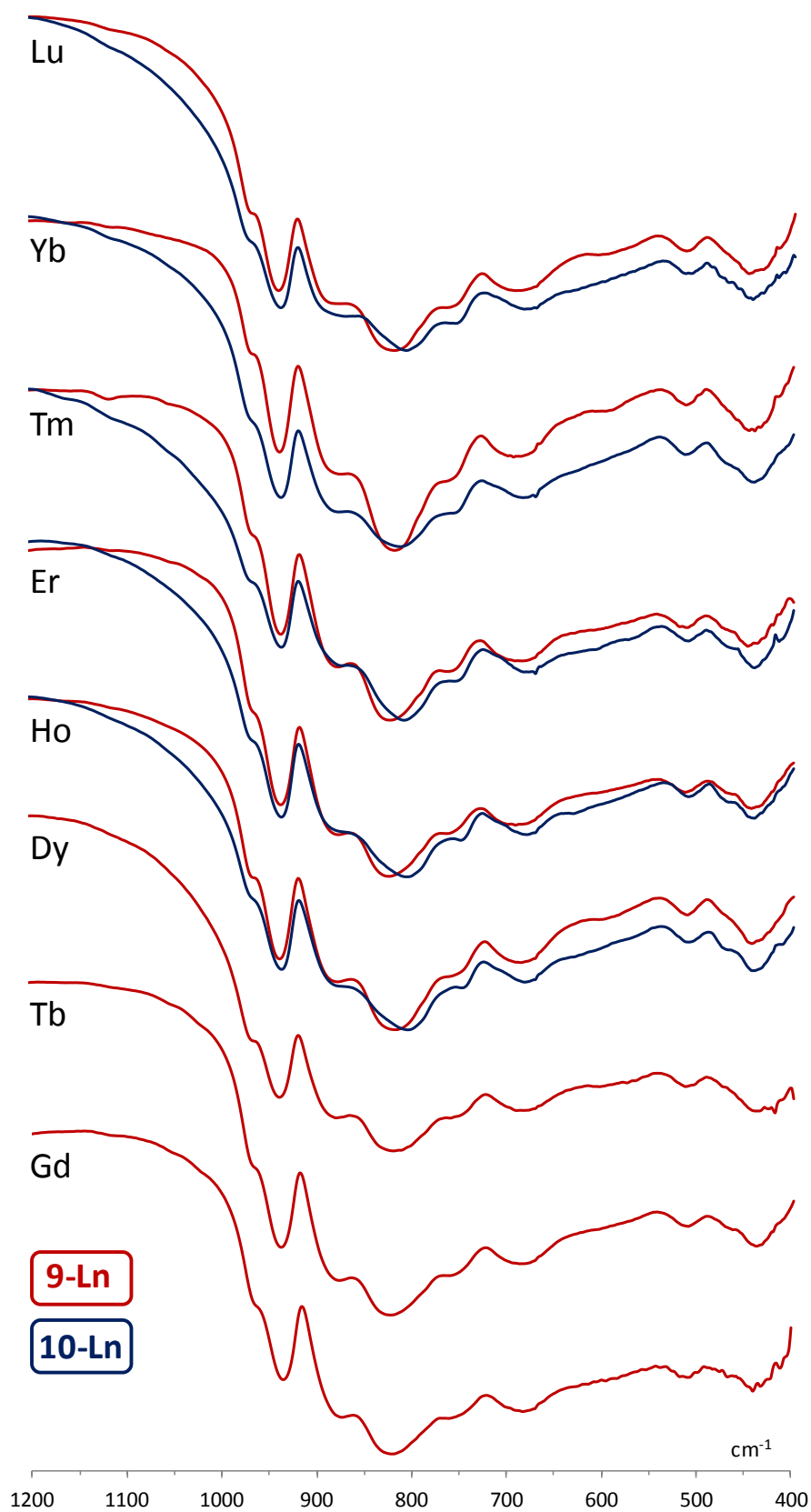


Figure A2.6. FT-IR spectra of some of the solid products obtained from the $\text{Ni}^{2+}/\text{Ln}^{3+}/\text{GeO}_2/\text{WO}_4^{2-}$ or $\text{Ln}^{3+}/\text{GeO}_2/\text{WO}_4^{2-}$ reactions upon addition of alkaline cations compared to those of the hexameric **6-Nd** and the dodecameric **8-Nd**. For the labeling see Table 3.1 in Chapter 3.

Assemblies containing mid-to-late lanthanides**Figure A2.7.** FT-IR spectra of compounds **9-Ln** and **10-Ln**.

CHAPTER 4. Heterometallic 3d-4f POMs derived from the Krebs-type structure

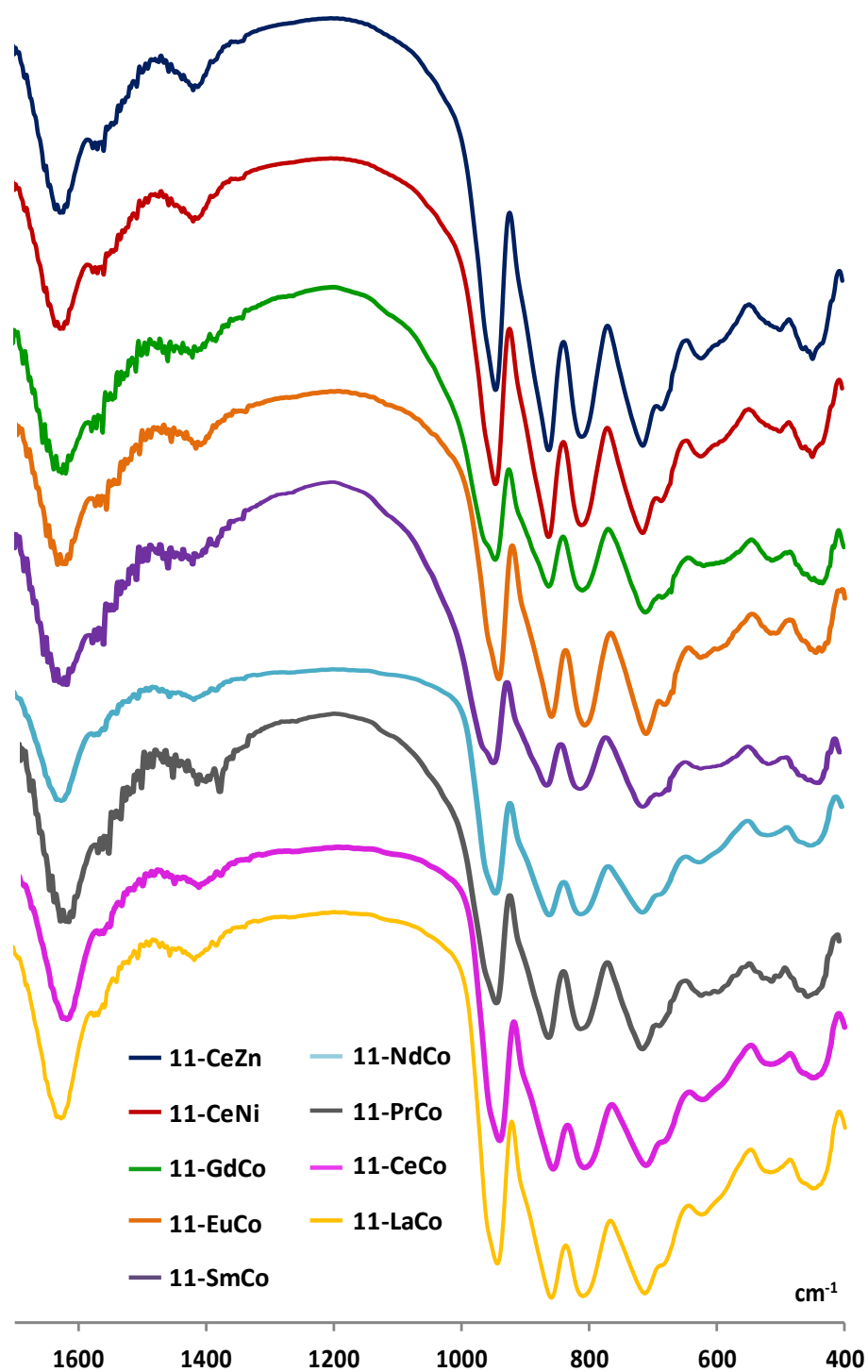


Figure A2.8. FT-IR spectra of compounds 11-LnM.

APPENDIX 2

A2.2.III. Thermal analyses

Thermogravimetric and differential thermal analyses (TGA/DTA) were carried out from room temperature to 700 °C at a rate of 5 °C min⁻¹ on a TA Instruments SDT 2960 thermobalance with a 150 mL min⁻¹ flow of synthetic air. β -alumina crucibles were used for approximately 20 mg of crystalline samples. All the TGA/DTA curves of the compounds studied in this work are shown in the following pages in Figures A2.9 to A2.13.

CHAPTER 2: Krebs-type hybrid POMs

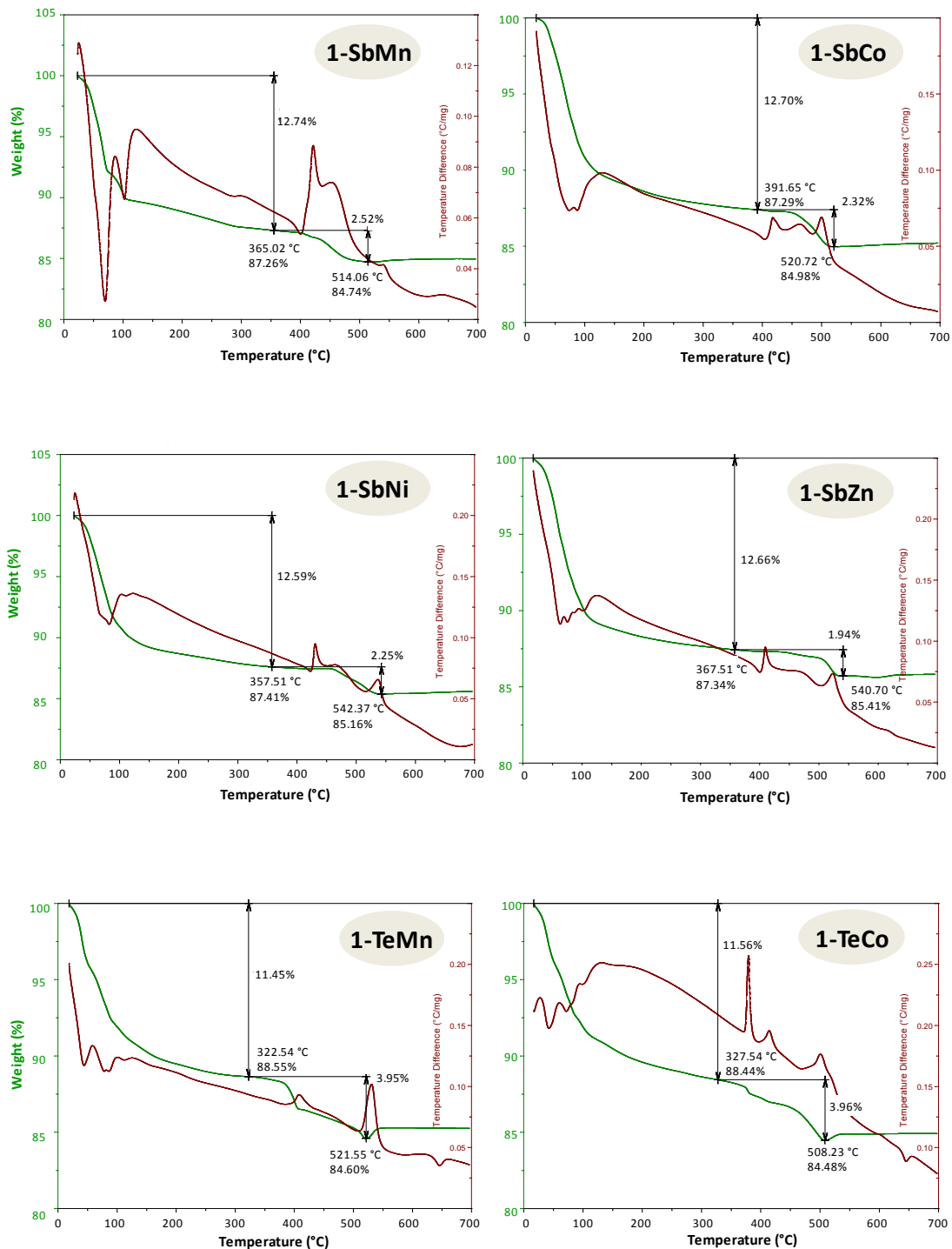


Figure A2.9. TGA/DTA curves for compounds 1-SbM and 1-TeM.

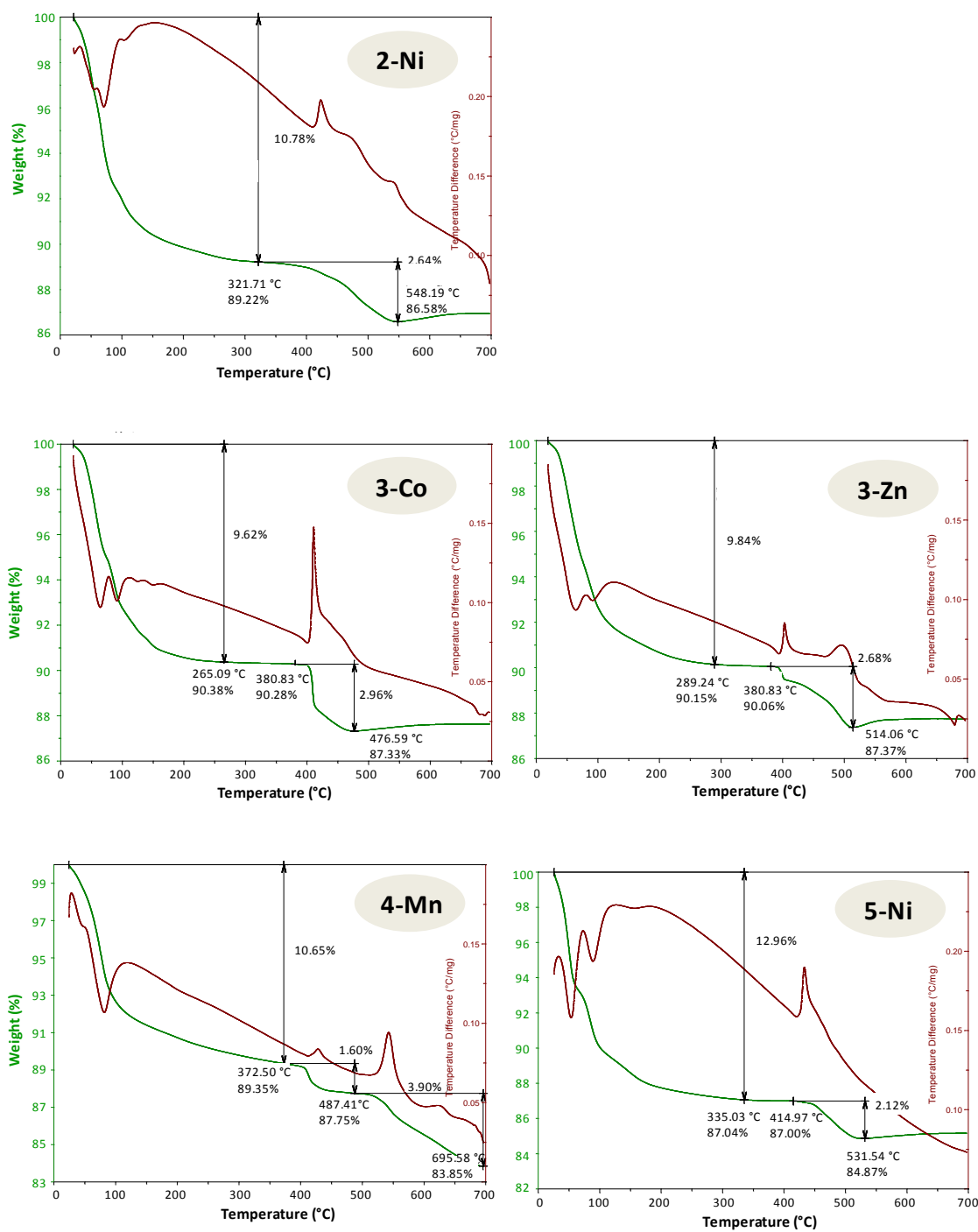


Figure A2.10. TGA/DTA curves for compounds 2-Ni, 3-M, 4-Mn and 5-Ni.

APPENDIX 2

CHAPTER 3: Lanthanide containing tungstogermanates

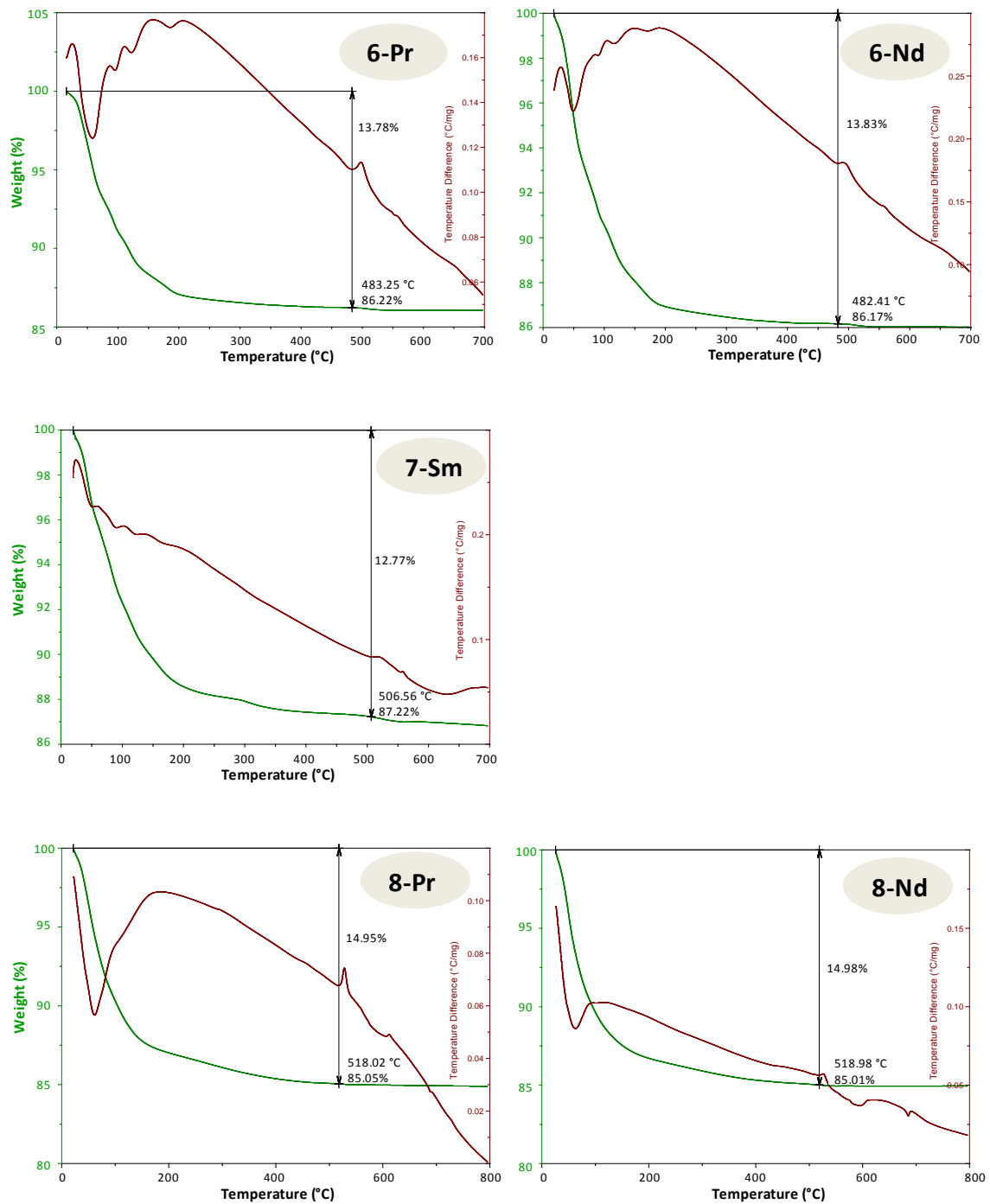
Assemblies containing early lanthanides

Figure A2.11. TGA/DTA curves for compounds 6-Ln, 7-Sm and 8-Ln.

Assemblies containing mid-to-late lanthanides

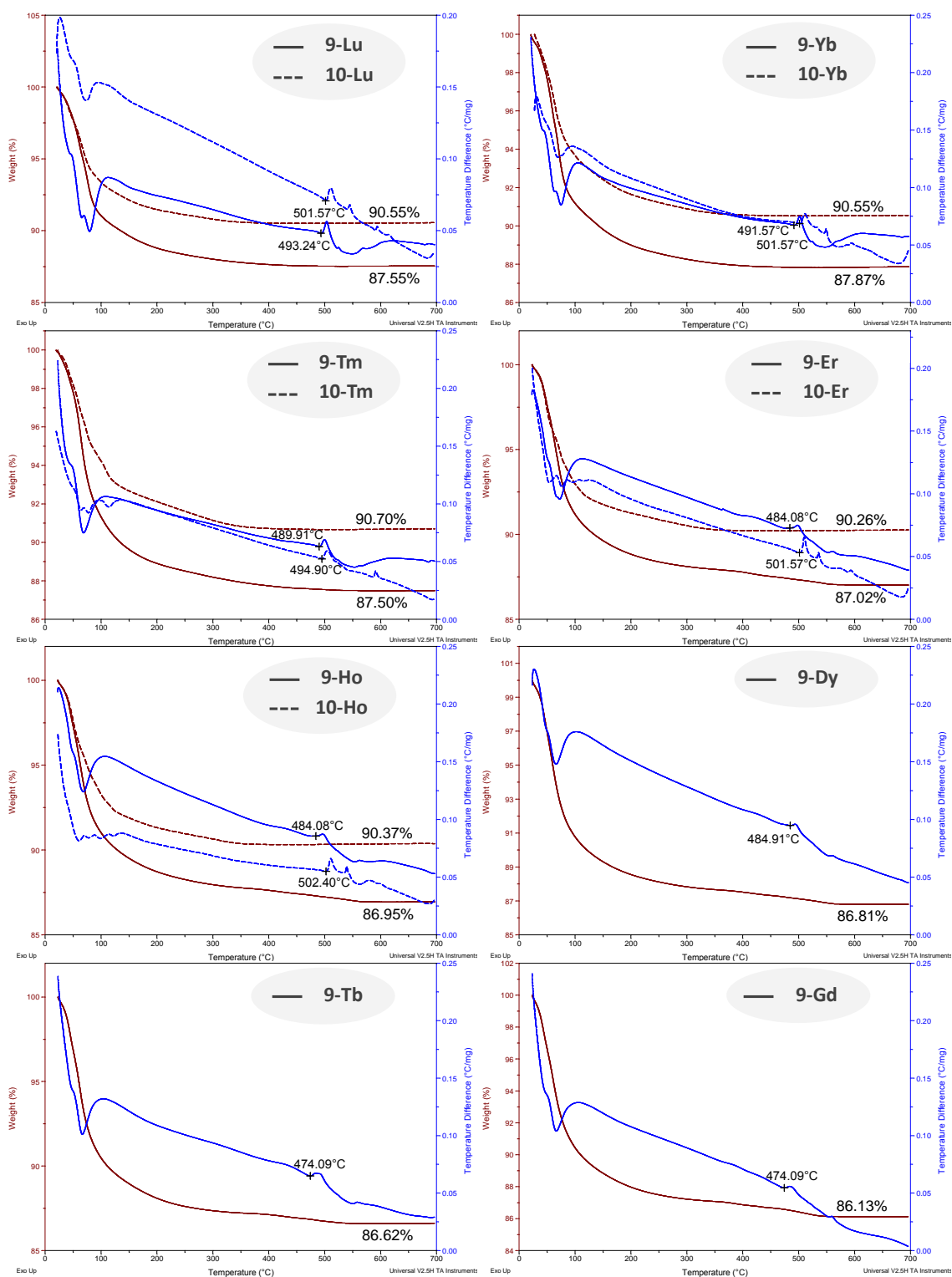


Figure A2.12. TGA/DTA curves for compounds 9-Ln and 10-Ln.

CHAPTER 4: Heterometallic 3d-4f POMs derived from the Krebs-type structure

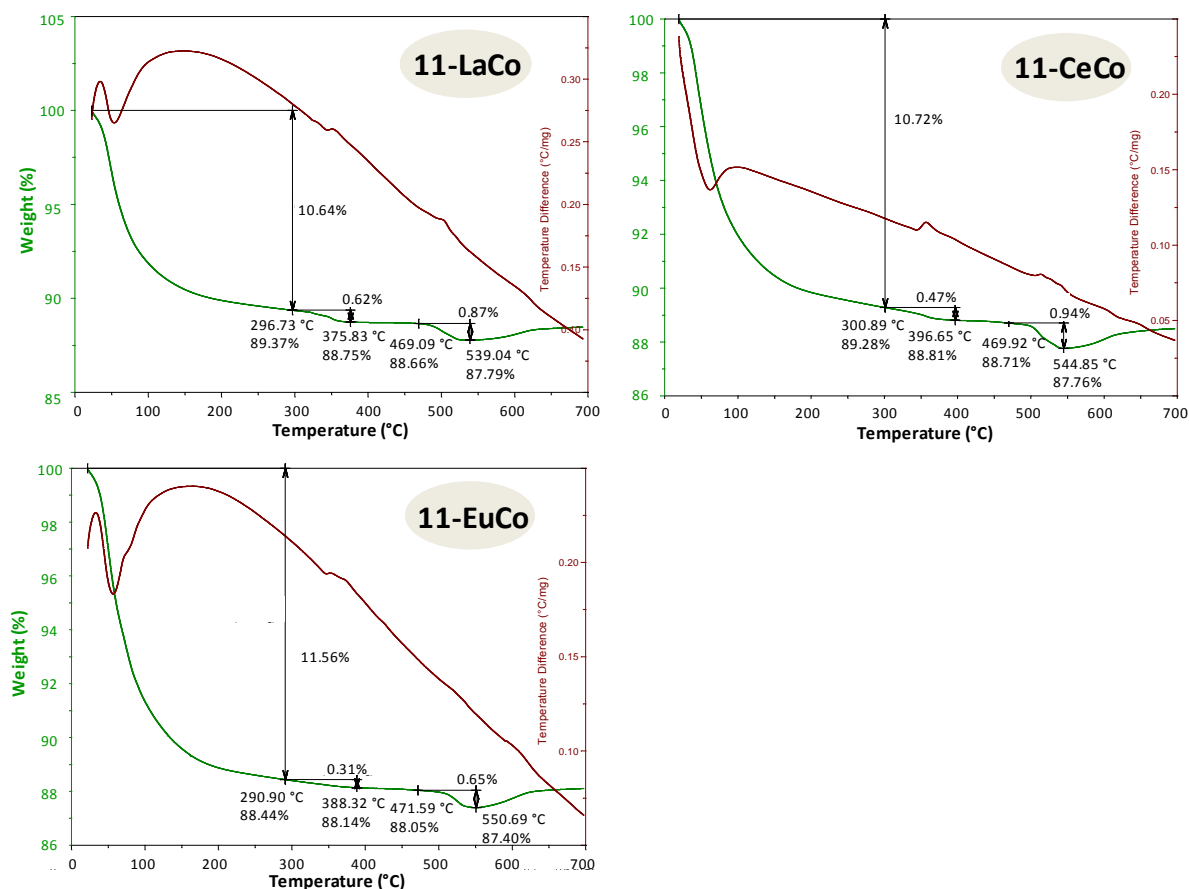


Figure A2.13. TGA/DTA curves for compounds 11-LnM.

A2.2.IV. Nuclear magnetic resonance spectroscopy

$^1\text{H-NMR}$: Solution ^1H -nuclear magnetic resonance ($^1\text{H-NMR}$) spectra were measured for **1-SbZn** and **3-Zn** on a Bruker AVANCE 500 spectrometer (D_2O , 500 MHz, one-bay). Two-dimensional spectra were recorded for the ligands to confirm the assignment of the signals.

$^{183}\text{W-NMR}$: ^{183}W -Nuclear magnetic resonance spectrum of **9-Lu** ($^{183}\text{W-NMR}$) was recorded at 16.688 MHz on a 400 MHz JEOL ECP400H instrument using solid samples dissolved in 0.5 M NaOAc buffer (pH = 4.8) and D_2O as solvent reference.

A2.2.V. Powder X-ray diffraction

Powder X-ray diffraction patterns for **9-Ln** were collected from $2\theta = 4$ to 60° (0.02606° step size, 30 s per step) using a Philips X'PERT PRO automatic diffractometer operating at 40 kV-40 mA in θ - θ configuration with monochromated Cu-K α radiation ($\lambda = 1.5418 \text{ \AA}$) and a PIXcel solid state detector (3.347° active length in 2θ). For the rest of compounds, Bruker D8 Advance Vario (CuK α_1) diffractometer (θ - 2θ geometry) equipped with a primary monochromator and a solid state SolX detector and a Philips X'Pert MPD diffractometer equipped with two independent θ - 2θ goniometers and a single X-ray source containing a secondary monochromator were used. Mercury¹ software was

employed to simulate the theoretical powder X-ray diffraction patterns from single-crystal X-ray diffraction data.

A2.2.VI. Photoluminescence measurements

Photoluminescence measurements were performed on crystalline samples at room temperature with a Edinburgh Instruments FLS920 spectrometer using a Kimmon IK3552R-G Helium Cadmium (HeCd, 325 nm) continuous laser as excitation source. Single-crystal emission spectra and photographs were taken in a micro-photoluminescence system included in an Olympus optical microscope illuminated with a HeCd laser or a Hg lamp.

A2.2.VII. Magnetic susceptibility measurements

Magnetic susceptibility measurements were performed for **4-Ni** and **9-Ln** in a Quantum Design MPMS-7 SQUID magnetometer using approximately 50 mg of crystalline powdered sample. Measurements were carried out in the 5-300 K temperature range under an applied direct current (dc) magnetic field of 0.1 T. Diamagnetic corrections were estimated from Pascal's constants.

The Van-Vleck's equation was employed to calculate the magnetic molar susceptibility (χ_m) for isolated 3d-metal centers:

$$\chi_m = \frac{N g^2 \beta^2 S(S+1)}{3 k T} \quad \text{Eq.1}$$

where N is the Avogadro's number, β is the Bohr magneton, k is the Boltzmann constant, g is the Landé factor and S is the spin quantum number.

The Curie-Weiss law was applied for paramagnetic regions:

$$\chi_m = \frac{C}{(T - \theta)} \quad \text{Eq.2}$$

where C is the Curie constant and θ is the Weiss temperature.

The magnetic molar susceptibility of isolated 4f-metals was estimated taking into account the spin-orbit coupling using Equations 3 and 4, as follows:

$$\chi_m = \frac{N g^2 \beta^2 J(J+1)}{3 k T} \quad \text{Eq.3}$$

where N , β and k have their usual meanings, J is the total angular momentum quantum number and g is the Landé factor defined as:

$$g = 1 + \frac{S(S+1) + J(J+1) + L(L+1)}{2J(J+1)} \quad \text{Eq.4}$$

where S and J have their usual meanings and L is the orbital quantum number.

A2.2.VIII. Electronic spin resonance spectroscopy

The ESR spectra for compounds **11-CeCo** and **11-GdCo** were recorded on powdered crystalline samples at X-band frequency, using a Bruker ELEXSYS 500 spectrometer (superhigh-Q resonator ER-4123-SHQ) equipped with a standard Oxford-low temperature device and calibrated by an NMR

probe for the magnetic field. The frequency was measured inside the cavity with a Hewlett-Packard 5352B microwave frequency counter. The spectra were fitted using WINEPR-Simfonia (Bruker Analytische Mes-technik, GmbH) software.

A2.2.IX. Electrospray ionization mass spectrometry

ESI-mass spectra were obtained on 10^{-5} M solutions of solid samples in the appropriate solvent. The spectra of **5-Ni**, **8-Ln** (Ln = Ce, Pr, Nd) and **11-CeCo** were carried out in pure water, whereas water-acetone mixtures were employed for **8-Nd**. In the case of **9-Ho** and **10-Ho** H₂O:CH₃CN mixtures were used in order to improve the resolution of the spectral peaks. The samples were introduced at a flow rate of 10 $\mu\text{L min}^{-1}$ in a Waters QTOF Premier instrument with orthogonal Z-spray electrospray interface operating with capillary voltage of 3.3 kV in the negative scan mode (V-mode) and N₂ as desolvation (300 L h⁻¹) and cone gas (30 L h⁻¹); typical desolvation (200 °C) and source block (120 °C) temperatures were used and the cone voltage (U_c) was set to 15 V to control the extent of fragmentation of the gas-phase detected species.

The ESI-spectra of those samples not included in the main text are depicted in Figures A2.14, A2.15 and A2.16.

8-Ce (water)

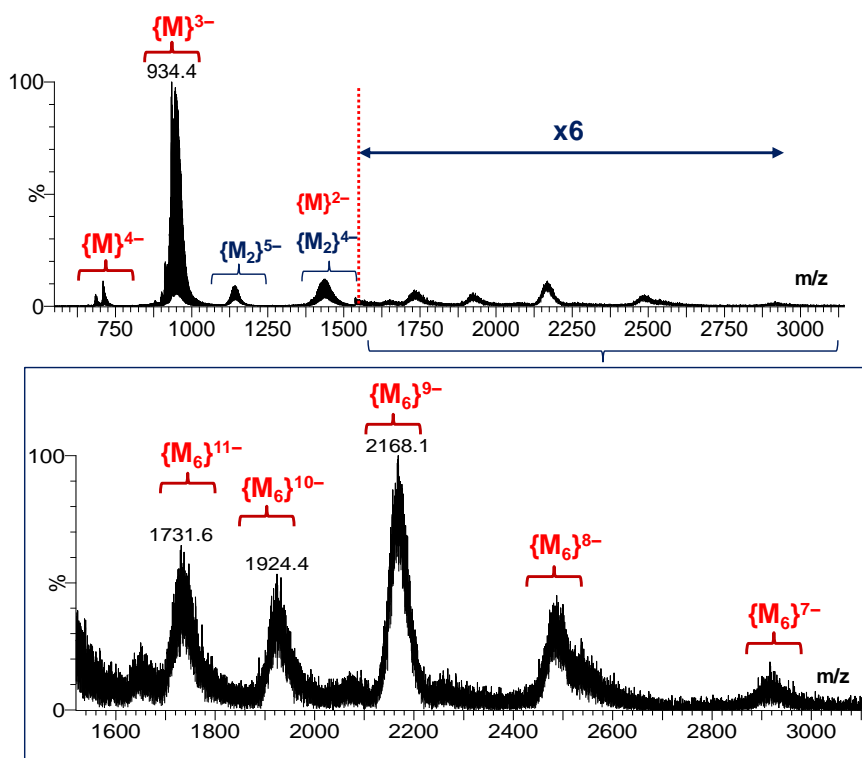


Figure A2.14. Top: Negative ESI mass spectrum of an aqueous solution of **8-Ce** ($U_c = 15$ V). The intensity of the m/z 1550-3100 range is increased (x6) for a better visualization. Bottom: Expanded m/z 1520-3100 region (note that dimeric and monomeric species are overlapped in the m/z 1400-1500 range). $\{M\}^{(6-n)-} = [\text{Ce}_2\text{GeW}_{10}\text{O}_{38} + x\text{H}_2\text{O} + m\text{K}^+ + (n-m)\text{Na}^+]^{(6-n)-}$; $\{M_2\}^{(12-n)-} = [(\text{Ce}_2\text{GeW}_{10}\text{O}_{38})_2 + x\text{H}_2\text{O} + m\text{K}^+ + (n-m)\text{Na}^+]^{(12-n)-}$; $\{M_6\}^{(36-n)-} = [(\text{Ce}_2\text{GeW}_{10}\text{O}_{38})_6 + x\text{H}_2\text{O} + m\text{K}^+ + (n-m)\text{Na}^+]^{(36-n)-}$.

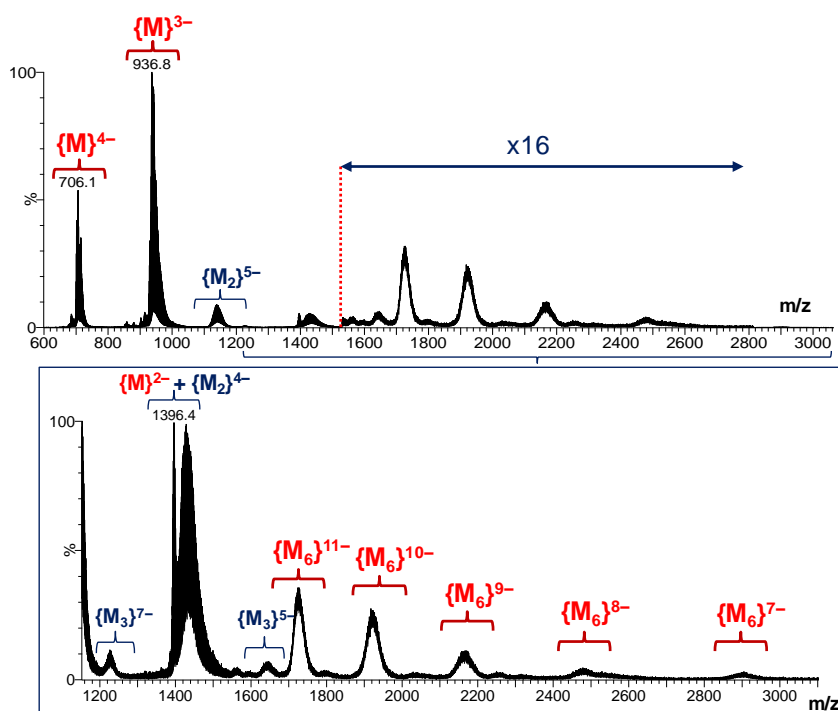
8-Nd (water)

Figure A2.15. Top: Negative ESI mass spectrum of an aqueous solution of **8-Nd** ($U_c = 15$ V). The intensity of the m/z 1520-2800 range is increased (x6) for a better visualization. Bottom: Expanded m/z 1150-3100 region (note that dimeric and monomeric species are overlapped in the m/z 1400-1500 range). $\{M\}^{(6-n)-} = [\text{Nd}_2\text{GeW}_{10}\text{O}_{38} + x\text{H}_2\text{O} + m\text{K}^+ + (n-m)\text{Na}^+]^{(6-n)-}$; $\{M_2\}^{(12-n)-} = [(\text{Nd}_2\text{GeW}_{10}\text{O}_{38})_2 + x\text{H}_2\text{O} + m\text{K}^+ + (n-m)\text{Na}^+]^{(12-n)-}$; $\{M_3\}^{(18-n)-} = [(\text{Nd}_2\text{GeW}_{10}\text{O}_{38})_3 + x\text{H}_2\text{O} + m\text{K}^+ + (n-m)\text{Na}^+]^{(18-n)-}$; $\{M_6\}^{(36-n)-} = [(\text{Nd}_2\text{GeW}_{10}\text{O}_{38})_6 + x\text{H}_2\text{O} + m\text{K}^+ + (n-m)\text{Na}^+]^{(36-n)-}$

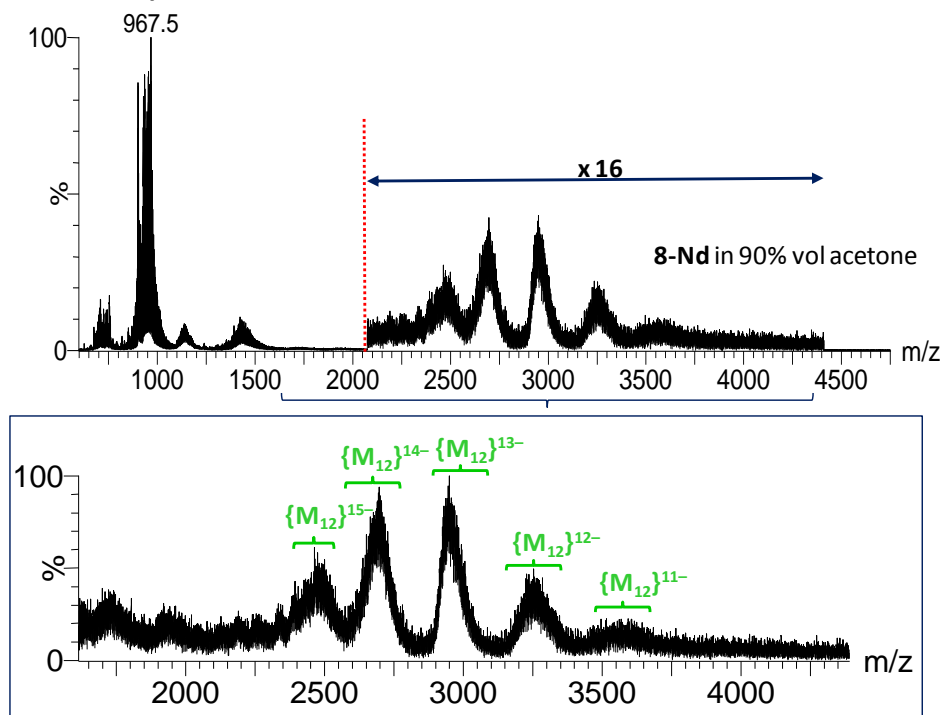
8-Nd (water/acetone)

Figure A2.16. Top: Negative ESI-mass spectrum of **8-Nd** dissolved in 90% vol. acetone solution. Note that the intensity of the m/z 2100-4400 range is increased (x16) for a better visualization. Bottom: Expanded m/z 1600-4400 region. $\{M_{12}\}^{(72-n)-} = [(\text{Nd}_2\text{GeW}_{10}\text{O}_{38})_{12} + x\text{H}_2\text{O} + m\text{K}^+ + (n-m)\text{Na}^+]^{(72-n)-}$

A2.2.VIII. Transmission electron microscopy

The TEM images were taken on a PHILIPS EM208S transmission electron microscope operated at 200 kV. Samples for the TEM analysis were prepared by dropping a small volume of the 0.1 mg ml⁻¹ aqueous solution of **8-Nd** and **11-CeCo** onto a holey carbon film on copper grid.

A2.3. X-RAY CRYSTALLOGRAPHY

Experimental conditions of the single-crystal X-ray diffraction studies, data acquisition and reduction details, methods for solution and refinement of the crystal structures and software and crystallographic databases employed are summarized in this section.

A2.3.I. Data acquisition and reduction

Intensity data for **1-SbMn**, **1-SbNi**, **1-SbZn**, **1-TeM**, **2-Ni**, **3-M**, **4-Ni**, **5-Mn**, **8-Pr**, **9-Ln**, **10-Ln** and **11-LnM** were collected at 100(2) K on a Agilent Technologies SuperNova diffractometer (mirror-monochromated Mo-K α radiation, $\lambda = 0.71073$ Å) equipped with Eos CCD surface detector. In the case of **1Sb-Co**, **6-Ln**, **7-Sm** and **8-Nd** the data collection was also carried out at 100(2) K, but the Supernova diffractometer was equipped with Cu-K α radiation ($\lambda = 1.54184$ Å) and Atlas CCD detector. Both diffractometers equipped with Oxford Cryosystems Cryostream 700 Plus (80–500K) devices. Pre-experiments were carried out (15 frames, ω scan, step 1°, exposition 5 s) in order to confirm the quality of the crystals, to determine the cell parameters and to optimize the experiment. Data collections, unit cell determinations, intensity data integrations, routine corrections for Lorentz and polarization effects and analytical absorption corrections with face indexing were performed using the CrysAlis Pro software package.²

A.2.3.II. Solution and refinement of crystal structures

The structures were solved by charge flipping methods using OLEX2³ and refined by full-matrix least-squares (F^2) with SHELXL-97⁴ as included in OLEX2 or the WinGX⁵ software package. Direct method solutions located the heaviest atoms and remaining atoms were found in subsequent Fourier difference maps. In all least-squares refinements, R and wR have been calculated using Equations 5 and 6.

$$R(F) = \frac{\sum ||F_o - F_c||}{\sum |F_o|} \quad (\text{Eq. 5})$$

$$wR(F^2) = \left\{ \frac{\sum [w(F_o^2 - F_c^2)^2]}{\sum [w(F_o^2)^2]} \right\}^{1/2} \quad (\text{Eq. 6})$$

A.2.3.III. Calculations

Final geometrical calculations were carried out with PLATON⁶ as integrated in WinGX. Bond Valence Sum (BVS) and Continuous Shape Measures (CShM) calculations were performed using BVSuCalc⁷ and SHAPE⁸ programs, respectively.

CShM calculations indicate the grade of distortion of a polyhedron with respect to an ideal shape. The 3d- or 4f-metal centers of the compounds included in this work exhibit coordination numbers ranging from 6 to 9. Ideal polyhedral geometries for such coordination numbers employed for the CShM calculations are detailed in Figure A2.17.

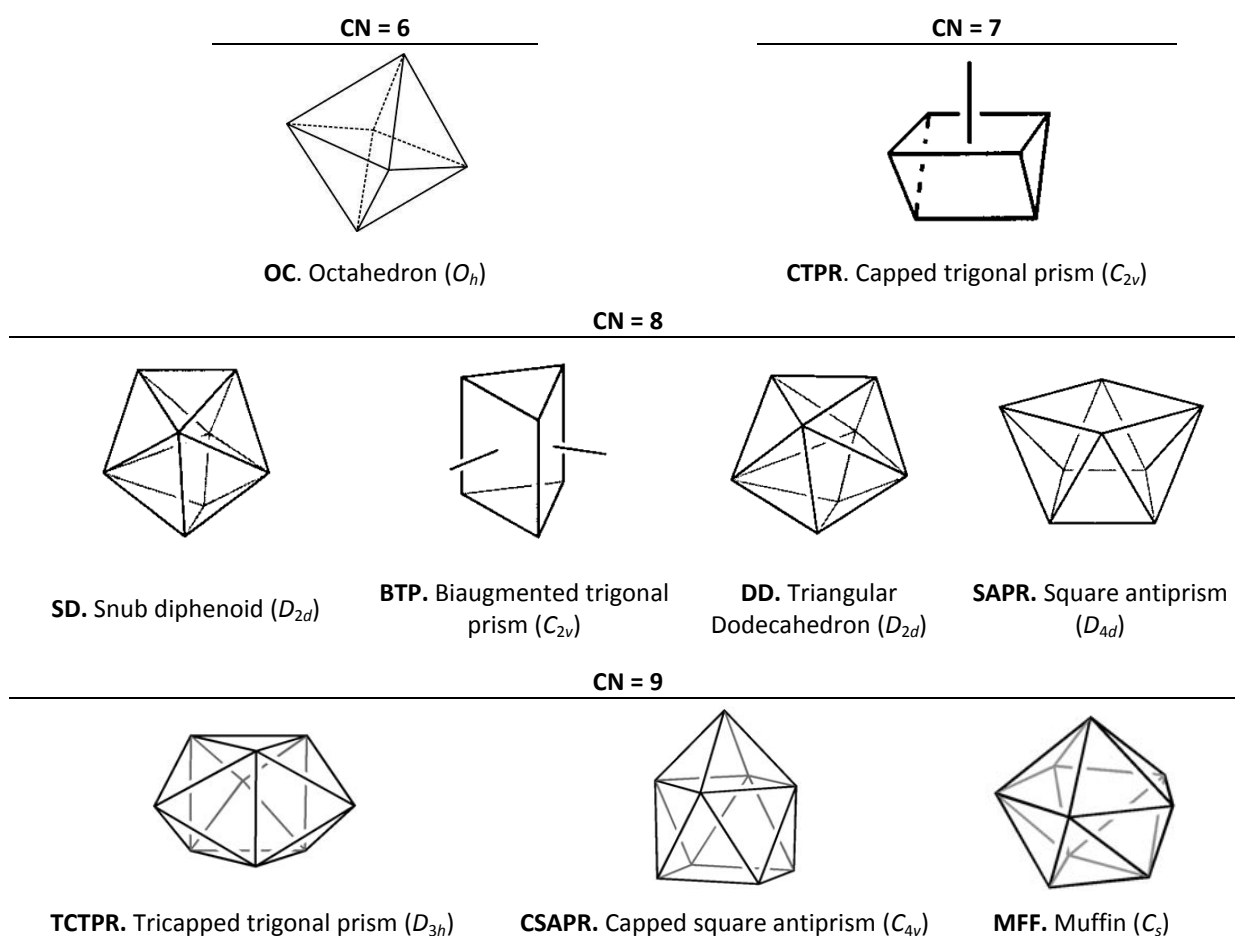


Figure A2.17. Ideal SHAPE geometries employed in CShM calculations.

A.2.3.III. Crystallographic software and databases

Ortep-3⁹, Crystal Maker¹⁰ and Diamond-3¹¹ were used as the graphic representation software. Moreover, the following structural (CSD, ICSD) and scientific (SciFinder) databases were employed in this work:

Cambridge Structural Database (CSD):¹² X-ray and neutron diffraction structures of organic, organometallic and coordination complexes are included in this database of the Cambridge Crystallographic Data Center (CCDC).

Inorganic Crystal Structure Database (ICSD):¹³ X-ray and neutron diffraction structures of completely inorganic compounds (including pure elements, minerals, metals, inorganic salts...) are included in this database of the Fachinformationszentrum (FIZ) Karlsruhe.

SciFinder:¹⁴ Multifunctional scientific database developed by the Chemical Abstract Service (CAS) for substances, reactions, and patent and journal references of chemistry and related fields.

A2.4. LASER LIGHT SCATTERING

Polyelectrolytic solutions are complicated systems. Despite the fact that the most popular method to describe a simple diluted ionic solution is the Debye-Hückel theory, it is only valid for very dilute solutions in which ions can be treated as point-like charges. In the case of POM type macroions, they cannot be considered point-charges due to their big size. Analogously, the behavior of charged colloids with sizes over 100 nm is usually described by the Derjaguin-Landau-Verwey-

APPENDIX 2

Overbeek (DLVO) theory. The DLVO theory is based on the competition between attractive van der Waals and repulsive Coulombian interactions. Nevertheless, size disparity between macroions and counterions (10 to 1) is much smaller compared to that of colloidal particles and their counterions (10^3 to 1), and therefore, POM solutions are not colloidal suspensions but real solutions. Thus, DLVO theory is not suitable for describing POM solutions.

It is known that POM type macroanions with sizes between ca. 2 to 6 nm show unique solution behaviors. Instead of distributing in the media to form stable and homogeneous solutions, they slowly self-assemble into spherical, hollow, single-layered and stable vesicles, named as “blackberry”-type structures. It seems to be unexpected that macroions with negative charge can self-assemble placing close to each other and overcoming coulombian repulsions. Therefore, it is interesting to study the solution behavior of macroions within the cited size range. Polyoxoanions usually have well-defined molecular structures, high negative charges (sometimes tunable charge), big size, high solubility and stability in polar solvents and no intramolecular-charge interactions. These features make POMs ideal models for understanding the broadly defined macroionic solutions, including not only polyelectrolites, but also biomolecular systems like the interaction between DNA and proteins and the formation of viral capsids.

Light scattering is based on the deflection of the straight ray by irregularities, particles or different refractive indexes in the media. Therefore, laser light scattering (LLS, traditionally used for polymers, biomolecules or colloidal suspensions) is the ideal technique to monitor diluted POM solutions. Static light scattering (SLS) can be used to determine the average molecular weight (M_w) and radius of gyration (R_g , defined as the root mean square distance of the particle's parts from its gravity center) of the aggregates by measuring the scattering intensity at different angles. Data is analyzed using different methods (Zimm, Berry, Guinier...). Performing a Zimm analysis on a single concentration (known as partial Zimm analysis) is a direct technique to calculate R_g in dilute solutions of strong point scatters. Inter-particle interactions given by the second virial coefficient (A_2) can also be calculated by SLS monitoring samples of different concentration. Dynamic Light Scattering (DLS) measures the intensity-intensity time correlation function from the scattered light, which is analyzed by the CONTIN method to calculate the average hydrodynamic radius (R_h) of the particles in solution as well as their size distribution. The ratio between R_h and R_g is widely used for predicting the shape of the aggregates, i.e. $R_h/R_g \approx 1$, for hollow spherical structures; 0.77, rigid spheres; 0.6-0.7, rod-like structures; 0.3-0.5, random polymer coils.

A2.4.1. Experimental details

Both Dynamic Light Scattering (DLS) and Static Light Scattering (SLS) were used to characterize aqueous solutions of **8-Ln** and **11-CeCo** and water-acetone samples of **8-Nd**. A commercial Brookhaven Instruments Inc. LLS spectrometer, equipped with a diode-pumped solid-state (DPSS) green laser operating at 532 nm was used.

DLS: A BI-9000AT multi-channel digital correlator was used for measuring the intensity-intensity time correlation function. The field correlation function $|g^{(1)}(\tau)|$ was analyzed by the constrained regularized CONTIN method to yield information on the distribution of the characteristic line width Γ from $|g^{(1)}(\tau)| = \int G(\Gamma) e^{-\Gamma\tau} d(\Gamma)$. The normalized distribution function of the characteristic line width, $G(\Gamma)$, so obtained, can be used to determine an average apparent translational diffusion coefficient, $D_{app} = \Gamma/q^2$. The hydrodynamic radius R_h is related to D via the Stokes–Einstein equation: $R_h = kT/(6\pi\eta D)$, where k is the Boltzmann constant and η the viscosity of the solvent at given

temperature. Using DLS measurements, we can obtain the particle-size distribution in solution from a plot of $\Gamma G(\Gamma)$ vs R_h . The R_h of the particles is obtained by extrapolating to the zero scattering angle.

SLS: The SLS was performed over a broad range of scattering angles from 20° to 120° , with a 2° interval. The raw data was analyzed with a partial Zimm plot derived from the Rayleigh–Gans–Debye equation to obtain the radius of gyration (R_g) of the large assemblies. The partial Zimm plot stems from the following approximate formula: $1/I = C(1 + R_g^2 q^2/3)$. Here R_g is determined from the slope and the intercept of a plot of $1/I$ vs q^2 . Similarly, the Berry plot was employed for larger assemblies of **8-Ce** in water. In this case, data from 20 to 30° scattering angles was removed in the final analysis due to the large fluctuations in the scattered intensities.

Sample preparation: solid samples were dissolved in 10 mL of the corresponding solvent and sonicated for 10 min. The solutions obtained were filtered using syringes capped with 100 nm pore size Millipore membrane filters and placed in a 20 mL dust-free clean vials for LLS analysis.

A2.4.II.Results

All the time resolved scattering intensity plots (at 90°) and partial Zimm plots resulting from SLS studies on water/acetone sample solutions of **8-Nd** (0.1 mg/mL) not included in the main text are displayed in Figures A2.18 to A2.22. Only high scattering angles were taken into account in the final analysis for the 10, 30 and 50% vol. acetone samples due to their best fit for such a small assemblies:

Time-resolved scattering intensity plots recorded at 90°

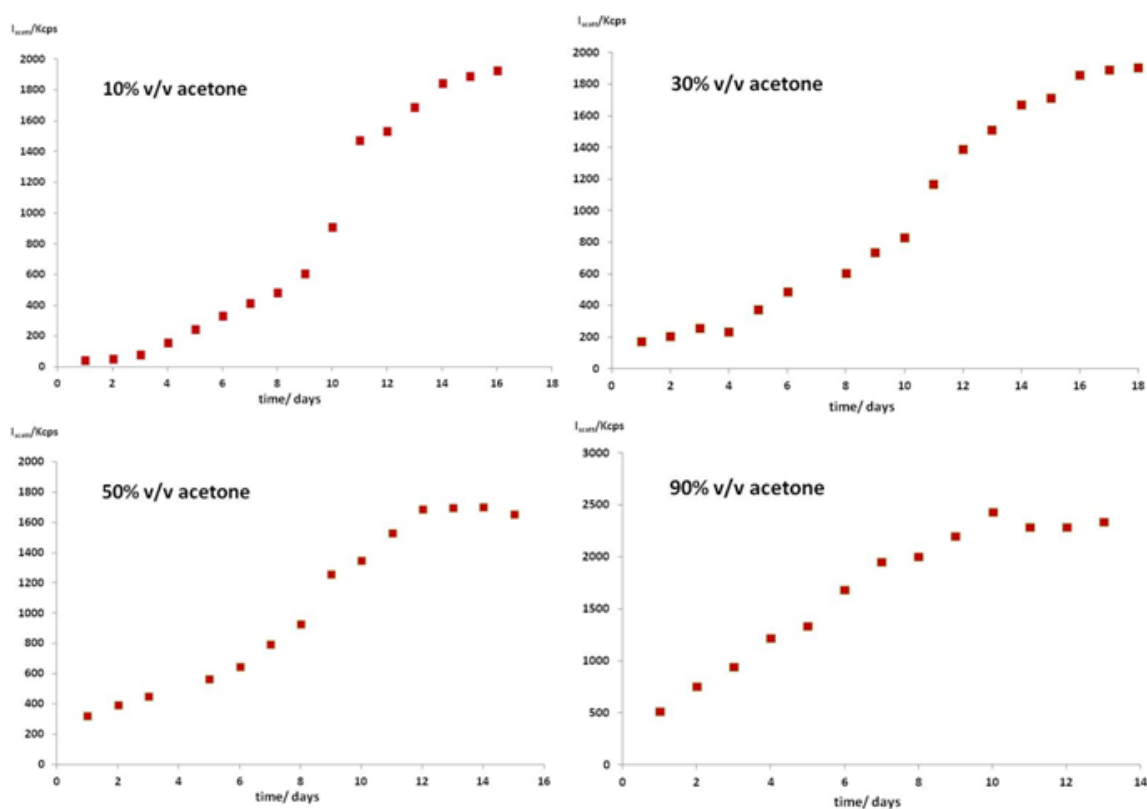
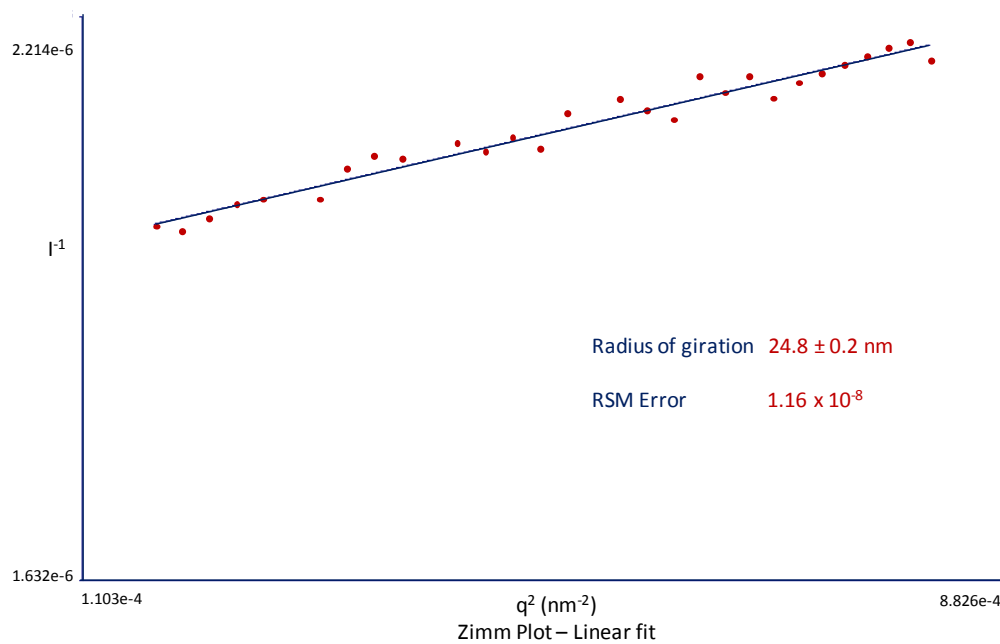


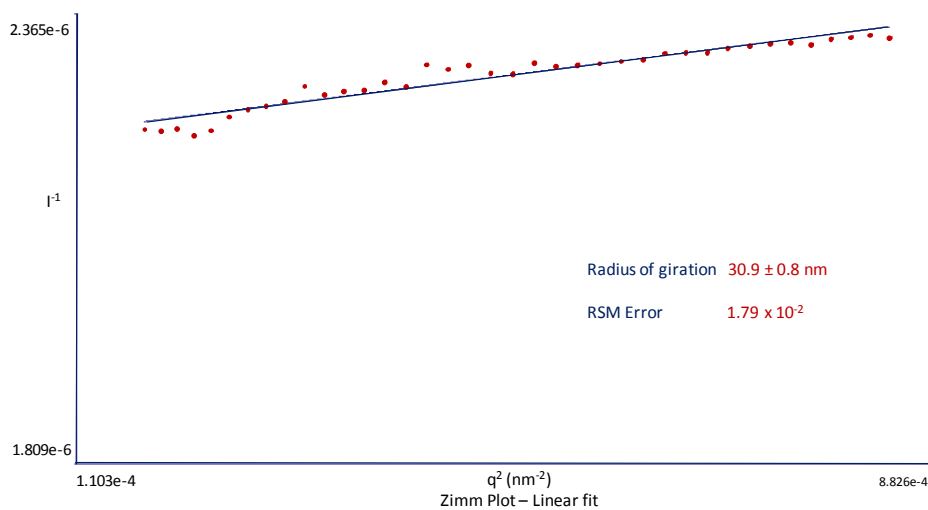
Figure A2.18. Time-resolved scattering intensity plots of water/acetone sample solutions of **8-Nd** (0.1 mg/mL).

Partial Zimm plots from SLS studies

1) 10% v/v acetone:

Figure A2.19. Partial Zimm plot from SLS studies of the 10% vol. acetone sample solutions of **8-Nd**.

2) 30% v/v acetone:

Figure A2.20. Partial Zimm plot from SLS studies of the 30% vol. acetone sample solution of **8-Nd**.

3) 50% v/v acetone:

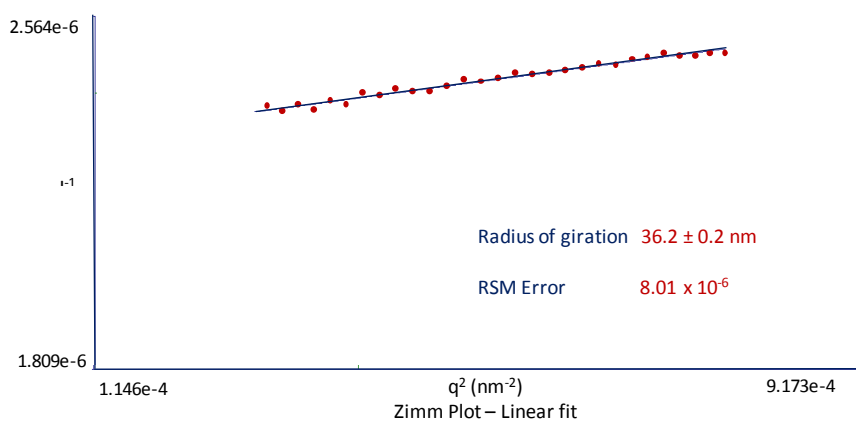


Figure A2.21. Partial Zimm plot from SLS studies of the 50% vol. acetone sample solution of **8-Nd**.

4) 90% v/v acetone:

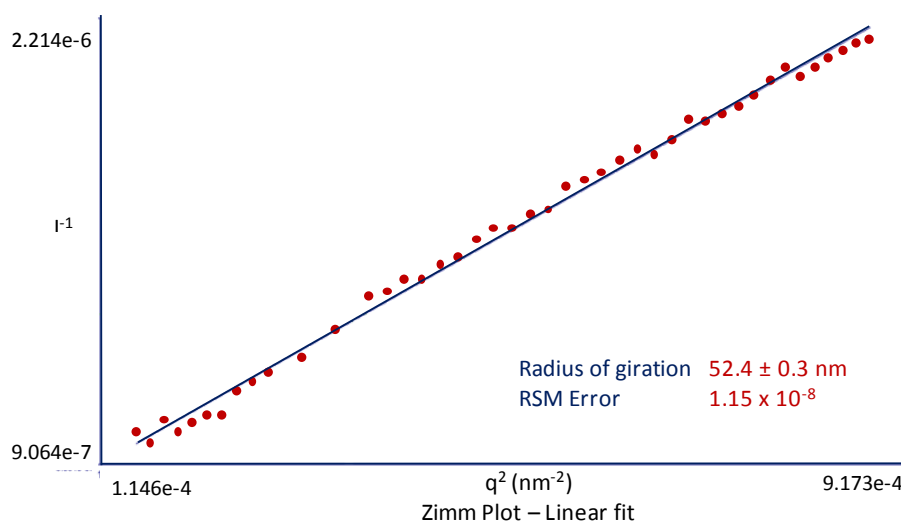


Figure A2.22. Partial Zimm plot from SLS studies of the 90% vol. acetone sample solution of **8-Nd**.

A2.5. REFERENCES

- [1] Macrae, C. F.; Bruno, I. J.; Chisholm, J. A.; Edgington, P. R.; McCabe, P.; Pidcock, E.; Rodriguez-Monge, L.; Taylor, R.; van de Streek, J.; Wood, P. A. *J. Appl. Crystallogr.* **2008**, *41*, 466.
- [2] *CrysAlisPro Software System*; Agilent Technologies UK Ltd.: Oxford, UK, 2012.
- [3] Dolomanov, O. V.; Bourhis, L. J.; Gildea, R. J.; Howard, J. A. K.; Puschmann, H. *J. Appl. Crystallogr.* **2009**, *42*, 339.
- [4] Sheldrick, G. M. *Acta Crystallogr.* **2008**, *A64*, 112.
- [5] Farrugia, L. J. *J. Appl. Crystallogr.* **1999**, *32*, 837.
- [6] Spek, A. L. *Acta Crystallogr.* **2009**, *D65*, 148.
- [7] *BVSumCalc program* is a courtesy of Dr. M. H. Dickman.

[8] Llunell, M.; Casanova, D.; Cirera, J.; Bofill, J. M.; Alemany, P.; Alvarez, S.; Pinsky, M.; Avnir, D. *SHAPE*, v2.1; Universitat de Barcelona: Barcelona, Spain and The Hebrew University of Jerusalem: Jerusalem, Israel, 2005.

[9] Farrugia, L. J. *J. Appl. Crystallogr.* **1997**, *30*, 565.

[10] *CrystalMaker*; CrystalMaker Software Ltd.: Yarnton, UK, 2010.

[11] Branderburg, K. *Diamond*; Crystal Impact GbR: Bonn, Germany, 2010.

[12] Allen, F. H. *Acta Crystallogr.* **2002**, *B58*, 380.

[13] <http://www.fiz-karlsruhe.de/icsd>

[14] <https://scifinder.cas.org>

Nomenclature of dilacunary units

A3.1. NOMENCLATURE OF DILACUNARY UNITS

This section explains the nomenclature used in numbering the addenda metal positions in dilacunary Keggin-type polyoxotungstate units included in Chapter 3. In 1998, Jeannin reported a review paper describing a general method to number the addenda metal positions following IUPAC recommendations, and consequently, also the vacancies of in a Keggin cluster. This method is as follows:¹

1- The reference axis is the highest order rotational axis of the idealized polyanion structure, which is oriented vertically. Therefore, the units are viewed from

- the top of the rotated trimer following the C_3 axis (β subunit).
- the top of the edge-sharing dimer following the C_2 axis (γ subunit).

2- Perpendicular to the reference axis, several skeletal planes are located. For β isomers, the numbering starts from the “bottom” corner-sharing tungsten triad, followed by the six central belt tungstens and ending with the three edge-sharing tungstens of the rotated trimer. For the γ isomer, it starts from the “top” edge-sharing dimer, followed by two edge-sharing tungsten pairs completing the rotated trimers, two octahedra of the two non-rotated trimers, and ending with the two edge-sharing tungsten pairs completing the non-rotated trimers.

3- Skeletal planes are numbered in the clockwise direction. After numbering one skeletal plane, the following tungsten atom is the one located closest to that with the lowest number in the clockwise direction.

4- The tungsten position number 1 is assigned in such a way that both vacancies have the lowest numbering possible.

Following these recommendations, each tungsten atom has been labeled indicating the number of the subunit to which they belong (i.e. subunit 1: from W1 to W12; subunit 2: from W21 to W32). Lanthanide atoms acquire the number of the vacant sites they occupy. Unfortunately, this method could only be applied for asymmetric units containing a maximum of five Keggin subunits, because the SHELX interface only allows the use of four characters for labeling each atom, and this made not possible to name the O atoms adequately. Therefore, compounds **9-Ln** and **10-Ln** were labeled following IUPAC rules, whereas **6-Ln**, **7-Sm** and **8-Ln** were named in a closely related way that is illustrated in Figure A3 as non-IUPAC.

¹ Jeannin, Y. P. *Chem. Rev.* **1998**, *98*, 51.

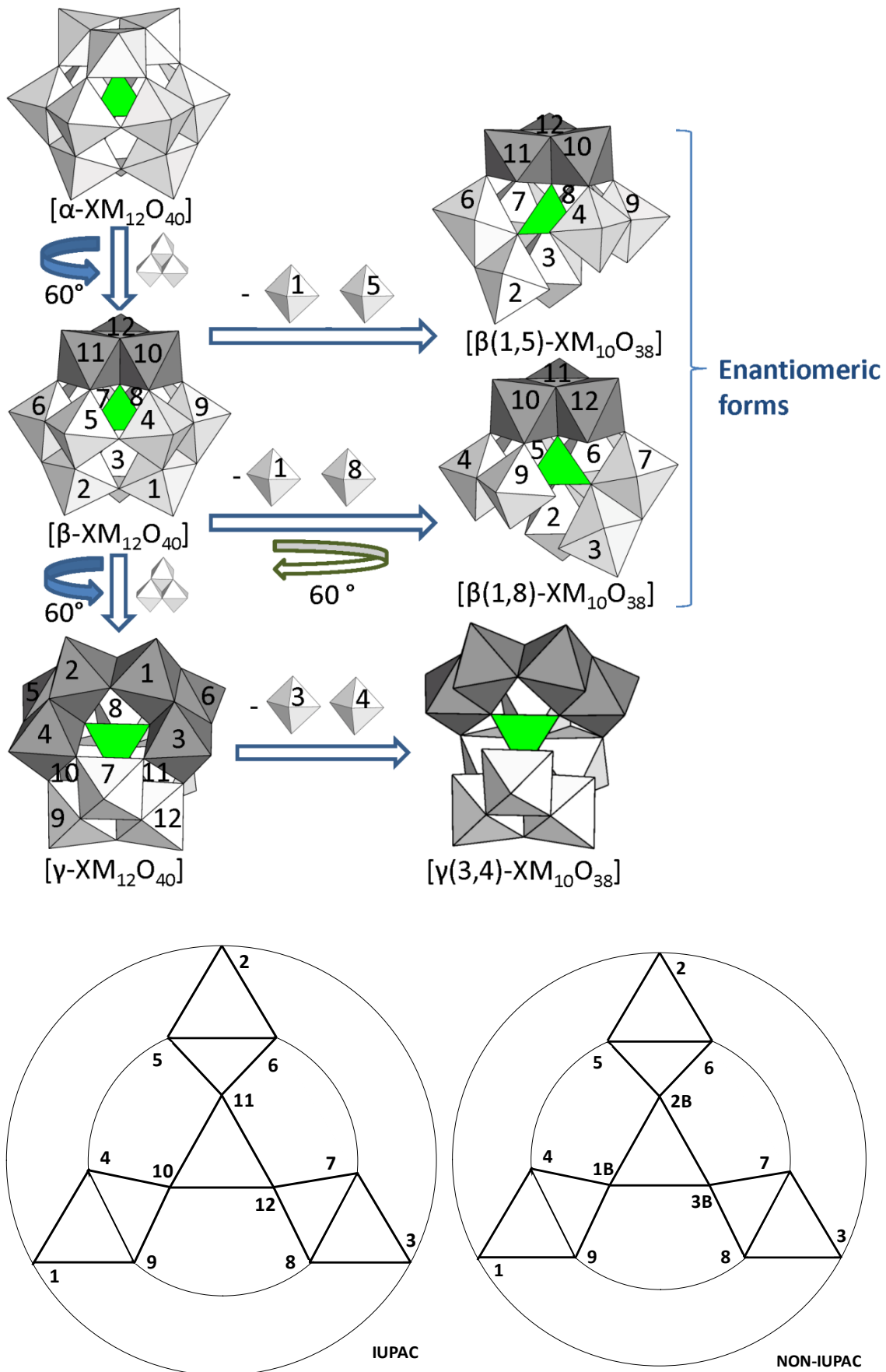


Figure A3. Notation and relationship between labeling schemes followed for Keggin type dilacunary subunits included in this work.

**Lanthanide-Oxygen bond lengths of
compounds included in Chapter 3**

A4. Selected bond lengths

Assemblies with early lanthanides

Table A4.1. Ln—O bond lengths and Ln···Ln distances in **6-Ln** (Ln = Pr, Nd) and **7-Sm**.

	6-Pr	6-Nd	7-Sm		6-Pr	6-Nd	7-Sm	
$\beta(1,8)$ subunit	Ln1—O12	2.464(12)	2.435(10)	2.376(11)	Ln8—O38	2.419(12)	2.392(10)	2.369(13)
	Ln1—O13	2.369(11)	2.346(10)	2.314(12)	Ln8—O78	2.447(12)	2.423(11)	2.412(13)
	Ln1—O14	2.414(11)	2.392(9)	2.358(12)	Ln8—O82	2.434(13)	2.412(11)	2.356(15)
	Ln1—O19	2.406(10)	2.384(9)	2.377(12)	Ln8—O89	2.356(12)	2.342(10)	2.295(12)
	Ln1—O119 ⁱ	2.547(11)	2.541(10)	2.572(11)	Ln8—O23T	2.526(12)	2.535(11)	2.476(14)
	Ln1—O19T ⁱ	2.510(11)	2.479(10)	2.425(11)	Ln8—O2F	2.528(12)	2.517(11)	2.469(14)
	Ln1—O1C	2.647(11)	2.615(11)	2.517(12)	Ln8—O3F	2.525(16)	2.492(13)	2.59(2)
	Ln1—O1F	2.596(12)	2.570(10)	2.590(12)	Ln8—O4F	2.59(2)	2.572(17)	2.515(19)
$\beta(1,8)$ subunit	Ln11—O112	2.412(12)	2.398(10)	2.394(11)	Ln18—O138	2.352(12)	2.336(11)	2.319(13)
	Ln11—O113	2.387(12)	2.345(10)	2.335(13)	Ln18—O178	2.415(12)	2.391(10)	2.391(12)
	Ln11—O114	2.428(10)	2.424(10)	2.368(11)	Ln18—O182	2.447(12)	2.412(11)	2.354(13)
	Ln11—O119	2.418(11)	2.407(10)	2.394(11)	Ln18—O189	2.287(12)	2.285(11)	2.233(13)
	Ln11—O214	2.540(11)	2.576(10)	2.614(12)	Ln18—O2T ⁱ	2.499(14)	2.465(11)	2.442(14)
	Ln11—O24T	2.513(11)	2.489(10)	2.445(12)	Ln18—O13B ⁱⁱ	2.455(13)	2.412(11)	2.375(13)
	Ln11—O2C	2.663(11)	2.628(10)	2.538(12)	Ln18—O6F	2.561(14)	2.542(12)	2.555(15)
	Ln11—O5F	2.563(13)	2.546(11)	2.504(13)				
$\beta(1,5)$ subunit	Ln21—O212	2.402(12)	2.364(10)	2.350(13)	Ln25—O225	2.414(13)	2.402(11)	2.319(13)
	Ln21—O213	2.422(11)	2.423(10)	2.386(12)	Ln25—O245	2.364(12)	2.352(10)	2.243(12)
	Ln21—O214	2.427(11)	2.396(10)	2.366(12)	Ln25—O251	2.441(13)	2.404(11)	2.358(13)
	Ln21—O219	2.428(11)	2.396(9)	2.388(13)	Ln25—O256	2.438(13)	2.420(11)	2.385(12)
	Ln21—O9T	2.477(12)	2.466(10)	2.401(12)	Ln25—O12T	2.537(12)	2.506(11)	2.482(12)
	Ln21—O19	2.574(10)	2.574(10)	2.654(12)	Ln25—O22B ⁱⁱⁱ	2.449(14)	2.460(12)	2.373(13)
	Ln21—O3C	2.689(11)	2.646(9)	2.525(11)	Ln25—O8F	2.598(15)	2.573(13)	2.554(14)
	Ln21—O7F	2.546(11)	2.536(10)	2.521(12)	Ln25—O9F	2.560(16)	2.522(14)	
Ln1···Ln11 ⁱⁱⁱ	4.699(7)	4.703(6)	4.743(6)	Ln1···Ln1 ⁱⁱⁱ	9.372(13)	9.369(10)	9.478(14)	
Ln11···Ln21	4.720(4)	4.722(5)	4.773(7)	Ln11···Ln11 ⁱⁱⁱ	9.444(6)	9.439(4)	9.603(6)	
Ln21···Ln1	4.577(3)	4.741(2)	4.839(3)	Ln21···Ln21 ⁱⁱⁱ	9.522(13)	9.515(12)	9.623(13)	
Ln···Ln mean	4.665	4.722	4.785	Ln···Ln mean	9.446	9.441	9.568	
O7T···O7T ⁱⁱⁱ	25.428(47)	25.406(38)	25.395(48)					
O17T···O17T ⁱⁱⁱ	25.456(26)	25.474(23)	25.544(29)					
O26T···O26T ⁱⁱⁱ	25.618(31)	25.626(26)	25.660(32)					
<O···O _{trans} >	25.500	25.502	25.533					

[a] Symmetry Code. i: -x, -y, 1-z; ii: -x, 1-y, 1-z; iii: -x, -y, -z

APPENDIX 4

Table A4.2. Ln—O bond lengths and Ln⋯Ln distances in the β -subunits of **8-Ln** (Ln = Pr, Nd). Note that the different asymmetric units for the two isostructural compounds are centrosymmetrically related.

8-Pr				8-Nd			
$\beta(1,8)$ subunits		$\beta(1,5)$ subunits		$\beta(1,5)$ subunits		$\beta(1,8)$ subunits	
Pr1—O12	2.409(14)	Pr11—O112	2.435(19)	Nd1—O12	2.381(13)	Nd11—O112	2.380(14)
Pr1—O13	2.394(17)	Pr11—O113	2.404(17)	Nd1—O13	2.381(14)	Nd11—O113	2.374(12)
Pr1—O14	2.400(16)	Pr11—O114	2.415(15)	Nd1—O14	2.405(13)	Nd11—O114	2.433(13)
Pr1—O19	2.438(14)	Pr11—O119	2.429(15)	Nd1—O19	2.414(13)	Nd11—O119	2.418(12)
Pr1—O14T	2.462(16)	Pr11—O24T ⁱ	2.460(17)	Nd1—O19T	2.450(12)	Nd11—O29T ^v	2.455(13)
Pr1—O114	2.597(15)	Pr11—O214 ⁱ	2.632(15)	Nd1—O119	2.592(12)	Nd11—O219 ^v	2.597(12)
Pr1—O1C	2.599(15)	Pr11—O2C	2.628(17)	Nd1—O1C	2.553(14)	Nd11—O2C	2.568(12)
Pr1—O1F	2.631(16)	Pr11—O4F	2.602(16)	Nd1—O1F	2.586(14)	Nd11—O4F	2.595(14)
Pr8—O38	2.415(17)	Pr15—O125	2.430(17)	Nd5—O25	2.402(13)	Nd18—O138	2.439(15)
Pr8—O78	2.452(16)	Pr15—O145	2.356(16)	Nd5—O45	2.362(13)	Nd18—O178	2.394(15)
Pr8—O82	2.514(16)	Pr15—O151	2.517(18)	Nd5—O52	2.433(15)	Nd18—O183	2.419(15)
Pr8—O89	2.365(15)	Pr15—O156	2.426(18)	Nd5—O56	2.425(15)	Nd18—O189	2.362(14)
Pr8—O23T	2.516(18)	Pr15—O2T	2.499(17)	Nd5—O22T	2.533(16)	Nd18—O3T	2.491(15)
Pr8—O37N	2.436(17)	Pr15—O47N	2.45(2)	Nd5—O37N	2.389(15)	Nd18—O47N	2.421(15)
Pr8—O2F	2.56(2)	Pr15—O5F	2.616(18)	Nd5—O2F	2.536(16)	Nd18—O5F	2.599(16)
Pr8—O3F	2.646(18)	Pr15—O6F	2.677(19)	Nd5—O3F	2.595(16)	Nd18—O6F	2.547(16)
		Pr21—O212	2.381(16)			Nd21—O212	2.396(14)
		Pr21—O213	2.404(17)			Nd21—O213	2.363(15)
		Pr21—O214	2.429(15)			Nd21—O214	2.402(13)
		Pr21—O219	2.425(15)			Nd21—O219	2.438(12)
		Pr21—O9T	2.474(15)			Nd21—O4T	2.464(13)
		Pr21—O19	2.616(14)			Nd21—O14	2.621(13)
		Pr21—O3C	2.600(16)			Nd21—O3C	2.576(13)
		Pr21—O7F	2.623(17)			Nd21—O7F	2.591(14)
		Pr25—O225	2.424(17)			Nd28—O238	2.402(15)
		Pr25—O245	2.347(17)			Nd28—O278	2.434(15)
		Pr25—O251	2.510(18)			Nd28—O283	2.461(15)
		Pr25—O256	2.437(18)			Nd28—O289	2.345(14)
		Pr25—O13T ⁱ	2.564(18)			Nd28—O12T ^v	2.477(14)
		Pr25—O57N	2.43(2)			Nd28—O57N ^v	2.382(16)
		Pr25—O8F	2.67(2)			Nd28—O8F	2.550(18)
		Pr25—O9F	2.57(2)			Nd28—O9F	2.653(15)
	Ln1⋯Ln11 ⁱⁱⁱ	4.803(5)		Ln1⋯Ln11 ⁱⁱⁱ	4.796(3)		
	Ln11⋯Ln21	4.833(5)		Ln11⋯Ln21	4.812(4)		
	Ln21⋯Ln1	4.839(4)		Ln21⋯Ln1	4.797(3)		
	<Ln⋯Ln>	4.825		<Ln⋯Ln>	4.802		

[a] Symmetry Codes. i: -x, 2-y, 2-z; ii: -x, 1-y, 2-z; iii: -x, -y, -z; iv: -x, 1-y, 1-z; v: 1-x, -y, 1-z.

Table A3.3. Ln—O bond lengths and Ln...Ln distances in the γ -subunits of **8-Ln** (Ln = Pr, Nd). Note that the different asymmetric units for the two isostructural compounds are centrosymmetrically related.

8-Pr				8-Nd			
$\gamma(3,4)$ -subunits				$\gamma(3,4)$ -subunits			
Pr33–O313	2.422(19)	Pr34–O324	2.453(18)	Nd33–O323	2.429(15)	Nd34–O314	2.38(2)
Pr33–O332	2.359(18)	Pr34–O345	2.455(19)	Nd33–O332	2.421(16)	Nd34–O345	2.430(19)
Pr33–O336	2.46(2)	Pr34–O347	2.387(17)	Nd33–O336	2.490(16)	Nd34–O347	2.425(15)
Pr33–O337	2.403(17)	Pr34–O349	2.431(17)	Nd33–O337	2.335(16)	Nd34–O349	2.360(17)
Pr33–O22T	2.434(16)	Pr34–O6T ⁱⁱ	2.501(15)	Nd33–O7T ^{iv}	2.482(15)	Nd34–O23T	2.433(15)
Pr33–O10F	2.62(2)	Pr34–O3B	2.472(16)	Nd33–O2B	2.465(16)	Nd34–O12F	2.65(2)
Pr33–O11F	2.66(2)	Pr34–O13F	2.59(2)	Nd33–O10F	2.601(17)	Nd34–O13F	2.49(2)
Pr33–O12F	2.52(2)	Pr34–O14F	2.569(19)	Nd33–O11F	2.536(18)	Nd34–O14F	2.617(19)
Pr43–O413	2.49(2)	Pr44–O424	2.39(2)	Nd43–O423	2.364(17)	Nd44–O414	2.409(19)
Pr43–O432	2.42(2)	Pr44–O445	2.45(2)	Nd43–O432	2.379(16)	Nd44–O445	2.452(18)
Pr43–O436	2.45(2)	Pr44–O447	2.40(2)	Nd43–O436	2.427(17)	Nd44–O447	2.331(15)
Pr43–O437	2.398(12)	Pr44–O449	2.41(2)	Nd43–O437	2.390(16)	Nd44–O449	2.396(17)
Pr43–O13B	2.447(19)	Pr44–O3T	2.502(17)	Nd43–O2T	2.431(14)	Nd44–O13B	2.469(16)
Pr43–O15F	2.55(3)	Pr44–O18F	2.60(3)	Nd43–O15F	2.64(2)	Nd44–O18F	2.53(2)
Pr43–O16F	2.62(3)	Pr44–O19F	2.59(4)	Nd43–O16F	2.57(2)	Nd44–O19F	2.422(18)
Pr43–O17F	2.45(3)	Pr44–O20F	2.55(4)	Nd43–O17F	2.53(2)	Nd44–O20F	2.60(2)
Pr53–O513	2.44(2)	Pr54–O524	2.43(3)	Nd53–O523	2.420(15)	Nd54–O514	2.381(17)
Pr53–O532	2.44(2)	Pr54–O545	2.42(2)	Nd53–O532	2.425(15)	Nd54–O545	2.444(18)
Pr53–O536	2.46(2)	Pr54–O547	2.39(2)	Nd53–O536	2.473(18)	Nd54–O547	2.423(15)
Pr53–O537	2.38(2)	Pr54–O549	2.38(2)	Nd53–O537	2.369(15)	Nd54–O549	2.358(19)
Pr53–O22B	2.39(2)	Pr54–O12T ⁱ	2.449(18)	Nd53–O23B ^{iv}	2.458(16)	Nd54–O13T	2.419(14)
Pr53–O21F	2.52(3)	Pr54–O24F	2.45(3)	Nd53–O21F	2.54(2)	Nd54–O24F	2.49(3)
Pr53–O22F	2.50(2)	Pr54–O25F	2.60(2)	Nd53–O22F	2.496(18)	Nd54–O25F	2.587(17)
Pr53–O23F	2.65(3)	Pr54–O26F	2.86(3)	Nd53–O23F	2.62(2)	Nd54–O26F	2.701(2)

[a] *Symmetry Codes*. i: -x, 2-y, 2-z; ii: -x, 1-y, 2-z; iii: -x, -y, -z; iv: -x, 1-y, 1-z; v: : 1-x, -y, 1-z.

APPENDIX 4

Assemblies with mid-to-late lanthanides

Table A4.4. Ln–O bond lengths and Ln⋯Ln distances (Å) in compounds 9-Ln (Ln = Dy to Lu).

	β (1,8) subunit			β (1,5) subunit			
	9-Dy	9-Ho	9-Er	9-Tm	9-Yb	9-Lu	
Ln1–O12	2.282(11)	2.269(10)	2.23(2)	Ln1–O12	2.214(8)	2.197(10)	2.207(10)
Ln1–O13	2.255(10)	2.231(9)	2.220(19)	Ln1–O13	2.263(8)	2.259(10)	2.244(11)
Ln1–O14	2.283(9)	2.292(9)	2.28(2)	Ln1–O14	2.285(8)	2.272(9)	2.277(11)
Ln1–O19	2.312(10)	2.308(9)	2.320(18)	Ln1–O19	2.285(8)	2.272(10)	2.267(10)
Ln1–O238	2.311(10)	2.304(9)	2.276(18)	Ln1–O225	2.292(8)	2.274(10)	2.279(11)
Ln1–O1F	2.378(11)	2.350(11)	2.32(2)	Ln1–O1F	2.313(9)	2.310(12)	2.279(11)
Ln1–O1G1	2.569(11)	2.551(9)	2.515(19)	Ln1–O1G1	2.567(8)	2.550(9)	2.533(10)
Ln1–O1FF	2.576(11)	2.579(10)	2.52(2)	Ln1–O1FF	2.536(9)	2.520(11)	2.505(12)
Ln8–O38	2.287(10)	2.280(9)	2.239(18)	Ln5–O25	2.250(8)	2.253(10)	2.227(10)
Ln8–O78	2.298(11)	2.289(9)	2.25(2)	Ln5–O45	2.222(8)	2.205(10)	2.207(10)
Ln8–O82	2.362(11)	2.340(10)	2.34(2)	Ln5–O51	2.300(8)	2.291(11)	2.281(11)
Ln8–O89	2.241(10)	2.218(9)	2.20(2)	Ln5–O56	2.254(8)	2.247(10)	2.233(10)
Ln8–O219	2.368(10)	2.359(9)	2.37(2)	Ln5–O214	2.323(8)	2.311(10)	2.293(11)
Ln8–O8F	2.380(10)	2.374(9)	2.35(2)	Ln5–O5F	2.347(8)	2.339(10)	2.321(11)
Ln8–O3G1	2.578(10)	2.559(9)	2.51(2)	Ln5–O2G1	2.547(8)	2.522(10)	2.519(10)
Ln8–O2FF	2.585(11)	2.588(10)	2.62(2)	Ln5–O2FF	2.555(8)	2.549(10)	2.545(10)
Ln21–O212	2.315(10)	2.310(10)	2.307(16)	Ln21–O212	2.200(8)	2.184(9)	2.180(11)
Ln21–O213	2.251(10)	2.227(9)	2.15(2)	Ln21–O213	2.293(8)	2.267(10)	2.293(11)
Ln21–O214	2.314(10)	2.311(9)	2.28(2)	Ln21–O214	2.269(8)	2.271(10)	2.258(10)
Ln21–O219	2.297(10)	2.289(9)	2.273(17)	Ln21–O219	2.284(8)	2.278(10)	2.284(10)
Ln21–O38	2.336(10)	2.322(9)	2.29(2)	Ln21–O25	2.302(8)	2.272(10)	2.291(11)
Ln21–O21F	2.368(11)	2.348(10)	2.31(2)	Ln21–O21F	2.330(9)	2.318(11)	2.288(11)
Ln21–O1G2	2.601(10)	2.594(9)	2.52(2)	Ln21–O1G2	2.571(8)	2.553(10)	2.542(10)
Ln21–O2FF	2.697(11)	2.704(10)	2.693(18)	Ln21–O2FF	2.716(8)	2.721(11)	2.728(11)
Ln28–O238	2.289(10)	2.280(9)	2.254(17)	Ln25–O225	2.219(8)	2.224(10)	2.221(10)
Ln28–O278	2.298(12)	2.288(10)	2.275(19)	Ln25–O245	2.218(8)	2.209(10)	2.209(10)
Ln28–O282	2.334(11)	2.333(10)	2.30(2)	Ln25–O251	2.299(9)	2.294(11)	2.297(12)
Ln28–O289	2.245(10)	2.226(9)	2.29(2)	Ln25–O256	2.258(9)	2.258(10)	2.252(11)
Ln28–O19	2.342(10)	2.307(9)	2.282(18)	Ln25–O14	2.323(8)	2.299(10)	2.306(11)
Ln28–O28F	2.356(11)	2.328(10)	2.332(19)	Ln25–O25F	2.316(9)	2.304(11)	2.300(11)
Ln28–O3G2	2.534(10)	2.514(9)	2.509(17)	Ln25–O2G2	2.529(8)	2.517(10)	2.509(10)
Ln28–O1FF	2.694(10)	2.696(9)	2.65(2)	Ln25–O1FF	2.729(8)	2.724(10)	2.719(11)
Ln1⋯Ln28	3.6040(10)	3.5883(9)	3.569(2)	Ln1⋯Ln25	3.5608(7)	3.5540(9)	3.5409(10)
Ln8⋯Ln21	3.6099(10)	3.5988(9)	3.5979(19)	Ln5⋯Ln21	3.5619(7)	3.5615(9)	3.5500(9)
<Ln⋯Ln>	3.6070	3.5936	3.583	<Ln⋯Ln>	3.5614	3.5578	3.5454

Table A4.5. Ln–O bond lengths and Ln⋯Ln distances (Å) in compounds **10-Ln** (Ln = Ho to Lu).^[a]

	<i>β</i> (1,5) subunit				<i>β</i> (1,8) subunit	
	10-Ho	10-Tm	10-Yb	10-Lu		10-Er
Ln1–O12	2.259(11)	2.233(9)	2.221(9)	2.203(8)	Ln1–O12	2.28(3)
Ln1–O13	2.308(11)	2.297(10)	2.292(10)	2.285(9)	Ln1–O13	2.19(3)
Ln1–O14	2.305(11)	2.259(9)	2.269(9)	2.253(9)	Ln1–O14	2.31(3)
Ln1–O19	2.269(13)	2.245(11)	2.245(11)	2.237(10)	Ln1–O19	2.30(3)
Ln1–O214	2.297(11)	2.281(9)	2.281(9)	2.273(8)	Ln1–O219	2.35(2)
Ln1–O29T ⁱ	2.280(12)	2.280(9)	2.289(9)	2.263(9)	Ln1–O24T ⁱⁱ	2.30(3)
Ln1–O1G1	2.564(13)	2.561(10)	2.558(11)	2.545(10)	Ln1–O1G1	2.59(3)
Ln1–O1FF	2.698(12)	2.688(9)	2.681(10)	2.675(9)	Ln1–O1FF	2.59(3)
Ln5–O25	2.269(11)	2.245(9)	2.245(9)	2.231(8)	Ln8–O38	2.29(3)
Ln5–O45	2.237(12)	2.217(10)	2.192(10)	2.179(10)	Ln8–O78	2.29(3)
Ln5–O51	2.291(18)	2.290(13)	2.274(14)	2.274(12)	Ln8–O82	2.31(4)
Ln5–O56	2.274(13)	2.266(11)	2.246(11)	2.244(10)	Ln8–O89	2.23(3)
Ln5–O225	2.344(12)	2.336(9)	2.315(10)	2.323(9)	Ln8–O238	2.34(3)
Ln5–O5F	2.341(13)	2.327(11)	2.328(12)	2.290(11)	Ln8–O8F	2.36(4)
Ln5–O2G1	2.554(12)	2.556(9)	2.539(10)	2.540(9)	Ln8–O3G1	2.55(3)
Ln5–O2FF	2.562(13)	2.574(10)	2.574(11)	2.544(9)	Ln8–O2FF	2.56(3)
Ln21–O212	2.209(12)	2.193(9)	2.178(10)	2.166(9)	Ln21–O212	2.32(3)
Ln21–O213	2.290(11)	2.286(10)	2.278(10)	2.261(9)	Ln21–O213	2.22(3)
Ln21–O214	2.269(11)	2.257(9)	2.242(9)	2.234(8)	Ln21–O214	2.32(3)
Ln21–O219	2.297(12)	2.287(9)	2.274(9)	2.275(8)	Ln21–O219	2.25(2)
Ln21–O14	2.354(12)	2.319(9)	2.318(10)	2.293(9)	Ln21–O19	2.35(3)
Ln21–O21F	2.383(14)	2.355(11)	2.345(11)	2.314(10)	Ln21–O21F	2.39(4)
Ln21–O1G2	2.565(12)	2.557(9)	2.553(9)	2.554(8)	Ln21–O1G2	2.55(3)
Ln21–O1FF	2.505(11)	2.476(9)	2.475(10)	2.465(9)	Ln21–O1FF	2.61(3)
Ln25–O225	2.294(12)	2.250(9)	2.258(9)	2.244(9)	Ln28–O238	2.25(3)
Ln25–O245	2.225(11)	2.223(9)	2.191(9)	2.194(8)	Ln28–O278	2.23(3)
Ln25–O251	2.327(12)	2.306(10)	2.295(10)	2.283(9)	Ln28–O282	2.28(3)
Ln25–O256	2.293(12)	2.261(9)	2.258(10)	2.256(9)	Ln28–O289	2.20(3)
Ln25–O25	2.320(11)	2.304(9)	2.312(9)	2.310(8)	Ln28–O38	2.36(3)
Ln25–O25F	2.303(14)	2.277(11)	2.289(11)	2.256(10)	Ln28–O28F	2.32(3)
Ln25–O2G2	2.534(11)	2.539(9)	2.517(9)	2.515(8)	Ln28–O3G2	2.52(3)
Ln25–O2FF	2.633(13)	2.613(10)	2.602(10)	2.597(9)	Ln28–O2FF	2.72(3)
Ln1⋯Ln21	3.5842(11)	3.5559(8)	3.5446(8)	3.5268(8)	Ln1⋯Ln21	3.589(3)
Ln5⋯Ln25	3.5709(12)	3.5412(9)	3.5368(9)	3.5233(8)	Ln8⋯Ln28	3.562(3)
<Ln⋯Ln>	3.5776	3.5486	3.5407	3.5250	<Ln⋯Ln>	3.576

[a] Symmetry Codes. i: 3–x, 1–y, 2–z; ii: –x, –y, 1–z.

CURRICULUM VITAE

Beñat Artetxe Arretxe

Departamento de Química Inorgánica

Facultad de Ciencia y Tecnología

Universidad del País Vasco/Euskal Herriko Unibertsitatea UPV/EHU

Campus de Leioa, B° Sarriena s/n

48940, Leioa, Spain.

e-mail: benat.artetxe@ehu.es

• **Personal Information:**

Gender: Male

Date of Birth: December 11th, 1986.

Language skills: English, Spanish, Basque (native)

➤ **RESEARCH TOPICS:**

Polyoxometalate Chemistry. Strong background in the synthesis and characterization (single crystal X-ray diffraction, IR, TGA, luminescence measurements, laser light scattering techniques) of inorganic metal clusters and hybrid organic-inorganic compounds based on POMs.

➤ **EDUCATION:**

PhD	University of the Basque Country UPV/EHU (2010-PRESENT)
Thesis title	Systematic Studies on 3d- and 4f-Metal Containing Polyoxometalates Suitable for Organic Derivatization
Advisors	Prof. Juan M. Gutiérrez-Zorrilla (UPV/EHU) Dr. Santiago Reinoso (UPV/EHU)
M.Sc. New Materials	University of the Basque Country UPV/EHU (2009/2010)
B.Sc. Chemistry	University of the Basque Country UPV/EHU (2004-2009)

➤ **AWARDS:**

B.Sc. Chemistry. 1) Extraordinary Award. *UPV/EHU* (2009/2010)

2) National Awards for Excellence in University Academic yield. Special Mention. *Spanish Ministry of Education*. (2009/2010)

M.Sc. New Materials. Best Student. *UPV/EHU* (2009/2010)

➤ **FELLOWSHIPS AND SCHOLARSHIPS:**

1) Recipient of Basque Government Predoctoral Fellowship.

Advisor: Prof. Juan M. Gutiérrez-Zorrilla. 2010-2013

2) Recipient of UPV/EHU collaboration scholarship.

Advisor: Prof. Juan M. Gutiérrez-Zorrilla. 2008/2009

➤ **MEMBERSHIPS:**

- Member of the Spanish Royal Society of Chemistry (RSEQ, N° 5211).

➤ **RESEARCH STAYS ABROAD:**

The University of Akron, Akron, OH, USA. 2013 (Three months)

Topic: The self-assembly of large polyoxometalates in solution.

Advisor: Prof. Tianbo Liu

➤ **SCIENTIFIC PUBLICATIONS:**

- 1) *Cation-Directed Dimeric vs. Tetrameric Assemblies of Lanthanide-Stabilized Dilacunary Keggin Tungstogermanates*. Artetxe, B.; Reinoso, S.; San Felices, L.; Lezama, L.; Gutiérrez-Zorrilla, J. M.; García, J. A.; Galán-Mascarós, J. R.; Haider, A.; Kortz, U.; Vicent, C. *Chem. Eur. J.* **2014**, 12144.
- 2) *Reversible Dehydration in Polyoxometalate-Based Hybrid Compounds: A Study of Single-Crystal to Single-Crystal Transformations in Keggin-Type Germanotungstates Decorated with Copper(II) Complexes of Tetradentate N-Donor Ligands*. Iturraspe, A.; San Felices, L.; Reinoso, S.; Artetxe, B.; Lezama, L.; Gutiérrez-Zorrilla, J. M. *Cryst. Growth Des.* **2014**, 14, 2318.
- 3) *trans-Diaquabis(pyrazine-3-carboxylato- κ^2N,O) cobalt(II) dihydrate*. Artetxe, B.; Reinoso, S.; San Felices, L.; Martín-Caballero, J.; Gutiérrez-Zorrilla, J. M. *Acta Crystallogr.* **2013**, E69, m94.
- 4) *Copper(II) Complexes of Tetradentate Pyridyl Ligands Supported on Keggin Polyoxometalates. Single-Crystal to Single-Crystal Transformations Promoted by Reversible Dehydration Processes*. Iturraspe, A.; Artetxe, B.; Reinoso, S.; San Felices, L.; Vitoria, P.; Lezama, L.; Gutiérrez-Zorrilla, J. M. *Inorg. Chem.* **2013**, 52, 3084.
- 5) *Diaqua bis(1-H-4-imidazolecarboxylate- κ^2N^3,O) cobalt(II)*. Artetxe, B.; San Felices, L.; Pache, A.; Reinoso, S.; Gutiérrez-Zorrilla, J. M. *Acta Crystallogr.* **2013**, E69, m94.
- 6) *Tetrakis(μ^2 -ferrocenecarboxylato- $\kappa^2O:O'$)bis[(methanol- κO)copper(II)] methanol disolvate*. Artetxe, B.; Vitoria, P.; Pache, A.; Reinoso, S.; Gutiérrez-Zorrilla, J. M. *Acta Crystallogr.* **2011**, E67, m1840.

➤ **CONTRIBUTIONS TO MEETINGS:**

- 1) Poster Presentation at *International Polyoxometalate Symposium* (Bremen, Germany, 2009).
- 2) Poster Presentation at *International Symposium on Metal Complexes. XXI Italian- Spanish Congress on Thermodynamics of Metal Complexes*. (Bilbao, Spain, 2010).
- 3) Poster Presentation at *14^a Reunión Científica Plenaria de Química Inorgánica. 8^a Reunión Científica Plenaria de Química de Estado Sólido*. (Cartagena, Spain, 2010).
- 4) Poster Presentation at *XXII Congress and General Assembly of the International Union of Crystallography* (Madrid, Spain, 2011).
- 5) Poster Presentation at *4th EuCheMS Chemistry Congress* (Prague, Czech Republic, 2012).
- 6) Poster Presentation at *15^a Reunión Científica Plenaria de Química Inorgánica. 9^a Reunión Científica Plenaria de Química de Estado Sólido*. (Girona, Spain, 2012).
- 7) Poster Presentation at *XXXIV Reunión Bienal de la Real Sociedad Española de Química*. (Santander, Spain, 2013).
- 8) Oral communication at *IV. Jornadas de Investigación de la Facultad de Ciencia y Tecnología* (Leioa, Spain, 2014).

Polyoxometalates (POMs) are a well-known class of metal-oxo clusters that show a wide range of properties and applications due to their large variety in terms of size, structure and composition. The organic derivatization of POMs has been identified as a key factor for these clusters to be suitably incorporated into different materials. In the first part of this work, systematic studies on the organic functionalization of the Krebs-type $[\{M(H_2O)_3\}_2(WO_2)_2(SbW_9O_{33})_2]^{10-}$ POMs are discussed. As a result, 11 novel hybrid POMs have been synthesized and characterized by elemental and thermal analyses, FT-IR spectroscopy and single-crystal X-ray diffraction. Moreover, their solution behavior has also been studied by 1H -NMR and ESI-MS.

The second part of this dissertation includes the synthesis of new POM clusters with accessible 3d- and 4f-metal centers suitable for further organic derivatization. In a first stage, the preparation of four series of 4f-metal containing assemblies is reported, whereas the heterometallic 3d-4f clusters obtained from the reaction of Krebs-type POMs with lanthanides are described later on. The 28 novel POMs have also been characterized by elemental and thermal analyses, FT-IR spectroscopy and single-crystal X-ray diffraction. Some interesting properties of these clusters, such as photoluminescence or magnetism have also been analyzed. The solution behavior has been studied by a combination of ESI-MS experiments and ^{183}W -NMR spectroscopy. Furthermore, the gigantic and highly charged polyoxotungstates obtained in this section have shown the ability to self-assemble in solution into hollow, single-layered and vesicle-like blackberry-type structures. The formation of the blackberries has been monitored by laser light scattering techniques (DLS and SLS).

